The University of Sheffield

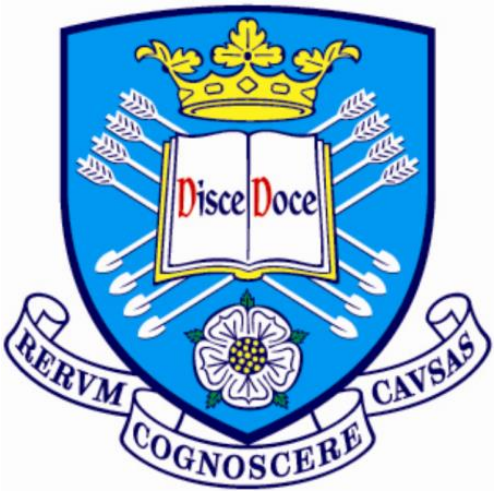

Novel Stator Permanent Magnet and DC Field Excited Synchronous Machines

Juntao Shi

A thesis submitted for the degree of Doctor of Philosophy

Department of Electronic and Electrical Engineering

The University of Sheffield

Mappin Street, Sheffield, S1 3JD, UK

March 2016

ABSTRACT

This thesis investigates the electromagnetic performance of novel stator permanent magnet (PM) and DC field excited synchronous machines which are evolved from the variable flux reluctance machines (VFRMs). All theoretical analyses are carried out by the finite element method and validated by experiments.

The influence of stator and rotor pole arcs on electromagnetic torque of VFRMs having different stator and rotor pole combinations is firstly investigated. It is found that the optimal rotor pole arc to rotor pole pitch ratio is ~1/3, while the optimal stator pole arc is equal to or slightly smaller than the optimum rotor pole arc. Then, by introducing the multi-tooth structure, novel multi-tooth VFRM is proposed and investigated, which exhibits more sinusoidal phase back-EMF, lower torque ripple and higher torque density at relatively low copper loss when compared with the optimized single-tooth VFRM.

A novel biased flux PM machine (BFPMM) is also proposed and investigated. The influence of PM locations in the stator, i.e. in stator yoke, in the stator pole, and on stator pole surface, is analysed and the result shows that maximum torque density is achieved when the PMs located in the stator yoke. Furthermore, various flux focusing configurations are employed in BFPMM to further enhance the torque density and PM utilization efficiency.

Similar to other stator PM synchronous machines, the confliction among the slot area, PMs and stator irons also exists in BFPMM and limits the possibility of further enhancing the torque density. As an effective solution, the partitioned stator configuration, which fully utilizes the inner space, is introduced in BFPMM as novel partitioned stator BFPMM (PS-BFPMM). It shows that the torque density is enhanced significantly without scarifying the PM utilization efficiency. Meanwhile, two PM stator configurations, i.e. SPM stator and Spoke-IPM stator, are proposed and investigated. It is found that PS-BFPMM with Spoke-IPM stator exhibits larger torque density while PS-BFPMM with SPM stator has higher PM utilization efficiency. For partitioned stator PM synchronous machines, since the PMs and armature windings are separately located in the inner and outer stators, the ratio of inner/outer stator poles (N_{is}/N_{os}) and the relative position of inner/outer stators are free and their influences on electromagnetic performance are investigated and compared based on Spoke-IPM stator configuration and minimum 6-pole inner and outer stators. The conditions to obtain the bipolar symmetrical phase flux-linkage and phase back-EMFs as well as maximum torque are derived for different N_{is}/N_{os}.

ACKNOWLEDGEMENTS

Foremost, I would like to express my sincere gratitude to my supervisor, Professor Zi-Qiang Zhu, for his continuous encouragement and support during my Ph.D. study. His invaluable advice and guidance on my research will also be preciously important to me for the rest of my life.

I would also like to thank all my fellows of Electrical Machines and Drives Group at The University of Sheffield for their help and inspired discussions. Particularly, I would like to express my thanks to Mr. John Ash Wilkinson for his assistance in building the prototype machines.

Finally, I would like to thank my parents for their love, financial supports and encouragements to conquer all challenges in my Ph.D. study.

CONTENTS

NOMENCLATURE

F	Magnetic motive force (A)
GCD	Greatest common divisor
I_a	Armature current (A)
I_{arms}	Phase current in RMS (A)
I_d	D-axis current (A)
I_f	DC field current (A)
I_q	Q-axis current (A)
K_d	Distribution factor
K_{dp}	Winding factor
K_p	Pitch factor
L_{aa}	Active axial length (mm)
L_{ag}	Length of air-gap (mm)
m	Number of phases
n	Number of small teeth per stator pole
n'	Ratio of inner stator pole number to outer stator pole number
N_a	Number of turns per phase for armature winding
N_c	Number of cogging torque cycles over one electric period
N_{is}	Number of inner stator poles
N_f	Number of turns per phase for DC field winding
N_{os}	Number of outer stator poles
N_p	Number of turns per phase
N_{pp}	Spatial span number of stator pole pitch between the two coils
N_r	Number of rotor poles
N_{rb}	Order of rotor poles
N_s	Number of stator poles
N_{sa}	Order of stator poles
N_{sscs}	Number of stator structure cyclic symmetry
p_a	Armature copper loss (W)
p_c	Copper loss (W)
p_f	Excitation copper loss (W)

P_0	Average air-gap permeance (Wb/A)
P_{Nsa}	Permeance between a stator pole N_{sa} and the complete rotor (Wb/A)
P_{sp}	Permeance between a single stator tooth and the complete rotor (Wb/A)
P_v	Permeance of v^{th} harmonic (Wb/A)
R_{isi}	Inner radius of inner stator (mm)
R_{iso}	Outer radius of inner stator (mm)
R_{osi}	Inner radius of outer stator (mm)
R_{oso}	Outer radius of outer stator (mm)
T	Electromagnetic torque (Nm)
T_{bri}	Thickness of lamination bridge
T_{ostto}	Thickness of outer stator tooth tip (slot opening) (mm)
T_{osttb}	Thickness of outer stator tooth tip (tooth body) (mm)
T_{osy}	Thickness of outer stator yoke (mm)
T_{PM}	Minimum thickness of PM (mm)
T_{rr}	Radial thickness of rotor (mm)
W_{rp}	Rotor pole width (mm)
W_{so}	Slot opening width (mm)
W_{sp}	Stator pole width (mm)
α_0	Initial angles of the phase current (°)
α_e	Electrical degree between two adjacent coil-EMF vectors (°)
α_m	Mechanical degree between two adjacent coil-EMF vectors (°)
θ	Rotor position (°)
θ_0	Initial rotor position (°)
θ_d	Angular phase difference between two coils belong to the same phase (°)
θ_{osr}	Relative position difference between the middle of one stator pole and one rotor pole referred to the aligned position (°)
θ_{ostb}	Pole arc of outer stator tooth body (°)
θ_{ostt}	Pole arc of outer stator tooth tip (°)
θ_{PM}	PM inner pole arc (°)
θ_{rop}	Rotor outer pole arc (°)
θ_{rip}	Rotor inner pole arc (°)
θ_{sr}	Position difference between the middle of the single stator tooth and rotor

	pole referred to the aligned position (°)
θ_{srki}	Position difference between the middle of i^{th} small stator tooth and the rotor pole referred to the aligned position (°)
ω	Rotor angular speed (rad/s)
σ	Leakage flux factor
Φ	Flux per phase(Wb)
ψ^{a}_{arm}	Armature reaction flux-linkage(Wb)
ψ_{DC}	DC field flux-linkage (Wb)
ψ^{a}_{PM}	PM flux-linkage (Wb)

BFPMMs	Biased flux permanent magnet machines
DSDSMs	Doubly fed doubly salient machines
DSPMMs	Doubly salient permanent magnet machines
FRPMMs	Flux reversal permanent magnet machines
MT-VFRMs	Multi-tooth variable flux reluctance machines
PS-BFPMMs	Partitioned stator biased flux permanent magnet machines
PS-SFPMMs	Partitioned stator switched flux permanent magnet machines
SFPMMs	Switched flux permanent magnet machines
VFRMs	Variable flux reluctance machines
WFSFMs	Wound field switched flux machines

CHAPTER 1
GENERAL INTRODUCTION

1.1 Introduction

With the development of high energy permanent magnet (PM) materials, improvement of power electronics and modern control theories, PM machines have been investigated extensively over the last four decades [JAH86] [BIA06a] [ZHU07] [ELR10]. Due to the inherent merits of high torque and power densities, as well as high efficiency, PM machines have been popular for various applications, such as automotive, renewable energy, industrial and domestic appliance [ZHU07] [LI08] [ELR11] [CAO12]. However, the rare earth PM materials are monopolized by few countries and the price have been increasing significantly in the last decade due to the tighter global supplies which are caused by the reducing export quotas of these resources [KOM12] [HUR10] [LEV10]. Therefore, it becomes increasingly attraction to consider less or no rare earth PM machines, although their torque/power density and efficiency are lower than PM machines. Conventional machines, including induction machine (IMs), switched reluctance machines (SRMs) and wound field synchronous machines (WFSMs) are currently being re-examined for various applications, particularly for wind power generation, domestic appliance, and so on [ZHU15]. Overall, the trade-off between electrical machine performance and cost is one of the key factors which should be considered in the design for applications with different performance indexes. Hence, investigation and development of novel machine topologies are important and can provide more options for different application requirements.

This thesis investigates the electromagnetic performance of both novel stator PM and DC field excited synchronous machines which are evolved from the variable flux reluctance machines (VFRMs).

1.2 Synchronous Machines with Alternate Excitation Sources

Synchronous machines with alternate excitation sources can be classified into four categories according to the locations and types of excitation sources, i.e. rotor DC field excited synchronous machines, rotor PM synchronous machines, stator DC field excited synchronous machines and stator PM synchronous machines, as shown in Fig. 1.1. The development of synchronous machines with alternate excitation sources will be reviewed in the following sub-sections, particularly for stator DC field excited synchronous machines and

stator PM synchronous machines.

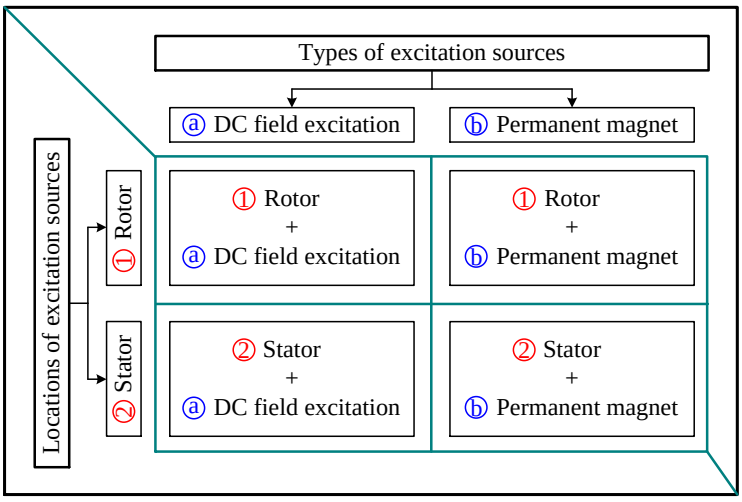

Fig. 1.1. Synchronous machines with alternate excitation sources.

1.2.1 Rotor DC Field Excited Synchronous Machines

Rotor DC field excited synchronous machines are widely used as generators in power generation system, such as steam turbine generators, hydroelectric generators and wind turbine generators [KOM12] [POL06a] [LI08]. The electrical energy generated by rotor DC field excited synchronous machines occupies the majority of electricity market [KOM12] [BOL06]. Meanwhile, rotor DC field synchronous machines can also be used for driving applications, such as steel mills, pumps, ship propulsion and electric vehicles [KOM12] [LIU12a] [ROS06]. Moreover, with the development of high-temperature superconducting (HTS) materials, rotor DC field excited synchronous machines also become the major research objects in HTS applications since they will offer several prominent advantages such as machine size reduction and life-cycle cost reduction [SCH08] [QU13].

Conventional distributed overlapping armature windings are usually employed in rotor DC field excited synchronous machines, as shown in Fig. 1.2. For the rotor structure, there are two types: non-salient pole rotor and salient pole rotor. Generally, non-salient pole rotor is used for high speed and large power applications with a small number of poles ($2p < 4$), such as steam turbine generators, while salient pole rotor is made for low speed and small to mid-size power applications with a large number of poles ($2p > 4$), such as hydroelectric generators [KOM12].

There are three independent control variables in rotor DC field excited synchronous machines, i.e. *d*-axis armature current, *q*-axis armature current and DC excitation current. By appropriately coordinating these three independent control variables, a near unity power

factor can be achieved. Meanwhile, the flux weakening performance is also excellent since the excitation field is adjustable. However, the efficiency will be limited by the existing excitation loss, and the reliability is also influenced by the lifetime of brushes/slip rings.

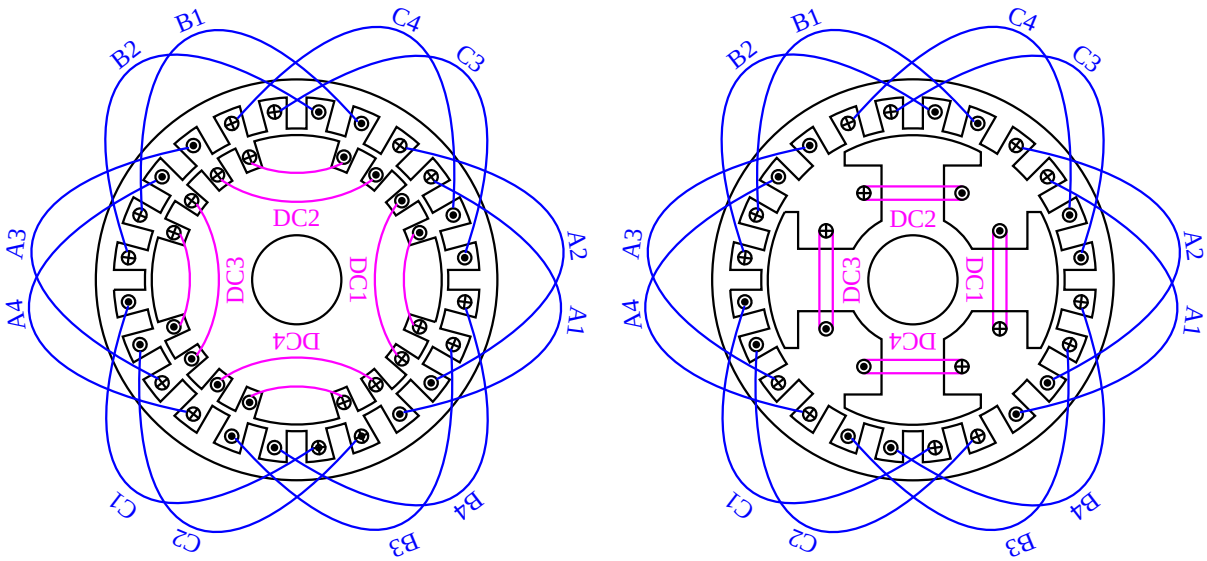

(a) Non-salient pole (b) Salient pole

Fig. 1.2. Topologies of rotor DC field synchronous machines.

1.2.2 Rotor PM Synchronous Machines

Due to the merits of high torque/power densities and high efficiency, rotor PM synchronous machines have been extensively used for various applications, such as aerospace, automotive and domestic appliance [ZHU07] [LI08] [ELR11]. Different from rotor DC field excited synchronous machines, the magnetic fields in rotor PM synchronous machines are established by PMs without energy consumption.

According to the number of slots per pole per phase q, rotor PM synchronous machines can be classified into integer slot machines (q equals an integer, i.e. q = 2) and fractional slot machines (q equals a fraction, i.e. q = 1/2), as shown in Fig. 1.3 (a) and (b). To maximize the flux linkage (torque performance), the coil-pitch is desirable to close the pole-pitch as much as possible [ZHU11a]. Therefore, the slot and pole numbers differed by one ($N_s = 2p \pm 1$) should be the optimal selection, as shown in Fig. 1.3(c). However, unbalanced magnetic forces (UMF) exist in fractional slot machines with $N_s = 2p \pm 1$. Hence, the most appropriate slot and pole numbers for fractional slot machine are related by $N_s = 2p \pm 2$ [BIA06a] [ZHU11a], as shown in Fig. 1.3(d). Compared with conventional integer slot machines, fractional slot machines with $N_s = 2p \pm 1$ and $N_s = 2p \pm 2$ exhibits lower copper loss, higher

torque density and efficiency due to short end windings. Meanwhile, due to the larger smallest common multiple of slot and pole numbers, they also have lower cogging torque and torque ripple [ZHU00].

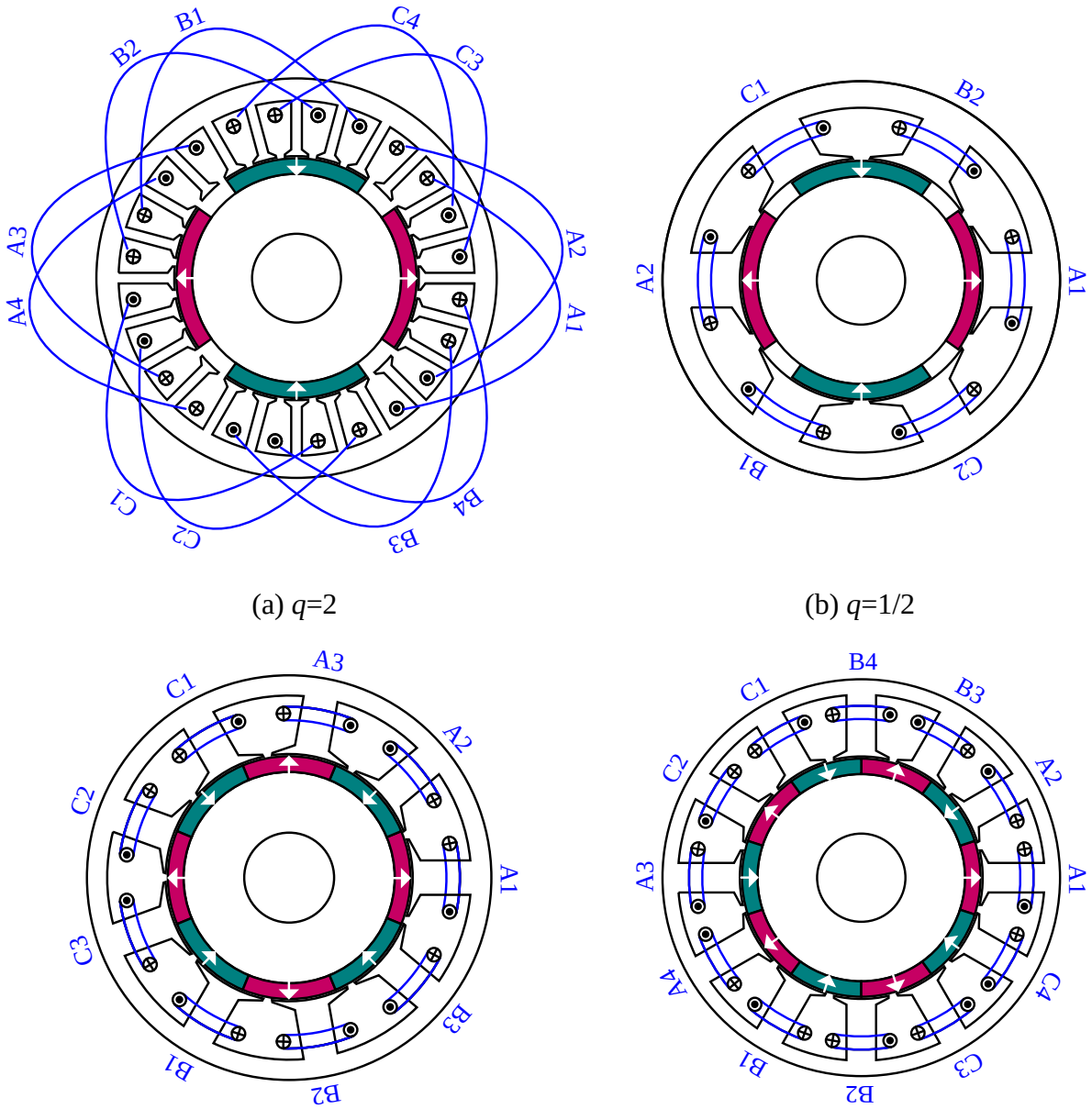

(a) q=2 (b) q=1/2

(c) N_s=$2p$±1 (d) N_s=$2p$±2

Fig. 1.3. Typical slot/pole number combinations of rotor PM synchronous machines.

According to the placement of PMs in the rotor, the rotor topologies could be classified into four basic configurations: surface-mounted rotor, interior-radial rotor, surface-inset rotor and interior-circumferential rotor, as shown in Fig. 1.4. For the surface-mounted PM (SPM) machines, due to the large equivalent air-gap (including PMs), the armature reaction field is relatively small while the d-axis and q-axis inductances are also comparatively low. Due to

the similar flux paths for *d*-axis and *q*-axis armature fluxes, the inductances of *d*-axis and *q*-axis are almost the same. Consequently, the reluctance torque is negligible. Meanwhile, since the PMs are directly exposed to the armature reaction field, the capability of demagnetization withstanding is also relatively low. For the interior PM (IPM) machines with radially magnetized direction, the *q*-axis inductance is larger than the *d*-axis inductance since the iron parts which are close to the air-gap offer extra *q*-axis flux paths for armature reaction. Therefore, the saliency ratio will increase the reluctance torque and improve the flux-weakening performance. Since the PMs are buried inside the rotor iron, the leakage flux in IPM machines is significantly larger than that in SPM machines. However, the capability of demagnetization withstanding is improved since the PMs are effectively shielded from demagnetization armature reaction field [ZHU07]. Moreover, the rotor mechanical structure of IPM machines is more robust than that of SPM machines. As a compromise between SPM machines and IPM machines, the surface-inset PM machines are proposed. As shown in Fig. 1.4(c), the surface-inset rotor removes the iron region above the PMs but retains the iron region between adjacent PMs. Similar to IPM machines, the reluctance torque also exists in surface-inset PM machines since the *q*-axis inductance is larger than the *d*-axis inductance. Furthermore, protected sleeves are also required in surface-inset machines for high speed application, which is similar to SPM machines. The interior PM machines with circumferential magnetized direction (Spoke-IPM machines) can be considered as one special type of IPM machines. The air-gap flux density can be increased by flux focusing (airgap field may become higher than the magnet remanence), and thus high torque density is achieved. Due to flux focusing and large inner space for PMs in the Spoke-IPM machines, low energy PMs with low cost, such as ferrite magnets, can be employed [ZHU07].

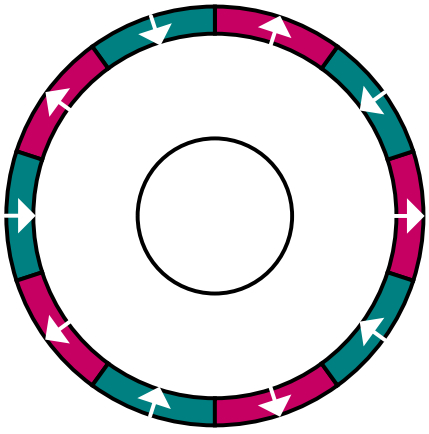

(a) Surface-mounted (SPM)

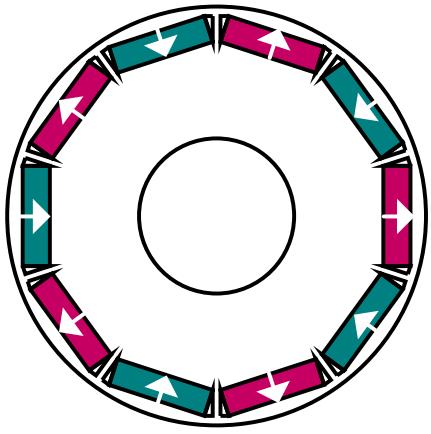

(b) Interior-radial (IPM)

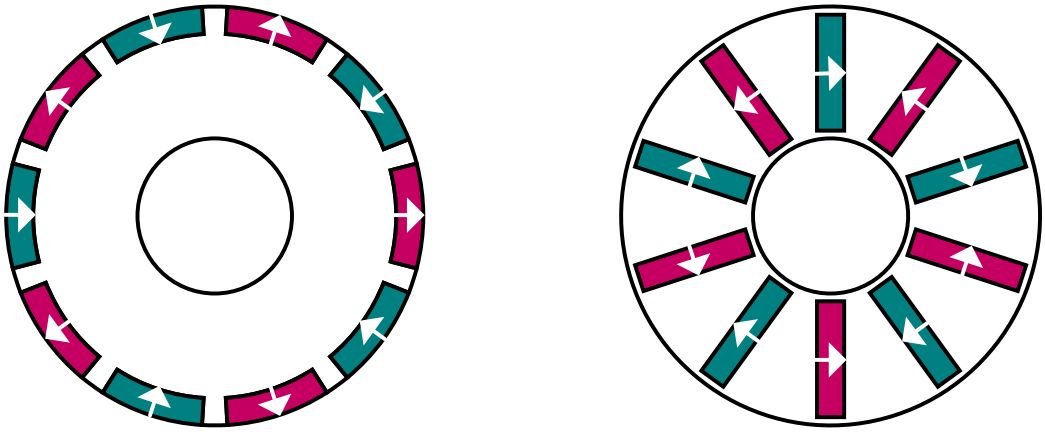

(c) Surface-inset (d) Interior-circumferential (Spoke-IPM)

Fig. 1.4. Typical rotor topologies of rotor PM synchronous machines.

1.2.3 Stator DC Field Excited Synchronous Machines

Stator DC field excited synchronous machines are one type of special synchronous machines, where the DC field winding and AC armature windings are both located in the stator [LI93] [POL99] [CHE10a] [ZHU10] [LIU12a] [FUK12] [ZHO13a]. Meanwhile, simple and robust salient pole rotor without any coils or PMs is employed. Therefore, the slip-rings/brushes, which are usually required in the conventional rotor DC field excited synchronous machine, are eliminated in stator DC field excited synchronous machines. Consequently, potential high reliability and low maintenance cost can be expected. Moreover, since all excitation sources are located in the stator, the heat can be easily dissipated from the stator iron and housing. Thus, better thermal management can be achieved in stator DC field excited synchronous machine when compared with rotor DC field excited synchronous machine. Moreover, the flux weakening capability of stator DC field excited synchronous machines is similar to that of rotor DC field excited synchronous machine since the air-gap flux density can also be adjusted.

With long-term development and in-depth research, various machine topologies have been proposed, which have been reviewed in [ZHU15]. Reference [ZHU15] also presents one concept that all three-phase stator DC field excited synchronous machine topologies can be summarized by a 3 × 3 matrix according to the coil-pitches of DC field and armature windings. In the following sub-sections, doubly fed doubly salient machines (DFDSMs), wound field switched flux machines (WFSFMs) and variable flux reluctance machines (VFRMs) will be reviewed as three special representatives of stator DC field synchronous

machines which have the unipolar/unipolar, bipolar/bipolar and unipolar/bipolar coil/phase flux-linkage waveforms.

1.2.3.1 Doubly Fed Doubly Salient Machines

Doubly fed doubly salient machines (DFDSMs) were firstly introduced in [LI93], in which full coil-pitched DC field windings and concentrated armature windings are located in the stator, as shown in Fig. 1.5. The coil/phase flux-linkage waveforms are unipolar while the coil/phase back-EMF waveforms are close to trapezoidal [LI95] [FAN08]. Therefore, DFDSM is more suitable for brushless DC (BLDC) operation. Since the flux paths for each phase in the stator are not identical, unbalance exists between different phases of DFDSMs, particularly under heavy magnetic saturation [LIU13]. It also leads to the large cogging torque and high torque ripple. Moreover, due to the unipolar coil/phase flux-linkages, the torque density of DFDSMs is relatively poor compared to that of the wound field switched flux machines (WFSFMs) which have bipolar coil/phase flux-linkages [ZHU07]. In order to enhance the torque density, unequal-slot stator structure can be employed in DFDSMs since some slots contain both DC field winding and armature winding while some slots contain armature windings only (a trade-off is required between DC field current and armature current under the same total copper loss) [KON05]. Reference [KON05] also points out that rotor skewing can effectively improve the back-EMF waveforms to be sinusoidal, which means DFSDMs are also suitable for brushless AC (BLAC) operation.

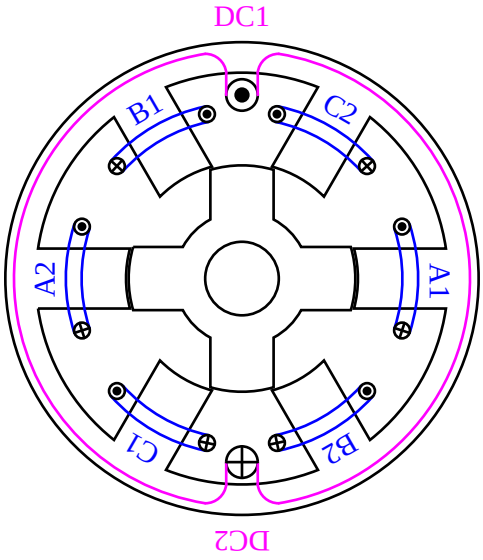

Fig. 1.5. Machine topology of DFDSMs, field coil-pitch=3 slot-pitches, armature coil-pitch=1 slot-pitches.

1.2.3.2 Wound Field Switched Flux Machines

Wound field switched flux machines (WFSFMs) were firstly introduced in [POL99] as a single phase machines in which fully pitched DC field windings and armature windings are both located in the stator. However, the single-phase WFSFMs have the problems of low starting torque, large torque ripple and fixed rotating direction [POL99] [POL03] [POL06a]. To solve these problems, three-phase WFSFMs were proposed and investigated in [CHE10a] based on the same operation principle. Since the field coil-pitch and the armature coil-pitch are both equal to 2 slot-pitches as shown in Fig. 1.6(a), this type WFSFMs can be designated as F2A2 WFSFMs. The stator and rotor pole combinations of F2A2 WFSFMs are more flexible than those of DFDSMs, in which the rotor pole number can be any integers except the phase number and its multiples. Different from the DFDSMs with unipolar coil flux-linkage, the coil flux-linkage of F2A2 WFSFMs is bipolar, which means higher torque density can be expected in F2A2 WFSFPMs. Moreover, due to the existing even harmonics, the coil flux-linkage and coil back-EMFs waveforms of F2A2 WFSFMs are asymmetric. To obtain the symmetrical bipolar phase flux-linkage and sinusoidal phase back-EMF waveforms, two conditions should be satisfied [CHE08]. Firstly, the coil number per phase must be even. Secondly, the pair of coils belong to same phase must have 180 electrical degrees phase shifting (opposite induced polarities). In other word, the ratio of stator pole number to the greatest common divisor (GCD) of stator- and rotor-pole numbers should be even integers.

Fig. 1.6(b) shows a WFSFM with the field coil-pitch and the armature coil-pitch equal to 1 and 3 slot-pitches respectively, which can be designated as F1A3 WFSFM [ZHO13a]. Similar to F2A2 WFSFMs, F1A3 WFSFMs also have the flexible stator/rotor pole combinations and bipolar coil flux-linkage as well as the same conditions for symmetrical bipolar phase flux-linkage and sinusoidal phase back-EMF waveforms. According to the analyses shown in [CHE10a] and [ZHO13a], for both 24-solt/10-pole F2A2 WFSFM and 18-slot/10-pole F1A3 WFSFM as shown in Fig. 1.6 (a) and (b) respectively, the torque densities are limited by the high flux leakage between adjacent stator teeth and severe magnetic saturation in the stator tooth. Therefore, higher torque density can be expected by halving the numbers of stator slots and rotor poles. The results show that the torque densities are increased by 30.9% and 20.7% respectively in the 12-slot/5-pole FA2A WFSFM and the 9-slot/5-pole F1A3 WFSFM when compared with the original 24-slot/10-pole FA2A WFSFM and 18-slot/10-pole F1A3 WFSFM under the same machine size and the same current density

of 20 A/mm^2 [ZHO13a]. Further, compared with the optimal 12-slot/7-pole F2A2 WFSFM under same copper loss, the 9-slot/5-pole F1A3 WFSFM has similar average torque but large torque ripple [ZHO13a].

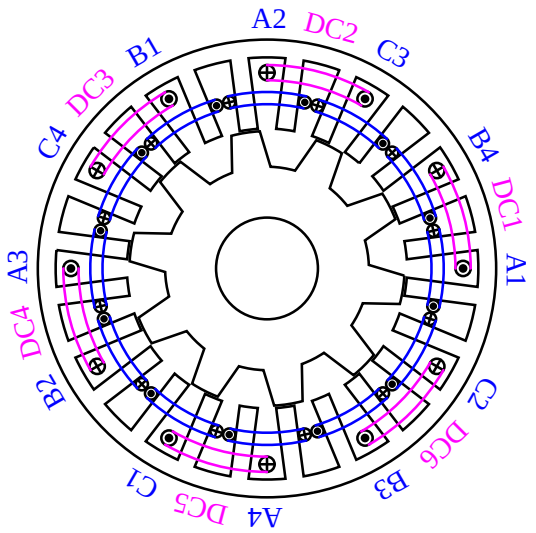

(a) F2A2 WFSFM, field coil-pitch=2 slot-pitches, armature coil-pitch=2 slot-pitches

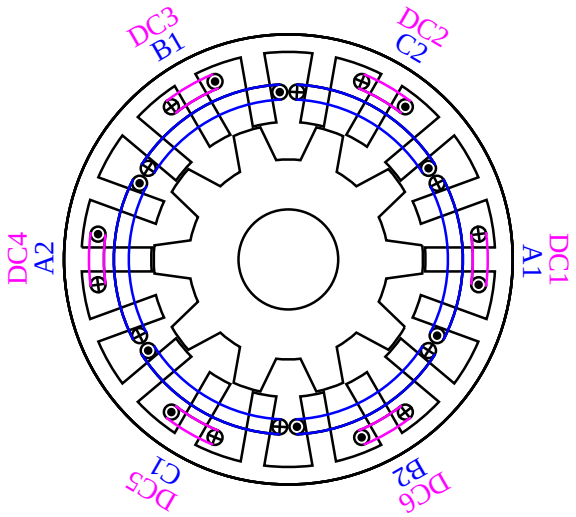

(b) F1A3 WFSFPM, field coil-pitch=1 slot-pitches, armature coil-pitch=3 slot-pitches

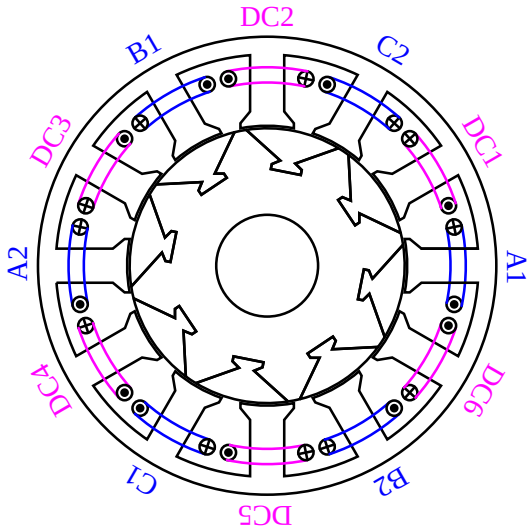

(c) F1A1 WFSFM with segment rotor, field coil-pitch=1 slot-pitches, armature coil-pitch=1 slot-pitches

Fig. 1.6. Machine topologies of WFSFMs.

A segment rotor WFSFM with concentrated DC field and armature windings was proposed in [ZUL10], as shown in Fig. 1.6(c). The DC field coils and armature coils are wound around the stator pole alternately. Therefore, this type machine can be designated as F1A1 WFSFM. According to the analyses shown in [ZUL10] [ZUL12a], the optimal rotor pole number for

12-slots F1A1 WFSFMs is 8 since the maximum average torque is achieved. However, asymmetric phase back-EMF and consequently high torque ripple are observed in the 12-slot/8-pole F1A1 WFSFM. Moreover, the torque density of F1A1 WFSFMs is relatively lower when compared with the F2A2 WFSFMs and the F1A3 WFSFMs [ZOU13a]

1.2.3.3 Variable Flux Reluctance Machines

Variable flux reluctance machines (VFRMs) were firstly introduced in [LIU12b] [FUK12] and have been systematically investigated in [LIU12c] [LIU12d] [LIU113] [LIU14] [AZA14]. As shown in Fig. 1.7, doubly salient stator and rotor structure with concentrated stator AC armature and DC field windings are adopted in VFRMs. Similar to the WFSFMs, the stator and rotor pole combinations of VFRMs remarkably exceed those in switched reluctance machines (SRMs) and DFDSMs, and the rotor pole number can be any integers except the phase number and its multiples [LIU12c]. Although the coil flux-linkage is unipolar and the coil back-EMF is asymmetric, symmetrical bipolar phase flux-linkage and sinusoidal phase back-EMF can be obtained in VFRMs by using specific stator/rotor pole combinations (such as 6/5, 6/7, 12/10, 12/11, 12/13 and 12/14 etc) since all the even order harmonics in a single coil are cancelled completely in the phase winding (the same conditions as required in WFSFMs as mentioned in section 1.2.3.2) [LIU12c] [LIU12d]. It means that VFRMs are suitable for BLAC operation. Moreover, reference [LIU13] also indicates that VFRMs exhibit larger torque density and lower torque ripple than DFDSMs under the same machine size and same coper loss.

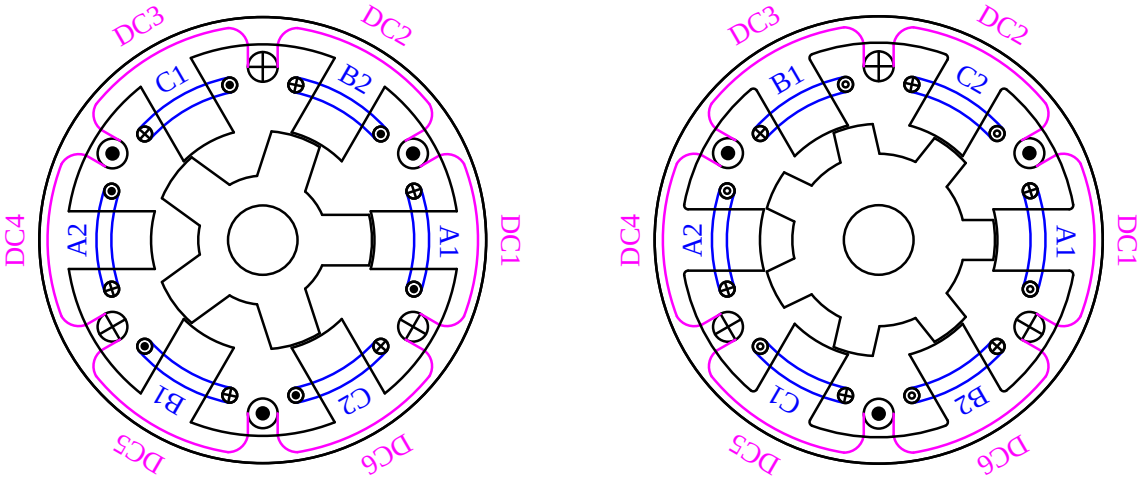

(a) 6S/5R VFRM (b) 6S/7R VFRM

Fig. 1.7. Machine topologies of VFRMs, field coil-pitch=1 slot-pitches, armature coil-pitch=1 slot-pitches.

1.2.4 Stator PM Synchronous Machines

PM synchronous machines having PMs located on the stator, nominated as stator PM synchronous machines, have been developed in the last decades [LIA95] [HOA97] [DEO97] [ZHU05] [ZHU07] [ZHU10] [CHE11c]. When the PMs are located in the stator, the rotor of stator PM synchronous machines usually have salient rotor pole geometry, similar to that of an SRM, which is simple and robust as well as suitable for high-speed operation [ZHU07]. The position of PM in the stator is flexible, which can be mounded in the stator yoke, placed on the inner surface of the stator teeth, or sandwiched in the stator teeth. However, irrespective of the PM locations, the armature windings in the stator are always non-overlapping and concentrated. Although the torque production mechanism for all stator PM synchronous machines is relied on the rotor saliency, the reluctance torque is negligible, which means that the torque of stator PM synchronous machines is predominantly generated by PM flux [ZHU07] [ZHU11b]. Moreover, since the heat can be easily dissipated from the stator iron and housing, effective management of magnet temperature rise can be achieved in stator PM synchronous machines. Consequently, the risk of demagnetization is reduced significantly [ZHU07] [ZHU10].

Basically, there are three types of stator PM synchronous machines, namely, doubly salient PM machines (DSPMMs) [LIA95], flux-reversal PM machines (FRPMMs) [DEO97] [WAN99] and switched flux PM machines (SFPMMs) [RAU55] [HOA97]. In the following sub-sections, these three machines will be reviewed separately.

1.2.4.1 Doubly Salient PM Machines

Doubly salient PM machines (DSPMMs) were firstly introduced in [LIA92], in which the PMs are located in the stator yoke at an interval of pole number equal to phase number and the concentrated windings are employed, as shown in Fig. 1.8. As the rotor rotates, the variation of the flux-linkage with each coil is unipolar, while the back-EMF waveform trends to be trapezoidal [LIA95] [ZHU07]. Thus, DSPMMs are more suitable for BLDC operation mode. However, the rotor-skewing method [LUO96] [CHE03] can be used to obtain a more sinusoidal back-EMF waveform. Consequently, DSPMMs can also be operated in BLAC mode. Due to the asymmetric flux paths in the stator, the flux-linkage and back-EMF waveforms for each phase are unbalanced, particularly under heavy magnetic saturation. Moreover, due to the unipolar flux-linkage, the torque density of DSPMMs is relatively poor compared to that of other PM synchronous machines [HUA05] [ZHU07]. In order to enhance

the toque density, various flux-focusing techniques are proposed and employed in DSPMMs [LIA95][LUO96] [CHE03].

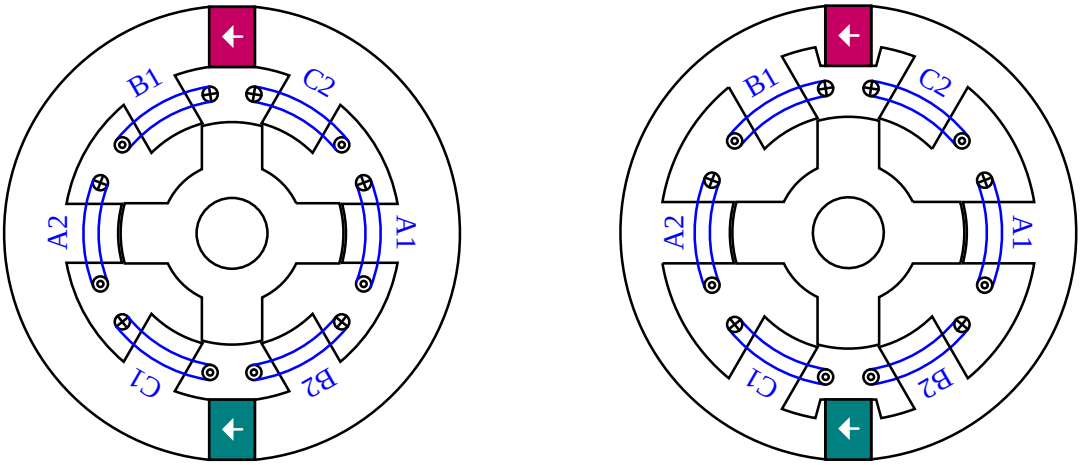

(a) (b)

Fig. 1.8. Machine topologies of DSPMMs.

1.2.4.2 Flux Reversal PM Machines

Flux reversal PM machines (FRPMMs) were firstly introduced in [DEO96], in which one or more pairs of PMs with alternate polarities are mounted on the surface of each stator tooth and the concentrated windings are employed, as shown in Fig. 1.9. When a coil is excited, the air-gap field under one PM is increased while that under the other PM (belong to the same stator pole) is reduced, and the salient rotor pole will rotate towards to the stronger magnetic field [ZHU07]. The coil and phase flux-linkage waveforms are both bipolar, while the coil and phase back-EMF waveforms are essentially trapezoidal. Therefore, the rotor-skewing method can also be used to improve the phase back-EMF to be more sinusoidal. Moreover, good fault-tolerance capability can be obtained in FRPMMs due to its natural isolation between the phases in a multi-phase configuration [DEO96]. Since the fluxes produced by PMs and the coils are in series, the PMs are more vulnerable to partial irreversible demagnetization. Meanwhile, significant eddy-current loss and large radial magnetic force will be observed in the PMs since they are directly exposed to the reluctance variation of the salient rotor poles [DOR03] [ZHU11b]. Compared with DSPMMs, FRPMMs exhibit higher torque density due to the bipolar phase flux-linkage [ZHA09].

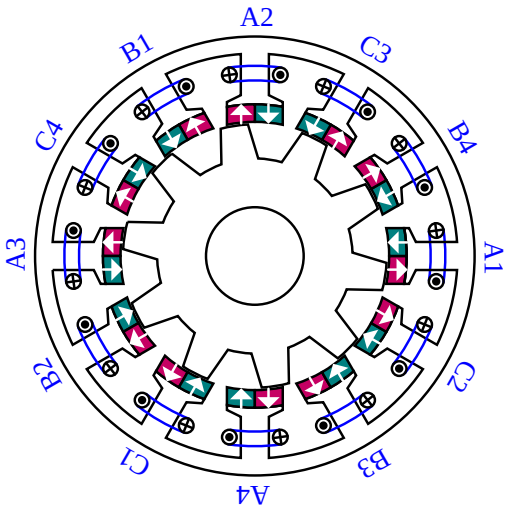

Fig. 1.9. Machine topology of FRPMM.

1.2.4.3 Switched Flux PM Machines

Switched flux PM machines [SFPMMs] were firstly introduced in [RAU55] as one of high frequency inductor generators which employs the switched flux principle. Then, extensive investigations were carried out in the field of polyphase SFPMMs, particularly for three phase SFPMMs [HOA97] [ZHU05] [FEI06] [ZHU08a] [CHE08] [CHE11a] [CHE11b] [ZUL12b]. Fig. 1.10(a) shows the typical three-phase SFPMMs with PMs sandwiched in the stator teeth. The stator consists of modular U-shaped laminated segments between which are placed circumferentially magnetized PMs alternatively with opposite polarity. The concentrated coils is wound around the stator pole comprises two adjacent laminated segments and a PM. Since the fluxes produced by PMs and the coils are in parallel, the influence of the armature reaction field on the working point of the PMs is minimal [ZHU07]. Consequently, the electric loading of SFPMMs can be every high. The polarity of the flux-linkage in the coil reverses when the rotor pole rotates from one stator tooth to another stator tooth belong to the same stator pole. Thus, bipolar phase flux-linkage is obtained in SFPMMs. Moreover, the back-EMF waveform of SFPMMs is essentially sinusoidal, which makes them suitable for BLAC operation. In addition, due to the utilisation of flux focusing and bipolar phase flux-linkage as well as sinusoidal phase back-EMF, SFPMMs exhibit significantly higher torque density and lower torque ripple when compared with DSPMMs and FRPMMs [ZHA09].

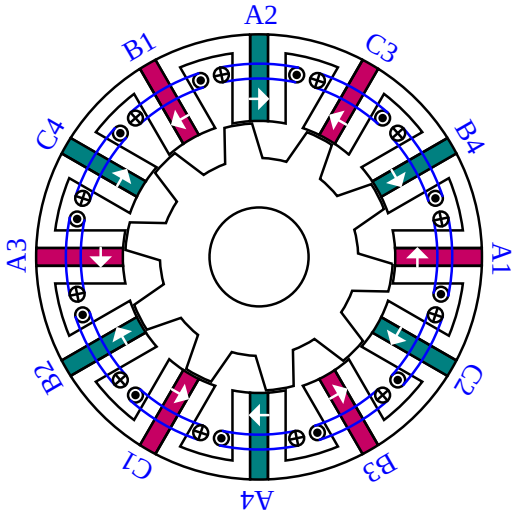

(a) Conventional SFPMM

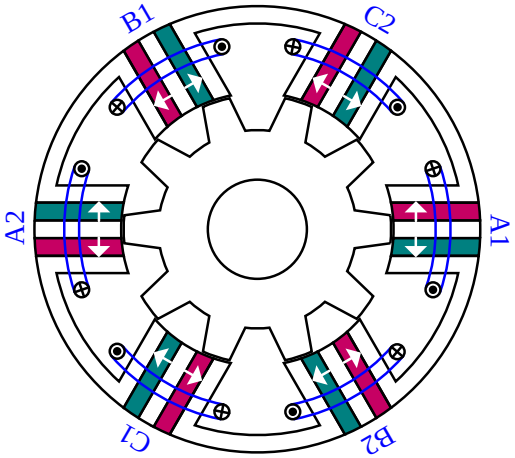

(b) Sandwiched SFPMM

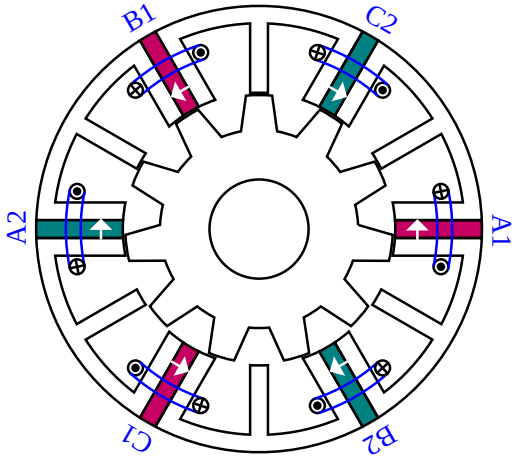

(c) E-core SFPMM

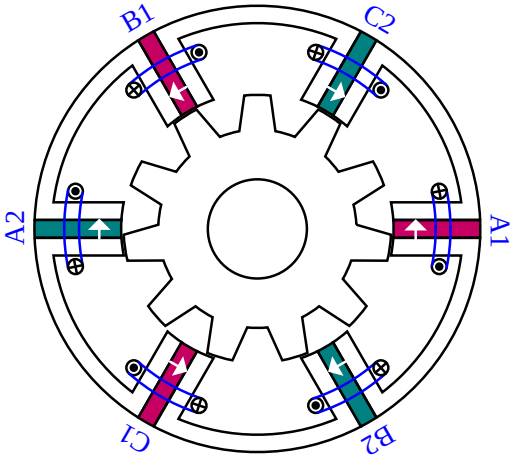

(d) C-core SFPMM

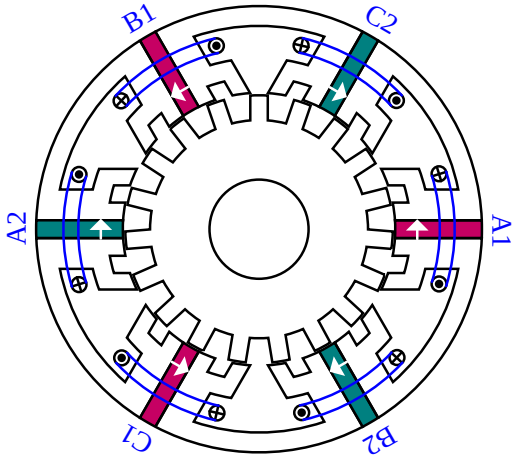

(e) Multi-tooth SFPMM

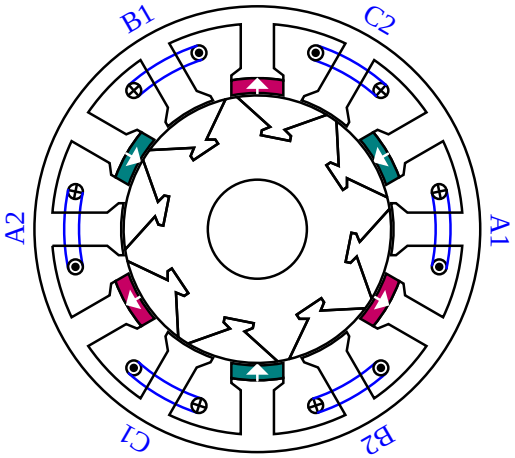

(f) Segment rotor SFPMM

Fig. 1.10. Machine topologies of SFPMMs.

Compared with the conventional PM brushless machines, the reluctance torque of SFPMMs is negligible [ZHU07] [ZHU08a]. Hence, the electromagnetic torque of SFPMMs mainly depends on the PM flux-linkage, armature current (q-axis) and rotor pole number. In other words, a trade-off among the PM volume (shape) and armature winding space (slot area) and rotor pole number under the same machine size and the same copper loss is the key factor on maximizing the torque of SFPMMs. Based on this guideline, various topologies of SFPMMs are proposed and investigated in [FEI06] [ZHU08a] [CHE08] [CHE11a] [CHE11b] [ZHO13b].

Sandwiched SFPMMs, as shown in Fig. 1.10(b), were firstly proposed in [FEI06]. This machine can be considered as developed from the conventional SFPMM as shown in Fig. 1.10(a) by combining two adjacent stator poles into one stator pole. Due to the reduced stator teeth, the slot area of Sandwiched SFPMMs is increased. Consequently, larger armature current can be achieved under the same copper loss. Meanwhile, the magnitude of PM flux-linkage is also increased in Sandwiched SFPMMs. Therefore, compared with conventional SFPMMs, sandwiched SFPMMs exhibit larger torque density and higher PM utilization efficiency [FEI06]. Moreover, by using the V-shape PM structure, the torque density and PM utilization efficiency of Sandwiched SFPMMs can be further enhanced [ZHO13b].

E-core SFPMMs, as shown in Fig. 1.10(c), were firstly proposed in [CHE11a]. This machine can be considered as developed from alternate poles wound SFPMM by removing the PMs which sandwiched in the stator poles without coils and changing the magnetization directions of the remaining PMs as alternate polarity. Due to the increased slot area together with the similar magnitude of PM flux-linkage, larger torque density is achieved in E-core SFPMMs when compared with conventional SFPMMs. Further, since half volume of PMs is removed, E-core SFPMMs also exhibit high PM utilization efficiency. Then, reference [CHE11b] shows that the stator teeth (stator pole without PMs) in the E-core can be removed as shown in Fig. 1.10(d), which can be designated as C-core SFPMMs. Due to further increased slot area together without sacrificing the PM flux-linkage, C-core SFPMMs have larger torque density than E-core SFPMMs and consequently larger than conventional SFPMMs [CHE11b].

Multi-tooth SFPMMs, as shown in Fig. 1.10(e), were firstly proposed in [ZHU08a]. This machine was developed from the conventional SFPMM by employing the multi-tooth stator structure. Obviously, the PM usage in multi-tooth SFPMM is reduced significantly, which is only half of that in conventional SFPMM. However, the slot area of multi-tooth SFPMM is almost the same as that of the conventional SFPMM due to the multi-tooth structure offsets

the increased slot area caused by reduced PM volume [ZHU08a] [CHE08]. Moreover, the increased stator tooth number will generally require more rotor tooth number. Due to the balance between reduced PM flux-linkage and increased rotor pole number, multi-tooth SFPMMs exhibit larger torque density and higher PM utilization efficiency than those of conventional SFPMMs when the electric loading is relative low.

Fig. 1.10(e) shows a segment rotor PM synchronous machine which also employs the switched flux principle [ZUL12b]. Hence, this machine can be designated as Segment rotor SFPMM. In this machine, alternate polarities PMs are mounted on the inner surface of stator poles together with concentrated coils wound around the adjacent stator poles. The results show that the torque density of Segment rotor SFPMM is about 62% that of IPM machine (or SPM machine) [ZUL12b]. Further, in [PAN97], the results show that the torque density of conventional SFPMM is similar to, or even larger than, that of the IPM machine. Therefore, the torque density of Segment rotor SFPMMs should be lower than that of conventional SFPMMs.

1.3 Scope of Research and Contributions of Thesis

1.3.1 Aims and Objectives

In this thesis, the investigation is focused on the electromagnetic performance of novel stator DC field excited and PM synchronous machines which are evolved from the VFRMs.

To further enhance the torque capability of VFRMs, the concepts of unequal stator pole arc and slot opening structure, multi-tooth stator structure, PMs replacing the DC field windings, flux focusing topologies, partitioned stator configuration together with unequal inner/outer stator pole ratio and relative position of inner and outer stator pole are introduced and investigated.

1.3.2 Outline of Thesis

Based on the research scope and methodology as illustrated in Fig. 1.11 together with the major investigated machine topologies as shown in Fig. 1.12, the thesis is organized as follows.

Chapter 1:

The major topologies of synchronous machines with alternate excitation source are reviewed, and the main objectives and contributions of this thesis are presented.

Chapter 2:

In this chapter, the influence of stator and rotor pole arcs on the flux-linkage, back-EMF, cogging torque and average torque in VFRMs with different stator/rotor pole combinations is comprehensively investigated. Then, the optimal rotor pole arc to rotor pole pitch ratio and the optimal stator pole arc are analyzed and summarized. Finally, prototype machines with optimal stator and rotor pole arcs are manufactured and measured to validate the analysis.

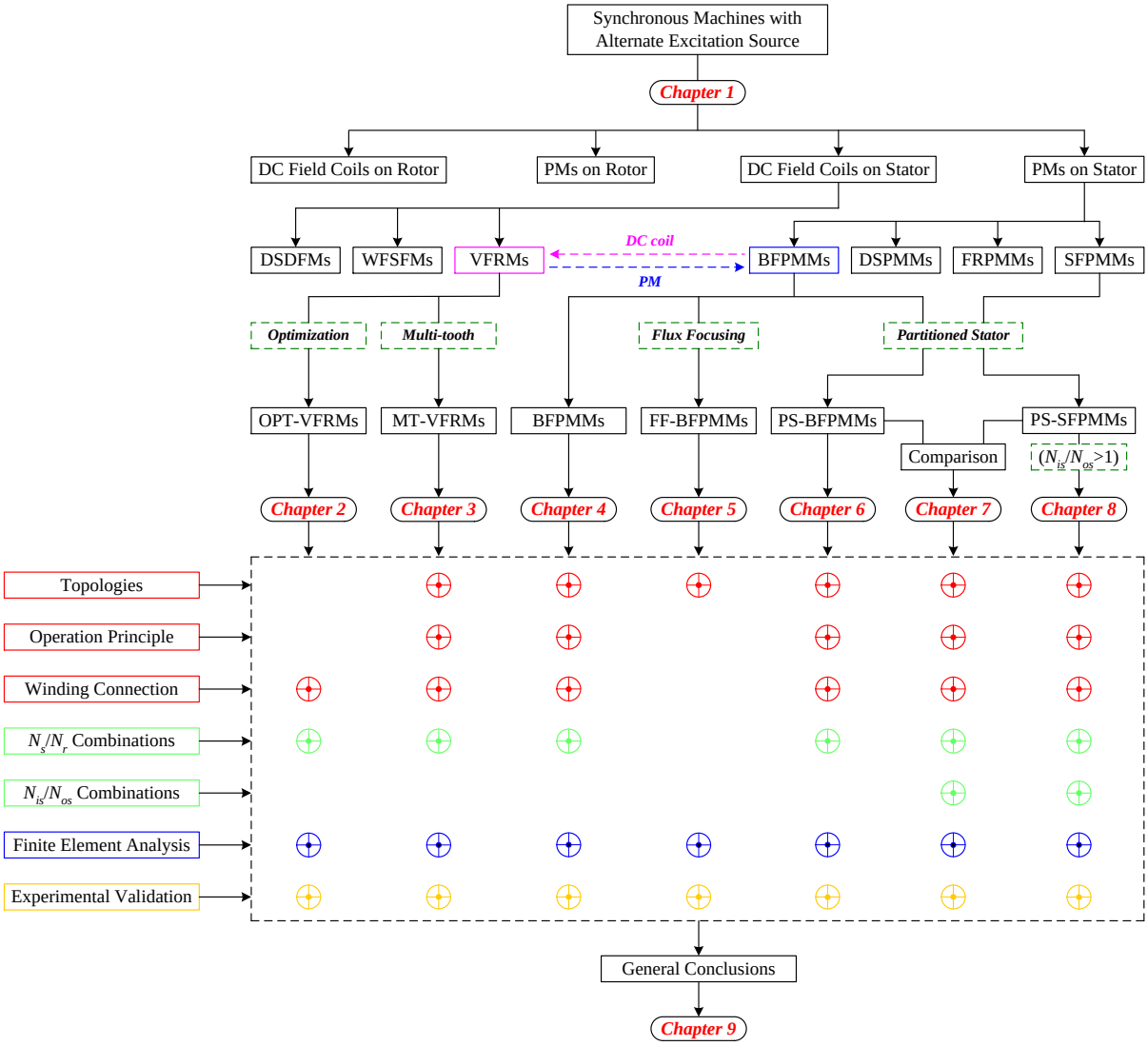

Fig. 1.11. Research scope and arrangement of chapters.

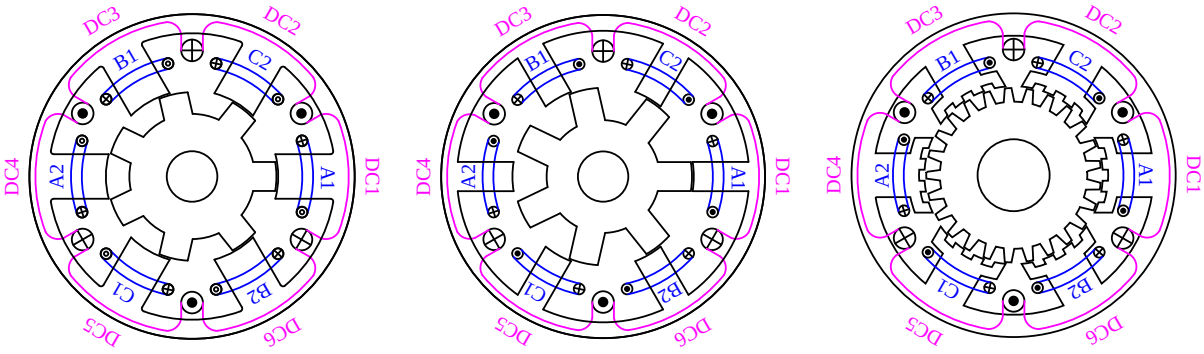

(a) Original VFRM (b) Optimized VFRM (c) Multi-tooth VFRM

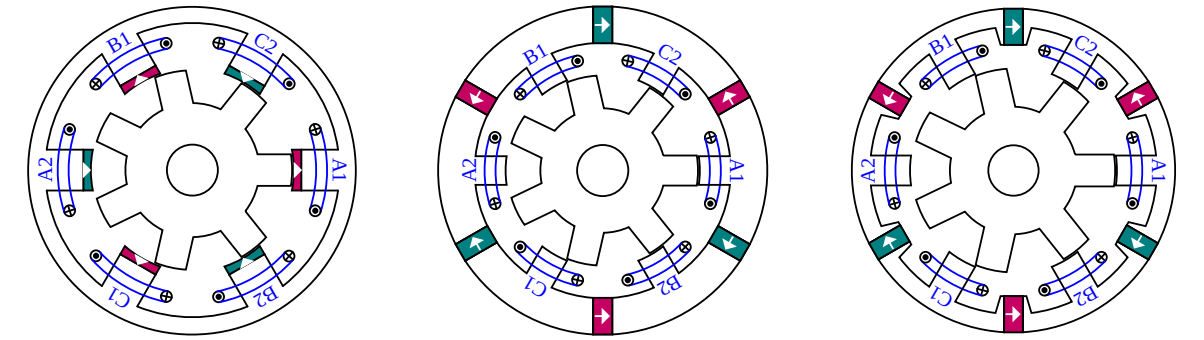

(d) BFPMM-I (SM) (e) BFPMM-II (SYM) (f) IT-BFPMM-II (SYM)

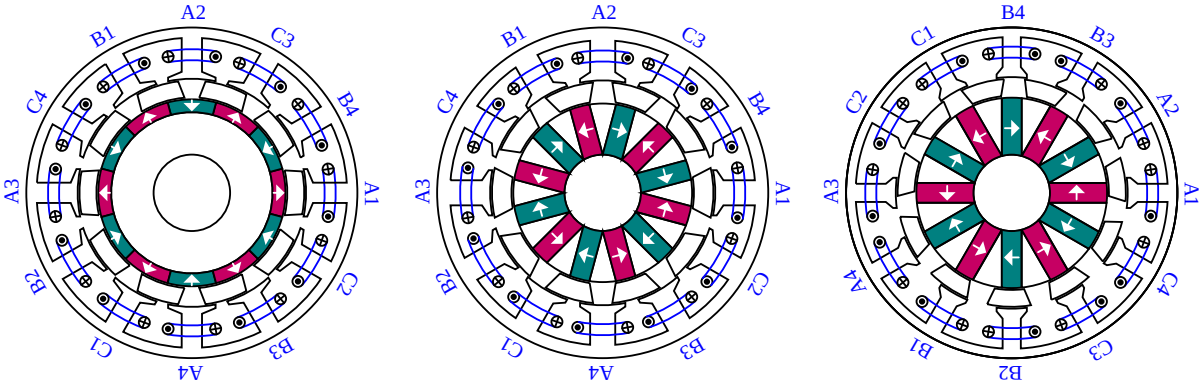

(g) PS-BFPMM-I (h) PS-BFPMM-II (j) PS-SFPMM (n=1)

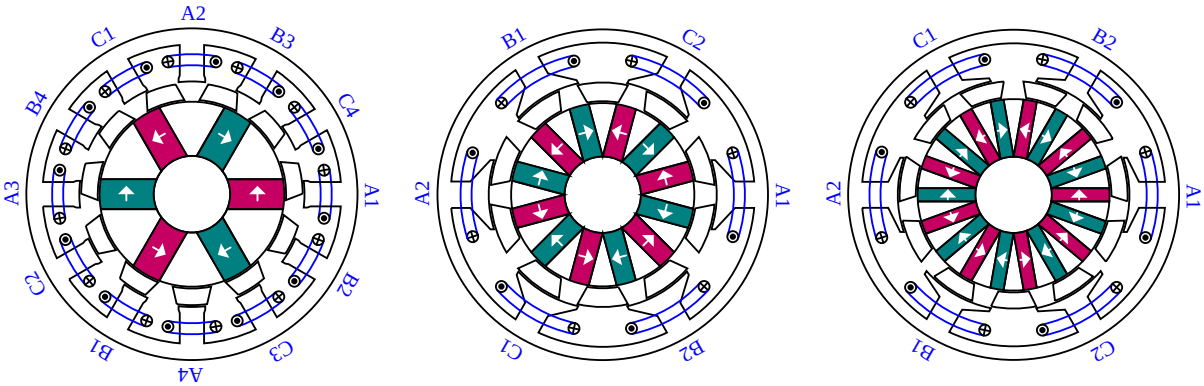

(j) PS-SFPMM (*n*=1/2) (k) PS-SFPMM (n=2) (l) PS-SFPMM (n=3)

Fig. 1.12. Examples of investigated machine topologies in this thesis.

Chapter 3:

In this chapter, novel multi-tooth VFRM is proposed and investigated. The operation principle and conditions for symmetrical back-EMF waveforms as well as average torque equations are firstly illustrated. Then, the optimal copper loss ratio between armature and DC field excitations to obtain the maximum average torque under the fixed copper loss is also analysed. Further, the influences of stator and rotor pole combinations together with number of smaller teeth per stator pole on electromagnetic performance are investigated. Moreover, based on the optimal stator/rotor pole combination, the electromagnetic performance of the multi-tooth VFRM is compared with that of the single-tooth VFRM. Finally, two prototype machines are manufactured and measured to validate the analyses.

Chapter 4:

Novel biased flux PM machine (BFPMM), which is developed from VFRM by replacing DC field windings with PMs, is proposed and investigated in this chapter. The operation principle, stator/rotor pole combinations, winding connections, winding factors and conditions for bipolar phase flux-linkage and symmetrical phase back-EMF waveforms are firstly analysed and summarized. Then, the influence of PM locations in the stator is investigated. Moreover, based on the optimal stator/rotor pole combination, the electromagnetic performances of BFPMMs with three typical PM locations are compared with that of the optimized VFRM. Finally, two prototype machines are manufactured and measured to validate the analyses.

Chapter 5:

In this chapter, the influence of flux focusing on the electromagnetic performance of BFPMM with PMs located in the stator yoke is investigated. Then, based on the inner type flux focusing structure, the electromagnetic performance of optimized BFPMM is compared with optimized DSPMM under the same rated copper loss and the same machine size as well as optimal current angles. Finally, the analyses are experimentally validated by the prototype machine.

Chapter 6:

By introducing the partitioned stator structure, novel partitioned stator BFPMMs (PS-BFPMMs) with two PM stator configurations, i.e. SPM stator and Spoke-IPM stator, are proposed and investigated in this chapter. The machine topologies and operation principle are firstly illustrated. Then, the electromagnetic performance in terms of phase flux-linkage and

back-EMF, *dq*-axis inductances and torque capability of PS-BFPMMs are investigated and compared with single stator BFPMMs (SS-BFPMMs) under the same (inner/outer) stator/rotor pole combination and the same machine size. Moreover, the main stator/rotor pole combinations of PS-BFPMMs are further analysed. Finally, two prototype machines having SPM and Spoke-IPM stators are manufactured and measured respectively to validate the analysis.

Chapter 7:

In this chapter, the influences of the ratio of inner/outer stator poles and the relative position of inner and outer stators on electromagnetic performance of partitioned stator PM synchronous machines will be analysed and compared based on spoke-IPM stator configuration and minimum 6-pole inner and outer stators. Firstly, the machine topologies and conditions for symmetrical bipolar phase flux-linkage and phase back-EMF under different inner/outer stator pole ratios are analysed. Then, based on the optimal rotor pole number, the electromagnetic performance of PS-BFPMM is compared with PS-SFPMMs with different inner/outer stator pole ratios (equal to 1, 1/2 and 2) under the same rated copper loss and machine size. Further, the influence of all pole wound windings and alternate pole wound windings on electromagnetic performance of PS-SFPMM with inner/outer stator pole ratios equal to 1/2 is analysed and compared. Finally, several prototype machines are manufactured and measured to validate the analysis.

Chapter 8:

In this chapter, the influences of inner stator and rotor pole combinations on electromagnetic performance of PS-SFPMMs with 6-pole outer stator are investigated. Firstly, the machine topologies and operational principle are illustrated. Then, the optimal inner stator and rotor pole combinations having different inner/outer stator pole ratios are investigated under the rated copper loss. Meanwhile, the guideline to search the optimal rotor pole number for PS-SFPMMs with different inner/outer stator pole ratios are derived and summarized. Further, based on the individual optimal inner stator and rotor pole combinations, the electromagnetic performance of PS-SFPMMs with inner/outer stator pole ratio equal to 1, 2, 3 and 4 are analyzed and compared. Finally, a prototype machine is manufactured and measured to validate the analyses.

Chapter 9:

It is the general conclusion which summarizes the research findings in this thesis and

outlines the future work.

Appendix A:

The methods for cogging torque and static torque measurement in this thesis are introduced.

Appendix B:

Novel consequent pole synchronous machines with concentrated windings and PM on stator pole surface is proposed and investigated. Meanwhile, the influence of unequal stator pole arc on electromagnetic torque is also analyzed.

Appendix C:

The influence of PMs and armature windings positions together with consequent pole PM stator configuration on electromagnetic performance of PS-BFPMMs with SPM stator is investigated.

Appendix D:

Drawings and parameters of laminations for all prototypes.

Appendix E:

Publications resulted from this Ph. D study.

1.3.3 Major Contributions of Thesis

<u>Major Contributions of Thesis:</u>

(1) For VFRMs, it reveals that the optimal rotor pole arc to rotor pole pitch ratio for the maximum average torque is ~1/3 and the optimal stator pole arc is always equal to or slightly smaller than the optimum rotor pole arc.

(2) Development of novel multi-tooth VFRM topologies.

(3) Development of novel BFPMM topologies.

(4) Development of novel PS-BFPMM topologies.

(5) Development of novel PS-SFPMM topologies.

(6) Systematical investigation of the influences of the ratio of inner/outer stator poles and the relative position of inner and outer stators on electromagnetic performance of partitioned stator PM synchronous machines. Meanwhile, the conditions for symmetrical bipolar phase flux-linkage and phase back-EMF under different inner/outer stator pole ratios are developed.

CHAPTER 2
INFLUENCE OF STATOR AND ROTOR POLE ARCS ON ELECTROMAGNETIC TORQUE OF VARIABLE FLUX RELUCTANCE MACHINES

Variable flux reluctance machines (VFRMs) are developed from switched reluctance machines (SRMs) by neglecting the current harmonics of orders higher than 2 and splitting the original winding into AC armature and DC field windings [LIU12b]. In previous investigation, the equal stator pole arc and stator slot opening, which is usually adopted in conventional 6/4 stator/rotor pole SRMs, is employed in VFRMs. However, since VFRMs can be considered as one type of stator DC excitation synchronous machines, equal stator pole arc and stator slot opening may not be the optimal design for VFRMs. Therefore, in this chapter, the influence of stator and rotor pole arcs on electromagnetic torque of VFRMs having different stator and rotor pole combinations is investigated.

2.1 Introduction

Due to high price of rare earth permanent magnet (PM), non-PM machines are being extensively researched. Among various electrical machines, switched reluctance machines (SRMs) are one of the candidates, which have been applied to many applications due to their simple and robust structure. However, SRMs suffer from high acoustic noise, vibration and torque ripple due to unipolar non-sinusoidal excitation [LIU12c].

Based on the conventional 6/4 stator/rotor-pole SRM, novel variable flux reluctance machines (VFRMs) have been proposed with both AC armature and DC field windings wound on the same stator pole [LIU12b] [LIU12c] [KAS11] [FUK12]. Meanwhile, the choice of rotor pole number in VFRMs is more flexible and can be any integer except the phase number and its multiples [LIU12b]. Since the DC field windings are identically wound on each stator pole, the flux path for each phase in the stator is the same. According to the test results shown in [LIU12c], the acoustic noise and vibration of 6/4 stator/rotor pole VFRM are reduced significantly due to the elimination of abrupt slope change of phase current. Moreover, by using specific stator/rotor pole combinations, such as 6/5 and 6/7, sinusoidal phase flux-linkages and back-EMFs can be obtained in VFRMs since the even order harmonics in a single coil are cancelled completely in the phase winding [LIU12c].

Further, lower torque ripple and better torque performance are obtained in VFRMs.

Since the VFRM was firstly developed from the conventional 6/4 stator/rotor pole SRM, previous investigations on VFRMs adopt the equal stator pole arc and stator slot opening [LIU12b] [LIU12c] [KAS11] [FUK12]. However, VFRMs can be considered as a type of stator DC excitation synchronous machines and are suitable for brushless AC (BLAC) operation, which is significantly different from SRMs. It hence suggests that the equal stator pole arc and stator slot opening may not be the optimal design for VFRMs. Therefore, in this chapter, the influence of stator and rotor pole arcs on the back-EMF, flux-linkage, cogging torque and average torque in VFRMs with different stator/rotor pole combinations is comprehensively investigated by 2D finite element analyses (FEA) and validated by experiments of the prototype machines.

2.2 Prototype Machines and Optimal Designs

VFRMs adopt doubly salient stator and rotor structure with non-overlapping stator AC armature and DC field windings and either odd or even rotor pole numbers with 6 stator poles as shown in Fig. 2.1. As one type of synchronous machines having negligible reluctance torque, the average torque is maximum under the $I_d = 0$ control and can be expressed by (2.1). Since the DC field and AC armature windings have identical contributions to the average torque, the average torque of VFRMs is the maximum when the DC excitation and armature copper losses are equal, i.e. $p_f = p_a$ (which can also be further explained as $N_a = N_f$ and $I_{arms} = I_f$) [LIU12d].

$$T = \frac{3}{2} N_r \psi_{DC} I_q \tag{2.1}$$

where N_r is the number of rotor poles, I_q is the q-axis current, ψ_{DC} is the DC field flux-linkage, N_a and N_f are the turns number per phase of armature winding and DC field winding respectively, I_{arms} is the root means square of armature current, and I_f is the DC field current.

In order to check whether the equal stator pole arc and stator slot opening, i.e. $W_{sp} = W_{so}$, is optimal for VFRMs, two sets of optimized designs are proposed individually and compared when they have the same outer diameter, axial length and total copper loss. The first set of designs, represented by ORI, is obtained when $W_{sp} = W_{so}$. Hence, there are four independent variables, e.g. split ratio, rotor pole arc, stator back iron thickness and rotor back iron thickness. The second set of designs, represented by OPT, is obtained without the constraint of $W_{sp} = W_{so}$. Hence, there are five independent variables, e.g. split ratio, stator pole arc, rotor pole arc, stator back iron thickness and rotor back iron thickness. Considering the thermal

condition under the machine size (45mm outer stator radium and 25 axial stack length) together with employing the force air cooling, the rated copper loss is chosen as 30W since the corresponding current density will be around 7-10 A/mm^2. In addition, due to the low rated electric frequency (corresponding to the rated speed 400rpm), the rated iron loss is relative small when compared with the rated copper loss. Therefore, in order to simplify the globe optimization, the iron loss is ignored. Then, two sets of machines are globally optimized with the purpose of maximum average torque under the same rated copper loss and the same machine size by genetic algorithm (ANSYS Maxwell, all of the variables are considered), and their main optimized geometric parameters and electromagnetic performance are listed in Table 2.1. It can be seen from Table 2.1 that OPT-VFRMs exhibit higher average torques than ORI-VFRMs for all the stator/rotor pole combinations. In other words, unequal stator pole arc and slot opening can boost the torque density of VFRMs.

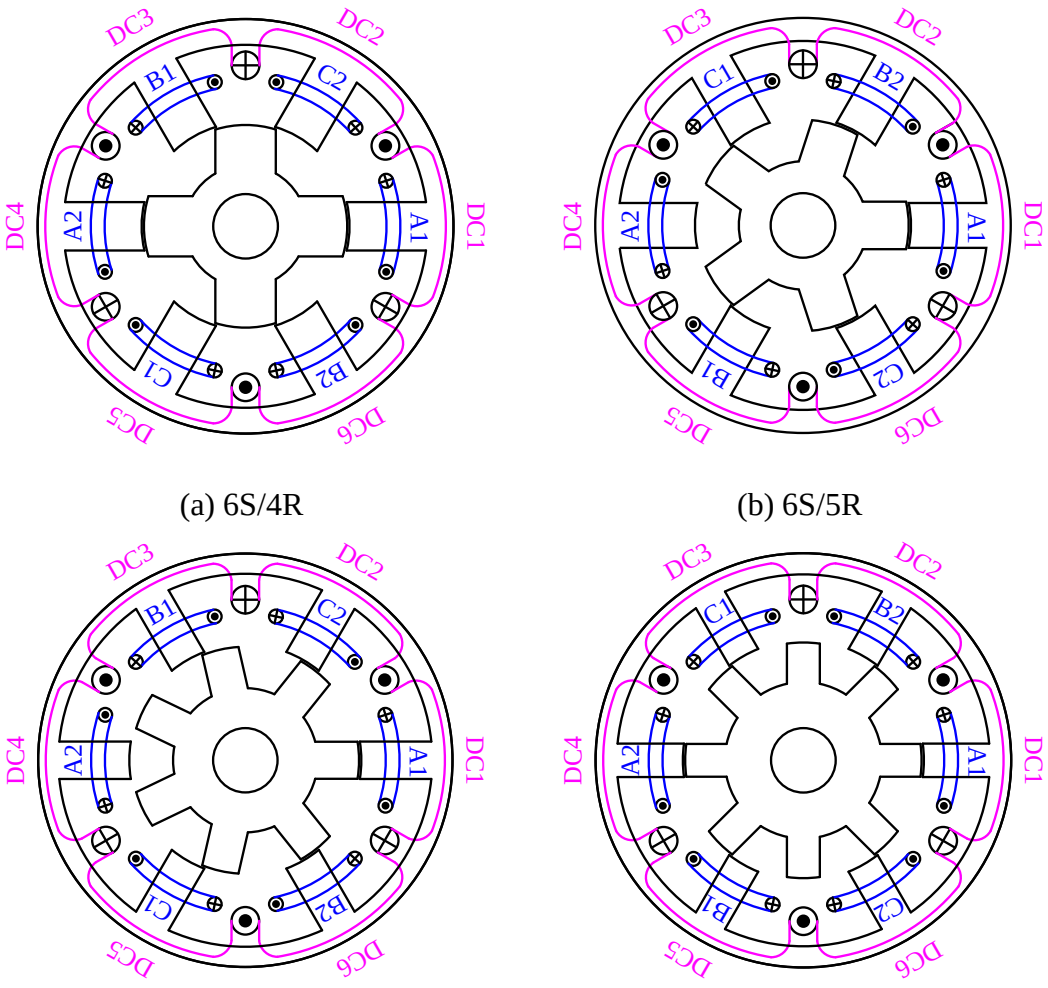

Fig. 2.1. Topologies of VFRMs with optimum stator and rotor pole arcs.

Table 2.1 Main parameters of VFRMs

Parameters	**VFRM**			
Number of phases	3			
Turns per coil (AC/DC)	36/36			
Rated speed (rpm)	400			
Packing factor	0.5			
Rated copper loss (W)	30			
Airgap length (mm)	0.5			
Active axial length (mm)	25			
Stator outer radius (mm)	45			
Number of stator poles N_s	6			
Number of rotor poles N_r	4	5	7	8
ORI/OPT designs	ORI/OPT	ORI/OPT	ORI/OPT	ORI/OPT
Split ratio	0.49/0.5	0.5/0.52	0.53/0.56	0.53/0.58
Stator pole arc (mech. deg)	30/27	30/24	30/18.6	30/16
Rotor pole arc (mech. deg)	32.4/34.6	26.8/26.0	19.8/18.8	16/16
Stator back iron (mm)	5.8/5.6	5.5/5.0	5.3/4.4	5.9/4.6
Slot area (mm^2)	353/369	352/389	330/405	313/394
Rated AC/DC current (A_{rms})	9.67/9.89	9.67/10.2	9.36/10.4	9.11/10.2
Rated AC/DC current density (A_{rms}/mm^2)	7.89/7.72	7.91/7.55	8.17/7.40	8.38/7.46
Rated electric frequency (Hz)	26.7/26.7	33.3/33.3	46.7/46.7	53.3/53.3
Rated core loss (W)	0.69/0.69	0.87/0.84	1.01/0.97	1.29/1.15
Fund. flux-linkage (Wb)	8.35/8.36	7.50/7.51	4.98/5.91	3.40/5.10
Fund. back-EMF (V)	1.40/1.41	1.57/1.58	1.46/1.73	1.14/1.71
Average torque (Nm)	0.62/0.63	0.71/0.74	0.63/0.82	0.46/0.79
Incremental rate (%)	1	4	30.7	72.9
Cogging torque (mNm)	35.3/53.9	46.4/17.0	44.5/40.0	32.8/72.2

2.3 Influence of Stator and Rotor Pole Arcs on Electromagnetic Torque

In order to quantify the influence of the stator and rotor pole arcs and hence further guide VFRMs designs, the variation of average torque with the stator and rotor pole arcs for different stator and rotor pole combinations is shown in Fig. 2.2. For each combination of

stator and rotor pole arcs, all the other variables are optimized for the maximum torque when the total copper loss is 30W (p_c = 30W). It can be seen that the influence of stator and rotor pole arcs on the average torque of VFRM is significant, especially when the rotor pole number N_r is larger than the stator pole number N_s. The average torques of 6/4, 6/5, 6/7 and 6/8 stator/rotor-pole VFRMs are maximized when the stator and rotor pole arcs are 27/34.6, 24/26, 18.6/18.8 and 16/16 mechanical degrees, respectively. The VFRMs with optimum stator pole arc have higher average torque than VFRMs having $W_{sp} = W_{so}$. The optimum rotor pole arc reduces as the number of rotor pole increases. Fig. 2.3 shows the variation of average torque with the rotor pole arc to rotor pole pitch ratio with all the other parameters being optimized. It can be seen that for all the stator/rotor pole combinations, the average torque always peaks when the rotor pole arc to rotor pole pitch ratio is ~1/3. Hence, the optimum rotor pole arc W_{rp} for maximum average torque in VFRM can be estimated by (2.2).

$$W_{rp} = 2\pi/(3N_r) \tag{2.2}$$

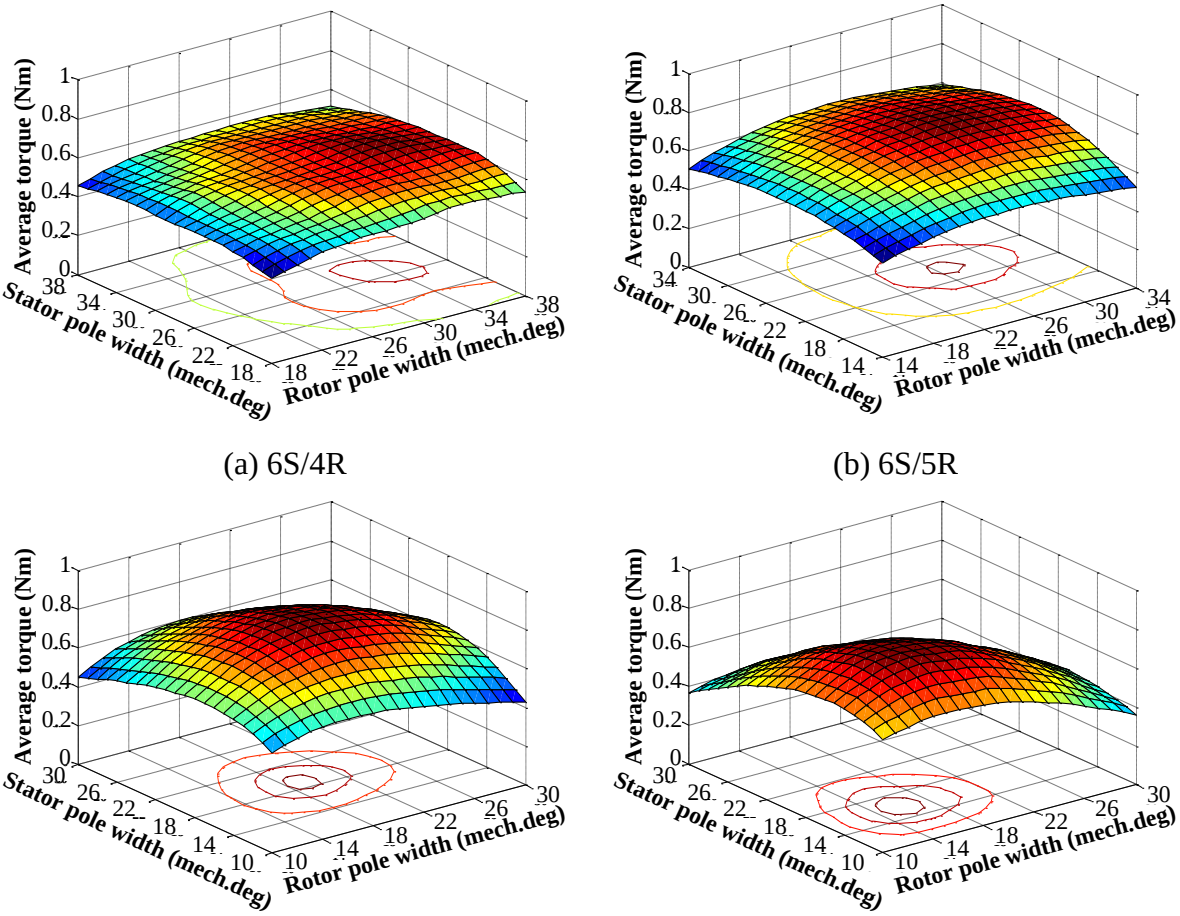

(a) 6S/4R (b) 6S/5R

(b) 6S/7R (d) 6S/8R

Fig. 2.2. Variation of average torque with stator and rotor pole arcs, $p_f = p_a$ = 1/2 p_c = 15W.

Furthermore, it can also be seen from Table 2.1 that the optimum stator pole arc is always equal to or slightly smaller than the optimum rotor pole arc. Based on these conclusions, the schematics of ORI- and OPT-VFRMs are illustrated in Fig. 2.4.

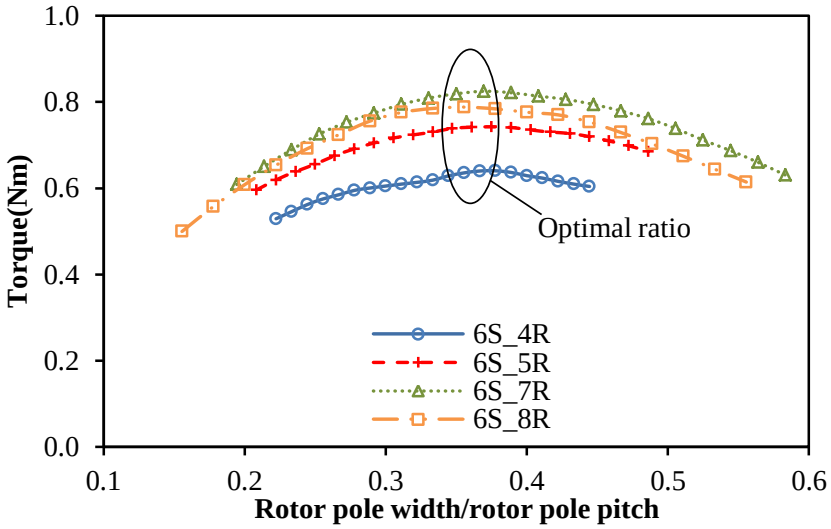

Fig. 2.3. Variation of average torque with rotor pole arc to rotor pole pitch ratio.

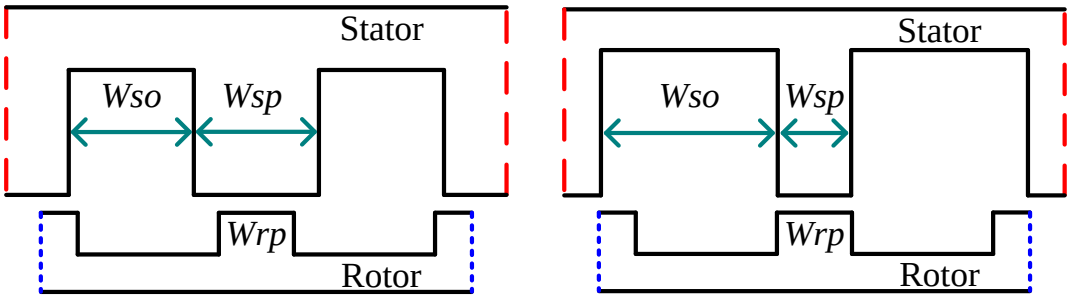

(a) ORI-VFRMs with equal stator pole arc and slot opening

(b) OPT-VFRMs with optimum stator and rotor pole arcs

Fig. 2.4. Schematics of ORI- and OPT-VFPMMs

2.4 Performance Comparison

In this section, ORI-VFRMs with W_{sp} = W_{so} and OPT-VFRMs are further compared to quantify the variations of electromagnetic quantities which contribute to the average torque.

2.4.1 Open-Circuit Field Distributions

Fig. 2.5 shows the open-circuit flux distributions of 6/4, 6/5, 6/7 and 6/8 stator/rotor pole VFRMs when a rotor pole is aligned with the stator pole having coil A1 and the field copper

loss is 15W. It can be seen that OPT-VFRMs have less flux leakage than ORI-VFRMs due to the increased slot openings, especially when $N_r > N_s$.

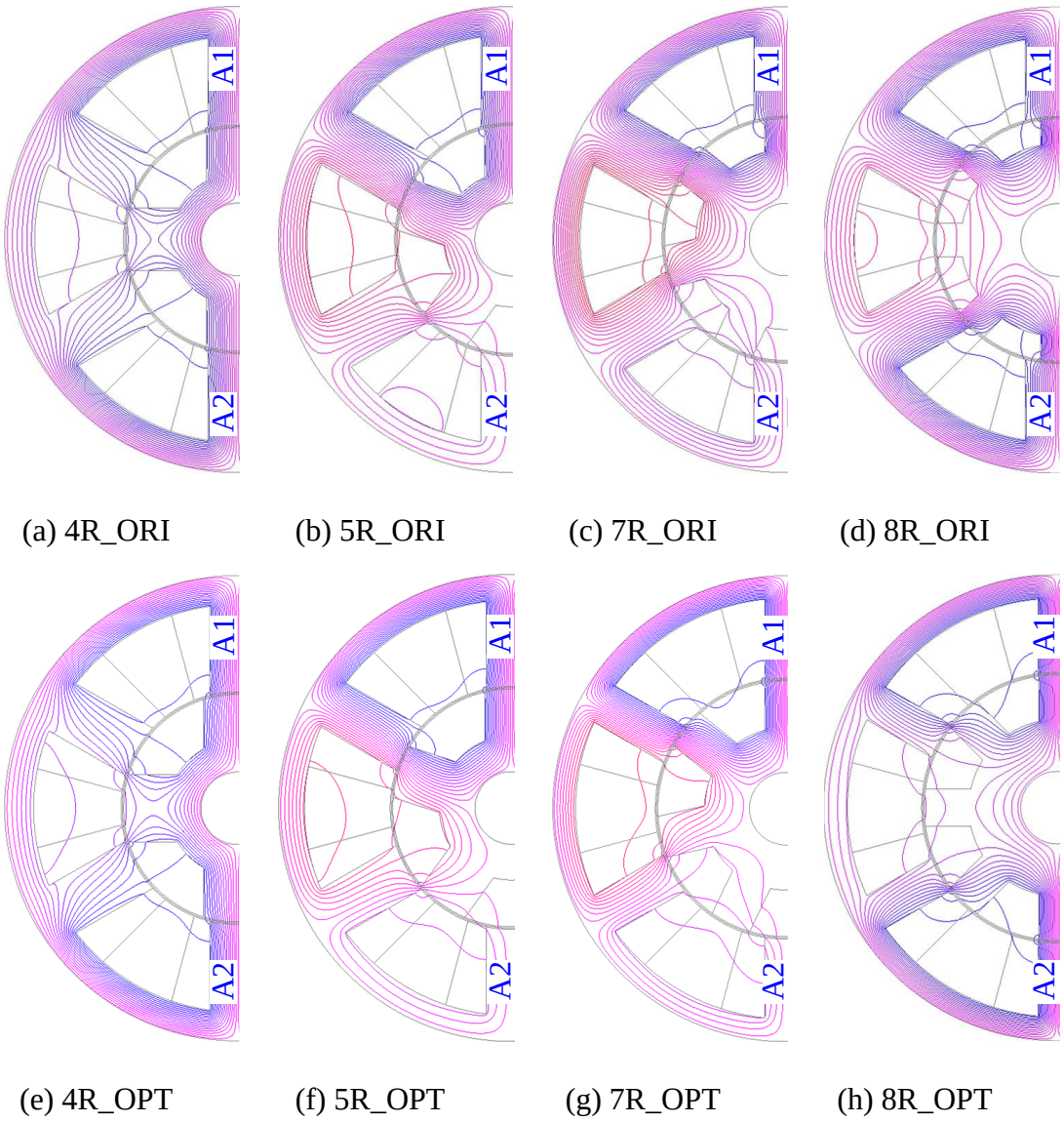

(a) 4R_ORI (b) 5R_ORI (c) 7R_ORI (d) 8R_ORI

(e) 4R_OPT (f) 5R_OPT (g) 7R_OPT (h) 8R_OPT

Fig. 2.5. Open-circuit flux equipotential Schematics of ORI- and OPT-VFPMMs

2.4.2 Flux-linkage and Back-EMF Waveforms

The flux-linkages of ORI- and OPT-VFRMs are given and compared in Fig. 2.6 and Table 2.1. The effective flux linkage component, which is the peak to peak value of the flux linkage variation, of OPT-VFRM is larger than that of ORI-VFRM, especially when $N_r > N_s$. It is due to two aspects. First, OPT-VFRMs have wider slot openings and hence larger slot areas. Consequently, OPT-VFRMs have larger field currents under the same copper loss. Thus, the flux-linkage, which is proportional to the DC current, increases. Second, due to narrower stator poles, the slot leakage flux is reduced in OPT-VFRMs, which helps to further increase

the main flux-linkage.

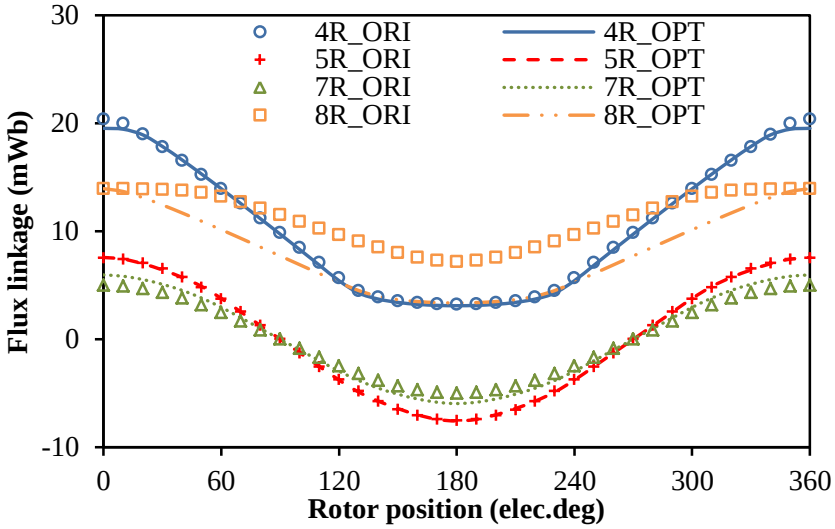

(a) Waveform

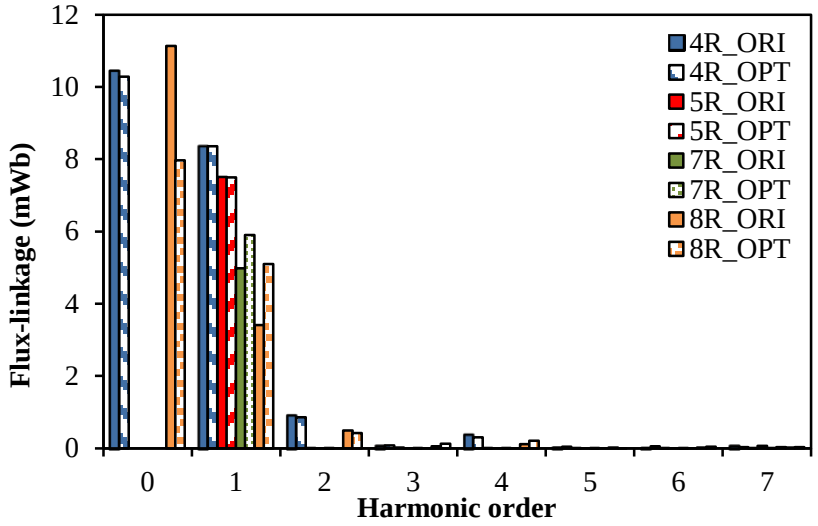

(b) Spectrum

Fig. 2.6. Open-circuit flux-linkages of phase A at rated DC field currents as given in Table 2.1, p_f = 15W.

Due to the increased effective flux linkages, for the same N_s/N_r combination, the fundamental back-EMF of OPT-VFRM is larger than ORI-VFRM, especially when $N_r > N_s$, which is confirmed by Fig. 2.7 and Table 2.1. In order to explain the back-EMF variations between different N_s/N_r combinations, it is necessary to consider the fundamental electrical frequency which depends on the rotor pole number. For example, the 6/7 stator/rotor-pole OPT-VFRM exhibits higher fundamental back-EMF than that of 6/5 stator/rotor-pole OPT-VFRM despite of a lower fundamental flux-linkage. It is due to that the fundamental

electrical frequency of 7-rotor pole VFRM is 1.4 times of the one for 5-rotor pole VFRMs under the same speed.

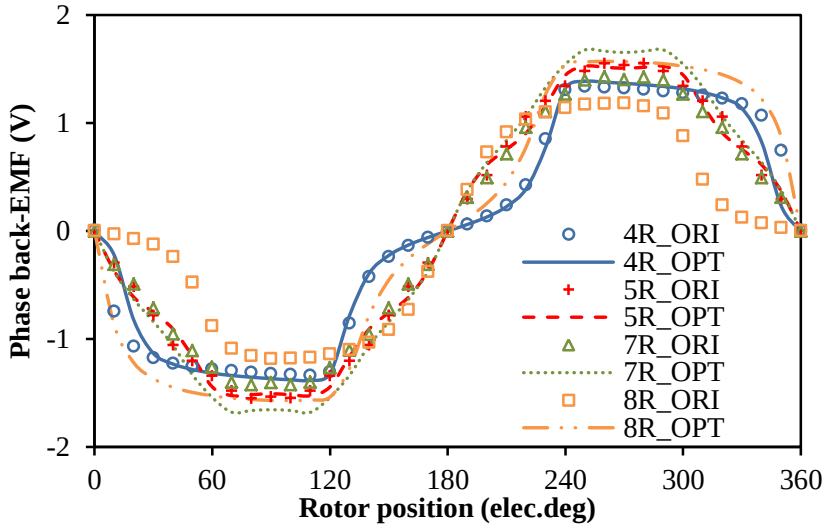

(a) Waveform

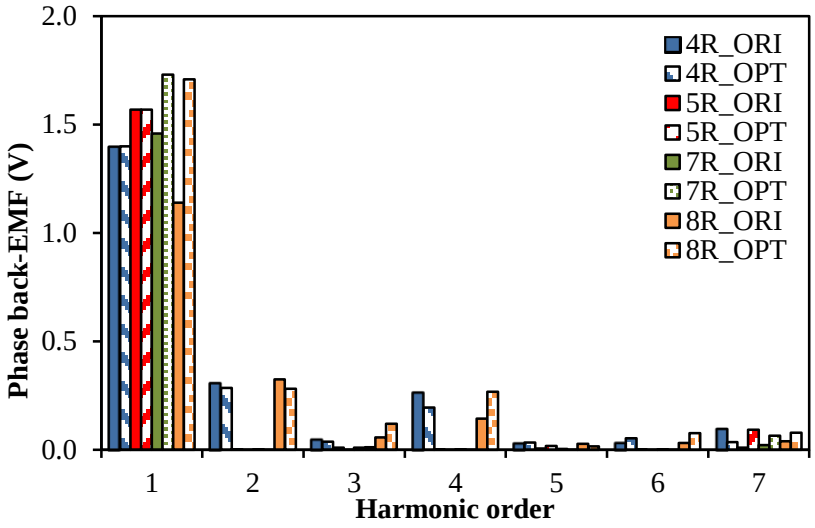

(b) Spectrum

Fig. 2.7. Open-circuit back-EMFs of phase A at rated DC field currents as given in Table 2.1, p_f = 15W.

2.4.3 Cogging Torque

In VFRMS, the cogging torque is defined as the static torque when DC field windings are excited with the DC currents while the AC armature coils are not excited. Fig. 2.8 shows the cogging torque waveforms over one electric period for all the machines with rated DC current when p_f =15W. Compared with ORI-VFRMs, the cogging torques of OPT-VFRMs are enlarged when $N_s = N_r \pm 2$ but reduced when $N_s = N_r \pm 1$, as shown in Fig. 2.8 and Table 2.1.

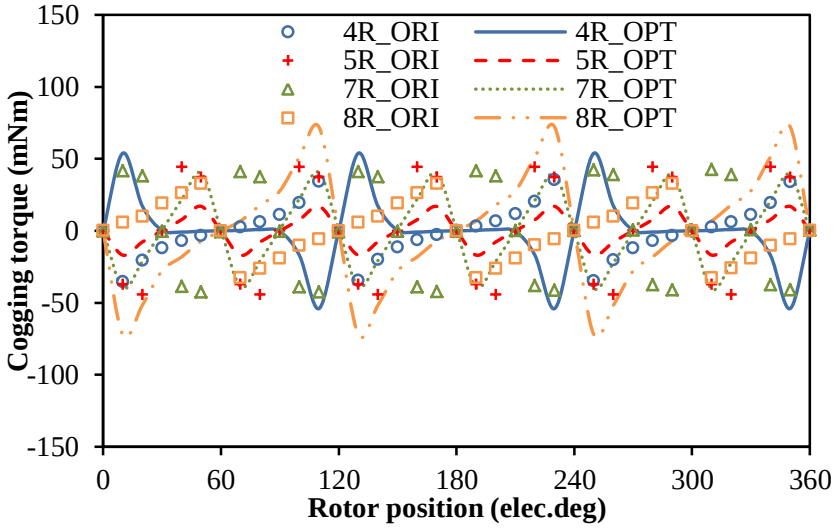

Fig. 2.8. Open-circuit cogging torques at rated DC field currents as given in Table 2.1, p_f=15W.

2.4.4 Electromagnetic Torque Characteristics

The torques of ORI- and OPT-VFRMs when the total copper loss is 30W and I_d = 0 are compared in Fig. 2.9 and Table 2.1. The variations of the average torque with the copper loss for all the VFRMs are further shown in Fig. 2.10. The dashed line indicates the rated copper loss, which is used during the optimization. It can be seen that for the whole copper loss range shown in Fig. 2.10, OPT-VFRMs exhibit higher torque than ORI-VFRMs for all the N_s/N_r combinations, excepting the 6/4 stator/rotor pole combination. For example, when the total copper loss is 30W, the average torques of OPT-VFRMs are 1%, 4%, 30.7% and 72.9% higher than the torques of ORI-VFRMs having 4-, 5-, 7- and 8-rotor poles, respectively. This is due to the increases of both the fundamental DC field flux linkage and the armature current. For the 6/4 stator/rotor pole combination, OPT- and ORI-VFRMs have similar average torques. This is due to that the dimensions of ORI-VFRM are already very close to the ones of OPT-VFRM for the 6/4 stator/rotor pole VFRM.

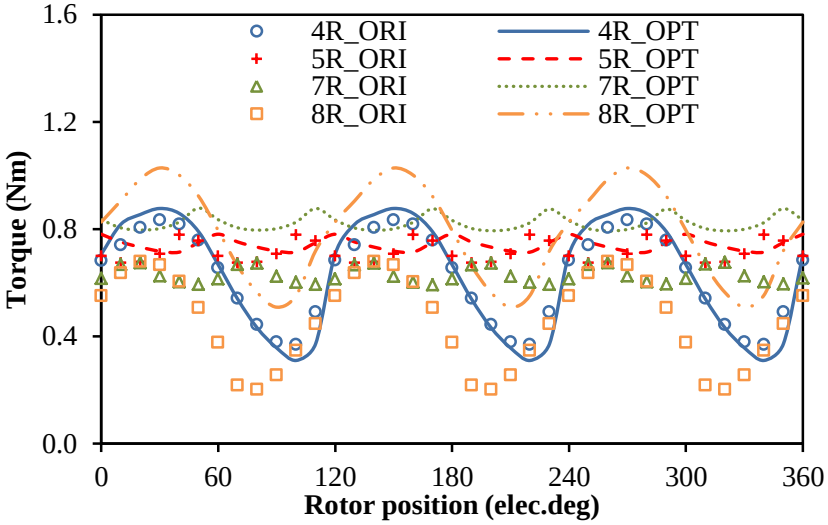

(a) Waveform

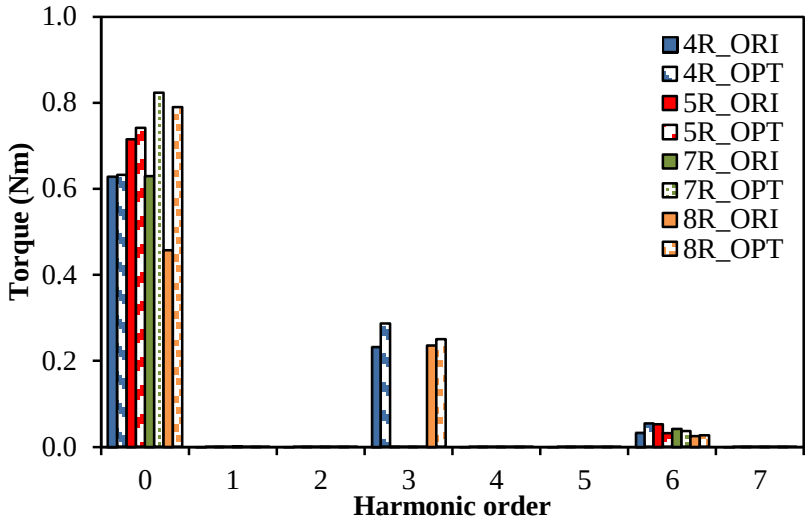

(b) Spectrum

Fig. 2.9. Electromagnetic torques at rated DC/AC currents as given in Table 2.1, p_f=p_a=15W.

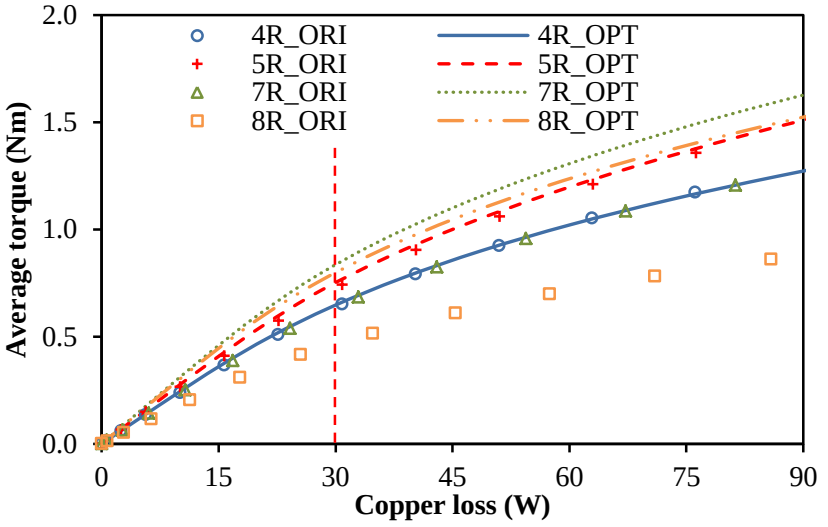

Fig. 2.10. Variation of average torques with copper loss, $p_f = p_a$.

Compared different stator/rotor pole number combinations, the 6/5 stator/rotor pole VFRM has the highest average torque when $W_{sp} = W_{so}$. However, when the constraint of $W_{sp} = W_{so}$ is removed, the 6/7 stator/rotor pole OPT-VFRM exhibits the highest average torque. Further, for VFRMs with 6/4, 6/5, 6/7 and 6/8 stator/rotor pole number combinations, the distribution factors (K_d) are all equal to 1 while the pitch factors (K_p) are 0.5, 0.87, 0.87 and 0.87 respectively. Then, the corresponding winding factors (K_{dp}) for VFRMs with 6/4, 6/5, 6/7 and 6/8 stator/rotor pole number combinations are 0.5, 0.87, 0.87 and 0.5 respectively. Therefore, considering the winding factors and rated currents (corresponding to p_c=30W), 6/7 stator/rotor pole VFRM exhibits higher torque capability than the 6/8 stator/rotor pole VFRM in both designs with or without the constraint of $W_{sp} = W_{so}$.

2.5 Experimental Verification

In order to validate the foregoing analyses, two prototype machines, 6/7 and 6/5, are made and shown in Fig. 2.11. For the 6/7 stator/rotor pole machine, it is the optimal design without the constraint of $W_{sp} = W_{so}$ and shown in Fig. 2.1(c) and Table 2.1. For the 6/5 stator/rotor pole machine, the stator is the same as the one of 6/7 stator/rotor pole prototype machine while the rotor is re-optimized according to the stator. The rotor pole arc is adjusted to 28.8° mechanical.

(a) 6-pole Stator

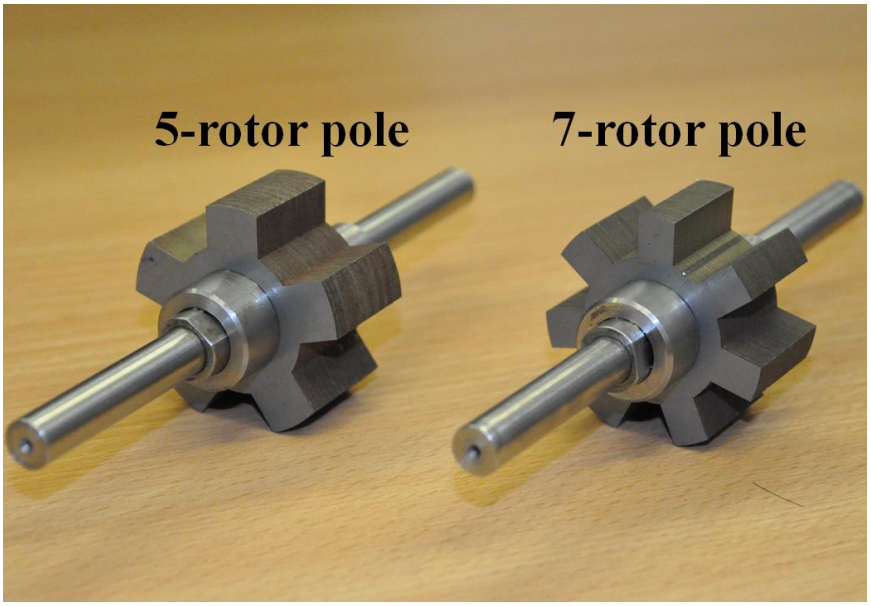

(b) 5- and 7-pole Rotors

Fig. 2.11. Prototypes of VFRMMs.

Fig. 2.12 shows the measured and predicted phase back-EMFs at two different field currents (5.2A and 10.4A corresponding to half and full rated DC currents) when the speed is 400rpm. The measured and predicted open-circuit cogging torque waveforms are shown in Fig. 2.13. It can be seen that the measured peak to peak values are slightly larger than the FE predictions in both two machines. It is acceptable when considering the measurement error and assembling tolerance, as well as the 3-dimensional end effect. Fig. 2.14 shows the variations of the static torque with rotor position at different field and armature currents (I_f = I_{arms} and I_a = I_A= -2I_B = -2I_C). Based on Fig. 2.14, the variations of the static torque at 270° rotor position with the total copper loss are shown in Fig. 2.15. Overall the measured and FE predicted results match well. The minor difference under higher current is due to the increased influence of end-effect.

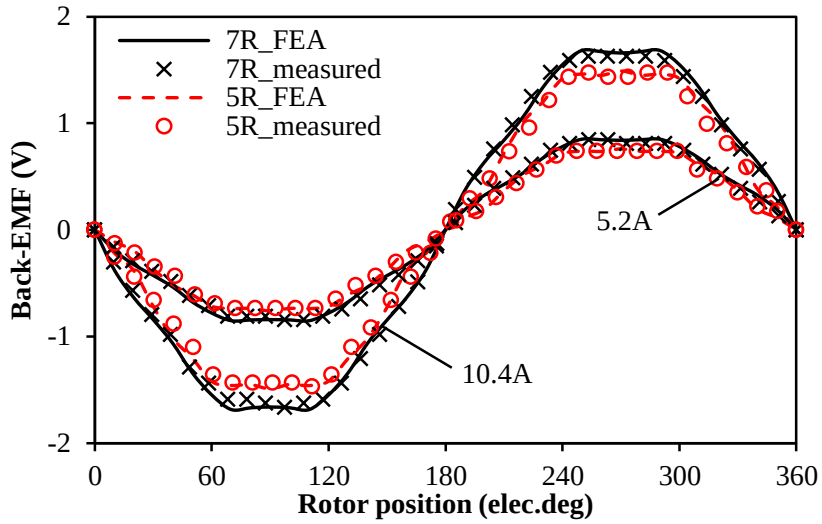

Fig. 2.12. Measured and FE predicted phase back-EMFs at 400rpm.

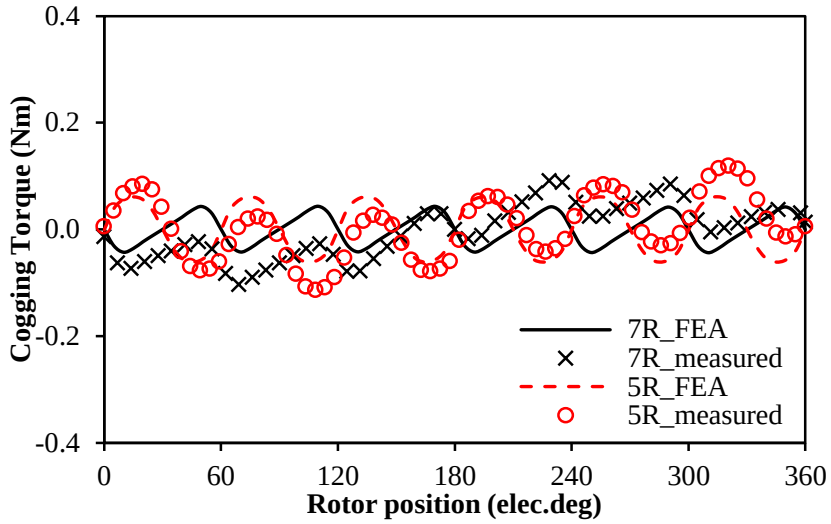

Fig. 2.13. Measured and FE predicted cogging torques at rated DC field currents, I_f = 10.4A.

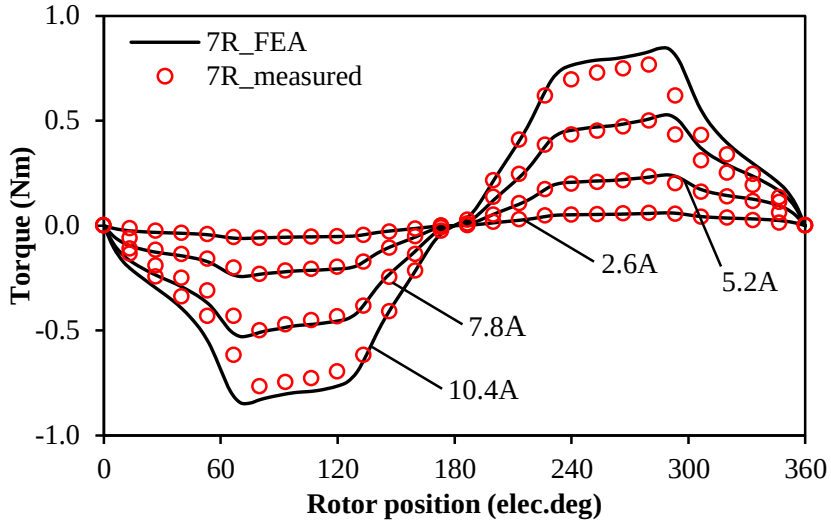

(a) 7-pole rotor

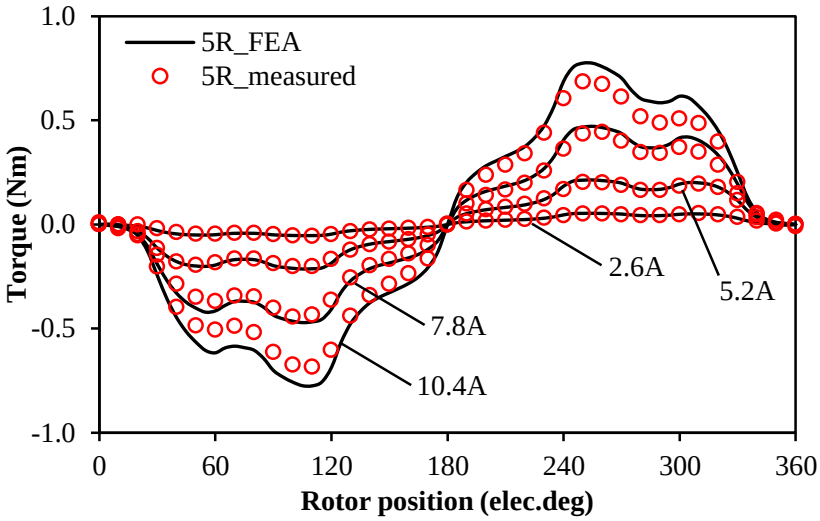

(b) 5-pole rotor

Fig. 2.14. Measured and FE predicted static torques when $I_f = I_{arms}$ and $I_a = I_A = -2I_B = -2I_C$.

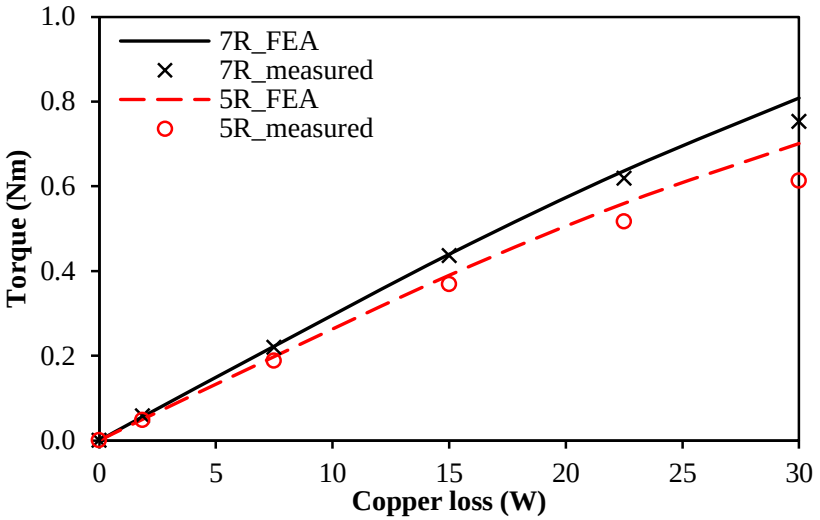

Fig. 2.15. Measured and FE predicted torque-copper loss characteristics at 270° rotor position.

2.6 Summary

The influence of stator and rotor pole arcs on electromagnetic torque of VFRMs having different stator and rotor pole combinations is investigated. It can be concluded that: (1) by employing unequal stator pole arc and slot opening, the average torque can be enhanced compared with the machines having equal stator pole arc and slot opening; (2) the optimal rotor pole arc to rotor pole pitch ratio for the maximum average torque is ~1/3 and the optimal stator pole arc is always equal to or slightly smaller than the optimum rotor pole arc; (3) without the constraint of equal stator pole arc and slot opening, the 6/7 stator/rotor-pole VFRM exhibits the highest average torque. All the analyses have been validated by both the FEA and measurements.

CHAPTER 3
ANALYSIS OF MULTI-TOOTH VARIABLE FLUX RELUCTANCE MACHINES WITH DIFFERENT STATOR AND ROTOR POLE COMBINATIONS

The multi-tooth stator pole structure is widely employed to further improve the torque capability, such as in hybrid stepper machines, switched reluctance machines and switched flux machines. Therefore, this concept can also be introduced in variable flux reluctance machines (VFRMMs). In this chapter, novel multi-tooth variable flux reluctance machines which adopt doubly salient stator and rotor structure with non-overlapping stator AC armature and DC field windings are investigated.

3.1 Introduction

Switched reluctance machines (SRMs) have been widely applied to applications from aerospace to domestic appliances over the past decades due to simple and robust structure [MIL93] [VIJ08]. However, due to unipolar non-sinusoidal excitation, SRM suffers from high torque ripple, acoustic noise and vibration [ZHU07]. Further, in order to improve the torque performance, an idea which splits the original armature windings in SRM into AC armature and DC field windings is presented in [PUL88]. Doubly fed doubly salient machine (DFDSM) [LI95] is one of the proposed machine topologies, in which full-pitched DC field windings and concentrated armature windings are located in the stator. However, since the flux path in the stator is asymmetric, DFDSM has the non-sinusoidal and asymmetric back-EMF as well as large torque ripple, particularly under heavy magnetic saturation.

Similarly, variable flux reluctance machine (VFRM) which adopts doubly salient stator and rotor structure with non-overlapping stator AC armature and DC field windings is proposed in [LIU12b] [LIU12c] [LIU13] [KAS12] [FUK12]. In reference [FUK12], VFRM is evolved from dual-winding reluctance machine by using non-overlapping stator armature and field windings. Meanwhile, VFRM can also be considered as developed from SRM by neglecting the current harmonics of orders higher than 2 and splitting the original winding into AC armature and DC field windings [LIU12b] [LIU12c] [LIU13]. The choice of rotor pole number is much more flexible than those in conventional SRM and DFDSM and can be any integers except the phase number and its multiples. Different from DFDSM, the flux paths for

each phase in the stator of VFRM are the same since the DC field windings are identically wound on each stator pole. Moreover, sinusoidal phase flux-linkage and back-EMF waveforms are obtained in VFRMs by using specific stator/rotor pole combinations (such as 6/5, 6/7, 12/10, 12/11, 12/13 and 12/14 etc) since all the even order harmonics in a single coil are cancelled completely in the phase winding [LIU12b]. Hence, VFRM exhibits lower torque ripple and higher torque capability than DFDSM [LIU13].

The multi-tooth stator pole structure is widely adopted to further improve the torque capability, such as in hybrid stepper machines, SRMs and switched flux machines (SFMs) [KUO75] [FAI95] [FIN84] [LEE13] [ZHU08a] [CHE08]. Therefore, this concept can also be introduced in VFRMs. In this chapter, novel three phase multi-tooth VFRMs are proposed and investigated. Firstly, the operation principle and conditions for symmetrical back-EMF waveforms as well as average torque equations are illustrated. Then, the optimal number of small teeth per stator pole n is investigated under the rated copper loss and 6-pole stator when the number of total small stator teeth and rotor pole differs by one ($N_r=nN_s\pm1$). Meanwhile, the electromagnetic performance of a 4-tooth VFRM with 6/25 stator/rotor pole is investigated and compared with a single-tooth VFRM with 6/7 stator/rotor pole. The main stator and rotor pole combinations of 4-tooth VFRM with 6-pole stator are analyzed and compared under the same rated copper loss as well. Finally, several prototype machines are manufactured and measured to validate the analyses.

3.2 Operation Principle of Single- and Multi-tooth VFRMs

3.2.1 Operation Principle

Doubly salient stator and rotor structure with non-overlapping stator AC armature and DC field windings are adopted in single-tooth VFRMs as shown in Fig. 3.1(a). Meanwhile, multi-tooth structure, which has been widely used in [KUO75] [FAI95] [FIN84] [LEE13] [ZHU08a] [CHE08], can also be introduced in VFRMs. With n representing the number of small teeth on each stator pole, several configurations of multi-tooth VFRMs are shown in Fig. 3.1 (b), (c) and (d) as examples.

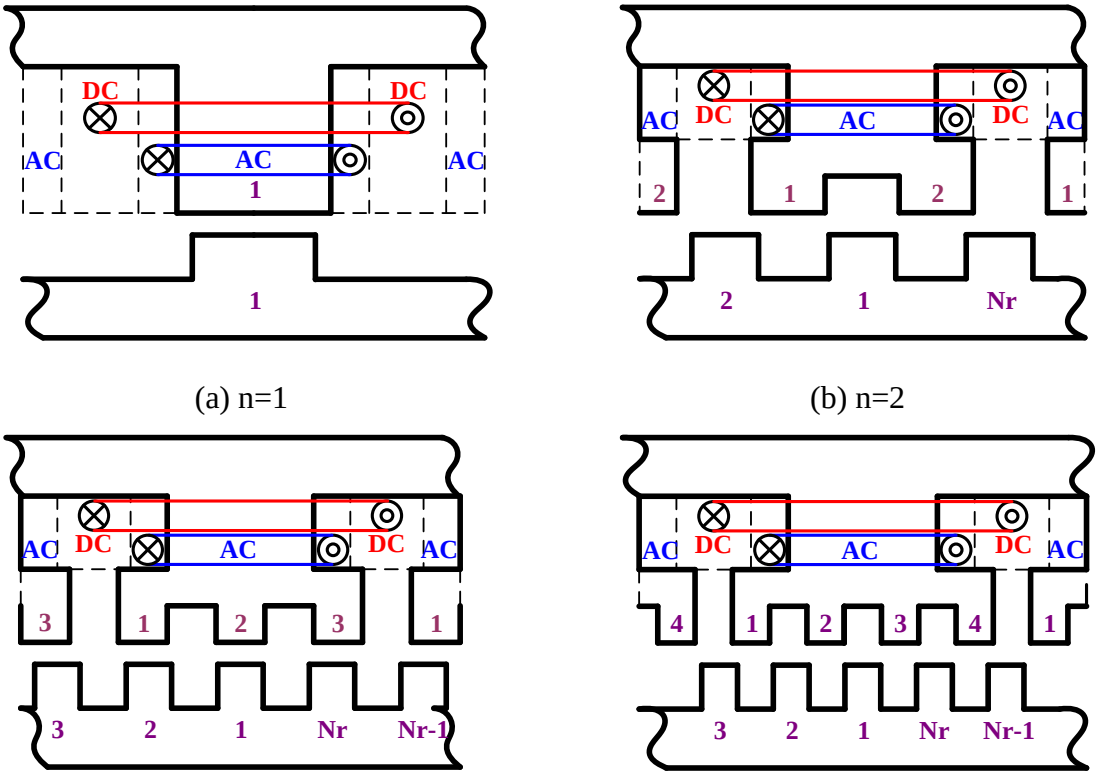

(a) n=1 (b) n=2

(c) n=3 (d) n=4

Fig. 3.1. Schematics of single- and multi-tooth VFRMs.

Being the same as single-tooth VFRM, the choice of stator and rotor pole numbers (N_s and N_r) in multi-tooth VFRM is also flexible. N_r can be any integers except the phase number and its multiples. Hence, the selections of N_s and N_r can be normally summarized as

$$N_s = km \ (k = 1, 2\ldots) \tag{3.1}$$

$$N_r = nN_s \pm j \ (N_r \neq k_i m, j=1, 2\ldots, k_i=1.\ 2\ldots) \tag{3.2}$$

where m is the phase number, k, j and k_i are integers.

For all the stator and rotor pole combinations, their coil connections of the armature winding are determined by the conventional coil-EMF vector method, in which electrical degree α_e between two adjacent coil-EMF vectors [ZHU10] can be calculated from the mechanical degree α_m and N_r as,

$$\alpha_e = N_r \alpha_m \tag{3.3}$$

3.2.2 Conditions for Symmetrical Bipolar Phase Back-EMF

Among all the combinations for single-tooth VFRMs, symmetrical bipolar phase flux-

linkage and back-EMF waveforms can be obtained when $N_r = N_s \pm 1$ with 6-pole stator [LIU08a]. It is due to that individual coils in the same phase are connected in series with 180 electrical degrees shifting (opposite polarities) as shown in Fig. 3.2. Thus, all the even order harmonics in a single coil which cause the back-EMF waveform asymmetric and slant to right or left in half electrical cycle are cancelled completely in the phase winding, Fig. 3.3 and Fig. 3.4.

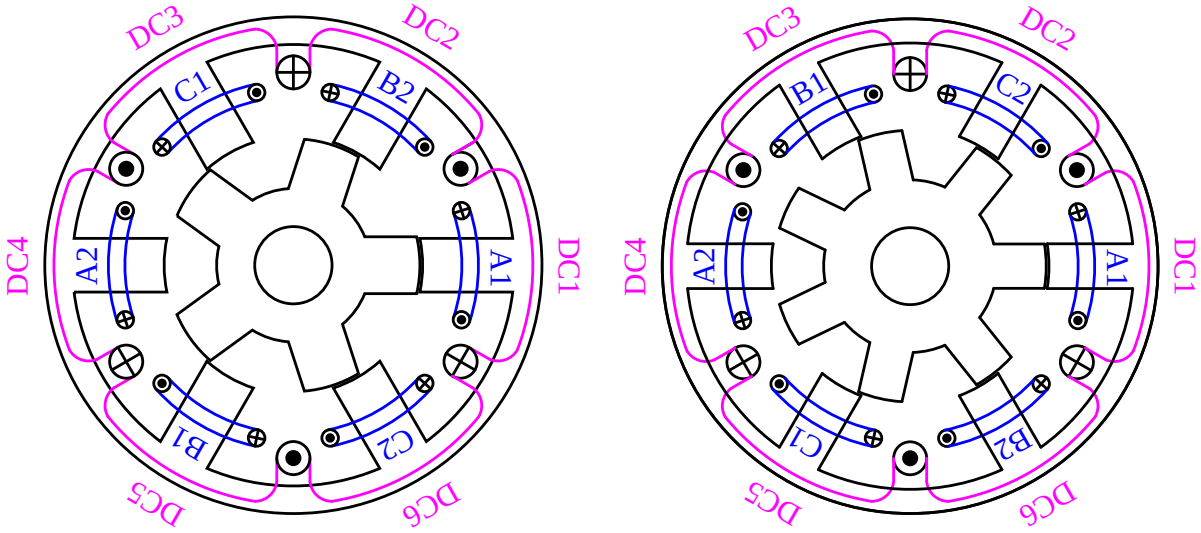

(a) 1×6S/5R (b) 1×6S/7R

Fig. 3.2. Topologies of single-tooth VFRMs with $N_r = N_s \pm 1$.

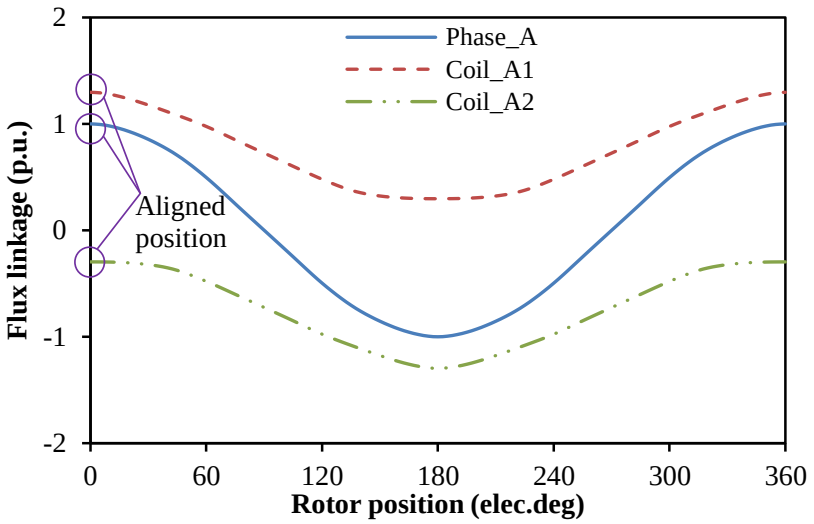

Fig. 3.3. Per-unit open-circuit flux-linkages of phase A, coil A1 and coil A2 when $N_r = N_s \pm 1$.

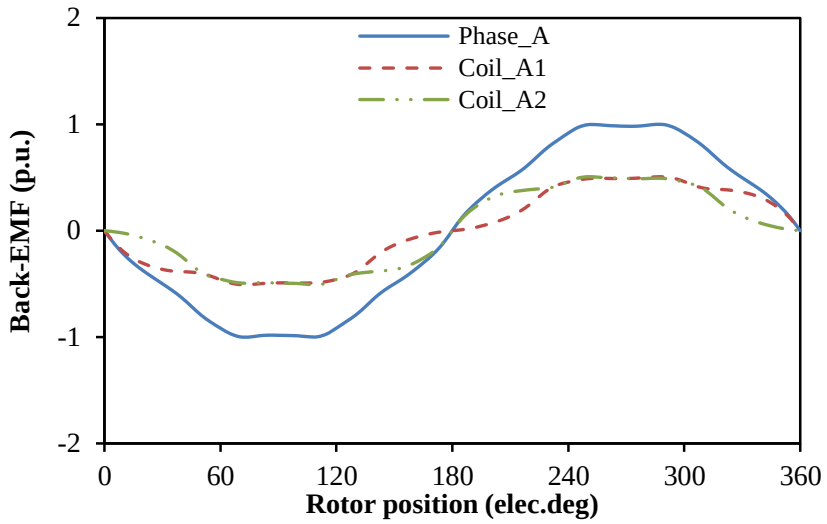

(a) Waveform

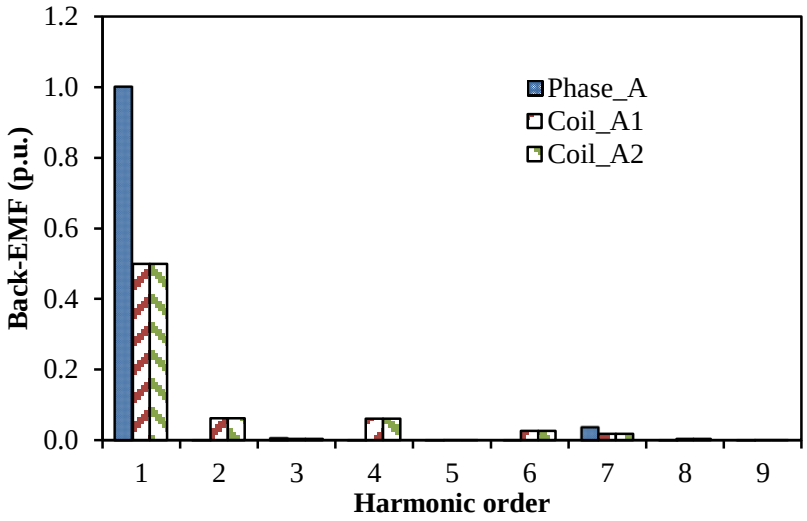

(b) Spectrum

Fig. 3.4. Per-unit open-circuit back-EMF of phase A, coil A1 and coil A2 when $N_r = N_s \pm 1$

For multi-tooth VFRMs, the flux linkage and back-EMF waveforms of a single coil may also be asymmetric in half electrical cycle. In order to obtain symmetrical bipolar phase flux-linkage and back-EMF waveforms by 180 electrical degrees phase shifting between the coils, two conditions should be satisfied. First, the number of coils per phase must be even. Second, the angular phase difference θ_d between two coils belong to the same phase must satisfy:

$$\theta_d = 2\pi N_r N_{pp}/N_s = (2k_j - 1)\pi \tag{3.4}$$

where k_j is an integer, and N_{pp} is the spatial span number of stator pole pitch between the two coils. Alternately, (Fig. 3.4) can be rewritten as

$$\frac{N_r}{N_s} = \frac{(2k_j - 1)}{2N_{pp}} \tag{3.5}$$

($2k_j$-1) and $2N_{pp}$ are odd and even integers respectively. As a conclusion, in order to obtain symmetrical phase back-EMF waveforms, the stator and rotor pole combinations should be satisfied by [CHE08]

$$\frac{N_s}{GCD(N_s,N_r)} = \text{even number} \tag{3.6}$$

where *GCD* means the greatest common divisor. By way of example, for the VFRM under investigation, 1×6/5, 1×6/7, 2×6/13, 4×6/23, and 4×6/25 *n*×stator/rotor pole combinations have symmetrical phase back-EMFs [LIU12b].

3.3 Analysis of Multi-Tooth VFRMs

In this section, in order to analyse the influence of N_s, N_r, n on the average torque of VFRM, the average output torque equation based on a simplified permeance and magnetic circuit model developed.

3.3.1 Torque Equation

Since VFRM is a special stator DC field excited synchronous machine having negligible reluctance torque [WU14], the average torque is maximum under zero *d*-axis current (I_d=0) control and can be expressed by:

$$T = \frac{3}{2} N_r \psi_{DC} I_q \tag{3.7}$$

where I_q is the *q*-axis current, ψ_{DC} is the DC field flux-linkage.

3.3.2 Permeance Model

Fig. 3.5 shows an ideal schematic of multi-tooth VFRM when N_s=6 and n=4. N_{sa} and N_{rb} are the integers representing all the stator and rotor poles respectively. The dashed line means the aligned position that the first stator pole N_{s1} is aligned with the middle of first rotor pole N_{r1}.

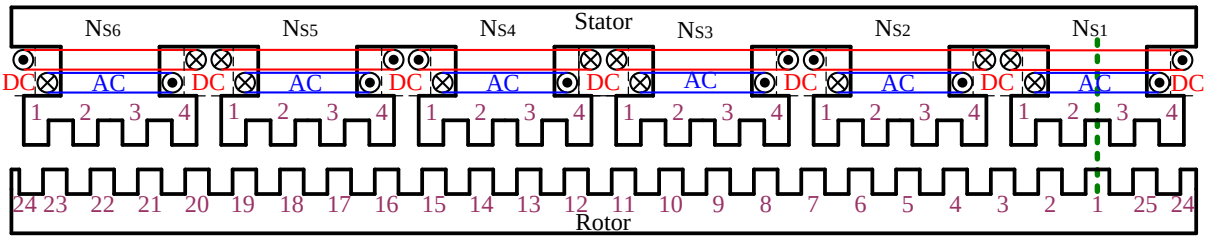

Fig. 3.5. Ideal schematic of multi-tooth VFRMs when n=4.

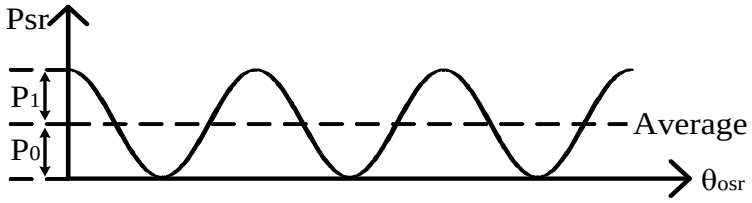

Fig. 3.6. Ideal permeance variation with rotor position.

As shown in Fig. 3.5, Fig. 3.6 and [CHE08], when n=1 (single-tooth VFRM), the permeance P_{sp} between a single stator tooth and the complete rotor can be expressed as

$$P_{sp}(\theta_{sr}) = P_0 + \sum_{v=1,3,5\ldots} P_v \cos(N_r v \theta_{sr}) \tag{3.8}$$

where P_0 is the average air-gap permeance, P_v is the magnitude of the v^{th} permeance harmonic, and θ_{sr} is the position difference between the middle of the single stator tooth and rotor pole referred to the aligned position. Then the permeance between a stator pole having n small teeth and the complete rotor is

$$P_{sp} = \sum_{i=1}^{n} P_{sp}(\theta_{srki}) \tag{3.9}$$

where θ_{srki} is the position difference between the middle of i^{th} small stator tooth and the rotor pole referred to the aligned position.

In this section, the influence *of* N_s, N_r, n will be focused on the average torque. Hence, high order permeance harmonics can be ignored. The permeance between one stator pole and complete rotor pole consisting the DC and fundamental components can be expressed as (3.10) according to the results shown in the section 3.8.1 of Appendix.

$$P_{sp} = nP_0 + P_1 \cdot \sum_{i=1}^{n} \cos\left(N_r \cdot \theta_{0sr} + \frac{n-(2i-1)}{2n} \cdot \frac{2\pi}{N_s} \cdot N_r + (n+1) \cdot \pi\right) \tag{3.10}$$

where θ_{osr} is the relative position difference between the middle of one stator pole and one rotor pole referred to the aligned position. The parameter of (n+1) π in (3.10) is employed to ensure the permeance is maximum at aligned position when θ_{osr} = 0 (at the aligned position, when n is even, the permeance of stator pole is minimum since the rotor pole is aligned with middle of the small slot in the stator pole, which is opposite with n is odd, as shown in Fig. 3.1(b) and (d)).

Based on (3.10), when considering the permeance of different stator pole P_{Nsa} to the complete rotor pole, the position difference between two stator poles should be considered. According to the results shown in the section 3.8.2 of Appendix, the permeance P_{Nsa} between

the stator pole N_{sa} and the complete rotor can be expressed as

$$P_{N_{sa}} = nP_0 + P_1 \cdot \sum_{i=1}^{n} \cos\left(N_r \cdot \theta_{0sr} + \frac{n-(2i-1)}{2n} \cdot \frac{2\pi}{N_s} \cdot N_r + (n+1) \cdot \pi + \frac{2\pi}{N_s} \cdot (Nsa-1) \cdot N_r\right) \tag{3.11}$$

3.3.3 Influence of Parameters on Average Torque

Since the single- and multi-tooth VFRMs satisfying (3.6) exhibits better EMFs than other combinations, the influence of parameters on the average torque is analyzed in this type of VFRM having 6-pole stator as an example. However, the following analysis methods are also applicable to the other stator/rotor pole combinations.

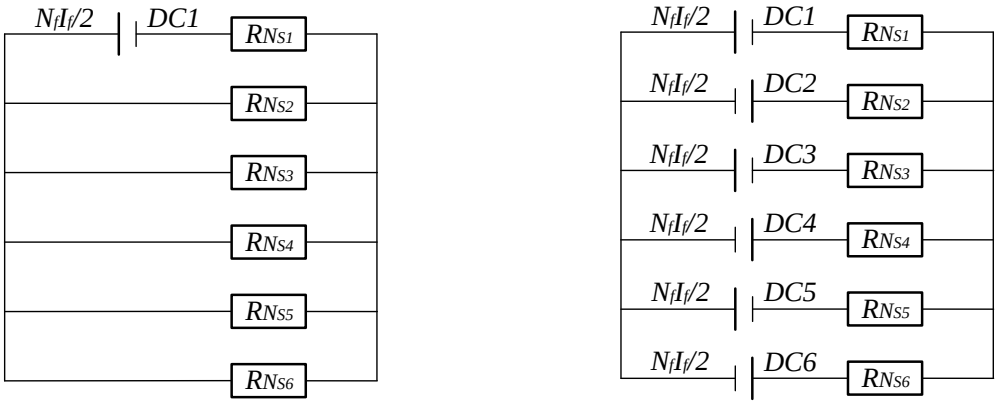

(a) With only one DC coil excited (b) With all DC coils excited

Fig. 3.7. Magnetic circuit model of 3 phase 6 stator pole VFRMs.

For VFRMs having 6-pole stator, the magnetic circuit models having only one or all DC coil excited are illustrated in Fig. 3.7(a) and (b) respectively. Based on (3.3), the winding configurations of 6-pole stator single- and multi-tooth VFRMs which stator and rotor pole combinations satisfying (3.6) are the same as the example shown in Fig. 3.2. Then, according to the Fig. 3.5 and Fig. 3.7(a), when only DC1 (DC coil wound around the stator pole N_{S1}) is excited, the direction and magnitude of induced MMFs in coils A1 and A2 are obtained and shown in section 3.8.3 of Appendix. "+" and "-" as shown in Table 3.3 refer to the same and opposite directions between MMF of DC coil and corresponding induced MMFs of coils A1 and A2 respectively. Based on the same means, the MMFs of coils A1 and A2 which are separately induced by DC2-DC6 can also be obtained. Further, according to Fig. 3.7(b), when all DC coils are excited, the induced MMFs of coils A1 and A2 can be obtained by adopting the superposition method as shown in section 3.8.3 of Appendix and expressed as (3.12) and

(3.13) respectively.

$$F_{(CA_1,DC_1\sim DC_6)} = N_f I_f \cdot \frac{P_{Ns2} + P_{Ns4} + P_{Ns6}}{\sum_{a=1}^{6} P_{Nsa}} \tag{3.12}$$

$$F_{(CA_2,DC_1\sim DC_6)} = -N_f I_f \cdot \frac{P_{Ns1} + P_{Ns3} + P_{Ns5}}{\sum_{a=1}^{6} P_{Nsa}} \tag{3.13}$$

Meanwhile, based on the waveforms of phase- and coil-flux linkages shown in Fig. 3.3, the peak value of open-circuit phase flux Φ_{PA} (or phase flux linkage, Ψ_{PA}) can be obtained by the sum of the coil fluxes Φ_{CA1} and Φ_{CA2} (or coil flux linkages, Ψ_{CA1}, Ψ_{CA2}) at aligned position (θ_{osr}=0) as

$$\Phi_{PA} = \Phi_{CA1} + \Phi_{CA2} \tag{3.14}$$

$$\Phi = FP \tag{3.15}$$

where Φ is flux, F is MMF and P is permeance.

Combined with equations (3.14), (3.15) and Fig. 3.7, the peak value of open-circuit phase flux Φ_{PA} can be given by

$$\Phi_{PA} = N_f I_f \cdot \left(\frac{P_{Ns2} + P_{Ns6}}{\sum_{a=1}^{6} P_{Nsa}} \cdot P_{Ns1} - \frac{P_{Ns3} + P_{Ns5}}{\sum_{a=1}^{6} P_{Nsa}} \cdot P_{Ns4} \right) \tag{3.16}$$

The peak value of open-circuit phase flux linkage Ψ_{PA} can then be obtained as

$$\Psi_{PA} = \frac{1}{2} N_a \cdot \Phi_{PA} \tag{3.17}$$

where N_a is the number of turns per phase of armature windings, N_f is the number of turns per phase of DC field windings (two DC field coils, the total numbers of turns of DC field windings is 3 N_f), I_f is DC field current.

Hence, based on (3.7), (3.11), (3.16) and (3.17), the average torque can be given as

$$T = \frac{3}{4\sigma} N_r N_a I_a N_f I_f \left(\frac{P_{Ns2} + P_{Ns6}}{\sum_{a=1}^{6} P_{Nsa}} \cdot P_{Ns1} - \frac{P_{Ns3} + P_{Ns5}}{\sum_{a=1}^{6} P_{Nsa}} \cdot P_{Ns4} \right) \tag{3.18}$$

where σ is a leakage flux factor. The leakage flux of VFRMs will be increased with the increase of small tooth number per stator pole n due to the reduced width of slot opening accordingly, as shown in Fig. 3.9. The leakage flux factor can be estimated by the ratio of the flux pass through one big stator tooth (stator pole) to the flux pass through the air-gap under one stator pole pitch.

Assume the ratio of AC peak value I_a to DC value I_f is $\sqrt{2}$ as (3.19) and the total number of turns per phase is N_p. Thus, the ratio of p_a/p_f (copper loss of armature winding to DC field

winding) under fixed copper loss can only be adjusted by changing the ratio of N_a/N_f since the total number of turns per phase is fixed as shown in (3.20). Then, combined with (3.20), equation (3.18) can be rewritten as (3.21). To obtain the maximum average torque under fixed copper loss, equation (3.22) should be zero. Equation (3.23) shows that $N_f = N_a$ is the optimal condition for maximum average torque under fixed copper loss when $I_a / I_f = \sqrt{2}$. Correspondingly, the optimal copper loss ratio of p_a to p_f is equal to 1 as shown in (3.24).

$$I_a/I_f = \sqrt{2} \tag{3.19}$$

$$N_p = N_a + N_f \tag{3.20}$$

$$T = \frac{3}{4\sigma} N_r N_a I_a (N_P - N_a) I_f \left(\frac{P_{Ns2} + P_{Ns6}}{\sum_{a=1}^{6} P_{Nsa}} \cdot P_{Ns1} - \frac{P_{Ns3} + P_{Ns5}}{\sum_{a=1}^{6} P_{Nsa}} \cdot P_{Ns4} \right) \tag{3.21}$$

$$\frac{\partial \mathrm{T}}{\partial \mathrm{N}_a} = \frac{3}{4\sigma} N_r (N_P - 2N_a) I_a I_f \left(\frac{P_{Ns2} + P_{Ns6}}{\sum_{a=1}^{6} P_{Nsa}} \cdot P_{Ns1} - \frac{P_{Ns3} + P_{Ns5}}{\sum_{a=1}^{6} P_{Nsa}} \cdot P_{Ns4} \right) \tag{3.22}$$

$$N_f = N_a = N_p/2 \tag{3.23}$$

$$p_f = p_a = p_C/2 \tag{3.24}$$

With constraint of fixed total copper loss and optimal condition for maximizing the average torque, the relationship between armature/excitation MMFs and slot area *S* can be given as

$$N_a I_a N_f I_f \propto S \tag{3.25}$$

According to (3.18), the average torque of single- and multi-tooth VFRMs can be obtained and is mainly dependent on the number of stator poles N_s, the number of rotor poles N_r, the number of small teeth per stator pole *n*, slot area *S* (proportional to $N_a I_a N_f I_f$ as shown in (3.25) under fixed copper loss) and leakage flux factor σ. Equation (3.18) can be used to explain the torque variation with N_s, N_r and *n* in the following sections. Equations (3.19), (3.22), (3.23) and (3.24) shows that the average torque of VFRM will be maximum under the fixed total copper loss when the excitation and armature copper losses are equal, i.e. $p_f = p_a$ ($N_a = N_f$, $I_{arms} = I_f$) [LIU12d] [ZHU00].

3.4 Main Stator and Rotor Pole Combinations of Multi-tooth VFRMs

In this section, the torque of VFRMs with different *n* while $N_r = nN_s \pm 1$ will be compared first. Then, as an example, the performance of 6/7 stator/rotor pole single-tooth VFRM and 6/25 stator/rotor pole 4-tooth VFRM will be compared.

3.4.1 Torque Performance of VFRMs with *n* when *Nr=nNs*±1

Since single-tooth VFRMs normally exhibit optimal torque capability when the number of rotor pole and stator pole differed by one, the torque variation of VFRMs with *n* in 6-pole stator is investigated when $N_r=nN_s\pm1$ in this section, as shown in Fig. 3.8. Obviously, 4-tooth VFRMs with $N_r=nN_s\pm1$ exhibits the largest average torque due to the combined influence of parameters listed in (3.18) and (3.25) at rated 30W total copper loss and same stator outer radius. Moreover, it should be noted that the average torque of VFRMs with $N_r=nN_s+1$ are larger than that of $N_r=nN_s-1$ when $n \leq 3$ but smaller when $n \geq 5$ due to the influence of leakage flux.

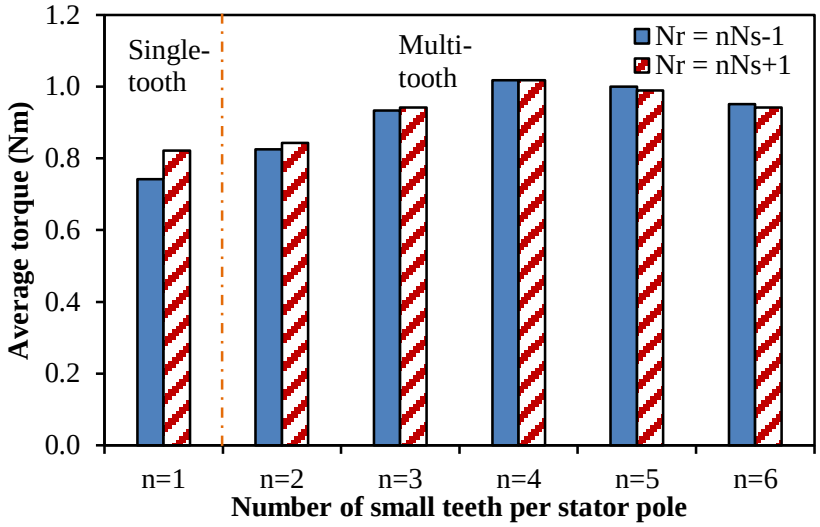

Fig. 3.8. Variation of average torque with number of small teeth per stator pole *n* when $N_r=nN_s\pm1$, $N_s=6$ and $p_f = p_a = 15$W.

In the following subsections, in order to further analyse the influence of N_s, N_r and *n*, the electromagnetic performance of single- and 4-tooth VFRMs with $N_r=nN_s+1$ are selected for comparison since the 6/7 stator/rotor pole VFRM exhibits the highest average torque among the 6-stator pole single-tooth VFRMs as shown in Fig. 3.8 [SHI14a]. All the machines are globally optimized with maximum average torque under the same rated copper loss and stator outer radius. Their main parameters are detailed in Table 3.1. For all the combinations, the winding configurations can be obtained based on the method mentioned in section 3.2. (The winding configuration of 6/25 stator/rotor pole 4-tooth VFRM is same as that of 6/7 stator/rotor pole single-tooth VFRM which shown in Fig. 3.2(b))

Table 3.1 Main parameters of single- and multi-tooth VFRMs

Parameter	**n=1**	**n=4**			
Number of phases	3				
Turns per coil (AC/DC)	36/36				
Rated speed (rpm)	400				
Rated copper loss (W)	30				
Packing factor	0.5				
Airgap length (mm)	0.5				
Active axial length (mm)	25				
Stator outer radius (mm)	45				
Stator pole number, N_s	6				
Rotor pole number, N_r	7	22	23	25	26
Split ratio	0.56	0.53	0.55	0.55	0.54
Rotor outer radius (mm)	24.7	23.35	24.25	24.25	23.8
Stator back iron (mm)	4.4	7.2	6.4	6.2	6.8
Stator small slot depth (mm)	-	1.6	1.5	1.5	1.4
Slot area (mm^2)	405	201	205	221	223
Rated AC/DC current (A_{rms})	10.40	7.31	7.39	7.67	7.71
Rated current density (A_{rms}/mm^2)	7.40	10.48	10.38	9.99	9.94
Stator big tooth width (mm)	8.1	12.4	12.8	12.2	11.6
Stator small tooth pole arc (mech.deg)	-	8.0	7.7	7.1	6.8
Rotor pole arc (mech.deg)	18.8	U:4.6 D:9.0	U:4.8 D:8.0	U:4.4 D:8.2	U:4.0 D:8.8
Rated electric frequency (Hz)	46.7	146.7	153.3	166.7	173.3
Power factor	0.44	0.16	0.14	0.13	0.12

3.4.2 Open-Circuit Field Distribution

Fig. 3.9 shows the open circuit equipotential and flux density distributions of single- and 4-tooth VFRMs at the aligned position under the rated DC field currents (p_f = 15W for both machines). It can be seen that when stator and rotor pole combination is determined by N_r=nN_s+1, both machines have short flux path and the coils belong to the same phase have completely independent flux loop.

The open-circuit air-gap flux density waveforms of two VFRMs at the aligned position are

shown in Fig. 3.10. It can be seen that the peak number of air-gap flux density under each coil depends on the number of small teeth per stator pole *n*, such as 4 peaks in multi-tooth VFRM with *n*=4.

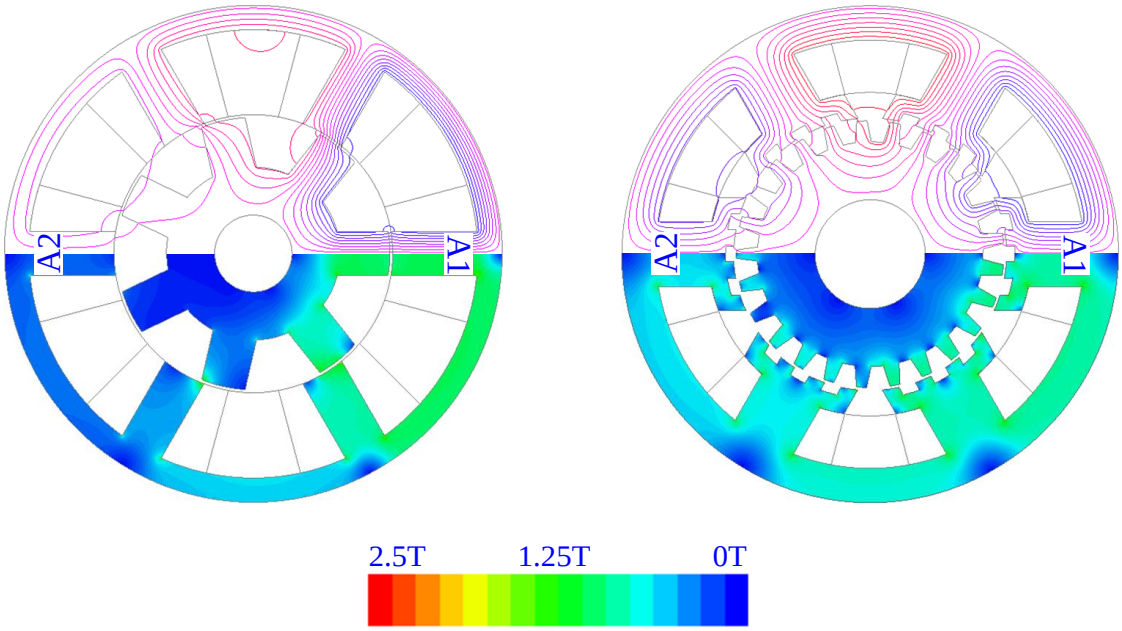

(a) 1×6S/7R (b) 4×6S/25R

Fig. 3.9. Open-circuit equipotential and flux density distributions of single- and multi-tooth VFRMs, p_f=15W.

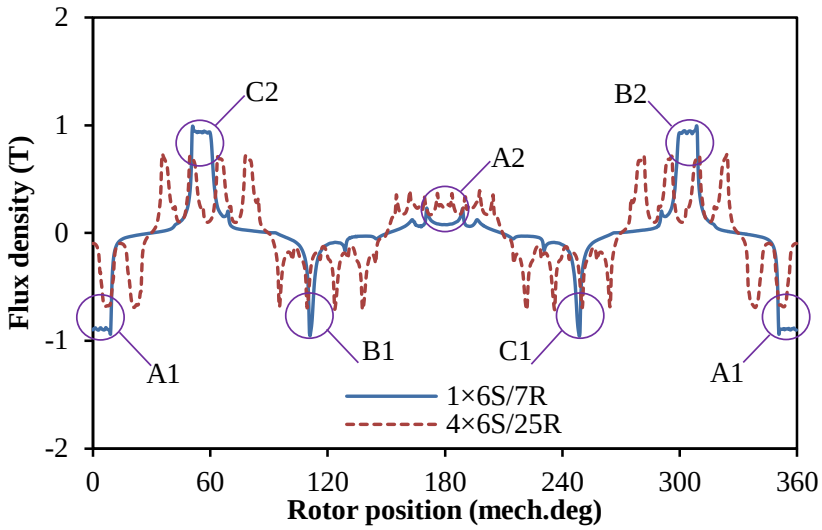

Fig. 3.10. Open-circuit air-gap flux density of single- and multi-tooth VFRMs at aligned position, p_f=15W.

3.4.3 Flux-Linkage and Back-EMF Waveforms

The flux-linkages and back-EMFs of 1×6/7 and 4×6/25 stator/rotor pole VFRMs are compared in Fig. 3.11, Fig. 3.12 and Table 3.2 respectively. It can be seen that the flux-

linkages of coils A1 and A2 in two machines are both unipolar and with 180 electric degree shifting as well as opposite polarity. However, the resultant phase flux-linkage (phase A) is bipolar and symmetric. Correspondently, the phase back-EMFs are symmetrical and essentially sinusoidal due to the cancellation of all even harmonics which cause the asymmetry in each coil. Hence, these two examples can be used to validate the (3.6). Moreover, due to the influence of rated electric frequency (46.7Hz in 1×6/7 stator/rotor pole VFRM and 166.7Hz in 4×6/25 stator/rotor pole VFRM), the 4×6/25 stator/rotor-pole VFRM exhibits 78% higher fundamental back-EMF than that of 1×6/7 stator/rotor pole VFRM while p_f=15W despite of a lower fundamental flux linkage as shown in Table 3.2 and Fig. 3.12.

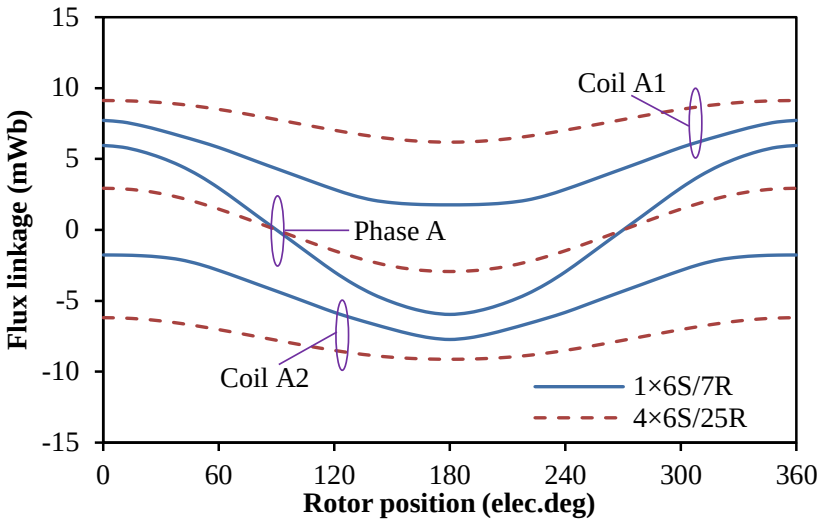

Fig. 3.11 .Open-circuit phase and coil flux-linkage of single- and multi-tooth VFRMs, p_f=15W.

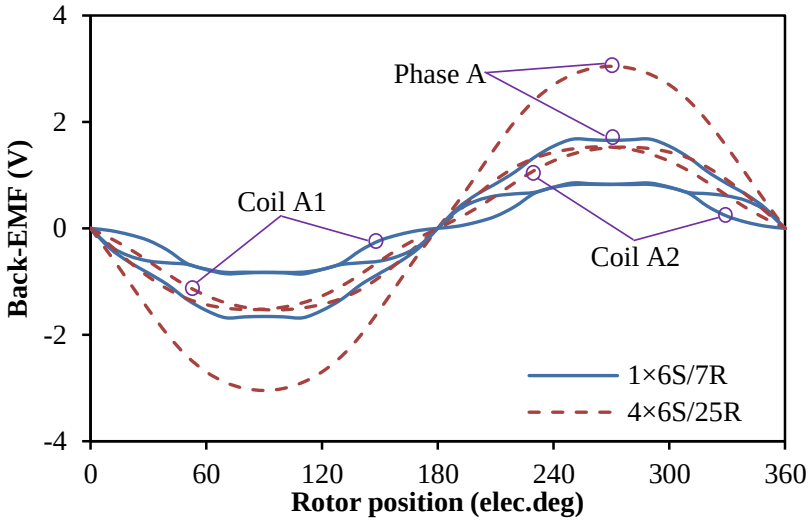

Fig. 3.12. Open-circuit phase and coil back-EMF of single-and multi-tooth VFRMs, p_f=15W, 400rpm.

3.4.4 Self- and Mutual-Inductances

The self- and mutual-inductances between armature windings of single- and 4-tooth VFRMs are shown in Fig. 3.13. p_a = 5W is corresponding to the copper loss produced by the positive DC current which is injected into the phase A winding. The 4×6/25 stator/rotor pole VFRM exhibits higher self- and mutual inductances, which is about 2.4 and 2.5 times of those for 1×6/7 stator/rotor pole VFRM, respectively.

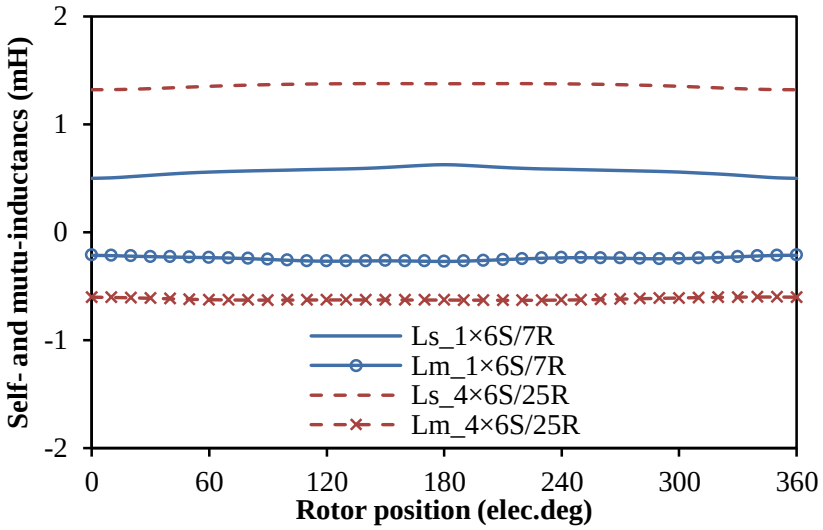

Fig. 3.13 .Self- and mutual inductances between armature windings of single- and multi-tooth VFRMs, p_f=15W, p_a=5W.

3.4.5 Torque Characteristics

In VFRMs, the cogging torque is defined as the static torque when DC field windings are excited with the DC currents while the AC armature coils are not excited [LIU12b]. Fig. 3.14 shows the cogging torque waveforms over one electric period for single-and 4-tooth VFRMs with rated DC current when p_f =15W. Compared with the single-tooth VFRM with 1×6/7 stator/rotor pole, the cogging torque of 4-tooth VFRM with 4×6/25 stator/rotor pole is much smaller and negligible.

Fig. 3.15 shows the waveforms of average torque against current angle at rated copper loss for single- and 4-tooth VFRMs. It can be seen that the optimal current angles of two machines are both close to 0°, which means the reluctance torques are negligible.

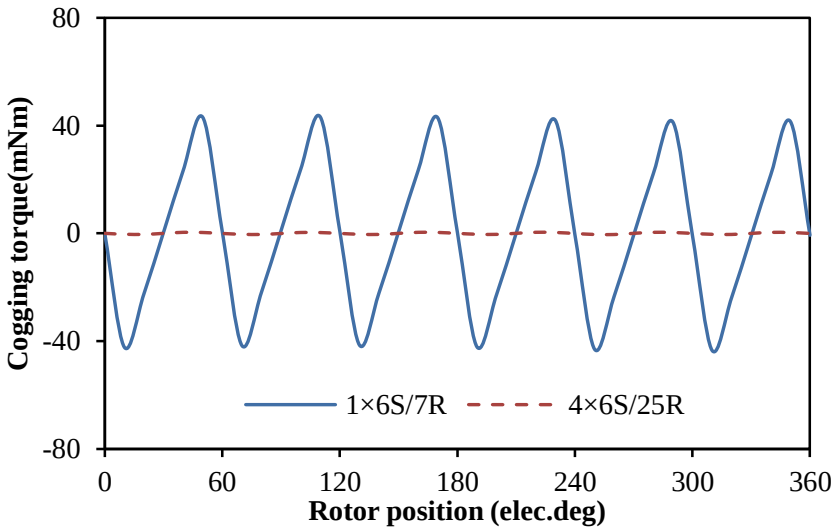

Fig. 3.14 .Open-circuit cogging torque of single- and multi-tooth VFRMs, p_f=15W.

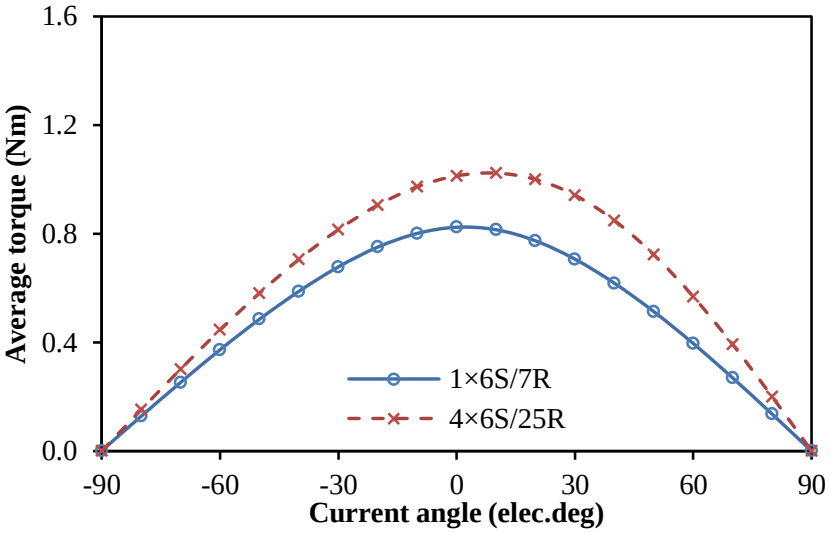

Fig. 3.15 .Variation of average torque with current angle in single-and multi-VFRMs, $p_f = p_a$ = 15W.

The torques of single- and 4-tooth VFRMs when the total copper loss is 30W and I_d = 0 control are compared in Fig. 3.16 and Table 3.2. It can be seen that the average torque of 4-tooth VFRM with 4×6/25 stator/rotor pole is about 24% higher than that of single-tooth VFRM with 1×6/7 stator/rotor pole. Meanwhile, the torque waveforms of both machines have six pulsations over one electric period. Further, the torque ripple of 4-tooth VFRMs is smaller than that of single-tooth VFRM, which are 4.6% and 10.4% respectively, as shown in Table 3.2.

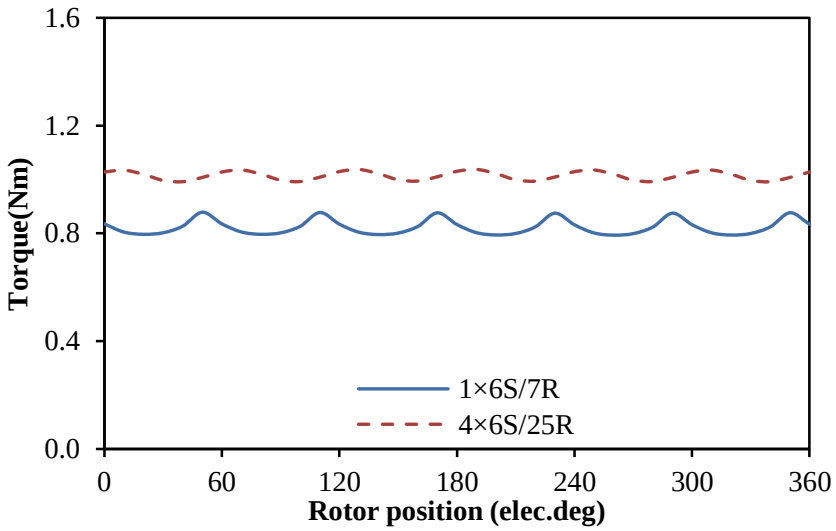

(a) Waveform

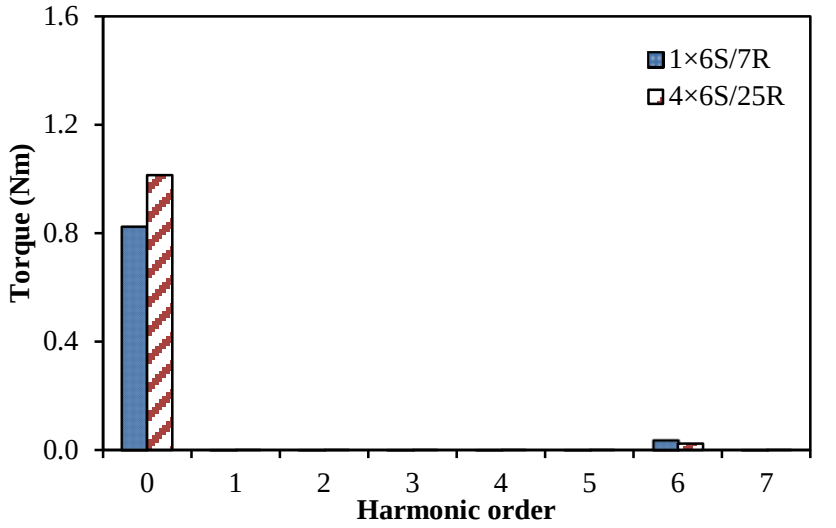

(b) Spectrum

Fig. 3.16 .Variation of electromagnetic torque with rotor position in single- and multi-VFRMs, $p_f = p_a$ = 15W, I_d = 0 control.

The variations of the average torque with the copper loss for two VFRMs are further shown in Fig. 3.17. The vertical dashed and dotted line indicates the rated copper loss, which is used during the optimization. According to (3.18) and (3.25), the phase armature- and DC field-current will be increased with the increase of copper loss, thus results in higher average torque as shown in Fig. 3.17. However, the increasing rate will gradually diminish for both machines due to magnetic saturation. Compared with single-tooth VFRM, the average torque of 4-tooth VFRM is larger at relatively low copper loss (electric loading) but smaller at high copper loss since the saturation of magnetic circuit is quicker due to bigger inductance and higher armature reaction.

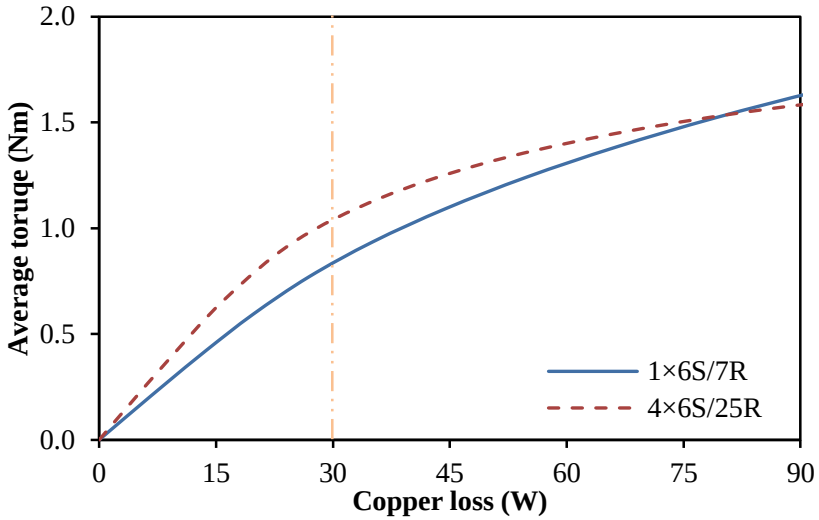

Fig. 3.17 .Variation of average torque with copper loss in single- and multi-VFRMs, $p_f = p_a$, $I_d = 0$ control.

3.4.6 Iron Loss and Efficiency

Fig. 3.18 shows the waveforms of iron loss against speed at rated copper loss for single- and 4-tooth VFRMs. It can be seen that the 4×6/25 stator/rotor pole VFRM exhibits larger iron loss than that of 1×6/7 stator/rotor pole VFRM at the same speed since the 4-tooth VFRM has higher frequency than the single-tooth VFRM. Moreover, as shown in Fig. 3.19, for both single-tooth and multi-tooth VFRMs, the saturation level and total saturation area in the stator are much heavier and larger than those in the rotor. Consequently, the iron loss in the stator will be higher than that in the rotor. It can be evidenced by the results shown in Fig. 3.18.

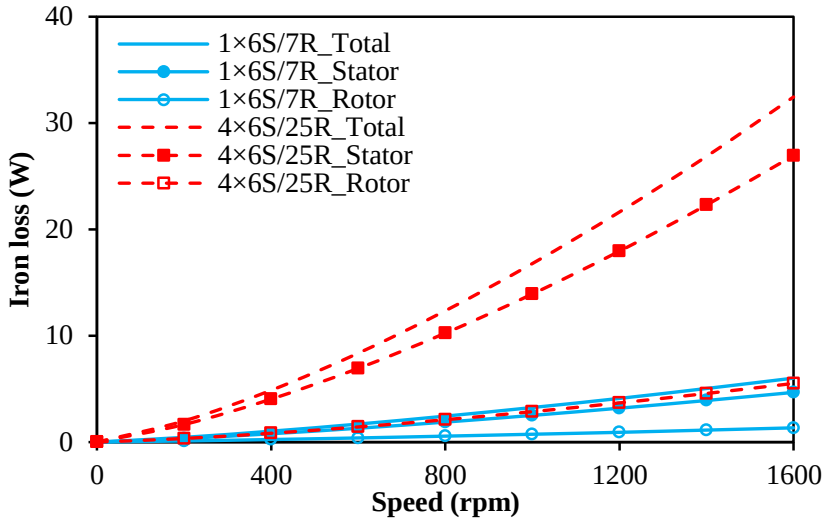

Fig. 3.18. Variation of iron loss with speed in single- and multi-VFRMs, $p_f = p_a$ 15W, $I_d = 0$ control.

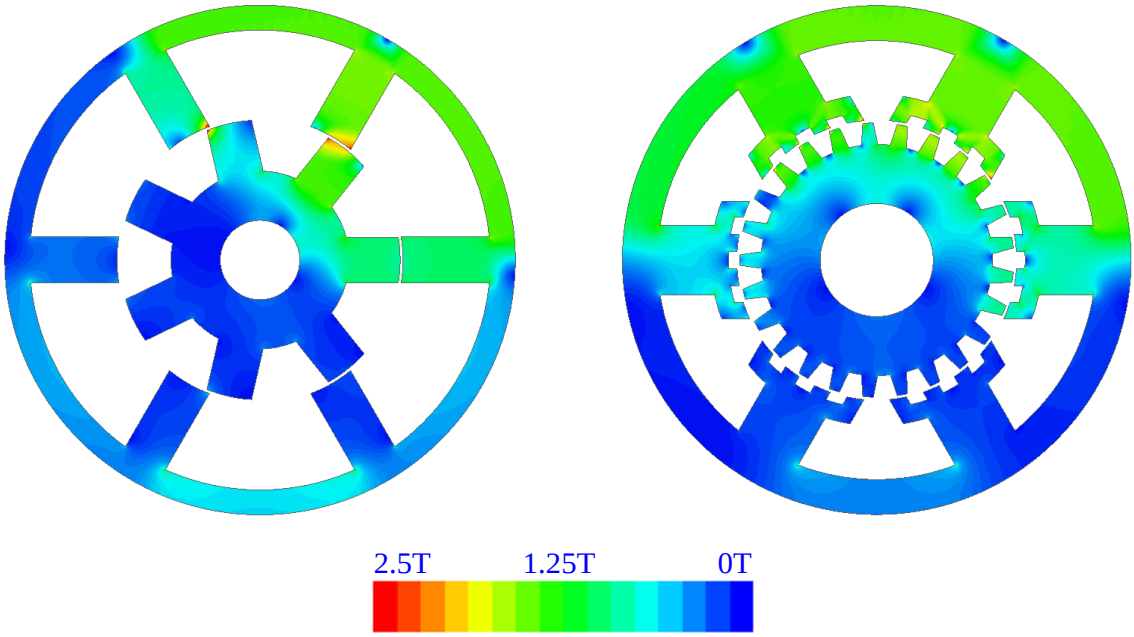

(a) 1×6S/7R (b) 4×6S/25R

Fig. 3.19. On-load flux density distributions of single- and multi-VFRMs, $p_f = p_a$ 15W, $I_d = 0$ control.

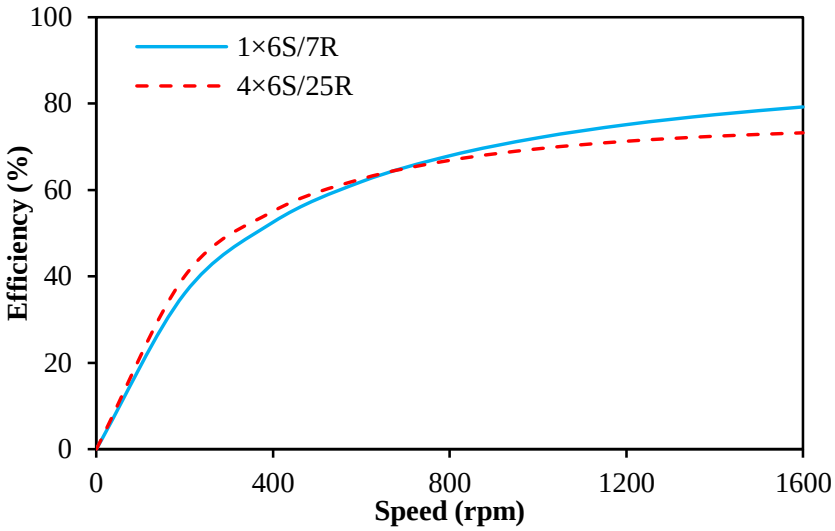

Fig. 3.20. Variation of efficiency with speed in single- and multi-VFRMs, $p_f = p_a$ 15W, $I_d = 0$ control.

The curves of efficiency against speed for single- and 4-tooth VFRMs at rated copper loss are compared in Fig. 3.20. Compared with 1×6/7 stator/rotor pole VFRM, the efficiency of 4×6/25 stator/rotor pole VFRM is higher at relatively low speed (< 670 rpm) but lower at high speed (> 670 rpm) since the increasing rate of iron loss in 4-tooth VFRM is larger than that of single-tooth VFRM. Meanwhile, the rated efficiency for 1×6/7 and 4×6/25 stator/rotor

pole VFRMs under the rated copper loss (30W) and rated speed (400rpm) are 52.5% and 55.1% respectively, as shown in Table 3.2.

Table 3.2 Main electromagnetic performance ($P_f = P_a$ =15W)

Parameter	**n=1**	**n=4**			
Rotor pole number, Nr	7	22	23	25	26
Rated electric frequency (Hz)	46.7	146.7	153.3	166.7	173.3
Fund. flux-linkage (Wb)	5.91	3.26	3.37	2.95	2.58
Fund. back-EMF (V)	1.73	3.0	3.24	3.08	2.81
Rated iron loss (W)	1.03	5.03	4.46	4.88	6.40
Rated efficiency (%)	52.5	51.8	55.4	55.1	50.6
Average torque (Nm)	0.82	0.90	1.02	1.02	0.89
Torque ripple (%)	10.4	74.4	4.4	4.6	79.5

3.5 Performance Comparison of 4-Tooth VFRMs

Among the 6-stator pole VFRM and different *n*, 4-tooth VFRMs exhibits the largest average torque at the conditions of rated 30W total copper loss and same stator outer radius according to $N_r=nN_s\pm1$ as shown in Fig. 3.8. Hence, the main stator and rotor pole combinations of 4-tooth VFRM with 6-stator pole will be compared in this section.

3.5.1 Main Stator and Rotor Pole Combinations while *n*=4

The main stator and rotor pole combinations of 4-tooth VFRM with 6-stator pole as $N_r=nN_s\pm1$ and $N_r=nN_s\pm2$ are shown in Fig. 3.21. Meanwhile, the main parameters of all the machines which are optimized for maximum average torque under rated copper loss are also listed in Table 3.1.

As shown in Fig. 3.21, the coil connections of 4-tooth VFRMs with $N_r=nN_s\pm1$ or $N_r=nN_s\pm2$ are satisfied with (3.3), by which the coils A1 and A2 belong to the same phase are connected in series with 180 electric degree shifting (opposite polarity) when $N_r=nN_s\pm1$ but with same polarity when $N_r=nN_s\pm2$.

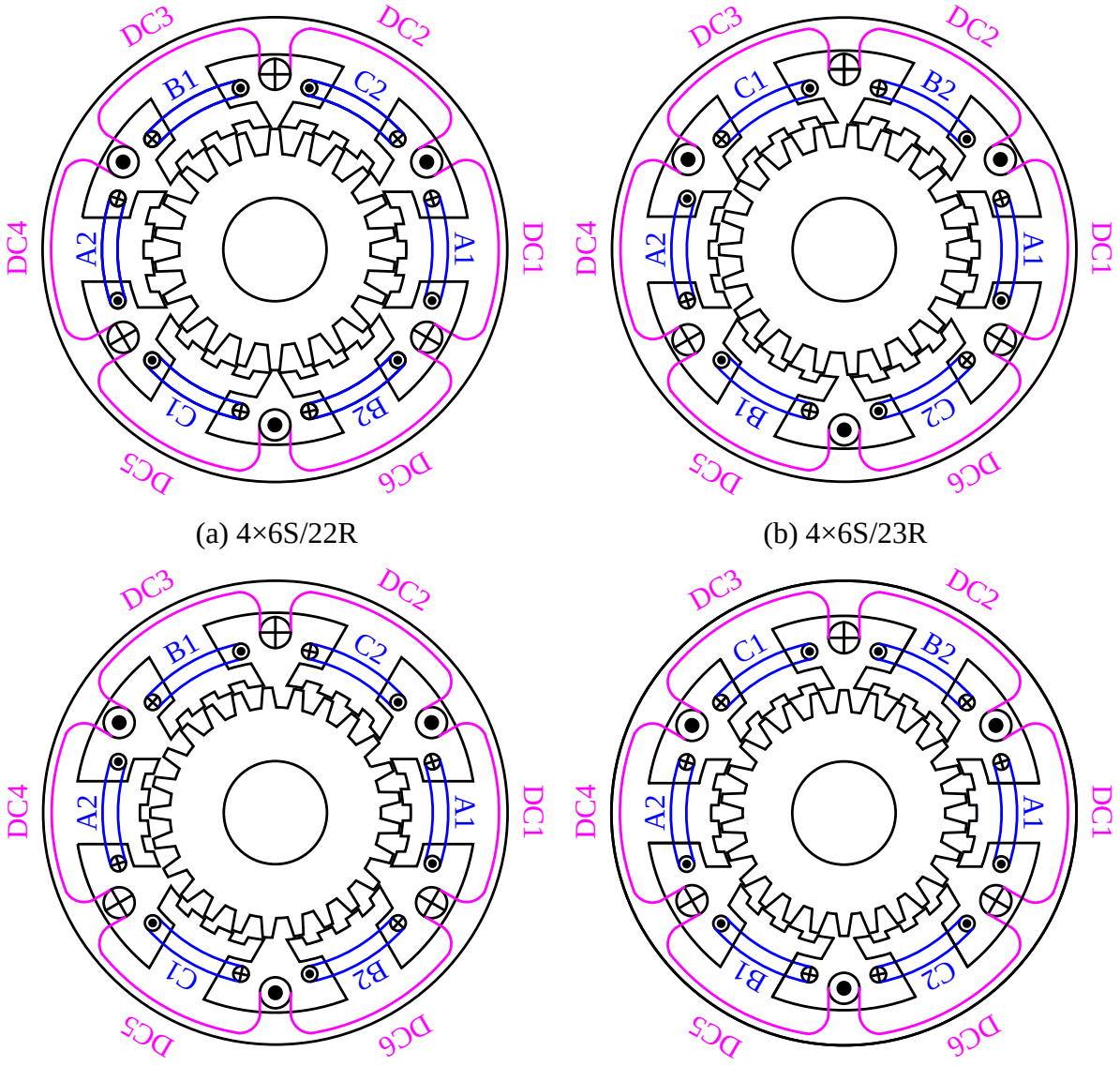

(a) 4×6S/22R (b) 4×6S/23R

(c) 4×6S/25R (d) 4×6S/26R

Fig. 3.21. Topologies of multi-tooth VFRMs, n=4, $N_r = nN_s \pm 1$ or $N_r = nN_s \pm 2$.

3.5.2 Flux-Linkage and Back-EMF Waveforms

The open-circuit phase flux-linkages of four machines are compared in Fig. 3.22 and Table 3.2. It can be seen that the phase flux-linkages of 4×6/23 and 4×6/25 stator/rotor pole ($N_r = nN_s \pm 1$) VFRMs are bipolar while those of 4×6/22 and 4×6/26 stator/rotor pole ($N_r = nN_s \pm 2$) VFRMs are unipolar, which are consistent with the conclusion of single tooth VFRMs. Moreover, the effective flux linkage component, which is the peak to peak value of the flux linkage variation, of 4×6/23 stator/rotor pole VFRM is the largest among the four machines, as show in Table 3.2. It caca be reflected by magnitudes of fundamental waveforms as shown in Fig. 3.22.

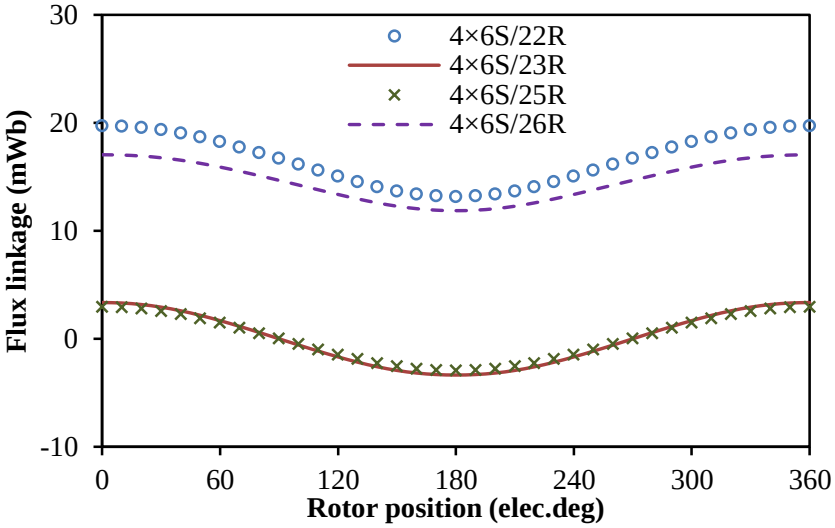

(a) Waveform

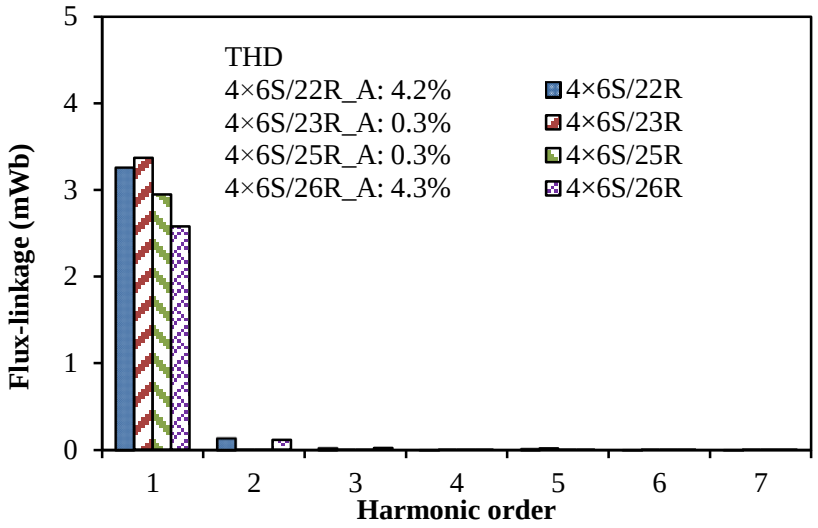

(b) Spectrum

Fig. 3.22. Open-circuit phase flux-linkages of multi-tooth VFRMs, n=4, p_f=15W.

Fig. 3.23 shows the open-circuit phase back-EMFs of four machines. The back-EMF waveforms of 4-tooth VFRMs with $N_r = nN_s \pm 1$ are more sinusoidal since the even harmonics in that of $N_r = nN_s \pm 2$ are cancelled. It is also confirmed by harmonic analysis and total harmonic distortion (THD) results shown in Fig. 3.23(b). Further, considering the influence of electric frequency under rated rotation speed (400 rpm), 4×6/23 stator/rotor pole VFRM still exhibits the largest magnitude of fundamental wave among the four machines.

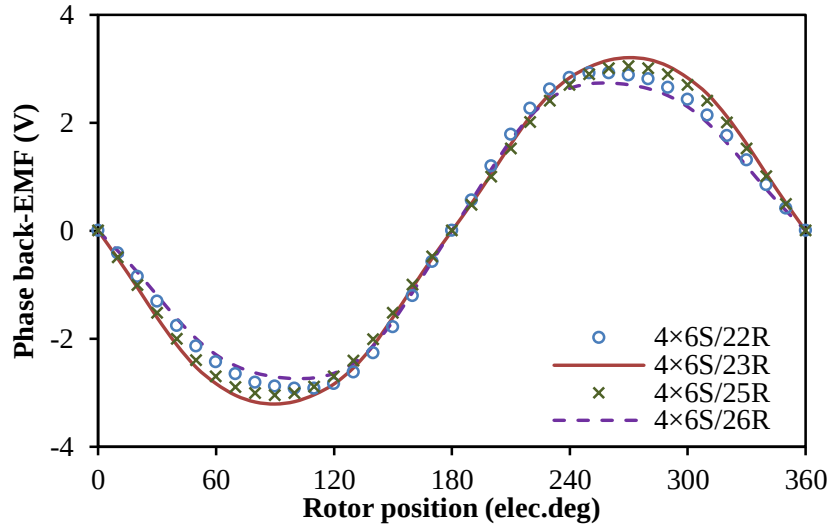

(a) Waveform

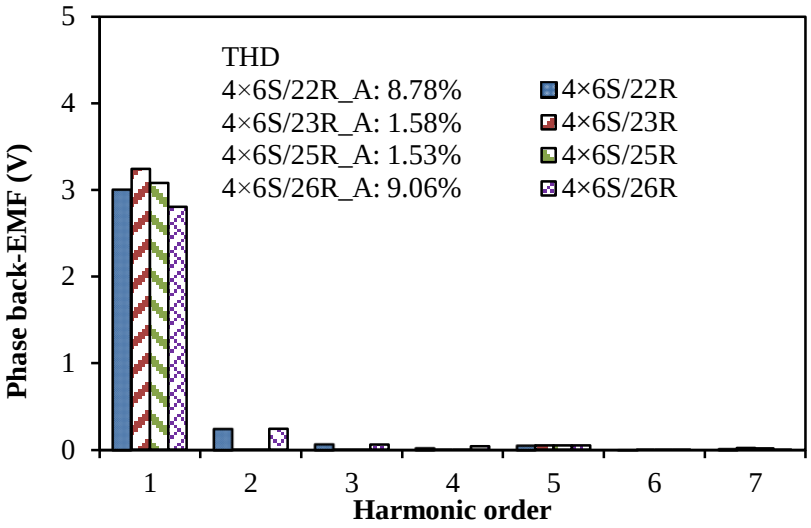

(b) Spectrum

Fig. 3.23. Open-circuit phase back-EMFs of multi-tooth VFRMs, n=4, 400rpm, p_f=15W.

3.5.3 Cogging Torque and Rated Torque

The cogging torque waveforms over one electric period for all machines are shown in Fig. 3.24. It can be seen that 4-tooth VFRMs with $N_r = nN_s \pm 1$ have very small cogging torque while that of $N_r = nN_s \pm 2$ have relatively large ones.

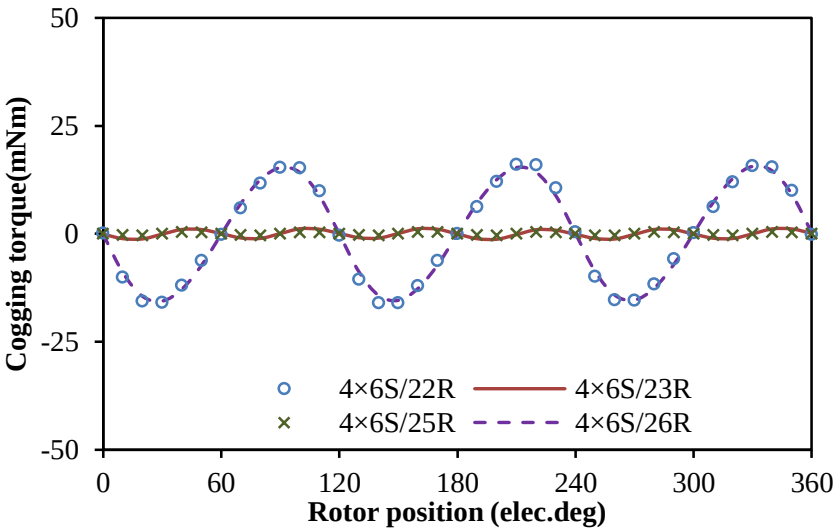

Fig. 3.24. Open-circuit cogging torque of multi-tooth VFRMs, n=4, p_f=15W.

As mentioned above, VFRMs are one type of synchronous machines in which DC field windings located in the stator slot. Hence, the number of cogging torque periods in conventional PM synchronous machines [ZHU00] can be extended to VFRMs. Thus, for both single- and multi-tooth VFRMs, the number of cogging torque cycles over one rotor pitch (one electric period) can be defined as

$$N_c = \frac{N_{sscs}}{GCD(N_{sscs}, N_r)} \tag{3.26}$$

where N_c is the number of cogging torque cycles over one electric period, N_{sscs} is the number of stator structure cyclic symmetry. By way of example, for 4×6/25 stator/rotor pole VFRM under investigation, N_r=25, N_{sscs}=6, N_c=6.

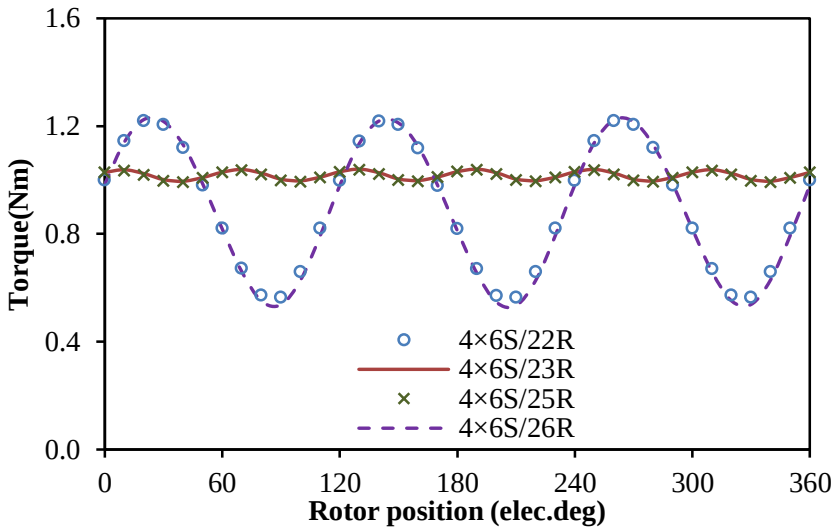

(a) Waveform

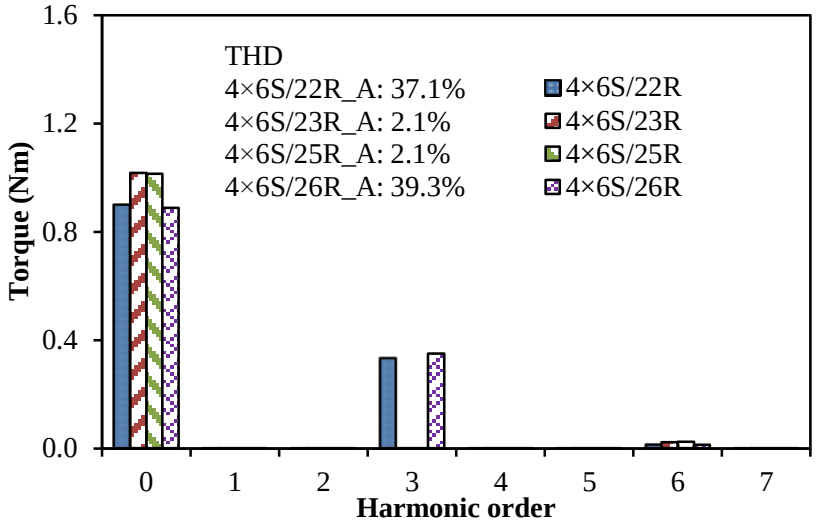

(b) Spectrum

Fig. 3.25. Electromagnetic torque of multi-tooth VFRMs, n=4, $p_f = p_a$ = 15W, I_d = 0 control.

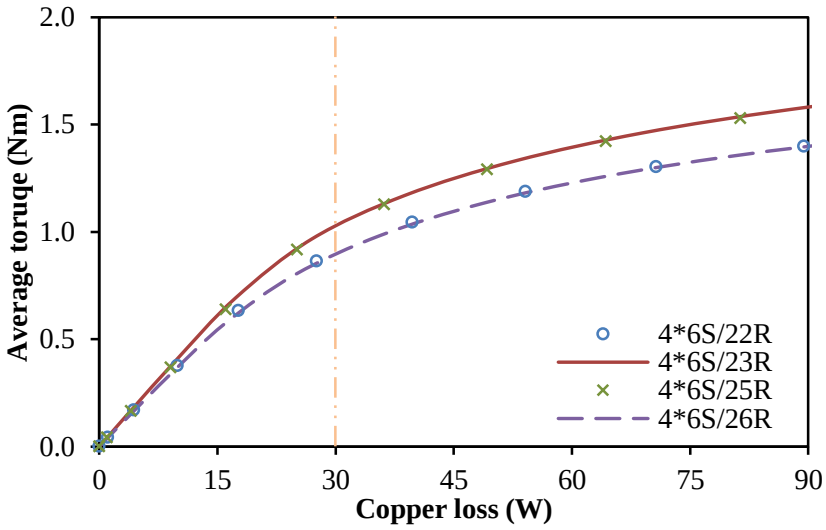

Fig. 3.26. Variation of average torque with copper loss in multi-VFRMs, n=4, $p_f = p_a$, I_d = 0 control.

The electromagnetic torques of 4-tooth VFRMs when the total copper loss is 30W and I_d=0 control are compared in Fig. 3.25 and Table 3.2. It can be seen that 4-tooth VFRMs with $N_r = nN_s \pm 1$ exhibit about 13.3% higher average torque than that of $N_r = nN_s \pm 2$. Further, as shown in Fig. 3.26, 4-tooth VFRMs with $N_r = nN_s \pm 1$ always have larger average torque than that of $N_r = nN_s \pm 2$. Meanwhile, the torque waveforms of 4-tooth VFRMs with $N_r = nN_s \pm 1$ have six pulsations over one electric period while that of $N_r = nN_s \pm 2$ are three pulsations, as shown in Fig. 3.25. This is caused by the combined influence of the harmonics of back-EMF and cogging torque. Further, the torque ripples of $N_r = nN_s \pm 1$ are much smaller than those of $N_r = nN_s \pm 2$ as shown in Fig. 3.25and Table 3.2. In addition, as shown in Table 3.2, 4-tooth

VFRMs with $N_r = nN_s \pm 1$ exhibit higher efficiency than that of $N_r = nN_s \pm 2$ since they have larger average torque and lower iron loss under the same rated copper loss and the same rated speed.

3.6 Experimental Verification

In order to validate the foregoing analyses, two prototype machines, 1×6/7 stator/rotor pole single-tooth VFRM and 4×6/25 stator/rotor pole 4-tooth VFRM are made and shown in Fig. 3.27, in which the parameters are same as shown in Table 3.1.

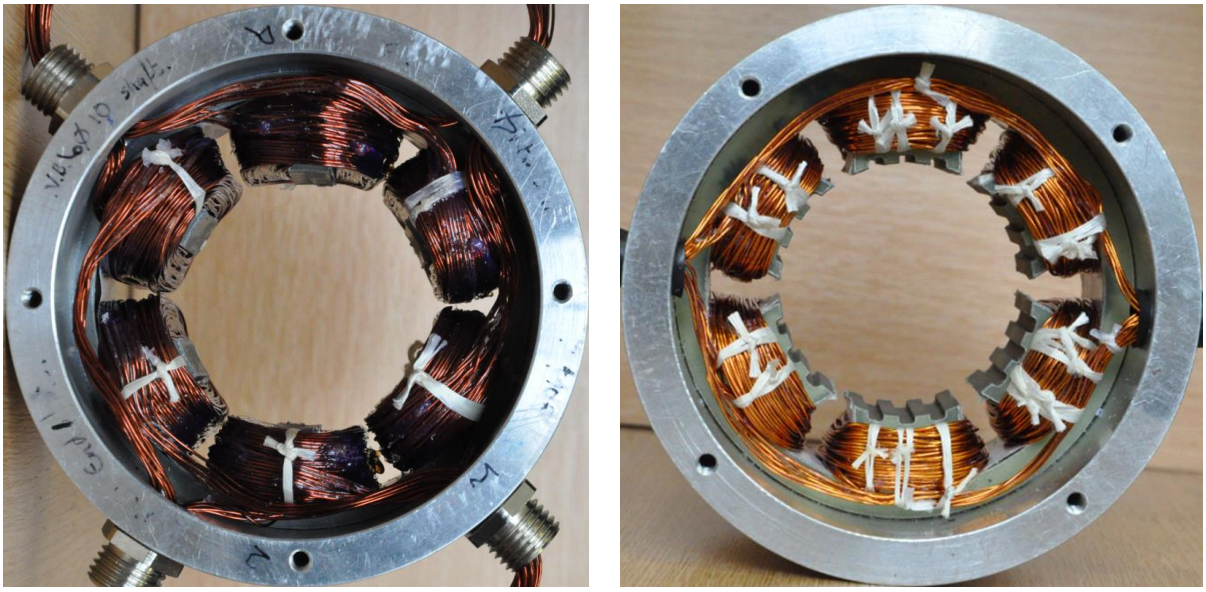

(a) Stator of single-tooth VFRM (b) Stator of 4-tooth VFRM

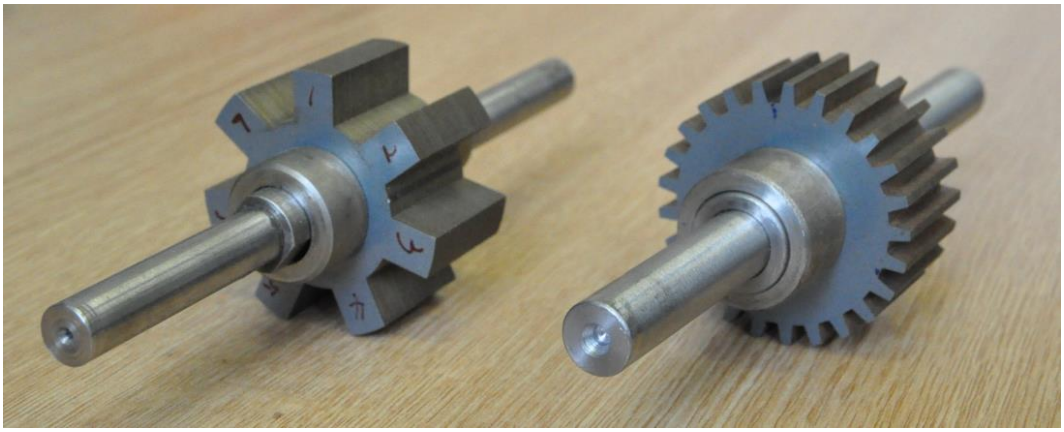

(c) 7-rotor pole (d) 25-rotor pole

Fig. 3.27. Prototypes of single- and 4-tooth VFRMs.

Fig. 3.28 shows the measured and predicted phase back-EMFs at two different field currents (half and full rated DC currents as shown in Table 3.1) when the speed is 400rpm.

Fig. 3.29 shows the variation of static torque with the rotor position at four different field and armature currents combinations, i.e. 25%, 50%, 75% and 100% of rated DC current with $p_f = p_a$ ($I_f = 0.707I_a$). Based on Fig. 3.29, the variation of the static torque at 270° rotor position with the total copper loss is obtained and shown in Fig. 3.30. Overall, the measured and FE predicted results match well, especially for phase back-EMF waveforms. The differences between the measured and FE predicted results of static torque under higher current (copper loss) are due to the increased influence of end-effect.

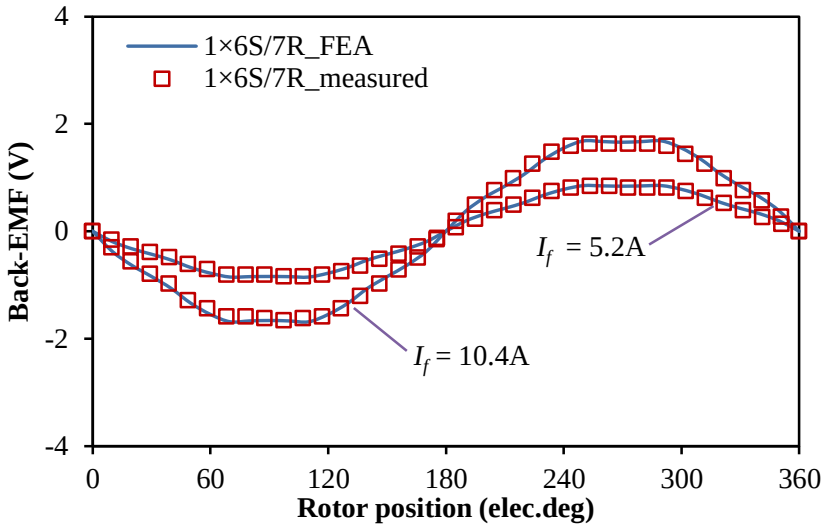

(a) Single-tooth VFRM, 1×6/7 stator/rotor pole.

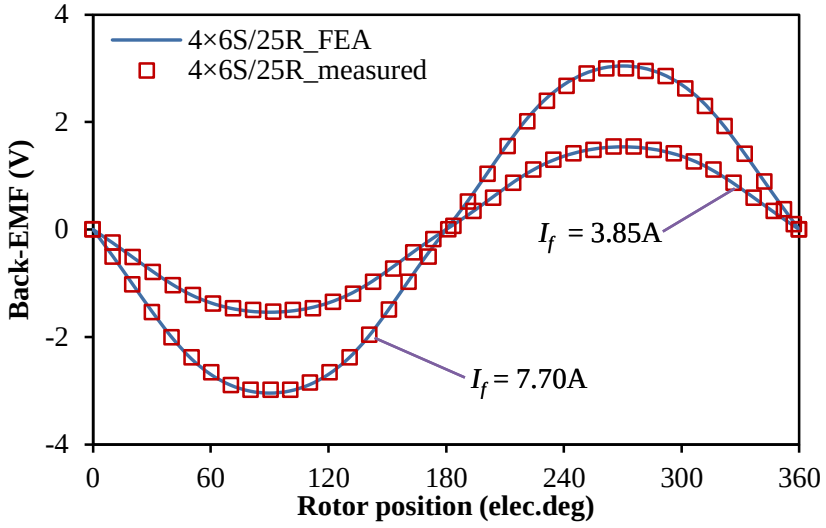

(b) 4-tooth VFRM, 4×6/25 stator/rotor pole.

Fig. 3.28. Measured and FE predicted phase back-EMFs at 400rpm.

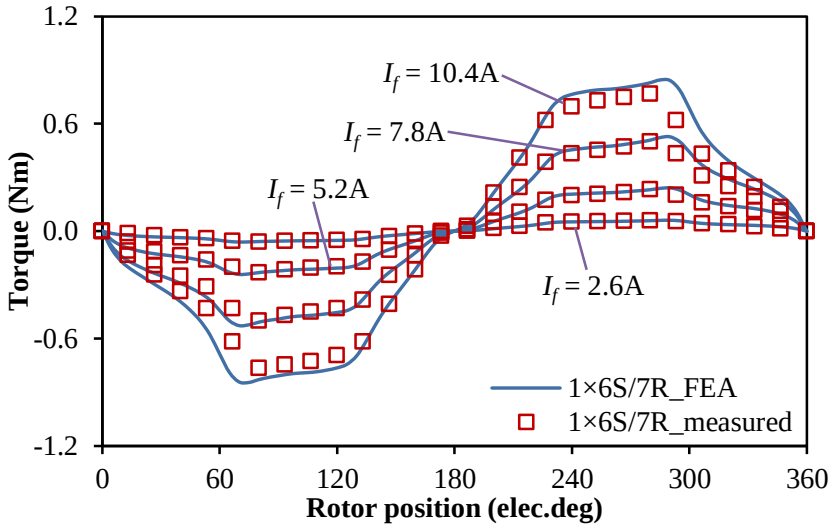

(a) Single-tooth VFRM, 1×6/7 stator/rotor pole.

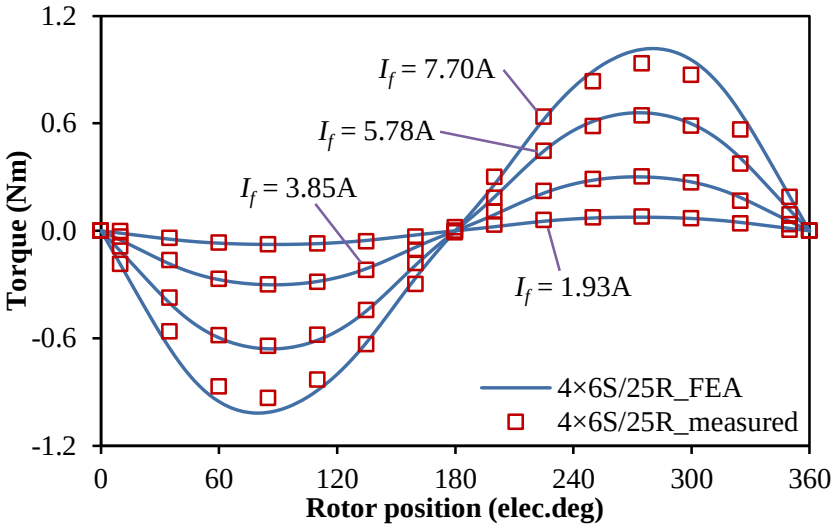

(b) 4-tooth VFRM, 4×6/25 stator/rotor pole.

Fig. 3.29. Measured and FE predicted phase static torques when p_f=p_a, I_f=0.707I_a, -1/2I_A=I_B=I_C.

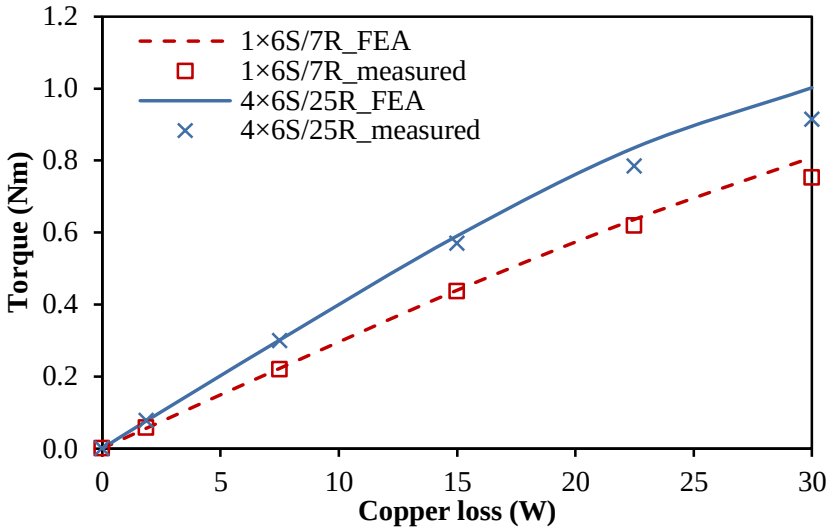

Fig. 3.30. Measured and FE predicted torque-copper loss characteristics when $p_f = p_a$ and rotor position is 270°.

3.7 Summary

In this chapter, novel multi-tooth VFRMs which adopt doubly salient stator and rotor structure with non-overlapping stator AC armature and DC field windings are investigated.

The choice of rotor pole number is flexible and can be any integers except the phase number and its multiples. Meanwhile, the symmetrical bipolar phase flux-linkage and back-EMF waveforms can be obtained when the ratio of stator pole number to GCD of stator- and rotor-pole numbers is even. Further, under the same rated copper loss and stator outer radius as well as 6-pole stator, 4-tooth per stator pole VFRMs exhibit the highest average torque if stator and rotor pole numbers satisfy $N_r=nN_s\pm1$. Furthermore, the 4×6/25 stator/rotor pole 4-tooth VFRM is compared with the 1×6/7 stator/rotor pole single-tooth VFRM when both are optimized. It can be concluded that: in 4×6/25 stator/rotor pole 4-tooth VFRM (1) the phase back-EMF is more sinusoidal and ~78% larger in magnitude of fundamental components than that of single-tooth VFRM, (2) the cogging torque and torque ripple is much lower than that of single-tooth VFRM, (3) it exhibits larger average torque at relatively low copper loss but smaller at high copper loss than that of single-tooth VFRM. Finally, among the main stator and rotor pole combinations in 4-tooth VFRMs, $N_r= nN_s \pm 1$ exhibit more sinusoidal and higher back-EMF, lower torque ripple and larger average torque than that of $N_r = nN_s \pm 2$. The analyses have been validated by both the FEA and measurements.

3.8 Appendix

3.8.1 Permeance between One Stator Pole and Complete Rotor

The permeance between one stator pole and complete rotor pole in different number of small tooth per stator pole *n* which correspond with Fig. 3.1 and Fig. 3.6 can be simplified as

n=1

$$P_{sp} = P_0 + P_1 \cdot cos(N_r \cdot \theta_{0sr} + 0 \cdot \frac{2\pi}{N_s} \cdot N_r)$$

n=2

$$P_{sp} = P_0 + P_1 \cdot cos\left(N_r \cdot \theta_{0sr} + \frac{1}{4} \cdot \frac{2\pi}{N_s} \cdot N_r + \pi\right) + P_0 + P_1 \cdot cos\left(N_r \cdot \theta_{0sr} - \frac{1}{4} \cdot \frac{2\pi}{N_s} \cdot N_r + \pi\right)$$

n=3

$$P_{sp} = P_0 + P_1 \cdot cos\left(N_r \cdot \theta_{0sr} + \frac{2}{6} \cdot \frac{2\pi}{N_s} \cdot N_r\right) + P_0 + P_1 \cdot cos\left(N_r \cdot \theta_{0sr} + 0 \cdot \frac{2\pi}{N_s} \cdot N_r\right) + P_0 + P_1 \cdot cos\left(N_r \cdot \theta_{0sr} - \frac{2}{6} \cdot \frac{2\pi}{N_s} \cdot N_r\right)$$

n=4

$$P_{sp} = P_0 + P_1 \cdot cos\left(N_r \cdot \theta_{0sr} + \frac{3}{8} \cdot \frac{2\pi}{N_s} \cdot N_r + \pi\right) + P_0 + P_1 \cdot cos\left(N_r \cdot \theta_{0sr} + \frac{1}{8} \cdot \frac{2\pi}{N_s} \cdot N_r + \pi\right) + P_0 + P_1 \cdot cos\left(N_r \cdot \theta_{0sr} - \frac{1}{8} \cdot \frac{2\pi}{N_s} \cdot N_r + \pi\right) + P_0 + P_1 \cdot cos\left(N_r \cdot \theta_{0sr} - \frac{3}{8} \cdot \frac{2\pi}{N_s} \cdot N_r + \pi\right)$$

where θ_{osr} is the relative position between the middle of one stator pole and one rotor-pole.

As a conclusion, the permeance between one stator pole and complete rotor pole whenever the number of small tooth *n* is selected can be expressed as

$$P_{sp} = nP_0 + P_1 \cdot \sum_{i=1}^{n} \cos\left(N_r \cdot \theta_{0sr} + \frac{n-(2i-1)}{2n} \cdot \frac{2\pi}{N_s} \cdot N_r + (n+1) \cdot \pi\right)$$

3.8.2 Permeance between Different Stator Pole and Complete Rotor

If assume the permeance P_{Ns1} as a base, the permeance P_{Nsa} between stator pole N_{sa} and the complete rotor can be expressed as following.

N_{sa}=N_{s1}=1 $$P_{N_{s1}} = nP_0 + P_1 \cdot \sum_{i=1}^{n} \cos\left(\begin{matrix} N_r \cdot \theta_{0sr} + \frac{n-(2i-1)}{2n} \cdot \frac{2\pi}{N_s} \cdot N_r \ + (n+1)\cdot\pi \\ + \frac{2\pi}{N_s} \cdot (1-1) \cdot N_r \end{matrix} \right)$$

N_{sa}=N_{s2}=2 $$P_{N_{s2}} = nP_0 + P_1 \cdot \sum_{i=1}^{n} \cos\left(\begin{matrix} N_r \cdot \theta_{0sr} + \frac{n-(2i-1)}{2n} \cdot \frac{2\pi}{N_s} \cdot N_r + (n+1)\cdot\pi \\ + \frac{2\pi}{N_s} \cdot (2-1) \cdot N_r \end{matrix} \right)$$

N_{sa}=N_{s3}=3 $$P_{N_{s3}} = nP_0 + P_1 \cdot \sum_{i=1}^{n} \cos\left(\begin{matrix} N_r \cdot \theta_{0sr} + \frac{n-(2i-1)}{2n} \cdot \frac{2\pi}{N_s} \cdot N_r + (n+1)\cdot\pi \\ + \frac{2\pi}{N_s} \cdot (3-1) \cdot N_r \end{matrix} \right)$$

******

N_{sa}=N_{sa} $$P_{N_{sa}} = nP_0 + P_1 \cdot \sum_{i=1}^{n} \cos\left(\begin{matrix} N_r \cdot \theta_{0sr} + \frac{n-(2i-1)}{2n} \cdot \frac{2\pi}{N_s} \cdot N_r + (n+1)\cdot\pi \\ + \frac{2\pi}{N_s} \cdot (Nsa-1) \cdot N_r \end{matrix} \right)$$

3.8.3 Model of MMF

The MMFs of coils A1 and A2 which induced by each excited DC coil under the conditions of 6-pole stator and the stator and rotor pole combinations satisfied with (3.6) are summarized in Table 3.3. Meanwhile, when all DC coils are excited, the corresponding induced MMFs of coils A1 and A2 are also obtained by adopting the superposition method.

Table 3.3 Open-circuit MMF of Coil A1 and A2

DC source	**Direction**	**MMF in coil A1**	**Direction**	**MMF in coil A2**
DC1	+	$\frac{1}{2}N_f I_f \cdot \left(1 - \frac{P_{Ns1}}{\sum_{a=1}^{6} P_{Nsa}}\right)$	-	$\frac{1}{2}N_f I_f \cdot \frac{P_{Ns1}}{\sum_{a=1}^{6} P_{Nsa}}$
DC2	+	$\frac{1}{2}N_f I_f \cdot \frac{P_{Ns2}}{\sum_{a=1}^{6} P_{Nsa}}$	+	$\frac{1}{2}N_f I_f \cdot \frac{P_{Ns2}}{\sum_{a=1}^{6} P_{Nsa}}$
DC3	-	$\frac{1}{2}N_f I_f \cdot \frac{P_{Ns3}}{\sum_{a=1}^{6} P_{Nsa}}$	-	$\frac{1}{2}N_f I_f \cdot \frac{P_{Ns3}}{\sum_{a=1}^{6} P_{Nsa}}$
DC4	+	$\frac{1}{2}N_f I_f \cdot \frac{P_{Ns4}}{\sum_{a=1}^{6} P_{Nsa}}$	-	$\frac{1}{2}N_f I_f \cdot \left(1 - \frac{P_{Ns4}}{\sum_{a=1}^{6} P_{Nsa}}\right)$
DC5	-	$\frac{1}{2}N_f I_f \cdot \frac{P_{Ns5}}{\sum_{a=1}^{6} P_{Nsa}}$	-	$\frac{1}{2}N_f I_f \cdot \frac{P_{Ns5}}{\sum_{a=1}^{6} P_{Nsa}}$
DC6	+	$\frac{1}{2}N_f I_f \cdot \frac{P_{Ns6}}{\sum_{a=1}^{6} P_{Nsa}}$	+	$\frac{1}{2}N_f I_f \cdot \frac{P_{Ns6}}{\sum_{a=1}^{6} P_{Nsa}}$
	Sum	$N_f I_f \frac{P_{NS2} + P_{NS4} + P_{NS6}}{\sum_{a=1}^{6} P_{Nsa}}$	Sum	$-N_f I_f \frac{P_{NS1} + P_{NS3} + P_{NS5}}{\sum_{a=1}^{6} P_{Nsa}}$

CHAPTER 4
COMPARATIVE STUDY OF NOVEL SYNCHRONOUS MACHINES HAVING PERMANENT MAGNETS IN STATOR

Similar to other DC field excitation machines, variable flux reluctance machines (VFRMs) also exhibit lower torque density compared with conventional permanent magnet (PM) machines [LIU12b]. Theoretically, by replacing DC field windings with PMs, higher torque density can be expected [GIN53]. Therefore, in this chapter, novel biased flux PM machines (BFPMMs) which are developed from VFRMs by replacing all DC field windings with PMs are proposed and investigated.

4.1 Introduction

Switched reluctance machines (SRMs) have been extensively investigated over the past decades due to the simple and robust structure as well as low cost [MIL93] [VIJ08]. However, due to the influence of unipolar non-sinusoidal excitation, SRMs suffer from high torque ripple, acoustic noise and vibration. In order to overcome these drawbacks, the idea which splits the original coils into two halves was proposed in [PUL88], in which half of phase windings is injected with DC current while the other half is connected to a bipolar drive circuit.

Based on this idea, doubly-fed doubly salient machines (DFDSMs), wound field switched flux machines (WFSFMs) and variable flux reluctance machines (VFRMs) were proposed [LI95] [POL06b] [CHE10a] [LIU12b] [KAS11]. For DFDSMs, the flux paths in the stator are asymmetric due to the full pitched DC field winding. Therefore, phase unbalance exists in DFDSMs, particularly under heavy magnetic saturation. Moreover, DFDSMs have the unipolar phase flux-linkages and asymmetric back-EMFs as well as large torque ripples [LI95]. Different from DFDSMs, bipolar phase flux-linkage and symmetrical back-EMF can be obtained in both WFSFMs and VFRMs by using typical stator and rotor pole combinations [POL06b] [CHE10a] [LIU12b] [KAS11]. Meanwhile, both WFSFMs and VFRMs exhibit lower cogging torques and torque ripples than those of DFDSMs [LIU13].

Nevertheless, the torque densities of these machines are relatively low when compared with the conventional permanent magnet (PM) machines. As a potential solution, PMs can be used to replace the DC field windings in the stator to further enhance the torque performance since the copper loss produced by the DC field windings can be eliminated. As a reverse proof,

when the PMs in the stator are replaced by the DC field windings, the torque performances of doubly salient PM machines (DSPMMs) and switched flux PM machines (SFPMMs) are weakened in the corresponding DFDSMs and WFSFMs respectively [LIA95] [HUA05] [RAU55] [HOA97] [CHE10a]. However, during the evolution process, the corresponding electromagnetic performance features are inherited.

Being the same as those in DSPMMs/DFDSMs and SFPMMs/WFSFMs, a type of PM machine is developed in this chapter by replacing the DC field windings with PMs in the VFRMs. Therefore, doubly salient structure and non-overlapping armature winding are still employed in this new machine while the PMs are mounted on the surfaces of adjacent stator poles with alternate polarities. Since all stator coils have biased PM flux-linkages with alternate polarities, this new machine can be designated as biased flux PM machine (BFPMM). Meanwhile, BFPMMs can also be considered as developed from flux-reversal PM machines (FRPMMs) [DEO97] by replacing the one or more pairs of alternate polarities PMs on the surface of single stator pole with one piece of PM. Further, the PM positions in BFPMMs can be located from the surface to the bottom of stator pole and even in the stator yoke since the main magnetic circuits are the same.

In this chapter, the operation principle and the stator and rotor pole combinations are illustrated first. Then, the influence of PM positions on electromagnetic performance of BFPMMs will be analysed and compared under the three representative positions with 6/7 (N_s/N_r) stator/rotor pole combination together with VFRMs. Finally, several prototype machines are manufactured and measured to validate the analysis.

4.2 Machine Operation Principle and Stator/Rotor Pole Combinations

4.2.1 Operation Principle

VFRM which adopts doubly salient stator and rotor structure with non-overlapping stator AC armature and DC field windings is shown in Fig. 4.1. The configuration of DC field winding shown in Fig. 4.1 is identical to that shown in Fig. 4.2(a). Therefore, they can be replaced by PMs in the adjacent stator poles with alternate polarities, as shown in Fig. 4.2(b).

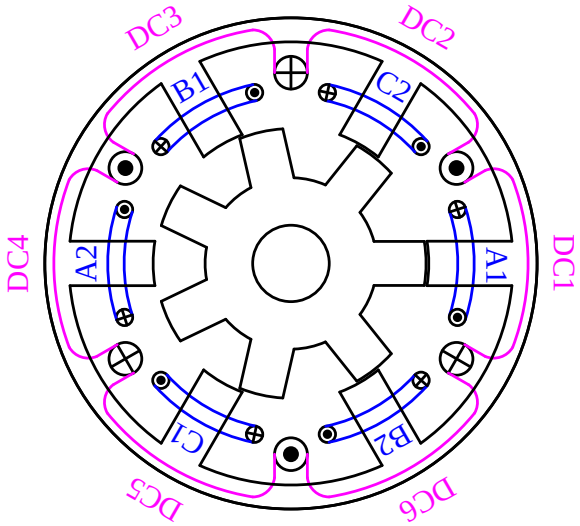

Fig. 4.1. Topology of 6/7 stator/rotor pole VFRM.

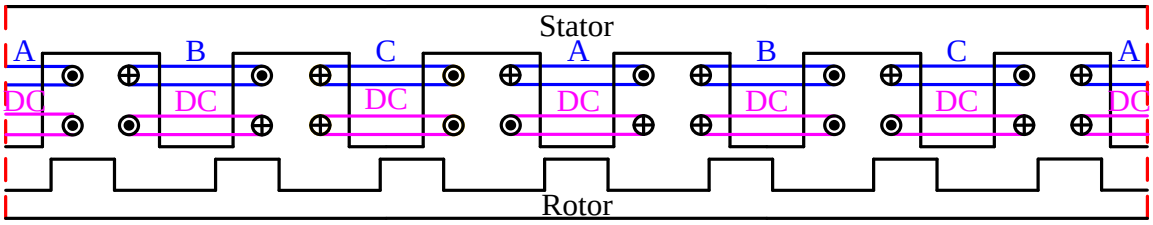

(a) Structure schematics of 6/7 stator/rotor pole VFRM.

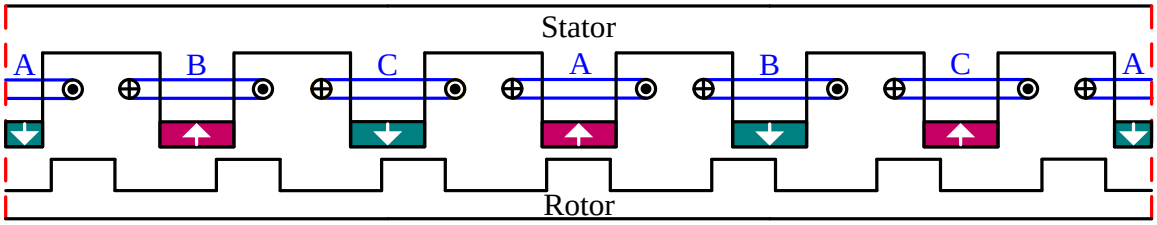

(b) Structure schematics of 6/7 stator/rotor pole BFPMM.

Fig. 4.2. Structures evolution from VFRM to BFPMM in 6/7 stator/rotor pole combination.

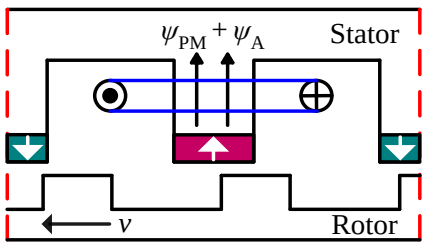

(a) Moving form unaligned to aligned position

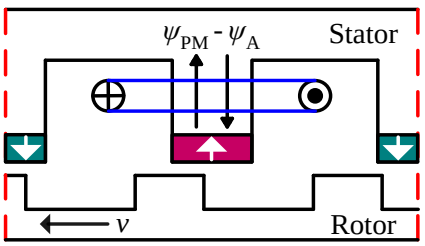

(b) Moving from aligned to unaligned position

Fig. 4.3. Operation principle schematics of BFPMM.

Similar to VFRM, if one rotor pole aligned with one stator pole, the corresponding rotor position can be designated as aligned position. For a single stator pole as shown in Fig. 4.3(a), when one rotor pole rotates from unaligned position to aligned position, the armature coil injected with positive current (its flux with same direction of PM flux) helps to enhance the airgap field and generate positive torque. On the contrary, when rotor rotates from aligned positon to unaligned position as shown in Fig. 4.3(b), negative current is injected into armature coil (its flux with opposite direction of PM flux) to weaken the airgap field to help moving the rotor smoothly. Therefore, a positive average torque is generated over one electric period. Further, as a combined result of three phase operation, more smooth output torque will be generated.

4.2.2 Topologies and Stator/Rotor Pole Combinations

Fig. 4.4 shows the topologies of 6-stator pole BFPMMs with different rotor pole numbers. It can be seen that doubly salient structure and non-overlapping armature windings are adopted in BFPMMs while the PMs are mounted on the surface of adjacent stator poles with alternate polarities. The rotor of BFPMMs is similar to SRM, which is simple and robust.

Being the same as VFRM, the choice of stator and rotor pole combinations in BFPMMs is flexible, in which the rotor pole number can be any integers except the phase number and its multiples. Hence, the selections of stator pole number N_s and rotor pole number N_r can be summarised as

$$N_s = km \text{ (k = 1, 2…)} \tag{4.1}$$

$$N_r = N_s \pm j \ (N_r \neq k_i m, j=1, 2\ldots, k_i=1.\ 2\ldots) \tag{4.2}$$

where m is the phase number, k, j and k_i are integers.

Since PMs have to be in pairs, a three phase BFPMM has at least 6 poles stator, which can be considered as a unit machine.

The coil connections of the armature winding can be determined by the conventional coil-EMF vector method. The electric degrees α_e between two adjacent coil-EMF vectors [ZHU10] can be derived from the mechanical degrees α_m and rotor pole number N_r according to equation following.

$$\alpha_e = N_r \alpha_m \tag{4.3}$$

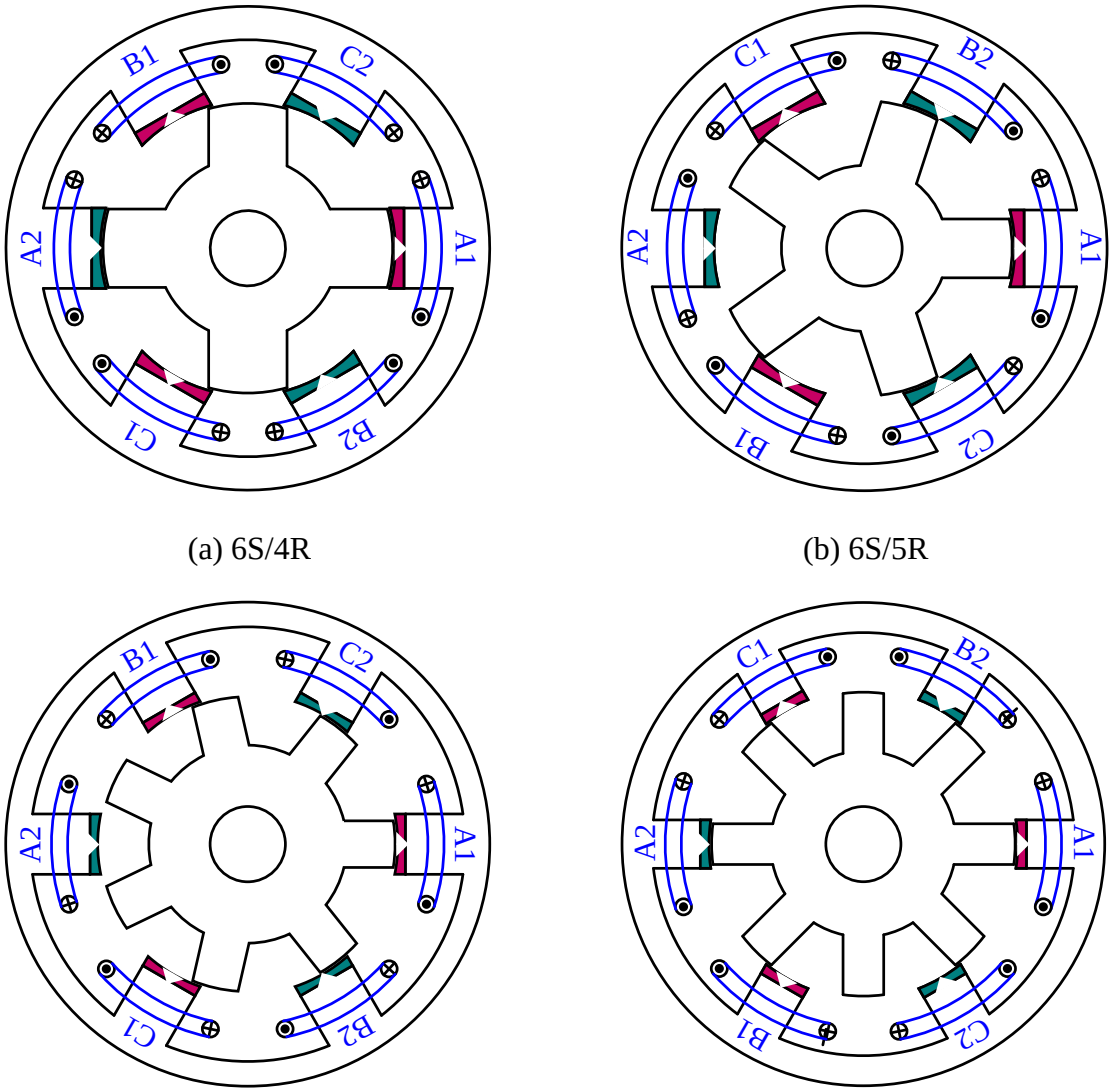

(a) 6S/4R (b) 6S/5R

(c) 6S/7R (d) 6S/8R

Fig. 4.4. Machine topologies for different number of rotor poles with 6-stator pole BFPMM.

For a 6-pole stator unit machine, the most feasible rotor pole numbers could be 4, 5, 7 and 8, as shown in Fig. 4.4. According to (4.3) with consideration of the alternate magnetization directions in adjacent stator pole, the coil EMF vectors of BFPMMs having different rotor pole numbers are shown in Fig. 4.5. Since all the coil-EMF vectors belong to the same phase are aligned as shown in Fig. 4.5, the distribution factors (K_d) for the stator/rotor pole combinations are all equal to one. Similar to the fractional slot PM machines [ISH06], the pitch factor (K_p) can be calculated by

$$K_p = \cos\left(\pi\left(\frac{N_r}{N_s} - 1\right)\right) \tag{4.4}$$

Based on (4.4), K_d, K_p and winding factor (K_{dp}) of BFPMM with different stator/rotor pole

combinations can be calculated. Table 4.1 shows the corresponding winding factors for the main stator/rotor pole combinations of BFPMMs with 6-pole stator. Obviously, when N_r is more close to N_s, the winding factor will be higher.

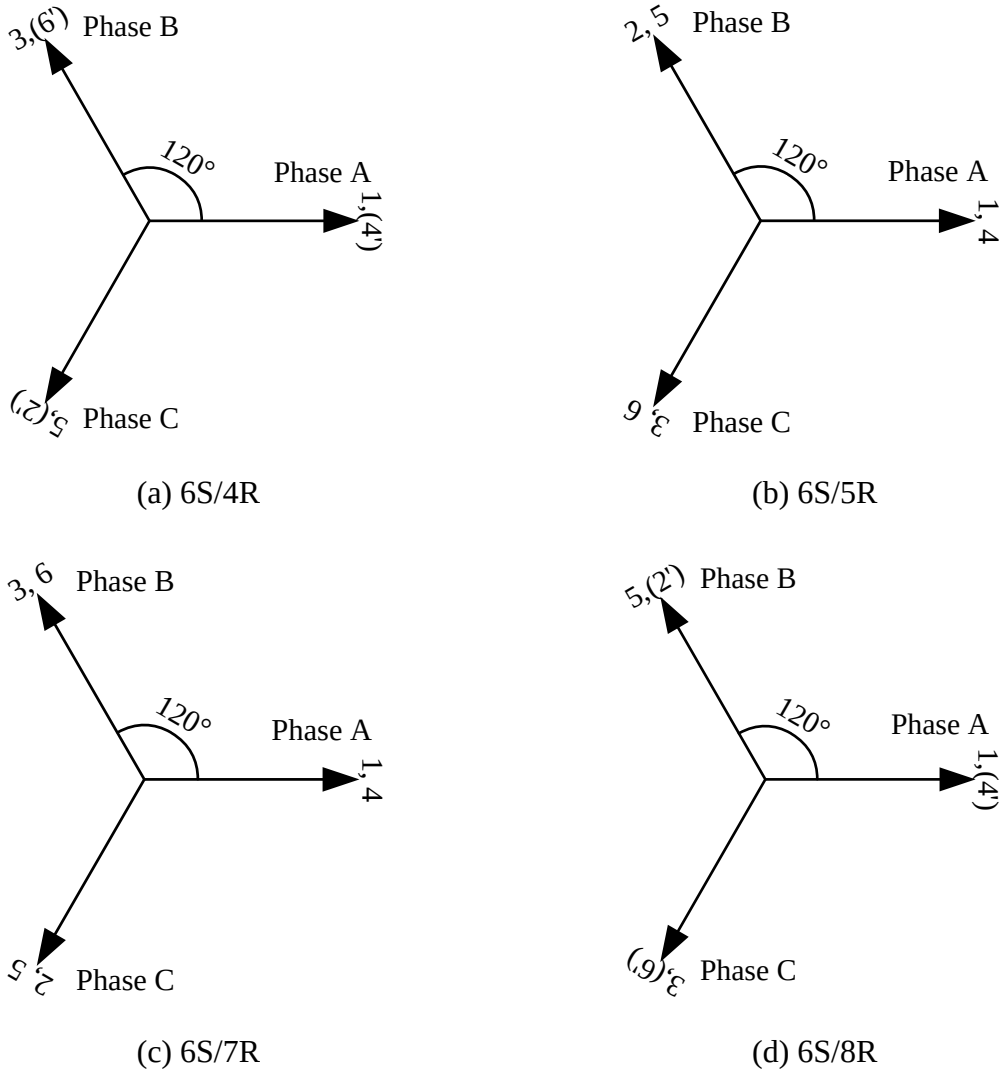

Fig. 4.5. Coil-EMF vectors for different rotor pole number with 6-pole stator (electric degree).

Table 4.1 Winding factors for different rotor pole numbers with 6-pole stator

N_r	**4**	**5**	**6**	**7**	**8**
K_d	1	1	1	1	1
K_p	0.5	0.87	1	0.87	0.5
K_{dp}	0.5	0.87	1	0.87	0.5

4.2.3 Coil and Phase Flux-Linkages and back-EMFs

Fig. 4.6 shows the typical coil and phase flux-linkages of BFPMMs with four stator/rotor pole combinations with per-unit value. It can be seen that coils A1 and A2 have the same biased flux-linkages for 4- and 8- pole rotors (N_r=N_s±2), while 5- and 7-pole rotors (N_r=N_s±1) have coil flux-linkages with opposite polarities (180 electric degrees shifting). This difference results in two different characteristics of phase flux-linkages for the different stator/rotor pole combinations. Obviously, the phase flux-linkage is unipolar when N_r=4 or 8 but bipolar when N_r=5 or 7, as shown in Fig. 4.6.

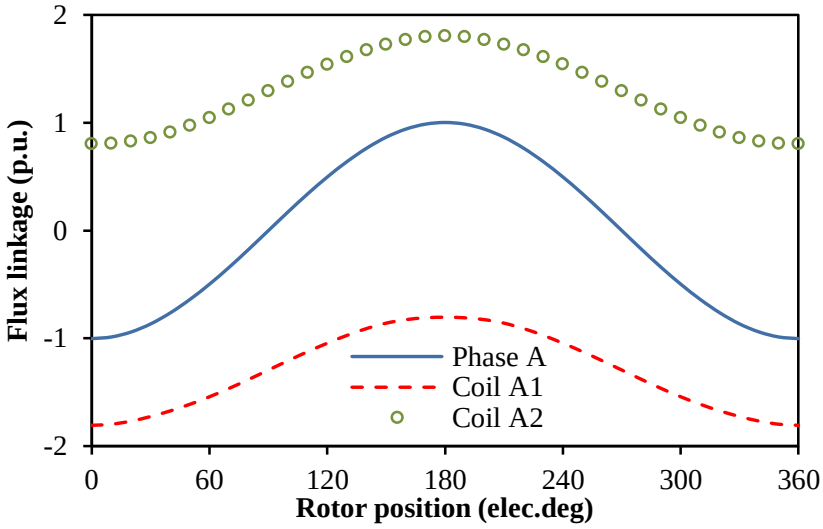

(a) N_r=5 or 7 (N_r=N_s±1).

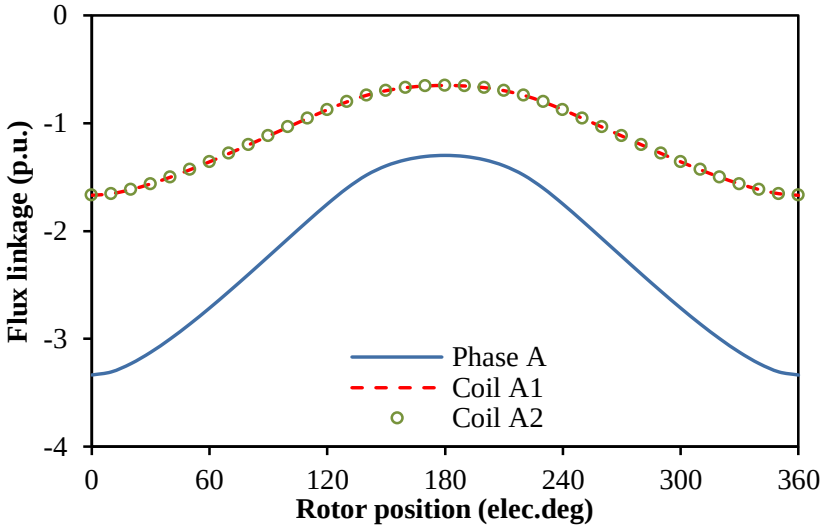

(b) N_r=4 or 8 (N_r=N_s±2).

Fig. 4.6. Per unit open-circuit phase and coil flux-linkages of 6-stator pole BFPMMs.

Further, the coil and phase back-EMFs of BFPMMs are shown in Fig. 4.7. It can be seen that the single coil back-EMF waveform is asymmetric (slant to right or left in half electric cycle) in all stator/rotor pole combinations due to the existing even harmonics. Similar to the conclusion of flux-linkage, symmetrical phase back-EMF is obtained when N_r=5 or 7 since all the even harmonics which cause the back-EMF waveform asymmetric in a single coil are cancelled completely in the phase winding by connecting the coils with opposite polarity.

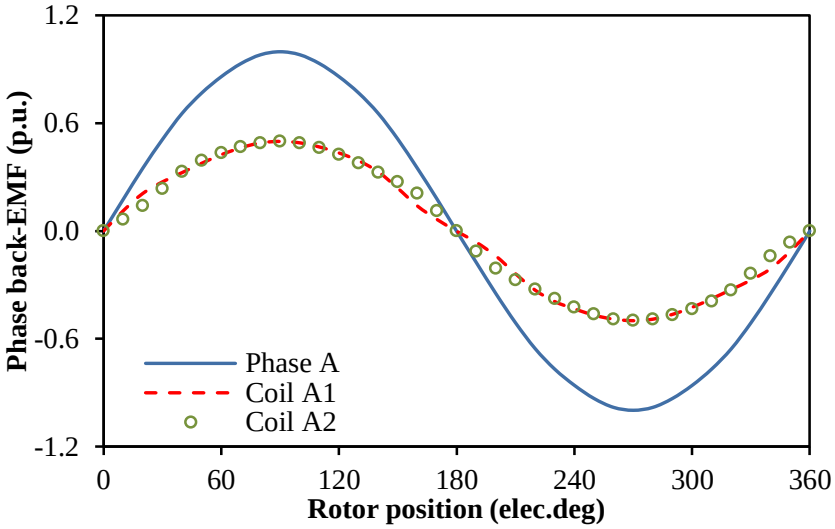

(a) N_r=5 or 7 (N_r=N_s±1).

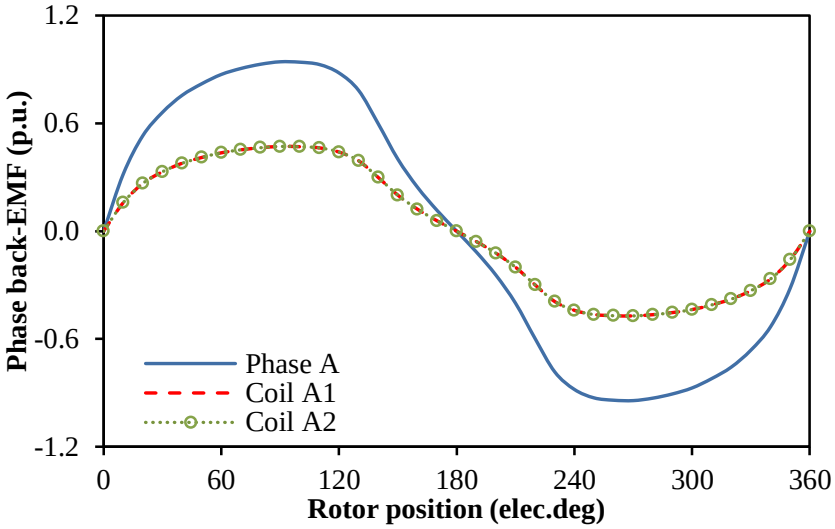

(b) N_r=4 or 8 (N_r=N_s±2).

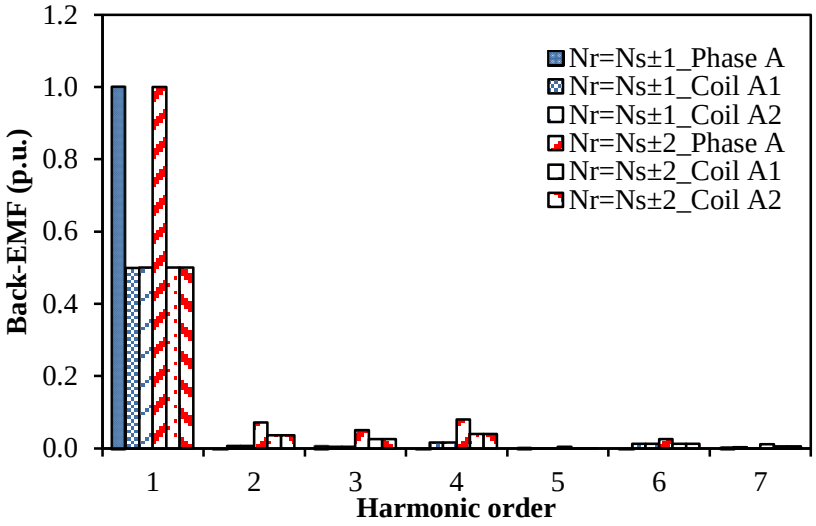

(c) Spectrum.

Fig. 4.7. Per unit open-circuit phase and coil back-EMFs of 6-stator pole BFPMMs.

Since BFPMMs are developed from VFRMs by replacing the DC field windings with PMs, the conditions for bipolar phase flux-linkage or symmetrical phase back-EMF in BFPMMs are also kept consistent. Thus, two conditions should be satisfied [SHI15]. First, the coil number per phase must be even. Second, the pair of coils belong to same phase must have 180 electrical degrees phase shifting (opposite induced polarities). In other word, the stator and rotor pole combinations should be satisfied with (4.5) [CHE08] [SHI15].

$$\frac{N_s}{GCD(N_s,N_r)} = Even \tag{4.5}$$

where *GCD* means the greatest common divisor. By way of example, for the BFPMM under investigation, 6/5 and 6/7 stator/rotor pole combinations are satisfied with (4.5).

4.2.4 Electromagnetic Torque Equation

According to energy conversion principle, if neglecting the magnetic saturation in the machine lamination and the energy variation in PM, the electromagnetic torque of one phase in BFPMM can be expressed as

$$\begin{aligned} T_a &= \frac{\partial W_a(\theta)}{\partial \theta} = \frac{\partial \int_0^{i_a} (\Psi_{arm}^a + \Psi_{PM}^a) di}{\partial \theta} \\ &= \frac{1}{2} i_a^2 \frac{dL_a}{d\theta} + i_a \frac{d\Psi_{PM}^a}{d\theta} \end{aligned} \tag{4.6}$$

where i_a, Ψ^a_{arm}, Ψ^a_{PM} and L_a stand for phase current, armature reaction flux-linkage, PM flux-linkage and self-inductance of phase A, and θ stands for rotor position. Assuming the armature winding is driven by sinusoidal current and only considering the fundamental wave

of phase flux linkage, that is

$$i_a = I_a \sin(N_r \omega t + \alpha_0) \tag{4.7}$$

$$\Psi_{PM}^a = \Psi_{PM} \cos(\theta + \theta_0) \tag{4.8}$$

where I_a and Ψ_{PM} stand for peak value of the phase current and amplitude of fundamental wave of PM flux-linkage, ω is rotor speed, α_0 and θ_0 are the initial angles of the phase current and the initial rotor position respectively.

To achieve the maximum average electromagnetic torque, the phase current should be aligned with phase back-EMF. Hence, current initial angle α_0 should be equal to initial rotor position θ_0. Then, the average electromagnetic torque of BFPMM can be expressed as

$$\begin{aligned} T_{ave} &= \frac{N_r}{2\pi} \int_0^{\frac{2\pi}{N_r}} (T_a + T_b + T_c)\, d\theta \\ &= \frac{3}{2} N_r \Psi_{PM} I_a \end{aligned} \tag{4.9}$$

Equation (4.9) indicates that the average electromagnetic torque of BFPMM is proportional to rotor pole number and phase current as well as PM flux-linkage. Since the definition of the pole pair number in BFPMMs is equal to N_r, this equation is the same as that in conventional PM synchronous machine, which means BFPMM is essentially a type of stator PM synchronous machine.

4.3 Torque Performance for Main Stator/Rotor Pole Combinations

Fig. 4.8 shows the waveforms of average torque against with current angle at rated 30W copper loss (p_c=30W) for BFPMMs for four main stator/rotor pole combinations. Being the same as VFRMs, the reluctance torque can be negligible in BFPMMs since the optimal current angles for all stator/rotor pole combinations are all close to 0°.

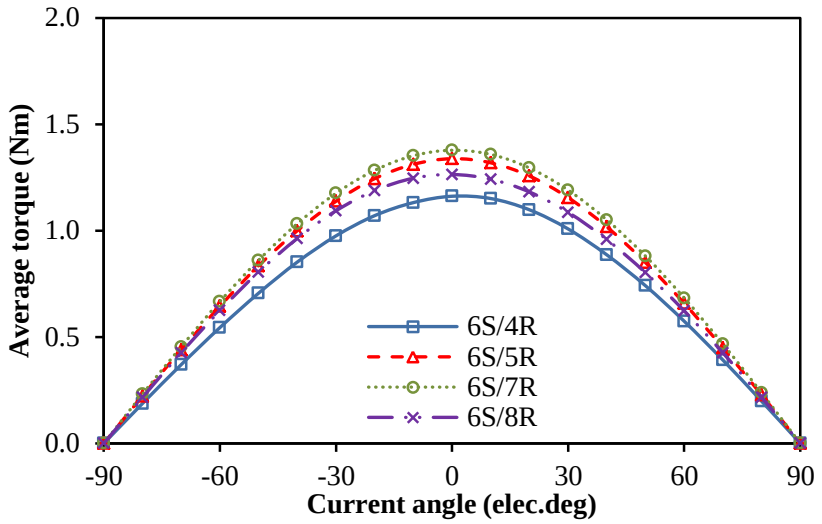

Fig. 4.8. Variation of average torque with current angle in BFPMM.

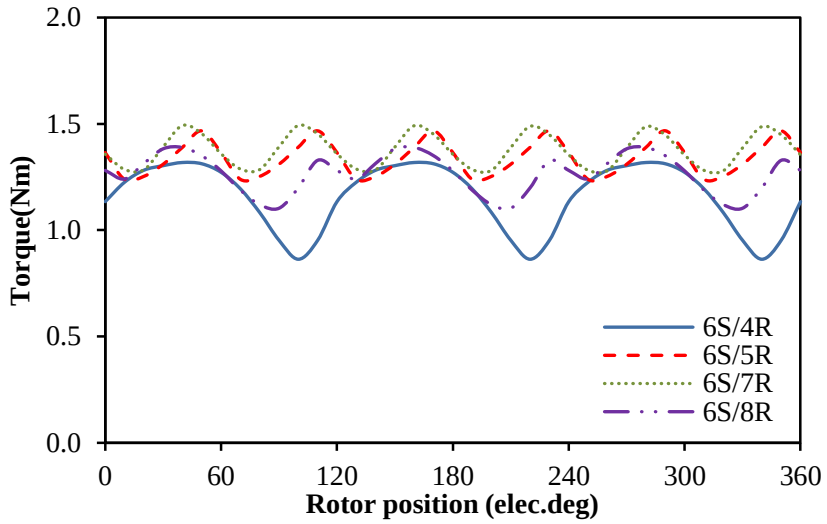

(a) Waveforms

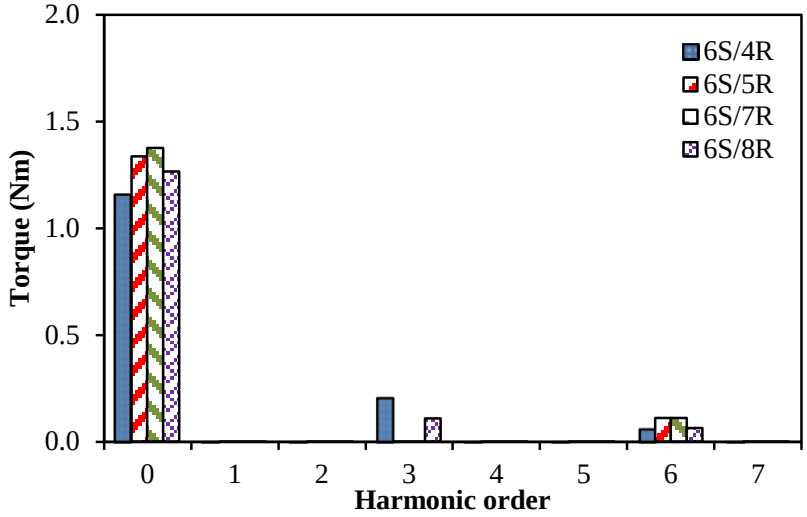

(b) Spectra

Fig. 4.9. Variation of torque with rotor position in BFPMM, p_c=30W, I_d =0 control.

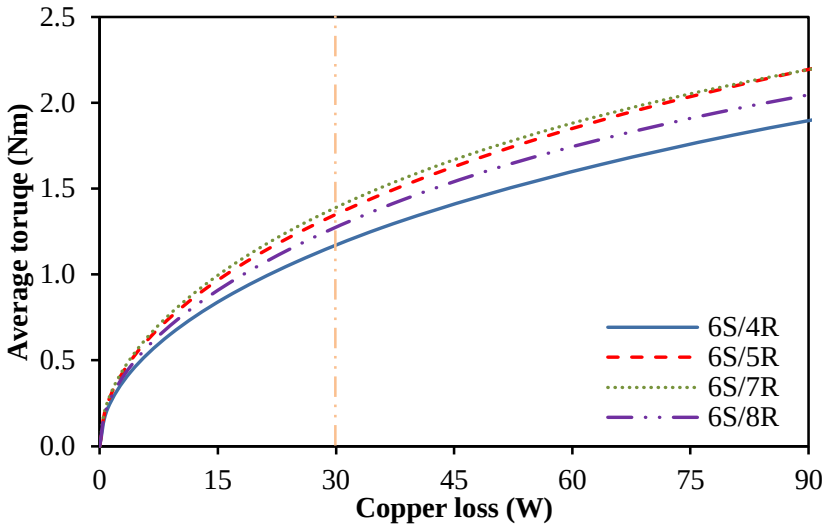

Fig. 4.10. Variation of average torque with copper loss in BFPMM.

Based on the rated copper loss and I_d =0 control, the waveforms of torque against with rotor position for four main stator/rotor pole combinations of BFPMMs are shown in Fig. 4.9. The torque ripples of BFPMMs with 6/4, 6/5, 6/7 and 6/8 stator/rotor pole combinations are 39.8%, 17.5%, 16.2% and 23.3% respectively. Obviously, BFPMMs with N_r=N_s±1 have lower torque ripple than those with N_r=N_s±2. Meanwhile, compared with BFPMMs with N_r=N_s±2 under rate copper loss, higher average torques are obtained in BFPMMs with N_r=N_s±1, as shown in Fig. 4.9. The torque performance also can be further reflected on the characteristic of average torque against with copper loss, as shown in Fig. 4.10. Among the four main stator/rotor pole combinations, the 6/7 stator/rotor pole BFPMM exhibits the highest average torque under the same copper loss during the whole copper loss range.

4.4 Comparison between VFRM and BFPMM Considering PM Locations

4.4.1 Alternate PM Locations

As shown in Fig. 4.11, the PMs in BFPMMs can be moved from surface to bottom of stator pole and even to stator yoke since the main magnetic circuits are consistent. In order to analyze the influence of PM locations on electromagnetic performance of BFPMMs, three typical PM locations are chosen as shown in Fig. 4.11. To simplify the comparison, the machine topologies corresponding to three typical PM locations as shown in Fig. 4.12 can be designated as surface mounted BFPMM (SM-BFPMM), middle tooth mounted (MTM-BFPMM) and stator yoke mounted BFPMM (SYM-BFPMM) respectively.

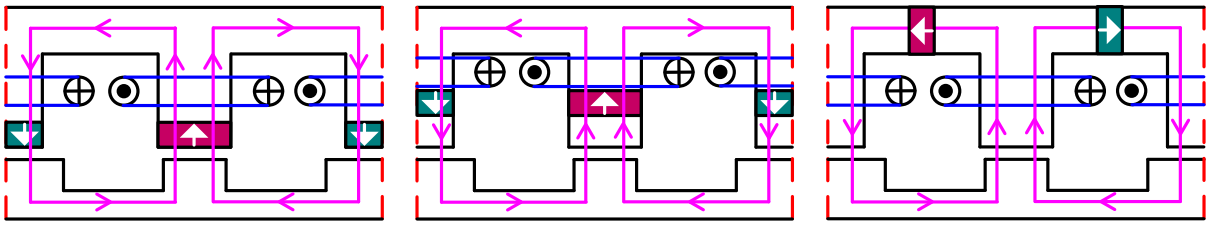

(a) Surface mounted BFPMM (b) Middle tooth mounted BFPMM (c) Stator yoke mounted BFPMM

Fig. 4.11. Structure schematics of BFPMMs with different PM locations.

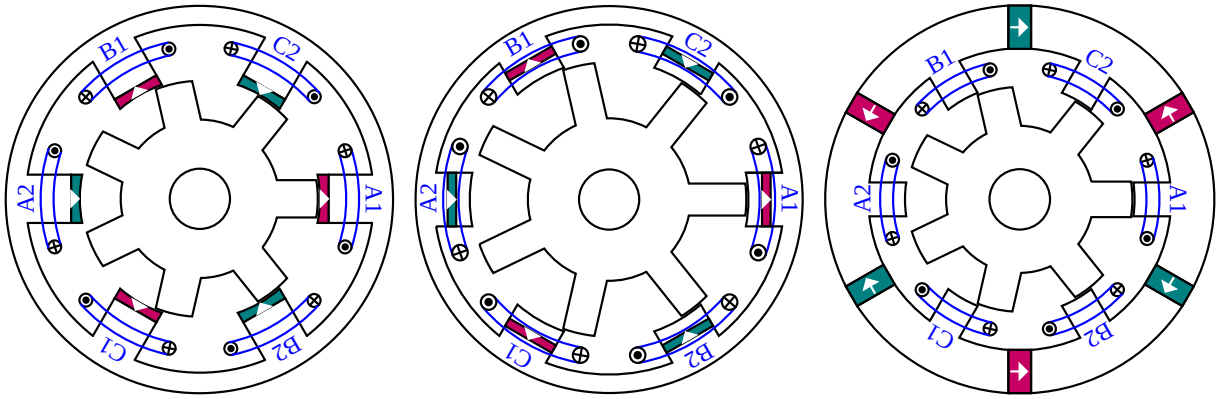

(a) SM-BFPMM (b) MTM-BFPMM (c) SYM-BFPMM

Fig. 4.12. Machine topologies of BFPMMs with different PM locations.

In the following sections, three types of BFPMMs will be analyzed and compared with VFRM (topology shown in Fig. 4.1) under the same rated total copper loss (30W) and machine size as the 6/7 stator/rotor pole combination (6/7 stator/rotor pole combination exhibits the highest torque capability among the main stator/rotor pole combinations in both VFRMs and SM-BFPMMs at the same copper loss). All the machines are globally optimized with the objective of maximum average torque under the 30W rated copper loss without the restriction on PM usage amount, and their main geometric parameters are listed in Table 4.2. According to the analysis in section 4.7 of Appendix, the minimum thickness of PM in SM-BFPMMs is chosen as 2mm to avoid irreversible demagnetization on load.

4.4.2 Open-circuit Field Distribution

The open-circuit flux equipotential for VFRM and three types of BFPMMs at the aligned position are shown in Fig. 4.13. Being the same as VFRM, short flux paths which could result in lower MMF drop in the stator are also achieved in BFPMMs. Meanwhile, the flux-loops of

the coils belong to the same phase are completely independent for all machines. Different from SM-BFPMM and MTM-BFPMM, the leakage flux exists outside of stator in SYM-BFPMM but is quite small when compared with the main flux. As shown in Fig. 4.14, the waveforms of open-circuit air-gap flux densities in VFRM and BFPMMs are consistent, and all three BFPMMs exhibit higher peak value of air-gap flux density than the VFRM.

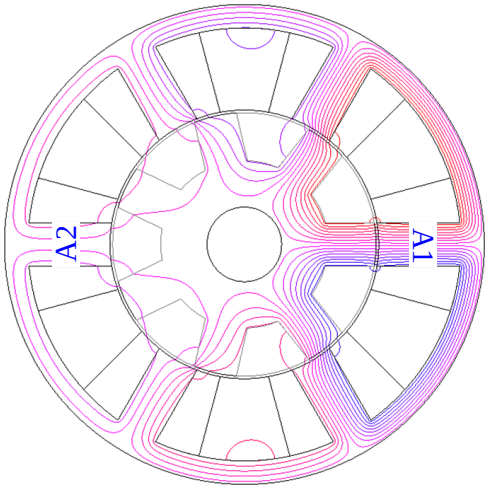

(a) VFRM

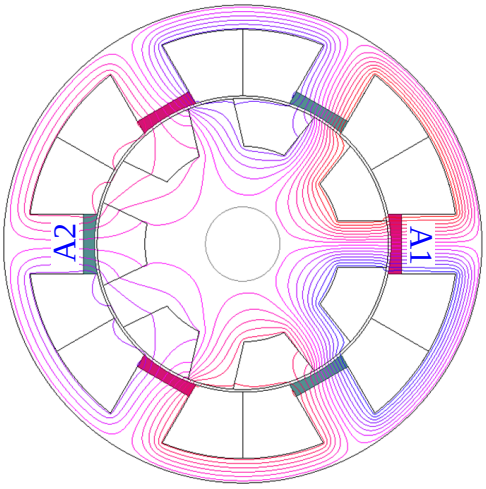

(b) SM-BFPMM

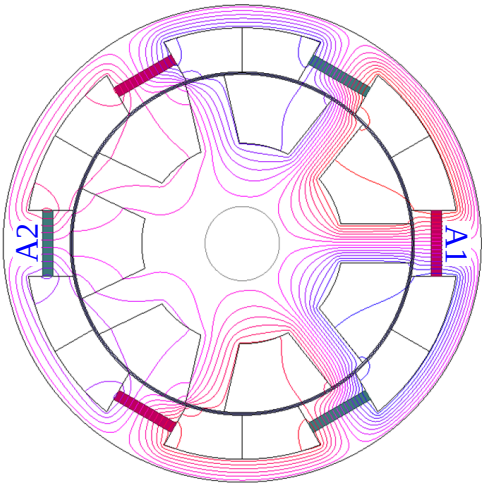

(a) MTM-BFPMM

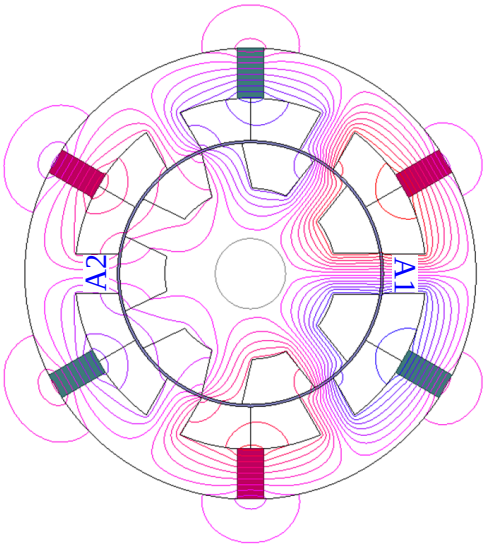

(b) SYM-BFPMM

Fig. 4.13. Open-circuit flux equipotential at aligned position, p_f=15W for VFRM.

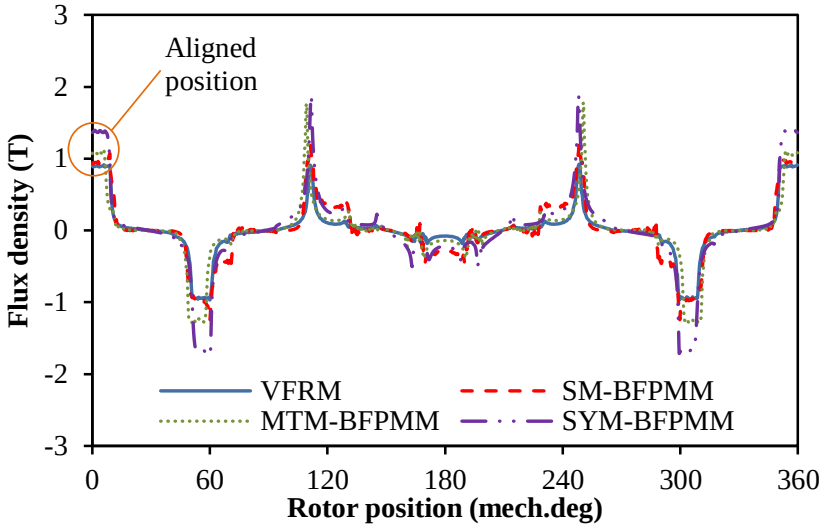

Fig. 4.14. Open-circuit air-gap flux density at aligned positon, p_f=15W for VFRM.

Table 4.2 Main parameters of VFRM and BFPMMs

Parameter	**VFRM**	**BFPMM**		
PM locations		**SM**	**MTM**	**SYM**
Stator pole number	6			
Rotor pole number	7			
Number of phases	3			
Turns per coil (AC/DC)	72			
Packing factor	0.5			
Rated copper loss (W)	30			
Airgap length (mm)	0.5			
Active axial length (mm)	25			
Rated speed (rpm)	400			
Outer radius of stator (mm)	45			
Split ratio	0.56	0.62	0.72	0.59
Stator pole arc (°)	18.6	23.2	22.2	17
Rotor pole arc (°)	18.8	18.2	13.4	18.2
Stator yoke thickness (mm)	4.4	4.6	4.3	10
Minimum PM thickness (mm)		2	2	5.2
Rated AC current (Arms)	5.2	9.0	7.5	7.4
Magnetic remanence (T)		1.2T	1.2T	1.2T
Relative PM permeability		1.05	1.05	1.05

4.4.3 Flux-Linkage and Back-EMF Waveforms

The open-circuit phase flux-linkage waveforms of the VFRM and three BFPMMs are compared in Fig. 4.15. Obviously, the polarities of phase flux-linkage for four machines with 6/7 stator/rotor pole combinations are all bipolar. Among the four machines, SYM-BFPMM has the highest fundamental phase flux-linkage while SM-BFPMM exhibit the lowest value, as shown in Fig. 4.15(b) and Table 4.3.

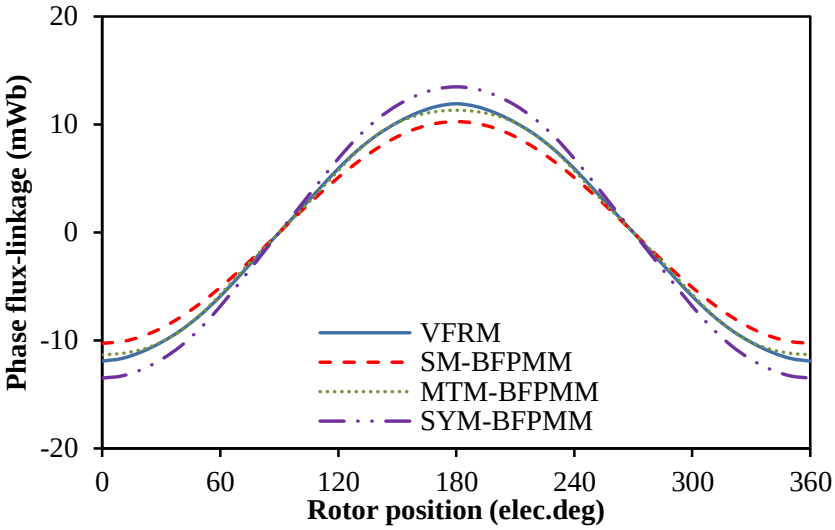

(a) Waveforms

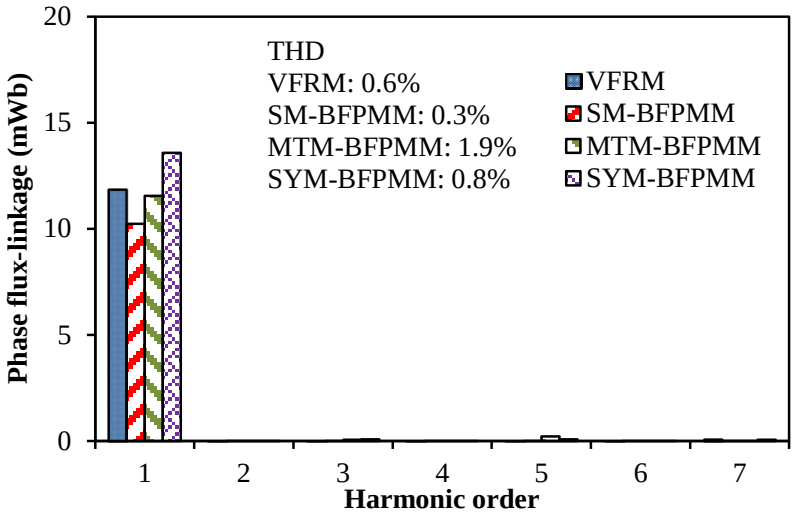

(b) Spectra

Fig. 4.15. Open-circuit phase flux-linkages, p_f=15W for VFRM.

Further, due to the same electric frequency (46.7Hz), SYM-BFPMM should also have the highest fundamental phase back-EMF, which is evidenced by the waveforms and FFT results shown in Fig. 4.16. Moreover, the phase back-EMF waveforms of four machines are all symmetrical since the even harmonics which cause the back-EMF waveform asymmetric are

cancelled completely. Compared with SYM- and MTM-BFPMMs, SM-BFPMM exhibits the most sinusoidal waveforms since the 3rd, 5th and 7th harmonics are lowest or negligible.

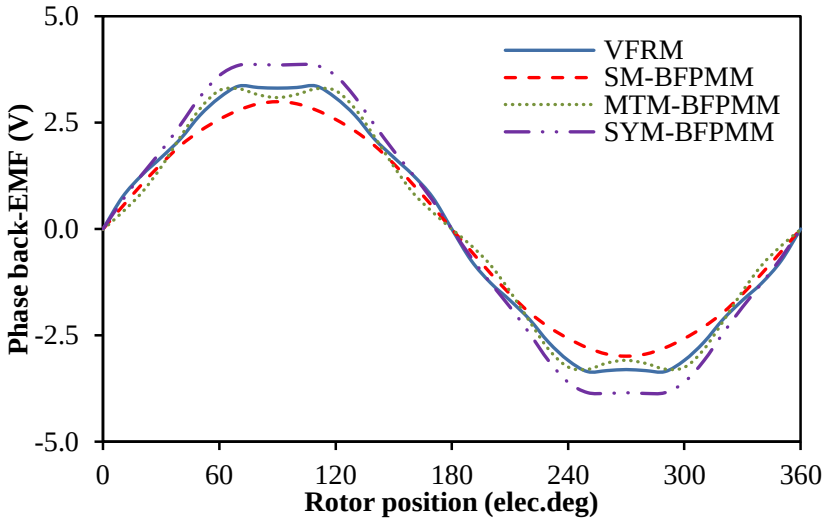

(a) Waveforms

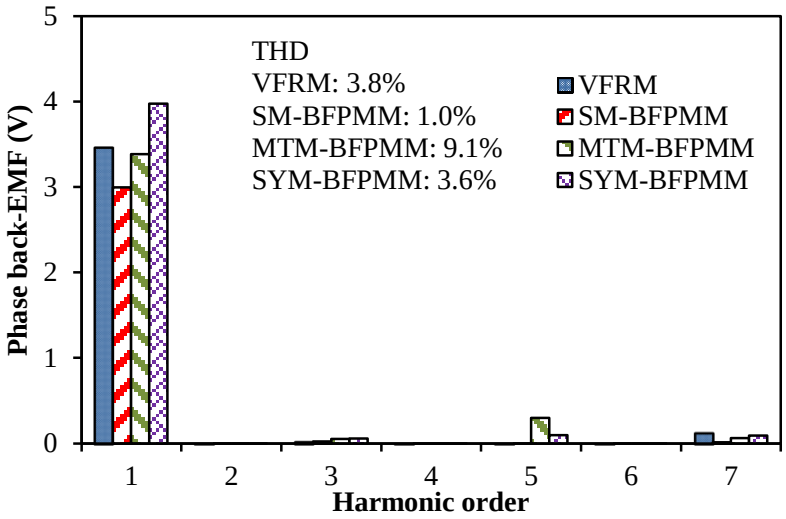

(b) Spectra

Fig. 4.16. Open-circuit phase back-EMFs at rated 400rpm, p_f=15W for VFRM.

4.4.4 *Dq*-Axis Inductances

According to torque equation shown in (4.9), BFPMM can be seen as one type of normal PM synchronous machines, which means it is suitable for vector control. Hence, *dq*-axis inductances are important parameters. Fig. 4.17 shows the *dq*-axis inductances with different current angles for all machines at rated currents as given in Table 4.2. Obviously, VFRM has much higher *dq*-axis inductances than BFPMM since the equivalent airgap in major flux loop of BFPMM is much larger due to the use of PMs. Further, among the three types of BFPMMs, SYM-BFPMM has the smallest *dq*-axis inductances. Similar to VFRM, the saliency ratios of

three BFPMMs are all close to 1 since the *d*-axis inductance is quite close to *q*-axis inductance, as shown in Fig. 4.17. This phenomenon implies that the potential reluctance torque of BFPMMs can be negligible as same as VFRM.

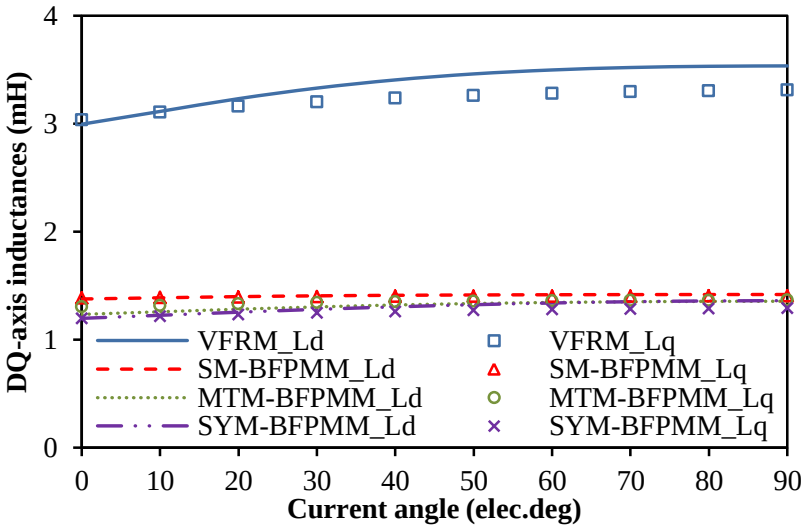

Fig. 4.17. *Dq*-axis inductances with current angle at rated currents of all machines.

4.4.5 Cogging Torque

Fig. 4.18 shows the cogging torque waveforms for VFRM and three types of BFPMMs. Obviously, SM-BFPMM exhibits the largest amplitudes of cogging torque while SYM-BFPMM has the smallest one.

According to the analysis mentioned above, BFPMM is one type of stator PM synchronous machines. Therefore, the formula which used to calculate the cycle number of the cogging torque waveform over one electric period in conventional PM synchronous machines can be extend to BFPMM as (4.10) [ZHU00].

$$N_c = \frac{N_S}{GCD(N_S, N_r)} \tag{4.10}$$

where N_c is the number of cogging torque cycles over one electrical period, GCD means the greatest common divisor. By way of example, for SM-BFPMMs under investigation, N_r=7, N_s=6, N_c=6. The result can be evidenced by Fig. 4.18(a). As shown in Fig. 4.18(b), the main harmonics of cogging torque in all machines are all 6n times, which indicate that the combined cogging torques will exhibit 6 cycles over one electric period.

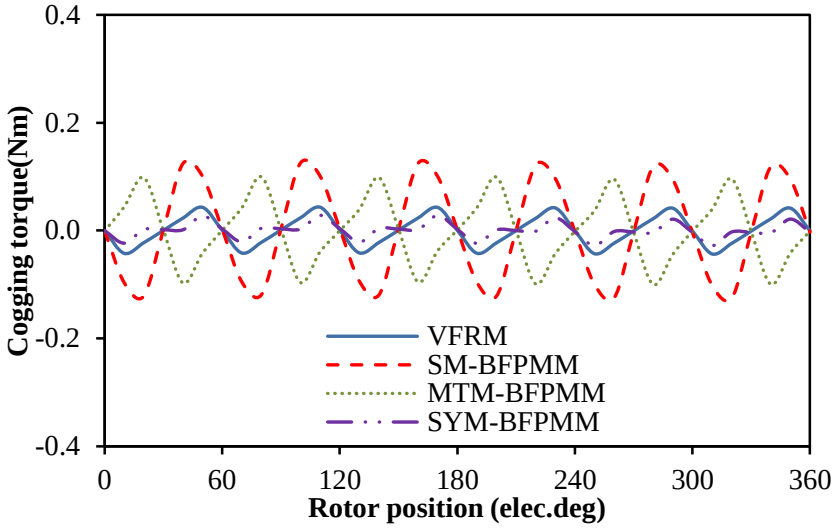

(a) Waveforms

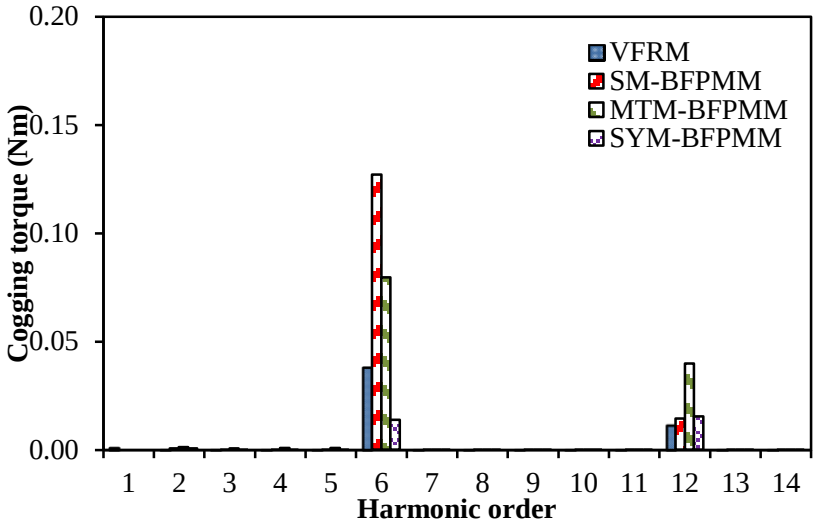

(b) Spectra

Fig. 4.18. Open-Circuit cogging torque, p_f=15W for VFRM.

4.4.6 Electromagnetic Torque Characteristics

Fig. 4.19 shows the waveforms of average torque against with current angle at rated currents (corresponding to p_c=30W) as given in Table 4.2. Similar to VFRM, the optimal current angles for three types of BFPMMs are all close to 0°. Hence, the reluctance torque can be negligible in both VFRMs and BFPMMs, which is consistent with the conclusion shown in section 4.4.4.

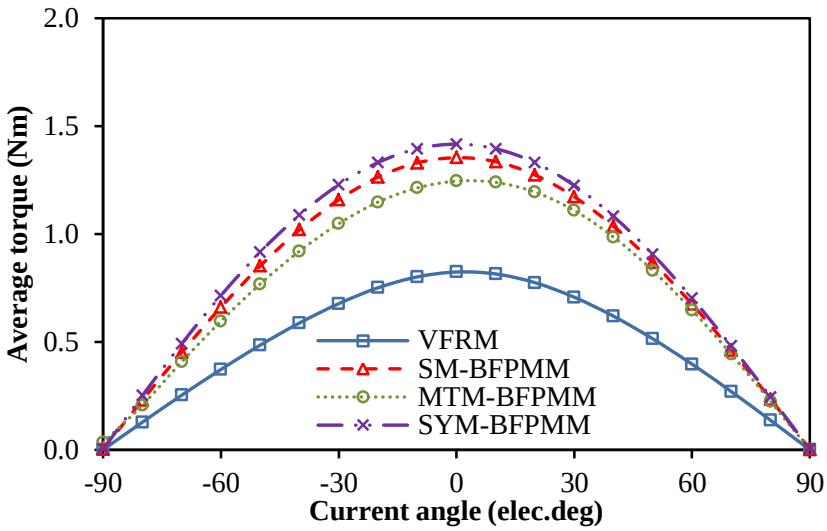

Fig. 4.19. Variation of average torque with current angle, p_c=30W.

Fig. 4.20 shows the waveform of torque against with rotor positon at rated currents (corresponding to p_c=30W) with I_d=0 control. Obviously, the cycle numbers of torque ripple over one electric period are six for all machines. It is mainly due to the combined influence of the 5th and 7th harmonics of back-EMF and the cogging torque. The torque ripples of VFRM, SM-BFPMM, MTM-BFPMM and SYM-BFPMM are 10.7%, 18.8%, 26.2% and 11.9% respectively. Obviously, BFPMM exhibits larger torque ripple than VFRM. Meanwhile, among three types of BFPMMs, MTM-BFPMM has the largest torque ripple while SYM-BFPMM exhibits the smallest one. Moreover, under the rated copper loss, the average torques of VFRM, SM-BFPMM, MTM-BFPMM and SYM-BFPMM are 0.82, 1.36, 1.25, 1.42 Nm respectively. Compared with VFRM, the average torques are enhanced by about 64.5%, 51.0% and 72.1% respectively in SM-BFPMM, MTM-BFPMM and SYM-BFPMM. Further, among the three types of BFPMMs, SYM-BFPMM has the highest torque capability while MTM-BFPMM has the lowest one. For the ratio of torque to PM volume as shown in Fig. 4.21, SM-BFPMM has the highest value among the three types of BFPMMs, which means that SM-BFPMM has the highest PM utilization efficiency.

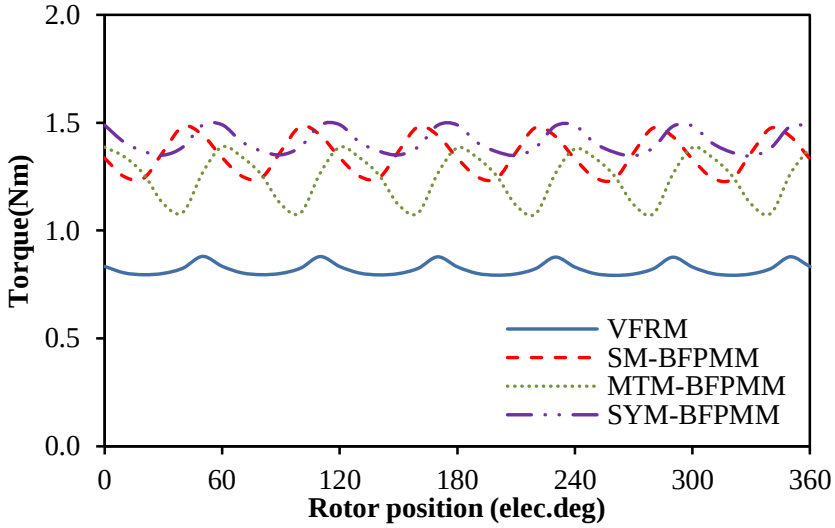

(a) Waveforms

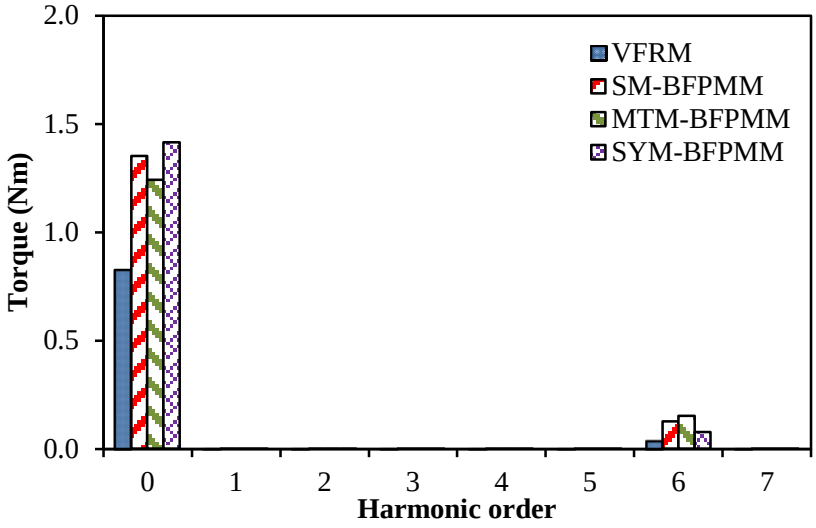

(b) Spectra

Fig. 4.20. Variation of torque with rotor position, p_c=30W, I_d=0 control.

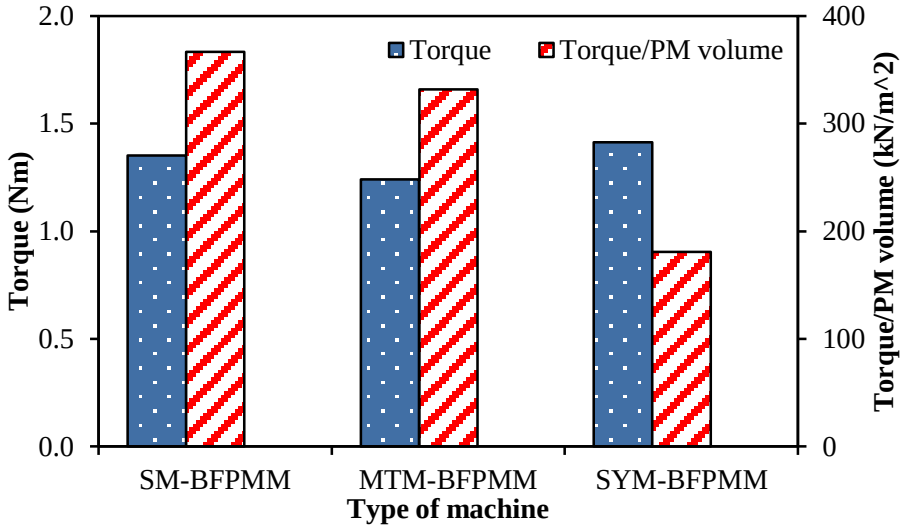

Fig. 4.21. Average torque and torque to volume of PM in BFPMMs, p_c=30W, I_d=0 control.

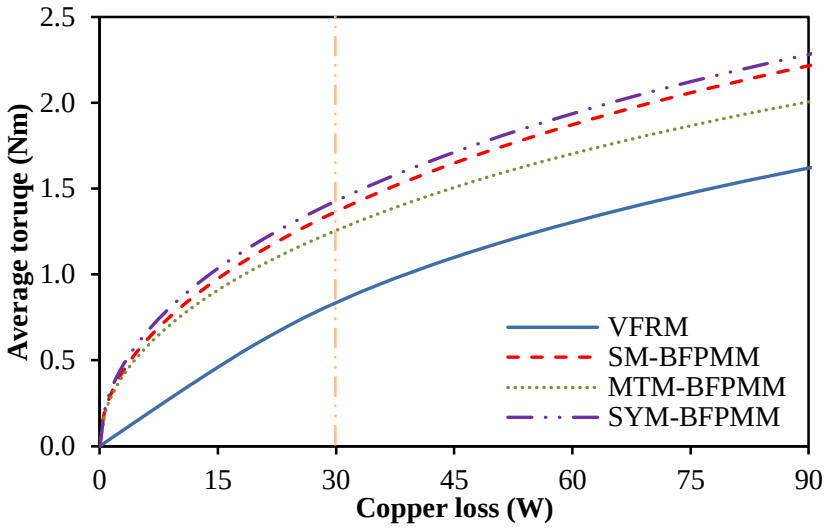

Fig. 4.22. Variation of average torque with copper loss.

Fig. 4.22 shows the waveforms of average torque against with copper loss for all machines. The dashed and dotted line indicates the rated copper loss which adopted in globe optimization. Obviously, the average torque is gradually saturated with the increase of copper loss (current) due to the saturation effect of magnetic circuit. Further, BFPMMs exhibit higher average torque than VFRM under the same copper loss during the whole copper loss range, especially in SYM-BFPMM.

Table 4.3 Main electromagnetic performances of VFRM and BFPMMs

Parameter	**VFRM**	**BFPMMs**		
PM locations		SM	MTM	SYM
Fund. flux-linkage (Wb)	11.9	10.2	11.6	13.6
Fund. back-EMF (V)	3.5	3.0	3.4	4.0
Cogging torque (Nm)	0.04	0.13	0.1	0.03
Average torque (Nm)	0.82	1.36	1.25	1.42
Torque ripple (%)	10.7	18.8	26.2	11.9
Torque/PM volume (kN/m2)		367	332	181

4.5 Experimental Verification

Two prototype machines are made to validate the foregoing analyses, which are 6/7 stator/rotor pole SM-BFPMM and SYM-BFPMM as shown in Fig. 4.23. The parameters of two prototype machines are the same as shown in Table 4.2.

Fig. 4.24 shows the measured and predicted open-circuit phase back-EMF of two machines at rated speed (400rpm). Fig. 4.25 shows the measured and predicted open-circuit cogging torque. Compared with SM-BFPMM, SYM-BFPMM exhibits higher phase back-EMF and lower cogging torque. The results are consistent with the previous analyses. Fig. 4.26 shows the variation of static torque with rotor position at four different armature current combinations, i.e. 25%, 50%, 75% and 100% of rated armature current. Based on Fig. 4.26, the variation of static torque at 90° rotor position with the copper loss is obtained and shown in Fig. 4.27. Overall, the measured and FE predicted results match well. The difference between the measured and FE predicted results of static torque under high current or copper loss are due to the increased influence of end-effect.

(a) Stator of SM-BFPMM

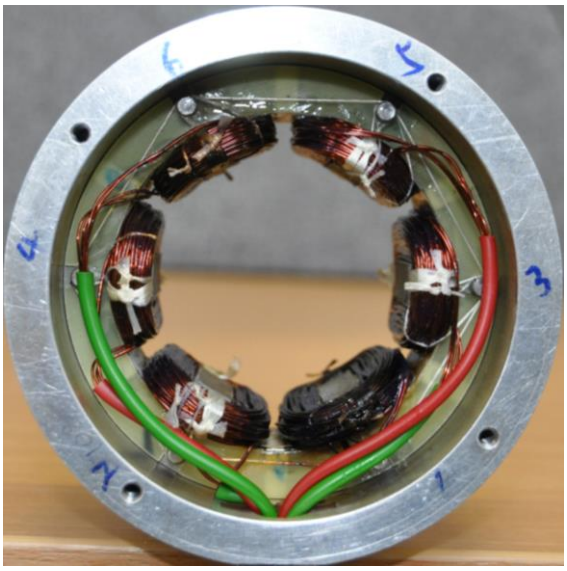

(b) Stator of SYM-BFPMM

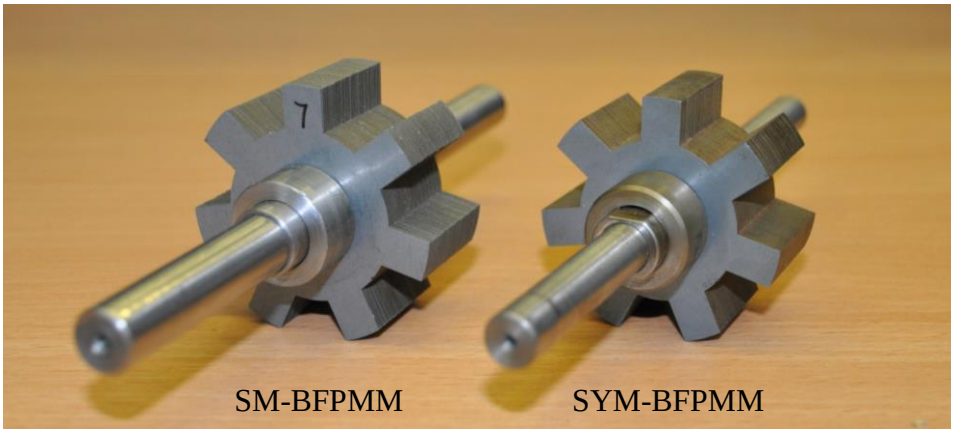

(c) 7-pole rotor SM-BFPMM (d) 7-pole rotor of SYM-BFPMM

Fig. 4.23. Prototypes of SM-BFPMM and SYM-BFPMM.

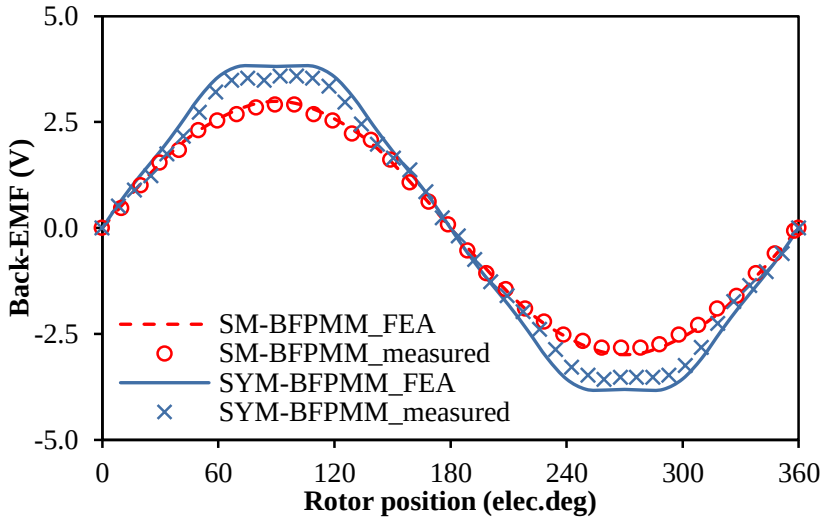

Fig. 4.24. Measured and FE predicted open-circuit phase back-EMFs at rated 400rpm.

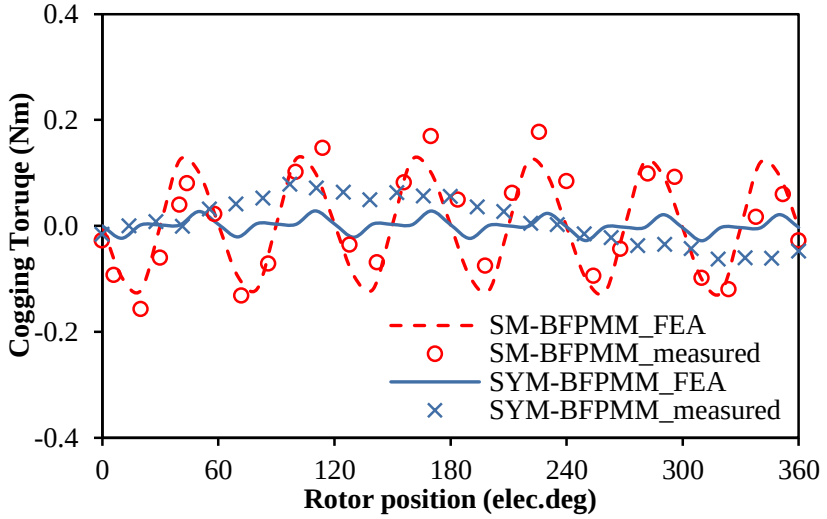

Fig. 4.25. Measured and FE predicted open-circuit cogging torque.

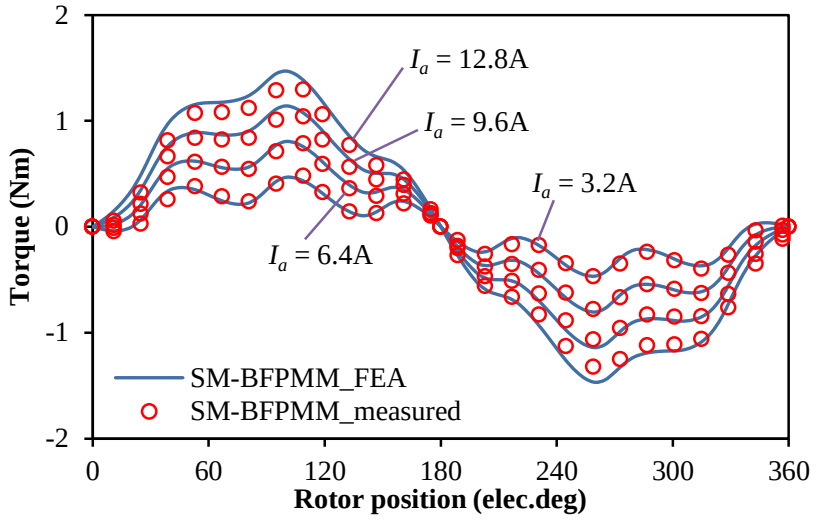

(a) SM-BFPMM with 7-pole rotor.

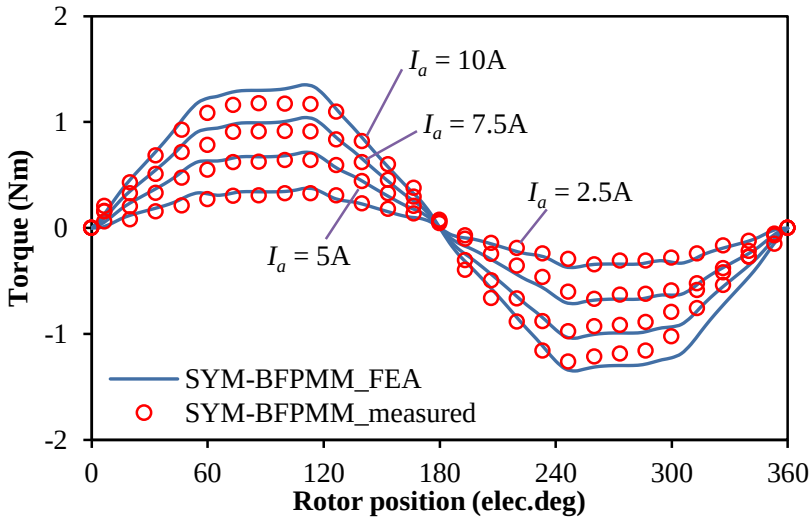

(b) SYM-BFPMM with 7-pole rotor.

Fig. 4.26. Measured and FE predicted phase static torques when -1/2I_A=I_B=I_C.

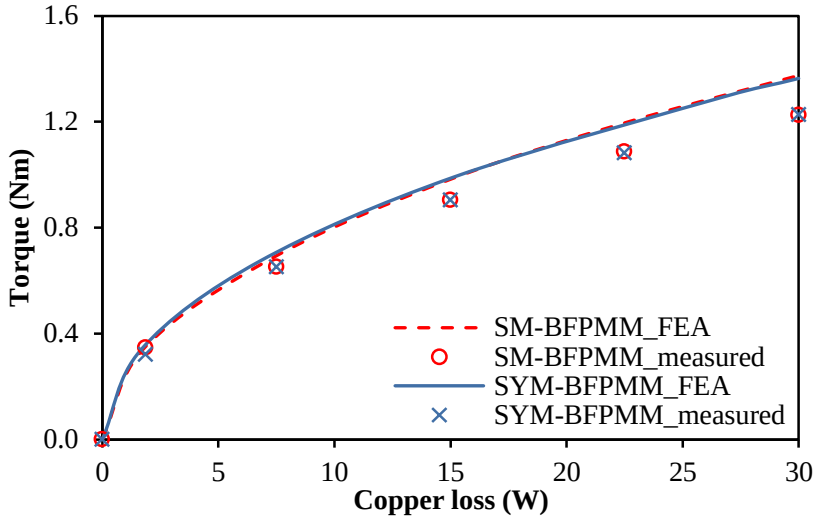

Fig. 4.27. Measured and FE predicted torque-copper loss characteristics when rotor positon is 90°

4.6 Summary

In this chapter, alternate BFPMMs having doubly salient stator and rotor structure and non-overlapping armature winding are proposed and investigated. Alternate polarity PMs are mounted on the surface of adjacent stator poles. The choice of rotor pole number is flexible and can be any integers except the phase number and its multiples. Meanwhile, the symmetrical bipolar phase flux-linkage and back-EMF waveforms can be obtained when the ratio of stator pole number to GCD of stator- and rotor-pole numbers is even.

Among the 6/4, 6/5, 6/7, and 6/8 stator/rotor pole combinations, 6/7 N_s/N_r SM-BFPMM has the largest average torque under the rated copper loss. Since the PM can be located from the surface to bottom of stator pole and even in stator yoke, three typical PM locations are chosen

to compare and analyze the influence of PM locations on electromagnetic performances under 6/7 N_s/N_r combination. The results show that SM-BFPMM has the highest PM utilization efficiency and the most sinusoidal phase back-EMF but the largest cogging torque. The SYM-BFPMM exhibits the largest average torque as well as the lowest torque ripple and cogging torque but the lowest PM utilization efficiency. Compared with VFRM, the average torques are enhanced by about 64.5%, 51.0% and 72.1% respectively in SM-BFPMM, MTM-BFPMM and SYM-BFPMM. Further, the reluctance torque is negligible in BFPMMs regardless of PM locations. Finally, the analyses have been validated by both FEA and measurements.

4.7 Appendix

In order to avoid the demagnetization under on-load condition, the thickness of PMs should be selected carefully. Corresponding to the maximum operating temperature which is assumed as 80℃, the magnetic remanence of PM with grade as N35SH is 1.08T. Then, the variation of minimum PM flux density with the thickness of PM under the rated 30W copper loss and 80℃ maximum operating temperature is indicated in Fig. 4.28, which is corresponding to the 6/7 stator/rotor pole SM-BFPMM. By the trade-off between the average torque (maximum at PM thickness is 1.4mm) and the minimum PM flux density at 80℃ maximum operating temperature, the minimum thickness of PM for SM-BFPMM is chosen to be 2mm. Similarly, the minimum thickness of PM in MTM-BFPMM can also be increased to 2mm to avoid the demagnetization.

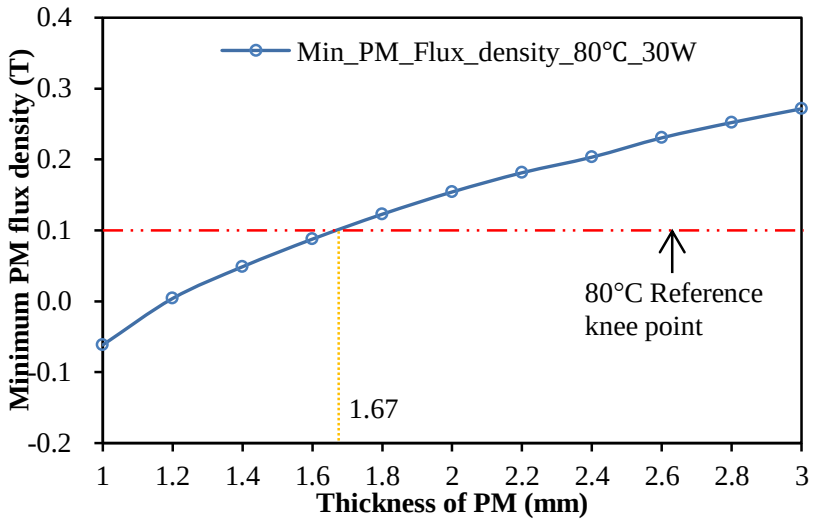

Fig. 4.28. Variation of minimum PM flux density with PM thickness under the rated 30W copper loss and 80℃ operating temperature for SM-BFPMM machines.

CHAPTER 5
COMPARATIVE STUDY OF NOVEL BIASED FLUX PM MACHINES WITH DOUBLY SALIENT PM MACHINES CONSIDERING INFLUENCE OF FLUX FOCSUING

In the previous chapter, the electromagnetic performances of biased flux permanent magnet (PMs) machines (BFPMMs) are analysed. The results show that the highest torque capability is obtained in BFPMM when the PMs are located in the stator yoke. Nevertheless, the flux densities in some part of the stator yoke are far below the saturation knee-point of steel B-H curve, which means that the material has not been fully utilized. Therefore, the part of stator yoke with low flux density can be reduced to enlarge the slot area, while has the feature of flux focusing. In this way, the increased slot area will result in larger rated current under same rated copper loss and enhance the torque performance.

In this chapter, the influences of flux focusing on the electromagnetic performance of BFPMM with PMs located in stator yoke will be analysed. Then, based on the inner type flux focusing structure, the electromagnetic performances of optimized BFPMM will be compared with optimized doubly salient PM machine (DSPMM) under the same rated copper loss and machine size since two types of machines have similar topology except the different interval number of stator poles between alternate polarity PMs in the stator yoke.

5.1 Introduction

Stator permanent magnet (PM) machines have been investigated extensively over the last decades due to the robust rotor structure, easy heat dissipation and low risk of demagnetization. Doubly salient PM machine (DSPMM) [LIA95] is one type of the stator PM machines, in which PMs are located in the stator back iron at an interval of pole number equal to phase number and the concentrated windings are employed. However, it has unipolar flux linkage, relative low torque density and large torque ripple.

References [CHE00] [CHE01a] analyse the principle of the electromagnetic torque generation and the influence of different geometry parameters of DSPMM in detail. The phase back-EMF waveform of DSPMM is trapezoidal [CHE00] [CHE01a] [CHE11c], which is suitable for brushless DC (BLDC) operation [LI07]. On the other hand, the rotor-skewing method [HUA08] can be used to make back-EMF waveform more sinusoidal. Consequently,

DSPMM can also be operated in the brushless AC (BLAC) mode [HUA08] [ZHA10]. Nevertheless, since the asymmetric flux path in the stator of DSPMM, the flux-linkages and back-EMFs of each phase are unbalanced, particularly under heavy magnetic saturation.

In this chapter, a novel biased flux PM machine (BFPMM) with doubly salient structure and alternate polarities of PMs circumferentially located in the stator back iron between adjacent stator poles is investigated, which can eliminate the asymmetric flux path in the stator of DSPMM. Firstly, the topologies and stator/rotor pole combinations are illustrated. Secondly, three types of flux focusing structure are proposed to enhance the torque performance. Then, based on the inner type flux focusing structure, the electromagnetic performances of BFPMM are compared with DSPMM. Finally, a prototype machine with 6/7 stator/rotor pole inner type flux focusing BFPMM is manufactured and measured to validate the analyses.

5.2 Machine Topologies and Stator/Rotor Pole Combinations

5.2.1 Machine Topologies

As shown in Fig. 5.1, the stator of biased flux permanent magnet (PM) machine (BFPMM) consists of T-shape laminated segments between which are placed by circumferentially magnetized PMs with alternate polarities. Non-overlapping windings are wound around each stator pole. The rotor pole of BFPMM is similar to SRM, which has excellent mechanical integrity and robustness. The main difference between BFPMM and doubly salient PM machine (DSPMM) is the interval number of stator pole between the alternate polarities PMs in the stator yoke, which is equal to one in BFPMM while that is equal to phase number in DSPMM.

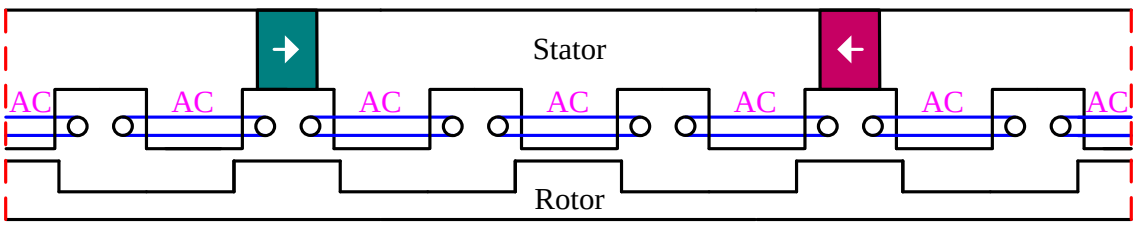

(a) Structure schematic of DSPMM

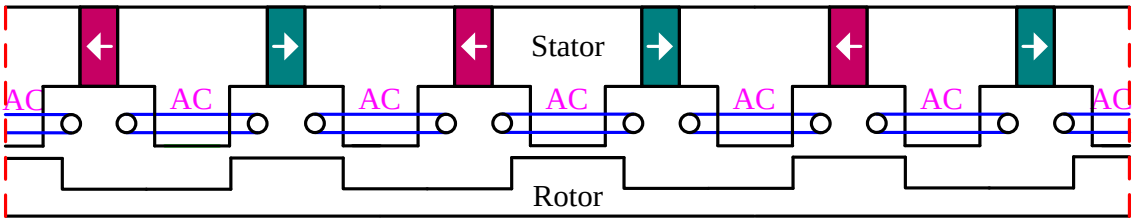

(b) Structure schematics of BFPMM

Fig. 5.1. Structure evolution from DSPMM to BFPMM.

5.2.2 Stator and Rotor Pole Combinations

Different from DSPMM in which the stator and rotor pole (N_s/N_r) combinations are restricted to equations (5.1) and (5.2) [FAN08], the stator and rotor pole combinations in BFPMM are more flexible. The rotor pole number can be any integers except the phase number and its multiples. Hence, the choices of stator and rotor pole combinations of BFPMM can be summarized as equations (5.1) and (5.3).

$$N_s = 2mk \tag{5.1}$$

$$N_r = N_s \pm 2k \tag{5.2}$$

$$N_r = N_s \pm j \ (N_r \neq k_i m, j=1, 2\ldots, k_i=1.\ 2\ldots) \tag{5.3}$$

where m is phase number, k, j and k_i are integers.

Being same as the analysis in previous chapter, the conventional coil-EMF vector method can be used in BFPMM to determine the armature windings [ZHU10]. The electric degrees α_e between two adjacent coil-EMF vectors can be derived from the mechanical degrees α_m and the rotor pole number N_r according to (5.4).

$$\alpha_e = N_r \alpha_m \tag{5.4}$$

For BFPMM with 6-pole stator, the most feasible rotor pole numbers could be 4, 5, 7 and 8, as shown in Fig. 5.2. All machines are optimized with maximum average torque under the rated 30W copper loss. According to (5.4), the coils belong to the same phase are connected in series with opposite polarity (180 electric degree shifting) in 5- and 7-rotor pole BFPMMs but with same polarity in 4- and 8-rotor pole BFPMMs, as shown in Fig. 5.2. This difference results in two different characteristics of phase flux-linkages and back-EMFs for the different stator/rotor pole combinations. Obviously, 5- and 7-rotor pole BFPMMs have bipolar phase flux-linkages and symmetic phase back-EMFs whilst 4- and 8-rotor pole BFPMMs exhibit

unipolar phase flux-linkages and asymmetric phase back-EMFs, as shown in Fig. 5.3 and Fig. 5.4. Further, among the four main stator/rotor pole combinations, the 6/7 stator/rotor pole BFPMM exhibits the highest average torque under the same copper loss during the whole copper loss range, as shown in Fig. 5.5.

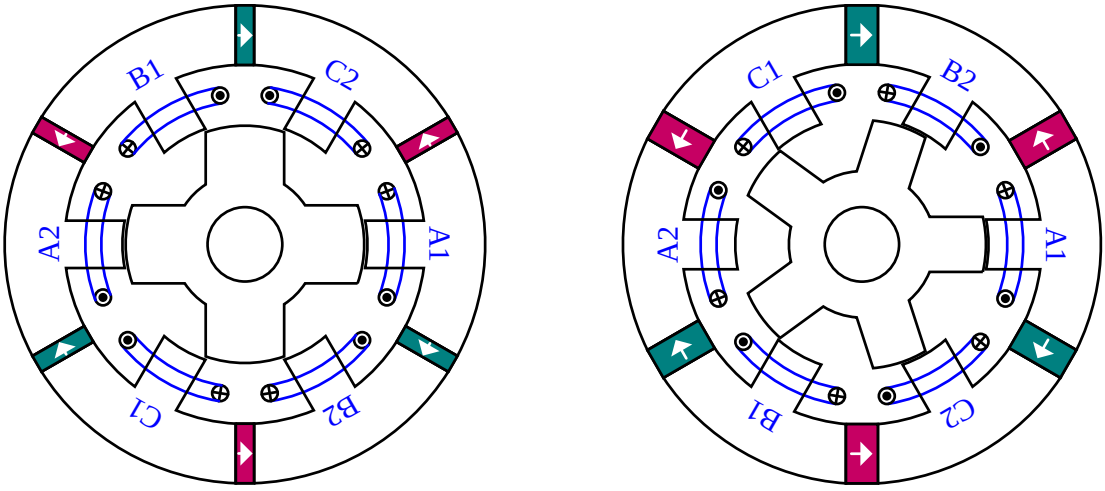

(a) 6S/4R (b) 6S/5R

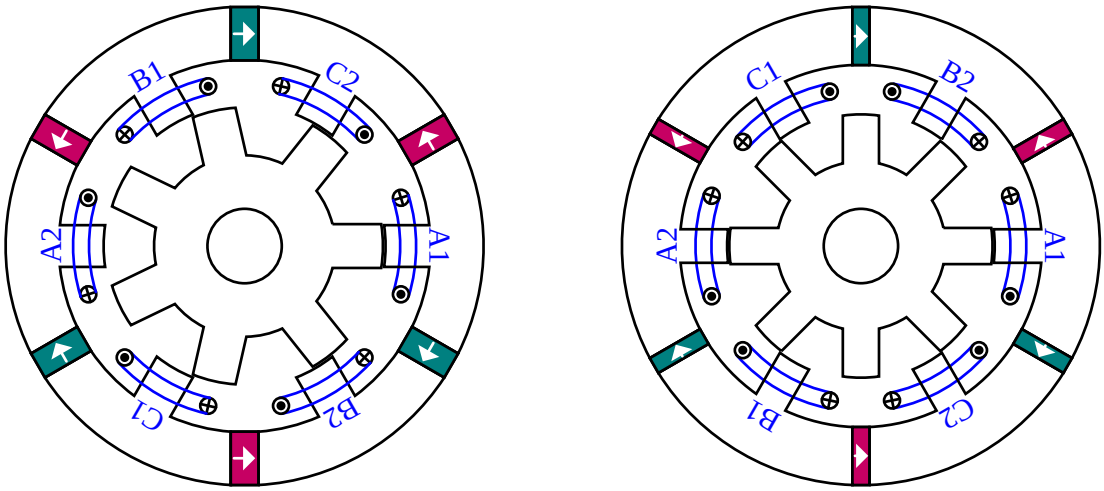

(a) 6S/7R (b) 6S/8R

Fig. 5.2. Topologies of 6-stator pole BFPMMs with different rotor pole number.

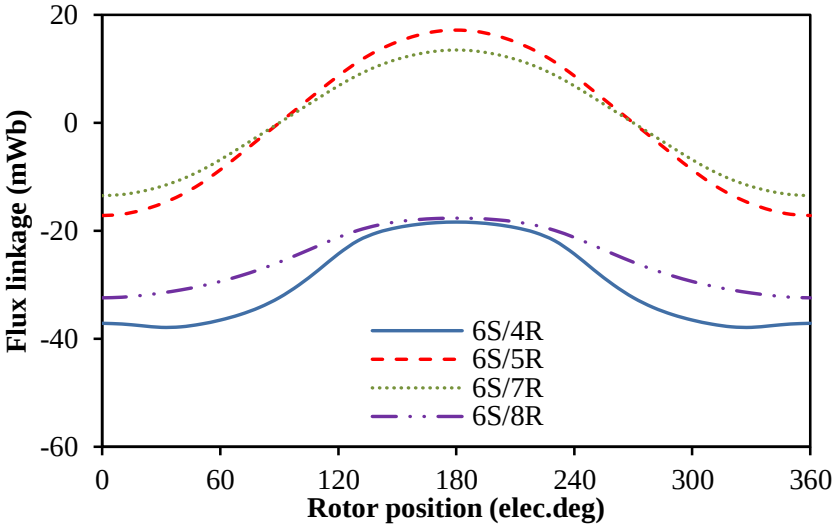

Fig. 5.3. Open-circuit phase flux-linkage of 6-stato pole BFPMMs.

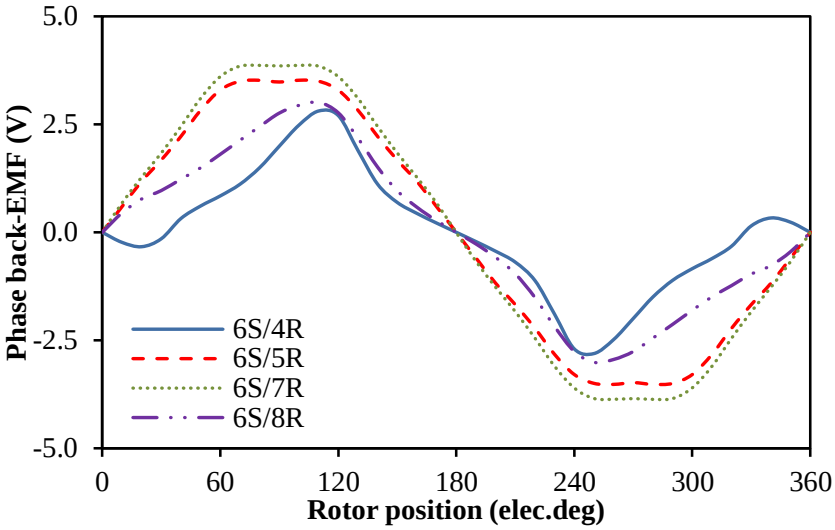

Fig. 5.4. Open-circuit phase-EMFs of 6-stator pole BFPMMs.

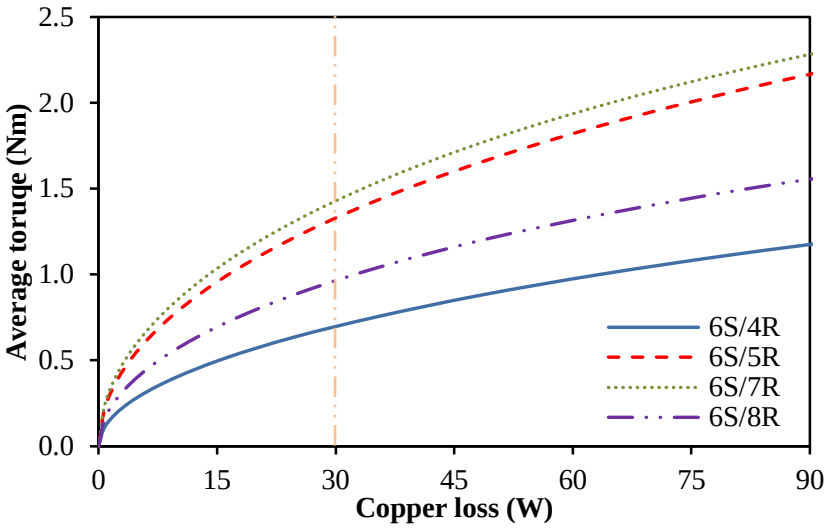

Fig. 5.5. Variation of average torque with copper loss in 6-sator pole BFPMM.

5.3 Comparison for BFPMMs with Different Flux Focusing Types

In this section, the influence of flux focusing on electromagnetic performance of BFPMMs will be analysed.

5.3.1 Alternate Flux Focusing Types

In the original design of BFPMM, the thickness of stator yoke is restricted by the thickness of PM as shown Fig. 5.2. Nevertheless, the flux densities in some part of the stator back iron of the original BFPMMs are far below the saturation knee-point of steel B-H curve, as shown in Fig. 5.6(a). It means that the material has not been fully utilized. Hence, the part of stator back-iron with low flux density can be reduced to enlarge the slot area as shown in Fig. 5.6(b) which has the feature of flux focusing. Under the fixed copper loss, the increased slot area will result in larger rated current and improve the torque performance. Meanwhile, the flux focusing types which are adopted in [LIA95] [CHE00] [CHE01a] can also be adopted in BFPMMs as shown in Fig. 5.6 (c). Further, this outer type flux focusing can be combined with Fig. 5.6(b) and form up a new topology as shown in Fig. 5.6(d). In order to simplify the comparison, these three flux focusing topologies can be designated as inner type (IT), outer type (OT) and combined type (CT). Since the 6/7 stator/rotor pole combination BFPMM exhibits the optimal average torque at the rated copper loss, the influence of flux focuisng on electromagnetic torque performance of BFPMM will be focused on this stator/rotor pole combination. The main geometric parameters of the origianal BFPMM and three flux focusing types of BFPMMs are listed in Table 5.1. All mahcines are optimized for maximum average toruqe unde the rated copper loss. Moreover, for OT-BFPMM and CT-BFPMM with feature of outer flux focusing, the radius of maximum inscribed circle of hexagonal stator structure is 45mm, which is same as the radius of outer stator of ORI-BFPMM and IT-BFPMM.

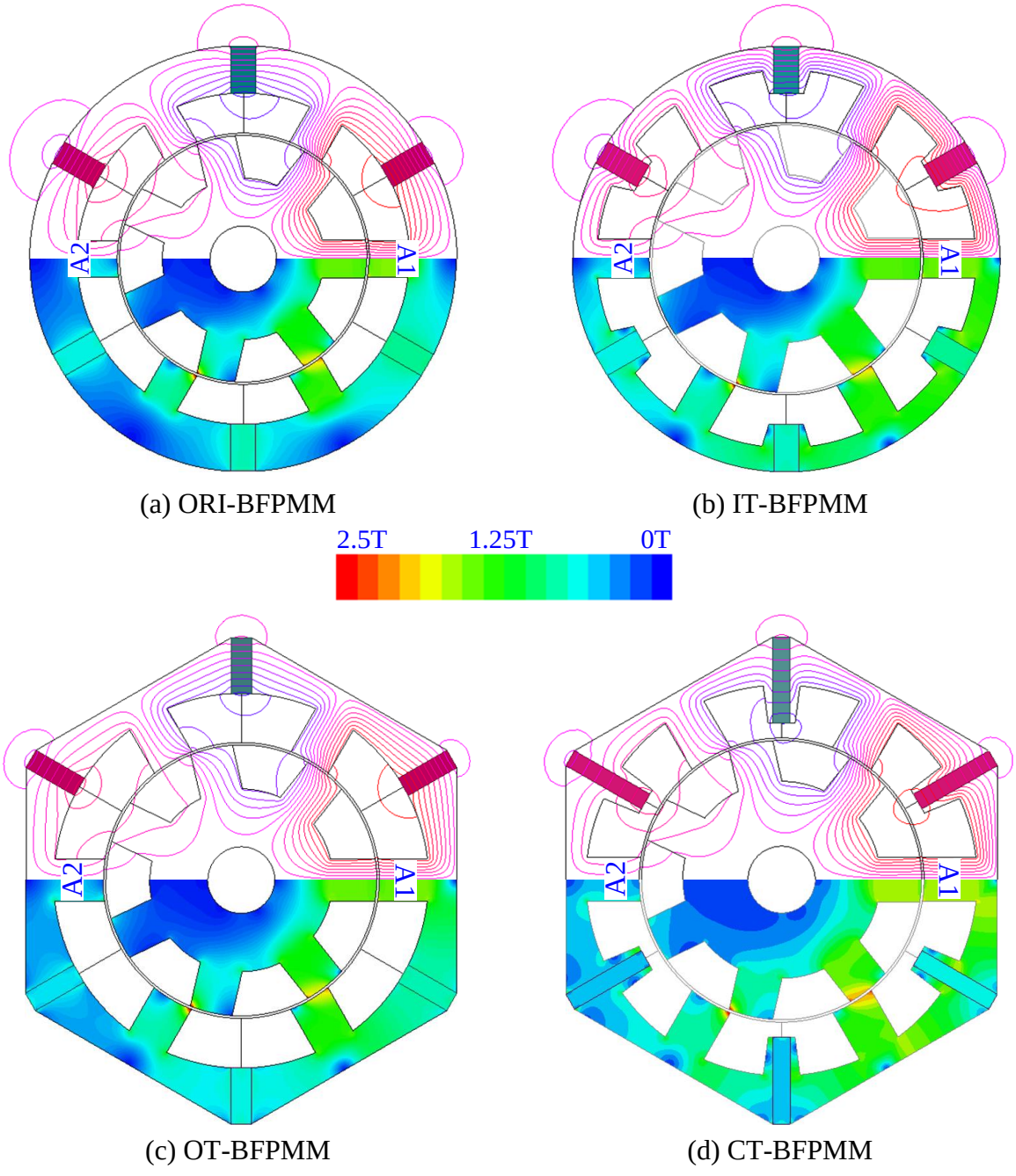

(a) ORI-BFPMM (b) IT-BFPMM

(c) OT-BFPMM (d) CT-BFPMM

Fig. 5.6. Open-circuit equipotential and flux distribution of BFPMM with the original design and different types of flux focusing.

Table 5.1 Main parameters of BFPMMs and DSPMMs

Parameters	**BFPMMs**				**DSPMMs**
Type of flux focusing	ORI	IT	OT	CT	IT
Number of phases	3				
Turns per coil	72				
Packing factor	0.5				
Rated copper loss (W)	30				
Airgap length (mm)	0.5				
Active axial length (mm)	25				
Rated speed (rpm)	400				
Outer radius of stator (mm)	45				
Stator pole number	6	6	6	6	6
Rotor pole number	7	7	7	7	4
Volume (10^{-6} m3)	159	159	175	175	159
Split ratio	0.59	0.64	0.64	0.66.	0.52
Stator pole arc (°)	17	16.6	18	18	30
Rotor pole arc (°)	18.2	18	18.8	18.4	30.8
Thickness of stator yoke (mm)	10	5.1	5.9	4.2	7.8
PM thickness (mm)	10	10	11.7	18.1	11.9
PM width (mm)	5.2	5.2	4.2	3.6	9.0
Total PM volume (mm^3)	7816.8	7816.8	7374.5	9807.5	5346.4
Rated AC current at 30W (Arms)	7.4	8.4	8.5	8.2	7.6
Rated current density (A_{rms}/mm^2)	10.34	9.13	8.97	9.32	10.01
Magnetic remanence (T)	1.2T				
Relative PM permeability	1.05				

5.3.2 Open-Circuit Field Distribution

Fig. 5.6 shows the open-circuit flux equiptotential and flux density field distributions for all machines at aligned position (one rotor pole alinged with the stator pole wound with coil A1). Obviously, short flux path, which could result in lower MMF drop in the stator, is observed in BFPMMs with 6/7 stator /rotor pole combination. Due to the reduced thickness of stator yoke, the saturation of the stator yoke in IT-BFPMM, OT-BFPMM and CT-BFPMM are hearvier than that in ORI-BFPMM.

5.3.3 Flux-Linkage and Back-EMF Waveforms

Fig. 5.7 shows the open-circuit bipolar phase flux-linkages of four machines. Obviously, CT-BFPMM has higher peak value of phase flux-linkage than other three machines since it employs largest magnet usage and thickness of PM. Due to the same electric frequency (46.7Hz), CT-BFPMM should also exhibits largest peak value of back-EMF among four machines according to the magnitude of flux-linkages as shown in Fig. 5.7. It is evidenced by the waveforms and FFT results shown in Fig. 5.8, in which CT-BFPMM has largest peak value and magnitude of fundamental wave. Overall, all three types of flux focusing can enhance the phase flux-linkage and back-EMF of BFPMMs when compared with original design, as show in Table 5.2. Moreover, the waveforms of phase back-EMF in ORI-BFPMM and BFPMMs with flux focusing are all close to sinusoidal due to the low odd harmonics and cancelled even harmonics as shown in Fig. 5.8(b).

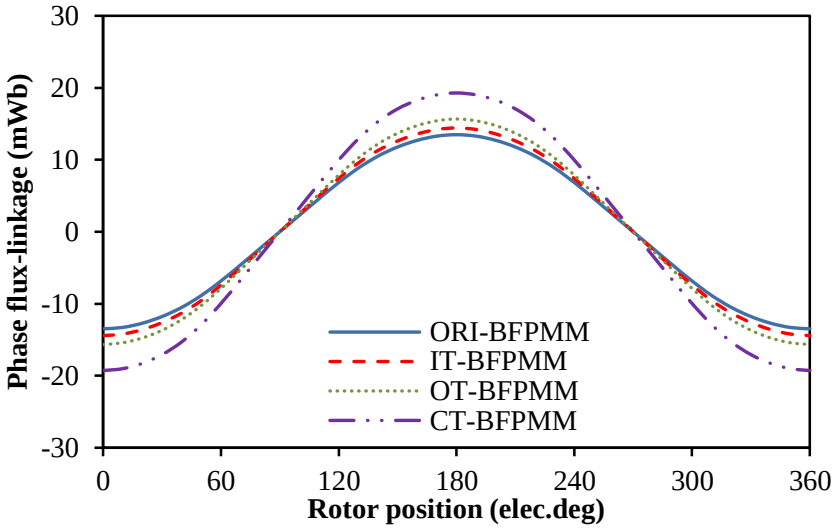

Fig. 5.7. Open-circuit phase flux-linkages of BFPMMs.

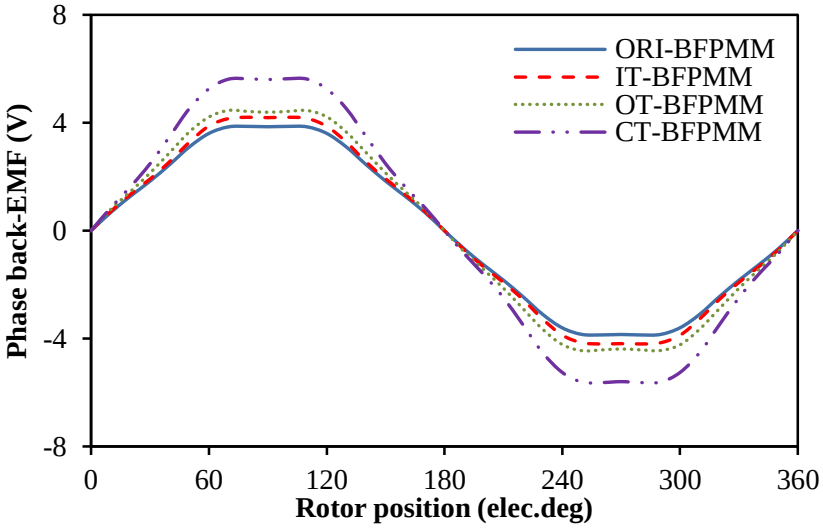

(a) Waveforms

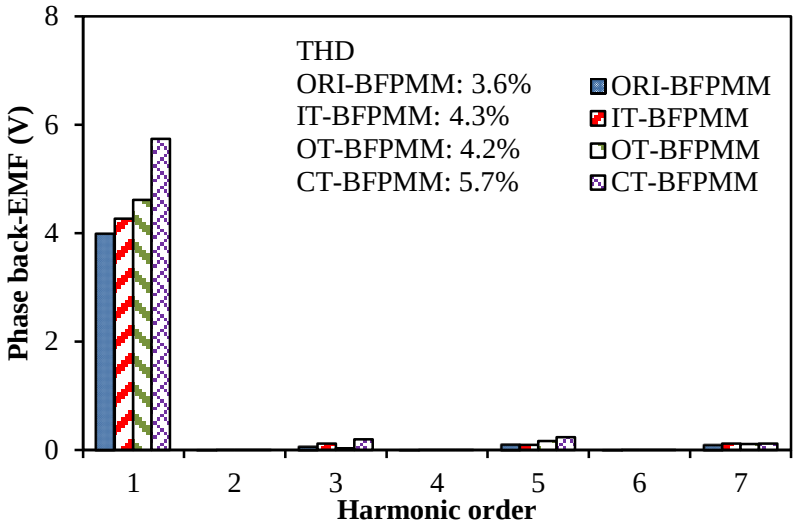

(b) Spectra

Fig. 5.8. Open-circuit phase back-EMFs of BFPMMs at rated 400rpm.

5.3.4 *Dq*-axis Inductances

The waveforms of *dq*-inductances with different current angles at rated currents of four machines are shown in Fig. 5.9. Compared with ORI-BFPMM, the *dq*-inductances are increased in BFPMMs with flux focusing structure, especially in OT-BFPMM and CT-BFPMM. It is mainly due to the reduced width of PM. Moreover, since the *q*-axis inductance is quite close to the *d*-axis inductance, the saliency ratios of four machines are all close to 1. Therefore, the potential reluctance torque of four machines can be negligible.

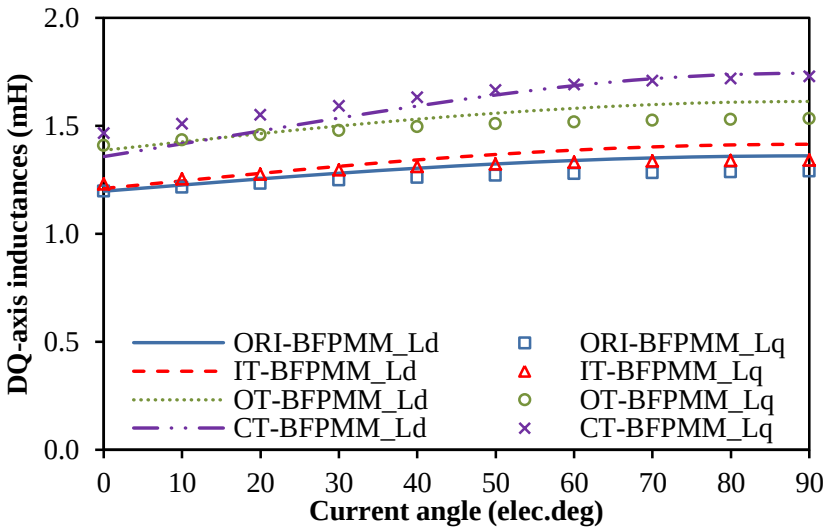

Fig. 5.9. Variation of *dq*-axis inductances with current angles at the rated currents as given in Table 5.1.

5.3.5 Cogging Torque

Fig. 5.10 shows the cogging torque waveforms over one electric period for four machines. Obviously, the magnitudes of cogging torque are enlarged in BFPMMs with flux focusing structure when compared with ORI-BFPMM, especially in BFPMM has the feature of outer flux focusing, e.g. CT-BFPMM and OT-BFPMMs. Moreover, the cycle numbers of torque ripple over one electric period for four machines are all equal to six. These results are further evidenced the (4.10).

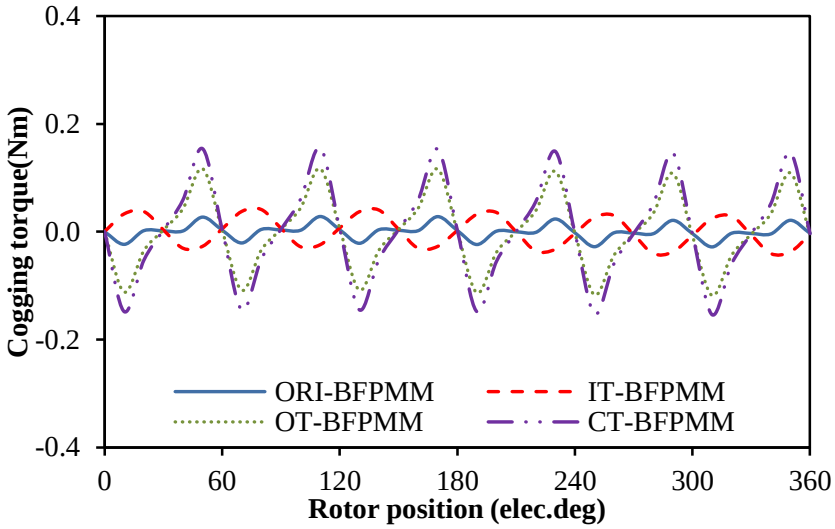

Fig. 5.10. Open-circuit cogging torques of BFPMMs.

5.3.6 Electromagnetic Torque Characteristics

Fig. 5.11 shows the waveforms of average torque against with current angle at rated currents of four machines. Obviously, the optimal current angles for four machines are all close to 0°, which can be used to evidence the conclusion about the negligible reluctance torque for BFPMMs as mentioned in section 5.3.4.

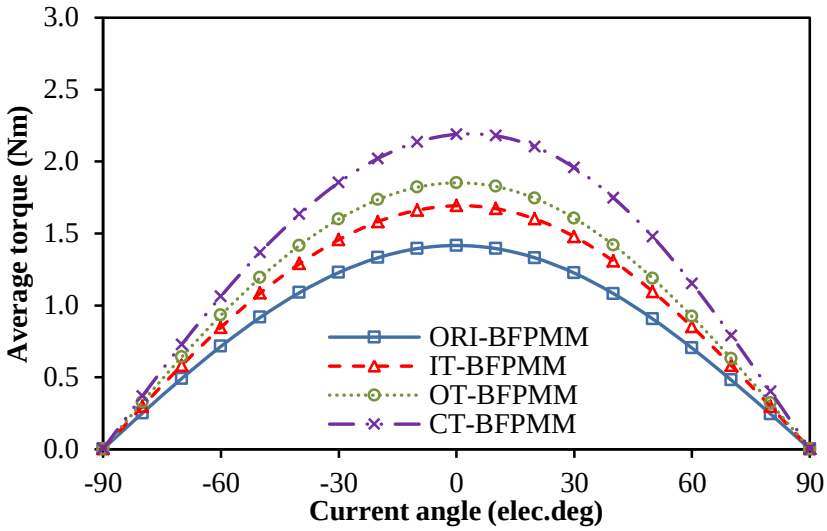

Fig. 5.11. Variation of average torque with current angle in BFPMMs, p_c=30W.

The waveforms of torque against with rotor position at rated currents and I_d=0 control for all machines are show in Fig. 5.12. The torque ripples of ORI-BFPMM, IT-BFPMM, OT-BFPMM and CT-BFPMM are 11.9%, 11.8%, 16.9% and 16.1% respectively, as shown in Table 5.2. Obviously, among the four machines, OT-BFPPMM and CT-BFPMM which have the feature of outer flux focusing structure exhibit higher torque ripple since they also have the larger magnitudes of cogging torque as shown in Fig. 5.10. Meanwhile, due to the increased PM volume and the enlarged slot area (result in increased current under the fixed copper loss), the average torques under the rated copper loss are enhanced about 19%, 30.3% and 54.2% respectively by using IT, OT and CT types of flux focusing structure in the original BFPMM. The torque performance can be further reflected on the characteristic of average torque against with copper loss, as show in Fig. 5.13. The results show that all three types of flux focusing can enhance the torque capability over the whole copper loss range.

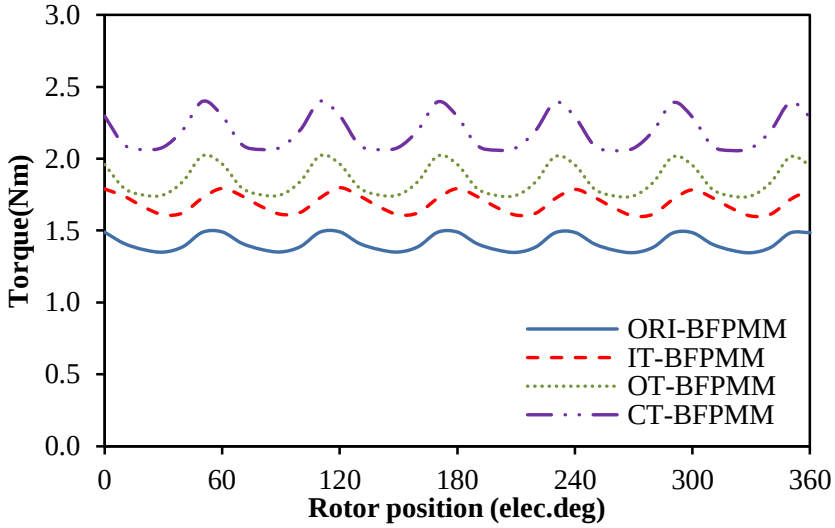

(a) Waveforms

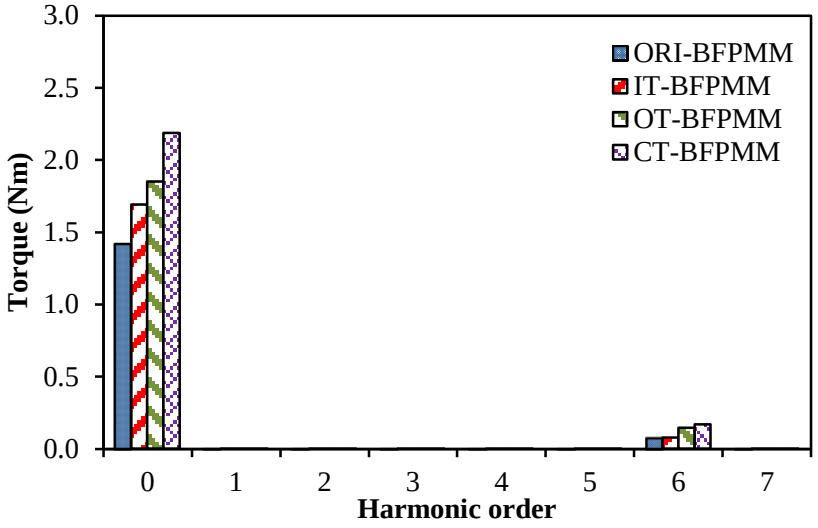

(b) Spectra

Fig. 5.12. Variation of torque with rotor positon in BFPMMs, p_c=30W, I_d=0 control.

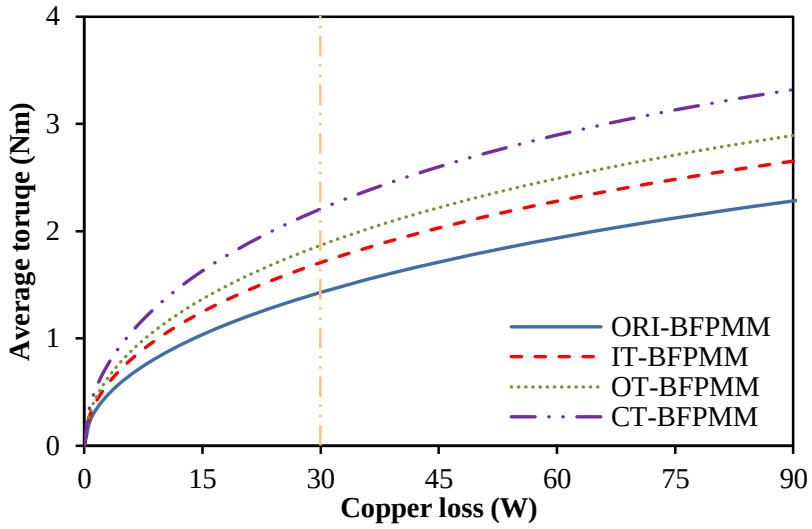

Fig. 5.13. Variation of average torque with copper loss in BFPMMs, I_d=0 control.

Based on the rated copper loss, the values of torque to PM volume and torque density of four machines are compared in Fig. 5.14. Obviously, all three types of flux focusing can improve the PM utilization efficiency and torque density of BFPMM. Among the four machines, OT-BFPMM exhibits the optimal PM utilization efficiency whist CT-BFPMM has the largest torque density.

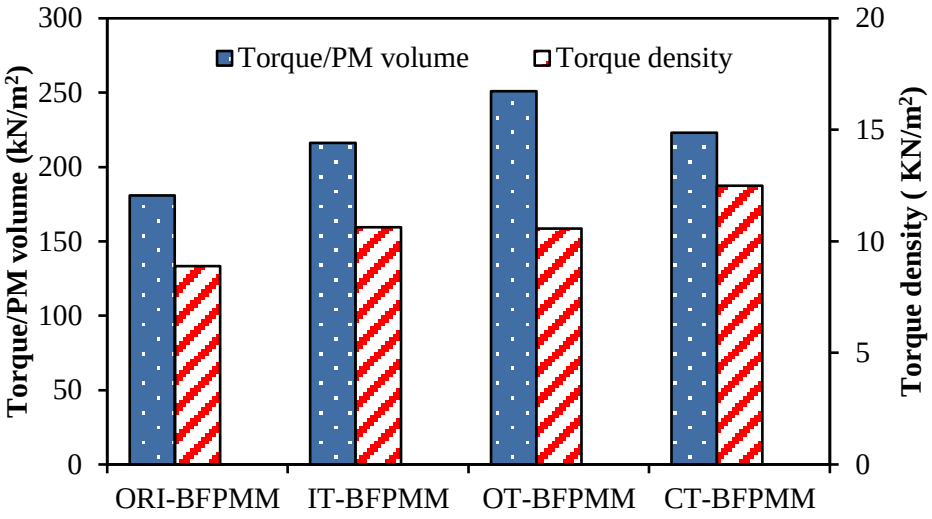

Fig. 5.14. Torque to volume of PM and torque density, p_c=30W, I_d=0 control.

5.3.7 Mechanical Integrity, Iron Loss and PM Loss

As mentioned in section 5.2.1, the rotor of BFPMMs is simple and robust. However, the stator of BFPMMs is composed by the laminated segments. This stator configuration increases the level of difficulty in the installation, especially in the precise positioning of each segment stator.

Fig. 5.15 shows the variation of iron losses against speed at rated copper loss for four BFPMMs. Iron loss is composed by hysteresis loss and eddy current loss, in which the hysteresis loss is proportional to the electric frequency while the eddy current loss is proportional to the square of electric frequency [ZHU04] [ISH05]. Consequently, as shown in Fig. 5.15, the iron loss will be increased as the speed increased. Further, as shown in Fig. 5.16, among the four BFPMMs, the CT-BFPMM has the heaviest saturation level (highest amplitude change of flux density) and largest total saturation area, and then followed by the OT-BFPMM and IT-BFPMM. Meanwhile, four BFPMMs have the same electric frequency under the same speed since they have the same 6/7 stator/rotor pole combination. Therefore, CT-BFPMM exhibits the largest iron loss among the four BFPMMs in the whole speed range while ORI-BFPMM has the smallest value. As shown in Table 5.2, the iron losses of ORI-BFPMM, IT-BFPMM, OT-BFPMM and CT-BFPMM under the rated copper loss (30W) and

the rated speed (400rpm) are 0.41, 0.55, 0.58 and 0.73W respectively.

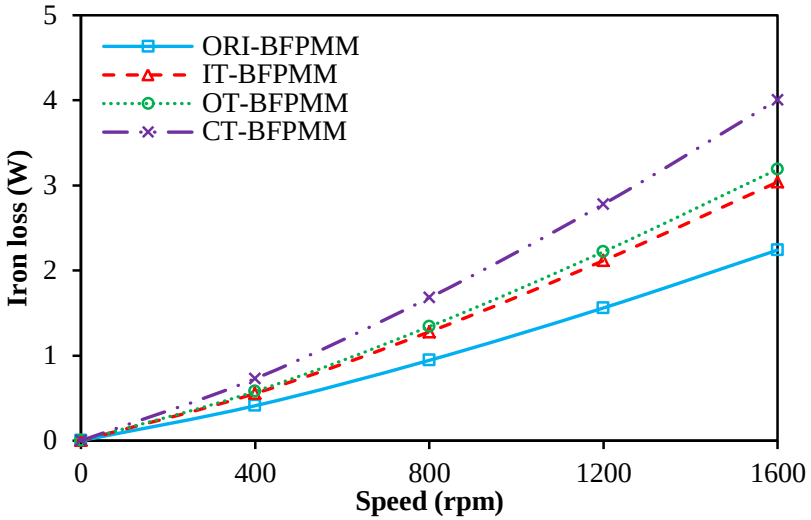

Fig. 5.15. Variation of iron loss with speed in BFPMMs, p_c =30W, I_d = 0 control.

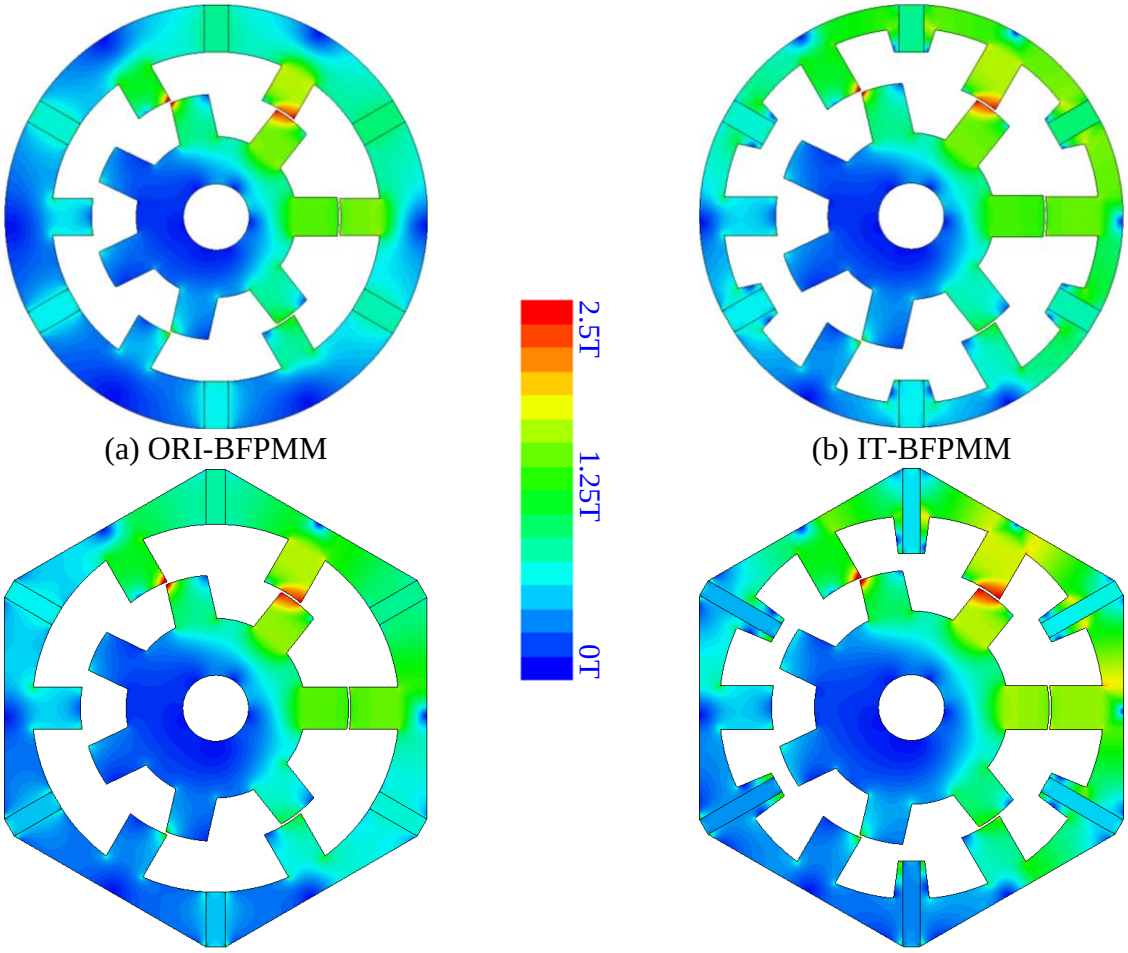

(a) ORI-BFPMM (b) IT-BFPMM

(c) OT-BFPMM (d) CT-BFPMM

Fig. 5.16. On-load flux density distributions of BFPMMs, p_c =30W, I_d = 0 control.

Fig. 5.17 shows the variation of PM losses against speed at rated copper loss for four BFPMMs. Obviously, the PM loss is increased as the speed increased since the PM loss is almost proportional to the square of the electric frequency [ZHU08b]. Further, as shown in Table 5.1, CT-BFPMM has the largest PM usage (total PM volume) among the four BFPMMs. Consequently, CT-BFPMM should also exhibit the highest PM loss in the whole speed range under the rated copper loss, as evidenced by the Fig. 5.17. As shown in Table 5.2, the PM losses of ORI-BFPMM, IT-BFPMM, OT-BFPMM and CT-BFPMM under the rated copper loss (30W) and the rated speed (400rpm) are 0.06, 0.07, 0.11 and 0.22W respectively.

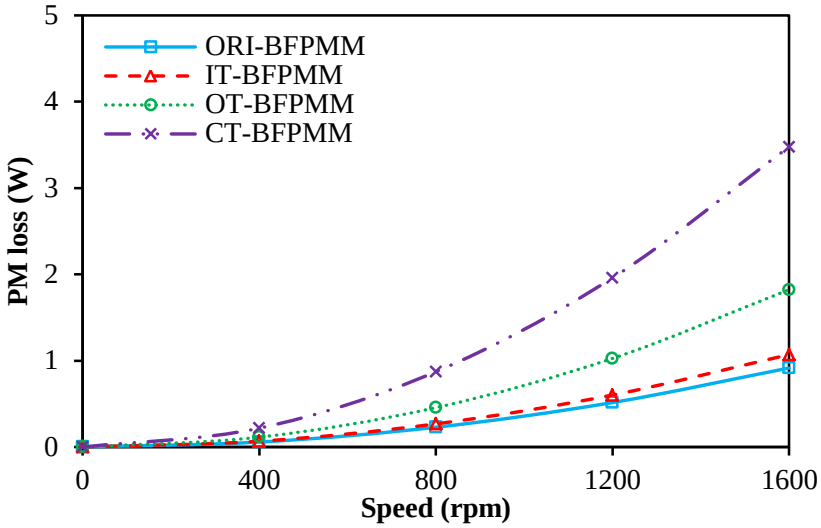

Fig. 5.17. Variation of PM loss with speed in BFPMMs, p_c =30W, I_d = 0 control.

Table 5.2 Main electromagnetic performance of BFPMMs and DSPMMs

Parameters	**BFPMMs**				**DSPMMs**
Type of flux focusing	ORI	IT	OT	CT	IT
Fund. flux-linkage (mWb)	13.6	14.6	15.8	19.6	23.48
Fund. back-EMF (V)	3.98	4.26	4.61	5.74	3.93
Cogging torque (Nm)	0.03	0.05	0.12	0.16	0.09
Average torque (Nm)	1.42	1.69	1.85	2.19	1.43
Torque ripple (%)	11.9	11.8	16.9	16.1	93.1
Torque/PM volume (kN/m^2)	180.9	216.2	250.8	222.97	267.9
Torque density (kN/m^2)	8.90	10.62	10.57	12.49	9.0
Rated iron loss (W)	0.41	0.55	0.58	0.73	-
Rated PM loss (W)	0.06	0.07	0.11	0.22	-

5.4 Performance Comparison between BFPMM and DSPMM

In this section, the electromagnetic performance of 6/7 stator/rotor pole BFPMM will be compared with conventional 6/4 stator/rotor pole DSPMM under the same machine size with inner type of flux focusing (IT).

5.4.1 Open-Circuit Field Distribution

Fig. 5.18 shows the open-circuit flux equipotential of IT-DSPMM and IT-BFPMM. It can be seen that the flux paths in two machines are different. Long flux path is exhibited in the 6/4 stator /rotor pole IT-DSPMM while short flux path is observed in the 6/7 stator/rotor pole IT-BFPMM. Therefore, IT-BFPMM has relative low MMF drop in the stator. Moreover, in both IT-DSPMM and IT-BFPMM, leakage fluxes exist outside the stators, but are quite small compared with the main flux.

The open-circuit air-gap flux density distributions of two machines are shown in Fig. 5.19. Obviously, the positive flux densities are observed in regions around the stator pole wound with coil A1 in both machines. However, in the regions around the stator pole wound with coil A2, the flux density is negative minimum in the 6/7 stator/rotor pole IT-BFPMM but negative maximum in the 6/4 stator/rotor pole IT-DSPMM.

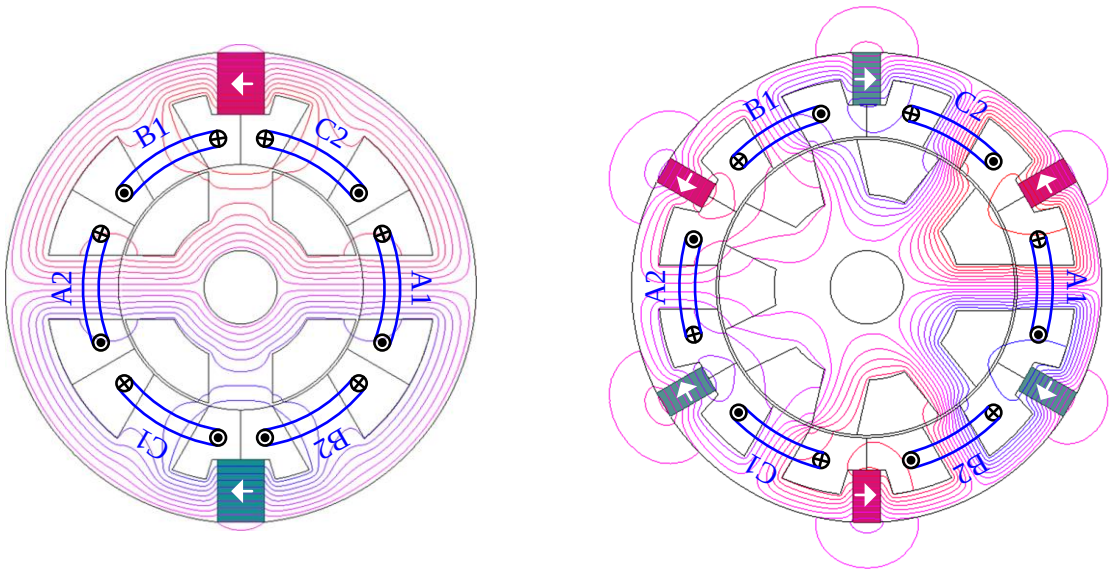

(a) IT-DSPMM (b) IT-BFPMM

Fig. 5.18. Topologies and open-circuit flux equipotential of IT-DSPMM and IT-BFPMM.

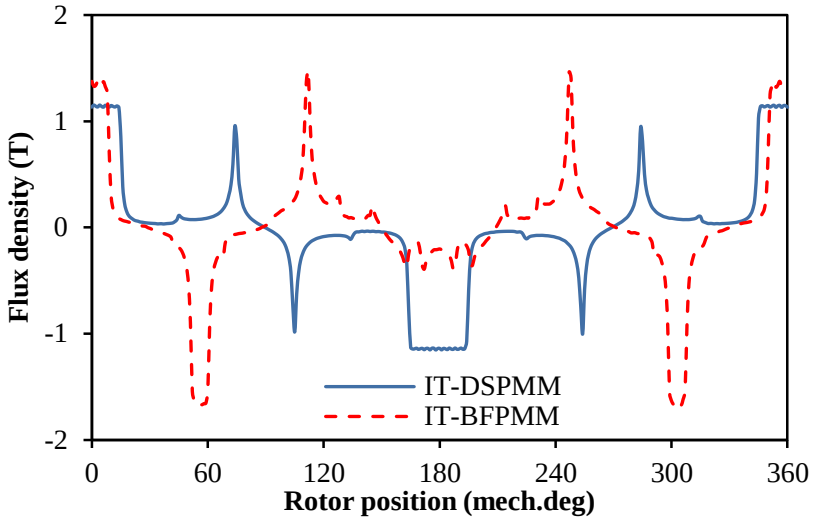

Fig. 5.19. Open-circuit air-gap flux densities of IT-DSPMM and IT-BFPMM at aligned position.

5.4.2 Open-Circuit Phase Flux-Linkage

Fig. 5.20 compares the open-circuit phase flux-linkages of two machines. It can be seen that the phase flux-linkage is unipolar in the 6/4 stator/rotor pole IT-DSPMM but bipolar in the 6/7 stator/rotor pole BFPMM. As shown in Table 5.2, IT-DSPMM exhibits the higher fundamental phase flux-linkage than that of IT-BFPMMs, which are 23.48 and 14.60mWb respectively.

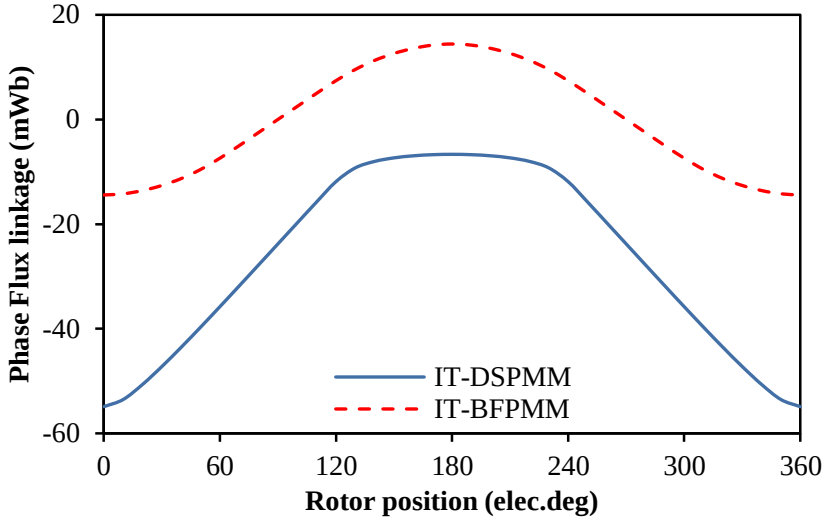

Fig. 5.20. Open-circuit phase flux-linkages of IT-DSPMM and IT-BFPMM.

5.4.3 Open-Circuit Phase Back-EMF and On-Load Terminal Voltage

Fig. 5.21 shows the open-circuit phase back-EMF waveforms of two machines at rated 400rpm. Obviously, the phase back-EMF waveform of 6/7 stator/rotor pole IT-BFPMM is

symmetrical since the even harmonics which cause the asymmetric waveform in single coil are completely cancelled in the phase winding by connecting the coils with opposite polarity. However, the even harmonics still exist in the phase back-EMF of the 6/4 stator/rotor pole IT-DSPMM, as shown in Fig. 5.21(b). Further, due to the influence of rated electric frequency, the 6/7 stator/rotor pole IT-BFPMM (46.7Hz) exhibits higher fundamental phase back-EMF than 6/4 stator/rotor pole IT-DSPMM (26.7Hz), which are 4.26 and 3.93V respectively, as shown in Fig. 5.21 and Table 5.2.

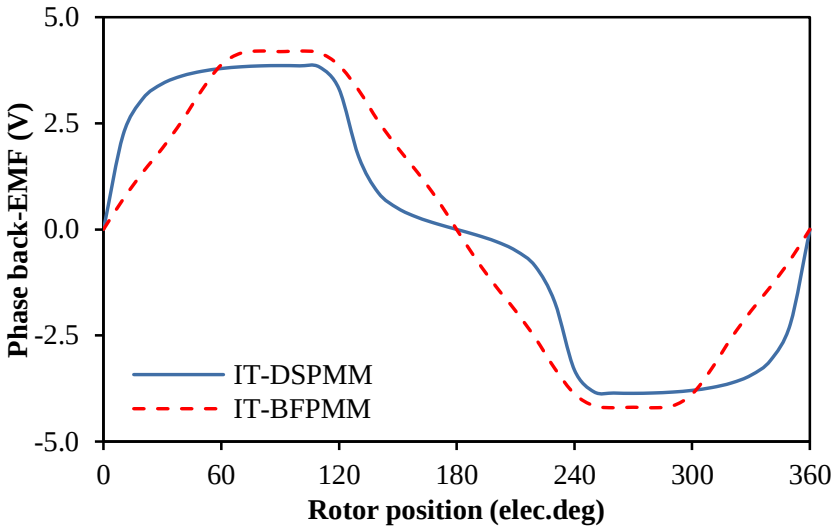

(a) Waveforms

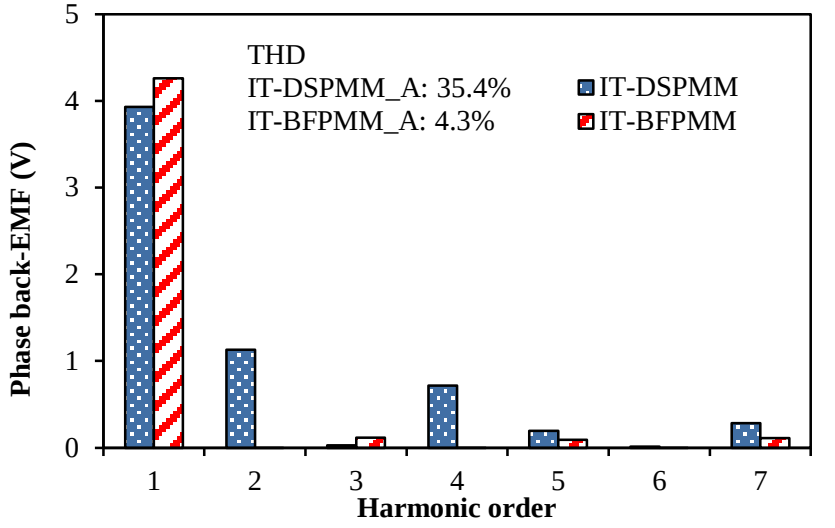

(b) Spectra

Fig. 5.21. Open-circuit phase back-EMFs of IT-DSPMM and IT-BFPMM at rated 400rpm.

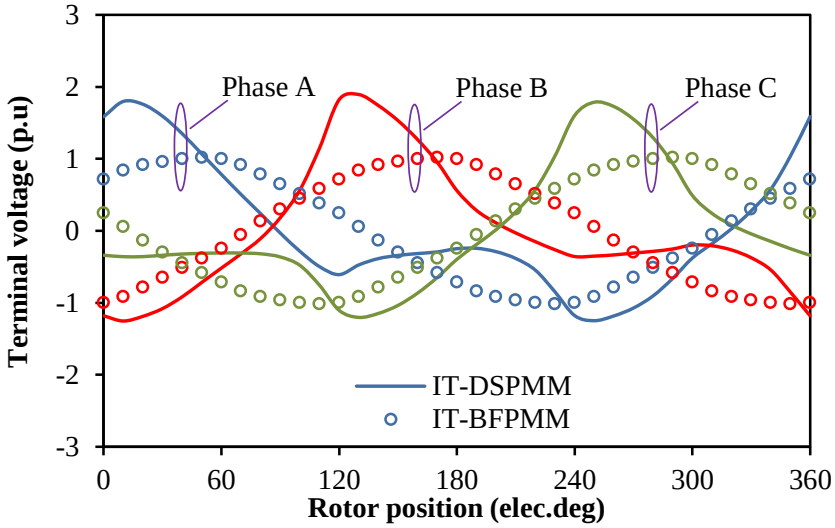

(a) Waveforms

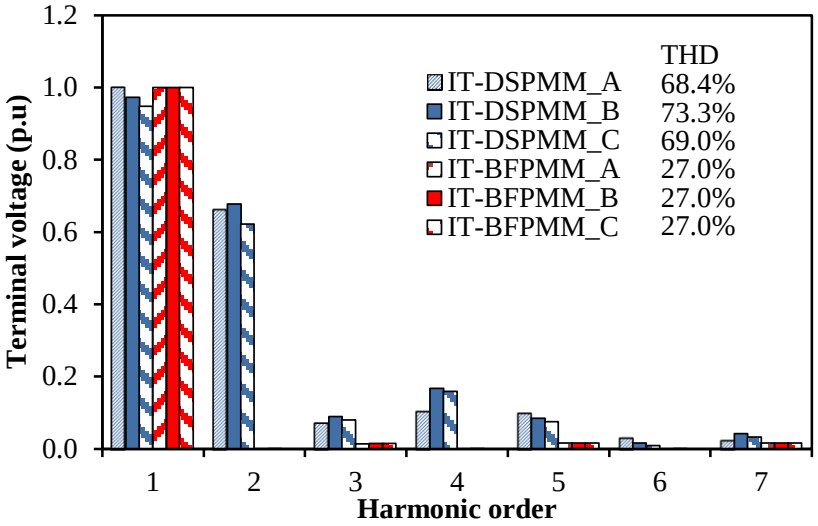

(b) Spectra

Fig. 5.22. On-load terminal voltages of IT-DSPMM and IT-BFPMM at rated current as given in Fig. 5.1, 400rpm, horizontal axis is per unit value.

The on-load terminal voltages of two machines are compared in Fig. 5.22 at rated currents as given in Table 5.1. The terminal voltages are expressed as per unit value, in which those base values are the maximum phase fundamental terminal voltage of two type machines respectively. As shown in Fig. 5.22, since the flux path of each phase is asymmetric in the stator, the terminal voltage waveforms of different phases in DSPMM are not identical. Further, the amplitude of each harmonic (including fundamental component) in the three phases are also different, Fig. 5.22. It means that unbalance exists between three phases of IT-DSPMM, particularly under heavy magnetic saturation. However, this drawback is overcome in BFPMM since the flux path of each phase in the stator is identical, in which can also be evidenced by the magnitude of each harmonic in Fig. 5.22. Moreover, compared with

DSPMM which has unequal positive and negative peak values of terminal voltage, the terminal voltage of BFPMM is almost sinusoidal and has a lower peak. Therefore, the usage efficiency of dc-link voltage in BFPMMs is much higher than that of DSPMMs since the requirement for the dc-link voltage is determined by the maximum peak value of terminal voltage.

5.4.4 *Dq*-Axis Inductances

The waveforms of *dq*-inductances with different current angles at rated currents of two machines are shown in Fig. 5.23. It can be seen that the *dq*-axis inductances of IT-DSPMM are both larger than those of IT-BFPMM. Moreover, the *q*-axis inductance is slightly larger than *d*-axis inductance in IT-DSPMM while those are nearly equal in IT-BFPMM. It means that the reluctance torque of IT-BFPMM is negligible since the saliency ratio is quite close to 1.

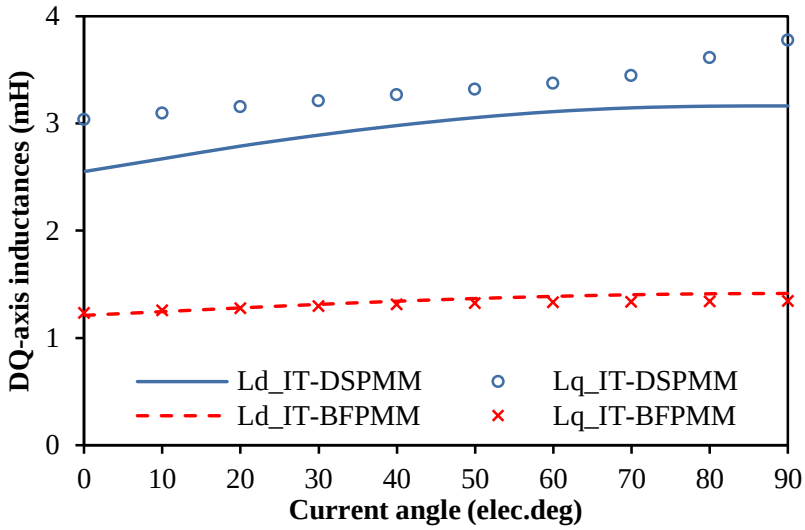

Fig. 5.23. Variation of *dq*-axis inductances with current angel at the rated currents as given in Table 5.1.

5.4.5 Cogging Torque

The waveforms of open-circuit cogging torque over one electric period are shown in Fig. 5.24. Obviously, IT-DSPMM exhibits larger magnitude of cogging torque than that of IT-BFPMM. As shown in Fig. 5.24(b), IT-DSPMM has 3n and 1n times harmonics in the cogging torque (here n is any integer). The 3n times harmonics are due to the 6/4 stator/rotor pole combination and the 1n times harmonics are due to the asymmetric flux path of each phase in the stator. Nevertheless, different from IT-DSPMM, the main harmonics of IT-BFPMM are 6n times. Therefore, the combined cogging torque of IT-DSPMM and IT-

BFPMM will exhibit one and six cycles during one electric period separately, as shown in Fig. 5.24(b).

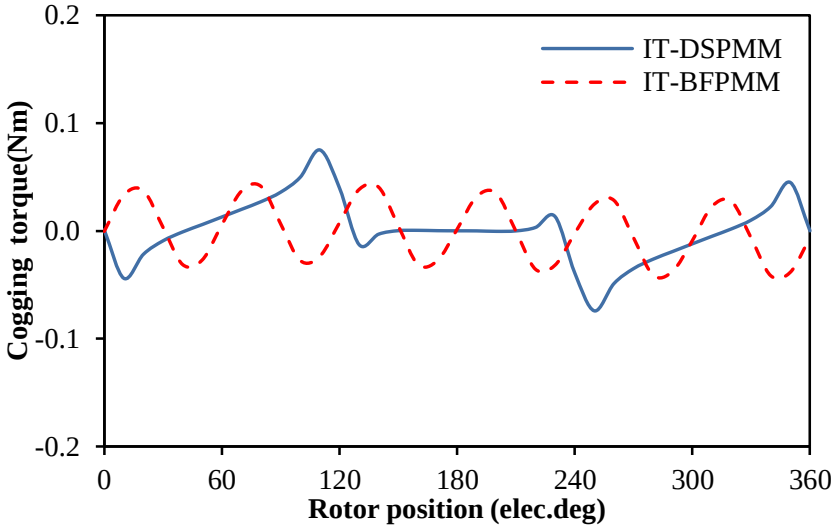

(a) Waveforms

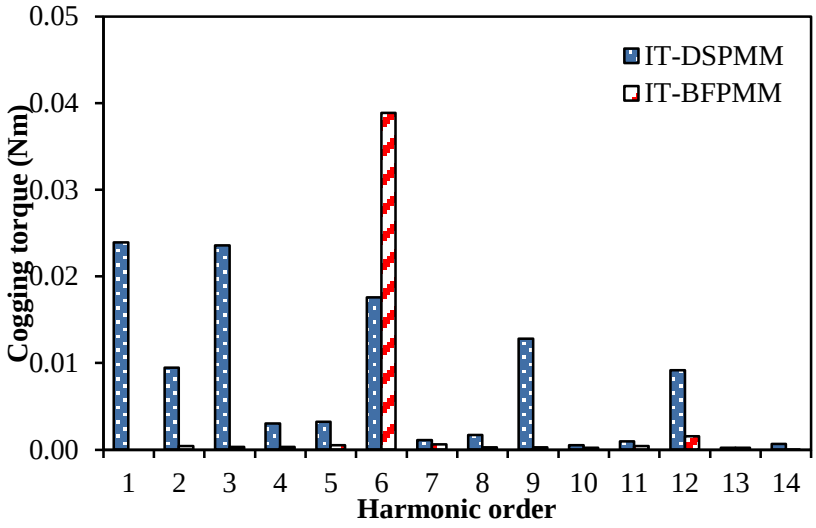

(b) Spectra

Fig. 5.24. Open-circuit cogging torques of IT-DSPMM and IT-BFPMM.

5.4.6 Electromagnetic Torque Characteristics

Fig. 5.25 shows the waveforms of average torque against current angle at rated currents as given in Table 5.1 (corresponding to p_c=30W) for two machines. Obviously, the optimal current angles for IT-DSPMM and IT-BFPMM are almost 15° and 0° respectively. It means that small reluctance torque exists in IT-DSPMM but negligible in IT-BFPMM, which are consistent with the previous analysis in section 5.4.4.

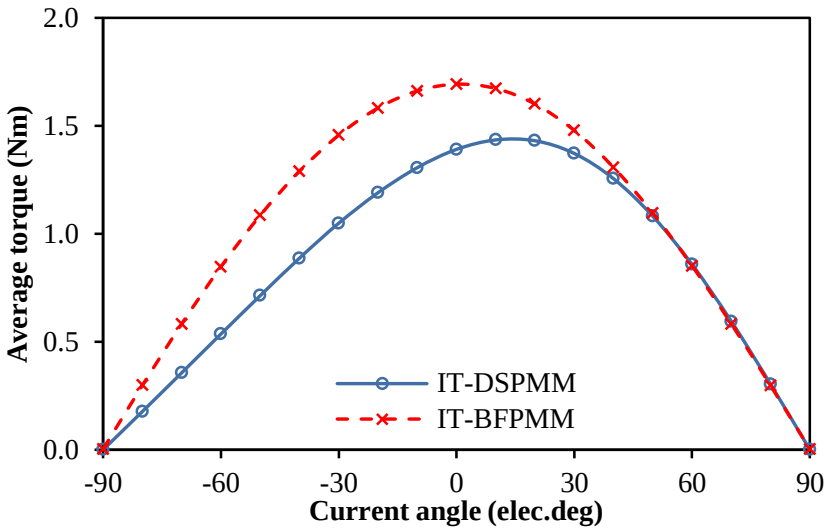

Fig. 5.25. Variation of average torque with current angle in IT-DSPMM and IT-BFPMM, p_c=30W.

The torque waveforms of two machines under the rated currents (p_c=30W) and optimal current angles are compared in Fig. 5.26. Obviously, due to the combined influence of the cogging torque and the harmonics of back-EMF (2^{th} and 4^{th} harmonics for IT-DSPMMs, 5^{th} and 7^{th} for IT-BFPMMs), the cycle numbers of torque ripple over one electric period are three in IT-DSPMM but six in IT-BFPMM. Moreover, the torque ripples of IT-DSPMM and IT-BFPMM are 93.1% and 11.8% respectively. It can be seen that the torque ripple is reduced significantly in IT-BFPMM when compared with IT-DSPMM. According to Fig. 5.26 and Table 5.2, IT-BFPMM exhibits ~18% higher average torque than IT-DSPMM under the same rated 30W copper loss, which is 1.69 and 1.43 Nm respectively.

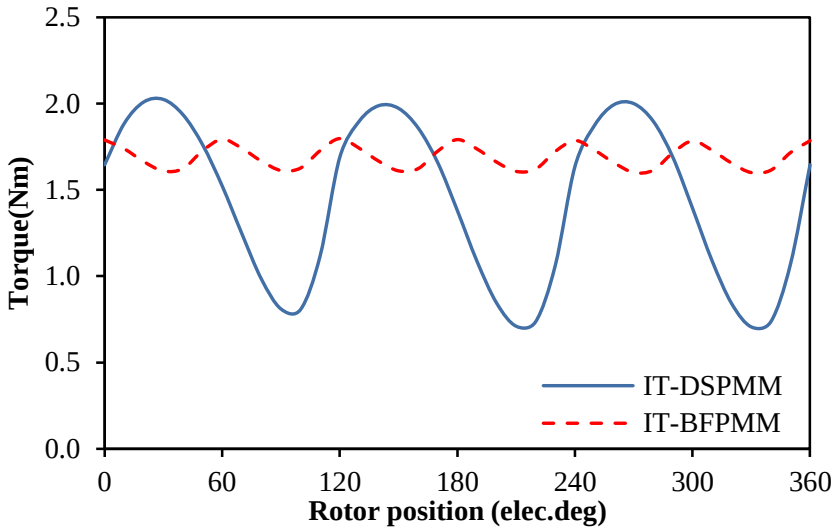

(a) Waveforms

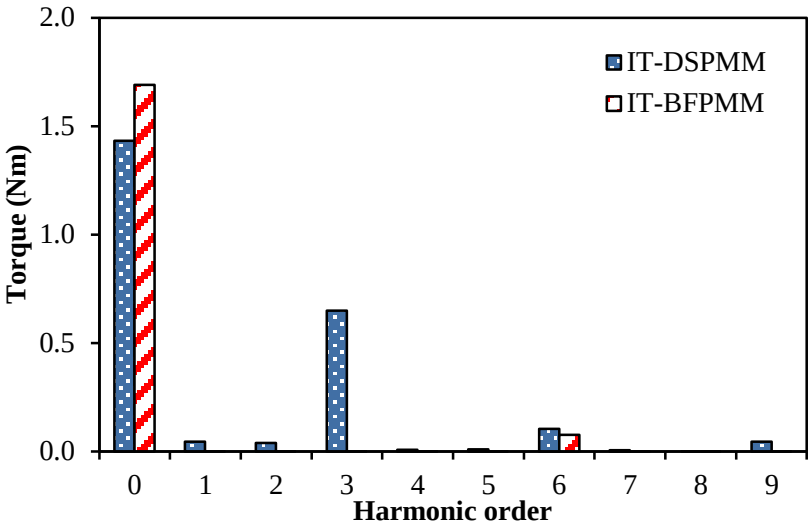

(b) Spectra

Fig. 5.26. Variation of electromagnetic torque with rotor position under the rated currents and optimal current angles in IT-DSPMM and IT-BFPMM, p_c=30W.

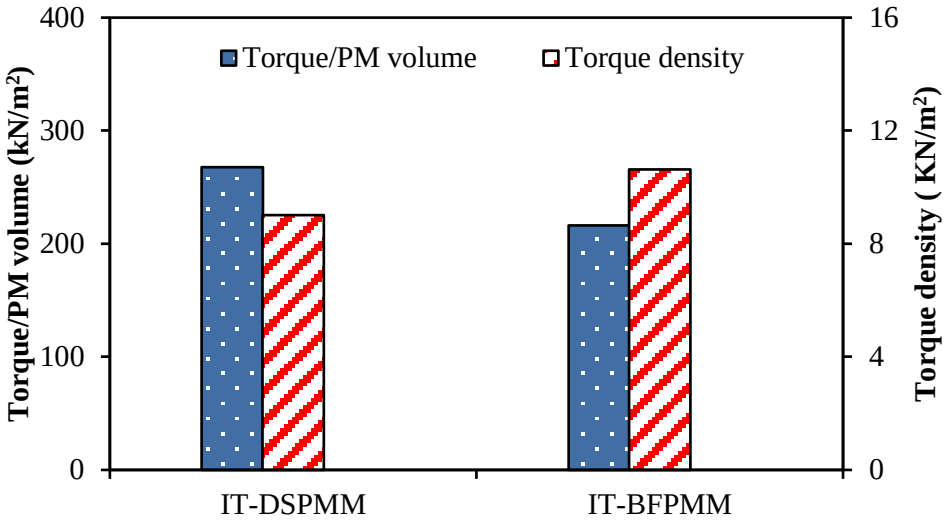

Fig. 5.27. Torque to volume of PM and torque density, p_c=30W and optimal current angles.

Fig. 5.27 compares the ratio of torque to PM volume and torque density of two machines at rated currents (p_c=30W) and optimal current angles. Compared with IT-DSPMM, IT-BFPMM exhibits higher torque density but lower ratio of torque to PM volume (lower PM utilization efficiency).

The variations of the average torque with the copper loss for two machines are further shown in Fig. 5.28. The vertical dashed and dotted line shows the rated copper loss which used to globe optimization. Due to the influence of magnetic saturation, the increasing rate of average torque will gradually diminish with the raised copper loss for both machines. Over

the whole copper loss range as shown in Fig. 5.28, IT-BFPMM exhibits larger average torque than IT-DSPMM under the same copper loss.

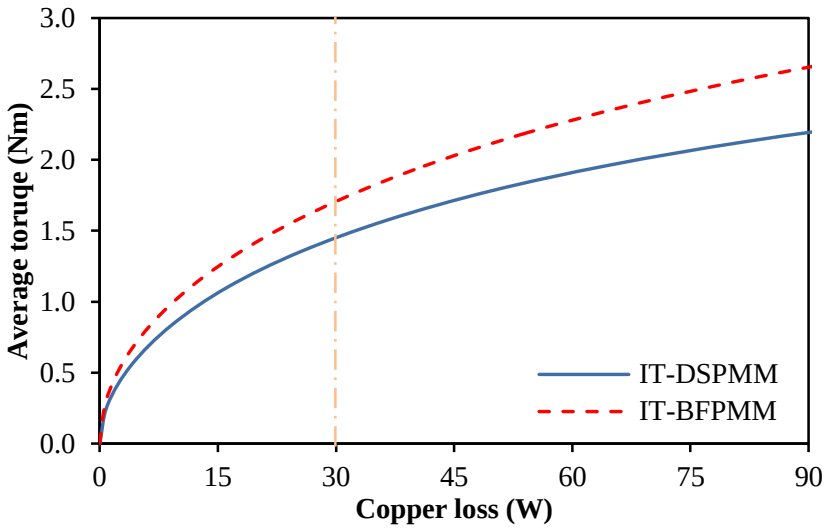

Fig. 5.28. Variation of average torques with copper loss at the optimal current angles.

5.5 Experimental Verification

Prototype machine of IT-BFPMM with 6/7 stator/rotor pole combination is made to validate the foregoing analysis, as shown in Fig. 5.29. The geometric parameters are the same as shown in Table 5.1.

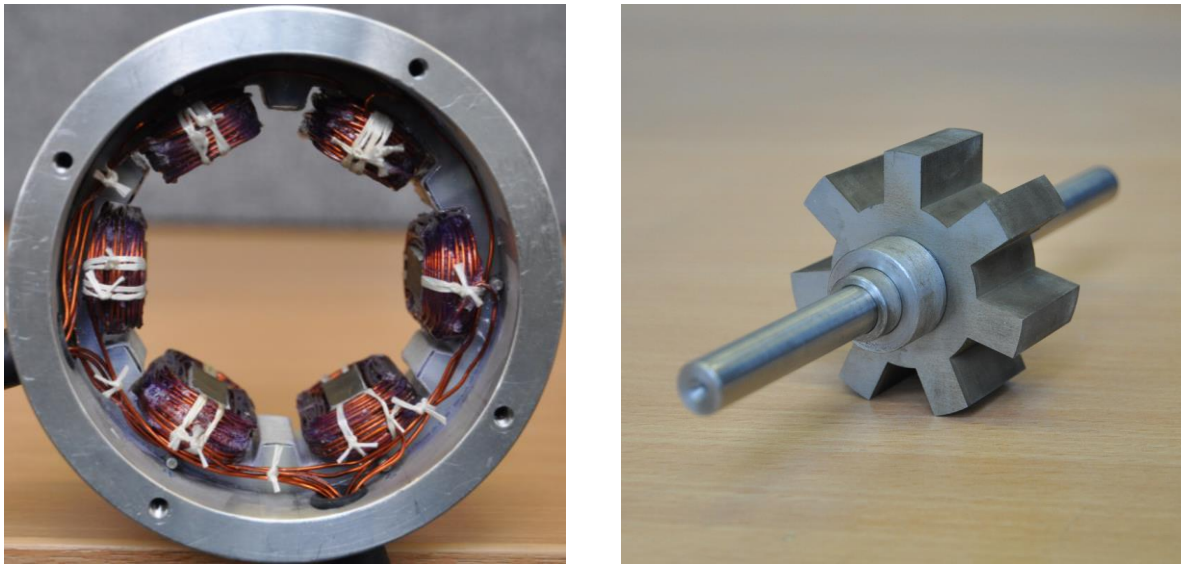

(a) 6-pole stator of IT-BFPMM (b) 7-pole rotor of IT-BFPMM.

Fig. 5.29. Prototype of IT-BFPMM with 6/7 stator/rotor pole combination.

Fig. 5.30 shows the measured and predicted open-circuit phase back-EMFs of IT-BFPMM at rated speed as 400rpm. It can be seen that the measured peak value is less than the FE

prediction due to the end-effect in 25 mm stack length machines. Fig. 5.31 shows the measured and predicted open-circuit cogging torques. The measured peak to peak value is slight larger than the FE prediction. This difference is acceptable when considering the measurement error and assembling tolerance. Fig. 5.32 shows the variation of static torques with the rotor position at four different armature currents combinations, i.e. 25%, 50%, 75% and 100% of the rated armature current. Further, based on Fig. 5.32, the variation of the static torque at 90° rotor position with the copper loss is obtained and shown in Fig. 5.33. Overall, the measured and FE predicted results match well. The difference between the measured and FE predicted results of static torque under high current (or copper loss) are due to the increased influence of end effect caused by aggravated saturation.

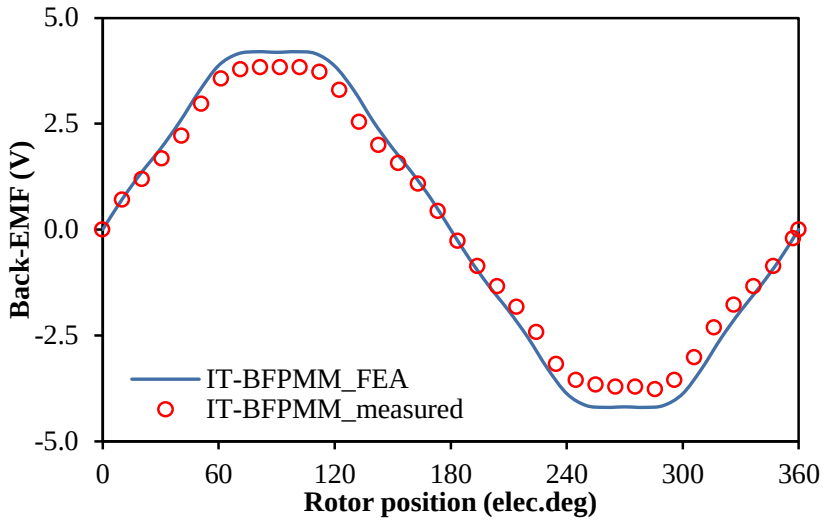

Fig. 5.30. Measured and FE predicted open-circuit phase back-EMFs at 400rpm.

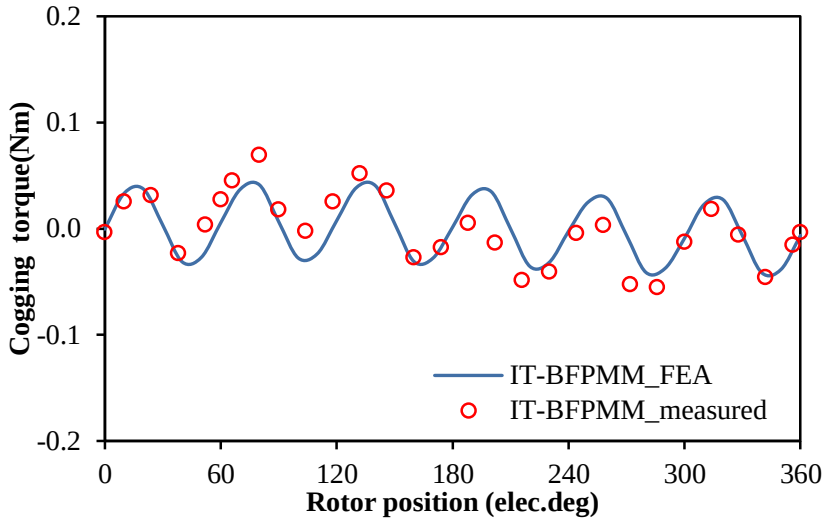

Fig. 5.31. Measured and FE predicted open-circuit cogging torques.

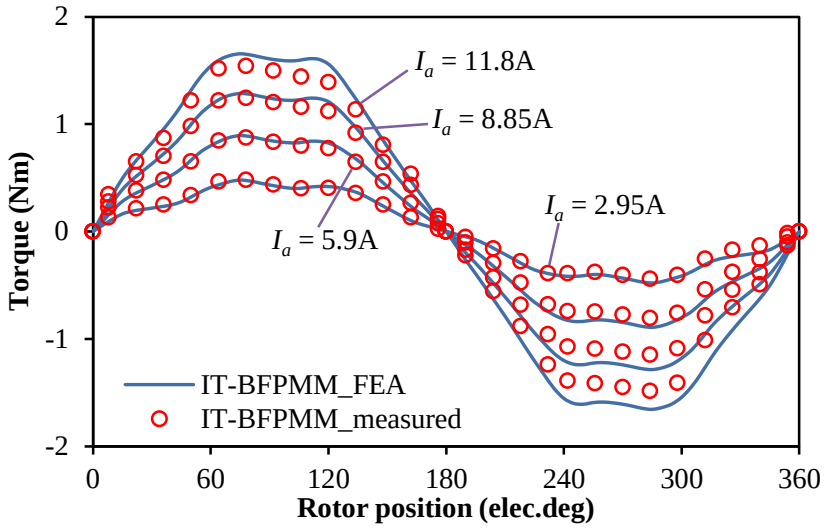

Fig. 5.32. Measured and FE predicted phase static torques when -1/2I_A=I_B=I_C.

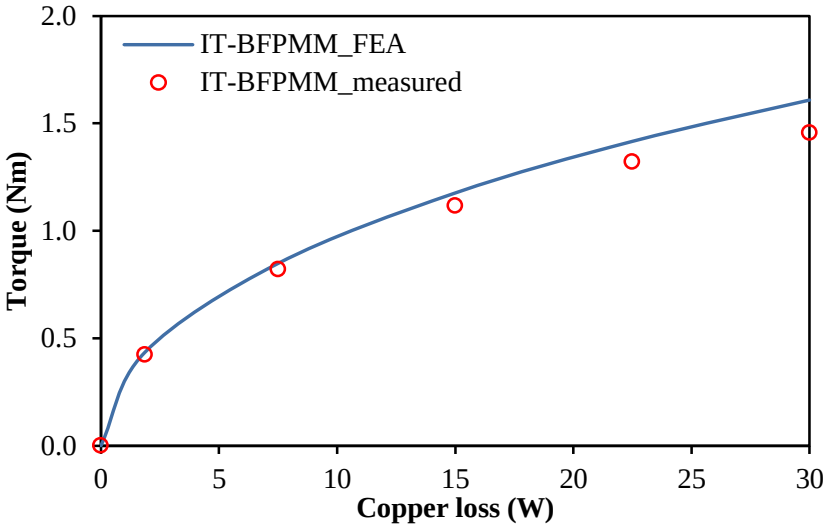

Fig. 5.33. Measured and FE predicted torque-copper loss characteristic when rotor position is 90°.

5.6 Summary

In this chapter, BFPMMs with doubly salient structure and non-overlapping armature windings are investigated. The PMs with alternate polarities are circumferentially located in the stator back iron between adjacent stator poles. Compared with DSPMMs, the selections of rotor pole number in BFPMMs are more flexible and can be any integers except the phase number and its multiples. When the numbers of stator and rotor poles differed by one, 6-stator pole BFPMMs exhibits bipolar phase flux-linkage and symmetrical phase back-EMF. Based on the optimal 6/7 stator/rotor pole combination and rated copper loss, the average torque of BFPMMs can be enhanced by ~19%, 30.3% and 54.2% respectively by adopting flux focusing with inner type, outer type and combined type. Correspondingly, the PM

utilization efficiency and torque density are also enhanced (by 19.5%, 38.6% and 23.3% for PM utilization efficiency while 19.3%, 18.8% and 40.3% for torque density). Moreover, optimized 6/4 stator/rotor pole IT-DSPMM is compared with optimized 6/7 stator/rotor pole BFPMM under the same rated copper loss and machine size as well as optimal current angle. The results show that IT-BFPMM exhibits about 18% higher average torque and 80% lower torque ripple than IT-DSPMM. Further, the unbalance between phases which is observed in DSPMMs is overcome in the BFPMMs. The analyses are experimentally validated by the prototype machine.

CHAPTER 6
NOVEL BIASED FLUX PERMANENT MAGNET MACHINES WITH PARTITIIONED STATOR

Similar to other stator permanent magnet (PM) machines, the torque performance of biased flux PM machines (BFPMMs) are also limited by the confliction among the PMs, coppers and stator irons due to the limited space. To solve this confliction and improve the potential torque performance under the same machine size, inner type flux focusing technique is employed in BFPMMs in the previous chapter by reducing the thickness of stator yoke which is not utilized effectively to increase the slot area. Nevertheless, the utilization ratio of whole machine space is still relatively low, especially for the inner space. As a more effective solution, the partitioned stator configuration is proposed in [EVA15], in which the PMs and armature windings in the original single stator are separated into inner and outer stators respectively. By introducing this configuration into BFPMM, high torque capability can be expected due to the reduced confliction by fully utilizing the inner space. In this chapter, novel partitioned stator BFPMMs (PS-BFPMMs) with different PM stator configurations are proposed and investigated.

6.1 Introduction

Theoretically, higher torque capability can be expected by replacing DC field windings with permanent magnets (PMs). Based on this concept, biased flux PM machines (BFPMMs) are evolved from VFRMs in [SHI14b]. The PMs are located in the adjacent stator poles with alternate polarities while concentrated armature windings are remained. Meanwhile, reference [SHI14b] indicates that the location of PMs can be moved from the surface to the bottom of stator pole due to the same main magnetic circuits. However, considering the influence of flux leakage in the stator slot, the optimal torque capability is obtained when PMs are mounted on the surface of stator pole [SHI14b]. Further, references [SHI14c] [WU14] also propose one type of BFPMM with PMs located in the stator yoke, which can overcome the drawback of unbalance between the phases in doubly salient PM machines (DSPMMs) and exhibits ~70% higher torque density than VFRMs.

Similar to other stator PM machines, the confliction among the slot area (coppers), PMs and stator irons also exists in BFPMMs and limits the possibility of further enhancing the torque performance. To solve this confliction and improve the potential torque performance,

inner type flux focusing technique is employed in BFPMM with PM located in stator yoke by reducing the thickness of stator yoke which is not utilized effectively [SHI14c]. Since the slot area is increased, the torque density under the same copper loss is also enhanced. Nevertheless, the utilization ratio of whole machine space is still relatively low, especially for the inner space. As a more effective solution, the partitioned stator configuration is proposed in [EVA15], in which the PMs and armature windings in the original single stator are separated into inner and outer stators respectively. Since the confliction is further reduced by fully utilizing of inner space, high torque capability is achieved [EVA15].

By introducing this configuration, novel partitioned stator BFPMMs (PS-BFPMMs) with two different PM configurations are proposed and investigated in this chapter. Firstly, the machine topologies and operation principle are illustrated. Secondly, based on the 2-D finite element analysis (FEA), the electromagnetic performance in terms of phase flux-linkage and back-EMF, *dq*-axis inductances and torque capability of PS-BFPMMs are investigated and compared with single stator BFPMMs (SS-BFPMMs) for the same (inner/outer) stator/rotor pole combination and the same machine size. Thirdly, the main stator/rotor pole combinations of PS-BFPMMs are further analysed. Finally, two prototype machines having PM configurations with surface mounted type and spoke type are manufactured and measured respectively to validate the analysis.

6.2 Machine Topologies and Operation Principle of PS-BFPMMs

6.2.1 Concepts of PS-BFPMMs

Fig. 6.1(a) and (b) show the basic models of original single stator BFPMMs (SS-BFPMMs) with PMs mounted on the surface of stator pole and located in the stator yoke respectively. Non-overlapping armature windings and salient pole rotors are employed. Partitioned stator configuration, which is proposed in [EVA15], can also be introduced in SS-BFPMM. Considering the different PM configurations as shown in Fig. 6.1(a) and (b), two corresponding basic models of partitioned stator BFPMMs (PS-BFPMMs) are shown in Fig. 6.1(c) and (d) respectively. It can be seen that the PMs and armature windings of PS-BFPMMs are located in two separate inner and outer stators while a modular rotor is adopted. Moreover, the second air-gap is introduced in PS-BFPMMs between the rotor and the PM stator to allow the rotor rotating. Overall, according to Fig. 6.1, the flux paths shown in two PS-BFPMMs are both consistent with those in two original SS-BFPMMs, which imply that the operation principle of PS-BFPMMs is similar to that of SS-BFPMMs.

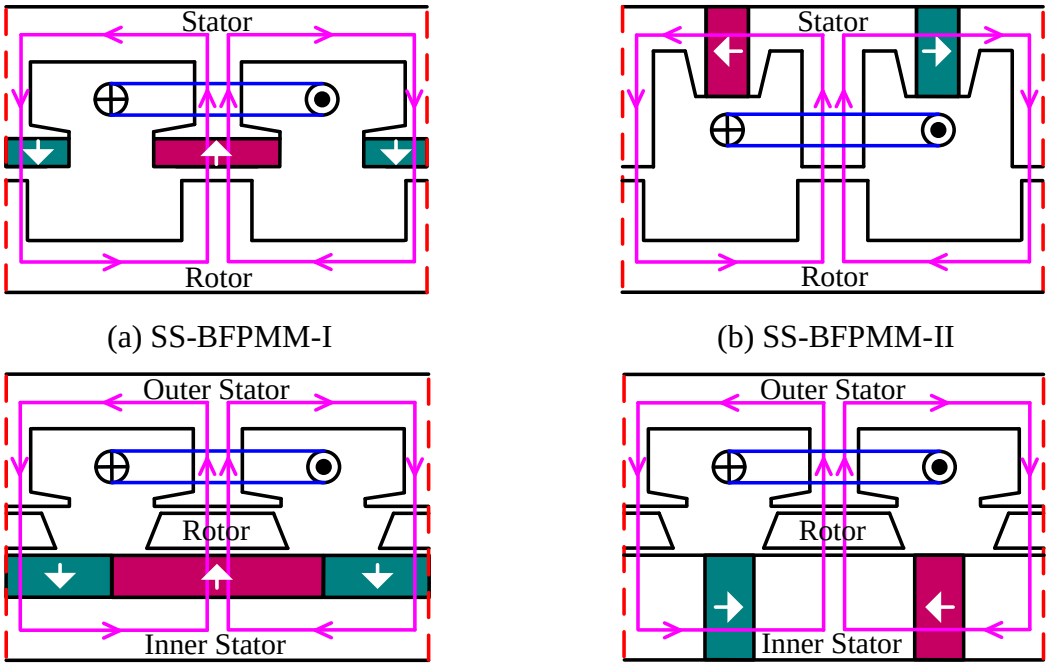

(a) SS-BFPMM-I (b) SS-BFPMM-II

(c) PS-BFPMM-I (d) PS-BFPMM-II

Fig. 6.1. Schematics of original SS-BFPMMs and PS-BFPMMs.

To simplify the comparison in the following sections, the machines corresponding to the basic models shown in Fig. 6.1(a), (b), (c) and (d) can be designated as SS-BFPMM-I, SS-BFPMM-II, PS-BFPMM-I and PS-BFPMMM-II respectively. Fig. 6.2 shows the topologies of 12/10 (inner/outer) stator/rotor pole SS-BFPMMs (12S/10R) and PS-BFPMMs (12I/12O/10R) with two PM configurations. All machines are globally optimized with maximum average torque under the same machine size and the same copper loss. The main geometric parameters are detailed in Table 6.1.

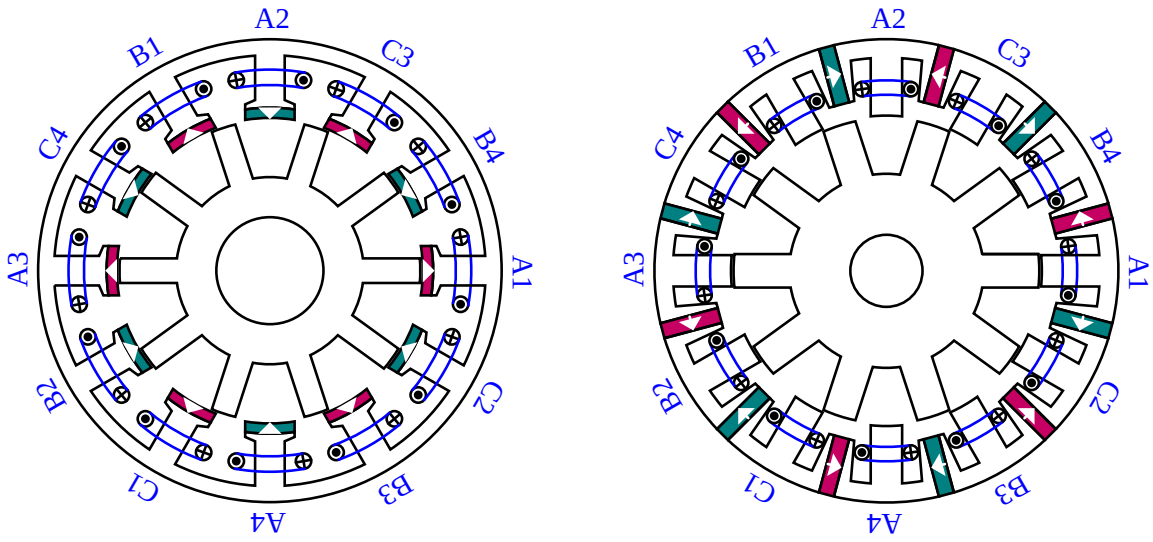

(a) SS-BFPMM-I (b) SS-BFPMM-II

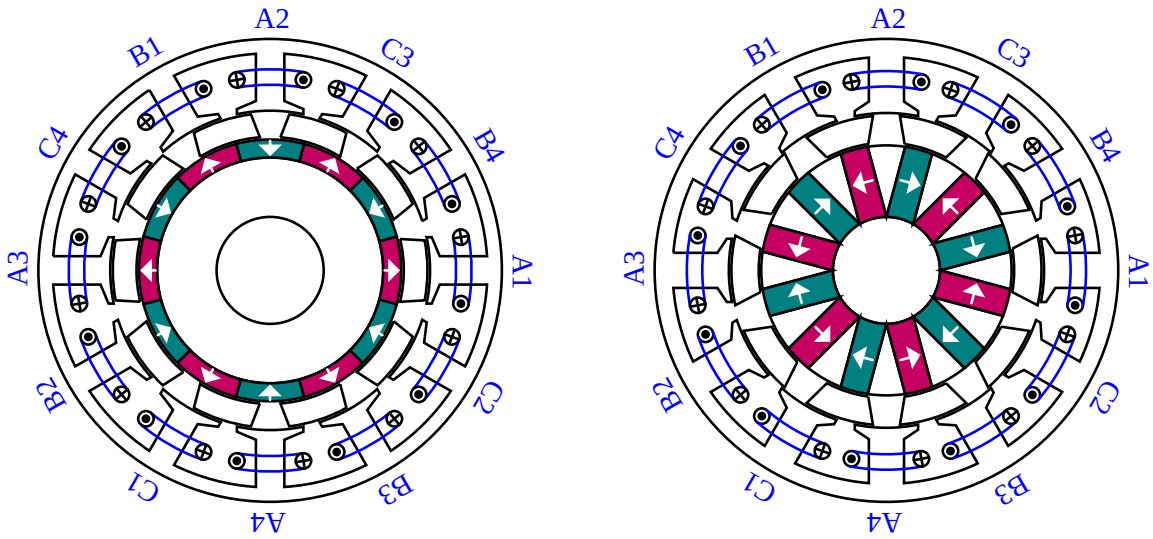

(c) PS-BFPMM-I (d) PS-BFPMM-II

Fig. 6.2. Topologies of SS-BFPMMs and PS-BFPMMs with 12/10 (inner/outer) stator/rotor pole combination.

Table 6.1 Main parameters of SS-BFPMMs and PS-BFPMMs.

Parameters	**BFPMMs**			
Topology	SS-I	SS-II	PS-I	PS-II
Number of phases	3			
Turns per phase	72			
Rated speed (rpm)	400			
Rated copper loss (W)	30			
Packing factor	0.5			
Air-gap length L_{ag} (mm)	0.5			
Active axial length L_{aa} (mm)	25			
Outer stator outer radius R_{oso} (mm)	45			
Radius of shaft (mm)	10.4	10.4		
Inner stator inner radius R_{isi} (mm)			10.4	10.4
Outer stator (OS) pole number, N_{os}	12	12	12	12
Inner stator (IS) pole number, N_{is}			12	12
Rotor pole number, N_r	10	10	10	10
OS inner radius R_{osi} (mm)	29.70	30.15	31.05	30.60
IS outer radius R_{iso} (mm)			25.45	24.30
OS tooth body pole arc θ_{ostb} (°)	10.4	11.6	10.2	12.8

OS tooth tip pole arc θ_{ostt} (°)	3.51		6.9	5.2
OS tooth tip thickness (Opening) T_{ostto} (mm)	1		1	1
OS tooth tip thickness (Body) T_{osttb} (mm)	1.6		2	2.4
Rotor outer pole arc θ_{rop} (°)	9.4	12.6	22	26
Rotor inner pole arc θ_{rip} (°)			27.2	19.6
Rotor radial thickness T_{rr} (mm)	11	10.8	4.6	5.3
OS yoke thickness T_{osy} (mm)	3.1	3.6	2.8	3.5
Rated AC current (A_{rms})	16.33	13.92	17.10	15.83
Rated current density (A_{rms}/mm^2)	9.35	10.99	8.92	9.64
PM inner pole arc θ_{PM} (°)	18.6	(3mm)	30	30
Minimum PM thickness T_{PM} (mm)	2	11.5	3.5	13.9
Magnetic remanence (T)	1.2			
Relative PM permeability	1.05			

6.2.2 Winding Configurations of PS-BFPMMs

Similar to SS-BFPMMs, the conventional coil EMF vector method [ZHU10] can also be used to determine the armature winding configuration of PS-BFPMMs, in which the electrical degree α_e between two adjacent coil-EMF vectors can be calculated from the mechanical degree α_m and the rotor pole number N_r according to (6.1) [CHE08].

$$\alpha_e = N_r \alpha_m \tag{6.1}$$

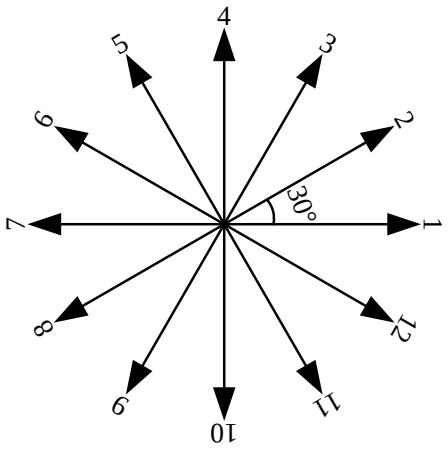

(a) Stator coil-EMF vectors (mech.deg.)

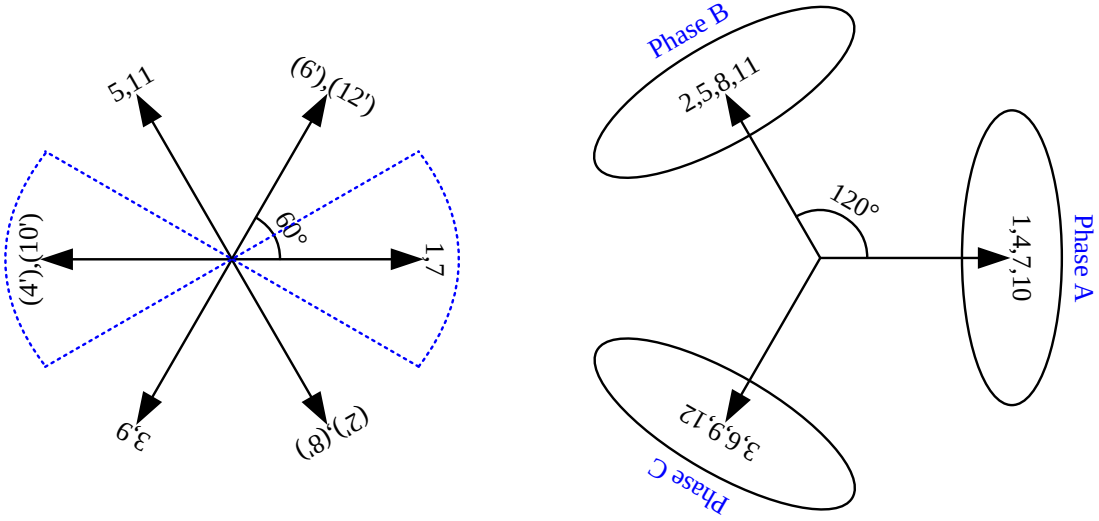

(b) Coil-EMF vectors (elec.deg.) and sectors for determining phase winding (dash lines)

(c) Phase windings

Fig. 6.3. Coil EMF vectors for SS-BFPMMs and PS-BFPMMs with 12/10 (inner/outer) stator/rotor pole combination.

By way of example, for the 12I/12O/10R PS-BFPMM under investigation, the coil-EMF vectors are shown in Fig. 6.3. Coil *n* and coil *n*' refer to the coils with opposite polarities, accounting for the alternate magnetization directions in adjacent stator poles, such as coils 1 and 2 as shown in Fig. 6.2 and Fig. 6.3(b).

6.2.3 Operation Principle of PS-BFPMMs

Fig. 6.4 shows the open-circuit flux equipotential of 12I/12O/10R PS-BFPMM-I at four different rotor positions. Fig. 6.5 shows the open-circuit coil flux-linkages for PS-BFPMM-I in per-unit value. Based on Fig. 6.4 and Fig. 6.5, the operation principle of PS-BFPMM-I can be explained in detail as follows. When one rotor pole aligns with the outer stator pole wound with coil A1 (defined as aligned position) as shown in Fig. 6.4(a), the fluxes flow from inner stator to outer stator and maximum negative coil flux-linkages are both achieved in coils A1 and A2 but with different peaks as shown in Fig. 6.5 at 0° rotor position. Correspondingly, the combined flux-linkage of coils A1+A2 also reaches the negative peak. When the rotor rotates through 1/4 rotor pole pitch from the aligned positon as shown in Fig. 6.4(b), the flux-linkages of coil A1 and coil A2 have the same peak values but opposite polarities due to the inverse flux directions. Thus, the combined flux-linkage of coils A1+A2 is zero, as shown in Fig. 6.5 with 90° rotor position. When the rotor rotates through 1/2 rotor pole pitch from the aligned positon as shown in Fig. 6.4(c), the directions of fluxes are both reversed (from outer

stator to inner stator) and maximum positive coil flux-linkages are achieved in coils A1 and A2 as well as the combined coils A1+A2, as shown in Fig. 6.5 at 180° rotor position. When the rotor rotates through 3/4 rotor pole pitch from the aligned positon as shown in Fig. 6.4(d), the flux-linkages of coil A1 and coil A2 have the same peak value but opposite polarities again, and the combined flux-linkage of coils A1+A2 is zero as shown in Fig. 6.5 at 270° rotor position. Therefore, due to the periodical variation of coil flux-linkages, back-EMF will be induced in the coils.

Furthermore, the operation principle of PS-BFPMM-II is consistent with PS-BFPMM-I since the only difference between two machines is the PM configuration in inner stator (surface mounted PM stator in PS-BFPMM-I while spoke type PM stator in PS-BFPMM-II), as shown in Fig. 6.2(c) and (d).

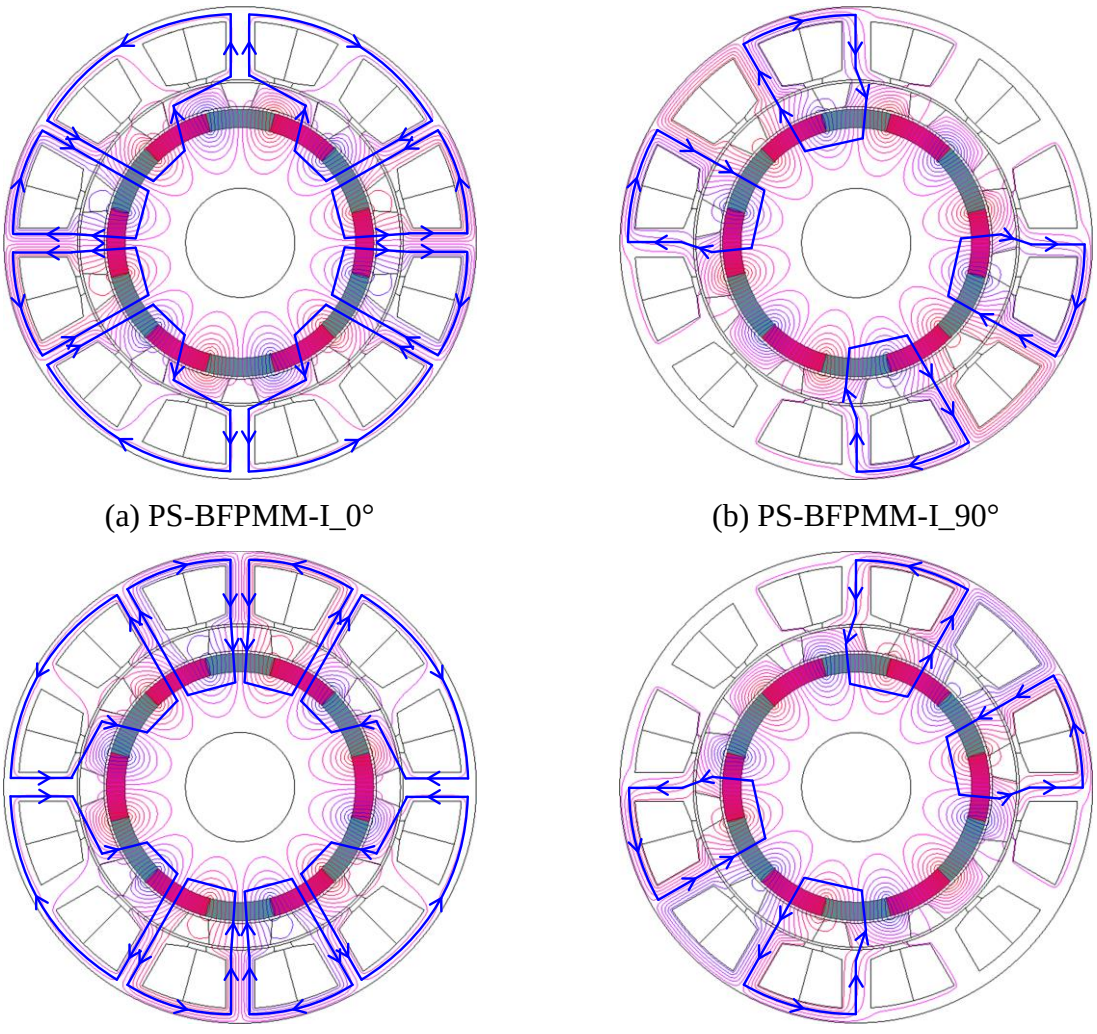

(a) PS-BFPMM-I_0° (b) PS-BFPMM-I_90°

(c) PS-BFPMM-I_180° (d) PS-BFPMM-I_270°

Fig. 6.4. Open-Circuit flux equipotential distributions at different rotor positions (elec.deg).

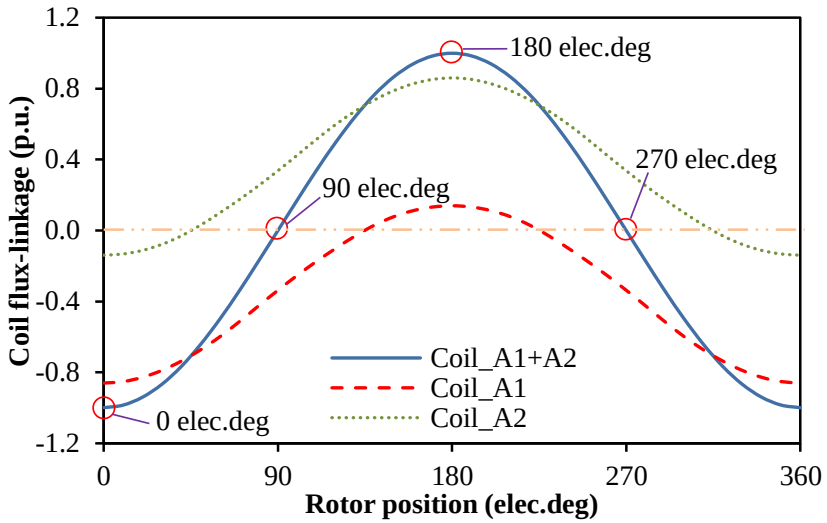

Fig. 6.5. Variation of open-circuit coil flux-linkages with rotor position in per-unit value.

6.2.4 Conditions for Bipolar Phase Flux-Linkage and Symmetrical Phase Back-EMF

Since PS-BFPMMs are evolved from SS-BFPMMs by introducing the partitioned stator configuration and two types of machines have the same operational principle, the conditions for bipolar phase flux-linkage and symmetrical phase back-EMF in SS-BFPMMs are also suitable for PS-BFPMMs. Hence, to obtain bipolar phase flux-linkage and symmetrical phase back-EMF in PS-BFPMMs, two conditions should be satisfied [SHI15]. First, the coil number per phase must be even. Second, the pair of coils belong to same phase must have 180 electrical degrees phase shifting (opposite induced polarities). In other word, the stator (stator wound with armature windings) and rotor pole combinations should be satisfied with (6.2) [CHE08] [SHI15].

$$\frac{N_{os}}{GCD(N_{os},N_r)} = Even \tag{6.2}$$

where N_{os} is the pole number of outer stator, *GCD* means the greatest common divisor.

6.3 Performance Comparison between SS-BFPMMs and PS-BFPMMs

In this section, the electromagnetic performance of the proposed PS-BFPMM-I and PS-BFPMM-II will be analysed and compared with the original SS-BFPMM-I and SS-BFPMM-II under the same 12/10 (inner/outer) stator/rotor pole combination and the same machine size as well as the same rated copper loss.

6.3.1 Open-Circuit Field Distribution

The open-circuit equipotential and flux density field distributions for all machines at aligned position are shown in Fig. 6.6. Obviously, the flux loop of each coil belong to the same phase is completely independent in PS-BFPMMs, which is consistent with SS-BFPMM. Meanwhile, short flux paths, which could result in lower MMF drop in the stator and thinner thickness of stator yoke, are also observed in both PS-BFPMMs and SS-BFPMMs. Moreover, due to the larger PM usage and spoke-IPM stator configuration (flux-focusing effect), the saturation in PS-BFPMM-II is much heavier than other three machines, especially in the regions of rotor which nearly aligns with PMs of inner stator.

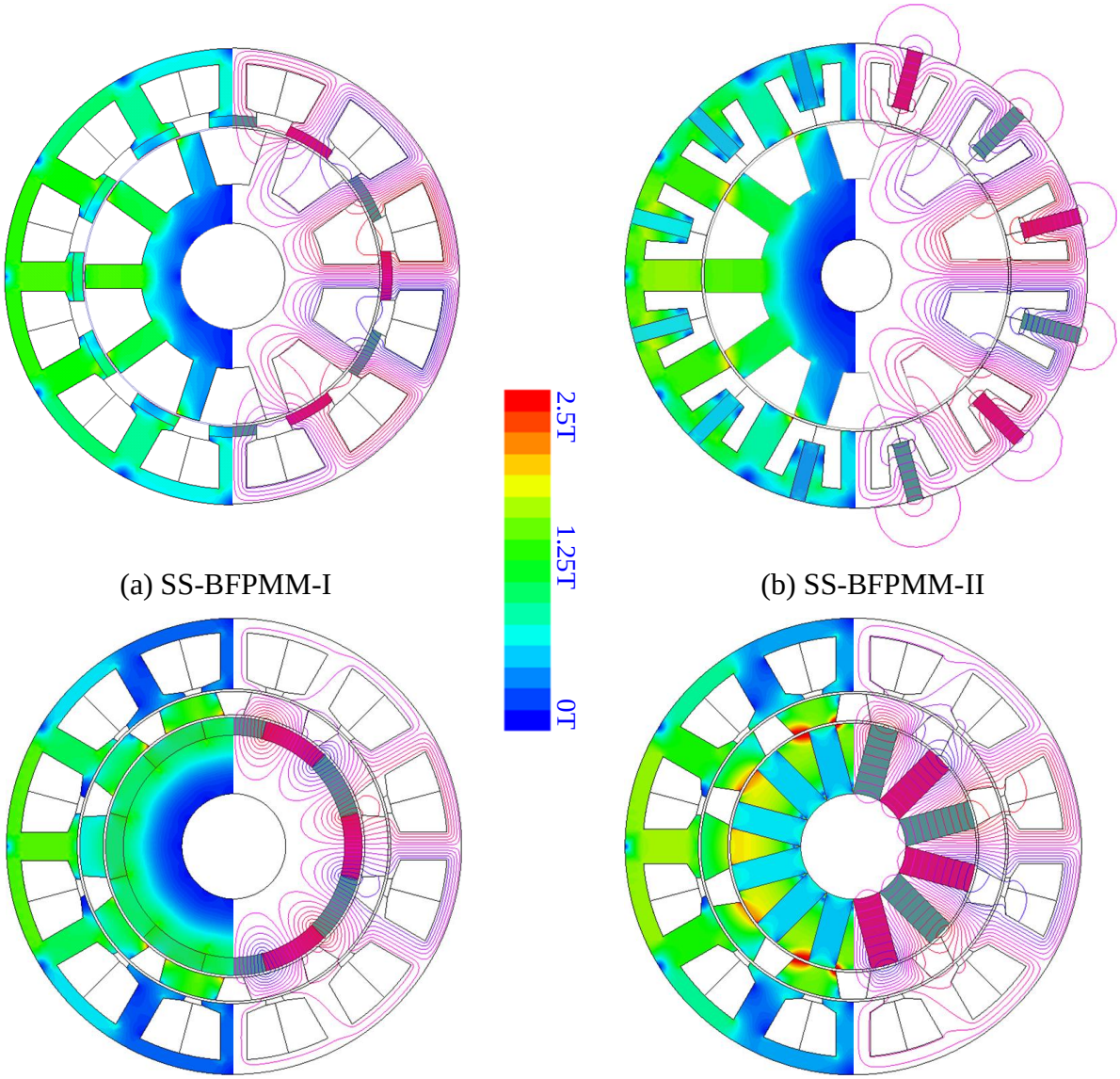

(a) SS-BFPMM-I (b) SS-BFPMM-II

(c) PS-BFPMM-I (d) PS-BFPMM-II

Fig. 6.6. Open-circuit equipotential and flux density field distributions at aligned position.

Fig. 6.7 shows the open-circuit air-gap flux density waveforms for all machines at aligned position. Since the PS-BFPMMs have two layers of air-gap, the corresponding waveforms shown in Fig. 6.7(b) are based on the layer which is close to the stator wound with armature windings (outer stator under investigation). It can be seen that the waveforms of two PS-BFPMMs are similar with those of two SS-BFPMMs. Meanwhile, due to the larger PM usage (especially for the larger PM cross section area), both SS-BFPMM-II and PS-BFPMM-II exhibits larger air-gap flux densities than SS-BFPMM-I and PS-BFPMM-I respectively.

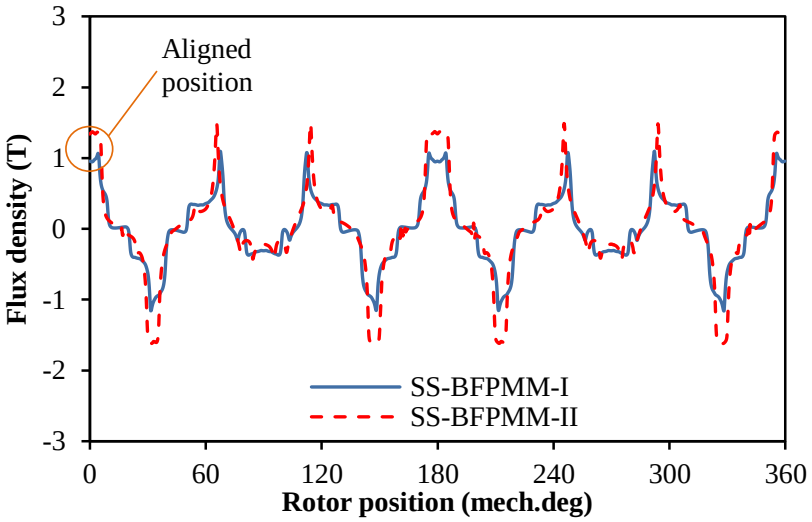

(a) SS-BFPMM-I and SS-BFPMM-II

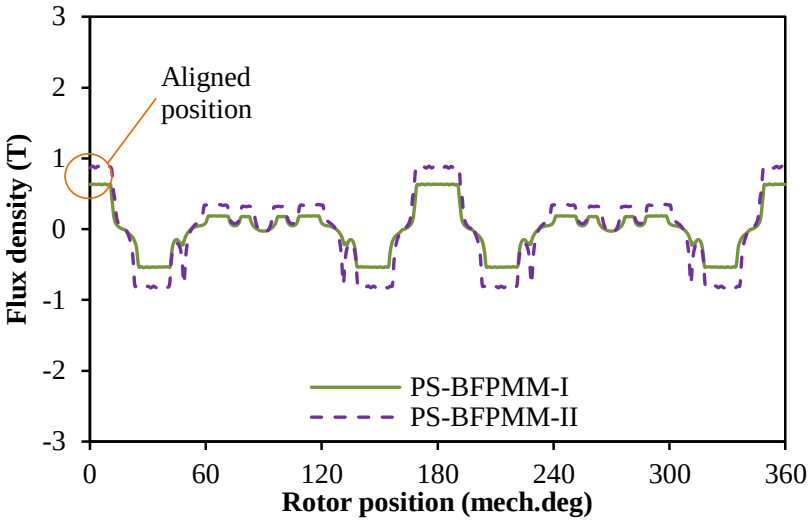

(b) PS-BFPMM-I and PS-BFPMM-II

Fig. 6.7. Open-circuit air-gap flux densities at aligned position.

6.3.2 Flux-Linkage and Back-EMF Waveforms

Fig. 6.8 shows the open-circuit phase flux-linkages of four machines. Obviously, symmetrical bipolar phase flux-linkages are obtained in 12I/12O/10R PS-BFPMMs, which

are the same as 12S/10R SS-BFPMMs. This result can be used as the evidence of equation (6.2) in section 6.2.4. According to Table 6.2, the magnitudes of fundamental phase flux-linkages for SS-BFPMM-I, SS-BFPMM-II, PS-BFPMM-I and PS-BFPMM-II are 3.84, 5.86, 8.46 and 12.88mWb respectively. By introducing the partitioned stator configuration into SS-BFPMM-I and SS-BFPMM-II, the fundamental phase flux-linkages are increased by ~120.3% and 119.8% respectively. Meanwhile, PS-BFPMM-II exhibits ~52.2% larger fundamental phase flux-linkage than PS-BFPMM-I. The increased phase flux-linkage is mainly due to the enlarged cross section and thickness of PMs as well as the benefit from the unequal top and bottom segment rotor pole arcs.

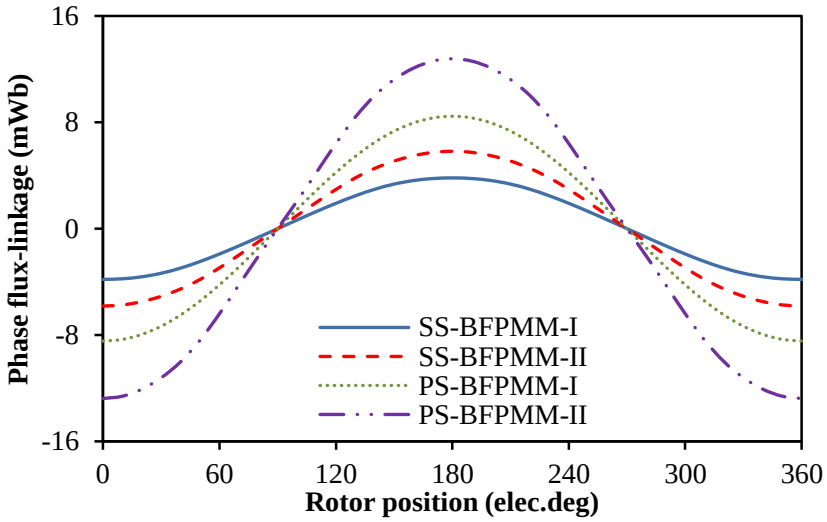

(a) Waveforms

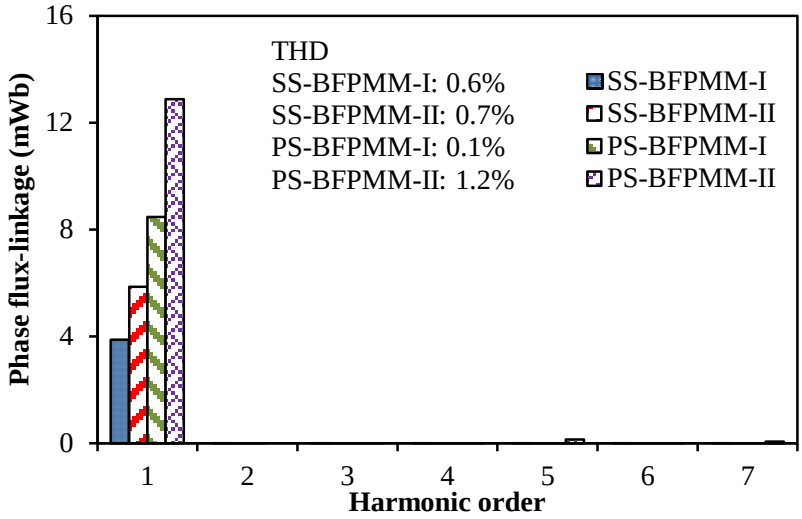

(b) Spectra

Fig. 6.8. Open-circuit phase flux-linkages of SS- and PS-BFPMMs.

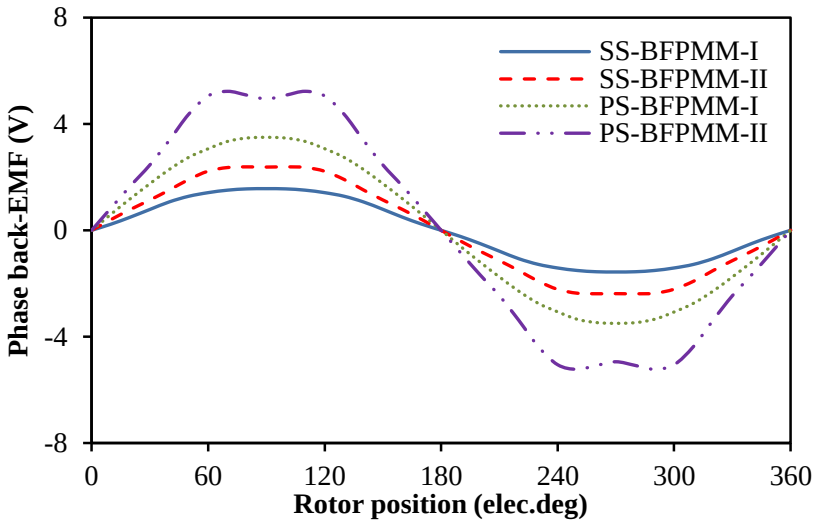

(a) Waveforms

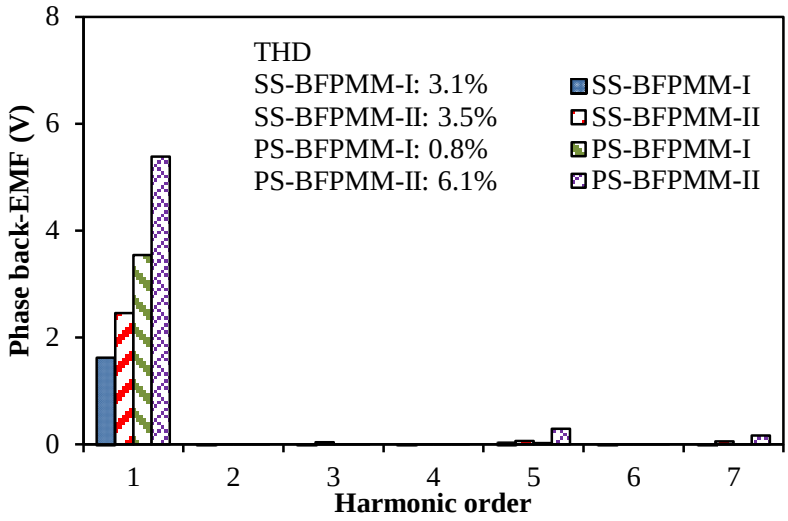

(b) Spectra

Fig. 6.9. Open-circuit phase back-EMFs of SS- and PS-BFPMMs at rated 400rpm.

The open-circuit phase back-EMF waveforms of four machines at rated speed (400rpm) are shown in Fig. 6.9. It can be seen that symmetrical phase back-EMFs are obtained in both PS-BFPMMs and SS-BFPMMs. The rated electric frequencies of four machines are the same and equal to 66.7Hz since they have the same stator/rotor pole combination. Hence, the increase rates of fundamental phase back-EMF in PS-BFPMM-I and PS-BFPMM-II are consistent with those in fundamental phase flux-linkage, which are ~120.3% and 119.8% higher than SS-BFPMM-I and SS-BFPMM-II respectively. Meanwhile, PS-BFPMM-II should also exhibit ~52.2% larger fundamental phase flux-linkage than PS-BFPMM-I. These conclusions can be evidenced by the fundamental phase back-EMFs shown in Table 6.2, which are 1.61,

2.45, 3.54 and 5.39V respectively for SS-BFPMM-I, SS-BFPMM-II, PS-BFPMM-I and PS-BFPMM-II.

6.3.3 *Dq*-Axis Inductances

Fig. 6.10 shows the *dq*-axis inductances at different current angles for all machines with rated currents as given in Table 6.1. Similar to SS-BFPMM, the *d*-axis inductance is quite close to *q*-axis inductance in PS-BFPMM and the saliency ratio is close to 1. Hence, the potential reluctance torque in PS-BFPMM can be negligible. Moreover, both PS-BFPMM-I and PS-BFPMM-II exhibit higher *dq*-axis inductances than SS-BFPMM-I and SS-BFPMM-II, as shown in Fig. 6.10. It is mainly due to the shorter equivalent air-gap length in main magnetic flux path of PS-BFPMM when compared with SS-BFPMM.

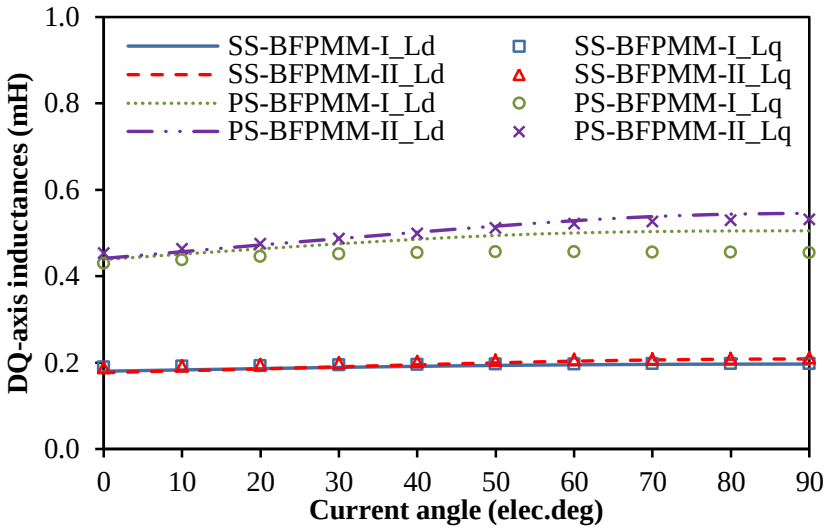

Fig. 6.10. Variation of *dq*-axis inductances with current angle under the rated currents, p_c=30W.

6.3.4 Cogging Torque

The cogging torque waveforms of all machines are shown in Fig. 6.11. Obviously, both PS-BFPMM-I and PS-BFPMM-II exhibit larger magnitudes of cogging torque than SS-BFPMM-I and SS-BFPMM-II, as shown in Fig. 6.11(a) and Table 6.2. Further, the main harmonics for all machines are 6n times as shown in Fig. 6.11(b), which means that the cogging torques will all exhibit 6 cycles over one electric period.

Since the operational principles of PS-BFPMMs are consistent with SS-BFPMMs, the equation (6.3) which is used to calculate the cycle number of cogging torque over one electric period in SS-BFPMMs can be extended to PS-BFPMMs.

$$N_C = \frac{N_{os}}{GCD(N_{os}, N_r)} \tag{6.3}$$

where N_c is the cycle number of cogging torque over one electrical period.

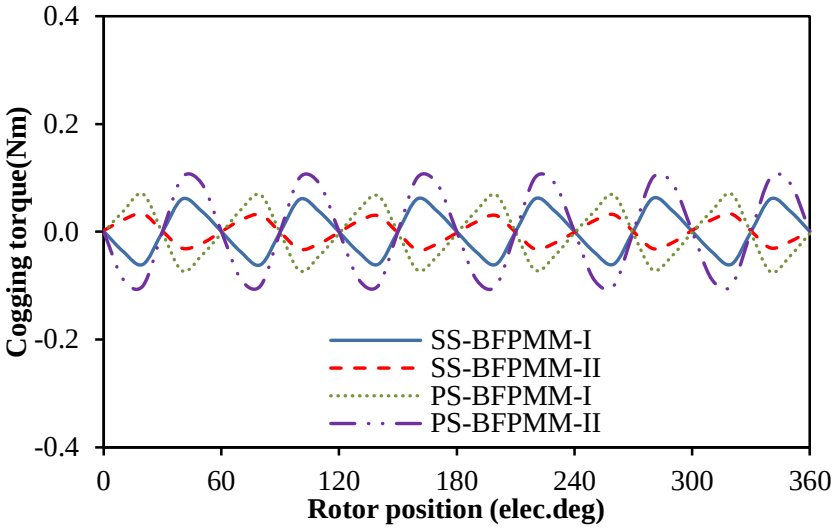

(a) Waveforms

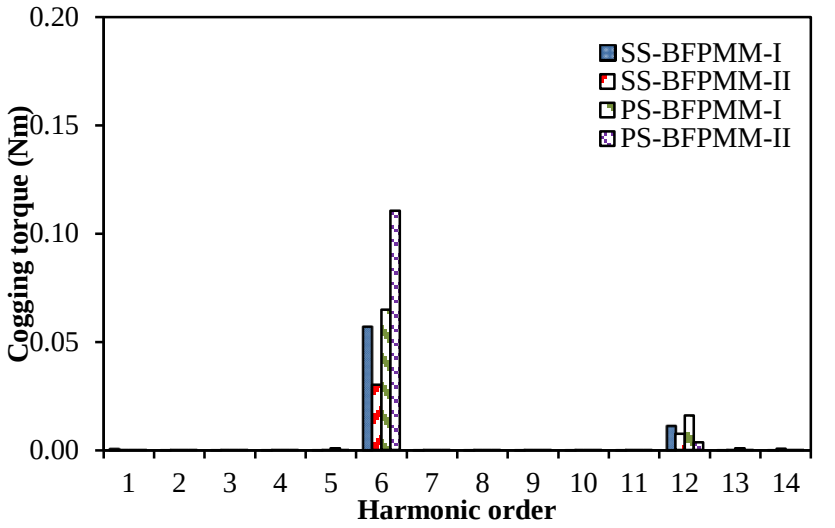

(b) Spectra

Fig. 6.11. Open-circuit cogging torques of SS-BFPMMs and PS-BFPMMs.

6.3.5 Electromagnetic Torque Characteristics

Fig. 6.12 shows the waveforms of average torque against current angle at rated currents (corresponding to p_c=30W) for all machines. Obviously, the optimal current angles of PS-BFPMMs are close to 0°, which are the same as those of SS-BFPMMs. The results indicate that the reluctance torque is negligible in PS-BFPMMs, which is consistent with the conclusion mentioned in section 6.3.3.

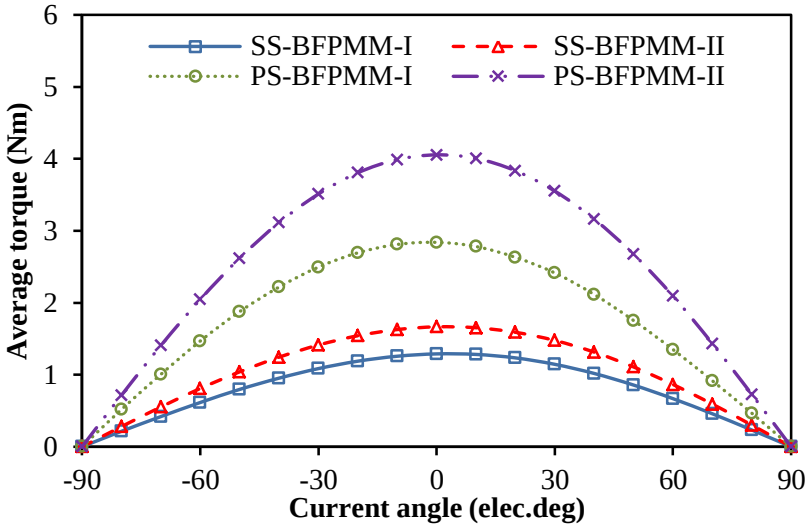

Fig. 6.12. Variation of average torque with current angle under the rated currents, p_c=30W.

Fig. 6.13 shows the waveforms of torque against rotor position at rated currents (p_c=30W) and I_d=0 control. Due to the combined influences of cogging torque and back-EMF harmonics (mainly in 5th and 7th), all machines have 6 torque ripples over one electric period. As shown in Table 6.2, the torque ripples of SS-BFPMM-I, SS-BFPMM-II, PS-BFPMM-I and PS-BFPMM-II are 10.0%, 9.4%, 14.0% and 9.0% respectively. It can be seen that the torque ripple is increased in BFPMM-I but decreased in BFPMM-II when partitioned stator configuration is employed. Meanwhile, PS-BFPMM-II has lower torque ripple when compared with PS-BFPMM-I.

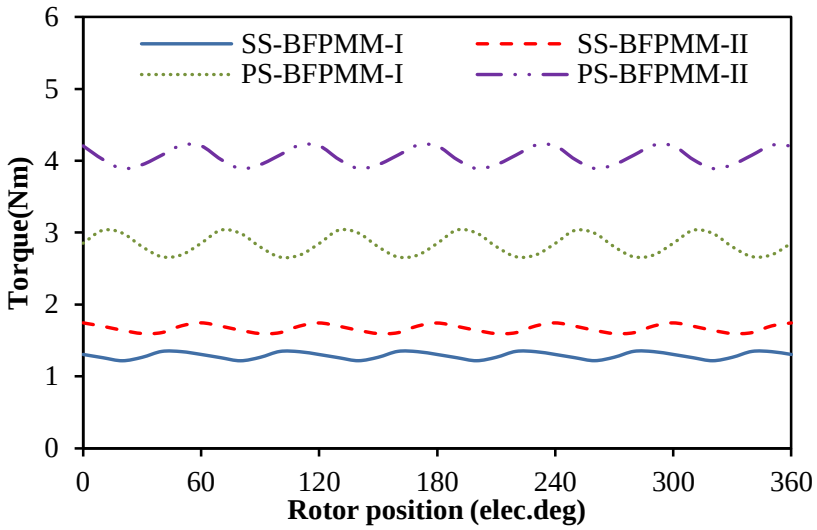

(a) Waveforms

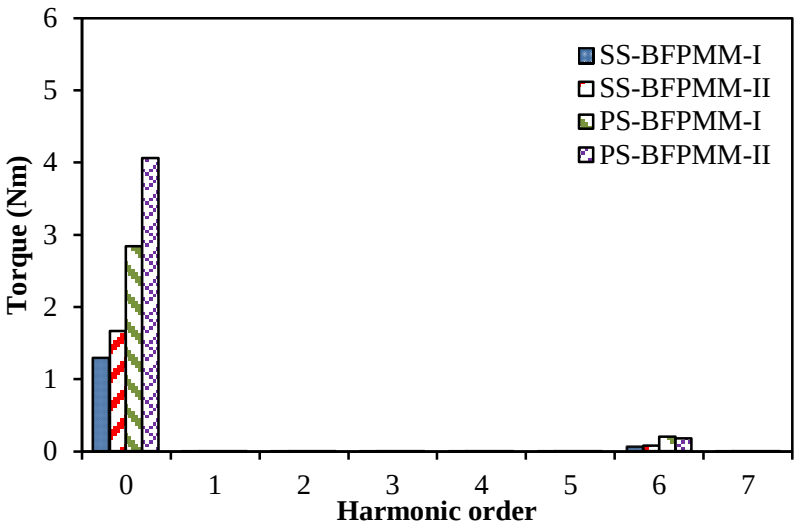

(b) Spectra

Fig. 6.13. Variation of electromagnetic torque with rotor position at rated currents, I_d=0 control, p_c=30W.

The average torque is enhanced significantly by using the partitioned stator configuration, as shown in Fig. 6.13. According to Table 6.2, the average torques for SS-BFPMM-I, SS-BFPMM-II, PS-BFPMM-I and PS-BFPMM-II under rated copper loss are 1.29, 1.66, 2.84 and 4.06Nm respectively. By employing the partitioned stator configuration in SS-BFPMM-I and SS-BFPMM-II, the average torques are enhanced by ~ 120% and 145% respectively due to the benefits from the enlarged PM cross section and unequal top and bottom rotor pole arcs. Moreover, PS-BFPMM-II exhibits ~43% larger average torque than PS-BFPMM-I.

Fig. 6.14 compares the torque density and torque to PM volume of four machines at the rated currents (p_c=30W) and I_d=0 control. Since four machines have the same machine size, the increase rates of torque density, which are caused by employing partitioned stator configuration, are consistent with the increase rates of average torque. As shown in Table 6.2, the torque densities for SS-BFPMM-I, SS-BFPMM-II, PS-BFPMM-I and PS-BFPMM-II under rated copper loss are 8.11, 10.47, 17.85 and 25.52 kN/m^2 respectively. Moreover, for the ratio of torque to PM volume (PM utilization efficiency), it is slightly decreased in PS-BFPMM-I but increased in PS-BFPMM-II when compared with SS-BFPMM-I and SS-BFPMM-II respectively. It also should be noted that the ratio of torque to PM volume (PM utilization efficiency) in PS-BFPMMM-II is ~ 17.4% lower than that in PS-BFPMM-I.

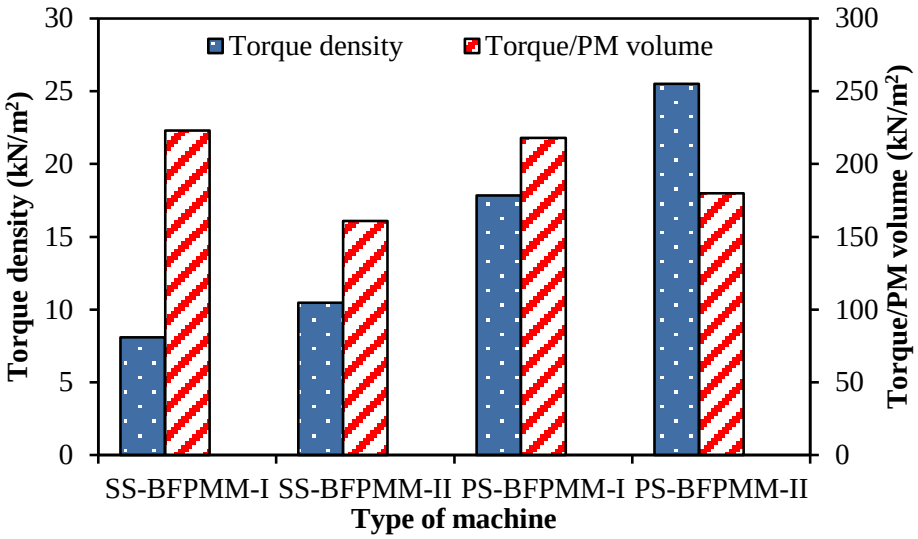

Fig. 6.14. Torque density and torque per PM volume, p_c=30W, I_d=0 control.

Fig. 6.15 compares the torque performance of four machines under different copper loss. The vertical dashed and dotted line shows the rated copper loss which is used for global optimization. Similar to SS-BFPMMs, the increase rate of average torque in PS-BFPMMs will be declined with the rising of copper loss (current) due to the aggravated magnetic saturation. As shown in Fig. 6.15, PS-BFPMMs exhibit larger average torque than SS-BFPMMs under the same copper loss over the whole copper loss range. Further, compared with PS-BFPMM-I under both low and high copper losses, PS-BFPMM-II always has higher torque capability since its higher PM usage and the additional flux focusing effect.

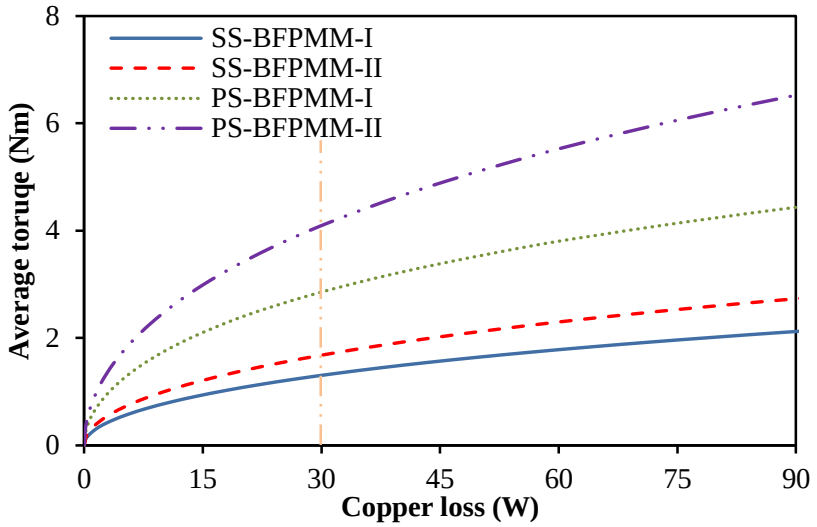

Fig. 6.15. Variation of average torque with copper loss, I_d=0 control.

Table 6.2 Main electromagnetic performances of SS-BFPMMs and PS-BFPMMs

Parameter	SS-I	SS-II	PS-I	PS-II
Fund. flux-linkage (mWb)	3.84	5.86	8.46	12.88
Fund. back-EMF (V)	1.61	2.45	3.54	5.39
Rated electric frequency (Hz)	66.7	66.7	66.7	66.7
Cogging torque (Nm)	0.062	0.033	0.070	0.107
Average torque (Nm)	1.29	1.66	2.84	4.06
Increment of torque (%)	0	-	120	-
	-	0	-	145
Torque ripple (%)	11.0	9.4	14.0	9.0
Torque density (kN/m^2)	8.11	10.47	17.85	25.52
Total PM volume (mm^3)	5783.1	10352.0	13029.8	22558.0
Torque/PM volume (kN/m^2)	223	161	218	180
Rated iron loss (W)	0.64	0.90	1.72	2.26
Rated PM loss (W)	0.23	0.14	0.07	0.06

6.3.6 Mechanical Integrity, Iron Loss and PM Loss

As shown in Fig. 6.2, for the original single stator BFPMMs, the mechanical integrity of SS-BFPMM-II is relatively poor than that of SS-BFPMM-I since the segmented stator configuration is employed. Then, when the partitioned stator configuration is introduced, the corresponding PS-BFPMMs are composed by three components, such as segment rotor, stator with armature windings and stator with PMs. Consequently, the assembling for PS-BFPMMs is more difficult than that for SS-BFPMMs due to the increased components. Compared with original SS-BFPMMs, the fabrication process of two stators of PS-BFPMMs is relative simple and convenience since the armature windings and PMs are separated into two stators. Further, the assembling and positioning of segmented rotor is more difficult although the fabrication is still easy. Therefore, as will be shown in later, to solve these problems and make the positioning easily as well as enhance the mechanical integrity, the segmented rotor is mechanically connected by 0.5mm lamination bridges at the side close to the stator with PMs, although it will reduce the electromagnetic torque performance. Similarly, for PS-BFPMM with spoke-IPM stator, 0.5mm lamination bridges are also added at both top and bottom edges of PMs to help fixing the PMs in the PM stator.

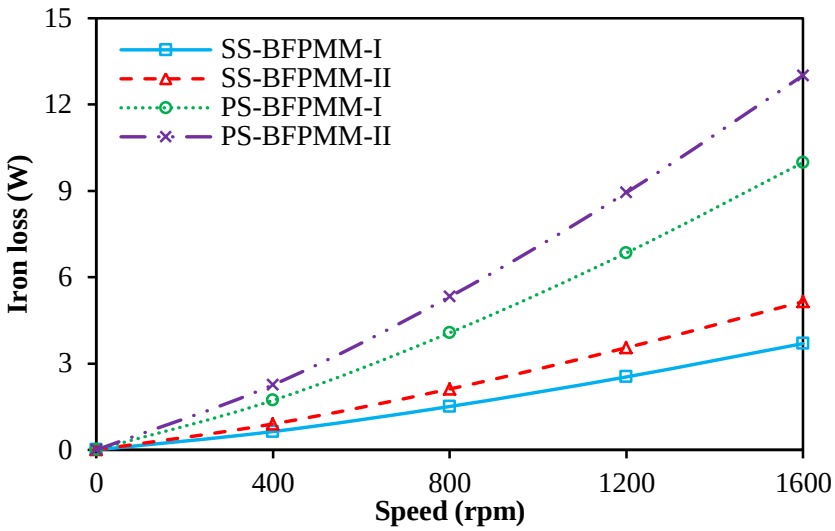

Fig. 6.16. Variation of iron loss with speed in SS- and PS-BFPMMs, p_c =30W, I_d = 0 control.

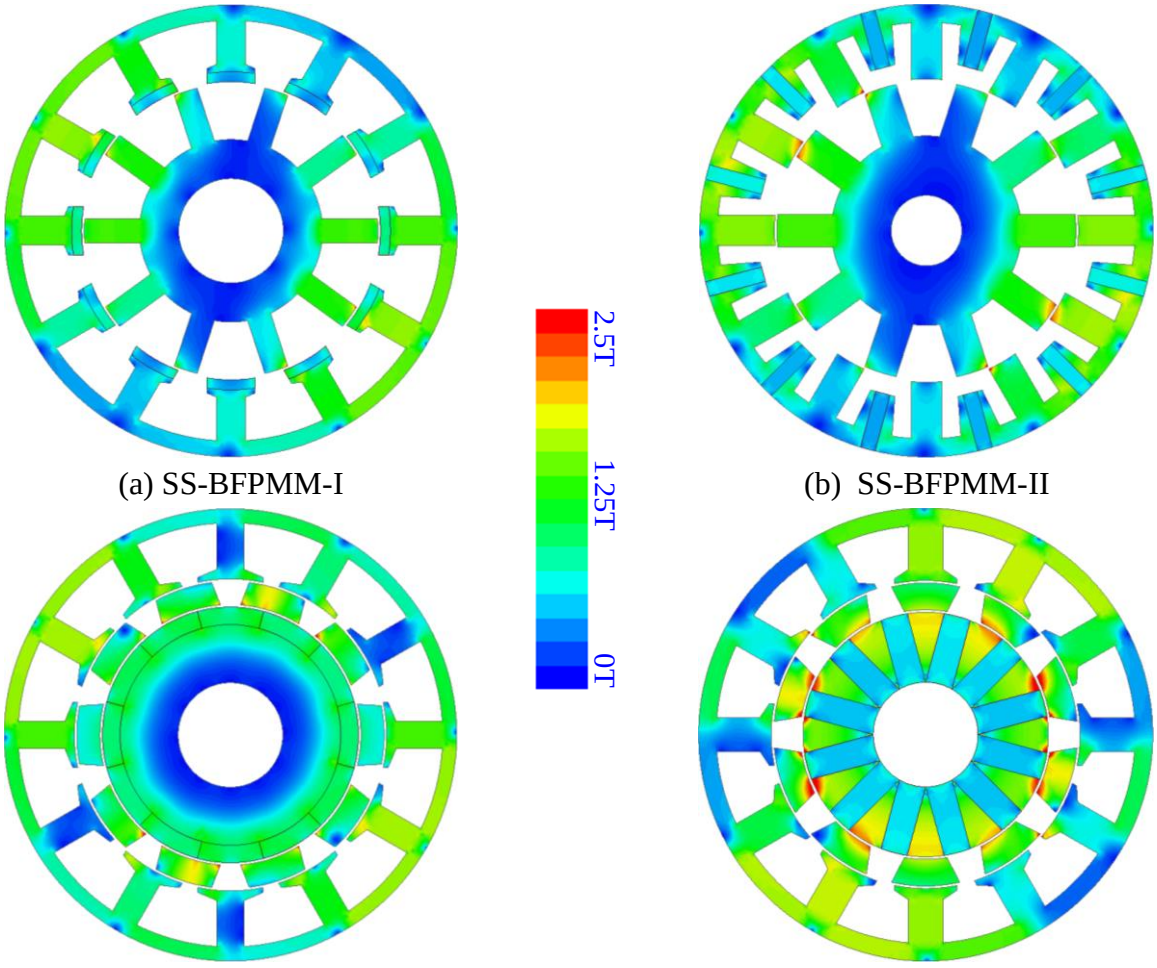

(a) SS-BFPMM-I (b) SS-BFPMM-II

(c) PS-BFPMM-I (d) PS-BFPMM-II

Fig. 6.17. On-load flux density distributions of SS- and PS-BFPMMs, p_c =30W, I_d = 0 control.

Fig. 6.16 shows the variation of total iron losses against speed at rated copper loss for four machines. According to the analyses shown in section 3.4.6 and section 5.3.7, the iron loss is

increased as the speed increased. Obviously, by introducing the partitioned stator configuration, the total iron loss is increased under the same speed when the copper loss is rated 30W. It is mainly due to that PS-BFPMMs have heavier saturation level and higher amplitude change of flux density over one electric period as well as larger total saturation area when compared with original SS-BFPMMs, as shown in Fig. 6.17. As shown in Table 6.2, the iron loss of SS-BFPMM-I, SS-BFPMM-II, PS-BFPMM-I and PS-BFPMM-II under the rated copper loss (30W) and the rated speed (400rpm) are 0.64, 0.90, 1.72 and 2.26W respectively.

The stator iron losses of SS-BFPMMs and PS-BFPMMs are compared in Fig. 6.18. Moreover, since PS-BFPMMs have two independent stators, the iron loss of each stator is further separated and also shown in Fig. 6.17. Obviously, due to much lower amplitude change of flux density over one electric period and much smaller total saturation area as shown in Fig. 6.17 (c) and (d), the iron loss produced in the inner stator (stator with PMs) is almost negligible when compared with that produced in the outer stator (stator with armature windings), as shown in Fig. 6.18.

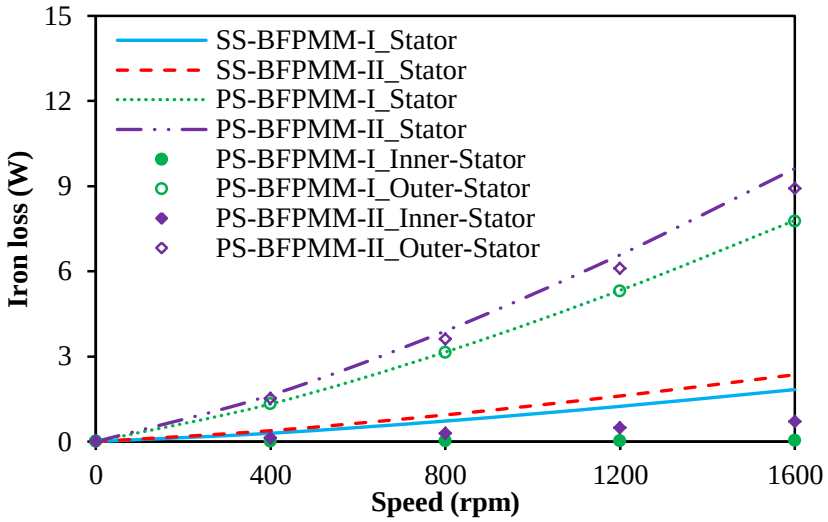

Fig. 6.18. Variation of stator iron loss with speed in SS- and PS-BFPMMs, p_c =30W, I_d = 0 control.

Fig. 6.19 shows the waveforms of PM losses against speed at rated copper loss for four machines. According to the analyses in section 5.3.7, the PM loss is increased as the speed increased. Compared with the SS-BFPMMs, the influence of armature reaction on the PM working point is much smaller in the PS-BFPMMs since the PMs and armature windings are separated into two stators and the second air-gap is introduced. In other word, the amplitude change of PM flux density over one electric period in PS-BFPMMs is much smaller than that

in SS-BFPMMs, as shown in Fig. 6.17. Consequently, PS-BFPMMs exhibit lower PM loss than SS-BFPMMs although PS-BFPMMs have larger total PM volume. As shown in Table 6.2, the PM loss of SS-BFPMM-I, SS-BFPMM-II, PS-BFPMM-I and PS-BFPMM-II under the rated copper loss (30W) and the rated speed (400rpm) are 0.23, 0.14, 0.07 and 0.06W respectively.

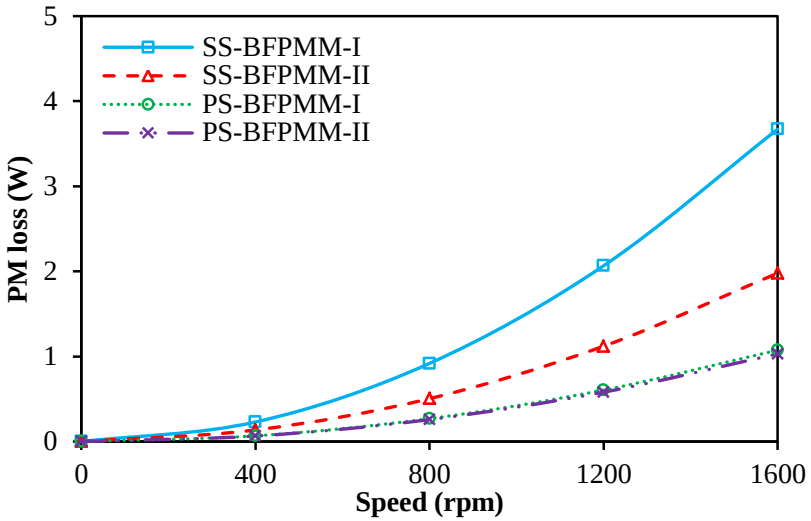

Fig. 6.19. Variation of PM loss with speed in SS- and PS-BFPMMs, p_c =30W, I_d = 0 control.

6.4 Influence of Stator/Rotor Pole Combinations on PS-BFPMM-I

In this section, the influence of stator/rotor pole combinations on electromagnetic performance of PS-BFPMM-I will be analysed and compared.

6.4.1 Main Stator/Rotor Pole Combinations

For the PS-BFPMM-Is with 12-pole inner/outer stator under investigation, the most feasible rotor pole numbers could be 10, 11, 13 and 14. According to (6.1) considering the alternate magnetization direction in adjacent stator pole, the coil EMF vectors of 12 inner/outer stator pole PS-BFPMM-Is having different rotor pole numbers are shown in Fig. 6.20. Meanwhile, the corresponding all topologies are shown in Fig. 6.21. All machines are globally optimized with maximum average torque under the same machine size and rated copper loss. The main geometric parameters are detailed in Table 6.3.

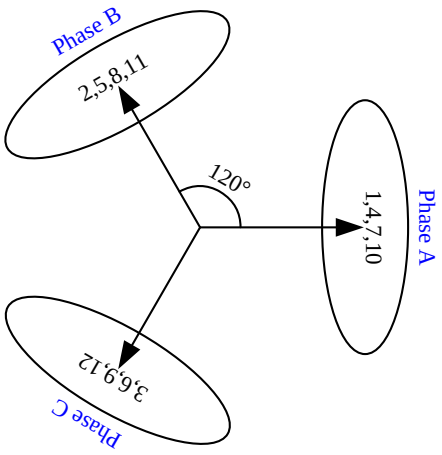

(a) 12I/12O/10R

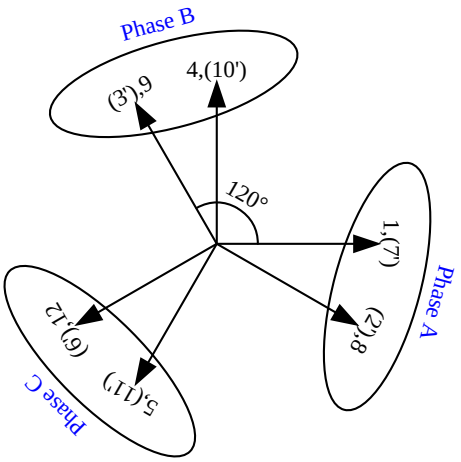

(b) 12I/12O/11R

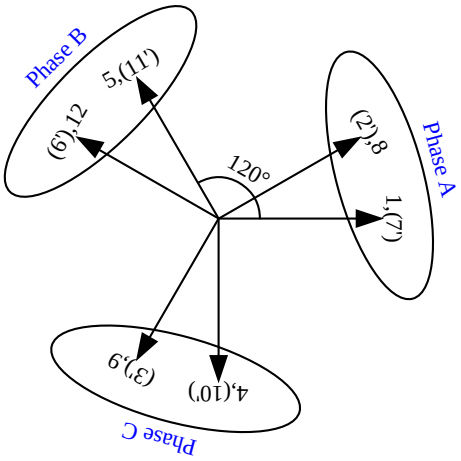

(c) 12I/12O/13R

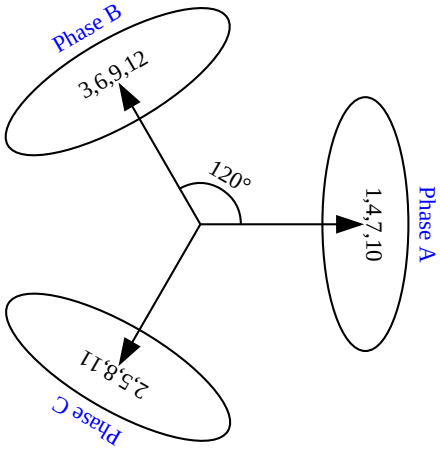

(d) 12I/12O/14R

Fig. 6.20. Coil-EMF vectors for PS-BFPMM-I with different stator/rotor pole combinations.

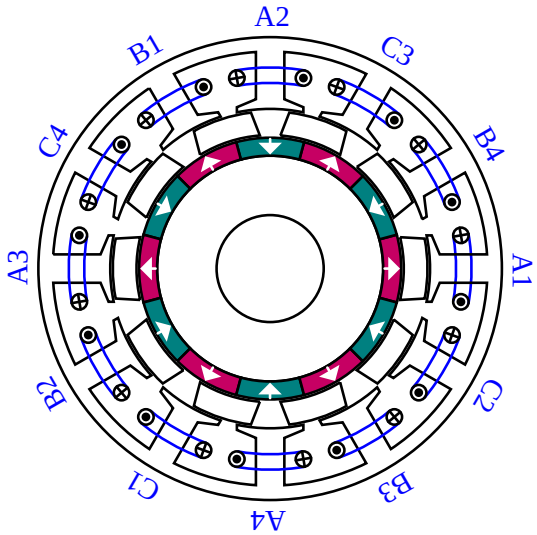

(a) 12I/12O/10R

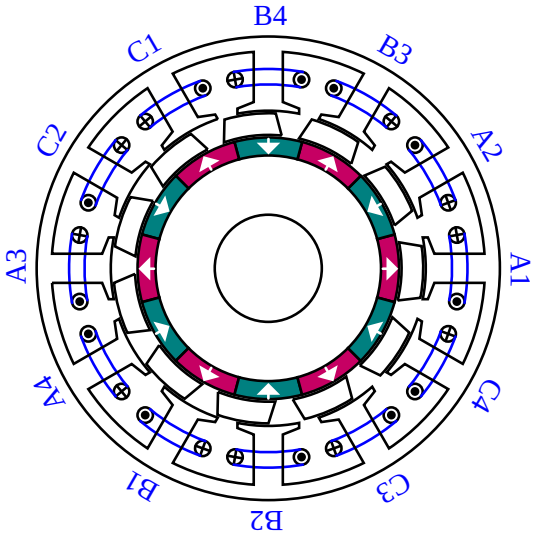

(b) 12I/12O/11R

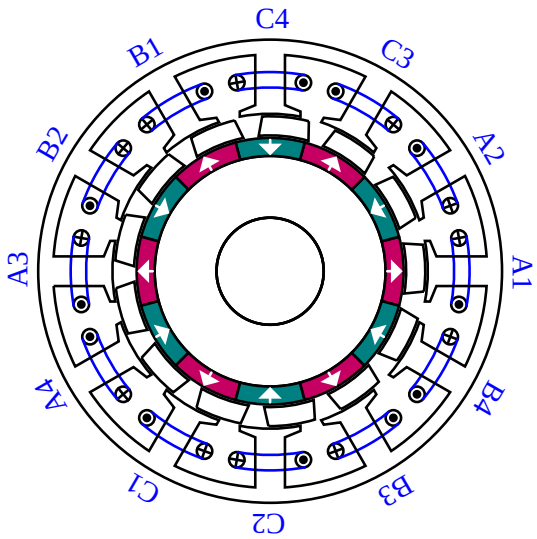

(c) 12I/12O/13R

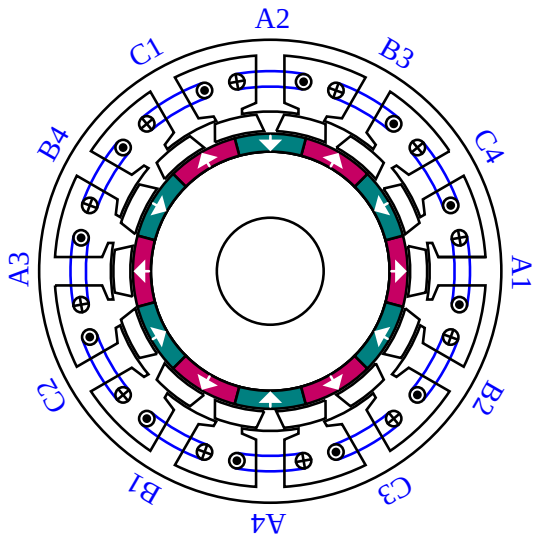

(d) 12I/12O/14R

Fig. 6.21. Topologies of PS-BFPMM-I with different stator/rotor pole combinations.

Table 6.3 Main parameters of PS-BFPMM-Is

Parameter	**12O/12I/10R**	**12O/12I/11R**	**12O/12I/13R**	**12O/12I/14R**
R_{OSI} (mm)	31.05	30.60	30.6	31.05
R_{ISO} (mm)	25.45	25.40	25.9	26.75
θ_{OSTB} (°)	10.2	10.6.	10.8	10.2
θ_{OSTT} (°)	6.9	6.0	5.7	5.1
T_{OSTTO} (mm)	1	1	1	1
T_{OSTTB} (mm)	2.0	1.8	1.8	1.8
θ_{ROP} (°)	22	19.2	17.4	15.6
θ_{RIP} (°)	27.2	25.2	21.2	20.8
T_{RR} (mm)	4.6	4.2	3.7	3.3
T_{OSY} (mm)	2.8	2.9	2.9	3.0
I_{arms}(Arms)	17.10	17.29	17.22	16.98
θ_{PM} (°)	30	30	30	30
T_{PM} (mm)	3.5	3.5	3.5	3.5

According to the coil-EMF vectors shown in Fig. 6.20, the distribution factors (K_d) for 12I/12O/10R and 12I/12O/14 are equal to 1 while 12I/12O/11R and 12I/12O/13R are equal to 0.97. Similar to the SS-BFPMMs, the pitch factor (K_p) of PS-BFPMMs can be calculated by

$$K_p = \cos\left(\pi\left(\frac{N_r}{N_s} - 1\right)\right) \tag{6.4}$$

Based on (6.4), K_p and winding factor (K_{dp}) of PS-BFPMMs with different stator/rotor pole combinations can be calculated. Table 6.4 shows the corresponding factors for the main stator/rotor pole combinations of 12 inner/outer stator pole PS-BFPMM-I. Obviously, when N_r is more close to N_s, the winding factor will be higher.

Table 6.4 Winding factors for 12 inner/outer stator pole PS-BFPMM-Is

N_r	10	11	12	13	14
K_d	1	0.97	1	0.97	1
K_p	0.87	0.97	1	0.97	0.87
K_{dp}	0.87	0.94	1	0.94	0.87

6.4.2 Flux-Linkage and Back-EMF Waveforms

Fig. 6.22 shows the open-circuit phase flux-linkages of PS-BFPMM-Is with four stator/rotor pole combinations. Obviously, the polarities of phase flux-linkages for four PS-BFPMM-Is are all bipolar since the (inner/outer) stator/rotor pole combinations all satisfy (6.2). Moreover, 12I/12O/10R PS-BFPMM-I has the largest fundamental phase flux-linkage among the four PS-BFPMM-Is, as shown in Fig. 6.22(b). According to Table 6.5, the magnitudes of fundamental phase flux-linkages for 12I/12O/10R-, 12I/12O/11R-, 12I/12O/13R- and 12I/12O/14R-PS-BFPMM-Is are 8.46, 7.72, 6.27 and 5.45mWb respectively.

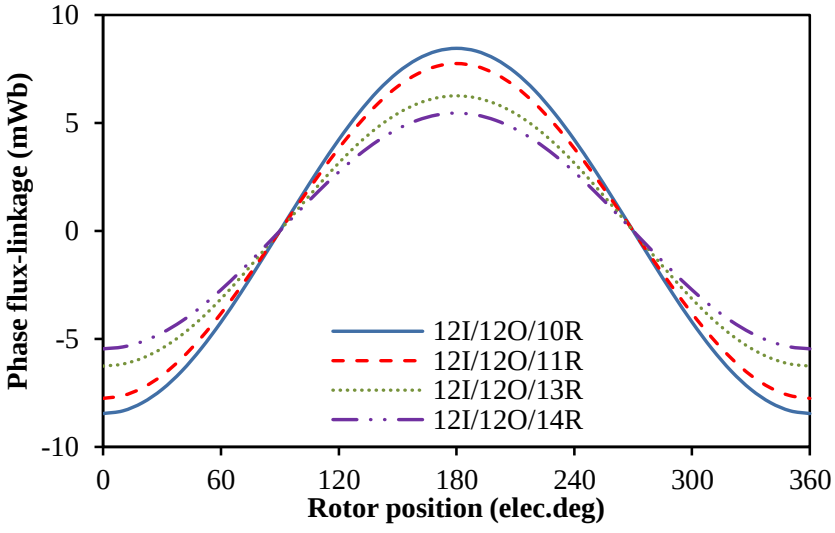

(a) Waveforms

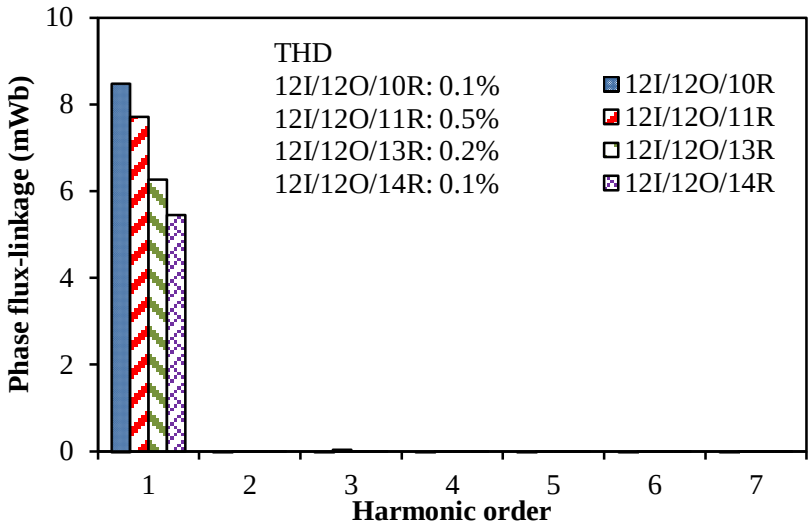

(b) Spectra

Fig. 6.22. Open-circuit phase flux-linkages of PS-BFPMM-Is.

Fig. 6.23 shows the open-circuit phase back-EMF waveforms of four machines at rated speed. It can be seen that all machines have the symmetrical phase back-EMFs since the even harmonics exist in single coils are completely cancelled. Due to the influence of rated electric frequency, 12I/12O/11R PS-BFPMM-I has the largest fundamental phase back-EMF among the four machines. As shown in Table 6.5, the magnitudes of fundamental phase back-EMFs for 12I/12O/10R-, 12I/12O/11R-, 12I/12O/13R- and 12I/12O/14R-PS-BFPMM-Is are 3.54, 3.55, 3.41 and 3.19V respectively.

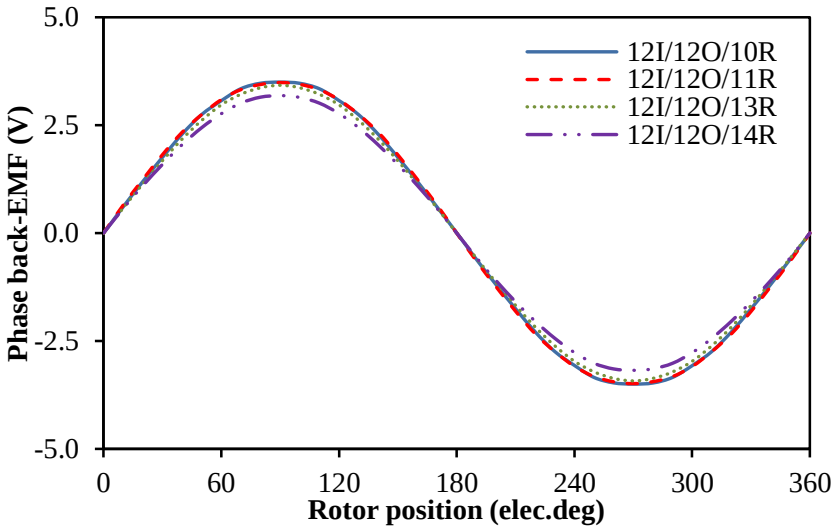

(a) Waveforms

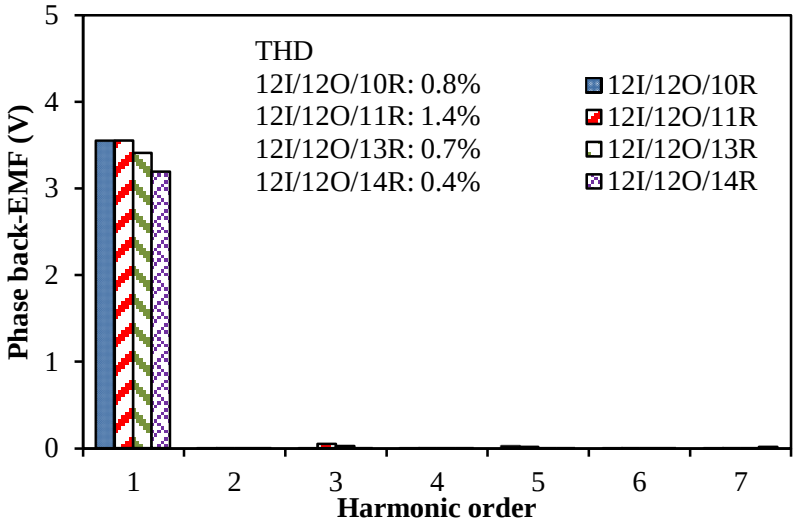

(b) Spectra

Fig. 6.23. Open-circuit phase back-EMFs of PS-BFPMM-I at rated 400rpm.

6.4.3 Cogging Torque

Fig. 6.24 shows the cogging torque waveforms of four machines. Obviously, 12I/12O/10R- and 12I/12O/14R-PS-BFPMM-Is exhibit larger magnitudes of cogging torque than 12I/12O/11R- and 12I/12O/13R-PS-BFPMM-Is. According to (6.3), the cycle numbers of cogging torque over one electric period are 6, 12, 12 and 6 respectively for 12I/12O/10R-, 12I/12O/11R-, 12I/12O/13R- and 12I/12O/11R-PS-BFPMM-Is. The results are evidenced by Fig. 6.24.

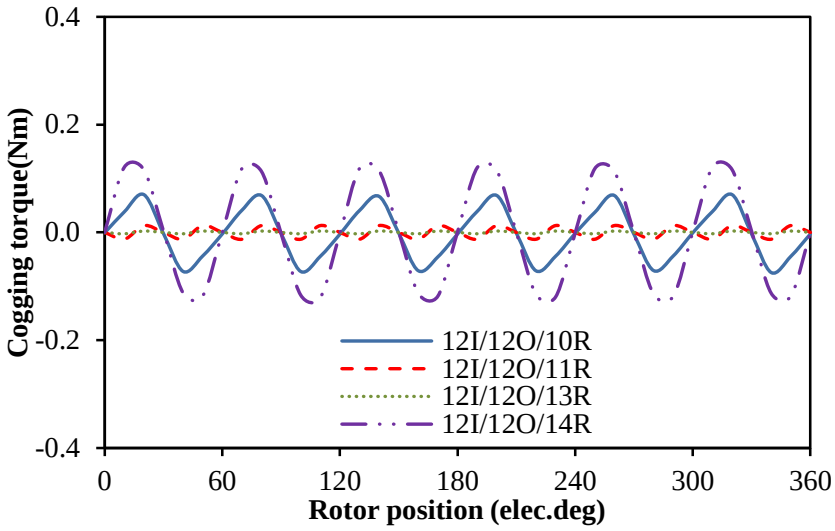

(a) Waveforms

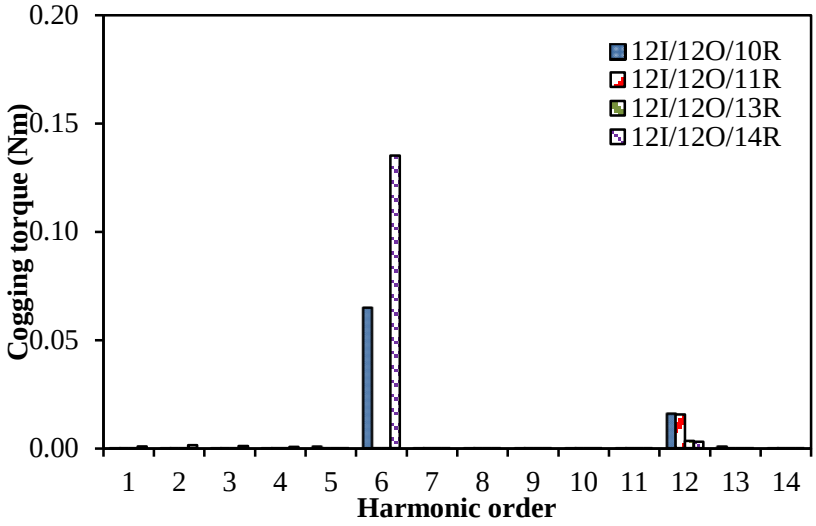

(b) Spectra

Fig. 6.24. Open-circuit cogging torques of PS-BFPMM-Is.

6.4.4 Electromagnetic Torque Characteristics

Fig. 6.25 shows the waveforms of static torque against with current angle at rated currents (p_c=30W) for four machines. It can be seen that the optimal current angles of four machines are all close to 0°, which means the reluctance torques are negligible in all stator/rotor pole combinations.

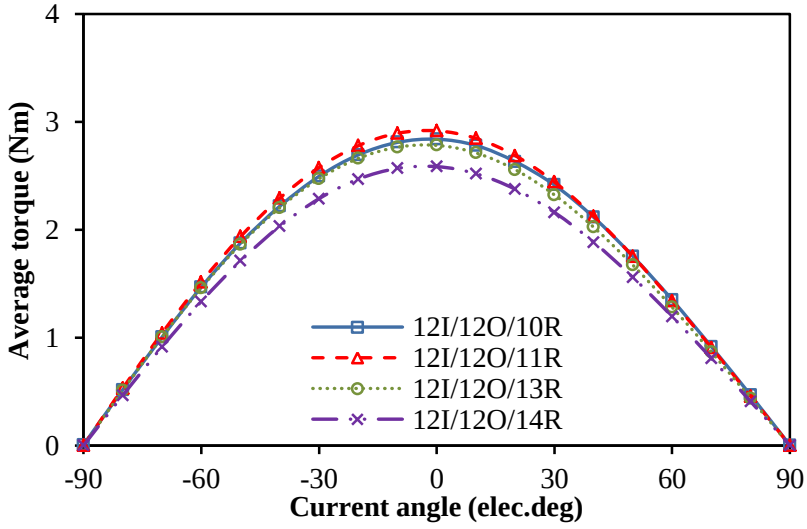

Fig. 6.25. Variation of average torque with current angle under the rated currents, p_c=30W.

Fig. 6.26 shows the torque against rotor position at rated currents (p_c=30W) and I_d=0 control for four machines. It can be seen that all machines have 6 torque ripples over one electric period, which is mainly due to the influence of back-EMF harmonics (mainly in 5th

and 7th). As shown in Table 6.5, the torque ripples of 12I/12O/10R-, 12I/12O/11R-, 12I/12O/13R- and 12I/12O/14R-PS-BFPMM-Is are 14.0%, 2.1%, 0.9% and 7.3% respectively. Obviously, among the four machines, 12I/12O/13R PS-BFPMM-I has the lowest torque ripple while 12/12O/10R exhibits the highest one.

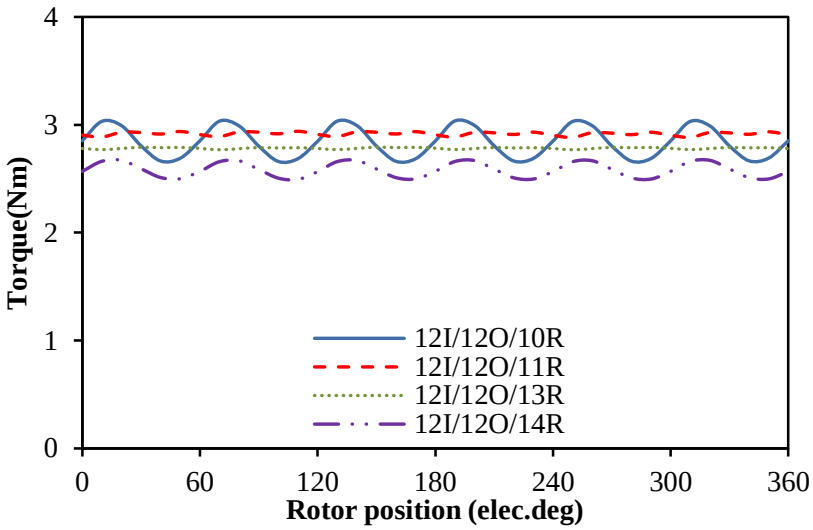

(a) Waveforms

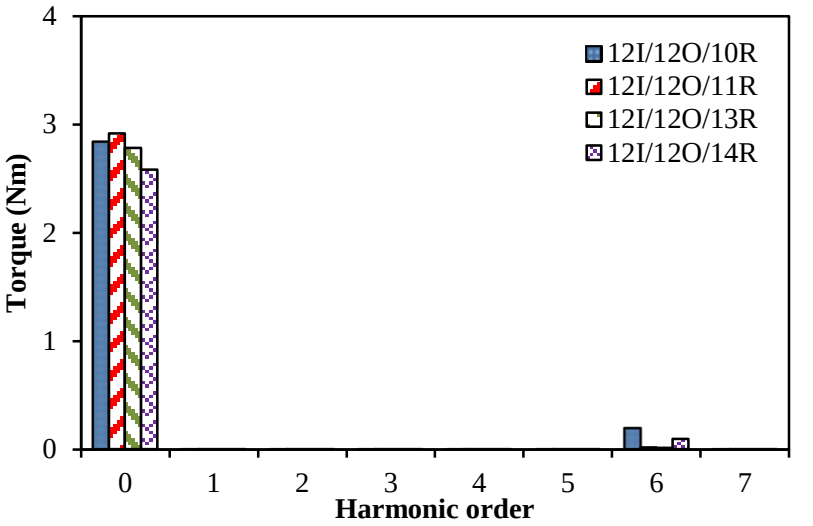

(b) Spectra

Fig. 6.26. Variation of torque with rotor position in PS-BFPMM-Is at rated currents, p_c=30W, I_d=0 control.

As shown in Fig. 6.27, among the four machines, 12I/12O/11R PS-BFPMM-I exhibits the largest average torque under the same copper loss over the whole copper loss range. According to Table 6.5, the average torques of 12I/12O/10R-, 12I/12O/11R-, 12I/12O/13R- and 12I/12O/14R-PS-BFPMM-Is under the rated copper loss are 2.84, 2.92, 2.78 and 2.58Nm respectively.

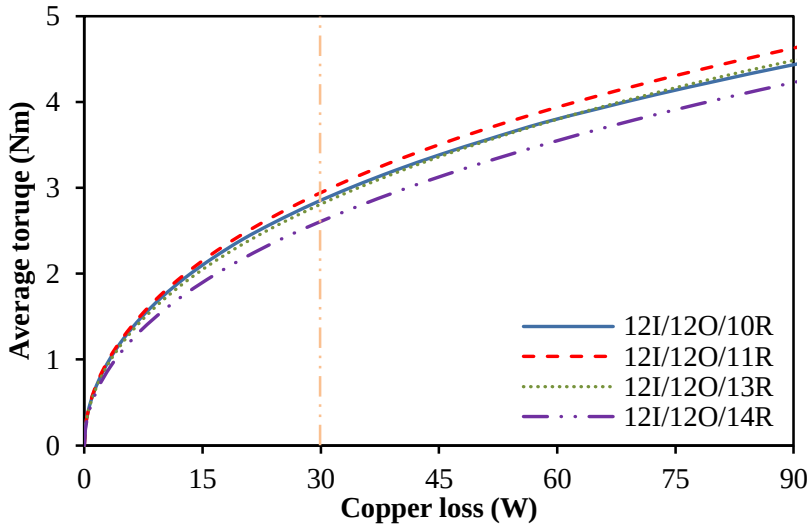

Fig. 6.27. Variation of average torque with copper loss in PS-BFPMM-Is, I_d=0 control.

Fig. 6.28 compares the torque density and torque to PM volume of four machines at the rated currents (p_c=30W) and I_d=0 control. Obviously, 12I/12O/11R PS-BFPMM-I has both the largest torque density and the highest ratio of torque to PM volume while 12I/12O/14R PS-BFPMM-I exhibits the both lowest values.

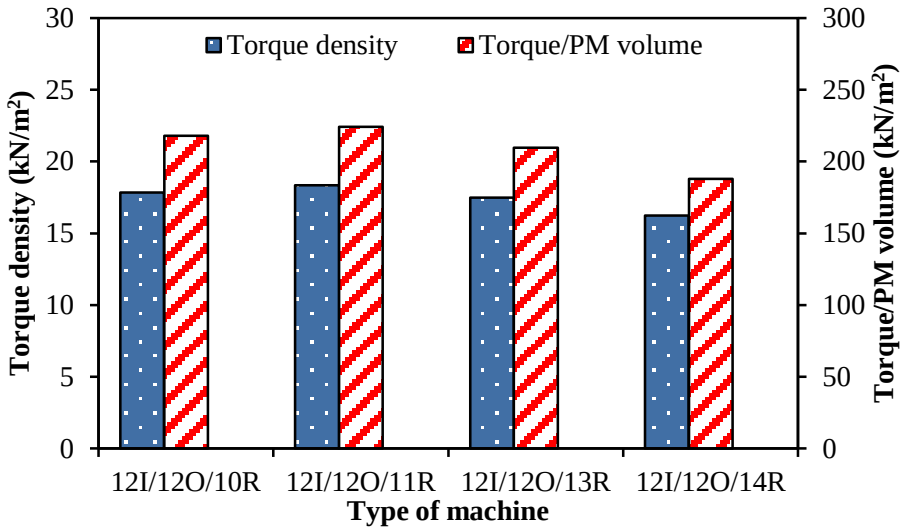

Fig. 6.28. Torque density and torque to PM volume, p_c=30W, I_d=0 control.

Table 6.5 Main electromagnetic performances of PS-BFPMM-Is

Parameter	12I/12O/10R	12I/12O/11R	12I/12O/13R	12I/12O/14R
Fund. flux-linkage (mWb)	8.46	7.72	6.27	5.45
Fund. back-EMF (V)	3.54	3.55	3.41	3.19
Rated electric frequency (Hz)	66.7	73.3	86.7	93.3
Cogging torque (Nm)	0.070	0.014	0.003	0.136
Average torque (Nm)	2.84	2.92	2.78	2.58
Torque ripple (%)	14.0	2.1	0.9	7.3
Torque density (kN/m^2)	17.85	18.34	17.50	16.24
Torque/PM volume (kN/m^2)	218	224	210	188

6.5 Influence of Stator/Rotor Pole Combinations on PS-BFPMM-II

In this section, the influence of stator/rotor pole combinations on electromagnetic performance of PS-BFPMM-II will be analysed and compared.

6.5.1 Main Stator/Rotor Pole Combinations

Similar to PS-BFPMM-I, the most feasible rotor pole numbers for PS-BFPMM-II with 12-pole inner/outer stator are 10, 11, 13 and 14. The topologies of PS-BFPMM-II with corresponding (inner/outer) stator/rotor pole combinations are shown in Fig. 6.29. All machines are globally optimized with maximum average torque under the same machine size and rated copper loss. The main geometric parameters are detailed in Table 6.6.

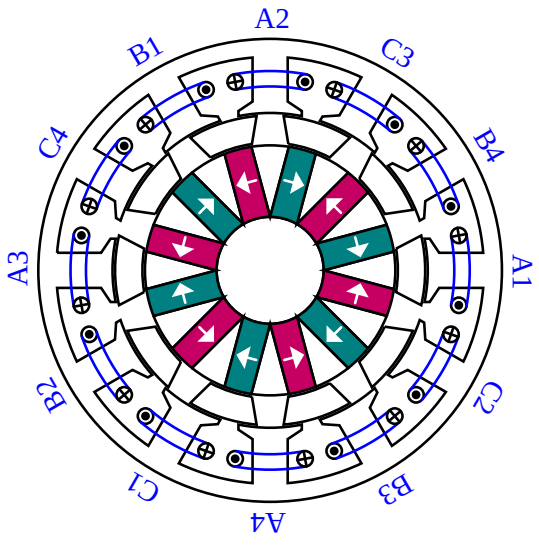

(a) 12I/12O/10R

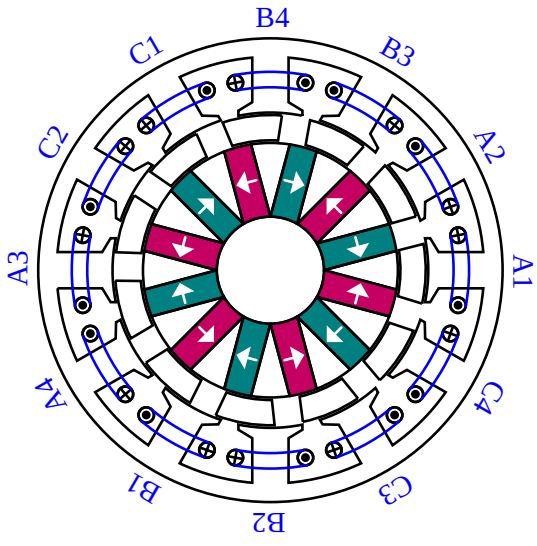

(b) 12I/12O/11R

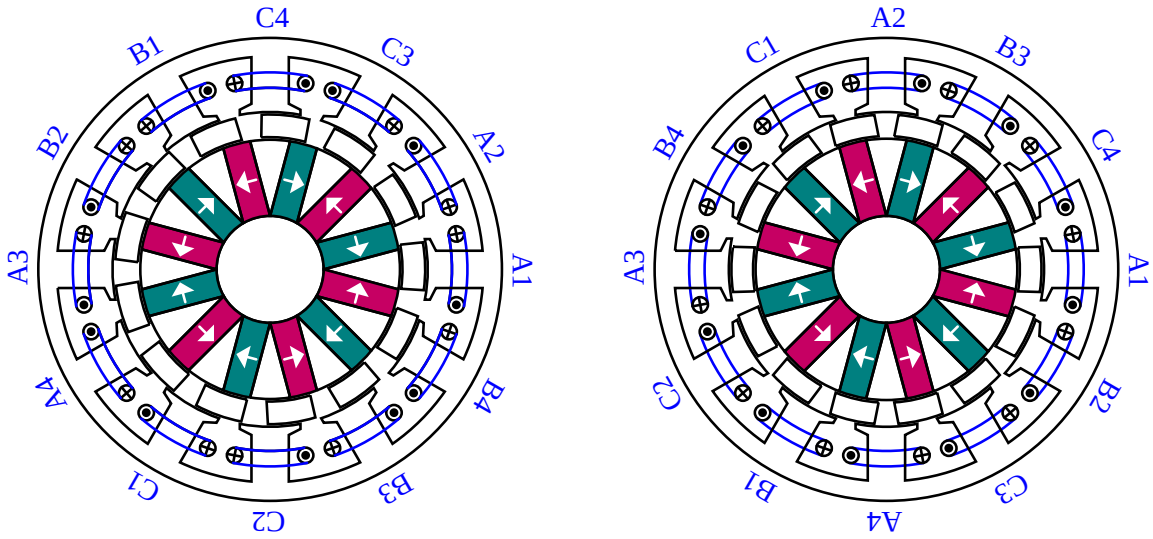

(c) 12I/12O/13R (d) 12I/12O/14R

Fig. 6.29. Topologies of PS-BFPMM-II with different stator/rotor pole combinations

Table 6.6 Main parameters of PS-BFPMM-IIs

Parameter	**12I/12O/10R**	**12I/12O/11R**	**12I/12O/13R**	**12I/12O/14R**
R_{OSI} (mm)	30.60	30.6	30.6	30.6
R_{ISO} (mm)	24.30	24.7	25.2	25.4
θ_{OSTB} (°)	12.8	13.2	13.6	13.6
θ_{OSTT} (°)	5.2	5.1	4.3	4.5
T_{OSTTO} (mm)	1	1	1	1
T_{OSTTB} (mm)	2.4	2.2	1.8	1.8
θ_{ROP} (°)	26	22.2	17.8	16.8
θ_{RIP} (°)	19.6	20.4	19.2	19
T_{RR} (mm)	5.3	4.9	4.4	4.2
T_{OSY} (mm)	3.5	3.6	3.6	3.8
I_{arms} (A)	15.83	15.63	15.58	15.38
θ_{PM} (°)	30	30	30	30
T_{PM} (mm)	13.9	14.3	14.8	15.0

6.5.2 Flux-Linkage and Back-EMF Waveforms

The phase flux-linkages and back-EMFs of PS-BFPMM-IIs with four main stator/rotor pole combinations are compared in Fig. 6.30 and Fig. 6.31 respectively. Similar to PS-

BFPMM-Is, bipolar phase flux-linkages and symmetrical phase back-EMFs are observed in PS-BFPMM-IIs with the four main stator/rotor pole combinations. Meanwhile, 12I/12O/10R PS-BFPMM-II exhibits the largest fundamental phase flux-linkage among the four main stator/rotor pole combinations. However, due to the influence of rated electric frequency, 12I/12O/11R PS-BFPMM-IIs have the same fundamental phase back-EMFs as 12I/12O/10R PS-BFPMM-II despite of a lower fundamental phase flux-linkage, as shown in Fig. 6.31(b) and Table 6.7.

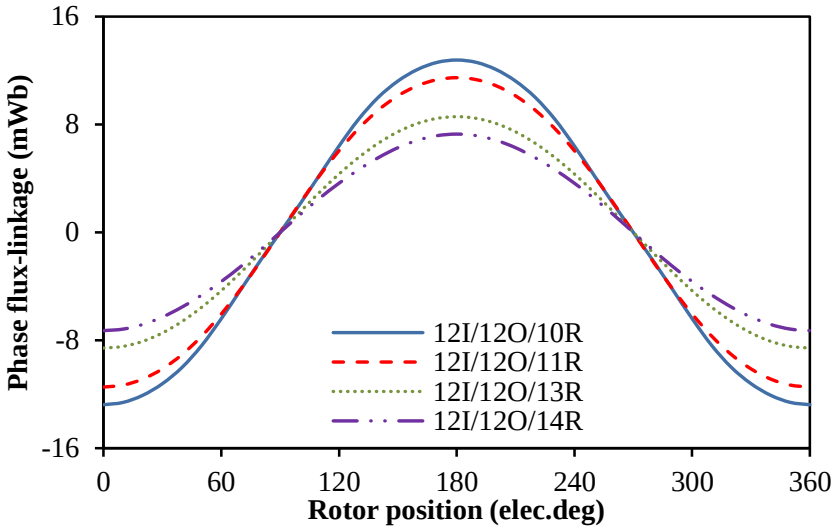

(a) Waveforms

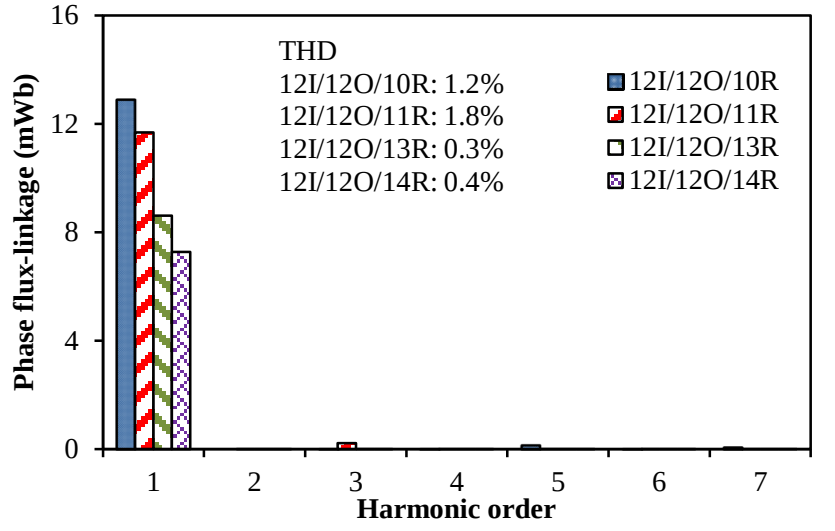

(b) Spectra

Fig. 6.30. Open-circuit phase flux-linkages of PS-BFPMM-IIs.

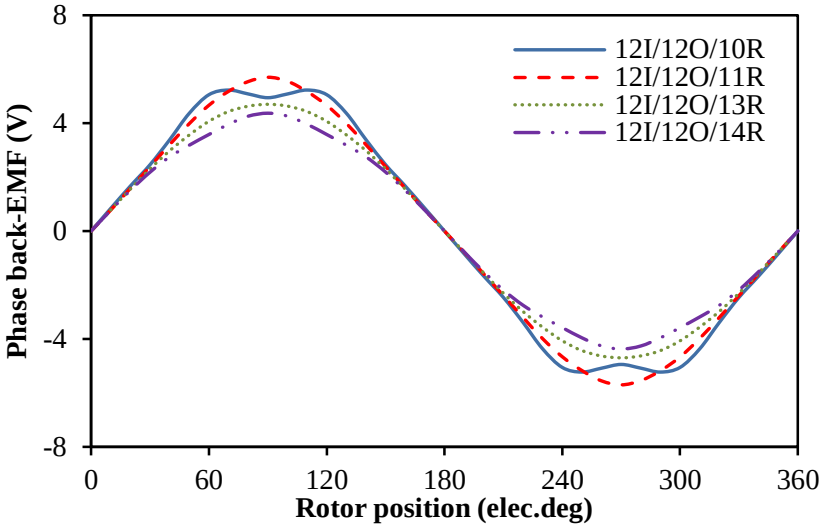

(a) Waveforms

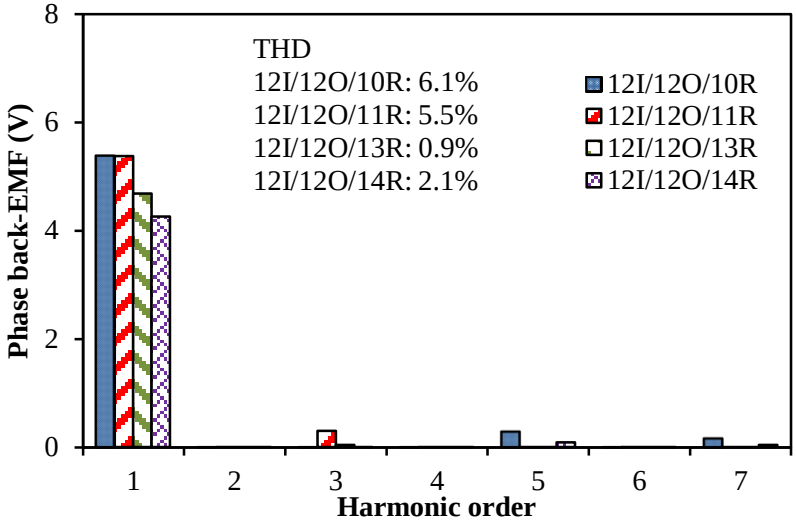

(b) Spectra

Fig. 6.31. Open-circuit phase back-EMFs of PS-BFPMM-II at rated 400rpm.

6.5.3 Cogging Torque

Fig. 6.32 compares the cogging torque of PS-BFPMM-IIs with four main stator/rotor pole combinations. It can be seen that 12I/12O/10R and 12I/12O/14R PS-BFPMM-IIs have larger magnitudes of cogging torque than 12I/12O/11R and 12I/12O/13R PS-BFPMM-IIs. Further, the cycle numbers of cogging torque over one electric period are 6 for 12I/12O/10R and 12I/12O/14R PS-BFPMM-IIs while 12 for 12I/12O/11R and 12I/12O/13R PS-BFPMM-IIs, which are same as the results calculated by (6.3).

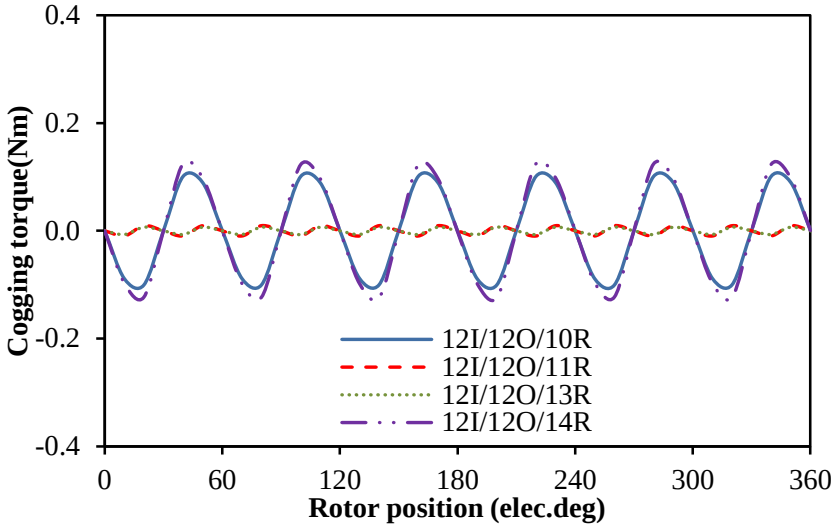

(a) Waveforms

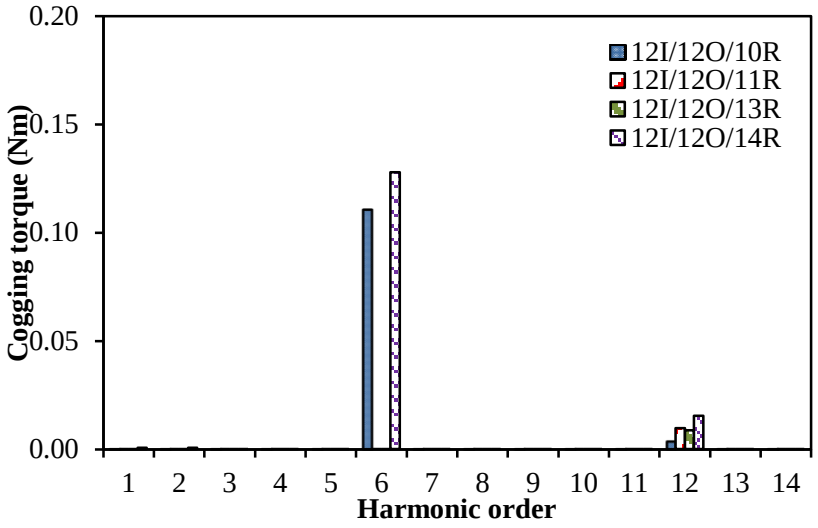

(b) Spectra

Fig. 6.32. Open-circuit cogging torques of PS-BFPMM-IIs.

6.5.4 Electromagnetic Torque Characteristics

The waveforms of torque against with current angle at rated currents (p_c=30W) for PS-BFPMM-IIs with four main stator/rotor pole combinations are shown in Fig. 6.33. Obviously, the optimal current angles for four machines are all close to 0°. Therefore, the reluctance torque is also negligible in PS-BFPMM-IIs with different inner/outer stator/rotor pole combinations.

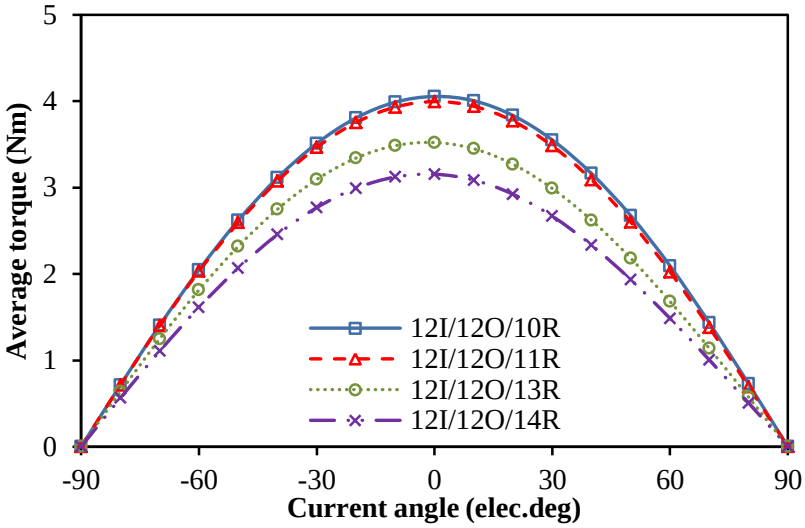

Fig. 6.33. Variation of average torque with current angle under the rated currents, p_c=30W.

Fig. 6.34 shows the waveforms of torque against with rotor position at rated currents (p_c=30W) and I_d=0 control for PS-BFPMM-IIs with four main stator/rotor pole combinations. Similar to the PS-BFPMM-Is, the four PS-BFPMM-IIs also have 6 torque ripples over one electric period. Meanwhile, 12I/12O/11R and 12I/12O/13R PS-BFPMM-II should exhibit lower torque ripples than 12I/12O/10R and 12I/12O/14R PS-BFPMM-II. It is evidenced by the data shown in Table 6.7, in which the torque ripples of 12I/12O/10R, 12I/12O/11R, 12I/12O/13R and 12I/12O/14R PS-BFPMM-IIs are 9.0%, 1.3%, 1.2% and 8.3% respectively.

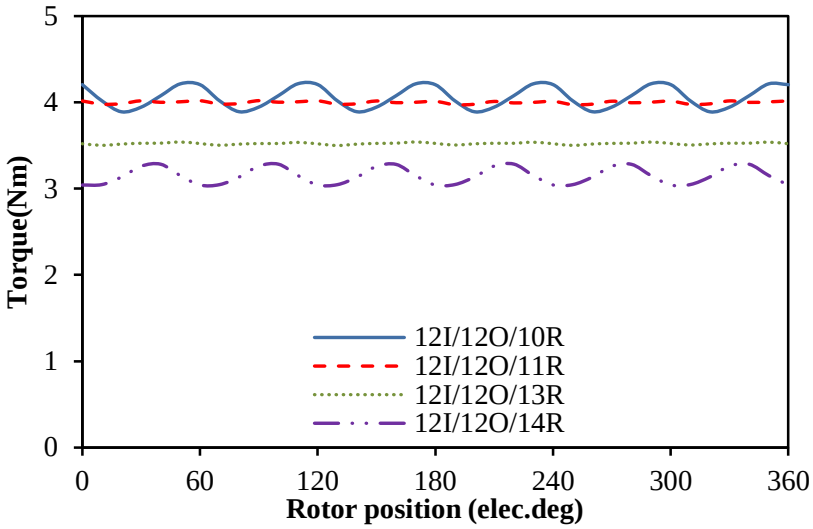

(a) Waveforms

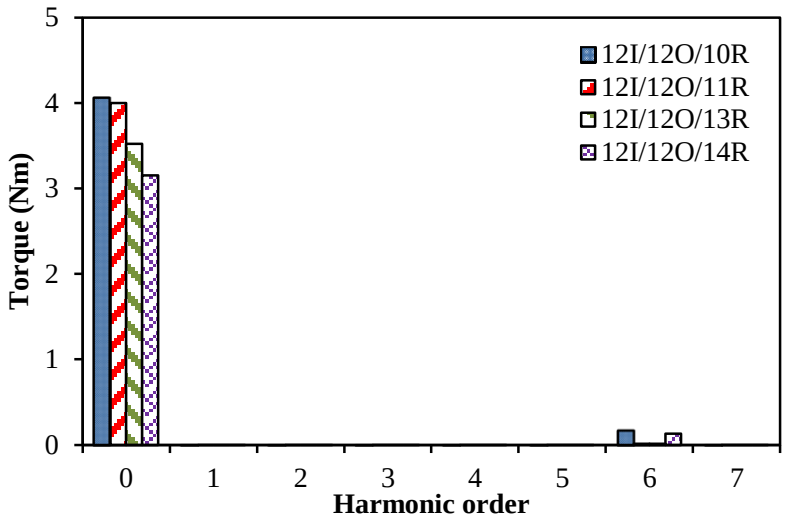

(b) Spectra

Fig. 6.34. Variation of torque with rotor position in PS-BFPMM-Is at rated currents, p_c=30W, I_d=0 control.

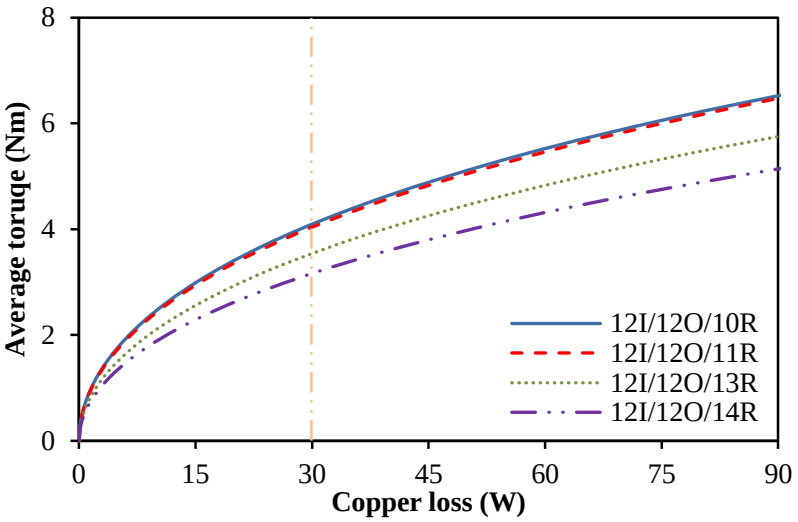

Fig. 6.35. Variation of average torque with copper loss in PS-BFPMM-Is, I_d=0 control.

As shown in Fig. 6.34(b), 12I/12O/10R PS-BFPMM-II exhibits the largest average torque among the PS-BFPMM-IIs with four main stator/rotor pole combinations. According to Table 6.7, the average torques of 12I/12O/10R, 12I/12O/11R, 12I/12O/13R and 12I/12O/14R PS-BFPMM-IIs under the rated copper loss are 4.06, 4.00, 3.52 and 3.15 Nm respectively. Then, Fig. 6.35 further indicates that 12I/12O/10R PS-BFPMM-II has the optimal torque capability over the whole copper loss range.

Fig. 6.36 compares the torque density and torque to PM volume of PS-BFPMM-IIs with four main stator/rotor pole combinations. Obviously, the largest torque density and highest ratio of torque to PM volume (PM utilization efficiency) are both observed in 12I/12O/10R

PS-BFPMM-II. Meanwhile, as the rotor pole number increased, the torque density and PM utilization efficiency are decreased.

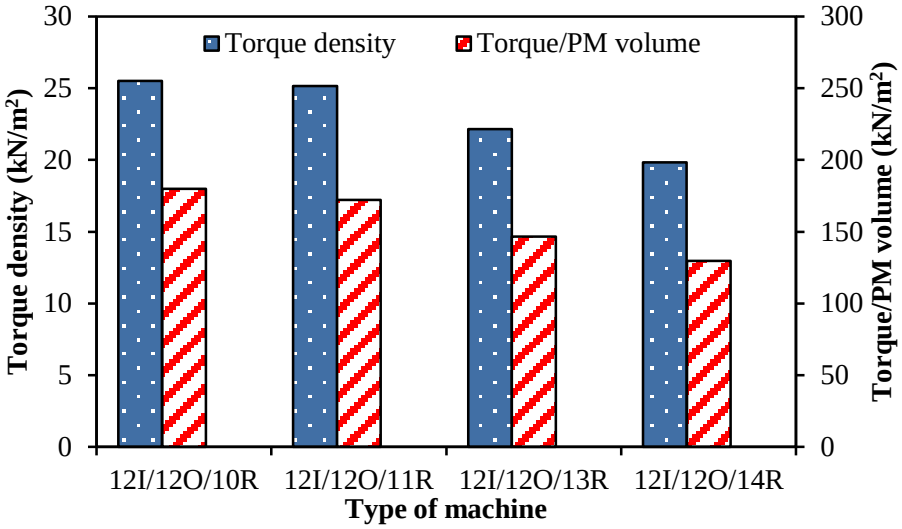

Fig. 6.36. Torque density and torque to PM volume, p_c=30W, I_d=0 control.

Table 6.7 Main electromagnetic performances of PS-BFPMM-IIs

Parameter	12O/12I/10R	12O/12I/11R	12O/12I/13R	12O/12I/14R
Fund. flux-linkage (mWb)	12.88	11.69	8.61	7.27
Fund. back-EMF (V)	5.39	5.38	4.68	4.26
Rated electric frequency (Hz)	66.7	73.3	86.7	93.3
Cogging torque (Nm)	0.107	0.010	0.008	0.130
Average torque (Nm)	4.06	4.00	3.52	3.15
Torque ripple (%)	9.0	1.3	1.2	8.3
Torque density (kN/m^2)	25.52	25.14	22.15	19.83
Torque/PM volume (kN/m^2)	180	172	147	130

6.6 Experimental Verification

Prototype machines of 12I/12O/10R PS-BFPMM-I and PS-BFPMM-II are made to validate the previous analyses, as shown in Fig. 6.37. To reduce the cost, two prototype machines are assembled by existing module rotor (10-pole), outer stator (12-pole) and two inner stators (12 PMs, surface mounted PM stator for PS-BFPMM-I and spoke type PM stator for PS-BFPMM-II). Hence, the parameters of prototype machines as shown in Table 6.8 are

different from the previous globally optimized parameters as shown in Table 6.1. Moreover, for easing the fabrication, 10-pole modular rotor is mechanically connected by the lamination bridges (T_{bri}=0.5mm) in the inner side, as shown in Fig. 6.37(b). Meanwhile, to help fixing the PMs in the inner stator of PS-BFPMM-II (spoke type PM stator), lamination bridges (0.5mm) are also added in both top and bottom edges of PMs, as shown in Fig. 6.37(d).

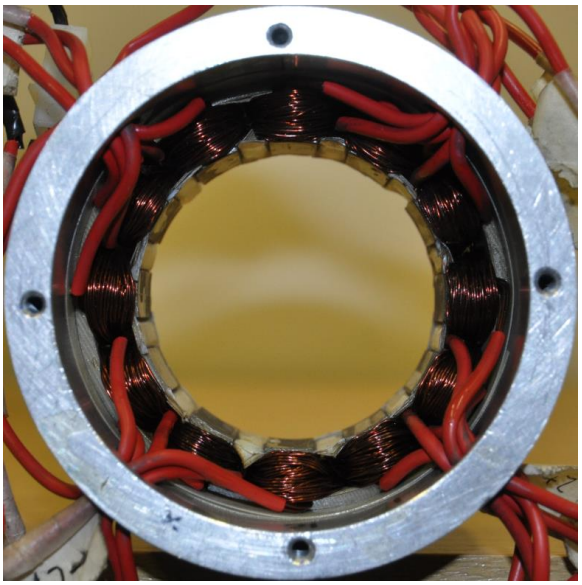

(a) 12-pole outer stator

(b) 10-pole rotor

(c) 12-pole inner stator of PS-BFPMM-I

(d) 12-pole inner stator of PS-BFPMM-II

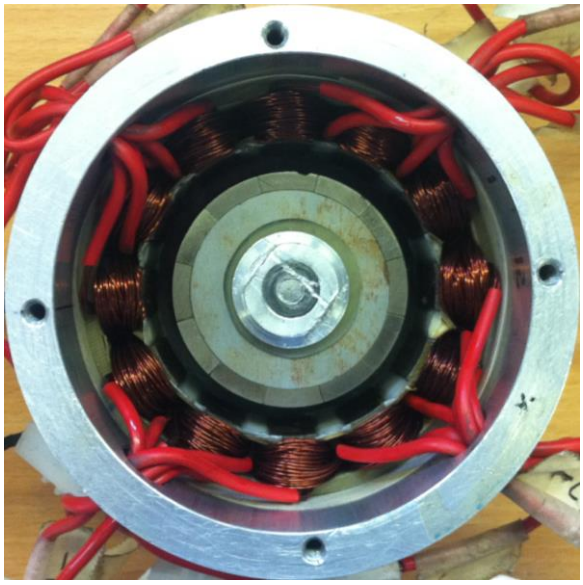

(e) Assembled stators of PS-BFPMM-I

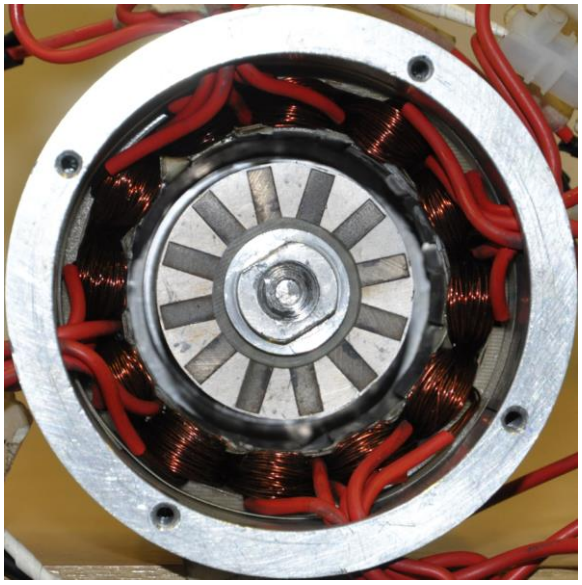

(f) Assembled stators of PS-BFPMM-II

Fig. 6.37. Prototypes of 12I/12O/10R PS-BFPMM-I and PS-BFPMM-II.

Table 6.8 Parameters of prototype machines

Parameter	**PS-I**	**PS-II**	**Parameter**	**PS-I**	**PS-II**
L_{ag} (mm)	0.5		T_{ostto} (mm)	1	
L_{aa} (mm)	25		T_{osy} (mm)	3	
R_{oso} (mm)	45		θ_{rop} (°)	18	
R_{ost} (mm)	31.75		θ_{rip} (°)	25.2	
R_{iso} (mm)	25.75		T_{rr} (mm)	5	
R_{ist} (mm)	10.4		θ_{PM} (°)	30	25.84 (5mm)
θ_{ostb} (°)	8.12		T_{PM} (mm)	4	14.35
θ_{ostt} (°)	4.94		T_{bri} (mm)	0.5	
T_{osttb}(mm)	3.0				

Fig. 6.38 shows the measured and predicted phase back-EMFs at rated speed (400rpm). It can be seen that the measured fundamental values are ~ 4% and 8% less than the predictions in PS-BFPMM-I and PS-BFPMM-II respectively due to the end-effect in 25mm stack length machines. Fig. 6.39 shows the measured and predicted open-circuit cogging torques of two machines. The measured peak to peak values are slightly larger than the FE predictions in both machines. This difference is acceptable when considering the measurement error and assembling tolerance. Fig. 6.40 shows the waveforms of static torque against with rotor positon at five different armature currents, i.e. 5A, 10A, 15A, 20A and 25A (I_{DC}=I_A=-2I_B=-

$2I_C$). Based on Fig. 6.40, the variation of the static torque at 90° rotor position with different currents is obtained and shown in Fig. 6.41. With injecting the DC current into the armature windings, more severe end effect will be caused by the armature reaction (higher saturation level) in 25mm stack length machines. The measured static torques are ~10% and 15% less than the predictions in PS-BFPMM-I and PS-BFPMM-II respectively and the difference will be gradually enlarged with the increased current. Furthermore, for PS-BFPMM-II with spoke-IPM stator, the large difference may also be caused by the manufacturing errors, such the thickness of lamination bridges at the top and bottom edges of PMs, residual gap between the PMs and lamination stator. Overall, the measured results match reasonably well with the FE predictions.

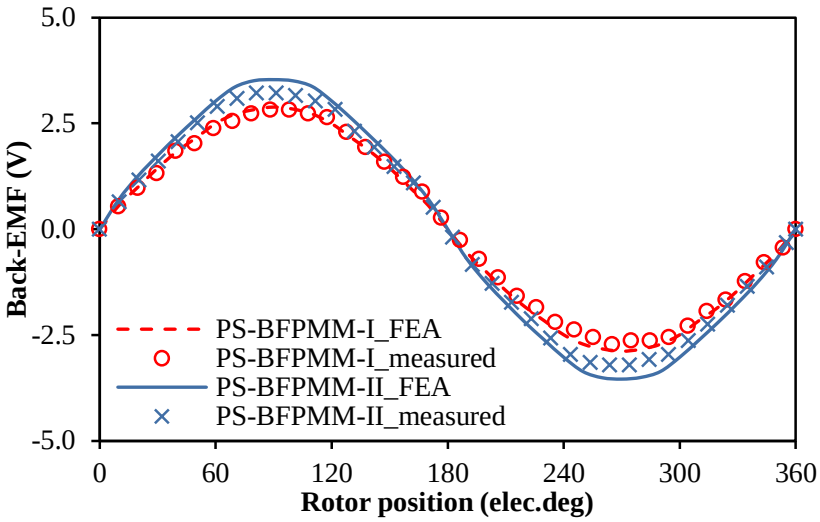

(a) Waveforms

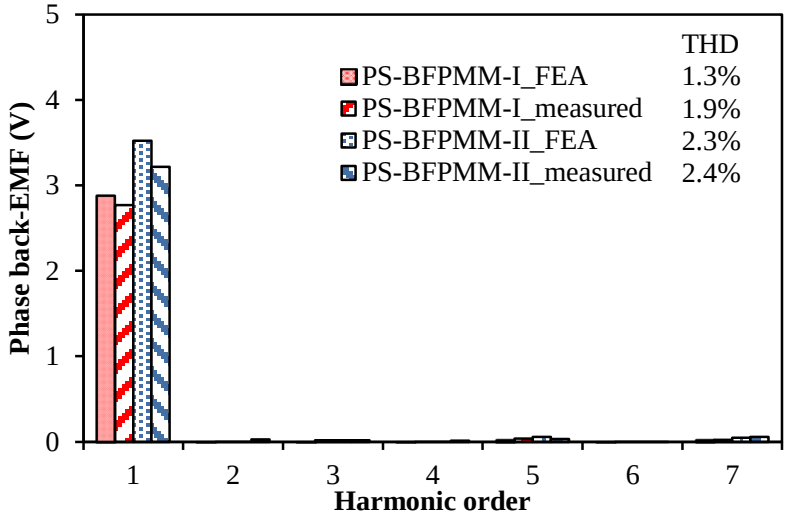

(b) Spectra

Fig. 6.38. Measured and FE predicted open-circuit phase back-EMFs at 400rpm.

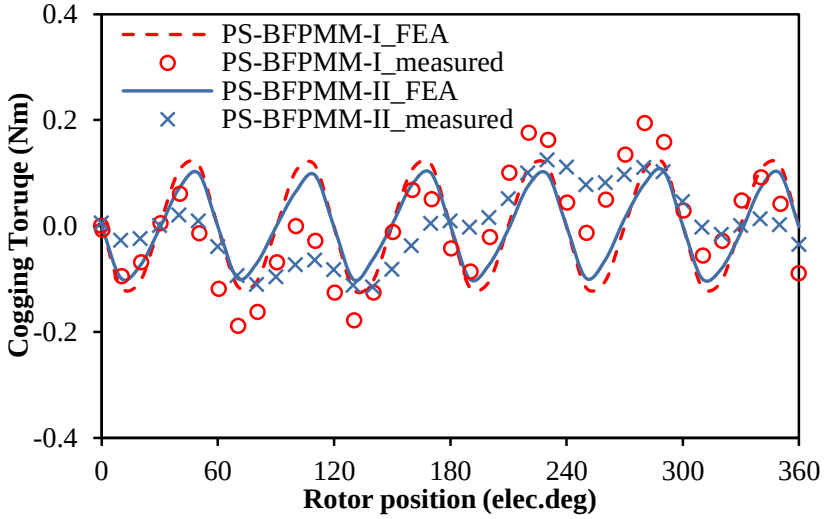

Fig. 6.39. Measured and FE predicted open-circuit cogging torques.

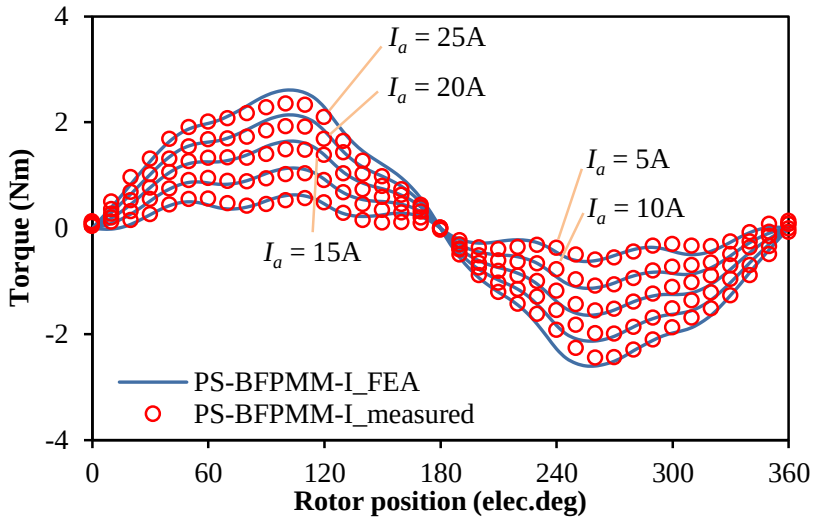

(a) 12I/12O/10R PS-BFPMM-I

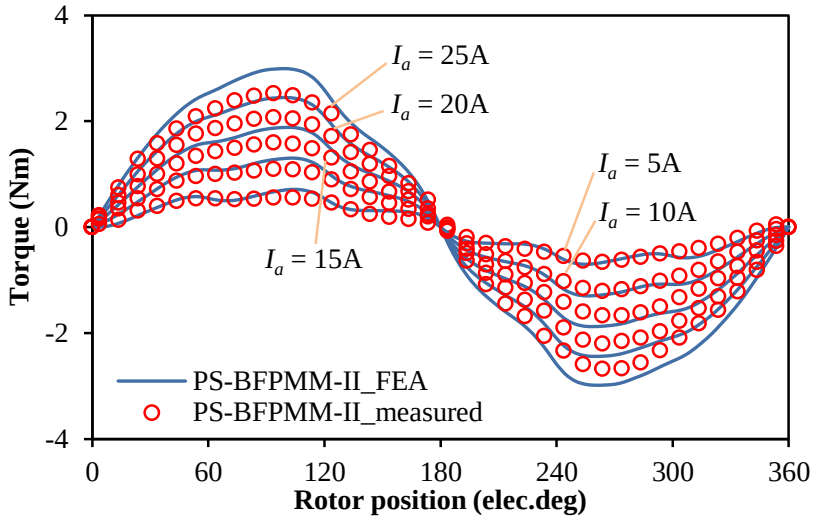

(b) 12I/12O/10R PS-BFPMM-II

Fig. 6.40. Measured and predicted static torque, $I_{DC}=I_A=-2I_B=-2I_C$.

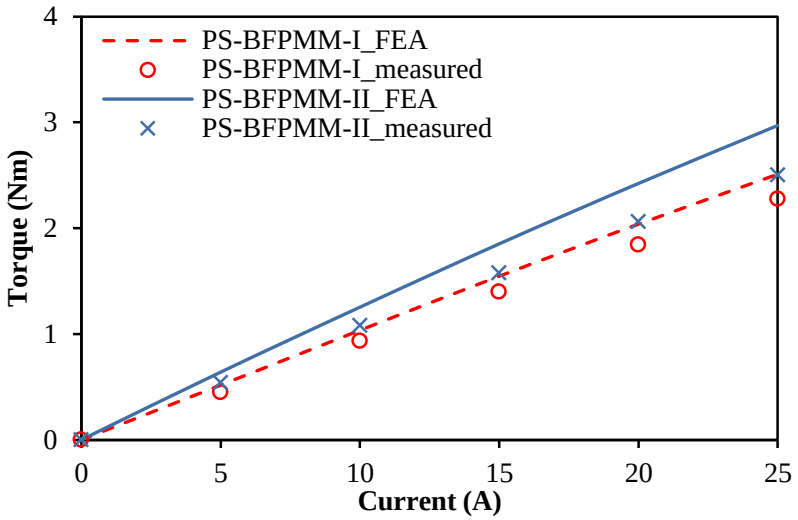

Fig. 6.41. Measured and predicted torque-current characteristics when rotor positon is 90°.

6.7 Summary

In this chapter, novel partitioned stator BFPMMs (PS-BFPMMs) with two PM stator configurations are proposed and compared with the original single stator BFPMMs (SS-BFPMMs). Similar to the original SS-BFPMMs, PS-BFPMMs also have bipolar phase flux-linkages and symmetrical phase back-EMFs due to the similar operational principle. The results show that PS-BFPMM-I and PS-BFPMM-II exhibit 120.3% and 119.8% higher phase back-EMFs as well as 120% and 145% larger average torque than SS-BFPMM-I and SS-BFPM-II respectively. Moreover, compared with PS-BFPMM-I, PS-BFPMM-II has 52.2% higher phase back-EMFs and 43% larger average torque but 17.4% lower PM utilization efficiency. Further, the reluctance torque is also negligible in PS-BFPMMs since the saliency ratio is quite close to 1, which is also consistent with the original SS-BFPMMs. In addition, for 12I/12O stator pole PS-BFPMMs, the optimal rotor pole numbers are 11 and 10 respectively in PS-BFPMM-I and PS-BFPMM-II since the highest torque densities and PM utilization efficiencies are achieved. Finally, the analyses have been validated by both FEA and measurement.

CHAPTER 7
COMPARATIVE STUDY OF PARTITIONED STATOR PM SYNCHRONOUS MACHINES WITH DIFFERERNT INNER/OUTER STATOR AND ROTOR POLE NUMBER COMBINATIONS

In the previous chapter, biased flux permanent magnet (PM) machines (BFPMMs) with partitioned stator (PS) configuration are proposed and investigated. Since PMs and armature windings are located in two separate (inner/outer) stators, the combinations of inner/outer stator pole numbers and the relative position of inner/outer stators are free to choose theoretically. Therefore, in this chapter, the influences of the combinations of inner/outer stator pole numbers and the relative position of inner/outer stators on electromagnetic performance of partitioned stator PM synchronous machines will be analysed and compared.

7.1 Introduction

Permanent magnet (PM) machines are popular in many applications due to high torque density and efficiency. Normally, PM machines can be classified into rotor PM machines and stator PM machines according to PM locations [ZHU07]. Compared with rotor PM machines, stator PM machines have many merits such as robust rotor structure, easy heat dissipation and low risk of demagnetization [ZHU05] [ZHU07] [HUA05] [CHE11c]. Hence, increasing attentions are paid to this type of machines in recent years.

However, compared with rotor PM machines, the stator space conflicts between PMs, armature windings and stator iron are more severe in the stator PM machines since the PMs are located in the stator [ZHU07] [ZHU08a]. Correspondingly, the limited stator space restricts the possibility of further enhancing the torque performance of stator PM machines. Reference [EVA15] proposes one concept of partitioned stator configuration to solve this conflict by fully utilising the inner space, in which the PMs and armature windings are separated into inner and outer stators respectively. Partitioned stator biased flux PM machines (PS-BFPMMs) [WU15] and partitioned stator switched flux PM machines (PS-SFPMMs) [EVA15] are two typical topologies of partitioned stator PM machines, which are evolved from the original single stator BFPMMs [WU15] and SFPMMs [HONG97] respectively by employing the partitioned stator configuration. Compared with two machine topologies, non-

overlapping armature windings and separate spoke type interior PM (spoke-IPM) stator are the common features while relative position between inner stator and outer stator is the only difference. The iron ribs are aligned with outer stator poles in PS-BFPMMs while the PMs are aligned with the outer stator pole in PS-SFPMMs. This difference causes the different polarities of coil flux-linkage in PS-BFPMMs (unipolar) and PS-SFPMMs (bipolar) [WU15] [EVA15]. However, symmetrical bipolar phase flux-linkage and phase back-EMF still can be obtained in both machines when the ratio of stator pole number (wound with armature windings) to the greatest common divisor of stator pole and rotor pole number is even.

Since the PMs and armature windings are separately located in the inner and outer stators, the ratio of inner/outer stator poles and the relative position of inner and outer stators will be free in the partitioned stator PM synchronous machines. However, the previous investigations only cover the inner/outer stator pole ratio equal to 1. Hence, in this chapter, the influences of the ratio of inner/outer stator poles and the relative position of inner and outer stators on electromagnetic performance of partitioned stator PM synchronous machines will be analysed and compared based on spoke-IPM stator configuration. Firstly, the machine topologies and conditions for symmetrical bipolar phase flux-linkage and phase back-EMF under different inner/outer stator pole ratios will be analysed. Secondly, based on the optimal rotor pole number, the electromagnetic performance of PS-BFPMMs will be compared with PS-SFPMMs with different inner/outer stator pole ratios (equal to 1, 1/2 and 2) under the same rated copper loss and the same machine size. Then, the influence of all pole wound windings and alternate pole wound windings on the electromagnetic performance of 6-inner/12-outer stator/11 rotor pole PS-SFPMM will be analysed and compared. Finally, several prototype machines are manufactured and measured to validate the analysis.

7.2 Machine Topologies and Conditions for Symmetrical Bipolar Phase Flux-Linkage

Based on the minimum 6-pole inner and outer stators, the machine topologies and conditions of symmetrical bipolar phase flux-linkage for partitioned stator PM synchronous machines with different inner/outer stator pole ratios (N_{is}/N_{os}) are illustrated and analysed in this section.

7.2.1 Inner/Outer Stator Pole Ratio N_{is}/N_{os} = 1

Partitioned stator biased flux PM machines (PS-BFPMMs) with N_{is}/N_{os}=1 is shown in Fig. 7.1(a). Obviously, the PMs and armature windings are located in two separated stators while

the rotor is modular. As mentioned in section 6.2.2, the conventional coil EMF vector method [ZHU10] can be used to determine the armature winding configuration of PS-BFPMMs. Hence, according to (6.1), the winding connection of 12-inner/12-outer stator/10 rotor pole (12I/12O/10R) PS-BFPMM is shown in Fig. 7.2.

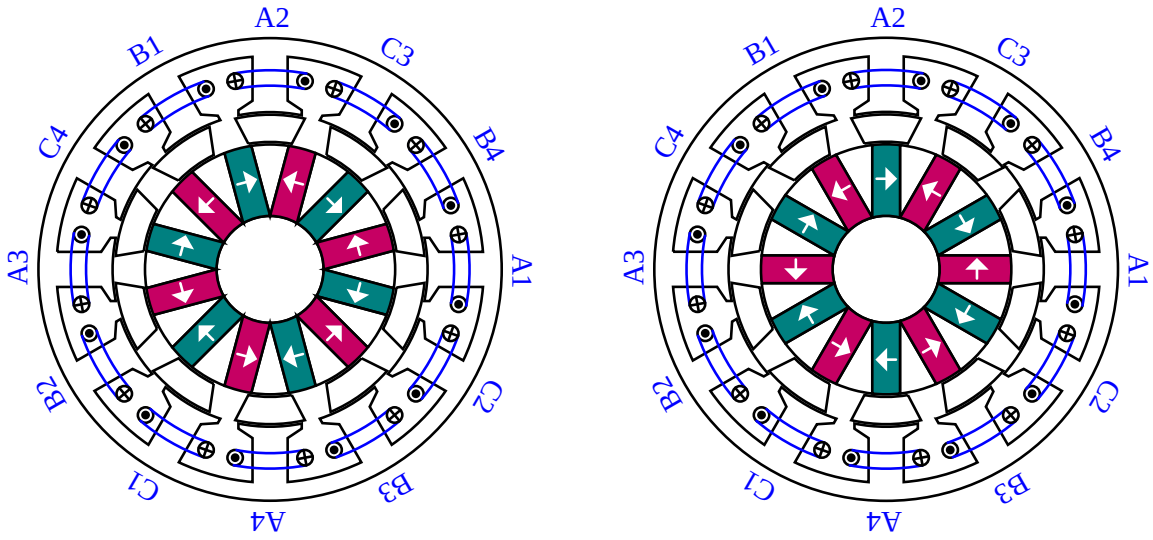

(a) 12I/12O/10R_PS-BFPMM (b) 12I/12O/10R_PS-SFPMM

Fig. 7.1. Topologies of 12I/12O/10R PS-BFPMM and PS-SFPMM.

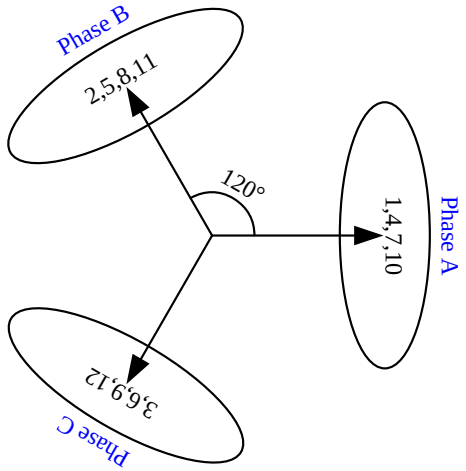

Fig. 7.2. Coil-EMF vectors for 12I/12O/10R PS-BFPMM and 12I/12O/10R PS-SFPMM.

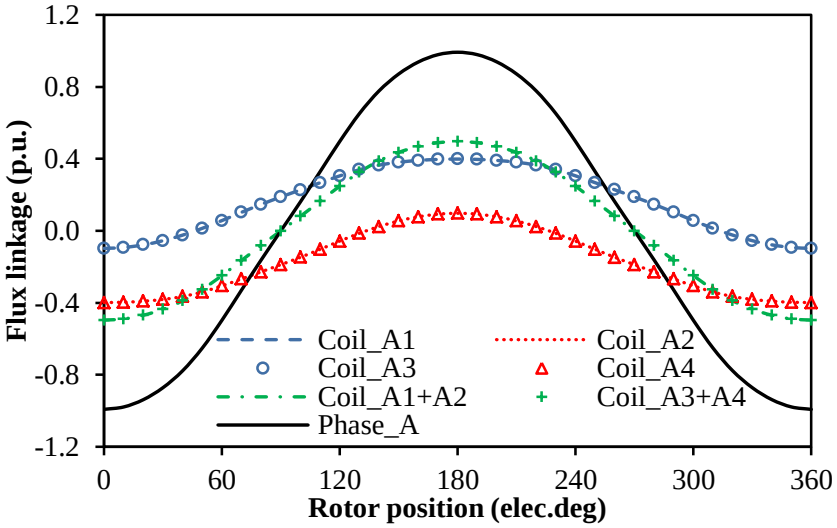

(a) Waveforms

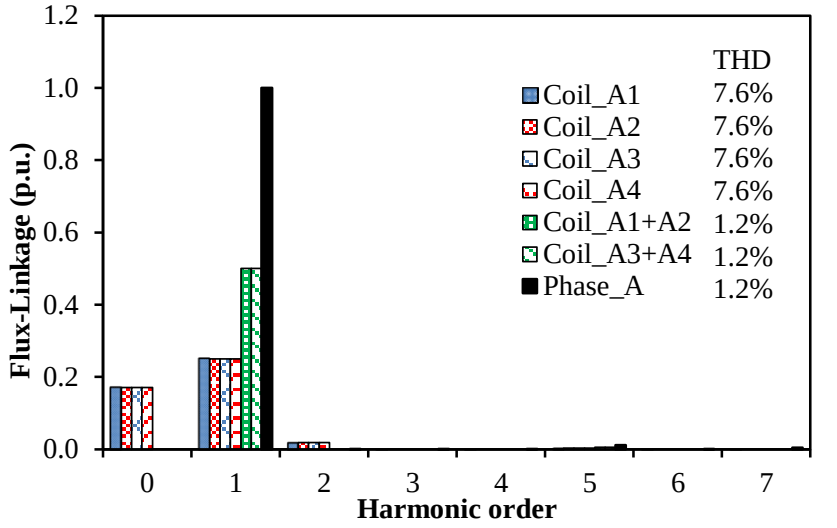

(b) Spectra

Fig. 7.3. Per unit open-circuit coil and phase flux-linkages of 12I/12O/10R PS-BFPMM.

Fig. 7.3 shows the open-circuit coil and phase flux-linkages of 12I/12O/10R PS-BFPMM in per unit value. It can be seen that the coil flux-linkage is nearly unipolar. However, the phase flux-linkage is bipolar and symmetrical since the even harmonics which cause the dc biased and asymmetry in each coil are completely cancelled in phase winding. As mentioned in section 6.2.4, to obtain symmetrical bipolar phase flux-linkage in PS-BFPMMs, two conditions should be satisfied. Firstly, the number of coils per phase must be even. Secondly, the pairs of coils belong to the same phase must have 180 electrical degrees phase shifting (opposite polarities). To achieve the two conditions, the stator and rotor pole combinations of PS-BFPMMs should be satisfied with (6.2) [CHE08] [SHI15]. Further, when considering the different inner/outer stator pole ratio N_{is}/N_{os}, equation (6.2) can be changed as (7.1).

$$\frac{MIN(N_{is}, N_{os})}{GCD(\,MIN(N_{is}, N_{os})\,, N_r)} = Even \tag{7.1}$$

where N_r is pole number of rotor, *GCD* means the greatest common divisor.

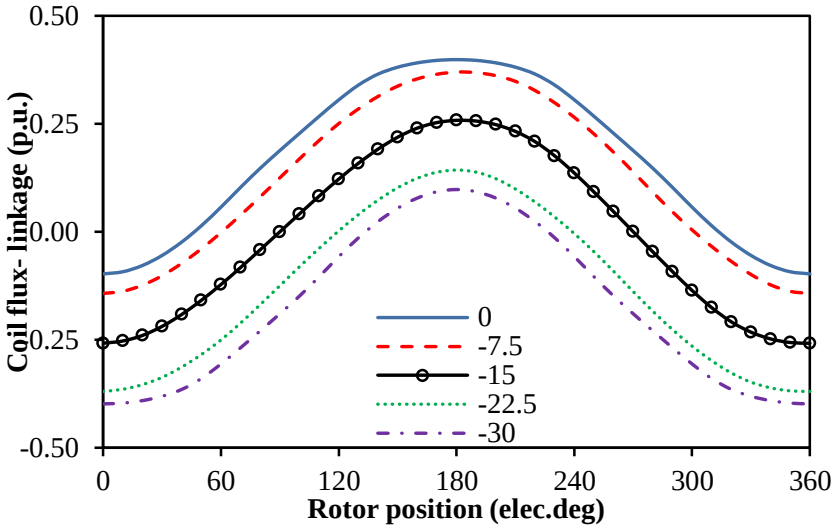

(a) Waveforms

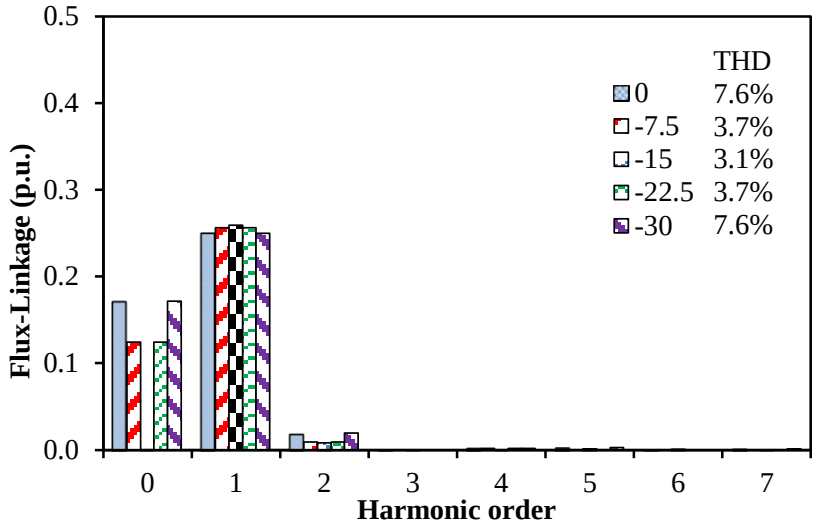

(b) Spectra

Fig. 7.4. Per unit open-circuit flux-linkage of coil A1 against with different rotation degree between inner and outer stators.

Since the PMs and armature windings of PS-BFPMM are located in separate inner and outer stators, the inner and outer stators are independent and the relative position of two stators is free and can be changed. Fig. 7.4 shows the waveforms of per unit open-circuit flux-linkage of coil A1 against with different relative position between inner and outer stators. The direction of rotation is clockwise which is shown as "–" in Fig. 7.4. Meanwhile, 0°, -7.5°, -15°, -22.5° and -30° mean that the inner stator of PS-BFPMM rotates by 0, 1/4, 1/2, 3/4 and

1 inner stator pole pitch respectively. It can be seen that the dc biased value of coil flux-linkage will be reduced to 0 and then increased again when the inner stator rotates from the original position to one inner stator pole pitch. In other word, bipolar coil flux-linkage will be obtained while the inner stator rotates half inner stator pole pitch. The corresponding machine topologies are shown in Fig. 7.1(b). Actually, this machine is named as partitioned stator switched flux PM machine (PS-SFPMM), which is proposed in [EVA15]. Further, PS-SFPMMs (N_{is}/N_{os}=1) exhibits higher fundamental coil flux-linkage than PS-BFPMMs (N_{is}/N_{os}=1) when the machine topologies are the same except the relative positons of inner and outer stator are different, as shown in Fig. 7.4.

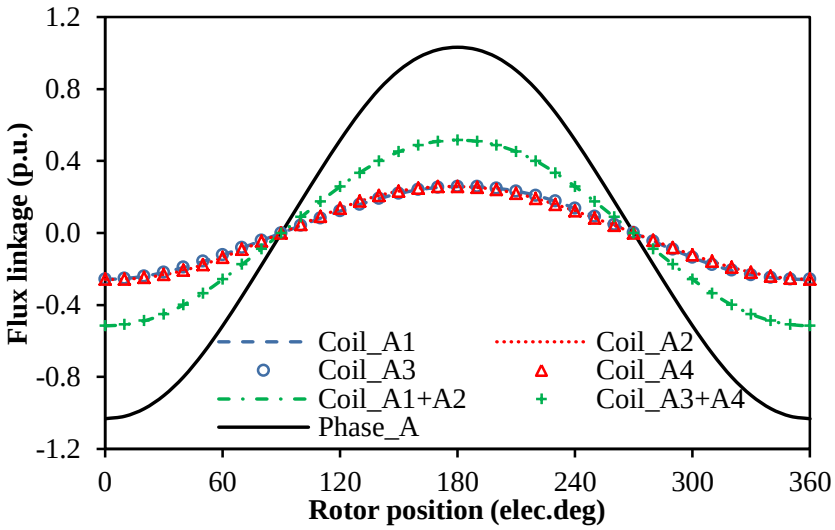

(a) Waveforms

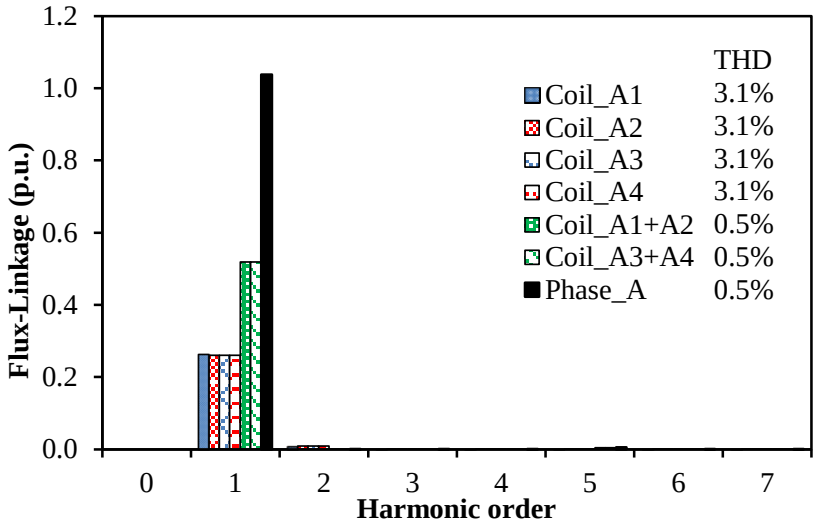

(b) Spectra

Fig. 7.5. Per unit open-circuit coil and phase flux-linkages of 12I/12O/10R PS-SFPMM.

Similar to PS-BFPMMs, the conventional coil EMF vector method and (6.1) can also be used to determine the armature winding configuration of PS-SFPMMs with N_{is}/N_{os}=1 [ZHU10]. Fig. 7.5 shows the open-circuit coil and phase flux-linkages of 12I/12O/10R PS-SFPMM in per unit value. The base value is selected as the magnitude of fundamental phase flux-linkage of 12I/12O/10R PS-BFPMM. Obviously, the coil flux-linkage of PS-SFPMM with N_{is}/N_{os}=1 is bipolar but slightly asymmetric in half cycle due to the even harmonics. To obtain the symmetrical bipolar phase flux-linkage, the conditions for PS-SFPMMs with N_{is}/N_{os}=1 are consistent with those for PS-BFPMMs, in which the (inner/outer) stator and rotor pole combinations should satisfy (7.1). By way of example, symmetrical bipolar phase flux-linkage is obtained in 12I/12O/10R PS-SFPMM as shown in Fig. 7.5 since the even harmonics are completely cancelled.

As a conclusion, for partitioned stator PM synchronous machines with N_{is}/N_{os}=1, symmetrical bipolar phase flux-linkage will be obtained when the (inner/outer) stator and rotor pole combinations satisfies (7.1). In addition, it should be noted that changing the relative position of inner and outer stators will mainly influence the even harmonics (including dc biased value) of coil flux-linkage and magnitude of fundamental coil flux-linkage.

7.2.2 Inner/Outer Stator Pole Ratio N_{is}/N_{os} = 1/2

The conventional coil-EMF vector method which is used to determine the winding configuration is also applicable to PS-SFPMMs with N_{is}/N_{os}=1/2. Fig. 7.6 shows the machine topology and coil-EMF vectors of 6I/12O/11R PS-SFPMM with N_{is}/N_{os}=1/2. As shown in Fig. 7.6(a), half of outer stator poles are aligned with PMs while the rest half of outer stator poles are aligned with iron ribs. According to the analysis in section 7.2.1, for 6I/12O PS-SFPMMs with N_{is}/N_{os}=1/2 shown in Fig. 7.6(a), bipolar coil flux-linkage could be observed when the coil-wound outer stator pole is aligned with PMs (such as coils A1 and A3), whilst unipolar coil flux-linkage would be found when the coil-wound outer stator pole is aligned with iron ribs (such as coils A2 and A4). This conjecture is evidenced by the waveforms of coil flux-linkage shown in Fig. 7.7, in which the flux linkages of coils A1 and A3 are bipolar while those of coils A2 and A4 are unipolar.

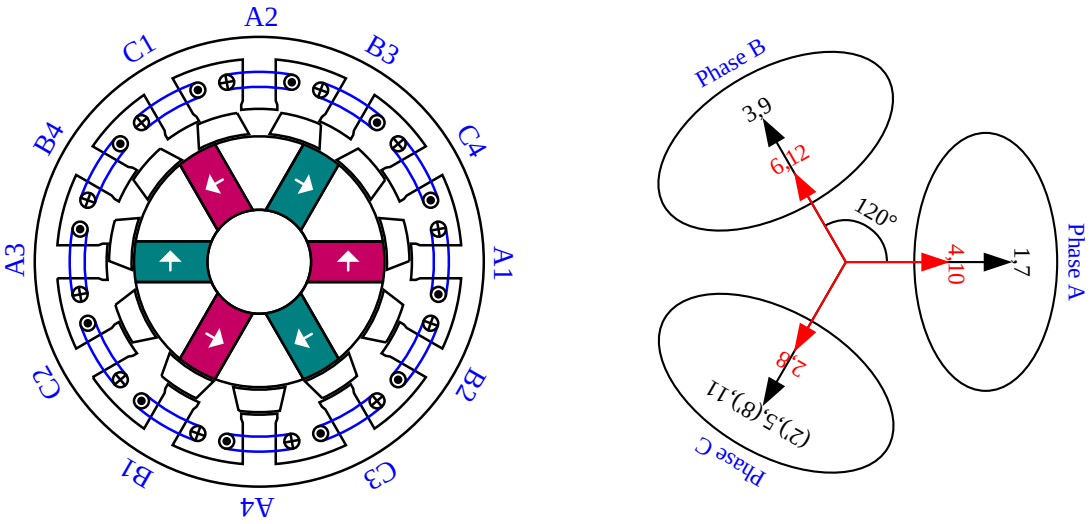

(a) Machine topology (b) Coil-EMF vectors

Fig. 7.6. Machine topology and coil-EMF vector of 6I/12O/11R PS-SFPMM.

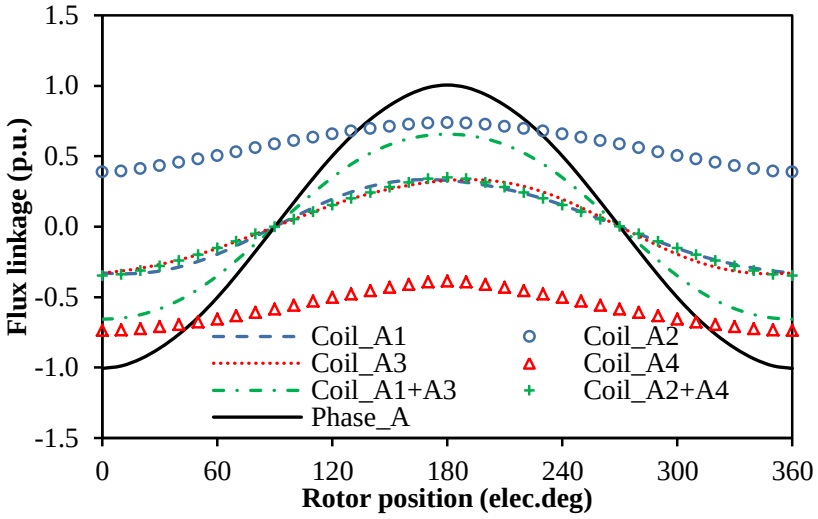

(a) Waveforms

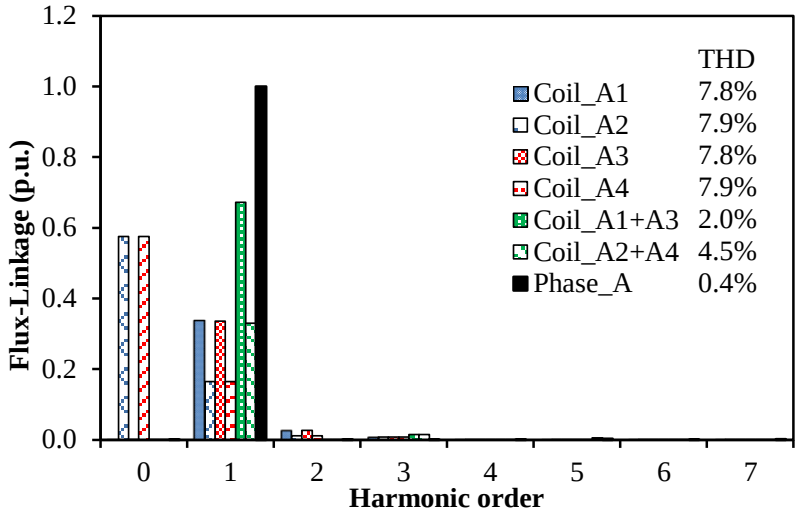

(b) Spectra

Fig. 7.7. Per unit open-circuit coil and phase flux-linkages of 6I/12O/11R PS-SFPMM.

According to the analysis shown in section 7.2.1, symmetrical bipolar phase flux-linkage can be obtained in both PS-BFPMMs (unipolar coil flux-linkage) and PS-SFPMMs (bipolar coil flux-linkage) with N_{is}/N_{os}=1 when the inner/outer stator and rotor pole combinations satisfy (7.1). Therefore, to obtain symmetrical bipolar phase flux-linkage in 6I/12O PS-SFPMM with N_{is}/N_{os}=1/2, three conditions should be satisfied. Firstly, for the coils belong to the same phase, the number of coils which have unipolar flux-linkages must be even (such as coils A2 and A4, one pair of coils with unipolar flux-linkage), while the number of coils which have bipolar flux-linkages also must be even (such as coils A1 and A3, one pair of coils with unipolar flux-linkage). Secondly, the pairs of coils belong to the same phase must have 180 electrical degree phase shifting (opposite polarities). Thirdly, the phase angles should be same for the resultant flux-linkages from unipolar ones and bipolar ones. To achieve three conditions, the inner/outer stator and rotor pole combinations should be satisfied with (7.1), which are same as those in PS-BFPMMs and PS-SFPMMs with N_{is}/N_{os}=1. By way of example, for 6I/12O/11R PS-SFPMM under investigation, symmetrical bipolar phase flux-linkage is obtained as shown in Fig. 7.7, in which the resultant flux-linkages from unipolar ones and bipolar ones are both symmetrical and bipolar as well as having same phase angles.

Moreover, as shown in Fig. 7.7, since the bipolar coil flux-linkage (coils A1 and A3) exhibits higher magnitude of fundamental wave than unipolar coil flux-linkage (coils A2 and A4), alternate pole wound winding configuration can be employed to enhance the torque performance of 6I/12O PS-SFPMMs. For example, the winding configuration of 6I/12O/11R PS-SFPMM shown in Fig. 7.6(b) can be divided into two sets as shown in Fig. 7.8 and the corresponding machine topologies are shown in Fig. 7.9. Meanwhile, the conditions for bipolar symmetrical phase flux-linkage of 6I/12O alternate pole wound PS-SFPMMs are consistent with 6I/12O all pole wound PS-SFPMMs.

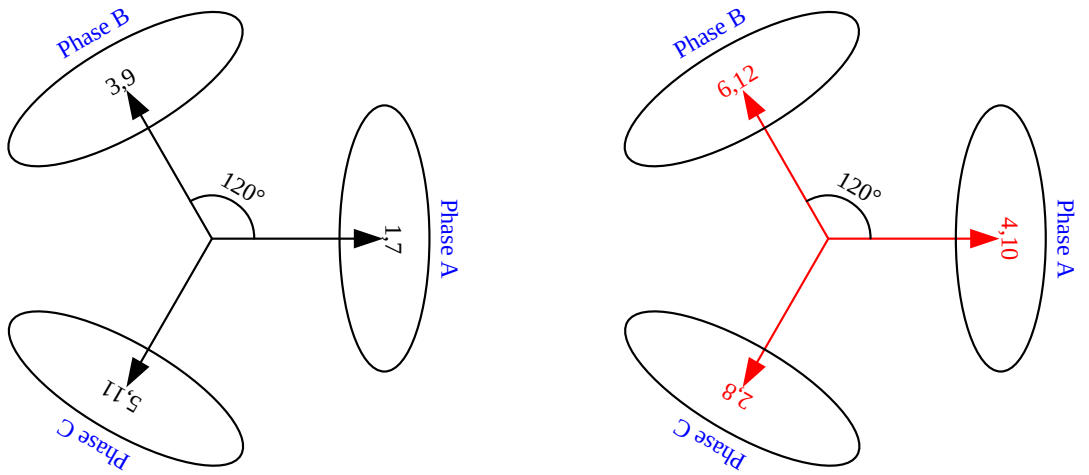

(a) 6I/12O/11R_PS-SFPMM-APW-I (b) 6I/12O/11R_PS-SFPMM-APW-II

Fig. 7.8. Coil-EMF vectors of two alternate pole wound 6I/12O/11R PS-SFPMMs.

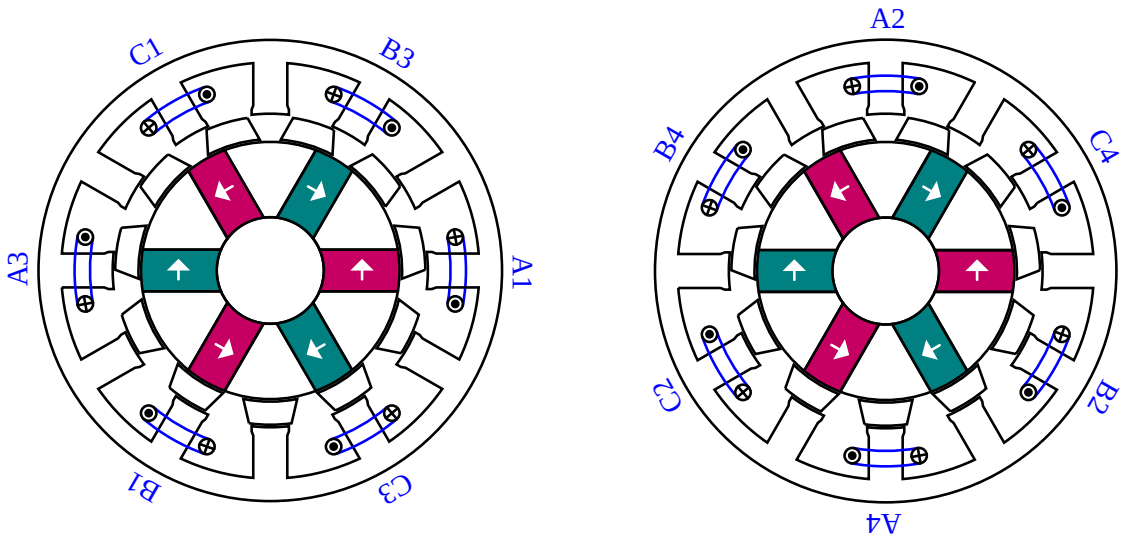

(a) 6I/12O/11R_PS-SFPMM-APW-I (b) 6I/12O/11R_PS-SFPMM-APW-II

Fig. 7.9. Machine topologies of two alternate pole wound 6I/12O/11R PS-SFPMM.

Similar to PS-BFPMMs and PS-SFPMMs with N_{is}/N_{os}=1, the relative position of two stators in 6I/12O PS-SFPMMs with N_{is}/N_{os}=1/2 are also free and can be changed. When the inner stator of 6I/12O PS-SFPMM with N_{is}/N_{os}=1/2 rotates half outer stator pole pitch in clockwise direction, one typical machine topology is proposed and shown in Fig. 7.10(a). The coil-EMF vectors of new 6I/12O/11R PS-SFPMMs are shown in Fig. 7.10(b), which is consistent with the original 6I/12O/11R PS-SFPMMs. Since all coil-wound outer stator poles are aligned with iron ribs, the coil flux-linkages in this new machine are unipolar, as shown in Fig. 7.11. According to the analysis shown in section 7.2.1, the conditions for symmetrical bipolar phase flux-linkage is kept consistent when changing the relative position of inner and outer stator. Therefore, when the inner/outer stator and rotor pole combinations satisfy (7.1),

symmetrical bipolar phase flux-linkage can be obtained in new 6I/12O PS-SFPMMs with N_{is}/N_{os}=1/2. By way of example, for new 6I/12O/11R PS-SFPMM under investigation, the phase flux-linkage is symmetrical and bipolar as shown in Fig. 7.11. In addition, since the base value corresponding to Fig. 7.11 is selected as the magnitude of fundamental phase flux-linkage of the original 6I/12O/11R PS-SFPMM, new 6I/12O/11R PS-SFPMM exhibits lower fundamental phase flux-linkage than the original 6I/12O/11R PS-SFPMM.

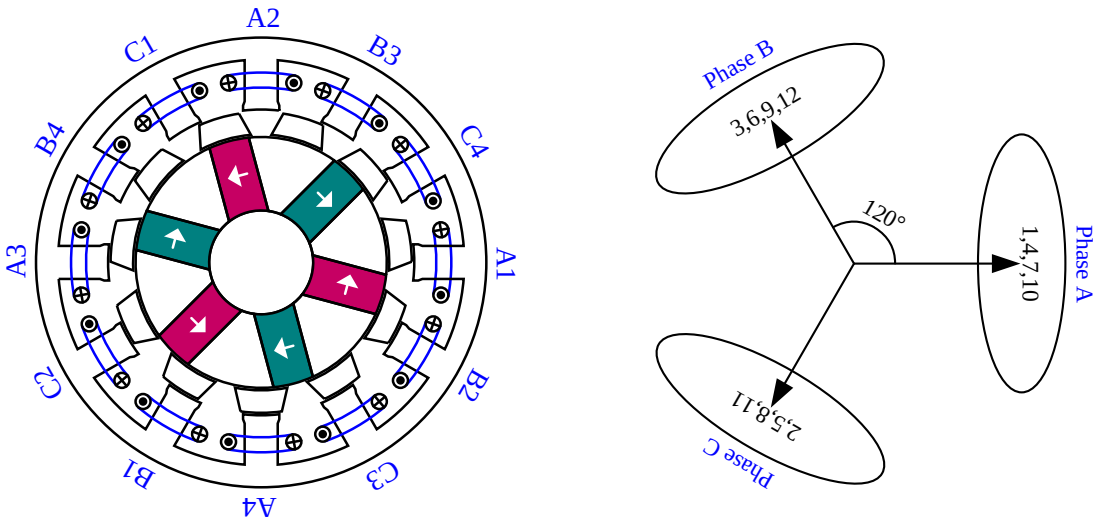

(a) Machine topology (b) Coil-EMF vectors

Fig. 7.10. Machine topology and coil-EMF vector of new 6I/12O/11R PS-SFPMM.

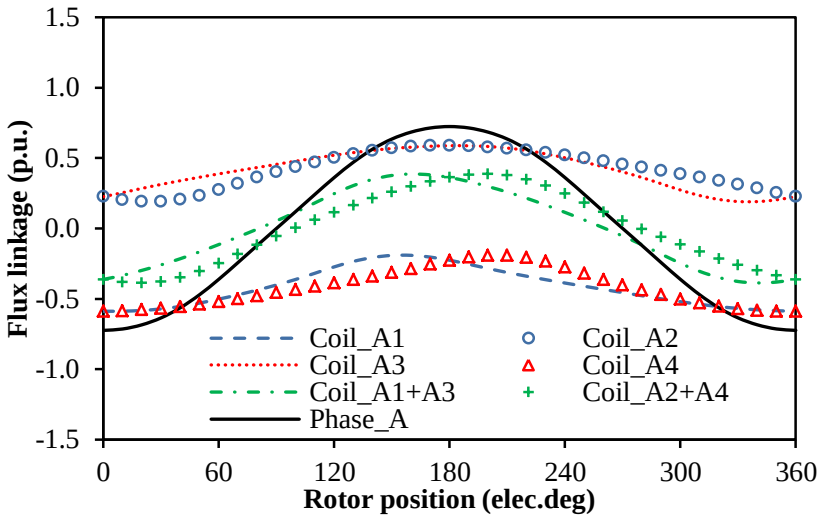

(a) Waveforms

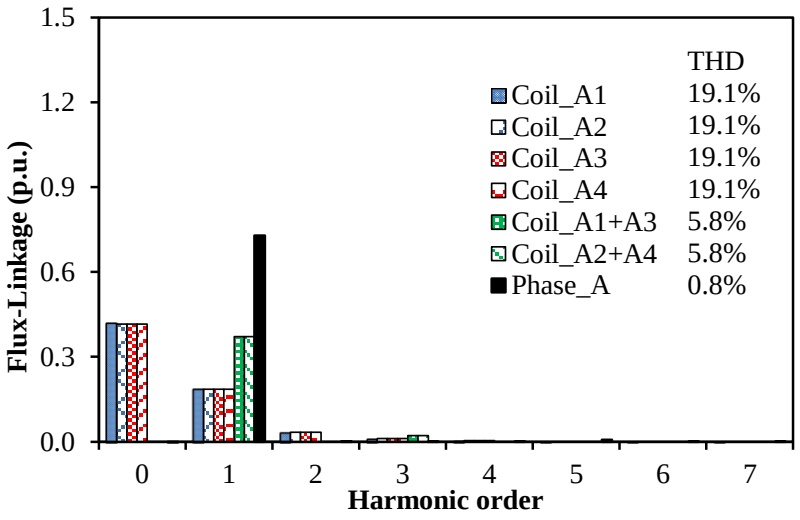

(b) Spectra

Fig. 7.11. Per unit open circuit coil and phase flux-linkage of 6I/12O/11R PS-SFPMM.

Overall, for partitioned stator PM synchronous machines with N_{is}/N_{os}=1/2, symmetrical bipolar phase flux-linkage will be obtained when the (inner/outer) stator and rotor pole combinations satisfy (7.1). Moreover, the relative position of inner and outer stators mainly influence on the even harmonics (including dc biased value) of coil flux-linkage and magnitude of fundamental coil flux-linkage.

7.2.3 Inner/Outer Stator Pole Ratio N_{is}/N_{os} = 2

Fig. 7.12 shows the machine topology and coil-EMF vectors of 12I/6O/11R PS-SFPMM with N_{is}/N_{os}=2. Similar to PS-BFPMMs and PS-SFPMMs with N_{is}/N_{os}=1, the conventional coil EMF vector method is also applicable to PS-SFPMM with N_{is}/N_{os}=2. Fig. 7.13 shows the open-circuit coil and phase flux-linkages of 12I/6O/11R PS-SFPMM in per unit value. It can be seen that the coil flux-linkage is nearly bipolar but slightly asymmetric in half cycle due to the even harmonics. However, by connecting the coils belong to same phase with 180 electrical degrees phase shifting, the phase flux-linkage is symmetrical and bipolar since the even harmonics in single coil are completely cancelled in phase winding, as shown in Fig. 7.12 and Fig. 7.13. Hence, the conditions for symmetrical bipolar phase flux-linkage of PS-SFPMMs with N_{is}/N_{os}=2 are consistent with those of PS-BFPMMs and PS-SFPMMs with N_{is}/N_{os}=1, in which the number of coils per phase must be even and the pairs of coils belong to the same phase must have 180 electrical degree phase shifting (opposite polarities). Therefore, when the inner/outer stator and rotor pole combinations satisfy (7.1), symmetrical bipolar phase flux-linkage can be obtained in PS-SFPMMs with N_{is}/N_{os}=2.

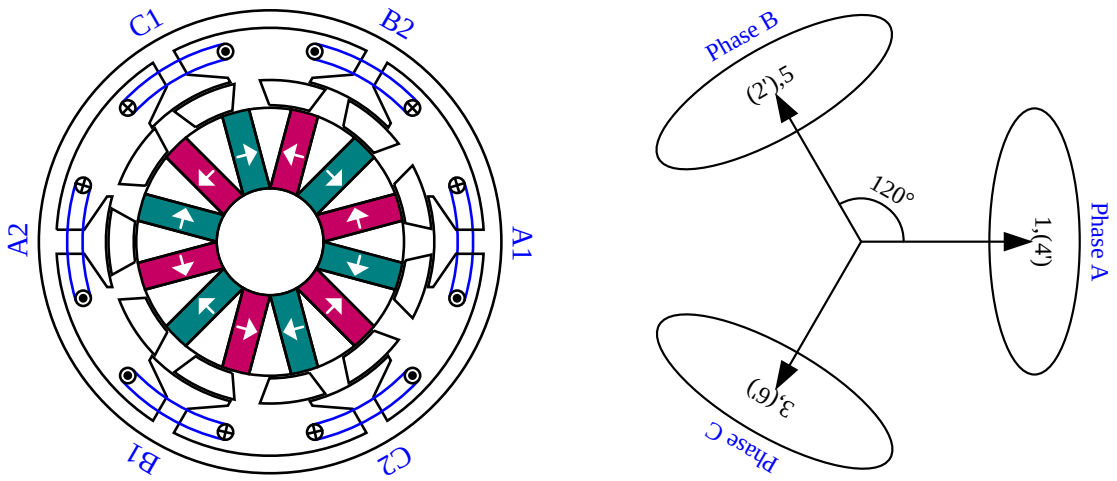

(a) Machine topology (b) Coil-EMF vectors

Fig. 7.12. Machine topology and coil-EMF vector of 12I/6O/11R PS-SFPMM.

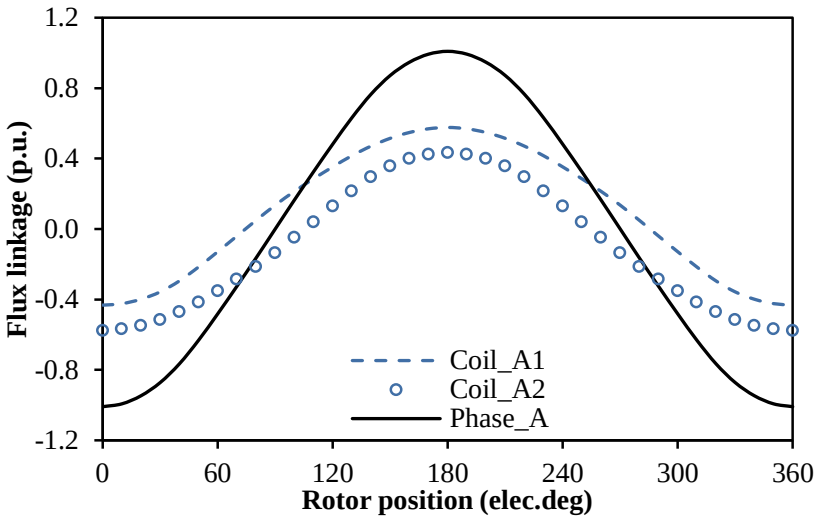

(a) Waveforms

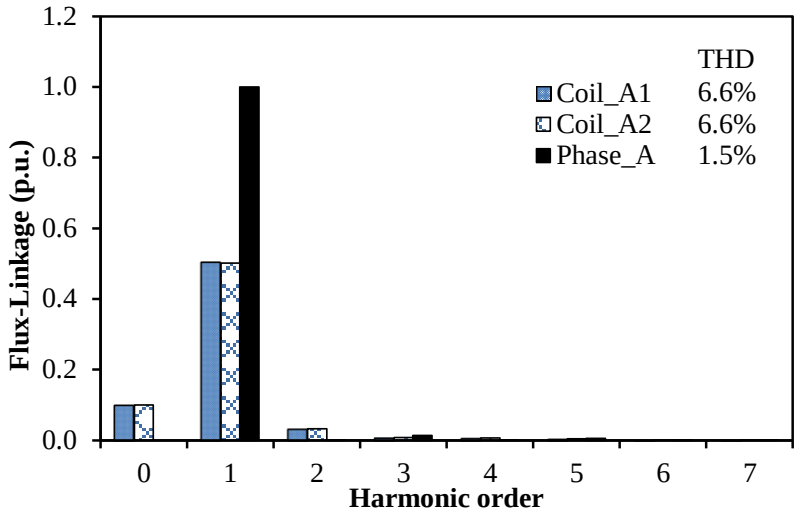

(b) Spectra

Fig. 7.13. Per unit open circuit coil and phase flux-linkage of 12I/6O/11R PS-SFPMM.

Similar to PS-BFPMMs and PS-SFPMMs with N_{is}/N_{os}=1, the relative position of two stators in PS-SFPMMs with N_{is}/N_{os}=2 are also free and can be changed. When the inner stator of 12I/6O PS-SFPMM with N_{is}/N_{os}=2 rotates half inner stator pole pitch in clockwise direction, one typical machine topology is proposed and shown in Fig. 7.14(a). The coil-EMF vectors of new 12I/6O/11R PS-SFPMM are shown in Fig. 7.14(b), which is consistent with the original 12I/6O/11R PS-SFPMM. According to the analysis shown in section 7.2.1, the conditions for symmetrical bipolar phase flux-linkage are kept consistent when changing the relative position of inner and outer stator. Therefore, when the inner/outer stator and rotor pole combinations satisfy (7.1), symmetrical bipolar phase flux-linkage can be obtained in new PS-SFPMMs with N_{is}/N_{os}=2. By way of example, for new 12I/6O/11R PS-SFPMM under investigation, the phase flux-linkage is symmetrical and bipolar as shown in Fig. 7.15. Moreover, since the base value corresponding to Fig. 7.15 is selected as the magnitude of fundamental phase flux-linkage of the original 12I/6O/11R PS-SFPMM, new 12I/6O/11R PS-SFPMM exhibits lower fundamental phase flux-linkage than the original 12I/6O/11R PS-SFPMM.

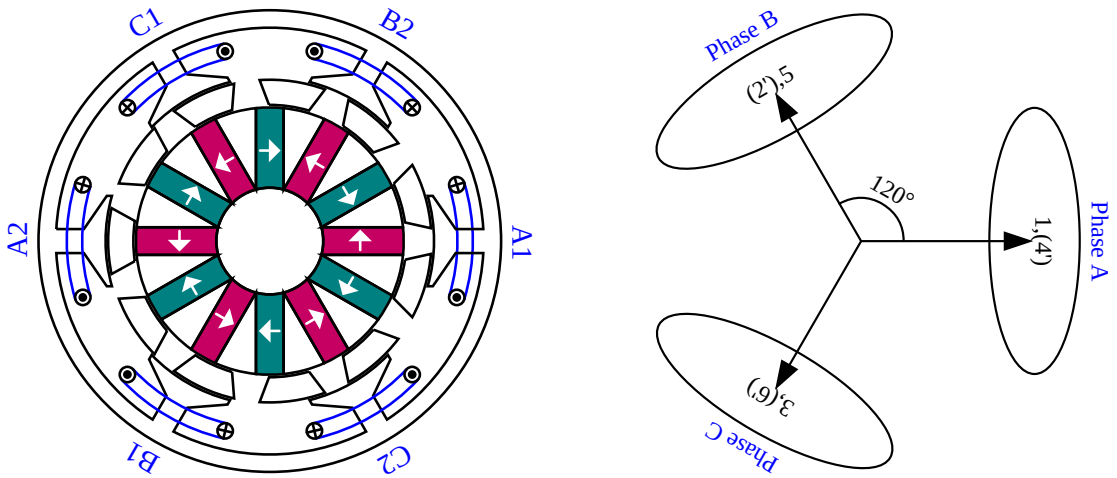

(a) Machine topology (b) Coil-EMF vectors

Fig. 7.14. Machine topology and coil-EMF vector of new 12I/6O/11R PS-SFPMM.

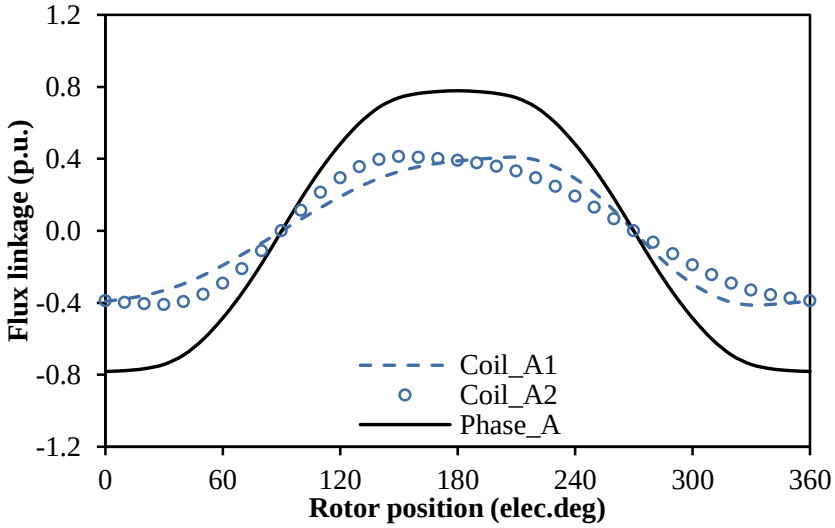

(a) Waveforms

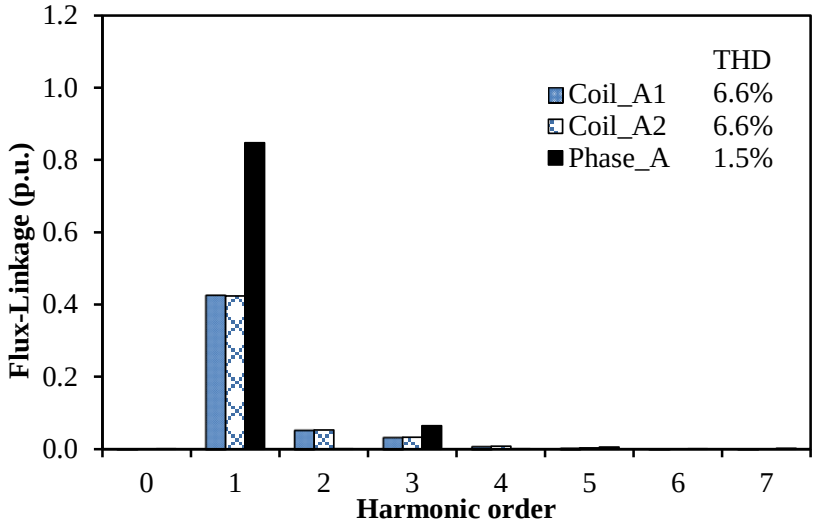

(b) Spectra

Fig. 7.15. Per unit open circuit coil and phase flux-linkage of new 12I/6O/11R PS-SFPMM.

As a conclusion, for partitioned stator PM synchronous machines with N_{is}/N_{os}=2, symmetrical bipolar phase flux-linkage will be obtained when the inner/outer stator and rotor pole combinations satisfy (7.1). In addition, it also should be noted that the relative position of inner and outer stators mainly influence the even harmonics (including dc biased value) of coil flux-linkage and magnitude of fundamental coil flux-linkage.

7.2.4 Conclusions for Symmetrical Bipolar Phase Flux-Linkage of Partitioned Stator PM Synchronous Machines

For partitioned stator PM synchronous machines in which the inner- and outer-stator poles are multiples of 6, the conditions for symmetrical bipolar phase flux-linkage under different inner/outer stator pole ratio N_{is}/N_{os} and relative position of inner and outer stators are

consistent according to the analyses shown in above and section 7.8 of Appendix. The coils per phase must be even and the pair of coils belong to the same phase should have 180 electrical degrees phase shifting (opposite polarities). In other word, to obtain the symmetrical bipolar phase flux-linkage, the inner/outer stator and rotor pole combinations must satisfy (7.1).

$$\frac{MIN(N_{is}, N_{os})}{GCD(\,MIN(N_{is}, N_{os})\,, N_r)} = Even \tag{7.1}$$

7.3 Performance Comparison between PS-BFPMMs and PS-SFPMMs

In this section, the electromagnetic performances of PS-BFPMMs and PS-SFPMMs with different inner/outer stator pole ratios (N_{is}/N_{os} equal to 1, 1/2 and 2) will be compared based on the optimal rotor pole numbers and all pole wound winding configuration.

7.3.1 Feasible Inner/Outer Stator and Rotor Pole Combinations for Different N_{is}/N_{os}

Similar to conventional BFPMMs and SFPMMs, the choice of rotor pole number is also flexible in PS-BFPMMs and PS-SFPMMs, which can be any integers except the phase number and its multiples. Further, for PS-BFPMMs and PS-SFPMMs with 12-pole (inner or outer) stator under investigation, the most feasible rotor pole numbers could be 10, 11, 13 and 14.

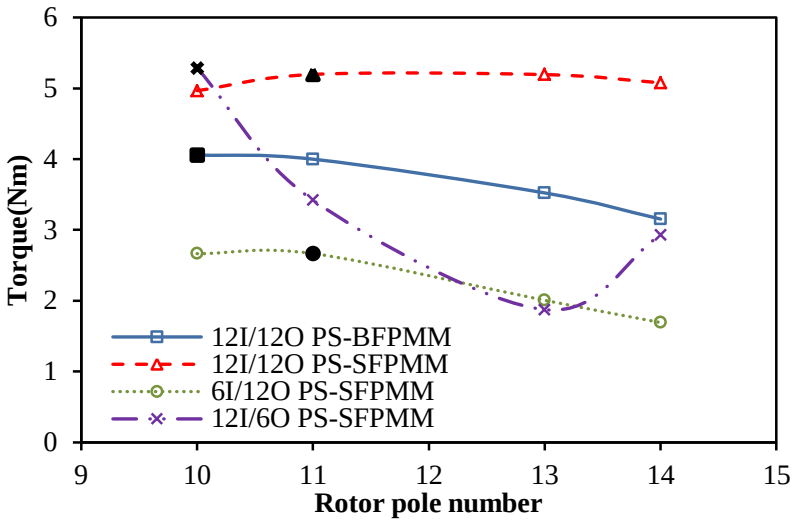

Fig. 7.16. Variation of average torque with rotor pole number in PS-BFPMMs and PS-SFPMMs with different inner/outer stator pole ratios, p_c = 30W.

Fig. 7.16 shows the torque variations of PS-BFPMMs and PS-SFPMMs with main rotor pole numbers under the rated 30W copper loss. It can be found that the optimal rotor pole numbers for 12I/12O PS-BFPMM, 12I/12O PS-SFPMM, 6I/12O PS-SFPMM and 12I/6O

PS-SFPMM are 10, 11, 11, and 10 respectively since the maximum average torques are achieved for each machine. Based on the respective optimal rotor pole numbers, the electromagnetic performance of PS-BFPMMs will be compared with PS-SFPMMs with different N_{is}/N_{os} (1/2 and 2) in the following sections.

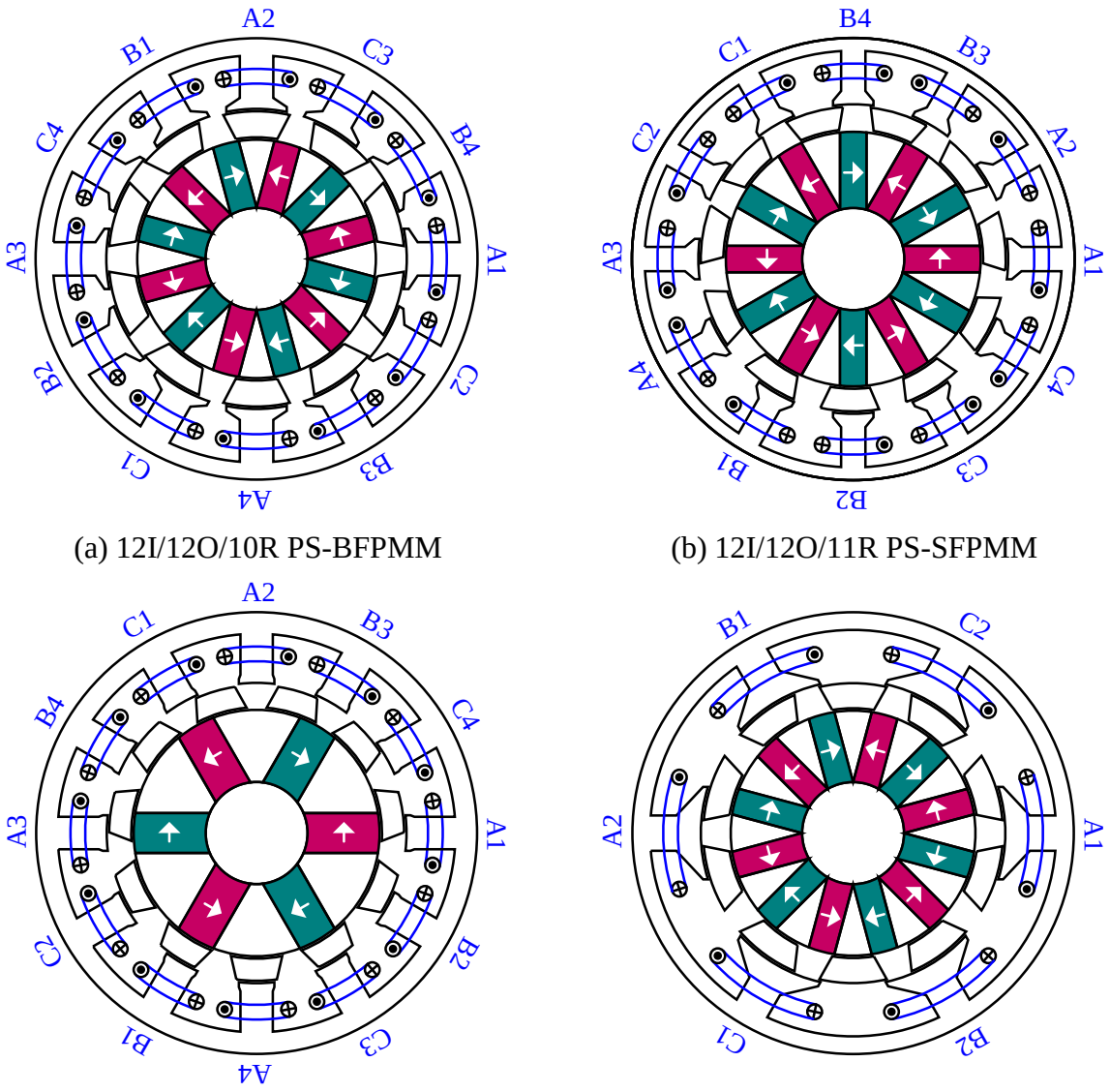

(a) 12I/12O/10R PS-BFPMM (b) 12I/12O/11R PS-SFPMM

(c) 6I/12O/11R PS-SFPMM (d) 12I/6O/10R PS-SFPMM

Fig. 7.17. Machine topologies of PS-BFPMMs and PS-SFPMMs with different N_{is}/N_{os}.

Fig. 7.17 shows the topologies of 12I/12O/10R PS-BFPMM, 12I/12O/11R PS-SFPMM, 6I/12O/11R PS-SFPMM and 12I/6O/10R PS-SFPMM. All machines are globally optimized with maximum average torque under the rated 30W copper loss and the same machine size. The main geometric parameters are detailed in Table 7.1. (According to the analyses shown in sections of 7.2.1 and 7.2.2, the relative positons of inner and outer stators for 6I/12O and 12I/6O PS-SFPMMs as shown in Fig. 7.17 are both optimal.)

Table 7.1 Main parameters of PS-BFPMMs and PS-SFPMMs with different N_{is}/N_{os}

Parameter	**PS-BFPMM**	**PS-SFPMM**		
Inner/outer stator pole ratio ($\boldsymbol{N_{is}/N_{os}}$)	**1**	**1**	**1/2**	**2**
Number of phases	3			
Turns per phase (N_{ph})	72			
Rated speed (rpm)	400			
Rated copper loss (W)	30			
Packing factor	0.5			
Air-gap length L_{ag} (mm)	0.5			
Active axial length L_{aa} (mm)	25			
Outer stator outer radius R_{oso} (mm)	45			
Inner stator inner radius R_{ist} (mm)	10.4			
Outer stator (OS) pole number, N_{os}	12	12	12	6
Inner stator (IS) pole number, N_{is}	12	12	6	12
Rotor pole number, N_r	10	11	11	10
OS inner radius R_{ost} (mm)	30.60	31.50	30.60	31.05
IS outer radius R_{iso} (mm)	24.30	25.90	25.10	24.95
OS tooth body pole arc θ_{ostb} (°)	12.8	9.0	12.4	13.3
OS tooth tip pole arc θ_{ostt} (°)	5.2	3.0	0.6	11.0
OS tooth tip thickness (Opening) T_{ostto} (mm)	1	1	1	1
OS tooth tip thickness (Body) T_{osttb} (mm)	2.4	2.8	1.8	5.2
Rotor outer pole arc θ_{rop} (°)	26	22.2	15.8	26
Rotor inner pole arc θ_{rip} (°)	19.6	17.4	23.6	19.2
Rotor radial thickness T_{rr} (mm)	5.3	4.6	4.5	5.1
OS yoke thickness T_{osy} (mm)	3.5	2.6	4.4	3.6
Rated AC current (A_{rms})	15.83	17.37	15.30	16.91
PM inner pole arc θ_{PM} (°)	30	30	46	30
Total PM volume (mm^3)	22558.0	25147.0	18116.7	23609.9
Magnetic remanence (T)	1.2			
Relative PM permeability	1.05			

7.3.2 Open-Circuit Field Distribution

Fig. 7.18 shows the open-circuit flux equipotential of PS-BFPMMs and PS-SFPMMs at aligned positions (negative *d*-axis). It can be seen that all machines have short flux path which could result in lower MMF drop in the stator. Meanwhile, the flux loop of the coils belong to same phase are completely independent. Moreover, leakage flux exists inside of the inner stator but is quite small compared with main flux. Fig. 7.19 shows the open-circuit air-gap flux density waveforms for all machines at aligned position. Since the partitioned stator PM synchronous machines have two layers of air-gap, the corresponding waveforms shown in Fig. 7.19 as based on the layers which is close to the stator wound with armature windings.

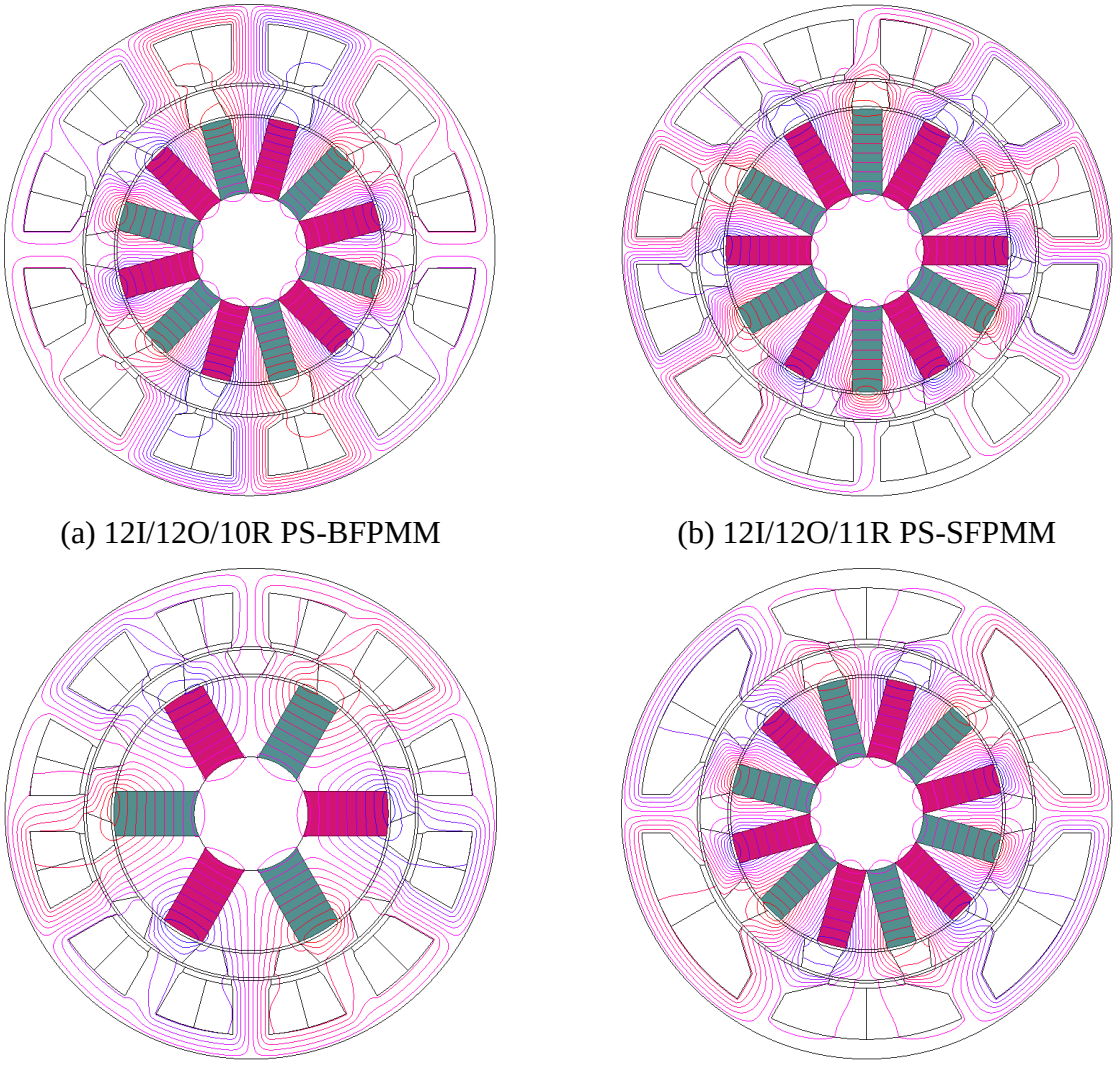

(a) 12I/12O/10R PS-BFPMM (b) 12I/12O/11R PS-SFPMM

(c) 6I/12O/11R PS-SFPMM (d) 12I/6O/10R PS-SFPMM

Fig. 7.18. Open-circuit flux equipotential distributions of PS-BFPMMs and PS-SFPMMs at aligned position

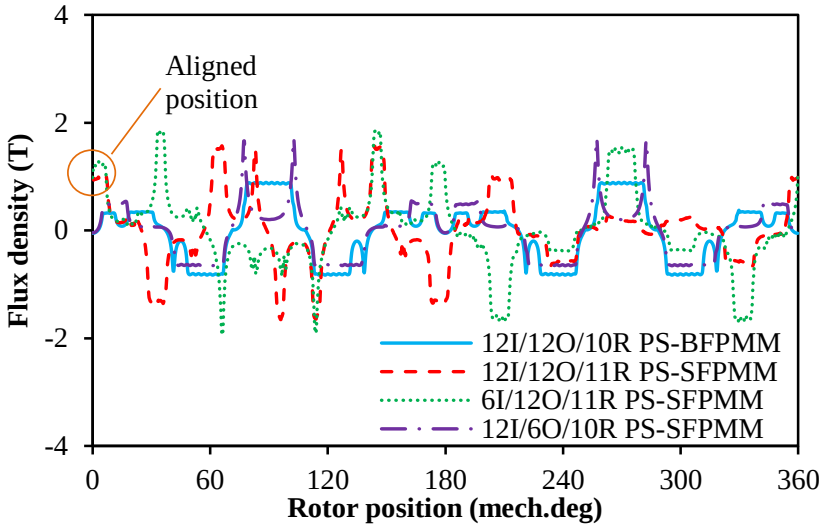

Fig. 7.19. Open-circuit air-gap flux densities of PS-BFPMMs and PS-SFPMMs at aligned position.

7.3.3 Flux-Linkage and Back-EMF Waveforms

The open-circuit phase flux-linkages of PS-BFPMMs and PS-SFPMMs are compared in Fig. 7.20. According to (7.1), symmetrical bipolar phase flux-linkages should be obtained in 12I/12O/10R PS-BFPMM, 12I/12O11R PS-SFPMM and 6I/12O/11R PS-SFPMM since the even harmonics which cause the dc biased and asymmetric in single coil are completely cancelled in the phase winding. It is evidenced by the waveforms and FFT results shown in Fig. 7.20. According to Table 7.2, the fundamental phase flux-linkages of 12I/12O/10R PS-BFPMM, 12I/12O/11R PS-SFPMM, 6I/12O/11R PS-SFPMM and 12I/6O/10R PS-SFPMM are 12.87, 13.33, 7.61 and 15.53mWb respectively. When N_{is}/N_{os}=1, 12I/12O/11R PS-SFPMM exhibit 3.3% higher fundamental phase flux-linage than 12I/12O/10R PS-BFPMM, as shown in Fig. 7.20 and Table 7.2. Further, compared with PS-SFPMMs with different N_{is}/N_{os}, 12I/6O/10R PS-SFPMM exhibits the highest fundamental phase flux-linkage while 6I/12O/11R has the lowest one due to the smallest PM usage.

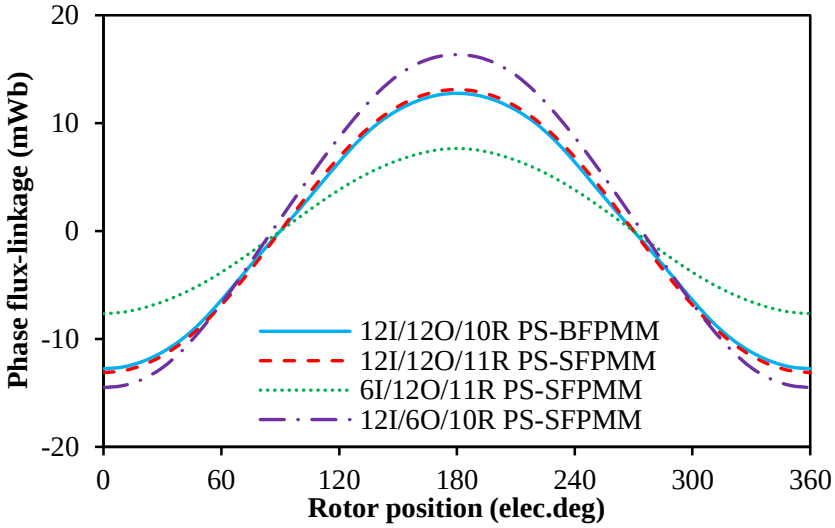

(a) Waveforms

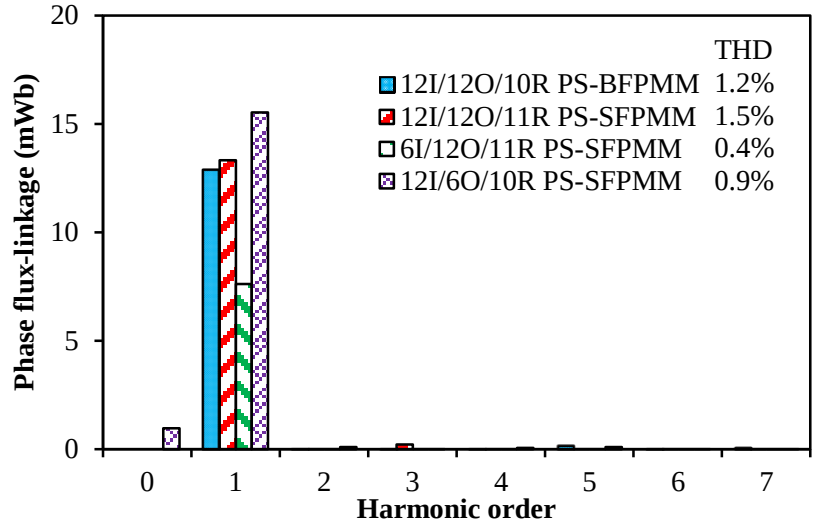

(b) Spectra

Fig. 7.20. Open-circuit phase flux-linkages of PS-BFPMMs and PS-SFPMMs.

Due to the same reason as phase flux-linkage, symmetrical phase back-EMFs are also obtained in 12I/12O/10R PS-BFPMM, 12I/12O11R PS-SFPMM and 6I/12O/11R PS-SFPMM, as shown in Fig. 7.21. According to Table 7.2, the fundamental phase back-EMFs of 12I/12O/10R PS-BFPMM, 12I/12O/11R PS-SFPMM, 6I/12O/11R PS-SFPMM and 12I/6O/10R PS-SFPMM are 5.38, 6.13, 3.50 and 6.50V respectively. Due to the influence of rated electric frequency, 12I/12O/11R PS-SFPMM exhibit 13.9% higher fundamental phase back-EMF than 12I/12O/10R PS-BFPMM when N_{is}/N_{os}=1. Meanwhile, among the PS-SFPMMs with different N_{is}/N_{os}, 12I/6O/10R PS-SFPMM still exhibits the highest fundamental phase back-EMF while 6I/12O/11R has the lowest one.

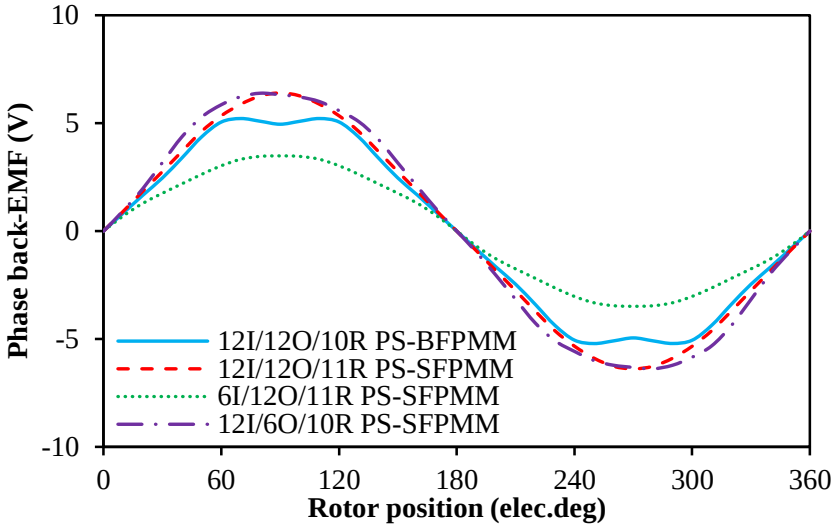

(a) Waveforms

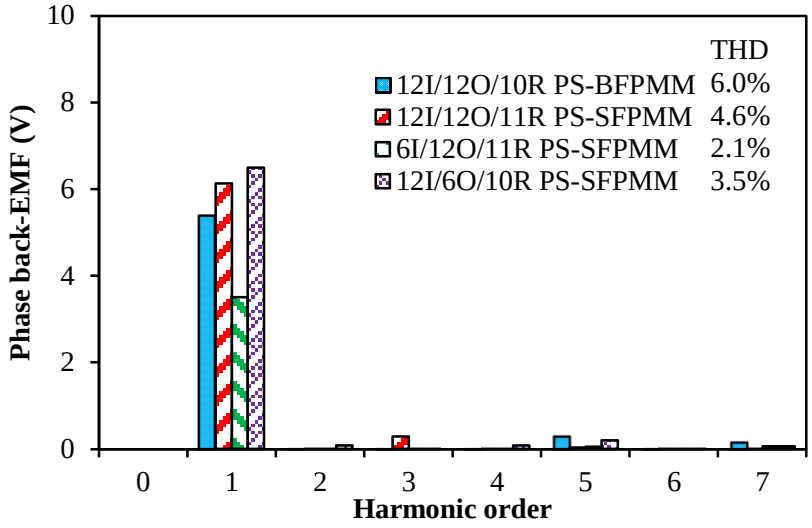

(b) Spectra

Fig. 7.21. Open-circuit phase back-EMFs of PS-BFPMMs and PS-SFPMMs.

7.3.4 *Dq*-Axis Inductances

Fig. 7.22 shows the *dq*-axis inductances at different current angles for all machines with rated currents as given in Table 7.1. It can be seen that the *d*-axis inductance is quite close to *q*-axis inductance in both PS-BFPMMs and PS-SFPMMs with different N_{is}/N_{os}. Since the saliency ratio is quite close to 1, the reluctance torque can be negligible in both PS-BFPMMs and PS-SFPMMs with different N_{is}/N_{os}.

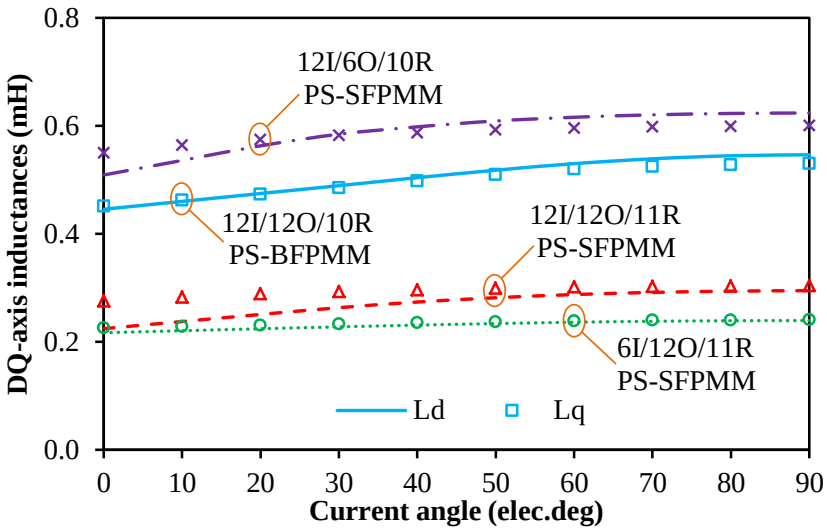

Fig. 7.22. Variation of *dq*-axis inductances with current angle under the rated currents as given in Table 7.1, p_c=30W.

7.3.5 Cogging Torque

Fig. 7.23 shows the open-circuit cogging torque waveforms of all machines. Obviously, for machines with N_{is}/N_{os}=1, 12I/12O/11R PS-SFPMM exhibit lower magnitude of cogging torque than 12I/120/10R PS-BFPMMs. In addition, among the PS-SFPMMs with different N_{is}/N_{os}, 12I/6O/10R PS-SFPMM has the largest magnitude of cogging torque, and then followed by 6I/12O/11R PS-SFPMM.

According to the analyses shown in section 7.2.1, the operational principles of PS-SFPMMs are similar to those of PS-BFPMMs. Therefore, equation (6.3) which is used to calculate the cycle number of cogging torque over one electric period in PS-BFPMMs can be extended to PS-SFPMMs. Considering the influence of inner/outer stator pole ratio N_{is}/N_{os}, equation (6.3) can be changed as

$$N_C = \frac{MIN(N_{is},\ N_{os})}{GCD(\ MIN(N_{is},\ N_{os})\ ,\ N_r)} \tag{7.2}$$

where N_c is the cycle number of cogging torque over one electrical period.

According to (7.2), the cycle numbers of cogging torque for 12I/12O/10R PS-BFPMM, 12I/12O11R PS-SFPMM, 6I/12O/11R PS-SFPMM and 12I/6O/10R PS-SFPMM are 6, 12, 6 and 3 respectively. It is evidenced by the waveforms and FFT results in Fig. 7.23.

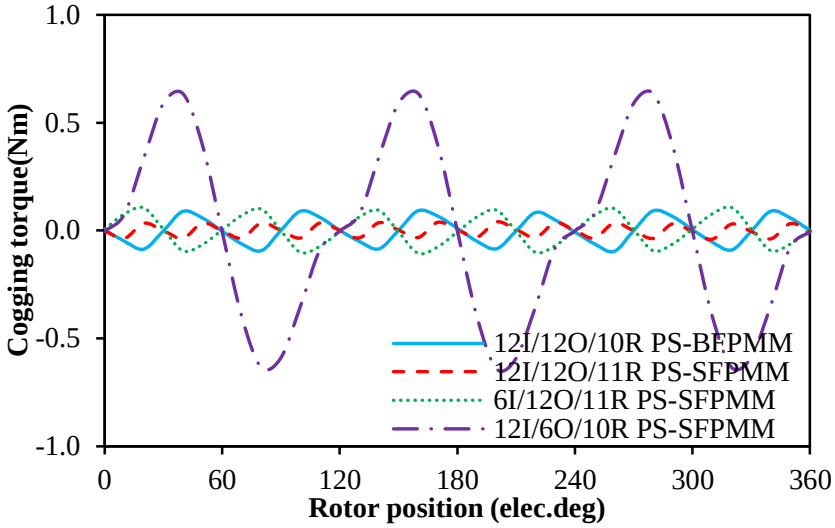

(a) Waveforms

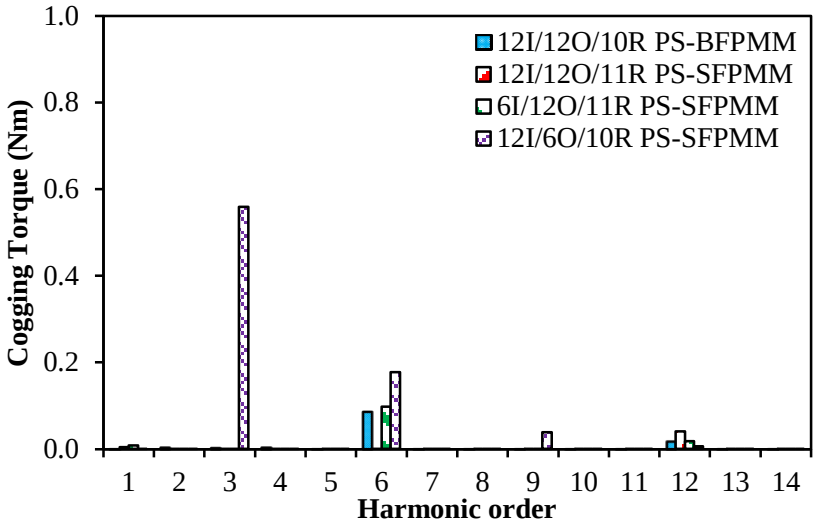

(b) Spectra

Fig. 7.23. Open-circuit cogging torques of PS-BFPMMs and PS-SFPMMs.

7.3.6 Electromagnetic Torque Characteristics

Fig. 7.24 shows the waveforms of average torque against with current angle at rated currents (corresponding to p_c=30W) for all machines. Obviously, the optimal current angles for PS-SFPMMs with different N_{is}/N_{os} are all close to 0°, which are similar to PS-BFPMMs. The results further indicate that the reluctance torque is negligible in PS-SFPMMs whatever the ratio of N_{is}/N_{os} is selected, which is consistent with the conclusion in section 7.3.4.

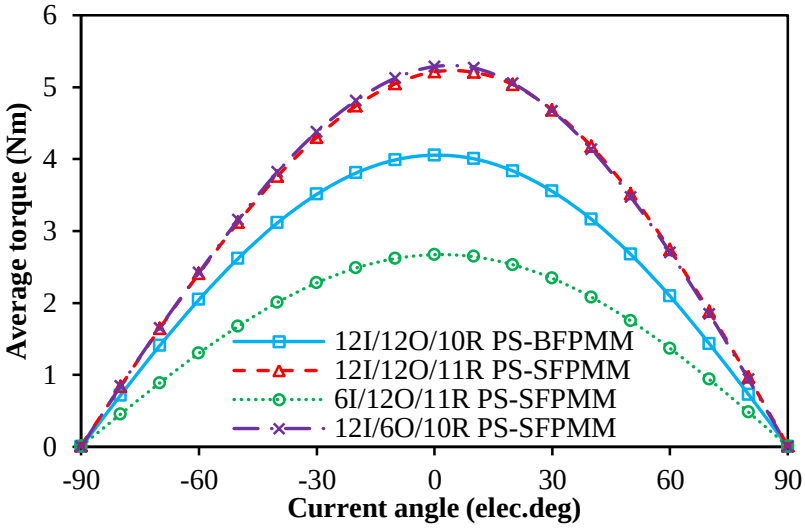

Fig. 7.24. Variation of average torque with current angle under the rated currents, p_c=30W.

Fig. 7.25 shows the waveforms of torque against with rotor position at rated currents (p_c=30W) and I_d=0 control. Due to the combined influences of cogging torque and back-EMF harmonics (mainly in 5^{th} and 7^{th}), 12I/12O/10R PS-BFPMM, 12I/12O/11R PS-SFPMM and 6I/12O/11R PS-SFPMM have 6 torque ripples over one electric period while 12I/6O/10R PS-SFPMM has 3 torque ripples. As shown in Table 7.2, the torque ripples of 12I/12O/10R PS-BFPMM, 12I/12O/11R PS-SFPMM, 6I/12O/11R PS-SFPMM and 12I/6O/10R PS-SFPMM are 7.3%, 2.3%, 9.8% and 26.9% respectively. Obviously, 12I/12O/11R PS-SFPMM exhibits the smallest torque ripple while 12I/6O/10R PS-SFPMM has the largest one.

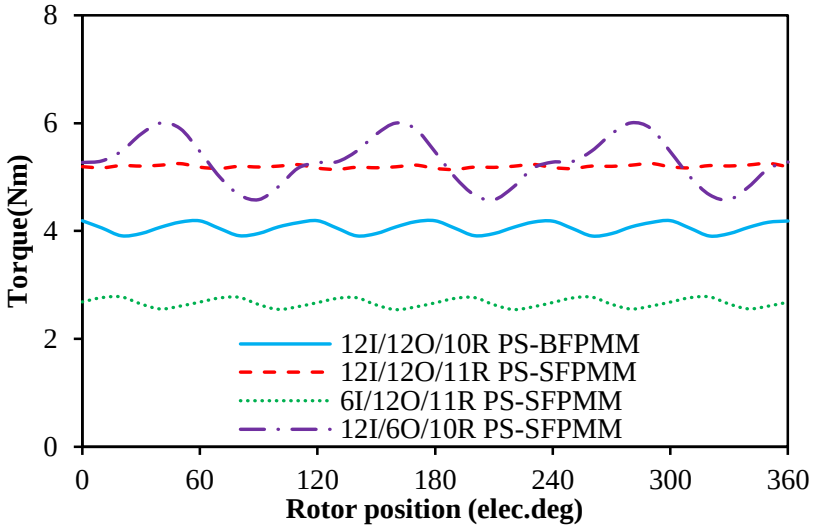

(a) Waveforms

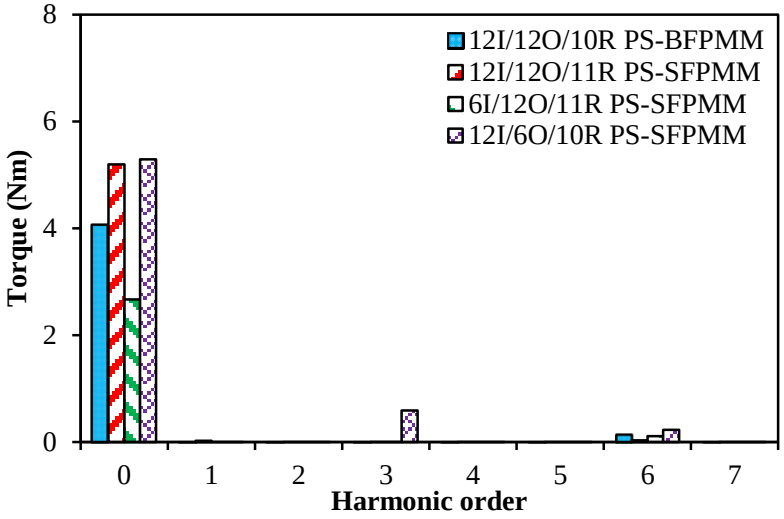

(b) Spectra

Fig. 7.25. Variation of electromagnetic torque with rotor position at rated currents, I_d=0 control, p_c=30W.

According to Table 7.2, the average torque for 12I/12O/10R PS-BFPMM, 12I/12O/11R PS-SFPMM, 6I/12O/11R PS-SFPMM and 12I/6O/10R PS-SFPMM are 4.06, 5.20, 2.67 and 5.29Nm respectively. According to the analyses shown in section 7.2.1 together with the larger PM usage and higher rated current under the same rated copper loss as well as the larger winding factor as shown in Table 7.1 and Table 6.4 respectively, 12I/12O/11R PS-SFPMM exhibits ~28% higher average torque than 12I/12O/10R PS-BFPMM. In addition, compared with 12I/12O/11R PS-SFPMM (N_{is}/N_{os}=1), ~2% higher average torque is obtained in 12I/6O/10R PS-SFPMM (N_{is}/N_{os}=2) while 49% lower average torque is found in 6I/12O/11R PS-SFPMM (N_{is}/N_{os}=1/2).

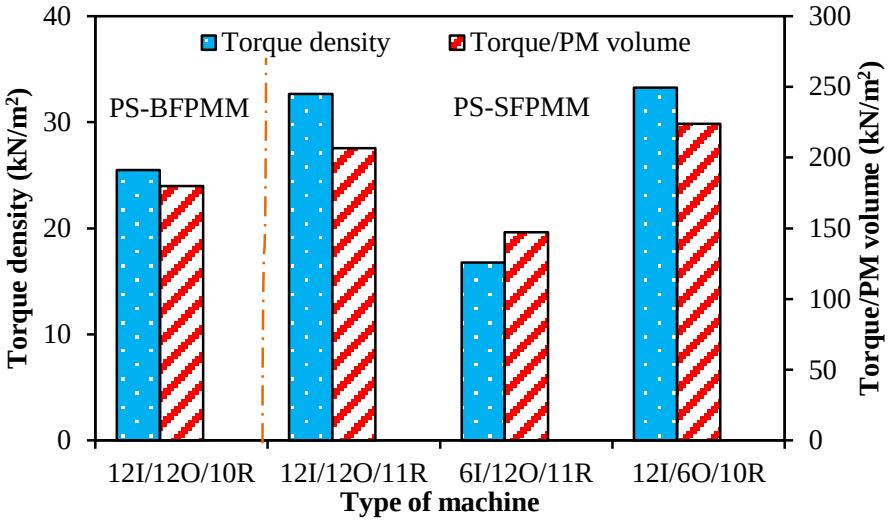

Fig. 7.26. Torque density and torque to PM volume, p_c=30W, I_d=0 control.

Fig. 7.26 compares the torque density and torque to PM volume of four machines at the rated currents (p_c=30W) and I_d=0 control. Compared with 12I/12O/10R PS-BFPMM, 12I/12O/11R PS-SFPMM exhibits ~28% larger torque density and ~15% higher PM utilization efficiency (ratio of torque to PM volume), as shown in Table 7.2. Among the three PS-SFPMMs with different N_{is}/N_{os}, 12I/6O/10R PS-SFPMM (N_{is}/N_{os}=2) exhibits the largest torque density and highest PM utilization efficiency while 6I/12O/11R PS-SFPMM (N_{is}/N_{os}=1/2) has the smallest torque density and lowest PM utilization efficiency.

The variations of average torque with copper loss are further shown in Fig. 7.27. The vertical dashed and dotted line shows the rated copper loss which is used to global optimization. As shown in Fig. 7.27, the increase rate of average torque in both PS-BFPMMs and PS-SFPMMs will be declined with the rising of copper loss (current) due to the aggravated magnetic saturation. In addition, for machines with N_{is}/N_{os}=1, 12I/12O/11R PS-SFPMM exhibits larger average torque than 12I/12O/10R PS-BFPMM under the same copper loss over the whole copper loss range, as shown in Fig. 7.27. Further, compared with 12I/12O/11R PS-SFPMM (N_{is}/N_{os}=1), the average torque of 12I/6O/10R PS-SFPMM (N_{is}/N_{os}=2) is slightly larger at relatively low copper loss (electric loading) but smaller at high copper loss since the saturation of magnetic circuit is quicker due to bigger inductance and higher armature reaction. Fig. 7.27 also indicates that 6I/12O/11R PS-SFPMM (N_{is}/N_{os}=1/2) has the smallest average torque over the whole copper loss range.

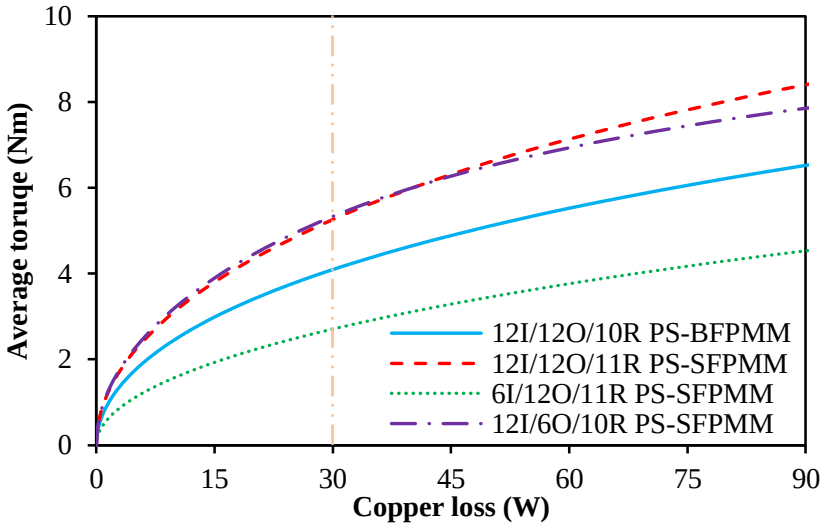

Fig. 7.27. Variation of average torque with copper loss, I_d=0 control.

Table 7.2 Main electromagnetic performances of PS-BFPMM and PS-SFPMMs

Parameter	**PS-BFPMM**	**PS-SFPMMs**		
$N_{is}/N_{os}/N_r$	**12I/12O/10R**	**12I/12O/11R**	**6I/12O/11R**	**12I/6O/10R**
Fund. flux-linkage (mWb)	12.87	13.33	7.61	15.53
Fund. back-EMF (V)	5.38	6.13	3.50	6.50
Rated electric frequency (Hz)	66.7	73.3	73.3	66.7
Cogging torque (Nm)	0.10	0.04	0.11	0.65
Average torque (Nm)	4.06	5.20	2.67	5.29
Torque ripple (%)	7.3	2.3	9.2	26.9
Torque density (kN/m^2)	25.5	32.7	16.8	33.3
Total PM volume (mm^3)	22558.0	25147.0	18116.7	23609.9
Torque/PM volume (kN/m^2)	180	207	147	224.0
Rated iron loss (W)	2.26	2.46	1.10	2.43
Rated PM loss (W)	0.064	0.041	0.044	0.236

7.3.7 Iron Loss and PM Loss

Fig. 7.28 shows the variation of total iron losses against speed at rated copper loss for four machines. According to the analyses shown in section 5.3.7, the iron loss is increased as the speed increased. Among these four machines, the 12I/12O/11R PS-SFPMM and 12I/6O/11R PS-SFPMM exhibit the similar highest total iron losses while the 6I/12O/11R PS-SFPMM has the lowest total iron loss in the whole speed range. As shown in Table 7.2, the iron loss of 12I/12O/10R PS-BFPMM, 12I/12O/11R PS-SFPMM, 6I/12O/11R PS-SFPMM and 12I/6O/10R PS-SFPMM under the rated copper loss (30W) and the rated speed (400rpm) are 2.26, 2.46, 1.10 and 2.43W respectively.

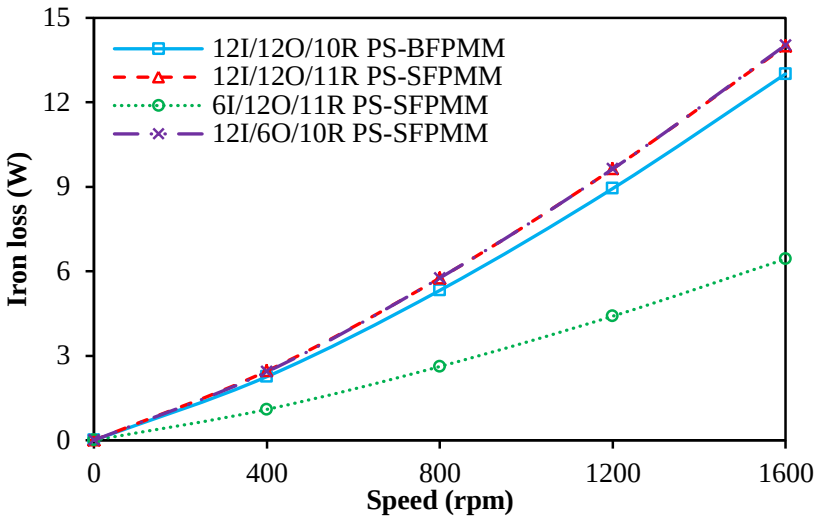

Fig. 7.28. Variation of iron loss with speed in PS-BFPMMs and PS-SFPMMs, p_c =30W, I_d = 0 control.

Fig. 7.29 shows the variation of PM losses against with speed at rated copper loss for four machines. According to the analyses in section 5.3.7, the PM loss is also increased as the speed increased. In addition, 12I/6O/10R PS-BFPMM exhibits the largest PM loss in the whole speed range among the four machines since it has the highest amplitude change of PM flux density during one electric period although its PM volume is lower than that of 12I/12O/11R PS-SFPMM. As shown in Table 7.2, the PM loss of 12I/12O/10R PS-BFPMM, 12I/12O/11R PS-SFPMM, 6I/12O/11R PS-SFPMM and 12I/6O/10R PS-SFPMM under the rated copper loss (30W) and the rated speed (400rpm) are 0.064, 0.041, 0.044 and 0.236W respectively.

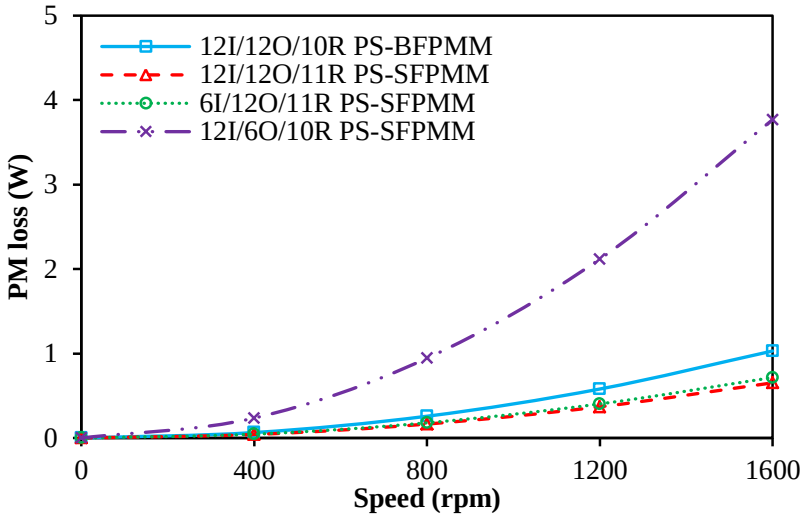

Fig. 7.29. Variation of PM loss with speed in PS-BFPMMs and PS-SFPMMs, p_c =30W, I_d = 0 control.

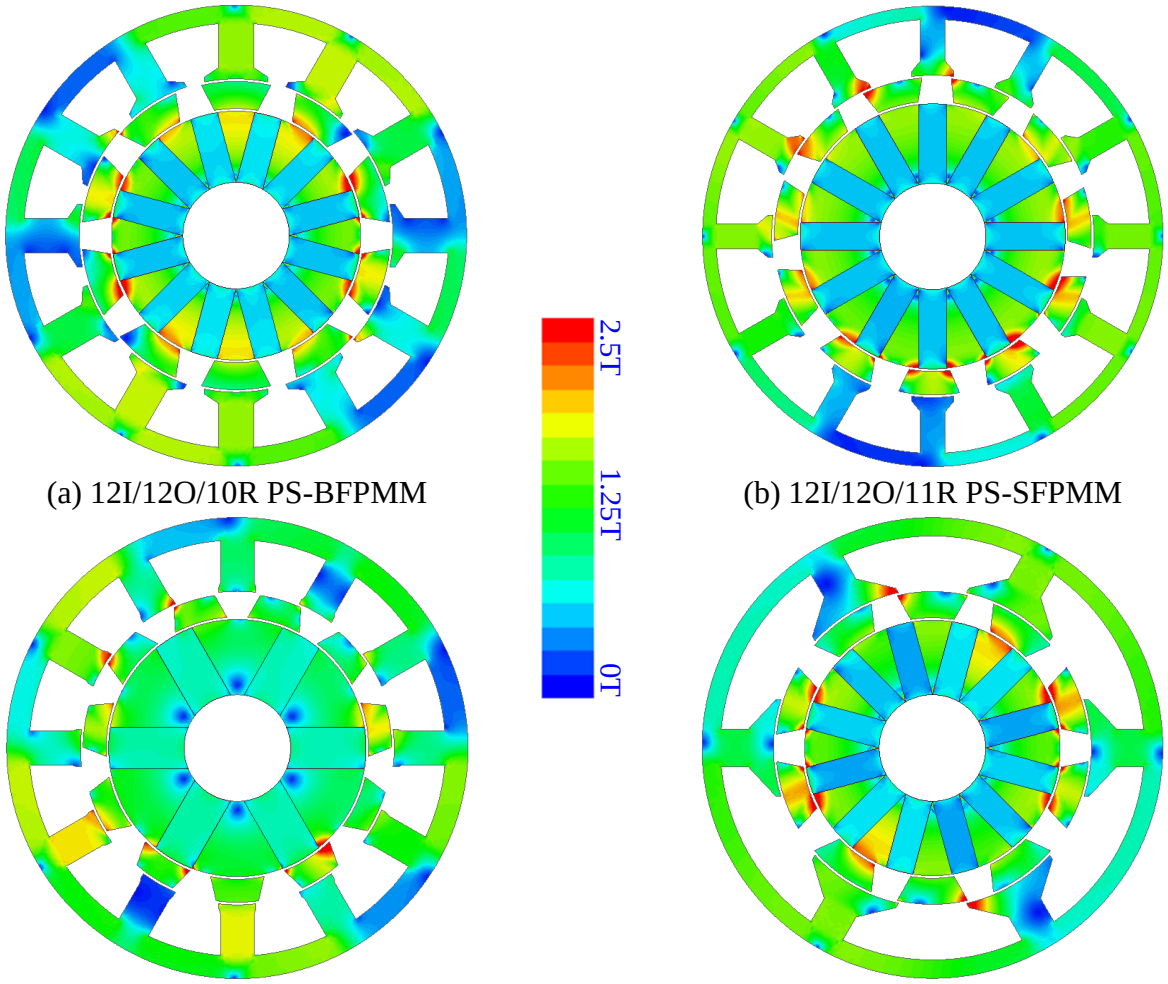

(a) 12I/12O/10R PS-BFPMM (b) 12I/12O/11R PS-SFPMM

(c) 6I/12O/11R PS-SFPMM (d) 12I/6O/10R PS-SFPMM

Fig. 7.30. On-load flux density distributions of PS-BFPMMs and PS-SFPMMs, p_c =30W, I_d = 0 control.

7.4 Winding Configurations of 6I/12O PS-SFPMMs with N_{is}/N_{os}=1/2

7.4.1 Machine Topologies and Windings Configurations

According to the analyses shown in section 7.2.2, symmetrical bipolar phase flux-linkage will be obtained in 6I/12O PS-SFPMMs (N_{is}/N_{os}=1/2) when the (inner/outer) stator and rotor pole combinations satisfy (7.1). Meanwhile, as shown in Fig. 7.7, the bipolar coil flux-linkage (coil-wound outer stator pole aligns with PMs) exhibits larger magnitude of fundamental wave than the unipolar coil flux-linkage (coil-wound outer stator pole aligns with iron ribs). Therefore, alternate pole wound winding configuration can be employed to enhance the torque performance of 6I/12O PS-SFPMM. Furthermore, the optimal rotor pole number which chosen to achieve maximum average torque for 6I/12O PS-SFPMM is 11, as shown in Fig. 7.16. Based on the optimal rotor pole number, the influence of winding

configurations on electromagnetic performance of 6I/12O PS-SFPMM (N_{is}/N_{os}=1/2) will be analysed and compared in the following sections.

Fig. 7.31 shows the machine topologies of 6I/12O/11R PS-SFPMMs with all pole wound and alternate pole wound winding configurations. To simplify the comparison in the following sections, the machine topologies corresponding to Fig. 7.31(a), (b) and (c) can be designated as 6I/12O/11R PS-SFPMM-ORI, 6I/12O/11R PS-SFPMM-APW-I and 6I/12O/11R PS-SFPMM-APW-II respectively. All machines are globally optimized with maximum average torque under the same rated 30W copper loss and the same machine size. The main geometric parameters are detailed in Table 7.3.

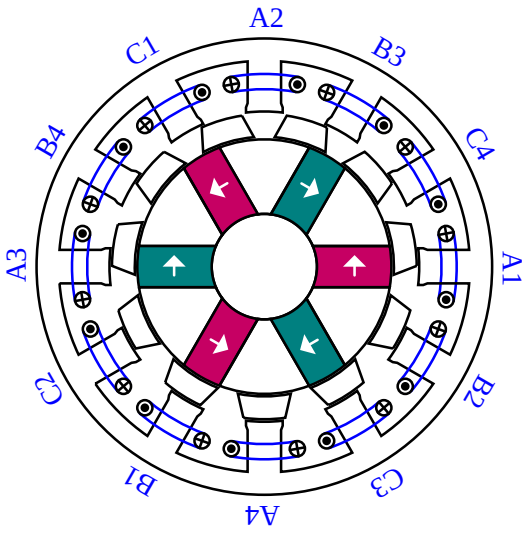

(a) 6I/12O/11R PS-BFPMM-ORI

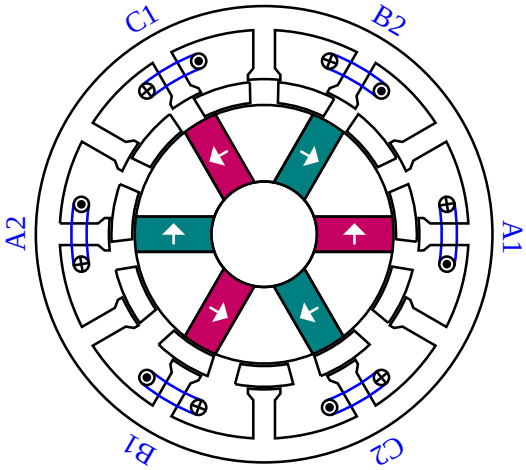

(b) 6I/12O/11R PS-SFPMM-APW-I

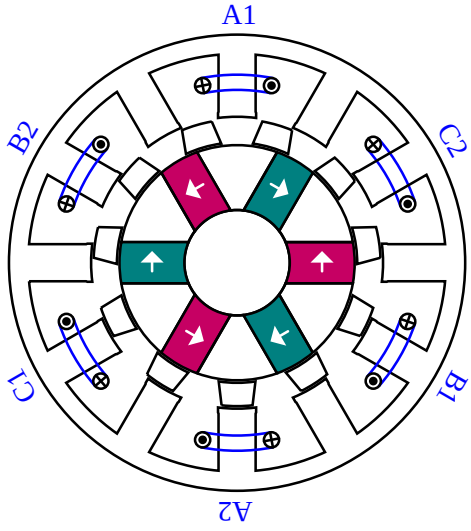

(c) 12I/6O/11R PS-SFPMM-APW-II

Fig. 7.31. Machine topologies of 6I/12O/11R PS-SFPMMs with all pole wound and alternate pole wound winding configurations.

Table 7.3 Main parameters of 6I/12O/11R alternate pole wound PS-SFPMMs

Parameter	**6I/12O/11R PS-SFPMMs**	
Winding Configuration	**APW-I**	**APW-II**
N_{ph}	72	72
R_{ost} (mm)	30.6	28.8
R_{iso} (mm)	25.5	23.2
θ_{ostb} (°)	8	14.6
θ_{ostt} (°)	2	0.2
T_{ostto} (mm)	1	1
T_{osttb} (mm)	2.2	1.2
θ_{rop} (°)	22	12.4
θ_{rip} (°)	20.7	17.6
T_{rr} (mm)	4.1	4.6
T_{osy} (mm)	4.7	3.8
I_{arms} (A)	16.30	16.50
θ_{PM} (°)	39	46

7.4.2 Flux-Linkage and Back-EMF Waveforms

According to the analyses in section 7.2.2, symmetrical bipolar phase flux-linkage can be obtained in both all pole wound and alternate pole wound 6I/12O PS-SFPMMs (N_{is}/N_{os}=1/2) when the (inner/outer) stator/rotor pole combinations are satisfied with (7.1). Therefore, for 6I/12O/11R PS-SFPMMs under investigation, symmetrical bipolar phase flux-linkages are obtained in both all pole wound and alternate pole wound winding configurations since the even harmonics are completely cancelled in phase windings, as shown in Fig. 7.32. Compared with 6I/12O/11R PS-SFPMM-ORI, the fundamental phase flux-linkages for 6I/12O/11R PS-SFPMM-APW-I and 6I/12O/11R PS-SFPMM-APW-II are enhanced by ~37% and reduced by ~33% respectively.

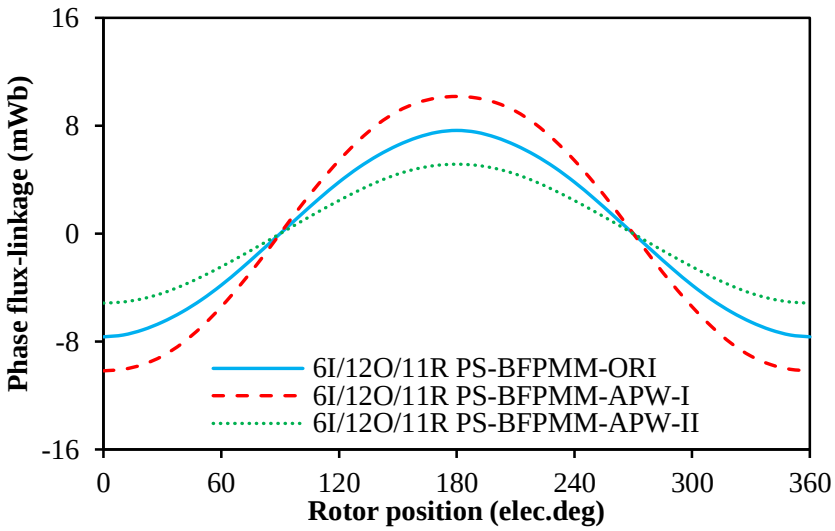

(a) Waveforms

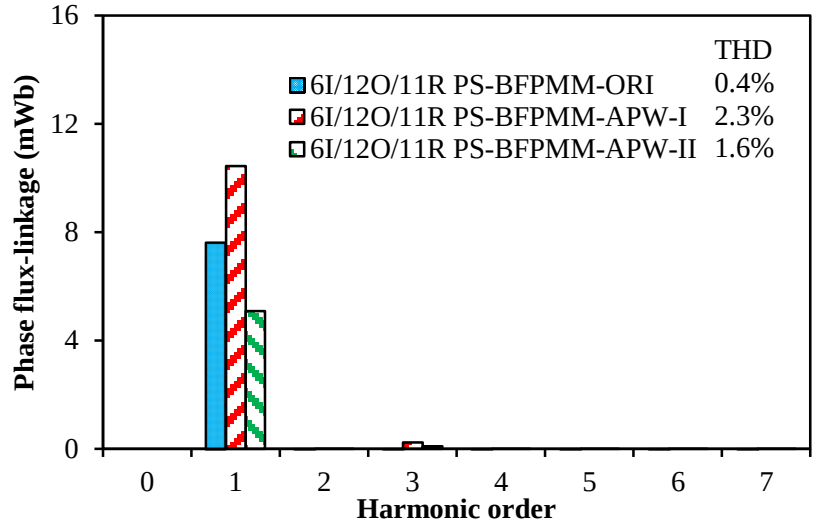

(b) Spectra

Fig. 7.32. Open-circuit phase flux-linkages of 6I/12O/11R PS-SFPMMs with all pole wound and alternate pole wound windings.

Similar to phase flux-linkage, symmetrical phase back-EMFs are also obtained in all three 6I/12O/11R PS-SFPMMs, as shown in Fig. 7.33. Due to the same rated electric frequency, the increase rate and decrease rate of fundamental phase back-EMFs in 6I/12O/11R PS-SFPMM-APW-I and 6I/12O/11R PS-SFPMM-APW-II are consistent with those in fundamental phase flux-linkages, which are ~37% higher and ~33% lower than 6I/12O/11R PS-SFPMM-ORI respectively.

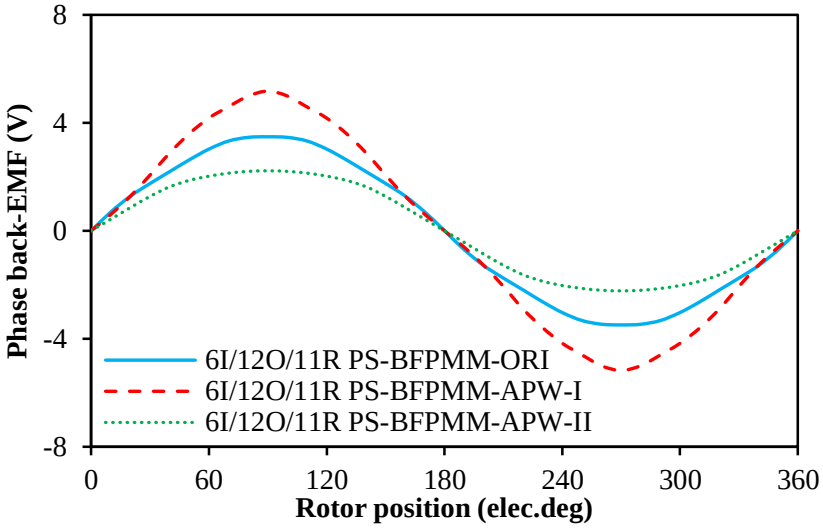

(a) Waveforms

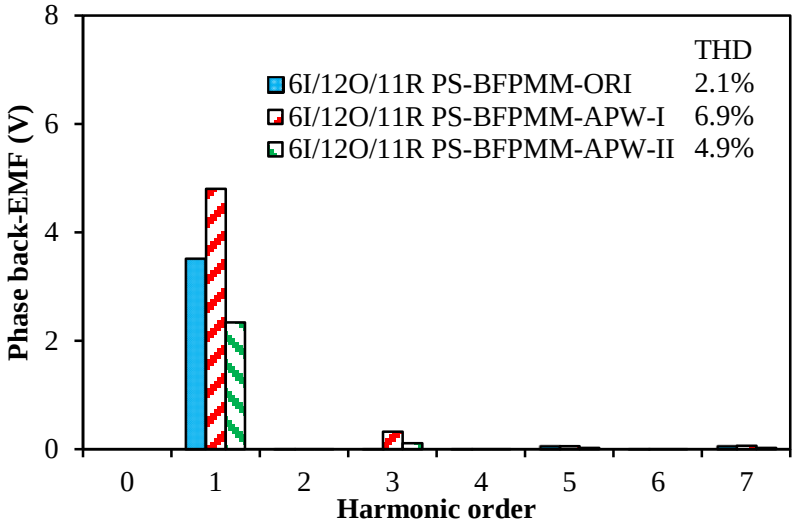

(b) Spectra

Fig. 7.33. Open-circuit phase back-EMFs of 6I/12O/11R PS-SFPMMs with all pole wound and alternate pole wound windings.

7.4.3 Cogging Torque

Due to the similar machine topologies, three machines should have the same cycle number of cogging torque over one electric period whatever the winding configurations are selected. According to (7.2), the cycle numbers of three machines are all equal to 6, which are consistent with the waveforms shown in Fig. 7.34. In addition, the magnitudes of cogging torque of 6I/12O/11R PS-SFPMM-APW-I and 6I/12O/11R PS-SFPMM-APW-II are both slightly smaller than that of 6I/12O/11R PS-SFPMM-ORI.

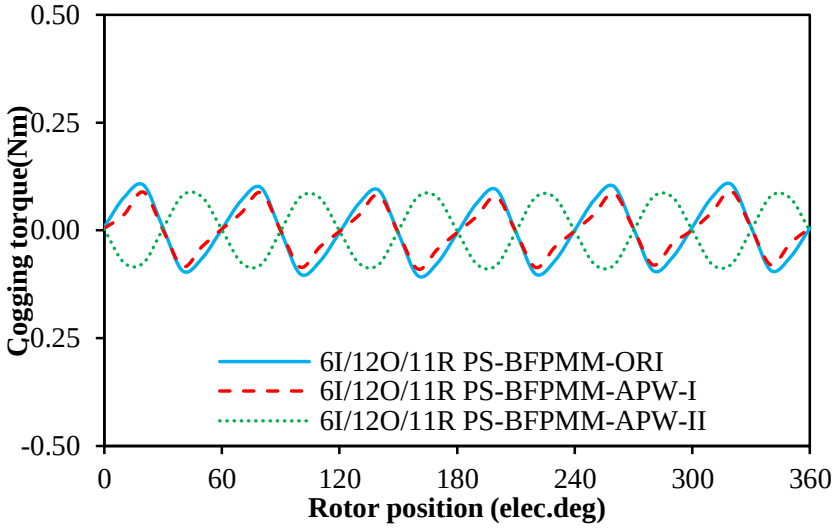

(a) Waveforms

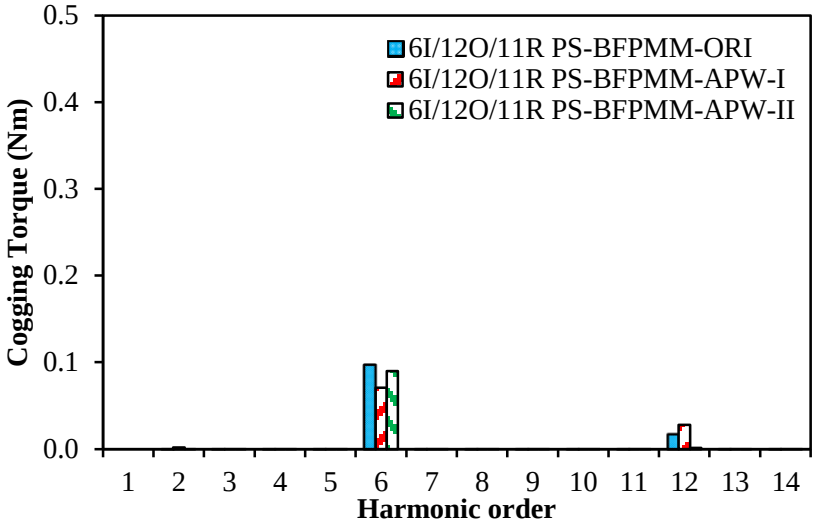

(b) Spectra

Fig. 7.34. Open-circuit cogging torque of 6I/12O/11R PS-SFPMMs with all pole wound and alternate pole wound windings.

7.4.4 Electromagnetic Torque Characteristics

Fig. 7.35 shows the waveforms of average torque against with current angle at rated currents (corresponding to p_c=30W) for three machines. Obviously, regardless of the selections of armature winding configurations, the reluctance torques are negligible in all three machines since the optimal current angles are all close to 0°.

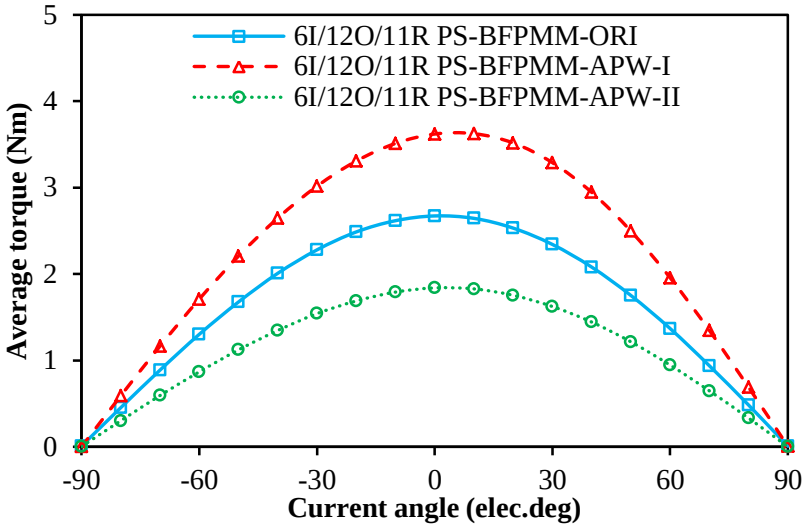

Fig. 7.35. Variation of average torque with current angle under the rated currents, p_c=30W.

Fig. 7.36 shows the waveforms of torque against rotor position at rated currents (p_c=30W) and I_d=0 control. Due to the combined influences of cogging torque and back-EMF harmonics (mainly the 5th and 7th harmonics), three machines all have 6 torque ripples over one electric period. As shown in Table 7.4, the torque ripples of 6I/12O/11R PS-SFPMM-ORI, 6I/12O/11R PS-SFPMM-APW-I and 6I/12O/11R PS-SFPMM-APW-II are 9.2%, 3.7% and 12.3% respectively. Compared with 6I/12O/11R PS-SFPMM-ORI, the torque ripple is reduced in 6I/12O/11R PS-SFPMM-APW-I but increased in 6I/12O/11R PS-SFPMM-APW-II.

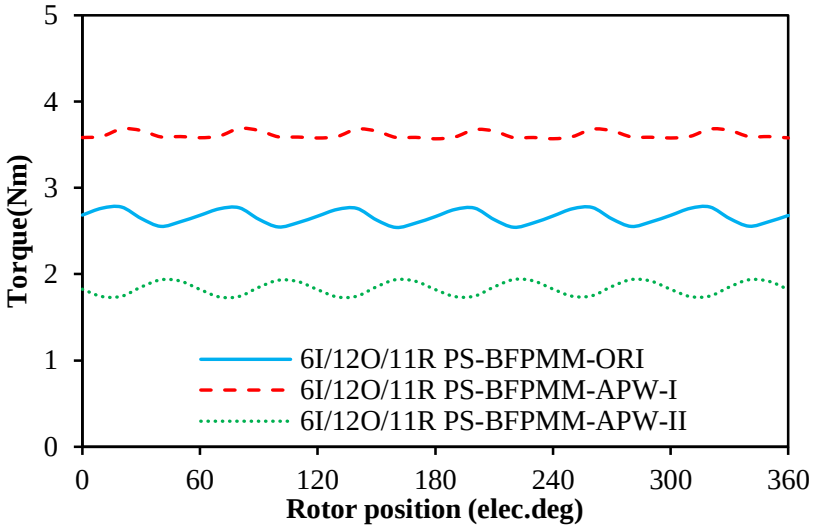

(a) Waveforms

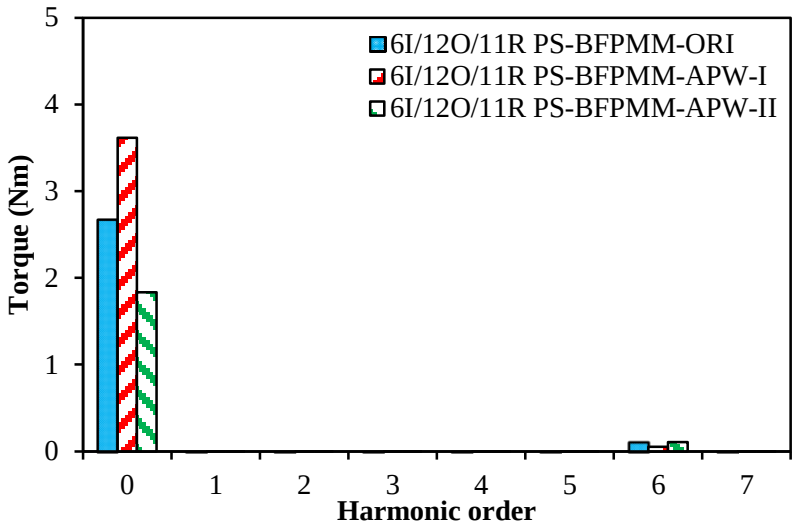

(b) Spectra

Fig. 7.36. Variation of electromagnetic torque with rotor position at rated currents, I_d=0 control, p_c=30W.

According to Table 7.4, the average torque for 6I/12O/11R PS-SFPMM-ORI, 6I/12O/11R PS-SFPMM-APW-I and 6I/12O/11R PS-SFPMM-APW-II are 2.67, 3.62 and 1.84Nm respectively. Compared with 6I/12O/11R PS-SFPMM-ORI, the average torque is enhanced by ~36% in 6I/12O/11R PS-SFPMM-APW-I but reduced by ~31% in 6I/12O/11R PS-SFPMM-APW-II.

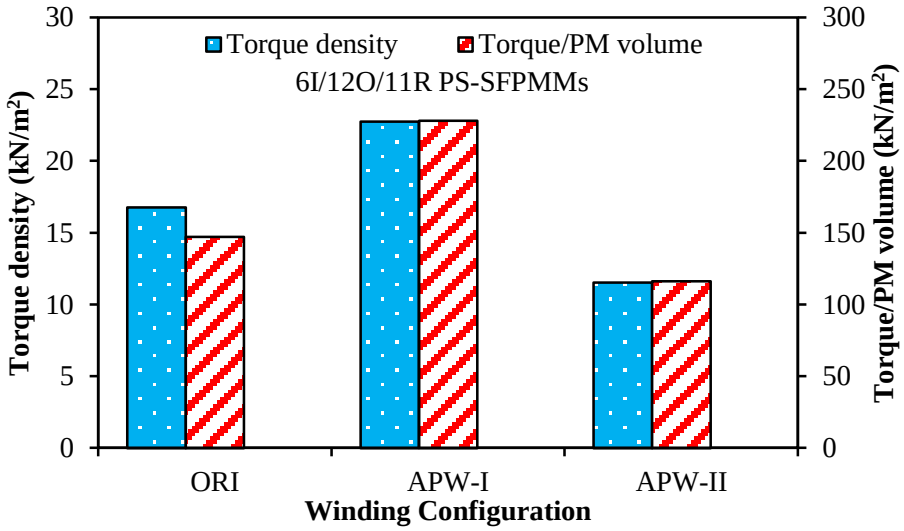

Fig. 7.37. Torque density and torque to PM volume, p_c=30W, I_d=0 control.

Fig. 7.37 compares the torque density and torque to PM volume of three machines at rated currents (p_c=30W) and I_d=0 control. Compared with 6I/12O/11R PS-SFPMM-ORI, 6I/12O/11R PS-SFPMM-APW-I exhibits ~36% larger torque density and ~55% higher PM

utilization efficiency (ratio of torque to PM volume) while 6I/12O/11R PS-SFPMM-APW-II has ~31% smaller torque density and ~21% lower PM utilization efficiency.

The torque performances of three machines under different copper loss are compared in Fig. 7.38. The vertical dashed and dotted line shows the rated copper loss which is used for global optimization. Obviously, among the three machines, 6I/12O/11R PS-SFPMM-APW-I exhibits the largest average torque under the same copper loss over the whole copper range while 6I/12O/11R PS-SFPMM-APW-II always has the smallest average torque. These results further evidence that alternate pole wound winding configuration coordinated with coils wound around the outer stator pole aligned with PMs of inner stator can both enhance the torque performance and PM utilization efficiency of 6I/12O PS-SFPMMs (N_{is}/N_{os}=1/2).

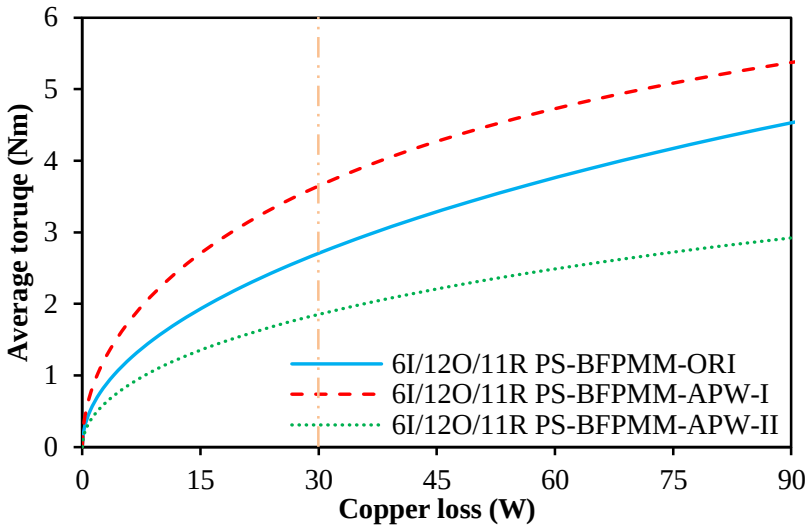

Fig. 7.38. Variation of average torque with copper loss, I_d=0 control.

Table 7.4 Main electromagnetic performances of 6I/12O/ PS-SFPMMs with all pole wound and alternate pole wound winding configurations

Parameter	**6I/12O/11R PS-SFPMMs**		
Winding Configuration	**ORI**	**APW-I**	**APW-II**
Fund. flux-linkage (mWb)	7.61	10.44	5.08
Fund. back-EMF (V)	3.50	4.81	2.34
Rated electric frequency (Hz)	73.3	73.3	73.3
Cogging torque (Nm)	0.107	0.091	0.093
Average torque (Nm)	2.67	3.62	1.84
Torque ripple (%)	9.2	3.7	12.3
Torque density (kN/m^2)	16.8	22.7	11.5
Torque/PM volume (kN/m^2)	147	228	116

7.5 Influence of Alternate Pole Wound Winding on Torque Performance of PS-BFPMM and PS-SFPMMs

Based on the optimal rotor pole numbers as mentioned in section 7.3, the influence of alternate pole wound winding on torque performance of PS-BFPMMs and PS-SFPMM with N_{is}/N_o equal to 1, 1/2 and 2 is compared in Fig. 7.39. Obviously, by employing the alternate pole wound winding, higher torque capabilities are obtained in 12I/12O/11R PS-SFPMM (distribution factor increased from 0.965 to 1) and 6I/12O/11R PS-SFPMM (APW-I) while lower torque capabilities are observed in 12I/12O/10R PS-BFPMM and 12I/6O/10R PS-SFPMM. In addition, among all machines with both all pole wound and alternate pole wound windings, 12I/12O/11R PS-SFPMM-APW exhibits the optimal torque capability under the copper loss over the whole copper loss range.

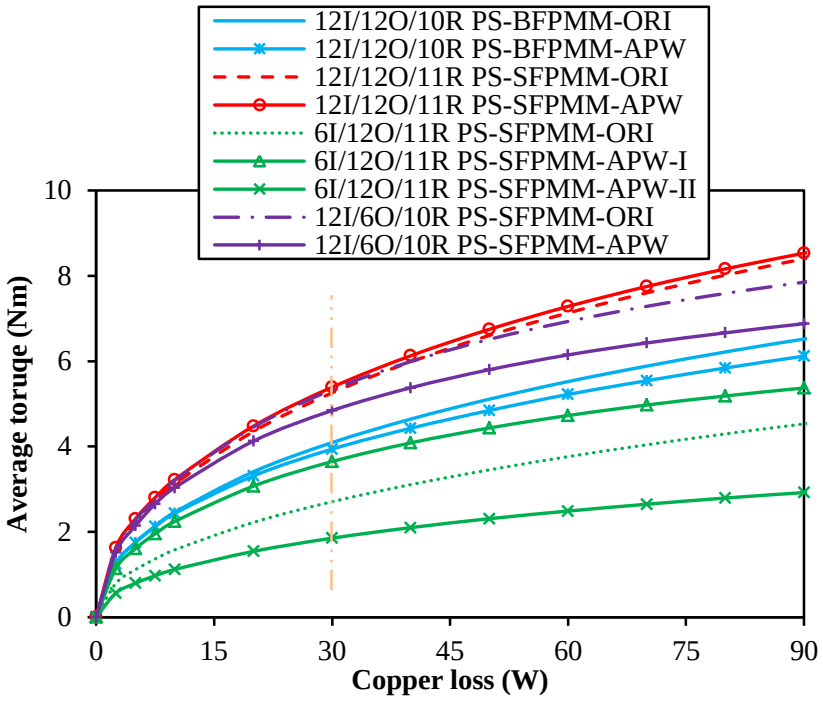

Fig. 7.39. Variation of average torque with copper loss for all machine with all pole and alternate pole wound windings, I_d=0 control.

Fig. 7.40 shows the variation of torque/PM volume against with copper loss for all machines with all pole wound and alternate pole wound windings. By employing the alternate pole wound winding, higher PM utilization efficiencies are obtained in 12I/12O/11R PS-SFPMM and 6I/12O/11R PS-SFPMM (APW-I) while lower PM utilization efficiencies are observed in 12I/12O/10R PS-BFPMM and 12I/6O/10R PS-SFPMM, which are similar to the conclusions on average torque. Moreover, 6I/12O/11R PS-SFPMM-APW-I has the highest

PM utilization efficiencies among all the machines, then followed by 12I/6O/10R PS-SFPMM.

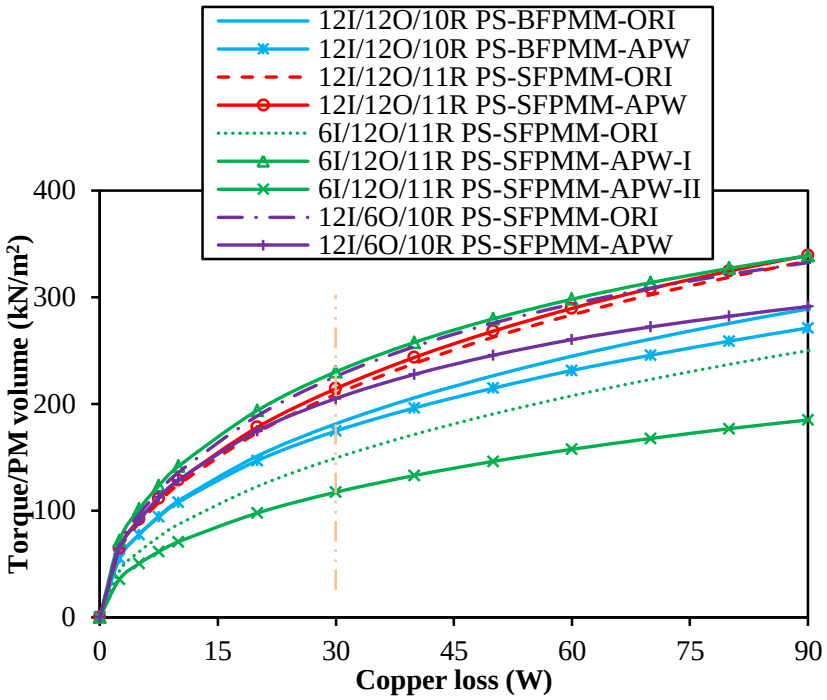

Fig. 7.40. Variation of torque/PM volume against with copper loss for all machines with all pole and alternate pole wound windings, I_d=0 control.

7.6 Experimental Verification

Prototype machines of 12I/12O/1OR PS-BFPMM and 12I/6O/10R PS-SFPMM are made to validate the foregoing analyses, and shown in Fig. 7.41. To reduce the cost, those existing inner stator with 12 PMs, 10-pole rotor and 12-pole outer stator are used to test and validate the FE results of 12I/12O/10R PS-BFPMM. For 12I/6O/10R PS-SFPMM, new 6-pole outer stator is made according to the re-optimized results when using the same existing inner stator and rotor as 12I/12O/10R PS-BFPMM. The parameters of two prototype machines are shown in Table 7.5, which are different from the previous globally optimized parameters as given in Table 7.1. Moreover, for easing the fabrication, 10-pole modular rotor is mechanically connected by lamination bridges with 0.5mm thickness (T_{BRI}) in the inner side of rotor, as shown in Fig. 7.41(d). Meanwhile, lamination bridges (0.5mm) are also added to both top and bottom edges of PMs to help fixing, as shown in Fig. 7.41(c).

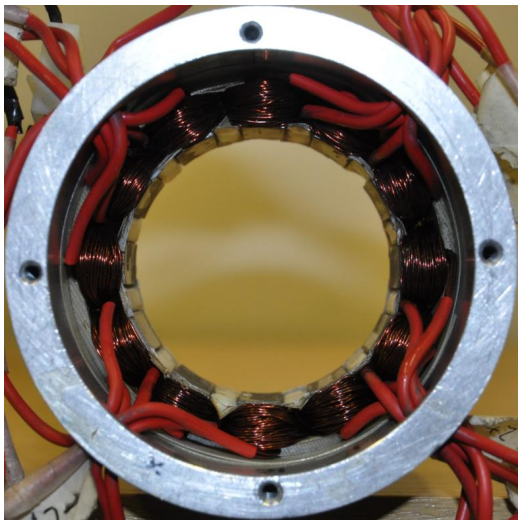

(a) 12-pole outer stator

(b) 6-pole outer stator

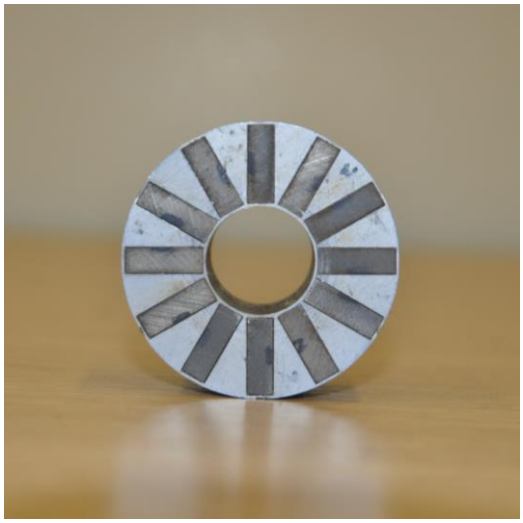

(c) Inner stator with 12 PMs

(d) 10-pole rotor

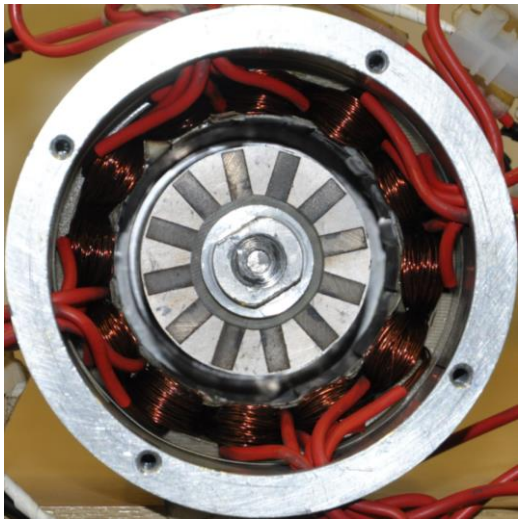

(e) Assembled stators of 12I/12O PS-BFPMM

(f) Assembled stators of 12I/6O PS-SFPMM

Fig. 7.41. Prototypes of 12I/12O/10R PS-BFPMM and 12I/6O/10R PS-SFPMM.

Table 7.5 Parameters of prototype machines for PS-BFPMM and PS-SFPMM

Parameter	**12I/12O/10R PS-BFPMM**	**12I/6O/10R PS-SFPMM**	**Parameter**	**12I/12O/10R PS-BFPMM**	**12I/6O/10R PS-SFPMM**
L_{ag} (mm)	0.5		T_{ostto} (mm)	1	1
L_{aa} (mm)	25		T_{osy} (mm)	3	3.4
R_{oso} (mm)	45		θ_{rop} (°)	18	
R_{osi} (mm)	31.75		θ_{rip} (°)	25.2	
R_{iso} (mm)	25.75		T_{rr} (mm)	5	
R_{ist} (mm)	10.4		T_{PM} (mm)	5	
θ_{ostb} (°)	8.12	13.20	L_{PM} (mm)	14.35	
θ_{ostt} (°)	4.94	14.30	T_{bri} (mm)	0.5	
T_{osttb} (mm)	3.0	5.8			

Fig. 7.42 shows the measured and predicted open-circuit phase back-EMFs at rated speed (400rpm). It can be seen that the measured fundamental values are ~8% less than the predictions in both prototype machines due to the end-effect in 25mm stack length machines. Meanwhile, different from 12I/12O/10R PS-BFPMM, the measured 2rd harmonic amplitude of 12I/6O/10R PS-SFPMM is higher than that of FE prediction but lower in 5th harmonic, which is caused by the imperfect manufacturing of 6-pole outer stator and end plates. Fig. 7.43 shows the measured and predicted open-circuit cogging torques of two machines. The maximum amplitudes of measured values match well with the FE predictions in both machines when considering measurement error and end-effect. Meanwhile, compared with 12I/12O/10R PS-BFPMM, the measured waveform of 12I/6O/10R PS-SFPMM is more close to the FE prediction since it has bigger cogging torque. Fig. 7.44 shows the variation of static torque with rotor position at three different armature currents, i.e. 15A, 20A and 25A (I_{DC}=I_A=-2I_B=-2I_C). Fig. 7.45 compares the measured and FE predicted peak torques at different current values. It can be observed that the differences between the measured and FE predicted results rise with the increased current since the influences of saturation and end-effect are enlarged together. Overall, the experimental results match well with the FE predictions.

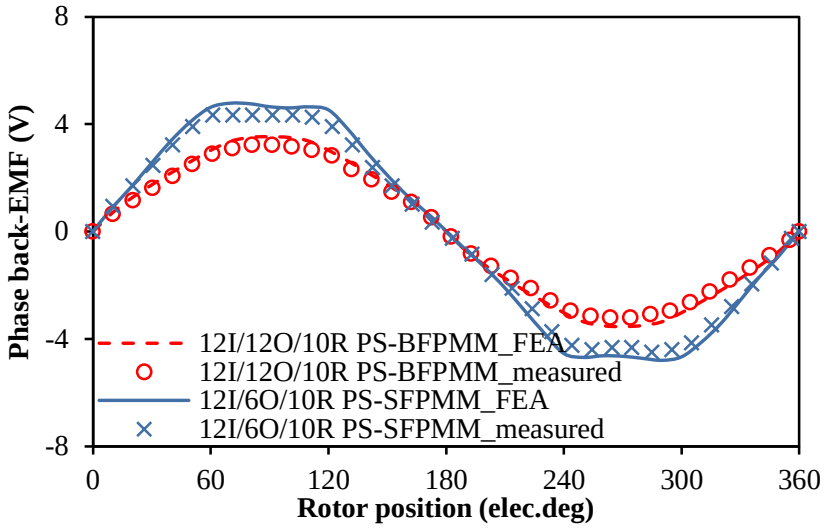

(a) Waveforms

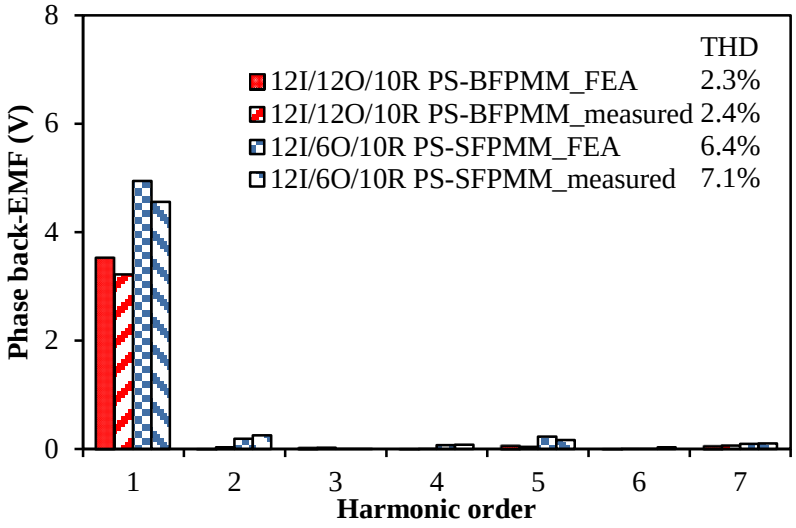

(b) Spectra

Fig. 7.42. Measured and FE predicted open-circuit phase back-EMFs at 400rpm.

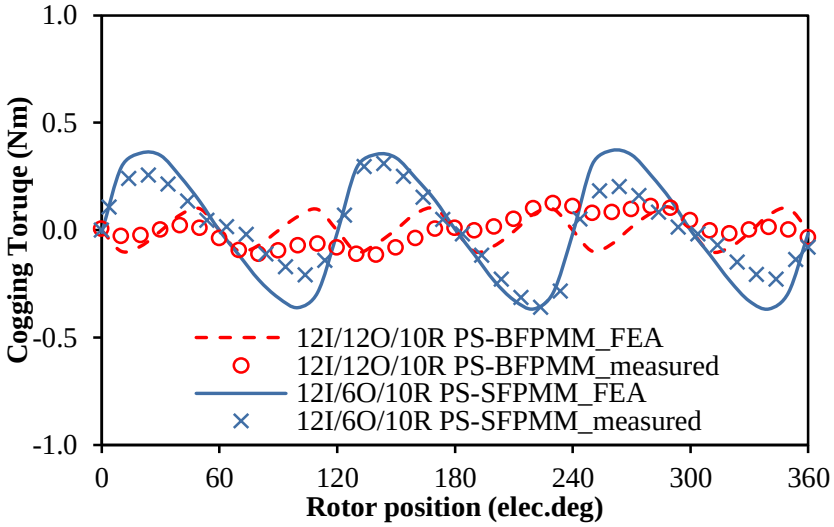

Fig. 7.43. Measured and FE predicted open-circuit cogging torques.

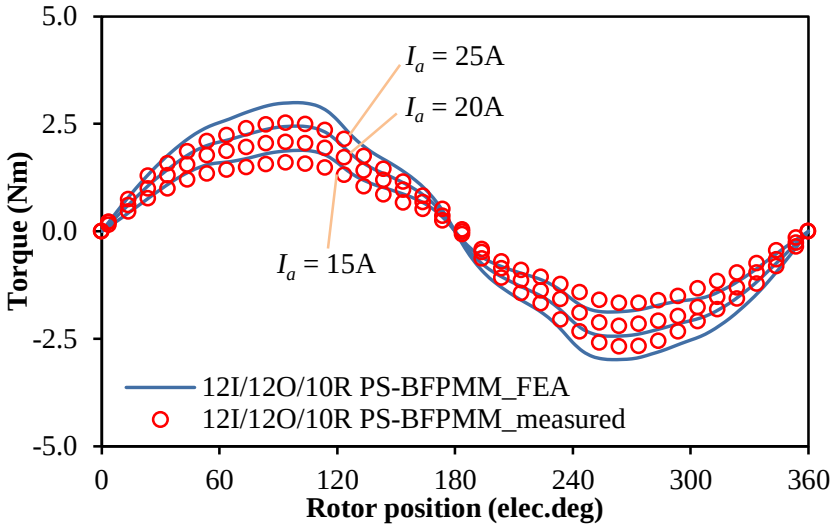

(a) 12I/12O/10R PS-BFPMM

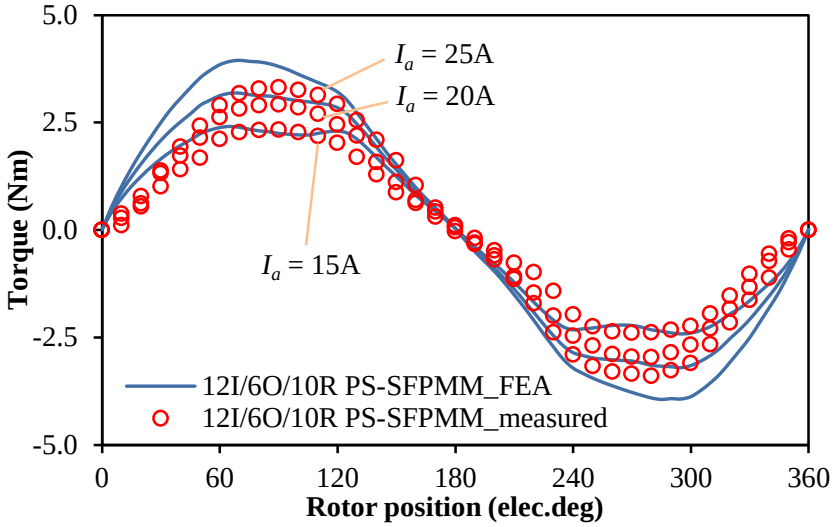

(b) 12I/6O/10R PS-SFPMM

Fig. 7.44. Measured and FE predicted static torques, I_{DC}=I_A=-2I_B=-2I_C.

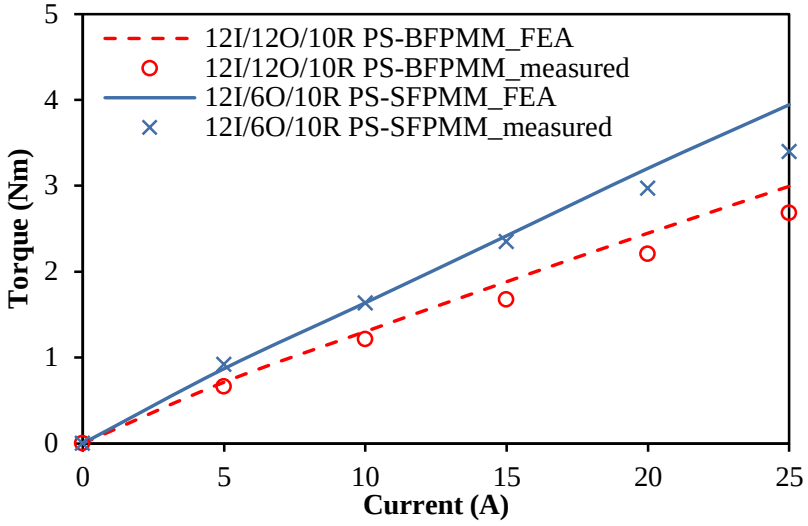

Fig. 7.45. Measured and predicted torque-current characteristics.

7.7 Summary

Based on spoke-IPM stator configuration and minimum 6-pole inner and outer stators, the influences of the ratio of inner/outer stator pole and the relative position of inner and outer stators on electromagnetic performance of partitioned stator PM synchronous machines are analysed and compared in this chapter.

For both PS-BFPMMs and PS-SFPMMs with different inner/outer stator pole ratios, the conditions for symmetrical bipolar phase flux-linkage (phase back-EMF) are consistent, in which the ratio of $Min(N_{os}, N_{is})$ to the greatest common divisor of $Min(N_{os}, N_{is})$ and rotor pole numbers N_r must be even.

The analysis results indicate that the optimal rotor pole number for 12I/12O PS-BFPMM, 12I/12O PS-SFPMM, 6I/12O PS-SFPMM and 12I/6O PS-SFPMM are 10, 11, 11, and 10 respectively. Compared with 12I/12O/10R PS-BFPMM (N_{is}/N_{os}=1), 12I/12O/11R PS-SFPMM exhibits ~13.9% higher fundamental phase back-EMF, ~28% larger average torque and ~15% higher PM utilization efficiency under the rated copper loss. Further, compared with 12I/12O/11R PS-SFPMM (N_{is}/N_{os}=1) under the rated copper loss, 12I/6O/10R PS-SFPMM (N_{is}/N_{os}=2) exhibits ~2% larger average torque and 8% higher PM utilization efficiency while 6I/12O/11R PS-SFPMM has 49% smaller average torque and 29% lower PM utilization efficiency.

By employing the alternate pole wound winding, the average torques are enhanced by about 2.5% and 36% in 12I/12O/11R PS-SFPMM and 6I/12O/11R PS-SFPMM while reduced by about 6.9% and 9.1% in 12I/12O/10R PS-BFPMM and 12I/6O/10R PS-SFPMM. Meanwhile, the PM utilization efficiencies are enhanced by about 2.5% and 55% in 12I/12O/11R PS-SFPMM and 6I/12O/11R PS-SFPMM while reduced by about 6.9% and 9.0% in 12I/12O/10R PS-BFPMM and 12I/6O/10R PS-SFPMM.

Finally, the analyses have been validated by both the FEA and measurements.

7.8 Appendix

The conventional coil EMF vector method can also be used to determine the winding configuration of PS-SFPMM with N_{is}/N_{os}=1/3. Fig. 7.46 shows the machine topology and coil-EMF vectors of 6I/18O/11R PS-SFPMM with N_{is}/N_{os}=1/3. As shown in Fig. 7.47, bipolar coil flux-linkage is observed when the coil-wound outer stator pole aligns with PMs (such as coils A1) whilst unipolar coil flux-linkage would be found when the coil-wound outer stator pole aligned with iron ribs (such as coils A2), which are similar to PS-SFPMM

with N_{is}/N_{os}=1/2 (such as 6I/12O PS-SFPMM shown in Fig. 7.6). Based on the analysis of PS-SFPMM with N_{is}/N_{os}=1/2, to obtain the symmetrical bipolar phase flux-linkage in PS-SFPMM with N_{is}/N_{os}=1/3, three conditions also should be satisfied. Firstly, the coils per phase must even. Secondly, the pairs of coils belong to the same phase must have 180 electrical degree phase shifting (opposite polarities). Thirdly, the phase angles should be same for the resultant flux-linkages for unipolar ones and for bipolar ones. Therefore, to achieve these conditions, the (inner/outer) stator/rotor pole combinations of PS-SFPMM with N_{is}/N_{os}=1/3 should be satisfied with (7.1). By way of example, for 6I/18O/11R PS-SFPMM under investigation, symmetrical bipolar phase flux-linkage is obtained as shown in Fig. 7.47.

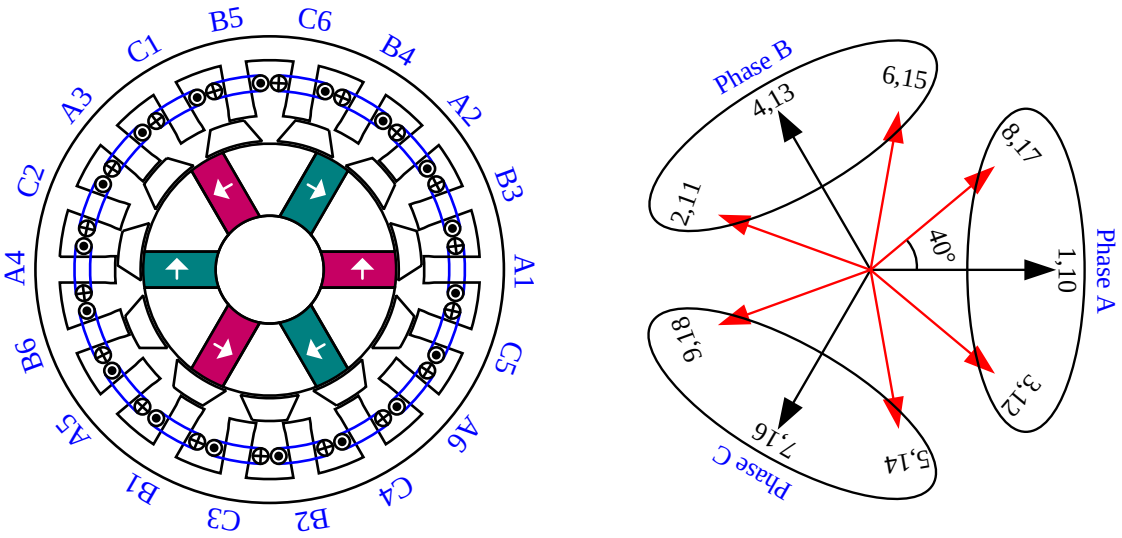

(a) Machine topology (b) Coil-EMF vectors

Fig. 7.46. Machine topology and coil-EMF vectors of 6I/18O/11R PS-SFPMM.

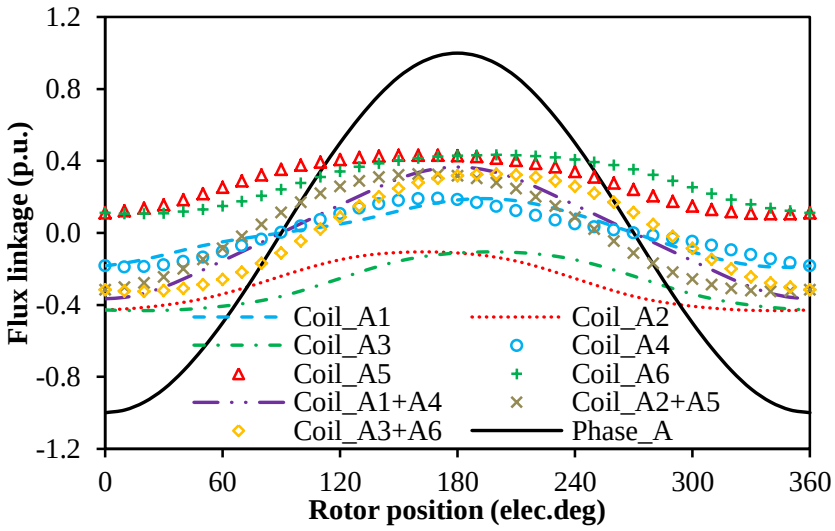

(a) Waveforms

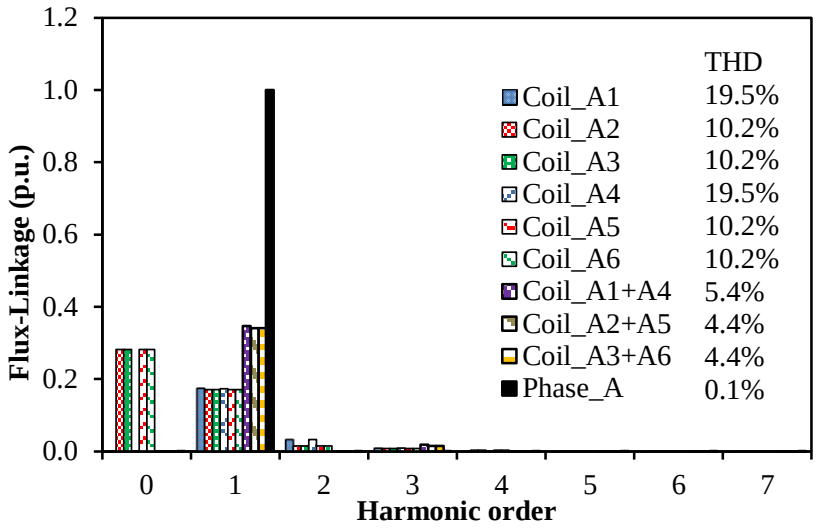

(b) Spectra

Fig. 7.47. Per unit open-circuit coil and phase flux-linkages of 6I/18O/11R PS-SFPMM.

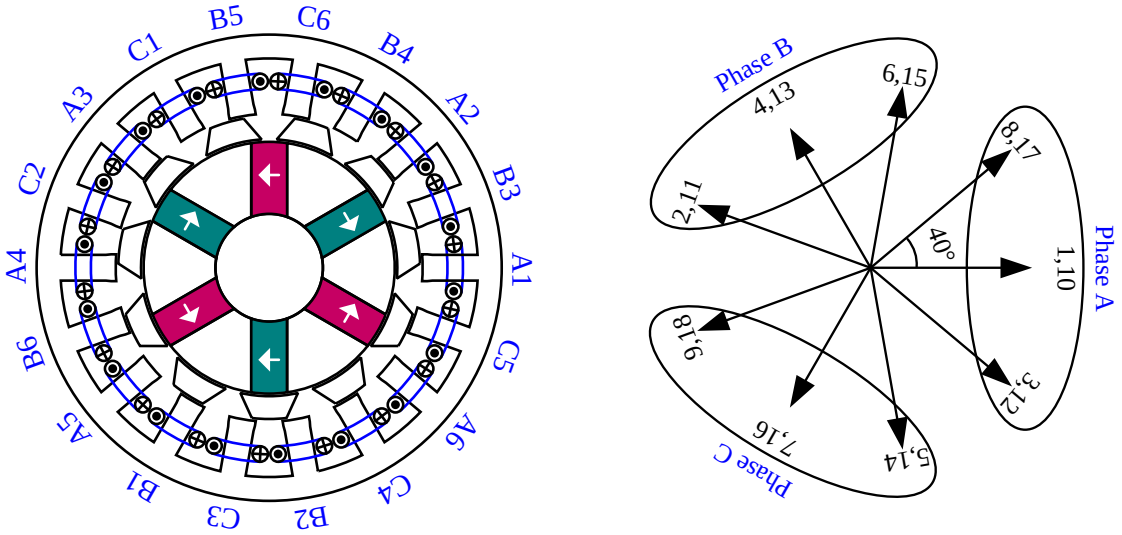

(a) Machine topology (b) Coil-EMF vectors

Fig. 7.48. Machine topology and coil-EMF vector of 6I/18O/11R PS-SFPMM SFPMM with relative position of inner and outer stator have half inner stator pole pitch shifting.

Similar to PS-SFPMM with N_{is}/N_{os}=1/2, the relative position of two stators for 6I/18O PS-SFPMM (N_{is}/N_{os}=1/3) are also free and can be changed. When the inner stator of 6I/18O PS-SFPMM rotates half inner stator pole pitch in clockwise direction, one typical machine topology is proposed and shown in Fig. 7.48(a). The coil-EMF vectors of new 6I/18O/11R PS-SFPMM are shown in Fig. 7.48(b), which is consistent with the original 6I/18O/11R PS-SFPMM. Since all coil-wound outer stator poles are aligned with iron ribs, the coil flux-linkages in this new machine are unipolar, as shown in Fig. 7.49(a). However, according to the analysis shown in section 7.2.1, the conditions of symmetrical bipolar phase flux-linkage

for new 6I/18O PS-SFPMM are the same as those of original 6I/18O PS-SFPMM, in which the (inner/outer) stator/rotor pole combinations of PS-SFPMM with N_{is}/N_{os}=1/3 should be satisfied with (7.1). By way of example, for new 6I/18O/11R PS-SFPMM shown in Fig. 7.49(a), the phase flux-linkage is symmetrical and bipolar as shown in Fig. 7.49. In addition, since the base value of Fig. 7.49 is selected as the magnitude of fundamental phase flux-linkage of original 6I/18O/11R PS-SFPMM, new 6I/18O/11R PS-SFPMM exhibits lower fundamental phase flux-linkage than original 6I/18O/11R PS-SFPMM.

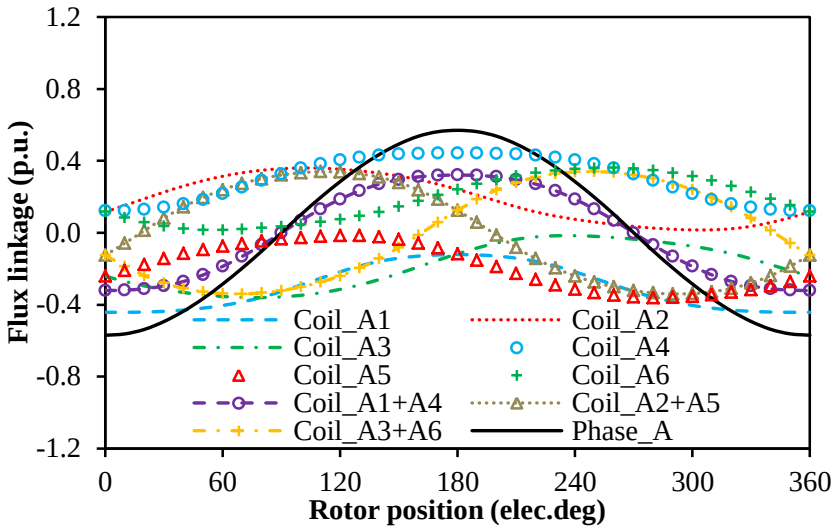

(a) Waveforms

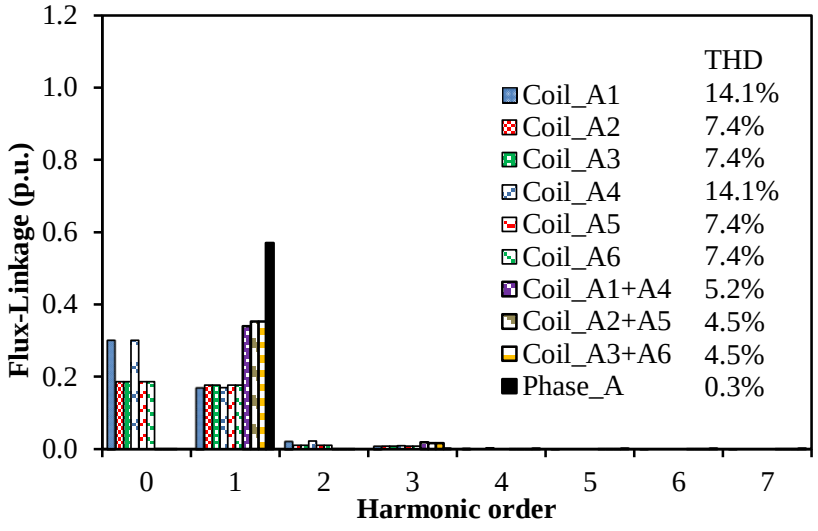

(b) Spectra

Fig. 7.49. Per unit open-circuit coil and phase flux-linkages of 6I/18O/11R PS-SFPMM with relative position of inner and outer stator have half outer stator pole pitch shifting.

CHAPTER 8
INFLUENCE OF INNER STATOR AND ROTOR POLE NUMBER COMBINATIONS ON ELECTROMANGETIC PERFORMANCE OF PARTITIONED STATOR SWITCHED FLUX PM MACHINES

Based on the spoke type interior permanent magnet (spoke-IPM) stator configuration and minimum 6-pole inner and outer stators, the influences of the ratio of inner/outer stator pole (N_{is}/N_{os}) and the relative position of inner and outer stators on electromagnetic performance of partitioned stator PM synchronous machines are analysed and compared in the previous chapter. Meanwhile, the results show that higher torque performance can be observed when $N_{is}/N_{os}>1$. Therefore, in this chapter, the influences of inner stator and rotor pole combinations on electromagnetic performance of partitioned stator switched flux PM machines (PS-SFPMMs) with 6-pole outer stator are investigated in detail.

8.1 Introduction

Switched flux permanent magnet (PM) machines (SFPMMs) have been investigated extensively over last decades due to high torque performance and efficiency as well as simple and robust rotor [RAU55] [HOA97] [ZHU05]. Since the PMs are located in the stator, easy heat dissipation and low risk of demagnetization also are the merits of SFPMMs [ZHU05]. Compared with the conventional PM brushless machines, the reluctance torque of SFPMMs is negligible [ZHO13b]. Hence, the electromagnetic torque of SFPMMs is mainly depending on the PM flux-linkage, armature current (q-axis) and rotor pole number. In other words, superior trade-off among the PM volume (shape) and armature winding space (slot area) and rotor pole number is the key factor on maximizing the torque of SFPMMs. Based on this guideline, different topologies of SFPMMs are proposed in [ZHO13b] [CHE11a] [CHE11b] [CHE08]. Compared with conventional SFPMM, C-core [CHE11b] and E-core [CHE11a] SFPMMs adopt the strategy of reducing the PM and stator tooth volume to increase the slot area whilst sandwiched SFPMM (SSFPMM) [4] combines two adjacent stator poles to achieve the same goal. In addition, splitting the original stator teeth into more small teeth per stator pole (reduce the slot area) and increasing the number of rotor poles are the designs which are used in multi-tooth SFPMM (MTSFPMM). Overall, the torque capabilities of

SFPMMs are enhanced by these means under the same machine size and rated copper loss [ZHU10].

However, the pursuit on higher torque capability is continuing forever. In order to further enhance the torque capability of SFPMMs, one effective solution is to increase the whole volume of stator within the same machine scale. The concept of partitioned stator configuration has been introduced, which is applied to the SFPMMs as partitioned stator SFPMMs (PS-SFPMMs) [EVA15]. In this way, the conflicts between PMs, armature windings and stator iron in conventional SFPMM which limit the torque capability are solved since the inner space is fully utilized. Thus, the torque capability is improved significantly in PS-SFPMMs when compared with conventional SFPMMs [EVA15].

Nevertheless, the previous investigation on PS-SFPMMs only considers the inner/outer stator pole ratio n' ($n'=N_{is}/N_{os}$) equal to 1. Actually, the inner/outer stator pole ratio n' can be any integers. Furthermore, by using the partitioned stator configuration, it is much easier to implement the designs when n' is bigger than 1, since the PMs are located in separated inner stator.

In this chapter, the influence of inner stator and rotor pole combinations on electromagnetic performance of PS-SFPMMs will be investigated. Firstly, the machine topologies and operational principle are illustrated. Then, the optimal inner stator and rotor pole combinations having different n' are investigated under the rated copper loss with the 6-pole outer stator. Further, based on the individual optimal inner stator and rotor pole combinations, the electromagnetic performance of PS-SFPMMs with n' equal to 1, 2, 3 and 4 are analyzed and compared. Finally, a prototype machine with 12-inner/6-outer stator/10 rotor pole (12I/6O/10R) PS-SFPMM is manufactured and measured to validate the analyses.

8.2 Operation Principle and Stator/Rotor Pole Number Combinations of PS-SFPMMS

8.2.1 Machine Topologies and Operation Principle

Partitioned stator switched flux permanent magnet machines (PS-SFPMMs) with inner/outer stator pole ratio n' ($n'=N_{is}/N_{os}$) equal to one is shown in Fig. 8.1(a). However, n can be any integers since the PMs are located in separated inner stator. Based on this conclusion, several configurations of PS-BFPMMs with $n' > 1$ are shown in Fig. 8.1(b), (c) and (d) as examples, which corresponds to n' equal to 2, 3 and 4 respectively. Further, according to the analyses in section of 7.2, to maximize the fundamental phase flux-linkage

(torque performance), the PM of inner stator pole should be aligned with outer stator pole when n' is odd while the iron rib of inner stator pole should be aligned with outer stator pole when n' is even, as shown in Fig. 8.1.

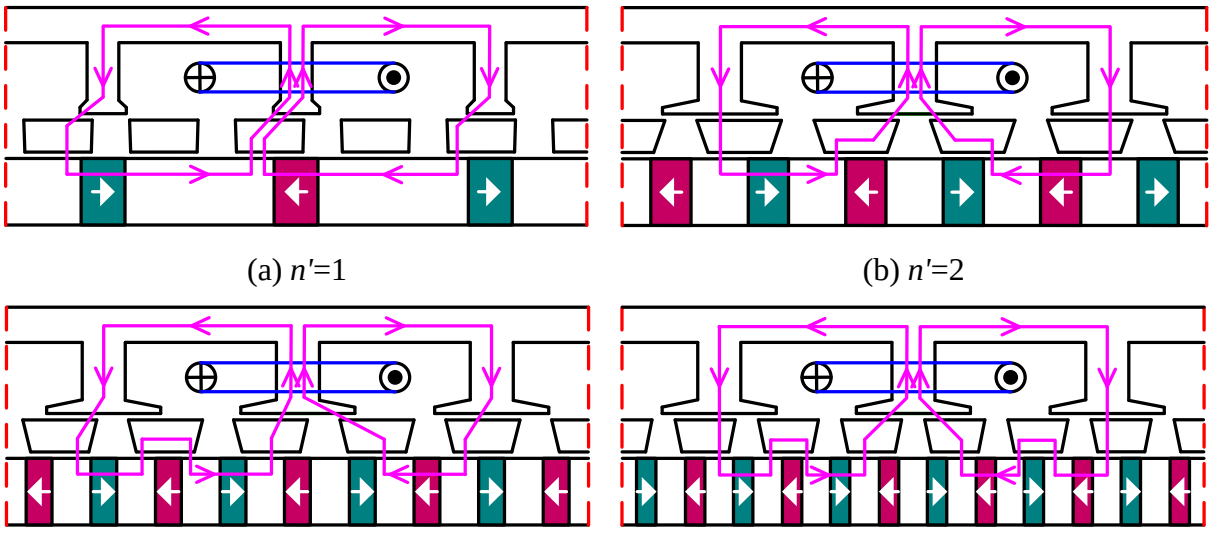

(a) n'=1 (b) n'=2

(c) n'=3 (d) n'=4

Fig. 8.1. Schematic diagrams of PS-SFPMMs with different n' at negative d-axis (negative maximum phase flux-linkage)

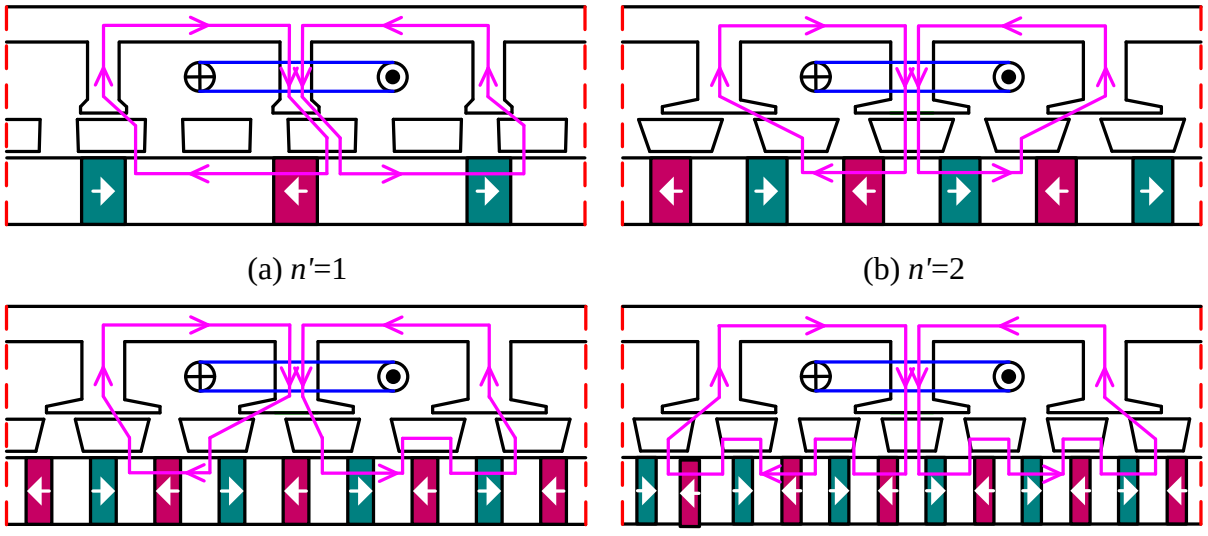

(a) n'=1 (b) n'=2

(c) n'=3 (d) n'=4

Fig. 8.2. Schematic diagrams of PS-SFPMMs with different n' at positive d-axis (positive maximum phase flux-linkage).

Based on the optimal relative positions of inner and outer stators, the main PM flux paths of PS-SFPMMs with different n' corresponding to the negative d-axis and positive d-axis are also illustrated in Fig. 8.1 and Fig. 8.2 respectively. It can be seen that the main flux passing

through one single coil are consisted with two separate flux loops in all PS-SFPMMs with different n'. Meanwhile, for one complete single flux loop of PS-SFPMMs with $n' > 2$, the flux has to pass through more than one PM, as shown in Fig. 8.1(c) and (d) as well as Fig. 8.2(c) and (d).

The basic operational principles of PS-SFPMMs with different n' are consistent. For PS-SFPMMs with n' being odd, it can be seen from Fig. 8.1(a) and (c) when the right edge of rotor is aligned with outer stator pole, the flux flows from inner stator side to outer stator side through the modular rotor, while in Fig. 8.2(a) and (c), when the left edge of rotor is aligned with outer stator pole, the direction of flux is reversed. Then, for PS-SFPMMs with n' being even, it can be seen from Fig. 8.1(b) and (d) when the rotor slot is aligned with outer stator pole, the flux flows from inner stator side to outer stator side through the modular rotor, while in Fig. 8.2(b) and (d), when the modular rotor is aligned with outer stator pole, the direction of flux is reversed. Therefore, for PS-SFPMMs with different n', back-EMF will be induced in the coils by periodical variation of flux-linkage (flux) with rotor position.

8.2.2 Inner Stator and Rotor Pole Number Combinations

Similar to the conventional SFPMMs, the choice of rotor pole number N_r is also flexible in PS-SFPMMs. No matter what n' is selected, N_r can be any integers except the phase number and its multiples. Meanwhile, considering the investigation in this chapter, the selections of N_{os}, N_{is}, and N_r can be normally summarized as

$$N_{os} = km \ (k = 1, 2\ldots) \tag{8.1}$$

$$N_{is} = n' N_{os} \ \ (n = 1, 2\ldots) \tag{8.2}$$

$$N_r = \mu N_{os} \pm j \ (N_r \neq k_i m, j=1, 2\ldots, k_i=1.\ 2\ldots) \tag{8.3}$$

where m is the phase number, k, n', μ, j and k_i are integers.

Based on the 6-pole outer stator (N_{os}=6, the minimum stator pole number in unit conventional SFPMM is normally defined as 6) and the optimal relative position of inner and outer stators, the torque variations of PS-SFPMMs with different n' and rotor pole number under the rated 30W copper loss are shown in Fig. 8.3. Obviously, for PS-SFPMMs with different n', the maximum average torque is improved with the increased n'. Meanwhile, PS-SFPMMs with n' equal to 3 and 4 have similar maximum average torque, which means the aggravated saturation and leakage flux caused by increased n' will also limit the enhancement of torque performance. Then, according to the maximum average torque as shown in Fig. 8.3

with black marks, the optimal inner stator/rotor pole combinations (N_{is}/N_r) for 6-pole outer stator PS-SFPMMs with n' equal to 1, 2, 3 and 4 are 6I/11R (6-inner stator/11-rotor pole), 12I/10R, 18I/11R and 24I/14R respectively. Further, based on the results mentioned above and shown in Fig. 8.3, the guideline to search for the optimal N_r in PS-SFPMMs with different n' can be roughly derived and summarized. Firstly, the optimal N_r is closed to $(N_{os}+N_{is})/2$. Secondly, optimal N_r is odd when n' is odd while it is even when n' is even.

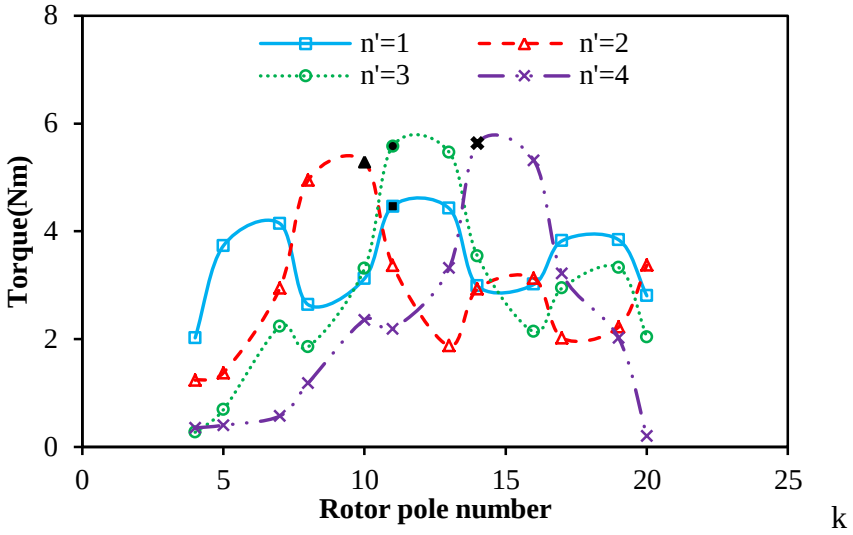

Fig. 8.3. Variation of average torque with rotor pole number under different n' and 6-pole outer stator, p_c=30W.

The topologies of 6-pole outer stator PS-SFPMMs with the optimal 6I/11R, 12I/10R, 18I/11R and 24I/14R inner stator/rotor pole combinations for n' equal to 1, 2, 3 and 4 are shown in Fig. 8.4. As mentioned in section 8.2.1 above, the PMs of inner stator poles are aligned with outer stator poles when n' is odd while the iron ribs of inner stator poles are aligned with outer stator poles when n' is even, as shown in Fig. 8.4. All the machines are globally optimized by generic algorithm with the objective of maximum average torque under the 30W rated copper loss and same machine size. The main geometric parameters are detailed in Table 8.1.

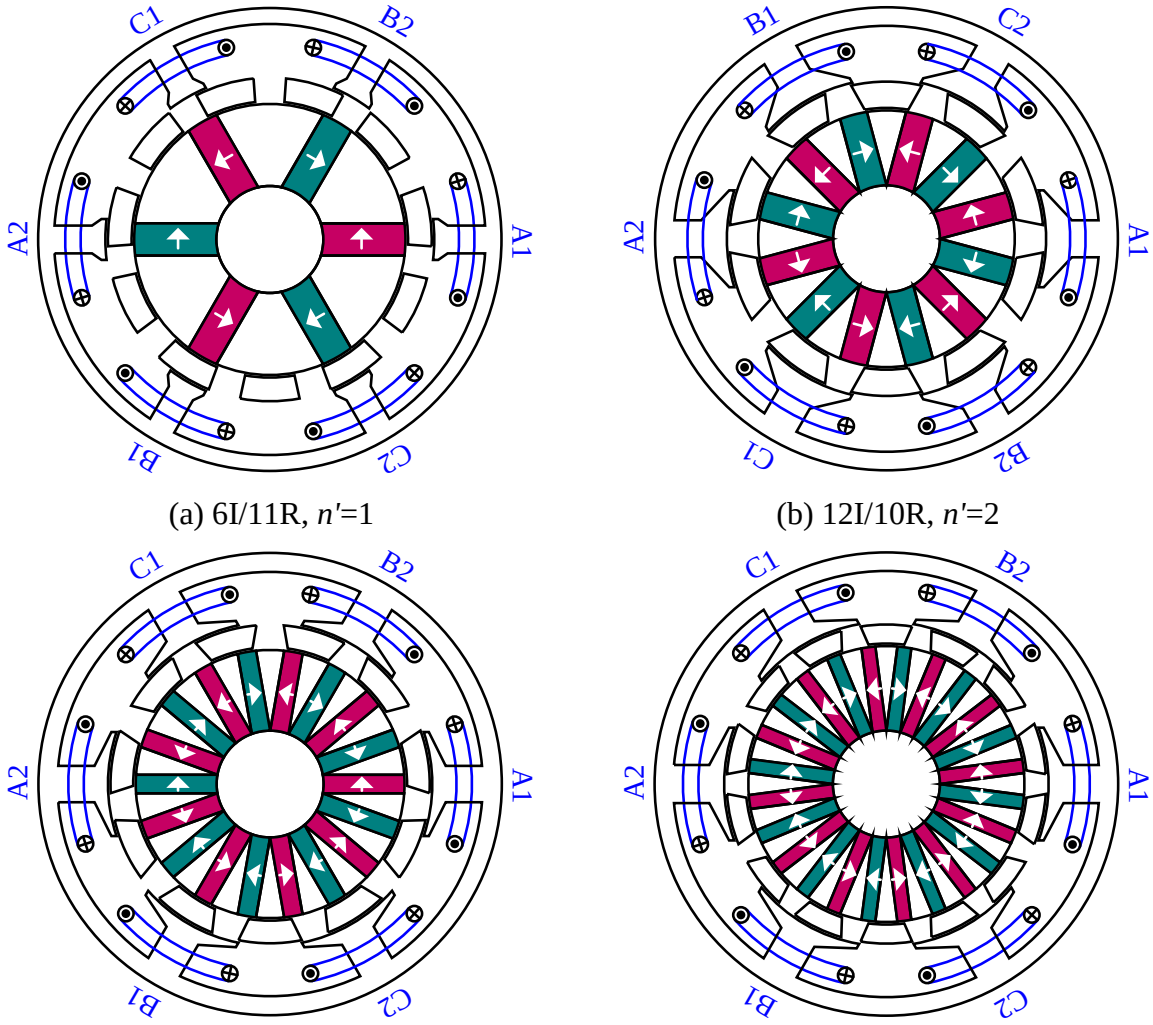

(a) 6I/11R, n'=1 (b) 12I/10R, n'=2

(c) 18I/11R, n'=3 (d) 24I/14R, n'=4

Fig. 8.4. Topologies of 6-pole outer stator PS-SFPMMs with different optimal inner stator/rotor pole combinations.

8.2.3 Winding Configurations

As mentioned in section 6.2 and section 7.2, the conventional coil-EMF vector method [ZHU10] can be used to determine the armature winding configuration of PS-SFPMMs with different N_{is}/N_{os}, in which the electrical degree α_e between two adjacent coil-EMF vectors can be calculated from the mechanical degree α_m and N_r. According to (6.1), the winding configurations of 6-pole outer stator PS-SFPMMs with 6I/11R, 12I/10R, 18I/11R and 24I/14R inner stator/rotor pole combinations are shown in Fig. 8.5, Fig. 8.6 and Fig. 8.7 as mechanical and electric degrees respectively. Coil k and coil k' refer to the coils with opposite polarities, accounting for the alternate magnetization directions in adjacent stator poles.

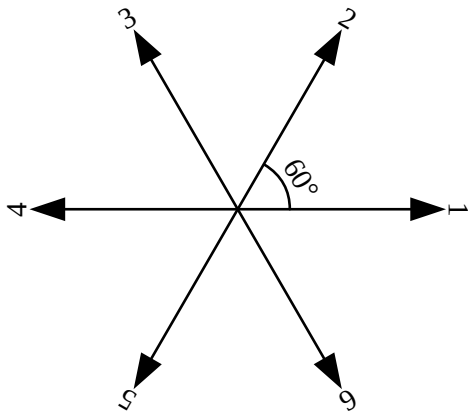

Fig. 8.5. Coil-EMF vectors of 6-pole outer stator PS-SFPMMs in mechanical degree.

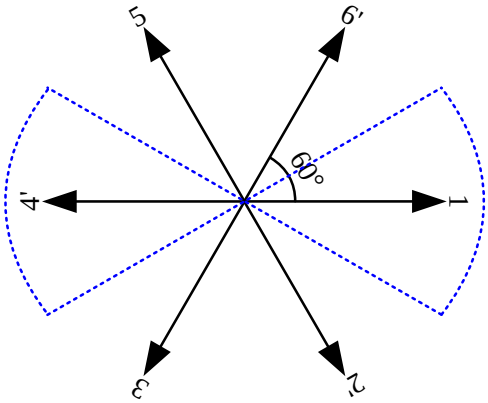

(a) 6I/11R, n'=1

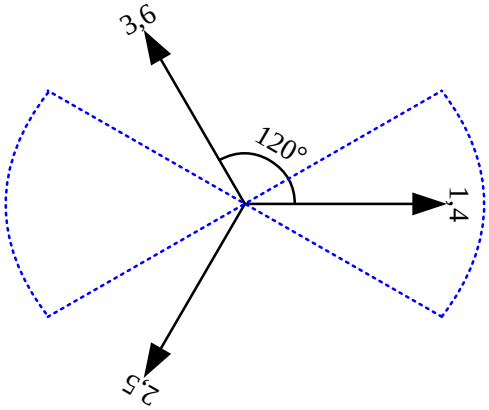

(b) 12I/10R, n'=2

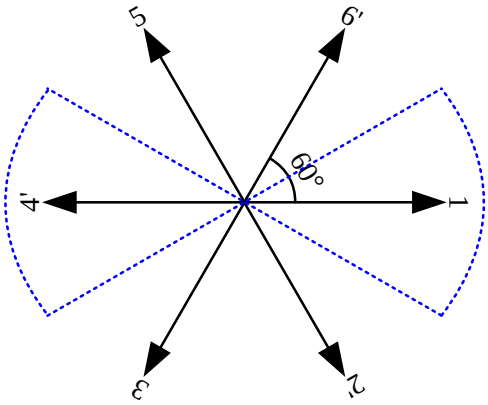

(c) 18I/11R, n'=3

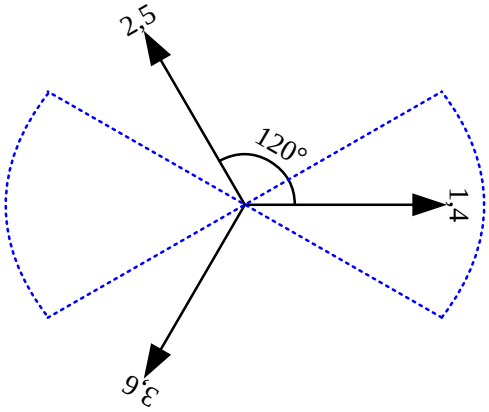

(d) 24I/14R, n'=4

Fig. 8.6. Coil-EMF vectors of 6-pole outer stator PS-SFPMMs in electric degree and sectors for determining phase winding.

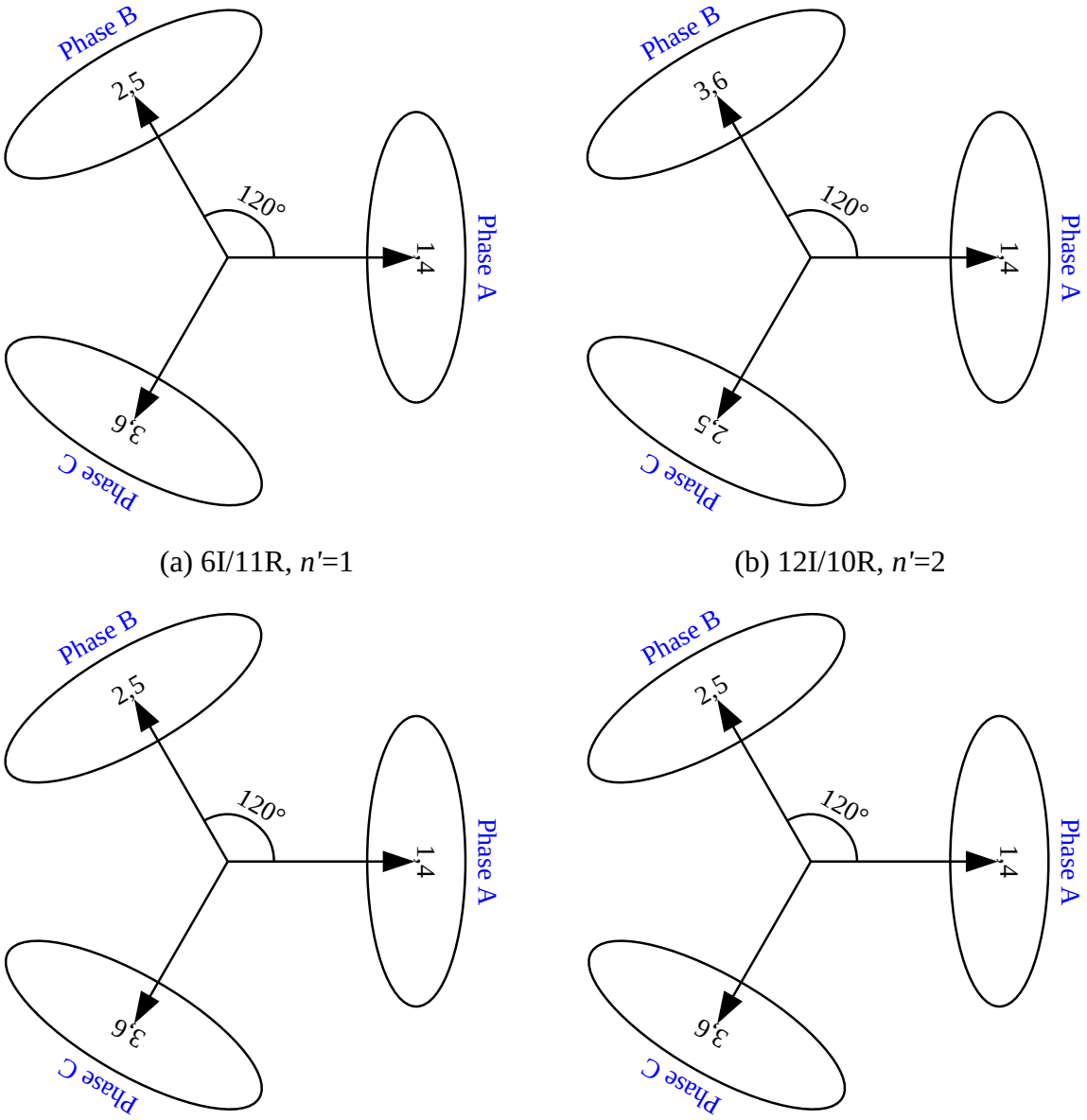

(a) 6I/11R, n'=1 (b) 12I/10R, n'=2

(c) 18I/11R, n'=3 (d) 24I/14R, n'=4

Fig. 8.7. Phase winding configurations of 6-pole outer stator PS-SFPMMs.

8.2.4 Conditions for Symmetrical Bipolar Phase Flux-Linkage and Phase Back-EMF

According to the analyses in section 7.2, symmetrical bipolar phase flux-linkage (phase back-EMF) can be obtained in PS-SFPMM with different N_{is}/N_{os} when the ratio of $Min(N_{os}, N_{is})$ to the greatest common divisor of $Min(N_{os}, N_{is})$ and rotor pole numbers N_r are even. In other word, the inner/outer stator/rotor pole combinations should be satisfied with (7.1). Therefore, among the four machines, symmetrical bipolar phase flux-linkage (phase back-EMF) will be obtained in 6-pole outer stator PS-SFPMMs with 6I/11R and 18I/11R inner stator/rotor pole combinations since the even harmonics which cause the dc biased value and asymmetric in single coils can be completely cancelled in phase winding by connecting the

coils belong the same phase with 180 electrical degree phase shifting (opposite polarities) as shown in Fig. 8.6 and Fig. 8.7.

Table 8.1 Main parameters of 6-pole outer stator PS-SFPMMs with optimal N_{is}/ N_r

Parameter	**6-pole outer stator PS-SFPMMs**			
Inner stator/rotor pole combinations	**6I/11R**	**12I/10R**	**18I/11R**	**24I/14R**
Number of phases	3			
Turns per phase (N_{ph})	72			
Rated speed (rpm)	400			
Rated copper loss (W)	30			
Packing factor	0.5			
Air-gap length L_{ag} (mm)	0.5			
Active axial length L_{aa} (mm)	25			
Outer stator outer radius R_{oso} (mm)	45			
Inner stator inner radius R_{ist} (mm)	10.4			
Outer stator (OS) pole number, N_{os}	6	6	6	6
Inner stator (IS) pole number, N_{is}	6	12	18	24
Rotor pole number, N_r	11	10	11	14
OS inner radius R_{ost} (mm)	31.95	31.05	31.50	31.50
IS outer radius R_{iso} (mm)	26.35	24.95	26.1	26.8
OS tooth body pole arc θ_{ostb} (°)	9.7	13.3	12.9	13.5
OS tooth tip pole arc θ_{ostt} (°)	2.3	11.0	12.3	13.6
OS tooth tip thickness (Opening) T_{ostto} (mm)	1	1	1	1
OS tooth tip thickness (Body) T_{osttb} (mm)	2.7	5.2	2.8	3.1
Rotor outer pole arc θ_{rop} (°)	21.2	26.0	22.9	18.6
Rotor inner pole arc θ_{rip} (°)	20.6	19.2	17.9	14.6
Rotor radial thickness T_{rr} (mm)	4.6	5.1	4.4	3.7
OS yoke thickness T_{osy} (mm)	3.1	3.6	3.7	3.6
Rated AC current (A_{rms})	17.84	16.91	16.87	16.81
Rated current density (A_{rms}/mm^2)	8.55	9.02	9.05	9.08
PM inner pole arc θ_{PM} (°)	35	30	20	15
Magnetic remanence (T)	1.2			
Relative PM permeability	1.05			

8.3 Performance Comparison between 6-Pole Outer Stator PS-SFPMMs with Optimal N_{is}/N_r

In this section, the electromagnetic performance of 6-pole outer stator PS-SFPMMs with 6I/11R, 12I/10R, 18I/11R and 24I/14R inner stator/rotor pole combinations will be analyzed and compared in detail since they represent the optimal inner stator/rotor pole combinations with n' equal to 1, 2, 3 and 4.

8.3.1 Open-Circuit Field Distribution

The open-circuit flux equipotential and flux density distributions for four PS-SFPMMs at the negative *d*-axis are shown in Fig. 8.8. It can be seen that all machines have short flux path which could result in lower MMF drop in the stator and thinner thickness of stator yoke. Meanwhile, the flux loop of the coils belong to same phase are completely independent. Since the PMs are located in the inner stator, leakage flux exists inside of the inner stator but is quite small compared with main flux. In addition, the heavy saturations for all machines are occurred on the positions when the rotor nearly aligns with PMs of inner stator and has contact surface with outer stator simultaneously. It also can be reflected by the waveforms of open-circuit air-gap flux density distributions at negative *d*-axis as shown in Fig. 8.9. Since the PS-SFPMMs have two layers of air-gap, the waveforms are focused on the layer which close to the stator wound with AC armature winding.

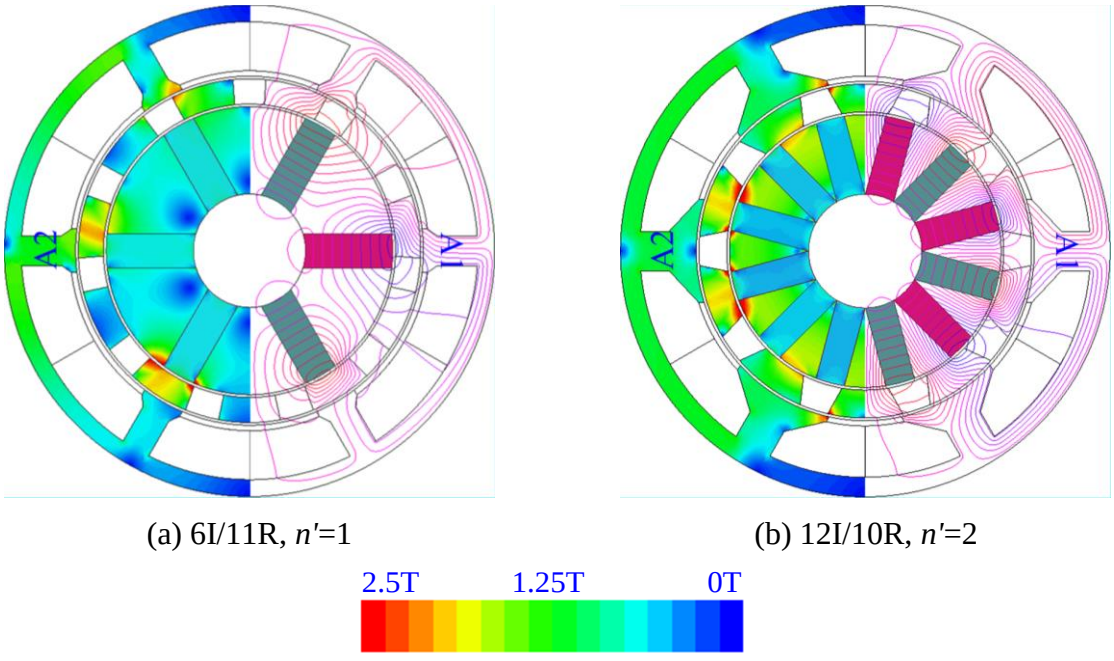

(a) 6I/11R, n'=1 (b) 12I/10R, n'=2

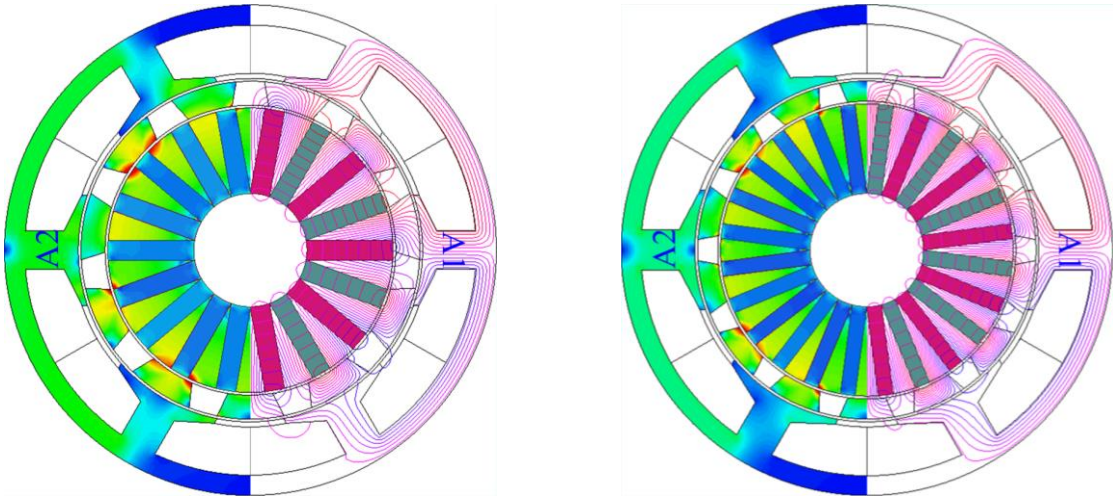

(c) 18I/11R, n'=3 (d) 24I/14R, n'=4

Fig. 8.8. Open-circuit equipotential and flux distributions at negative d-axis for all PS-SFPMMs.

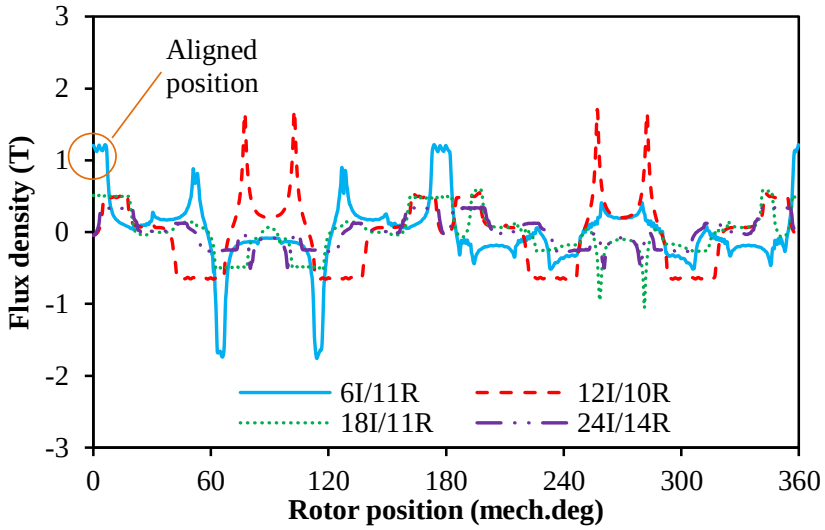

Fig. 8.9. Open-circuit air-gap flux density at negative *d*-axis for all PS-SFPMMs.

8.3.2 Flux-Linkage and Back-EMF Waveforms

As shown in Fig. 8.10 and Fig. 8.11, the coil and phase flux-linkages are bipolar in PS-SFPMMs whatever the selections of n' and rotor pole number. Meanwhile, it can be seen that the coil flux-linkage waveforms for all PS-SFPMMs are asymmetric (slant to right or left in half cycle when n' is odd while different positive and negative peak values in half cycle when n' is even) due to the even harmonics. However, with the influence of outer stator and rotor pole combinations, symmetrical bipolar phase flux-linkages are obtained in 6I/11R and 18I/11R PS-SFPMMs since the even harmonics are completely cancelled in phase winding by connecting the coils belong the same phase with 180 electrical degrees phase shifting (opposite polarities), as shown in Fig. 8.6 and Fig. 8.11. Therefore, these two examples can

be used to validate (7.1) and the conclusions mentioned in section 8.2.4. Further, among four machines, 12I/10R and 18I/11R PS-SFPMMs exhibit similar highest fundamental flux-linkages, and then followed by 24I/14R PS-SFPMM, as shown in Fig. 8.11(b) and Table 8.2.

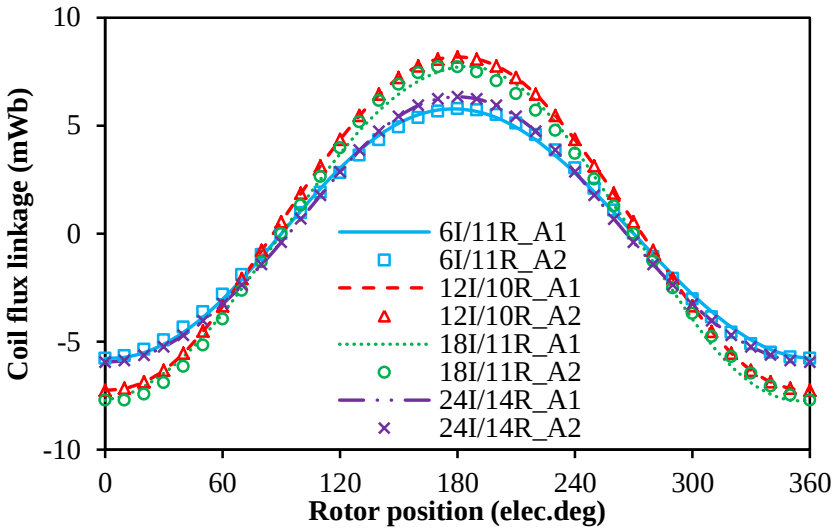

Fig. 8.10. Open-circuit coil flux-linkages of all PS-SFPMMs.

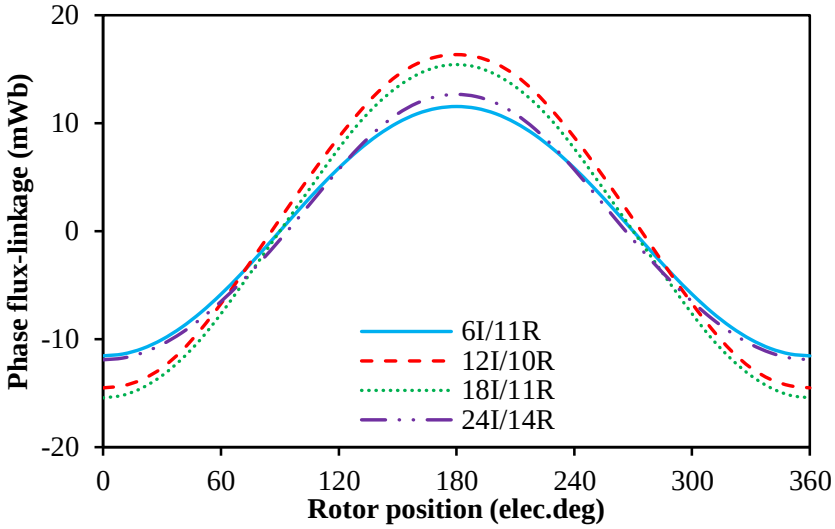

(a) Waveforms

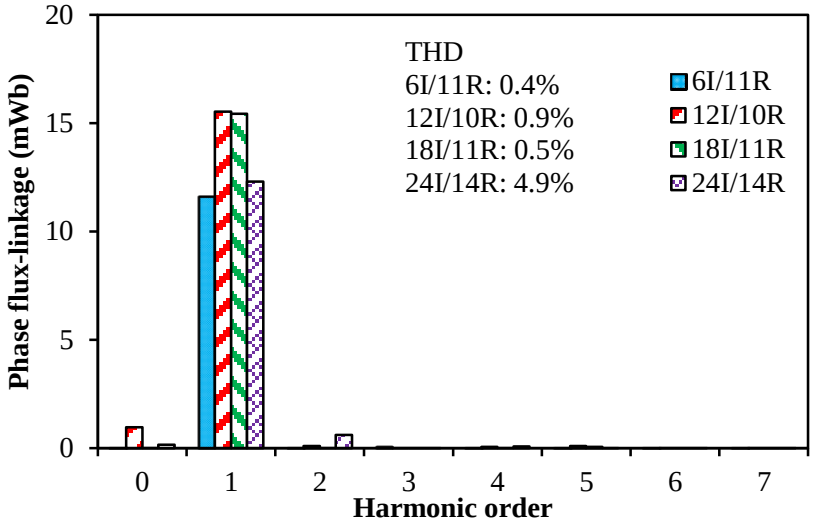

(b) Spectra

Fig. 8.11. Open-circuit phase flux-linkage of PS-SFPMMs for all PS-SFPMMs.

Based on the similar influence caused by even harmonics in coil flux-linkage, the coil back-EMF waveforms in four machines are also asymmetric, in which positive and negative peak values in half cycle are different when n' is odd while slant to right or left in half cycle when n' is even, as shown in Fig. 8.12. Similar to the phase flux-linkages, symmetrical phase back-EMFs are also obtained in 6I/11R and 18I/11R PS-SFPMMs since the even harmonics are completely cancelled in the phase windings, as shown in Fig. 8.13. Meanwhile, due to the influence of rated electrical frequency, 24I/14R and 18I/11R PS-SFPMMs exhibit similar highest fundamental back-EMF, and then followed by 12I/10R PS-SFPMM, as shown in Fig. 8.13(b) and Table 8.2.

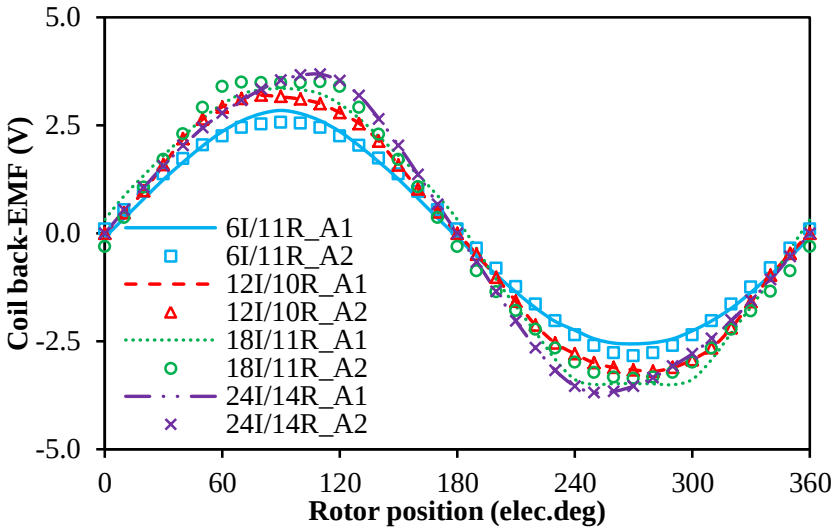

Fig. 8.12. Open-circuit coil back-EMFs for all PS-SFPMMs, 400rpm.

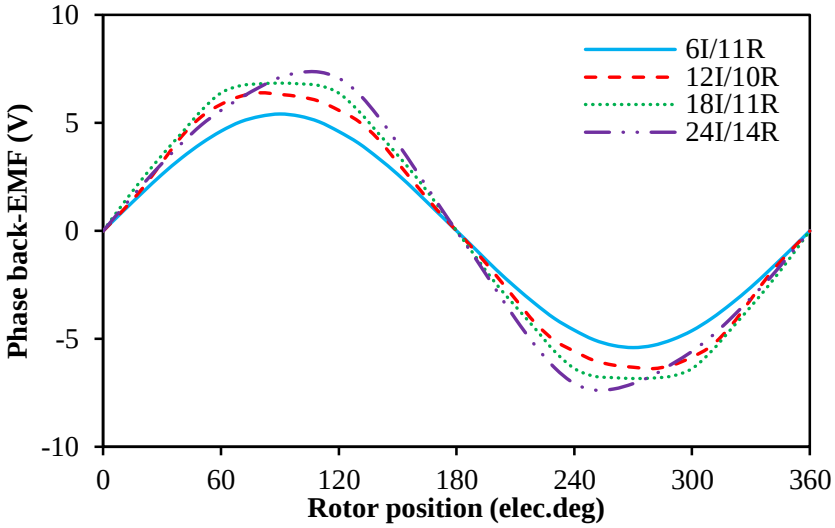

(a) Waveforms

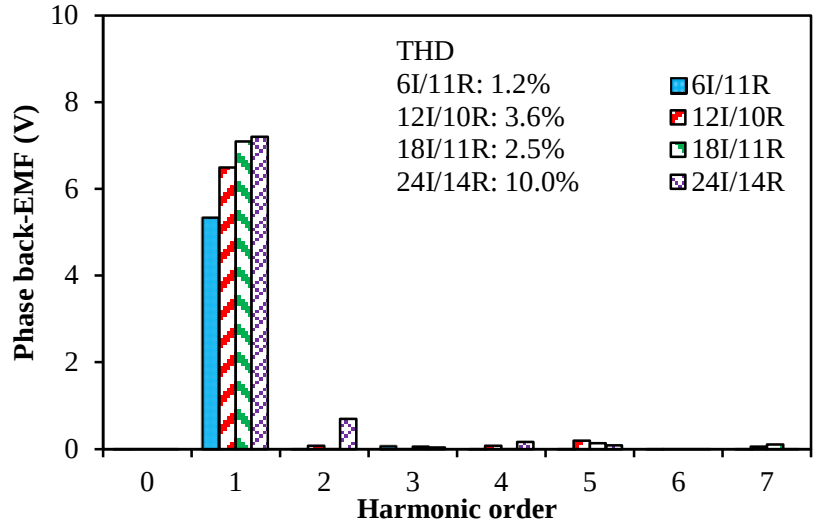

(b) Spectra

Fig. 8.13. Open-circuit phase back-EMFs for all PS-SFPMMs, 400rpm.

8.3.3 Dq-Axis Inductances

The *dq*-axis inductances against current angles for four PS-SFPMMs at rated currents (corresponding to 30W copper loss) are compared in Fig. 8.14. It can be seen that the *dq*-axis inductances of PS-SFPMMs are raised with the increase of *n'*. Meanwhile, the *q*-axis inductances are slightly larger than *d*-axis inductances when current angle close to 0° but reversed when current angle close to 90°. Further, the saliency ratios are close to 1 for all machines since difference between *dq*-axis inductances is quite small. Hence, the potential reluctance torque can be negligible in all PS-SFPMMs with different *n'*.

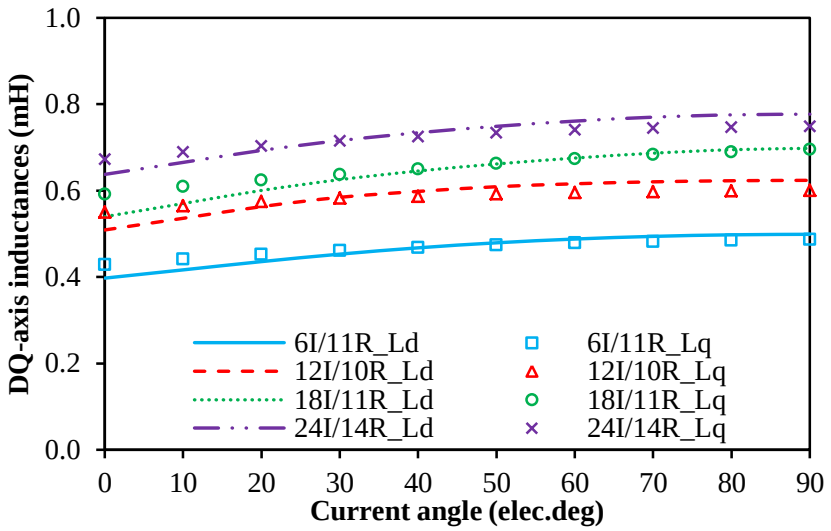

Fig. 8.14. Variation of *dq*-axis inductances with current angle under the rated currents as given in Table 8.1, p_c=30W.

8.3.4 Cogging Torque

Fig. 8.15 compares the cogging torque for four PS-SFPMMs over one electric period. It can be seen that 12I/10R PS-SFPMM exhibits the largest magnitude of cogging torque while 18I/11R PS-SFPMM has the smallest value.

According to the analyses shown in section 7.3.5, equation (7.2) can be used to calculate the cycle number of cogging torque over one electric period for PS-SFPMMs with different *n'*. Therefore, the cycle numbers of cogging torque for 6I/11R, 12I/10R, 18I/11R and 24I/14R PS-SFPMMs with 6-pole outer stator should be 6, 3, 6 and 3 respectively, and these results are evidenced by the waveforms of cogging torque shown in Fig. 8.15.

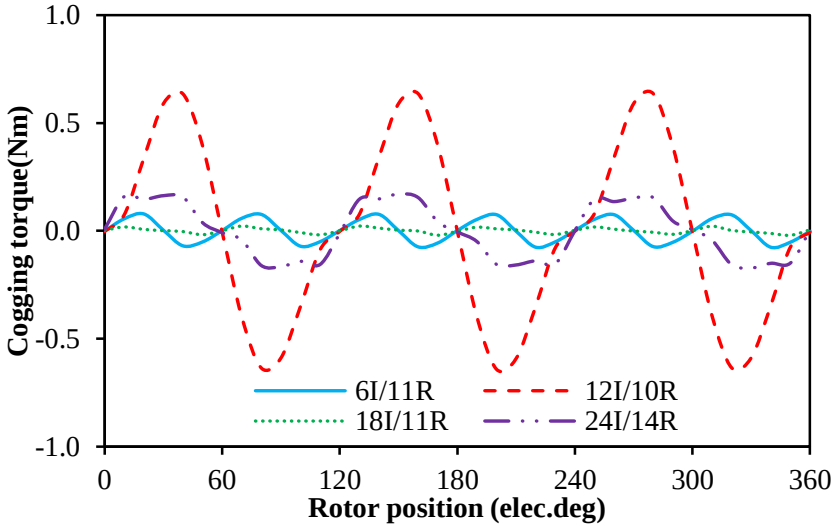

(a) Waveforms

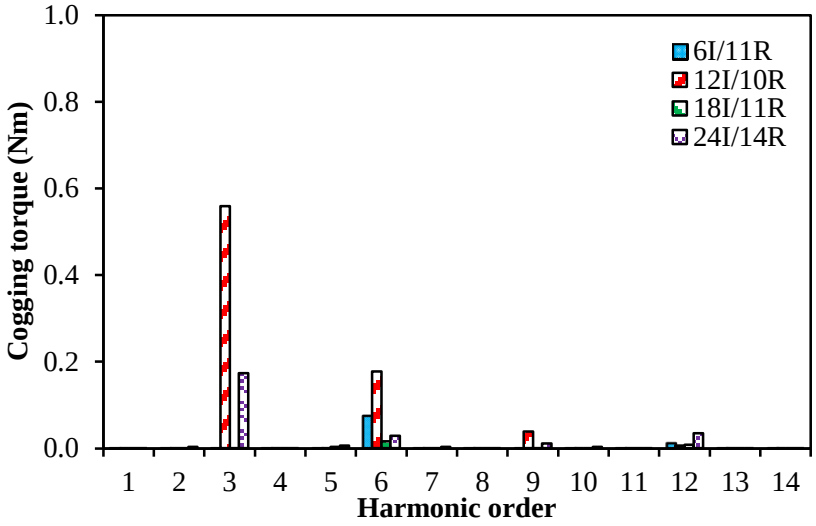

(b) Spectra

Fig. 8.15. Open-circuit cogging torque for all PS-SFPMMs.

8.3.5 Electromagnetic Torque Characteristics

Fig. 8.16 shows the waveforms of average torque against current angle at rated currents (corresponding to p_c=30W) for all machines. Obviously, the reluctance torque can be negligible in PS-SFPMMs whatever n' is selected since the optimal current angles are all close to 0°. This result is consistent with the conclusion mentioned in section 8.3.3.

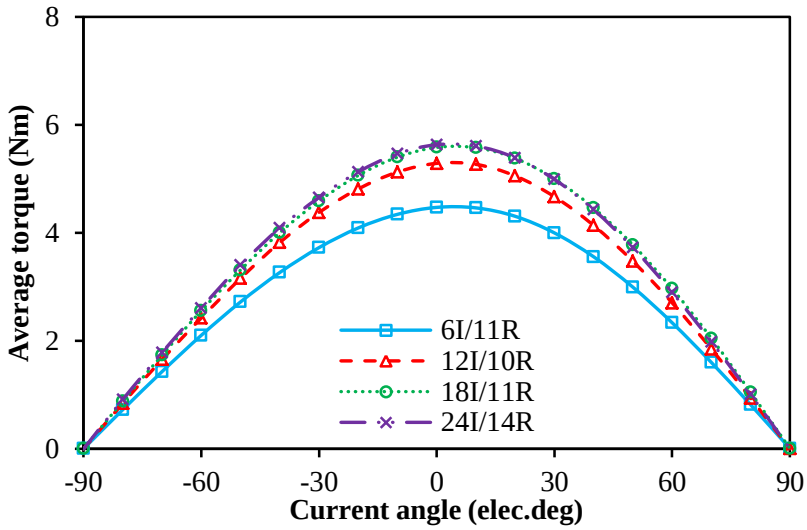

Fig. 8.16. Variation of average torque with current angle under the rated currents as given in Table 8.1, p_c=30W.

Fig. 8.17 shows the waveforms of torque against rotor position at rated currents (corresponding to p_c=30W) and I_d=0 control. Due to the combined influences of cogging torque and back-EMF harmonics, the cycle numbers of torque ripple over one electric period

are six for 6I/11R and 18I/11R PS-SFPMMs while those are three for 12I/10R and 24I/14R PS-SFPMMs. Further, as shown in Table 8.2, the torque ripple of 6I/11R, 12I/10R, 18I/11R and 24I/14R PS-SFPMMs are 2.1%, 26.9%, 3.6% and 20.4% respectively. Obviously, among those four machines, 6I/11R PS-SFPMM exhibits the smallest torque ripple while 12I/10R PS-SFPM has the largest one.

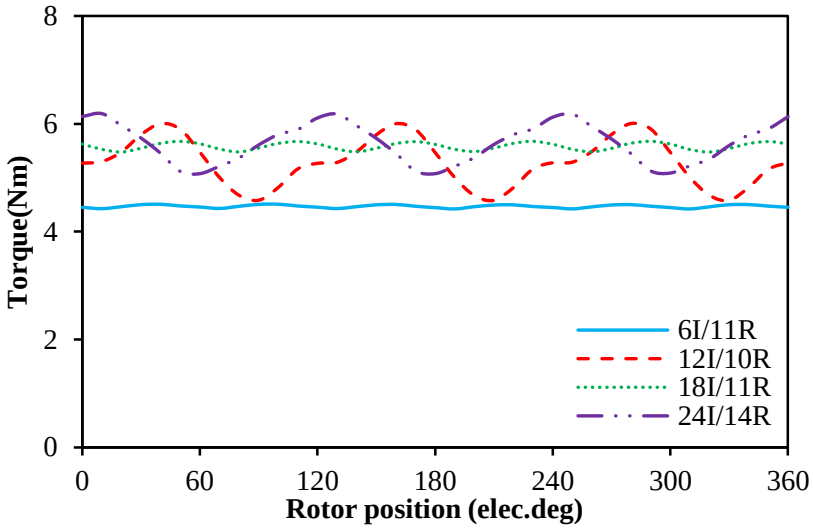

(a) Waveforms

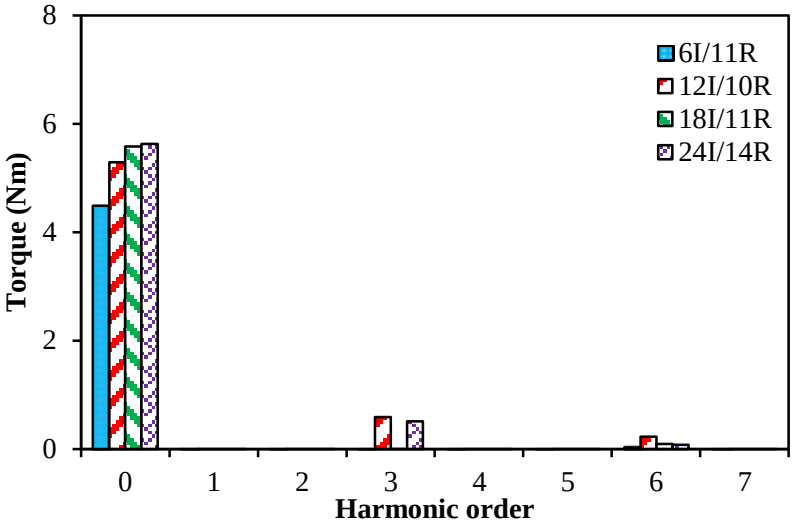

(b) Spectra

Fig. 8.17. Variation of electromagnetic torque with rotor position in PS-SFPMMs at rated current as given in Table 8.2, I_d=0 control, p_c=30W.

As shown in Table 8.2, the average torque for 6I/11R, 12I/10R, 18I/11R and 24I/14R PS-SFPMMs are 4.47, 5.29, 5.59 and 5.62 Nm respectively. Compared with the optimal 6-pole outer stator PS-SFPMMs with n' equal to 1, the optimal torque capability is enhanced by about 18.4%, 25.1% and 25.7% respectively corresponding to 6-pole outer stator PS-SFPMMs with

n' equal to 2, 3, and 4 due to the increased PM usage and enlarged slot area (corresponding to the increased rated current under the fixed rated copper loss).

Fig. 8.18 compares the torque density and torque to PM volume of four machines at the rated currents (p_c=30W) and I_d=0 control. Obviously, as n' increases, the torque density is enhanced whilst the PM utilization efficiency (torque to PM volume) is decreased. As shown in Table 8.2, the torque densities for 6I/11R, 12I/10R, 18I/11R and 24I/14R PS-SFPMMs are 28.1, 33.3, 35.1 and 35.4 kN/m^2 respectively. Since four machines have the same machine size, the increase rates of torque density for optimal 6-ople outer stator PS-SFPMMs with n' equal to 2, 3, and 4 are consistent with the increase rates of average torque, which are 18.4%, 25.1% and 25.7% respectively. Moreover, the torque to PM volume (PM utilization efficiency) for 6I/11R, 12I/10R, 18I/11R and 24I/14R PS-SFPMMs are 297, 224, 219 and 211kN/m^2 respectively. Compared with the optimal 6-pole outer stator PS-SFPMMs with n' equal to 1, the PM utilization efficiency is declined by about 24.5%, 26.3% and 29.0% respectively in 6-pole outer stator PS-SFPMMs with n' equal to 2, 3, and 4.

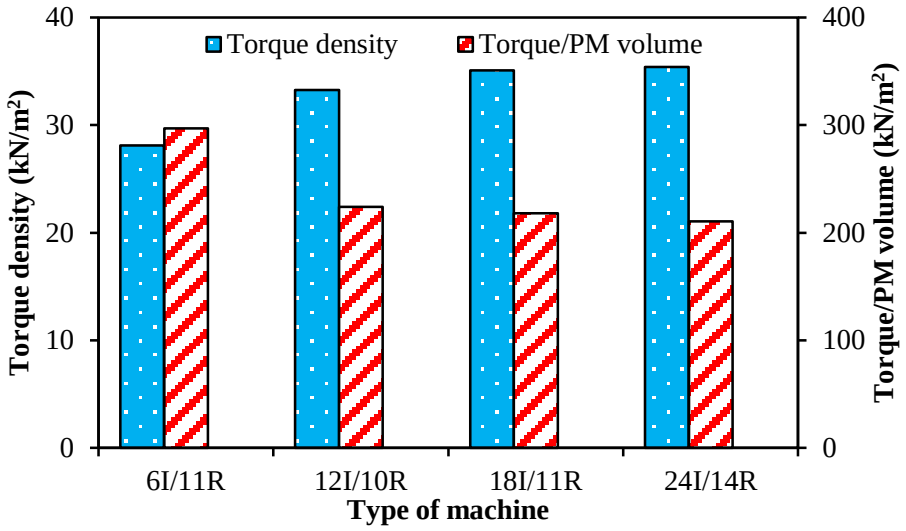

Fig. 8.18. Torque density and torque to PM volume, I_d=0 control, p_c=30W.

The variations of average torque with copper loss are further shown in Fig. 8.19. The vertical dashed and dotted line indicates the rated copper loss which is used during the optimization of PS-SFPMMs. Obviously, due to the effect of magnetic saturation, the increase rate of average torque will be decreased gradually with the rising of copper loss in all PS-SFPMMs. Compared with 6I/11R PS-SFPMM, 12I/10R, 18I/11R and 24I/14R PS-SFPMMs exhibit higher average torque under the same cooper loss over the whole copper loss range. The result indicates that PS-SFPMMs with $n' > 1$ can enhance the torque

performance not only in low electric loading but also in high electric loading. Further, compared with 18I/11R PS-SFPMM, the average torque of 24I/14R PS-SFPMMs is slightly larger at relatively low copper loss (lower than 40W) but smaller at high copper loss (higher than 40W) due to the more severe saturation (larger inductance) and leakage flux caused by the increased n'.

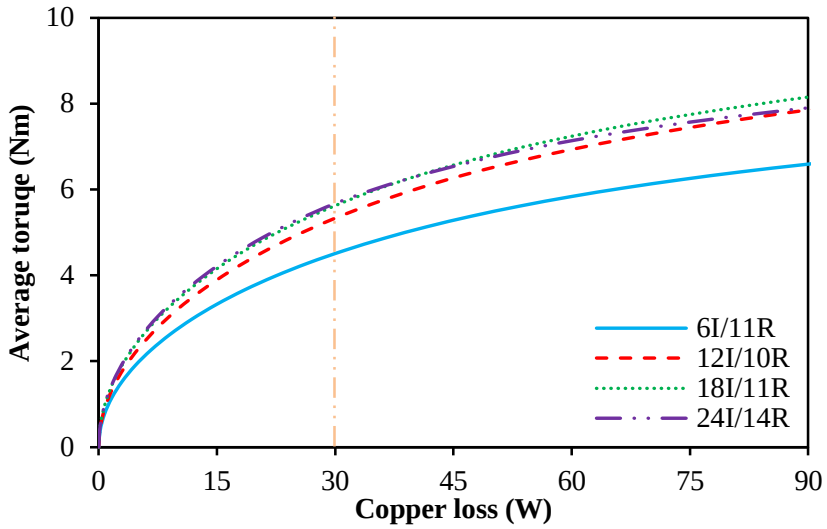

Fig. 8.19. Variation of average torque with copper loss in PS-SFPMMs, I_d=0 control.

Table 8.2 Main electromagnetic performance of 6-pole outer stator PS-SFPMMs with optimal N_{is}/N_r

Parameter	***n*=1**	***n*=2**	***n*=3**	***n*=4**
N_{is}/N_r	**6I/11R**	**12I/10R**	**18I/11R**	**24I/14R**
Fund. flux-linkage (mWb)	11.60	15.53	15.43	12.30
Fund. back-EMF (V)	5.36	6.50	7.10	7.20
Rated electric frequency (Hz)	73.3	66.7	73.3	93.3
Cogging torque (Nm)	0.08	0.65	0.03	0.18
Average torque (Nm)	4.47	5.29	5.59	5.62
Increment of torque (%)	0	18.4	25.1	25.7
Torque ripple (%)	2.1	26.9	3.6	20.4
Torque density (kN/m^2)	28.1	33.3	35.1	35.4
Total PM volume (mm^3)	15055.3	23609.7	25569.4	26744.6
Torque/PM volume (kN/m^2)	297	224	219	211
Rated iron loss (W)	1.78	2.43	2.78	3.45
Rated PM loss (W)	0.12	0.24	0.46	0.88

8.3.6 Electromagnetic Torque Characteristics

Fig. 8.20 shows the variation of total iron losses against with speed at rated copper loss for four machines. Obviously, based on the respective optimal rotor pole numbers (different electric frequency under the same speed), the saturation level and total saturation area are increased when n is increased, as shown in Fig. 8.21. Consequently, together with considering the influence of electric frequency, the iron loss of PS-BFPMM is also increased simultaneously with the increased n, as shown in Fig. 8.20. According to Table 8.2, the iron loss of 6I/11R, 12I/10R, 18I/11R and 24I/14R PS-SFPMMs under the rated copper loss (30W) and the rated speed (400rpm) are 1.78, 2.43, 2.78 and 3.45W respectively.

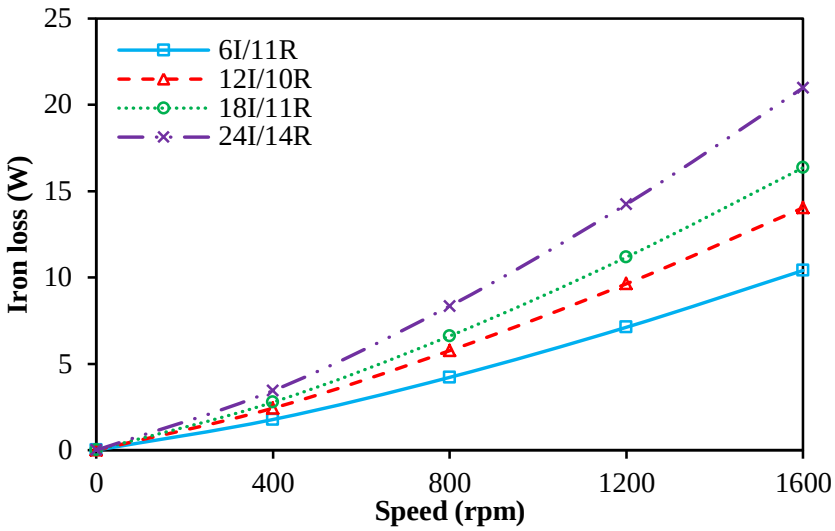

Fig. 8.20. Variation of iron loss with speed in PS-SFPMMs, p_c =30W, I_d = 0 control.

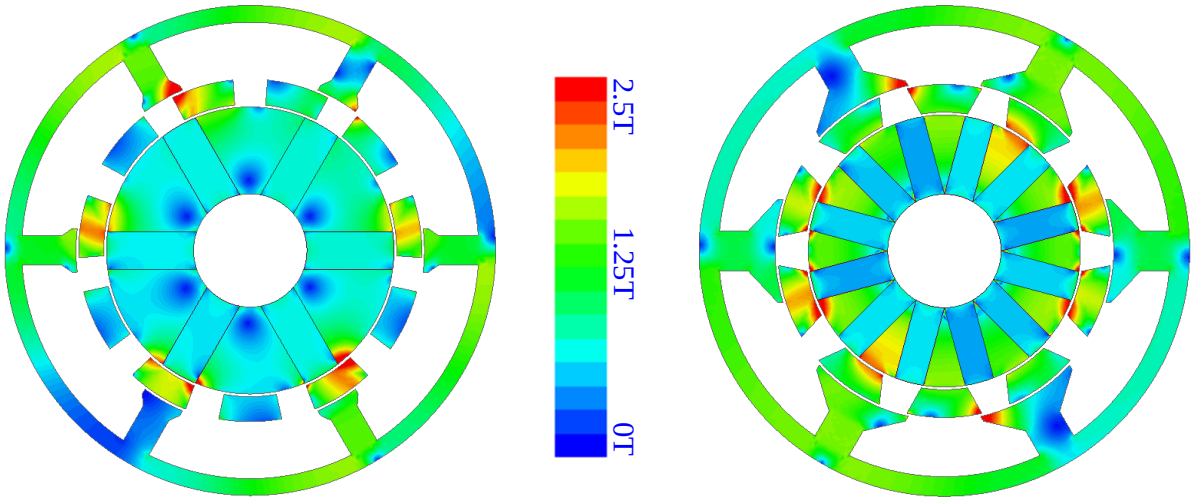

(a) 6I/11R (b) 12I/10R

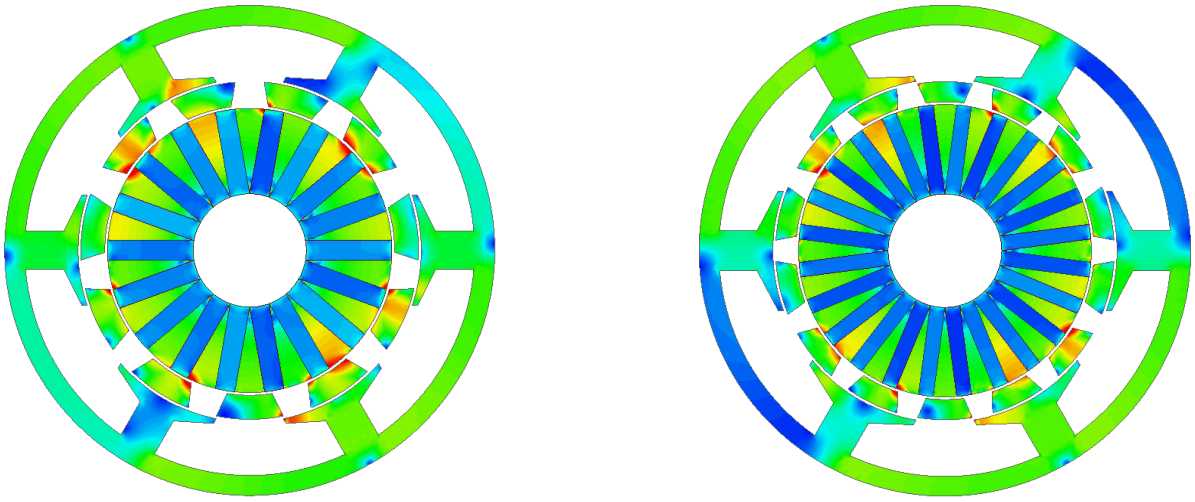

(c) 18I/11R (d) 24I/14R

Fig. 8.21. On-load flux density distributions of PS-SFPMMs, p_c =30W, I_d = 0 control.

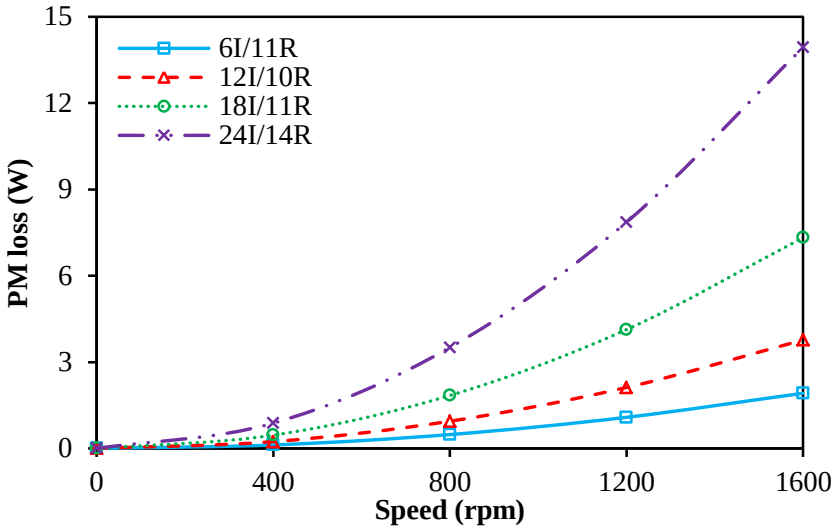

Fig. 8.22. Variation of PM loss with speed in PS-SFPMMs, p_c =30W, I_d = 0 control.

Fig. 8.22 shows the variation of PM losses against speed at rated copper loss for four machines. Obviously, the PM loss of PS-BFPMMs is increased as *n* increased, which is mainly due to the increased total PM volume simultaneously. As shown in Table 8.2, the PM loss of 6I/11R, 12I/10R, 18I/11R and 24I/14R PS-SFPMMs under the rated copper loss (30W) and the rated speed (400rpm) are 0.12, 0.24, 0.46 and 0.88W respectively.

8.4 Experimental Verification

Prototype machine of 12I/10R PS-SFPMM with 6-pole outer stator is made to validate the foregoing analyses, as shown in Fig. 8.23. To reduce the cost, existing inner stator with 12 PMs and 10-pole rotor are used for experiment, and new 6-pole outer is made according to

the re-optimized results. Therefore, the parameters of prototype machine as shown in Table 8.3 are different from the previous globally optimized parameters as given in Table 8.1. In addition, for easing the fabrication, lamination bridges with 0.5mm thickness (T_{BRI}) are added to both top and bottom edges of PMs to help fixing, as shown in Fig. 8.23(b). Meanwhile, 10-pole modular rotor is mechanically connected by lamination bridges in the inner side of rotor, as shown in Fig. 8.23(d).

(a) 6-pole outer stator

(b) Inner stator with 12 PMs

(c) Assembled stator

(d) 10-pole rotor

Fig. 8.23. Prototype of 12I/10R PS-SFPMM with 6-pole outer stator.

Table 8.3 Parameters of prototype machine for 12I/10R PS-SFPMM with 6-pole outer stator

Parameter	**12I/10R PS-SFPMM**	**Parameter**	**12I/10R PS-SFPMM**
L_{ag} (mm)	0.5	T_{Sostto} (mm)	1
L_{aa} (mm)	25	T_{osy} (mm)	3.4
R_{oso} (mm)	45	θ_{rop} (°)	18
R_{ost} (mm)	31.75	θ_{rip} (°)	25.2
R_{iso} (mm)	25.75	T_{rr} (mm)	5
R_{ist} (mm)	10.4	T_{PM} (mm)	5
θ_{ostb} (°)	13.20	L_{PM} (mm)	14.35
θ_{ostt} (°)	14.30	T_{bri} (mm)	0.5
T_{osttb} (mm)	5.8		

Fig. 8.24 shows the measured and predicted phase back-EMF at rated speed (400rpm). Due to the end-effect in 25mm stack length machines, the measured fundamental value is ~8% less than the prediction. Meanwhile, the measured amplitude of the 5th harmonic is lower than that of FE prediction but higher for the 2rd harmonic, which is caused by the imperfect manufacture. The measured and predicted open-circuit cogging torque waveforms are compared in Fig. 8.25. Considering the measurement error and end-effect, the measured peak to peak value agrees well with the FE perdition and the waveforms are relatively consistent. Fig. 8.26 shows the waveforms of static torque with rotor position at three different armature currents, i.e. 15A, 20A and 25A (I_{DC}=I_A=-2I_B=-2I_C). Furthermore, the measured and predicted peak torques corresponding to different currents are compared in Fig. 8.27. It can be seen that the differences between the measured and FE predicted results enlarge with increased current due to the more severe end effect caused by saturation. In general, the measured results agree well with the FE predictions.

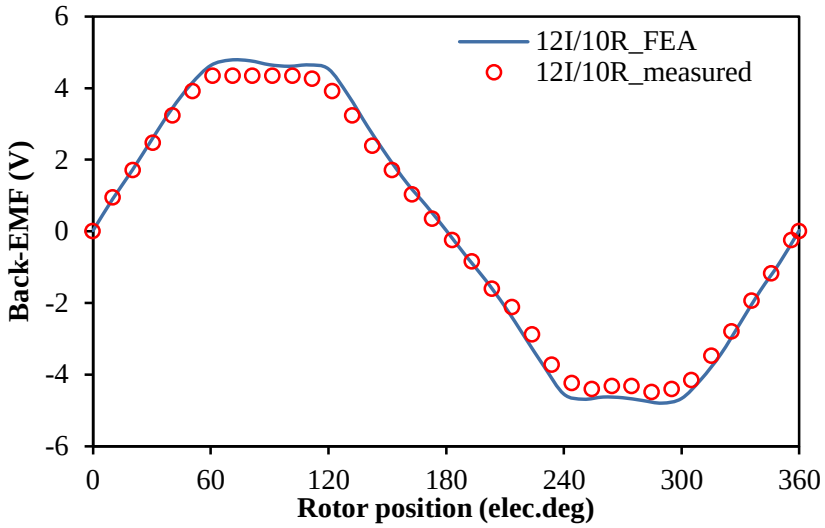

(a) Waveforms

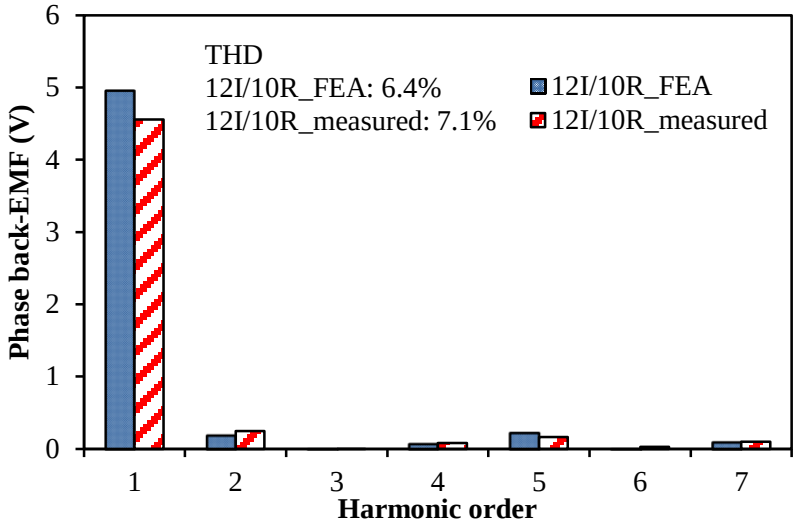

(b) Spectra

Fig. 8.24. Measured and FE predicted phase back-EMFs at 400rpm.

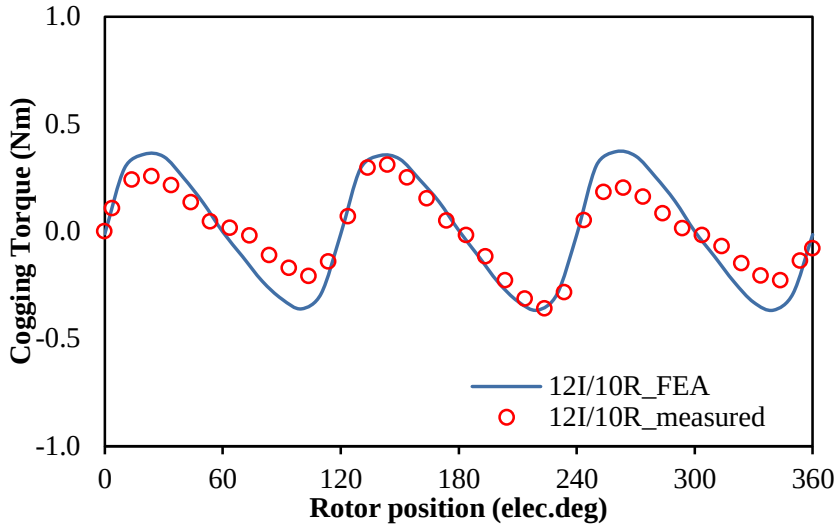

Fig. 8.25. Measured and FE predicted open-circuit cogging torques.

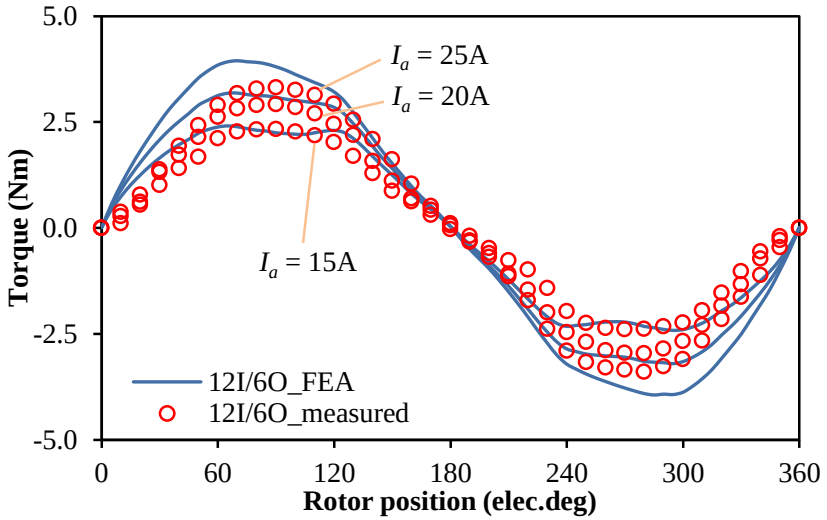

Fig. 8.26. Measured and FE predicted static torques, $I_{DC}=I_A=-2I_B=-2I_C$.

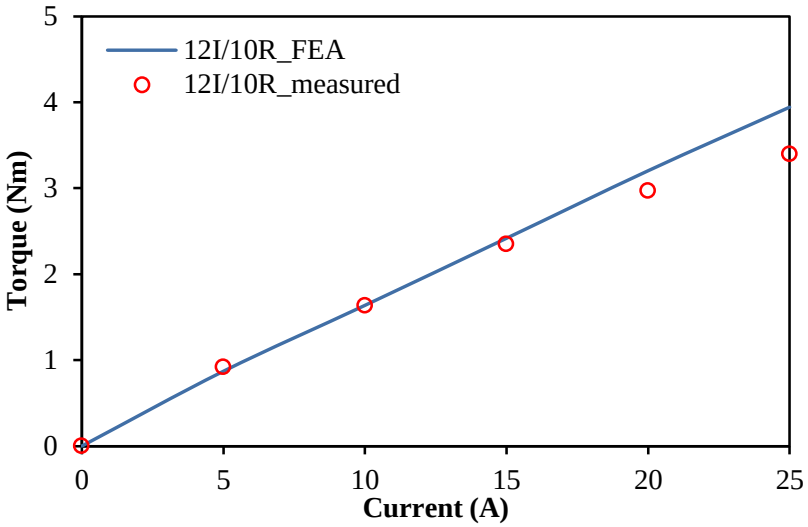

Fig. 8.27. Measured and FE predicted peak torque-current characteristics.

8.5 Summary

In this chapter, the influences of inner stator and rotor pole combinations on electromagnetic performance of PS-SFPMMs with 6-pole outer stator are investigated.

To maximize the torque performance, the PMs of inner stator pole should be aligned with outer stator pole when inner/outer stator pole ratio n' ($n'=N_{is}/N_{os}$) is odd while the iron rib of inner stator pole should be aligned with outer stator pole when n is even. No matter what n' is selected in PS-SFPMMs, the choice of rotor pole number N_r is flexible and can be any integers except the phase number and its multiples. The analysis results indicate that the optimal N_r is closed to $(N_{os}+N_{is})/2$ and it is odd when n' is odd while it is even when n' is even. Meanwhile, symmetrical bipolar phase flux-linkage and phase back-EMF waveforms will be

obtained when the ratio of $Min(N_{os}, N_{is})$ to the greatest common divisor of $Min(N_{os}, N_{is})$ and rotor pole numbers N_r is even. Further, based on the condition of maximum average torque under rated copper loss, 6I/11R, 12I/10R, 18I/11R and 24I/14R are the optimal inner stator/rotor combinations of 6-pole outer stator PS-SFPMMs with n' equal to 1, 2, 3 and 4 respectively. Compared with 6I/11R (n'=1) PS-SFPMM at rated copper loss and same machine size, the average torque is improved by about 18.4%, 25.1% and 25.7% respectively for 12I/10R (n'=2), 18I/11R (n'=3) and 24I/14R (n'=4) PS-SFPMMs. Among these four machines, 6I/11R and 18I/11R PS-SFPMMs exhibit more symmetrical phase back-EMF, smaller cogging torque and lower torque ripple. The analyses have been validated by both the FEA and measurements.

CHAPTER 9

General Conclusions and Future Works

9.1 General Conclusions

In this thesis, the investigation is focused on the electromagnetic performance of novel stator permanent magnet (PM) and DC field excited synchronous machines which are evolved from the variable flux reluctance machines (VFRMs). All theoretical analyses are carried out by the finite element method and validated by experiments. The details of each research topic are summarized in the following sub-sections.

9.1.1 Variable Flux Reluctance Machines

A. Influence of Stator and Rotor Pole Arcs on Electromagnetic Torque

Since the VFRM was firstly developed from the conventional 6/4 stator/rotor pole SRM by neglecting the current harmonics of orders higher than 2 and splitting the original winding into AC armature and DC field windings, previous investigations on VFRMs adopt the equal stator pole arc and stator slot opening. However, VFRMs can be considered as one type of stator DC field excited synchronous machines. Therefore, equal stator pole arc and stator slot opening may not be the optimal for VFRMs.

In Chapter 2, the influence of stator and rotor pole arcs on electromagnetic torque of VFRMs having different stator and rotor pole combinations is investigated. It is found that:

(1) The optimal rotor pole arc to rotor pole pitch ratio is ~1/3;

(2) The optimal stator pole arc is equal to or slightly smaller than the optimum rotor pole arc;

(3) Compared with 6-pole stator VFRMs having equal stator pole arc and stator slot opening under the rated 30W copper loss, the average torque of 4-, 5-, 7- and 8-pole rotor VFRMs with the optimal stator and rotor pole arcs are enhanced by 1%, 4%, 30.7% and 72.9% respectively;

(4) The 6/7 stator/rotor pole VFRM exhibits the largest torque density when the constraint of equal stator pole arc and stator slot opening is removed, which is different from the previous conclusion.

B. Novel Multi-tooth VFRMs

The multi-tooth stator pole structure is widely employed to further improve the torque capability, such as in hybrid stepper machines, switched reluctance machines and switched flux machines. By introducing the multi-tooth structure into VFRM, novel multi-tooth VFRM is proposed and investigated in Chapter 3. It is found that:

(1) Similar to the single-tooth VFRM, the choice of rotor pole number in multi-tooth VFRM is also flexible and can be any integers except the phase number and its multiples;

(2) Symmetrical bipolar phase flux-linkage and phase back-EMF waveforms can be obtained when the ratio of stator pole number to greatest common divisor (GCD) of stator- and rotor-pole numbers is even;

(3) Under the same rated copper loss and the same stator outer radius as well as 6-pole stator, 4-tooth per stator pole VFRMs exhibit the highest average torque when the stator and rotor pole numbers satisfy with $N_r=nN_s\pm1$ (n is the number of small teeth per stator pole);

(4) Compared with the optimal 6/7 stator/rotor pole single-tooth VFRM, the 6/25 stator/rotor pole 4-tooth VFRM has more sinusoidal and larger back-EMF, negligible cogging torque, lower torque ripple and higher torque capability at relatively low copper loss (24% higher under the rated 30W copper loss);

(5) Similar to single-tooth VFRMs, 4-tooth VFRMs with $N_r=nN_s\pm1$ exhibit more sinusoidal back-EMF, lower torque ripple and larger torque than those of VFRMs with $N_r=nN_s\pm2$.

9.1.2 Novel Biased Flux PM Machines

A. Machine Topologies and Influence of PM Location on Electromagnetic Performance

Generally, by replacing DC field windings with PMs, higher torque density can be expected. Therefore, novel biased flux PM machines (BFPMMs) which are developed from VFRMs by replacing all DC field windings with PMs are proposed and investigated in Chapter 4. Consequently, the features of VFRMs are inherited in the BFPMMs, and can be summarised as:

(1) Doubly salient structure;

(2) Concentrated non-overlapping armature windings;

(3) Flexible choice of rotor pole number, which can be any integers except phase number and its multiples;
(4) Symmetric bipolar phase flux-linkage and phase back-EMF waveforms can be obtained when the stator and rotor pole combinations satisfy with the ratio of stator pole number to greatest common divisor (GCD) of stator- and rotor-pole numbers equal to even.

The PM locations in the stator of BFPMMs are flexible and can be moved from surface to bottom of stator pole and even to stator yoke since the main magnetic circuits are consistent. Therefore, the influence of PM location on electromagnetic performance of BFPMMs is investigated. Then, BFPMMs with three typical PM locations are compared with VFRMs under the same rated copper loss and the same machine size. It is found that:

(1) The 6/7 stator/rotor pole is the optimal combination for both SM-BFPMM (PMs mounted on the surface of stator pole) and SYM-BFPMM (PMs located in the stator yoke), which are consistent with that of VFRM;
(2) Among the three BFPMMs, SYM-BFPMM has largest torque density while SM-BFPMM has the highest PM utilization efficiency;
(3) Compared with VFRM under 6/7 stator/rotor pole combination, the average torques are enhanced by 64.5%, 51.0% and 72.1% respectively in SM-BFPMM, MTM-BFPMM and SYM-BFPMM.

B. Influence of Flux Focusing on Electromagnetic Performance

In Chapter 5, various flux focusing configurations are employed in SYM-BFPMM to further enhance the torque density and PM utilization efficiency. The results show that:

(1) The average torque of SYM-BFPMM is enhanced by ~19%, 30.3% and 54.2% respectively by adopting flux focusing configurations with inner type (IT), outer type (OT) and combined type (CT);
(2) The PM utilization efficiency is enhanced by 19.5%, 38.6% and 23.3% respectively;
(3) The torque density is enhanced by 19.3%, 18.8% and 40.3% respectively.

C. Performance Comparison between BFPMM and DSPMM

Based on the inner type flux focusing configuration, the optimized 6/4 stator/rotor pole IT-DSPMM is compared with optimized 6/7 stator/rotor pole IT-BFPMM under the same rated copper loss and machine size as well as optimal current angle. The results show that:

(1) The selection of rotor pole number in BFPMM is more flexible than that in DSPMM;

(2) The phase flux-linkage waveform is bipolar in BFPMM while it is unipolar in DSPMM;
(3) The phase back-EMF waveforms is close to sinusoidal (symmetrical) in BFPMM while it is close to trapezoidal (asymmetric) in DSPMM;
(4) IT-BFPMM exhibits ~ 18% higher average torque and 80% lower torque ripple than IT-DSPMM;
(5) The unbalance between phases which is observed DSPMMs is overcome in the BFPMMs.

9.1.3 Novel Partitioned Stator PM Synchronous Machines

A. Novel Partitioned Stator Biased Flux PM Machine

The partitioned stator configuration, which fully utilized the inner space, is an effective solution to solve the confliction among the slot area, PMs and stator irons of BFPMM which limits the possibility of further enhancing the torque density. By introducing the partitioned stator configuration into BFPMM, novel partitioned stator BFPMM (PS-BFPMM) is proposed and investigated in Chapter 6. Two PM stator configurations, i.e. SPM stator and Spoke-IPM stator, which are evolved from BFPMMs with PM mounted on the surface of stator pole and located in the stator yoke, are proposed and investigated. The results show that:

(1) PS-BFPMM with SPM stator and PS-BFPMM with Spoke-IPM stator exhibit 120% and 145% larger average torque than SM-BFPMM and SYM-BFPMM respectively under the same machine size and the same rated copper loss as well as 12/10 (inner/outer) stator/rotor pole combination;
(2) Compared with PS-BFPMM with SPM stator, PS-BFPMM with Spoke-IPM stator has 52.2% higher phase back-EMFs and 43% larger average torque but 17.4% lower PM utilization efficiency;
(3) For 12I/12O stator pole PS-BFPMMs, the optimal rotor pole numbers are 11 and 10 respectively in PS-BFPMM with SPM stator and PS-BFPMM with Spoke-IPM stator since the highest torque densities and PM utilization efficiencies are achieved.

B. Influences of the Ratio of Inner/Outer Stator Pole and the Relative Position of Inner and Outer Stators on Electromagnetic Performance

Based on Spoke-IPM stator configuration and minimum 6-pole inner and outer stators, the influences of the ratio of inner/outer stator pole and the relative position of inner and outer

stators on electromagnetic performance of partitioned stator PM synchronous machines are analysed and compared in Chapter 7 and Chapter 8. The results show that:

(1) To obtain the bipolar symmetrical phase flux-linkage and phase back-EMFs, the ratio of $Min(N_{is}, N_{os})$ to the greatest common divisor of $Min(N_{is}, N_{os})$ and rotor pole numbers N_r should be even (N_{is} and N_{os} are the numbers of inner and outer stator pole);

(2) The optimal rotor pole number for 12I/12O PS-BFPMM (N_{is}/N_{os}=1), 12I/12O PS-SFPMM (N_{is}/N_{os}=1), 6I/12O PS-SFPMM (N_{is}/N_{os}=1/2) and 12I/6O PS-SFPMM (N_{is}/N_{os}=2) are 10, 11, 11, and 10 respectively;

(3) Compared with 12I/12O/10R PS-BFPMM (N_{is}/N_{os}=1), 12I/12O/11R PS-SFPMM (N_{is}/N_{os}=1) exhibits 28% larger average torque and 15% higher PM utilization efficiency under the rated copper loss;

(4) Compared with 12I/12O/11R PS-SFPMM ($\boldsymbol{N}_{is}/\boldsymbol{N}_{os}$=1) under the rated copper loss, 12I/6O/10R PS-SFPMM ($\boldsymbol{N}_{is}/\boldsymbol{N}_{os}$=2) exhibits ~2% larger average torque and 8% higher PM utilization efficiency while 6I/12O/11R PS-SFPMM has 49% smaller average torque and 29% lower PM utilization efficiency;

(5) When employing the alternate pole wound winding in 6I/12O/11R PS-SFPMM, the average torque and the PM utilization efficiency are enhanced by 36% and 55% respectively.

C. Influence of Inner Stator and Rotor Pole Combinations on Electromagnetic Performance of PS-SFPMMs

Since higher torque density can be observed in PS-SFPMMs when N_{is}/N_{os}>1, the influences of inner stator and rotor pole combinations on electromagnetic performance of PS-SFPMMs with 6-pole outer stator are also investigated in Chapter 8. It is found that:

(1) To maximize the torque performance, the PMs of inner stator pole should be aligned with outer stator pole when N_{is}/N_{os} is odd while the iron rib of inner stator pole should be aligned with outer stator pole when N_{is}/N_{os} is even;

(2) The optimal N_r is closed to $(N_{os}+N_{is})/2$ and it is odd when n is odd while it is even when n is even;

(3) Based on the condition of maximum average torque under rated copper loss, 6I/11R, 12I/10R, 18I/11R and 24I/14R are the optimal inner stator/rotor combinations of 6-pole outer stator PS-SFPMMs with N_{is}/N_{os} equal to 1, 2, 3 and 4 respectively;

(4) Compared with 6I/11R (N_{is}/N_{os}=1) PS-SFPMM at the rated copper loss and the same machine size, the average torque is improved by about 18.4%, 25.1% and 25.7%

respectively for 12I/10R (N_{is}/N_{os}=2), 18I/11R (N_{is}/N_{os}=3) and 24I/14R (N_{is}/N_{os}=4) PS-SFPMMs.

9.2 Comparison between Proposed Machines and Conventional Surface-Mounted PM machines

In this section, the main electromagnetic performance and material cost of selected proposed machines are compared with the conventional 12-slot 10-pole surface-mounted PM machine (SPMM).

9.2.1 Machine Topologies and Main Parameters of Conventional SPMM

Fig. 9.1 shows the topologies of selected proposed machines and conventional SPMM. All of the machines are globally optimized with the objective of maximum average torque under the same rated 30W copper loss and the same machine size by genetic algorithm (ANSYS Maxwell). To simplify the drawing in this section, the selected proposed machine and conventional SPMM are defined as M1 to M10 respectively, as shown in Fig. 9.1. Moreover, the main parameters of conventional SPMM are listed in Table 9.1.

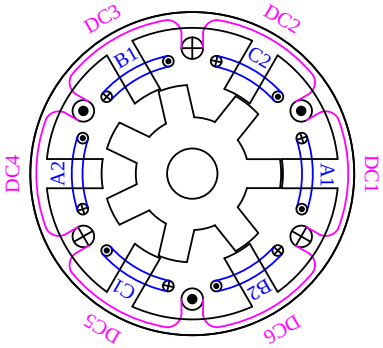

(a) 6S/7R VFRM (**M1**)

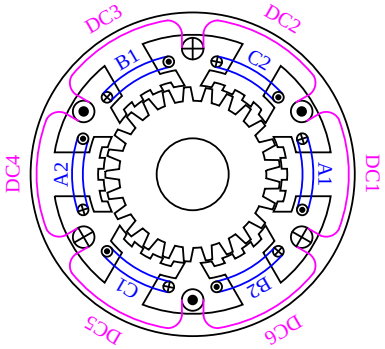

(b) 6S/25R MT-VFRM (**M2**)

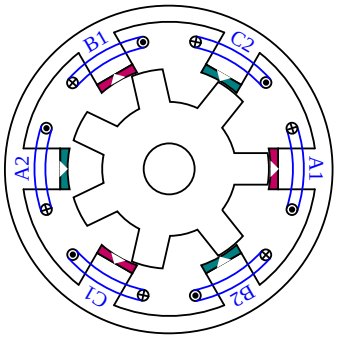

(c) 6S/7R BFPMM-I (**M3**)

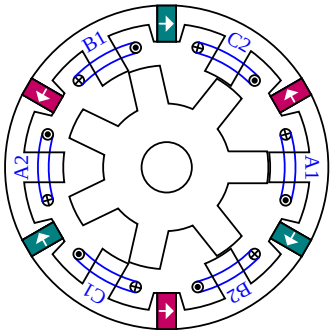

(d) 6S/7R BFPMM-II (**M4**)

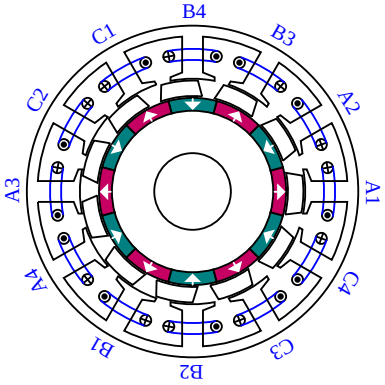

(e) 12I/12O/11R PS-BFPMM-I (**M5**)

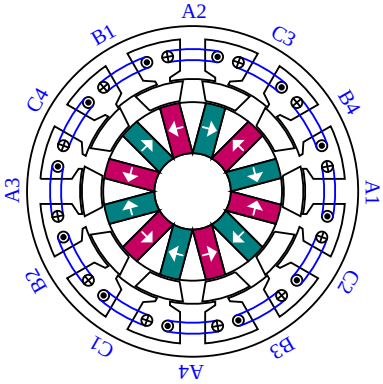

(f) I2I/12O/10R PS-BFPMM-II (**M6**)

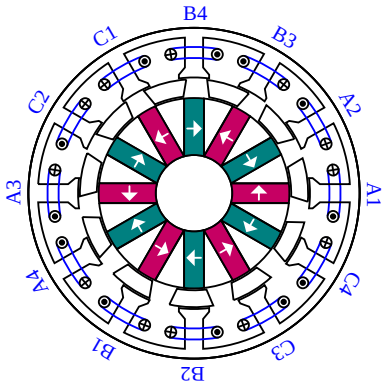

(g) 12I/12O/11R PS-SFPMM (**M7**)

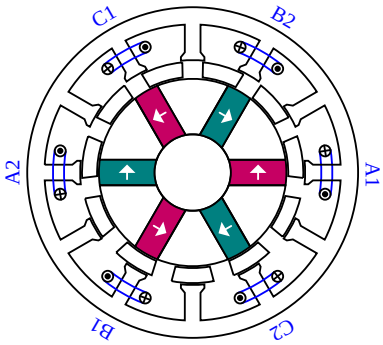

(h) 6I/12O/11R PS-SFPMM (**M8**)

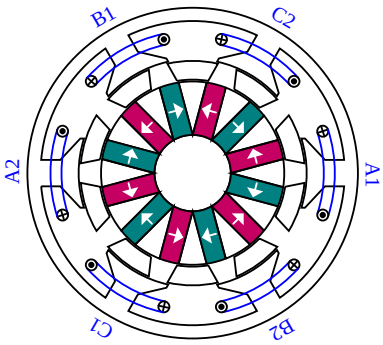

(j) 12I/6O/10R PS-SFPMM (**M9**)

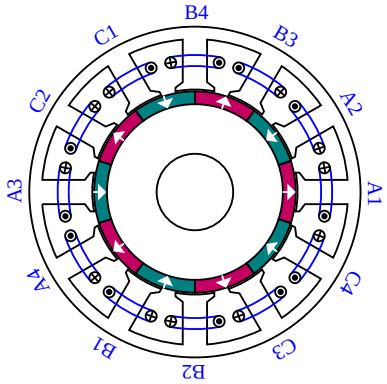

(k) 12S/10P SPMM (**M10**)

Fig. 9.1. Topologies of proposed machines and conventional SPMM.

Table 9.1 Main parameters of conventional 12S/10P SPMM (M10)

Conventional SPM machine (M10)			
Number of stator poles	12	Stator yoke thickness (mm)	3.4
Number of rotor poles	10	Stator tooth body pole arc (°)	13.6
Number of phases	3	Stator tooth tip pole arc (°)	4.1
Turns per phase	72	Stator tooth tip thickness (Opening) (mm)	1
Rated speed (rpm)	400	Stator tooth tip thickness (Body) (mm)	2.2
Rated copper loss (W)	30	Rated AC current (A_{rms})	17.7
Packing factor	0.5	Rated current density (A_{rms}/mm^2)	8.61
Air-gap length (mm)	0.5	PM pole arc (°)	36
Active axial length (mm)	25	PM thickness (mm)	3.5
Radius of shaft (mm)	10.4	Total PM volume (mm^3)	14101.8
Stator outer radius (mm)	45	Magnetic remanence (T)	1.2
Stator inner radius (mm)	27.9	Relative PM permeability	1.05

9.2.2 Electromagnetic Performance

A. Electromagnetic Torque

Fig. 9.2 shows the torque waveforms of selected proposed machines and conventional SPMM under the rated copper loss and I_d=0 control. Then, the average torque and torque ripple of all machines under the rated copper loss are further shown in Fig. 9.3. Obviously, among the selected proposed machines, 12I/12O/11R PS-SFPMM (M7) and 12I/6O/10R PS-SFPMM (M9) have the similar largest average torque. Then, compared with the conventional 12S/10P SPMM (M10), only the 12I/12O/10R PS-BFPMM-II (M6), 12I/12O/11R PS-SFPMM (M7) and 12I/6O/10R PS-SFPMM (M9) exhibit the relatively larger average torques.

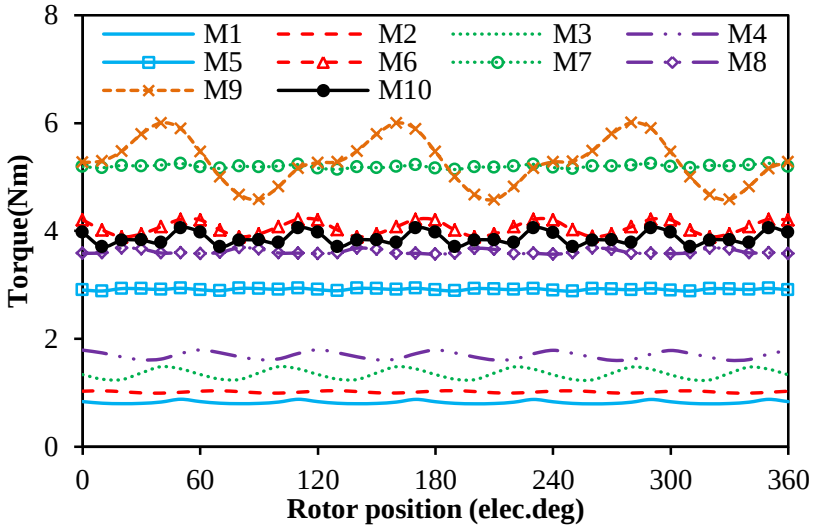

Fig. 9.2. Comparison of torque waveforms, I_d=0 control, p_c=30W.

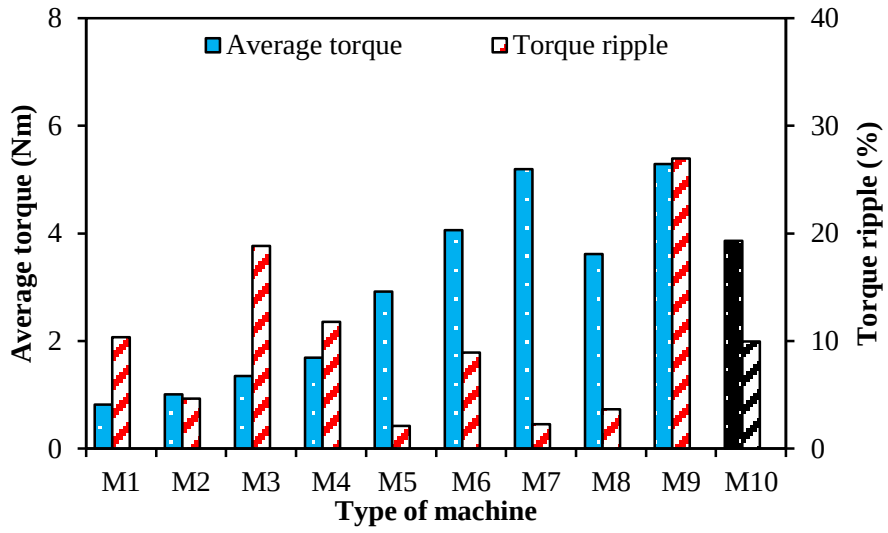

Fig. 9.3. Comparison of average torque and torque ripple, I_d=0 control, p_c=30W.

Moreover, as shown in Fig. 9.3, 12I/12O/11R PS-BFPMM-I (M5) and 12I/12O/11R PS-SFPMM (M7) have the lowest torque ripple among the selected proposed machines. Further, compared with conventional 12S/10P SPMM, 6S/7R VFRM (M1), 6S/7R BFPMM-I (M3), 6S/7R BFPMM-II (M4) and 12I/6O/10R PS-SFPMM (M9) exhibit larger torque ripples while the other selected proposed machines have lower torque ripples.

Fig. 9.4 compares the PM volume and the torque per PM volume (PM utilization efficiency) under the rated copper loss with I_d=0 control. It can be seen that 12I/12O/11R PS-SFPMM (M7) consumes the largest PM material among the selected proposed PM machines. In addition, compared with the selected proposed PM machines, conventional 12S/10P SPMM (M10) exhibits higher PM utilization efficiency except the 6S/7R BFPMM-I (M3).

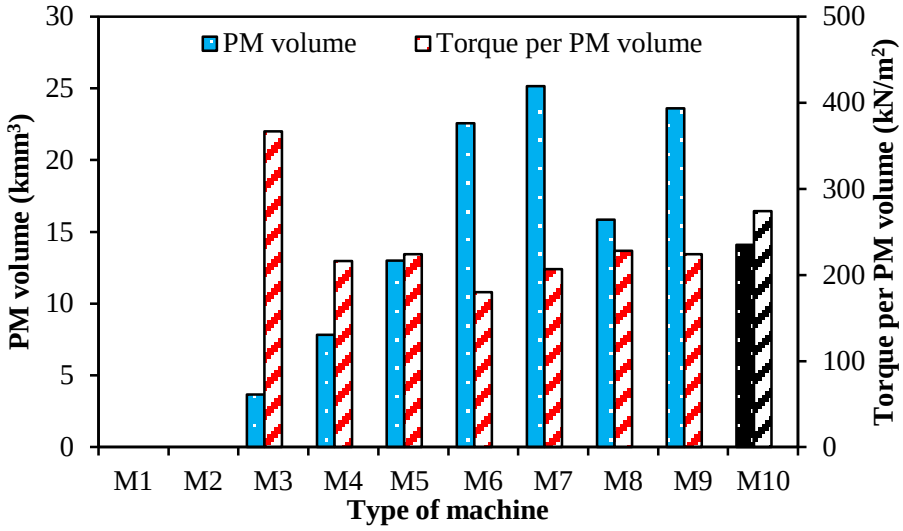

Fig. 9.4. Comparison of PM volume and torque per PM volume, I_d=0 control, p_c=30W.

The average torques of all machines under the different copper loss are further compared in Fig. 9.5. Obviously, among the selected proposed machines, 12I/6O/10R PS-SFPMM (M9) exhibit the largest torque capability during the relative low copper loss range while 12I/12O/11R PS-SFPMM (M7) exhibit the largest torque capability during the relative high copper loss range. In addition, compared with conventional 12S/10P SPMM, 12I/12O/11R PS-SFPMM (M7) and 12I/6O/10R PS-SFPMM (M9) exhibit the larger torque capability during the whole copper loss range while 12I/12O/10R PS-BFPMM-II (M6) has the similar torque capability.

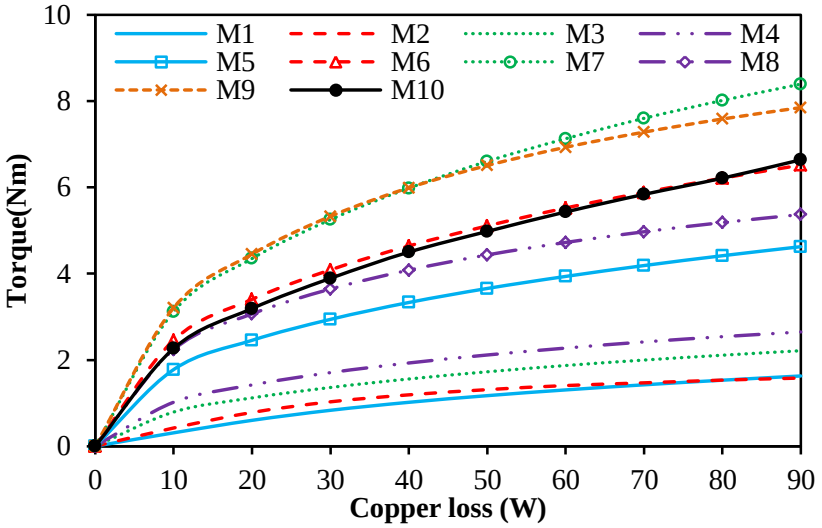

Fig. 9.5. Characteristic comparison of average torque against copper loss, I_d=0 control.

B. Iron Loss, PM Loss and Efficiency

The iron losses of selected proposed machines and conventional 12S/10P SPMM under different rotor speed are compared in Fig. 9.6. Obviously, in the whole speed range, 6S/25R MT-VFRM (M2) has the largest iron loss while 6S/7R BFPMM-I (M3) and 6S/7R BFPMM-II (M4) exhibit similar smallest values. Meanwhile, among all the selected proposed machines, only 6S/7R VFRM (M1), 6S/7R BFPMM-I (M3) and 6S/7R BFPMM-II (M4) have lower iron losses than that of conventional 12S/10P SPMM (M10).

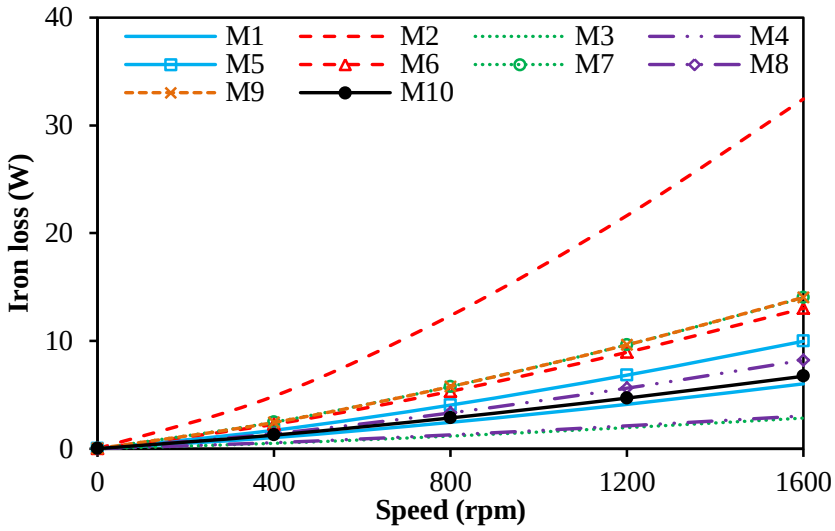

Fig. 9.6. Characteristic comparison of iron loss against speed, I_d=0 control, p_c=30W.

Fig. 9.7 compares the PM losses of selected proposed machines and conventional 12S/10P SPMM under the different rotor speed. It should be noted that 6S/7R VFRM (M1) and

6S/25R MT-VFRM (M2) have no PM losses since these two machine are DC field excited machines. Further, for the PM excited machines, 12I/12O/11R PS-SFPMM (M7) exhibits the lowest PM loss in the whole speed range while 6S/7R BFPMM-I (M3) and 12I/6O/10R PS-SFPMM (M9) have the similar highest values. Moreover, when compared with conventional 12S/10P SPMM (M10), only 6S/7R BFPMM-I (M3) and 12I/6O/10R PS-SFPMM (M9) exhibit larger PM losses.

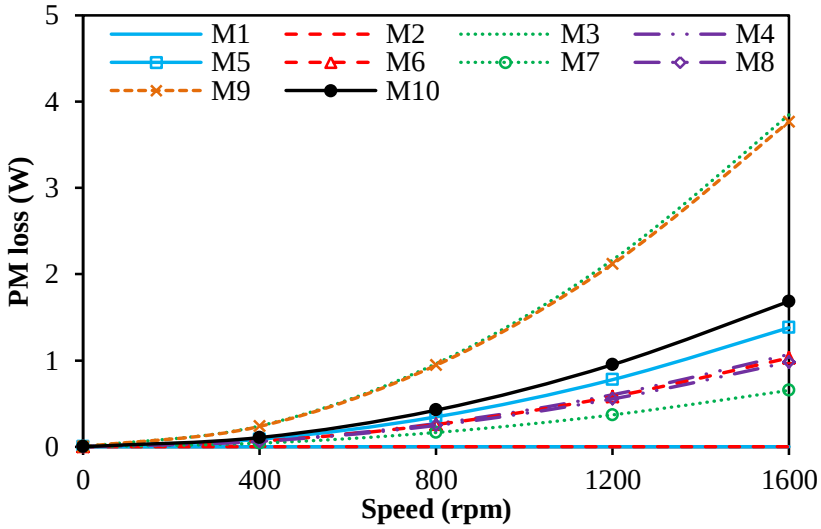

Fig. 9.7. Characteristic comparison of PM loss against speed, I_d=0 control, p_c=30W.

Based on the rated copper loss and the average torque, iron loss, PM loss as shown in Fig. 9.3, Fig. 9.6, and Fig. 9.7 respectively, the efficiency of selected proposed machines and conventional 12S/10P SPMM under different speed are shown in Fig. 9.8. Obviously, PM excited machines (M3-M10) have higher efficiency than those of DC field excited machines (M1-M2) since the copper loss produced by DC field windings are eliminated in the PM excited machines. Further, among the selected proposed PM machines, 12I/12O/11R PS-SFPMM (M7) and 12I/6O/10R PS-SFPMM (M9) have the highest efficiency in the whole speed range. Meanwhile, only these two machines exhibit higher efficiencies than the conventional 12S/10P SPMM (M10). Moreover, 12I/12O/10R PS-BFPMM-II (M6) has similar efficiency of 12S/10P SPMM (M10) in the whole speed range.

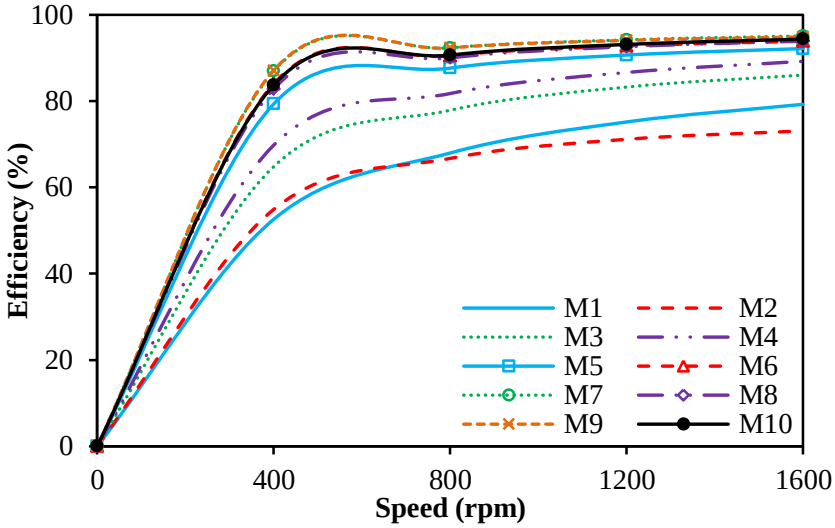

Fig. 9.8. Characteristic comparison of efficiency against speed, I_d=0 control, p_c=30W.

9.2.3 Material Weight and Cost Evaluation

According to [CHU14], the costs of lamination, copper and PM are £1/kg, £7/kg and £15/kg respectively (maybe different from the current costs). Therefore, together with considering the mass of materials as shown in Table 9.2, the cost evaluation of the selected proposed machines and conventional SPMM are obtained and shown in Fig. 9.9. Obviously, among the selected proposed machines, the 6S/25R MT-VFRM (M2) has the lowest total material cost while the 12I/6O/10R PS-SFPMM (M9) has the highest total material cost. Moreover, 12I/12O/10R PS-BFPMM-II (M6), 12I/12O/11R PS-SFPMM (M7), 6I/12O/11R PS-SFPMM (M8) and 12I/6O/10R PS-SFPMM (M9) all have higher total material costs than that of conventional 12S/10P SPMM.

Table 9.2 Mass of materials for proposed machines and SPMM

Mass of materials	M1	M2	M3	M4	M5	M6	M7	M8	M9	M10
Lamination (kg)	0.587	0.776	0.649	0.641	0.639	0.603	0.517	0.639	0.550	0.678
Copper (kg)	0.505	0.290	0.398	0.328	0.283	0.241	0.284	0.291	0.346	0.298
PM (kg)	0	0	0.027	0.058	00096	0.170	0.186	0.117	0.175	0.104

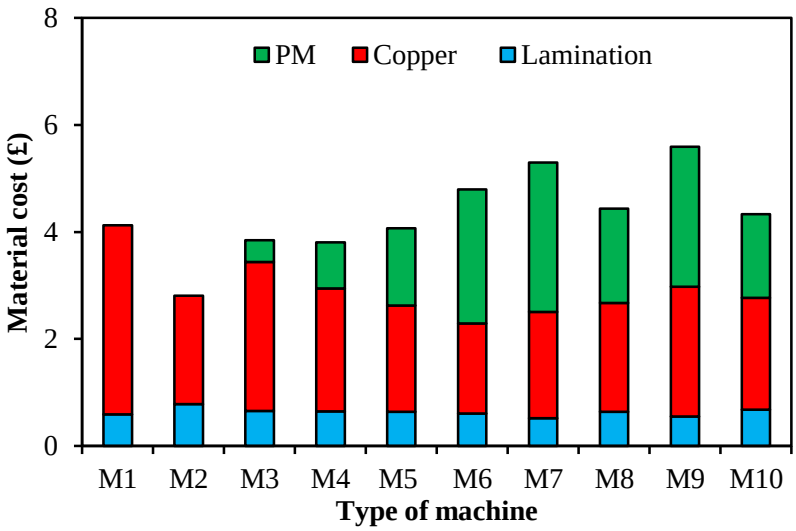

Fig. 9.9. Comparison of material costs.

9.3 Discussion on Potential Application Fields and Limitation

9.3.1 Scalability of the Designs and Findings

In this thesis, the investigations of proposed machines are based on the 45mm outer stator radius and 25mm stack length. Therefore, it should be noted that part of the findings may be subject to the limitation of machine size and inapplicable to the large or small scale machines since the rated operating conditions will be changed accordingly. The scalability of the findings in this thesis is briefly summarized as follows.

A. Potential Inapplicable Findings

(1) The optimal small tooth number per stator pole *n* in MT-VFRPMs.

(2) The optimal (inner/outer) stator/rotor pole number combinations for the proposed machines.

B. Applicable Findings

(1) The methods to enhance the torque performance: a) employing the unequal stator pole arc and slot opening stator structure in VFRMs; b) PM replacing the DC field coils in VFRMs; c) changing the PM locations in BFPMMs; d) employing the flux focusing stator structure in BFPMMs; 5) introducing the partitioned stator configuration in PS-BFPMM.

(2) The general conclusions about the influence of the relative position and ratio between the inner and outer stators on the electromagnetic performance of partitioned stator PM synchronous machines.

9.3.2 Potential Application Fields

A. VFRMs

The stator and rotor structures of VFRMs are simple and robust. Meanwhile, both the DC field and AC armature windings are located in the stator. Consequently, the slip-rings and brushes are eliminated in VFRMs. Therefore, VFRMs are suitable for the application fields which require high reliability under harsh operating environmental conditions. Moreover, VFRMs can also be considered as an alternative option of conventional rotor DC field excited synchronous machines.

B. BFPMMs

According to the analyses in Chapter 5, BFPMMs exhibit higher torque density and lower torque ripple than DSPMMs. Meanwhile, the drawback of phase unbalance in DSPMMs is also eliminated in BFPMMs. Further, the usage efficiency of dc-link voltage in BFPMMs is much higher than that of DSPMMs. Therefore, BFPMMs can be considered as an alternative option of DSPMMs.

C. PS-BFPMMs and PS-SFPMMs

According to the analyses shown in section 9.2, PS-BFPMMs (M6) and PS-SFPMMs (M7, M9) exhibit larger torque density and higher efficiency than conventional SPMM (M10). Therefore, PS-BFPMMs and PS-SFPMMs can be considered as an alternative option of conventional SPMMs. Moreover, PS-BFPMMs and PS-SFPMMs are also suitable for the application fields which require high torque capability within small machine size (high torque density).

9.3.3 Limitation and Challenge for Mechanical Integrity

A. VFRMs

As shown in Fig. 9.1, VFRMs (M1, M2) have the simple and robust mechanical structure. Therefore, the mechanical strength of VFRMs is desirable.

B. BFPMMs

As shown in Fig. 9.1, the mechanical integrity of BFPMM-I (M3) is relatively good since the stator and rotor structures are integrated and the PMs are mounted on the surface of stator pole. However, for BFPMM-II (M4) with PMs located in the stator yoke, the stator is

consisted by the segment pieces. Hence, the mechanical integrity of BFPMM-II (M4) is undesirable and poor than that of BFPMM-I (M3). Meanwhile, the segmented stator structure also causes the difficulty in the assembling and precise positioning. To solve this problem, 0.5mm lamination bridges can be added in the outer edge of stator to improve the mechanical integrity of stator. However, the electromagnetic performance will be reduced simultaneously.

C. PS-BFPMMs and PS-SFPMMs

As shown in Fig. 9.1, the partitioned stator (PS) machines are composed by three components, i.e. segment rotor, stator with armature windings and stator with PMs (or DC field coils). Due to increased components, the precise assembling for PS machines is more difficult than that for SS machines, especially for the segment rotor. Therefore, to enhance the mechanical integrity and convenient for the assembling, the segmented rotor is mechanically connected by the 0.5mm lamination bridges at the side close to the stator with PMs, although it will reduce the electromagnetic torque. Moreover, for PS machine with spoke-IPM stator (such as M6, M7), 0.5mm lamination bridges can also be added at the both top and bottom edges of PMs to help fixing the PMs and enhance the mechanical integrity.

9.4 Future Works

Based on the aforementioned investigation in this thesis, the future research can be listed as follows.

A. Comparative study of BFPMMs with single stator, partitioned stator and dual stator configurations.

The BFPMMs with single- and partitioned-stator configurations are investigated and compared in Chapter 4, Chapter 5 and Chapter 6 respectively. Correspondingly, for a systematic research, the investigation on BFPMMs with dual stator configuration is necessary. Therefore, comparative study of BFPMMs with single stator, partitioned stator and dual stator configuration is one topic of future research.

B. Investigation on novel topologies of hybrid excited BFPMMs, including both single stator and portioned stator configurations.

Generally, hybrid excited machines can be evolved from the original PM machines. Meanwhile, the PM utilization efficiency can be enhanced (or PM usage can be reduced) while the torque performance can be maintained similar to the original PM machines. Moreover, due to the introduced DC field windings, the flux weakening performance can be

enhanced since the excitation field is adjustable. Therefore, the investigation on the topologies and electromagnetic performance of hybrid excited BFPMMs considering the single- and partitioned-stator configurations is desirable and can be one topic of further research. Furthermore, the topologies of hybrid excited SFPMMs can be considered as the references of hybrid excited BFPMMs with single- and partitioned-stator configurations. It should be noted that the topologies of hybrid excited PS-BFPMMs will be more flexible than those of SS-BFPMMs since the PMs and armature windings are located in two separated inner and outer stators.

C. Dynamic simulation and control of BFPMMs

In this thesis, the investigation is focused on the electromagnetic performance of novel stator DC field excited and PM synchronous machines. Meanwhile, the experiments are also focused on the static performance. However, to be a systematic research, the investigation on the control strategy, dynamic simulation and experiment are necessary and can be considered as one topic of future research.

D. Measurement and comparison of efficiency in BFPMMs

Efficiency map is one of the key specifications for electric vehicle (EV) application. Therefore, when considering the application field of BFPMMs, the investigation of efficiency map of BFPMMs with single- and partitioned-stator configuration is desirable and can be one topic of further research.

E. Multi-PMs Combinations in BFPMMs

According to the analyses in Chapter 4 and Chapter 5, the PM location of BFPMMs can be moved from the surface to the bottom of stator pole and even to the stator yoke since the main magnetic circuit is similar. Moreover, according to the [AFI16], the PM also can be located in the stator slot. Since the machine topology proposed in [AFI16] is same as the BFPMMs except the PM location, the multi-PM combinations can be employed in BFPMMs, such as the PMs can be located in the stator yoke (stator pole) and stator slot simultaneously. Meanwhile, the flux focusing structure (such as used in M4 as shown in Fig. 9.1) can also be adopted in BFPMMs with multi-PM combinations (for both PM located in stator yoke and stator slot). Moreover, the Multi-PM combination also can be extended to PS-BFPMMs.

REFERENCES

[AFI16] I. A. A. Afinowi, Z. Q. Zhu, Y. Guan, J. C. Mipo, and P. Farah, "A novel brushless AC doubly salient stator slot permanent magnet machine," *IEEE Trans. Energy Convers*., vol. 31, mo. 1, pp. 283-292, Mar. 2016.

[AZA14] Z. Azar and Z. Q. Zhu, "Performance analysis of synchronous reluctance machines having nonoverlapping concentrated winding and sinusoidal bipolar with dc bias excitation," *IEEE Trans. Ind. Appl*., vol.50, no.5, pp.3346-3356, Sep./Oct. 2014.

[BES98] M. Bianchi, S. Bolognani, M. Pre, and G. Grezzani, "Design considerations for fractional-slot winding configurations of synchronous machines," *IEEE Trans. Ind. Appl.*, vol.42, no.4, pp.997-1006, Jul./Aug. 2006.

[BIA02] N. Bianchi and S. Bolognani, "Design techniques for reducing the cogging torque in surface-mounted PM motors," *IEEE Trans. Ind. Appl*., vol. 38, no.5, pp. 1259-1265, Sep./Oct. 2002.

[BIA06a] N. Bianchi, S. Bolognani, and P. Frare, "Design criteria for high-efficiency SPM synchronous motors," *IEEE Trans. Energy Convers*., vol. 21, no.2, pp. 396-404, Jun. 2006.

[BIA06b] N. Bianchi, S. Bolognani, M. D. Pre, and G. Grezzani, "Design considerations for fractional-slot winding configurations of synchronous machines," *IEEE Trans. Ind. Appl*., vol. 42, no. 4, pp. 997-1006, July/Aug. 2006.

[BOL06] I. Boldea, *The Electrical Generators Handbook: Synchronous Generators*. Boca Raton: Taylor & Francis, 2006.

[CAI03] W. Cai, P. Pillay, Z. Tang, and A. M. Omekanda, "Low-vibration design of switched reluctance motors for automotive application using model analysis," *IEEE Trans. Ind. Appl*., vol.39 no.4, pp. 971-977, Jul./Aug. 2003.

[CAM92] D. E. Cameron, J. H. Lang, and S. D. Umans, "The origin and reduction of acoustic noise in doubly Salient variable reluctance motor," *IEEE Trans. Ind. Appl.,* vol.26, no.6, pp.1250-1255, Nov./Dec. 2011.

[CAO11] R. Cao, M. Cheng, C. Mi, W. Hua, and W. Zhao, "A linear doubly salient permanent-magnet motor with modular and complementary structure," *IEEE Trans. Magn*., vol.47, no.12, pp.4809-4821, Dec. 2011.

[CAO12] W. P. Cao, B. C. Mecrow, G. J. Atkinson, J. W. Benett, and D. J. Atkinson, "Overview of electric motor technologies used for more electric aircraft (MEA)," *IEEE Trans. Ind. Electron*., vol. 59, no. 9, pp. 3523-3531, Sep. 2012.

[CHE00] M. Chen, K. T. Chao, C. C. Chan, E. Zhou and X. Huang, "Nonlinear varying network magnetic circuit analysis for doubly salient permanent-magnet motors," *IEEE Trans. Magn*.,vol.36, no. 1, pp. 339-348, Jan. 2000.

[CHE01a] M. Chen, K. T. Chao and C. C. Chan, "Design and analysis of a new doubly salient permanent magnet motor," *IEEE Trans. Magn*., vol. 37, no. 4, pp. 3012-3020, Jul. 2001.

[CHE01b] M. Cheng, K. T. Chau, and C. C. Chan, "Static characteristics of a new doubly salient permanent machine," *IEEE Trans. Energy Convers*., vol. 16, no. 1, pp. 20-25, Mar. 2001.

[CHE03] M. Cheng, K. T. Chau, C. C. Chan and Q. Sun, "Control and operation of a new 8/6-pole doubly salient permanent-magnet motor drive," IEEE Tran., Ind. Appl., vol. 39, no.. 5, pp.1363-1371, Sep./Oct. 2003.

[CHE08] J. T. Chen, Z. Q. Zhu and D. Howe, "Stator and rotor pole combinations for multi-tooth flux-switching permanent-magnet brushless AC machines," *IEEE Trans, Magn*., vol. 44, no.12, pp. 4659-4667, Dec. 2008.

[CHE09] J. T. Chen, "High-torque direct-drive flux-switching permanent magnet brushless AC machines," *Ph.D. Thesis*, University of Sheffield, Oct. 2009.

[CHE10a] J. T. Chen, Z. Q. Zhu, S. Iwasaki, and R. Deodhar, "Low cost flux switching brushless AC macahines," in *Proc. IEEE Veh. Power Propulsion Conf*., Sep. 3-5, 2010, pp.1-3.

[CHE10b] J. T. Chen and Z. Q. Zhu, "Winding configurations and optimal stator and rotor pole combination of flux-switching PM brushless ac machines,"*IEEE Trans. Energy Convers*., vol.25, no.2, pp. 293-302, Jun. 2010.

[CHE10c] J. T. Chen, Z. Q. Zhu, S. Iwasaki, and R. Deodhar, "Low cost flux-switching brushless AC machines," *IEEE Vehicle Power and Propulsion Conf*., 1-3 Sept., 2010, Lille, Fracnce, VPPC 2010, Paper RT6/95-13475

[CHE11a] J. T. Chen, Z. Q. Zhu, S. Iwasaki, and R. Deodhar, "A novel E-core flux-switching PM brushless AC machine," *IEEE Trans. Ind. Appl.*, vol.47, no.3, pp. 1273-1282, 2011.

[CHE11b] J. T. Chen, Z. Q. Zhu, S. Iwasaki, and R. Deodhar, "Influence of slot opening on optimal stator and rotor pole combination and electromagnetic performance of flux-switching PM brushless AC machines," *IEEE Trans Ind. Appl*., vol.47, no.4, pp.1681-1691, Jul./Aug. 2011.

[CHE11c] M. Cheng, W. Hua, J. Z. Zhang, and W. X. Zhao, "Overview of stator-permanent magnet brushless machines," *IEEE Trans. Ind. Electron*., vol. 58, no.11, pp. 5087-5101, Nov. 2011.

[CHU14] W. Q. Chu, Z. Q. Zhu, J. Zhang, X. Ge, X. Liu, D. Stone, and M. Foster, "Comparison of electrically excited and interior permanent magnet machines for hybrid electric vehicle application," in *Int. Conf. on Electrical Machines and Systems (ICEMS)*, pp. 401-407, China, Oct. 2014.

[DEO96] R. Deodhar, S. Anderson, I. Boldea, and T. J. E. Miller, "The flux-reversal machine: A new brushless doubly-salient permanent magnet machine," *Proc. IEEE Ind. Appl. Society Ann. Meeting*, pp. 786-793., Oct. 1996.

[DEO97] R. Deodhar, S. Anderson, I. Boldea, and T. J. E. Miller, "The flux-reversal machine: A new brushless doubly-salient permanent magnet machine," *IEEE Trans. Ind. Appl*., vol. 33, pp. 925–934, July./Aug. 1997.

[DOR03] D. G. Dorrell, I. Chindurza, and F. Butt, "Operation, theory and comparison of the flux reversal machine-Is it a viable proposition?," *in Proc. Int. Conf. Power Electron. Drive Syst*., 2003, PP. 253-258.

[ELR10] A. M. El-Refaie, "Fractional-slot concentrated-windings synchronous permanent magnet machines: opportunities and challenges," *IEEE Trans. Ind. Electron*., vol. 57, no. 1, pp. 107-121, Jan. 2010.

[ELR11] A. M. El-Refaie, "Motors/generators for traction/propulsion applications: a reiview," in *IEEE Int. Elect. Mach. Drives Conf*., Niagara Falls, Canada, 2011, pp. 490-497.

[EVA15] D. J. Evans and Z. Q. Zhu, "Novel partitioned stator switched flux permanent magnet machines," *IEEE Trans Magn*, vol. 51, no. 1, Jan. 2015.

[FAI95] J. Faiz, J. W. Finch and H. M. B. Metwally, "A novel switched reluctance motor with multiple teeth per stator pole and comparison of such motors," *J. Elect. Power Syst. Res*., vol. 34, pp. 197-203, 1995.

[FAN06] Y. Fan, K. T. Chau, and S. Niu, "Development of a new brushless doubly fed

doubly salient machine for wind power generation," *IEEE Trans. Magn.*, vol. 42, no. 10, pp. 3455-3457, Oct. 2006.

[FAN08] Y. Fan and K. T. Chau, "Design, modeling, and analysis of a brushless doubly fed doubly salient machine for electric vehicles," *IEEE Trans. Ind. Appl.*, vol. 44, no. 3, pp. 727-734, May/Jun. 2008.

[FEI06] W. Z. Fei and J. X. Shen, "Novel permanent magnet switching flux Motors," *Proc. 41st Int.Universities Power Eng. Conf.*, 2006, pp. 729-733.

[FIN84] J.W. Finch, M. R. Harris, A. Musoke and H.M.B. Metwally, "Variable speed drives using multi-tooth per pole switched reluctance motors," *13th Annu. Symp. Incremental Motion Control Syst. Devices*, University of Illinois, Urbana, IL, USA, pp. 12-18, 1984.

[FUK12] T. Fukami, Y. Matsuura and K, Shima, "A multipole synchronous machine with nonoverlapping concentrated armature and field windings on the stator," *IEEE Trans. Ind. Electron.*, vol. 59, no. 6, pp. 2583-2591, Jun. 2012.

[GIN53] D. Ginsberg and L. J. Misenheimer, "Design calculations for permanent-magnet generators-including discussion," *AIEE Trans. Power Apparatus and Systems*, vol. 72, no. 2, part III, pp. 670-676, Jan. 1953.

[HOA97] E. Hoang, A. H. Ben-Ahmed, and J. Lucidarme, "Switching flux permanent magnet polyphased synchronous machines," in *Proc. 7th Eur. Conf. Power Electronics and Applications*, vol. 3, 1997, pp. 903-908.

[HON02] J. Hong, K. Ha, and J. Lee, "Stator pole and yoke design for vibration reduction of switched reluctance motor," *IEEE Trans. Magn.*, vol. 38, no.2, pp.929-932, Mar. 2002.

[HUA05] W. Hua, Z. Q. Zhu, M. Cheng, Y. Pang , and D. Howe, "Comparison of flux-switching and doubly-salient permanent magnet brushless machines," in *Proc. Int. Conf. Electrical Machines and Systems*, China, Sep. 27-29, 2005, pp.165-170.

[HUA08] W. Hua and M. Cheng, "A new model of vector-controlled doubly-salient permanent magnet motor with skewed rotor," in *Proc. Int. Conf. Elect. Mach. Syst.*, 2008, pp. 3026-3031.

[HUR10] C. Hurst, "China's rare earth elements industry: what can the west learn?," *Institute for the Analysis of Global Security (IAGS)*, Mar. 2010.

[HUS02] I.Husain, "Minimization of torque ripple in SRM drive," *IEEE Trans. Ind. Electron.*, vol. 49, no.1, pp.28-39, Feb. 2002

[ISH05] D. Ishak, Z. Q. Zhu, and D. Howe, "Eddy-current loss in the rotor magnets of permanent-magnet brushless machines having a fractional number of slots per pole," *IEEE Trans. Magn.*, vol. 41, no. 9, pp. 2462-2469, Sep. 2005.

[ISH06] D. Ishak, Z. Q. Zhu, and D. Howe, "Comparison of PM brushless motor, having either all teeth or alternate teeth wound," *IEEE Trans. Energy Convers.*, vol. 21, no. 1, pp. 95-103, Mar. 2006.

[JAH86] T. M. Jahns, "Interior permanent-magnet synchronous motors for adjustable-speed drives," *IEEE Trans. Ind. Appl.*, vol. IA-22, no. 4, pp. 738-747, Jul./Aug. 1986.

[KAS11] Y. Kashitani and S. Shimomura, "Novel slipring-less winding-excited synchronous machine," in *Int. Conf. Electr. Machines Systems*, Sept. 2011, pp.1-6.

[KIM09] T. H. Kim, "A study on the design of an inset-permanent-magnet-type flux-reversal machine," *IEEE Trans. Magn.*, vol.45, no.6 , pp.2859-2862, Jun. 2009.

[KOM12] G. Komurgoz and T. Gundogdu, "Comparison of salient pole and permanent

magnet synchronous machines designed for wind turbines," in *IEEE Power Electron. Mach. Wind Appl*., Denver, USA, 2012, pp. 1-5

[KON05] X. G. Kong and M. Cheng, "Static characteristics of a novel stator-doubly-fed doubly salient motor for electric vehicles," *Proc. Int. Conf. Electrical Machines and Systems*, China, Sept. 2005, pp. 866-869.

[KUO75] B. C. Kuo and G. Singh, "A dc-type hybrid step motor for large power application," *IEEE Trans. Ind. Appl*., vol. 11, no. 4, pp. 365–372, Jul./ Aug. 1975.

[LAW80] P. J. Lawrenson, J. M. Stephenson, P. T Blenkinsop, J. Corda, and N. N. Futon, "Variable-speed switched reluctance motors", *IET Proc*., vol.127, no. 4, pp. 253-265, July 1980.

[LEE04] J. W. Lee, H. S. Kim, B. I. Kwon, and B. T. Kim, "New rotor shape design for minimum torque ripple of SRM using FEM," *IEEE Trans. Magn*., vol.40. no.2, pp. 754-757, Mar.2004.

[LEE13] C. H. T. Lee, K. T. Chau and C. H, Liu, "Design and analysis of a DC field multitooth switched reluctance machine by using soft-magnetic-composite material," in *Int. Symp. Ind. Electron. (ISIE),* May 2013, pp,:1-6.

[LEV10] L. Levkowitz, "China's rare earths industry and its role in the international market," *U.S.-China Economic and Security Review Commission Staff Background*, Nov. 2010.

[LI93] S. H. Li, F. Liang, Y. Zhao, and T. A. Lipo, "A doubly salient doubly excited variable reluctance motor," *Proc. IEEE Ind. Appl. Society Ann. Meeting*, pp. 137-143., Oct. 1993.

[LI95] S. H. Li, F. Liang, Y. Zhao, and T. A. Lipo, "A doubly salient doubly excited variable reluctance motor," *IEEE Trans. Ind. Appl*., vol. 31, no. 1, pp. 99–106, Jan./Feb. 1995.

[LI07] Y. Li and C. C. Mi, "Doubly salient permanent-magnet machine with skewed rotor and six-state commutating mode," *IEEE Trans. Magn*., vol. 43, no. 9, pp. 3623–3629, Sep. 2007.

[LI08] H. Li and Z. Chen, "Overview of different wind generator systems and their comparisons," *IET Renew. Power General*., vol.2 no. 2, pp. 123-138, 2008

[LIA92] Y. Liao, F. Liang, and T. A. Lipo, "A novel permanent magnet motor with doubly salient structure," *Proc. IEEE Ind. Appl. Society Ann. Meeting*, pp. 308-314., Oct. 1992.

[LIA95] Y. Liao, F. Liang, and T. A. Lipo, "A novel permanent magnet motor with doubly salient structure," *IEEE Trans. Ind. Appl*., vol. 31, no. 5, pp. 1069–1078, Sep./Oct. 1995.

[LIU12a] H. Liu, Liu, L. Xu, M. Shangguan, and W. N. Fu, "Finite element analysis of 1 mw high speed wound-rotor synchronous machine," *IEEE Trans. Magn*., vol. 48, no. 11, pp. 4650-4653, Nov. 2012.

[LIU12b] X. Liu and Z. Q. Zhu, "Electromagnetic performance of novel variable flux reluctance machines with DC-field coil in stator," *IEEE Trans. Magn*., vol. 49, no. 6, pp. 3020-3028, Aug. 2012.

[LIU12c] X. Liu, Z. Q. Zhu, M. Hasegawa, A, Pride, and R. Deodhar, "Vibration and noise in novel variable flux reluctance machine with DC-field coil in stator," in *Proc. Int. Conf. Power Electron. Motion Control*, Jun 2-5, 2012, pp.1100-1107.

[LIU12d] X. Liu, Z. Q. Zhu and Z. P. Pan, "Analysis of electromagnetic torque in sinusoidal excited switched reluctance machines having DC bias in excitation," in *Proc. Int. Conf. Elect. Mach*., 2012, pp. 2882-2888.

[LIU13] X. Liu and Z. Q. Zhu, "Comparative study of novel variable flux reluctance machines with doubly fed doubly salient machines," *IEEE Trans. Magn*., vol 49, no. 7, pp. 3838-3941, Jul. 2013.

[LIU14] X. Liu and Z. Q. Zhu, "Stator/rotor pole combinations and winding configurations of variable flux reluctance machines," *IEEE Trans Ind. Appl*., vol.50, no.6, pp.3675-3684, Nov./Dec. 2014.

[LON01] S. A. Long, Z. Q. Zhu, and D. Howe, "Vibration behavior of stators of switched reluctance machines," *Inst. Elect. Eng. Proc. Elect. Power Appl*., vol. 148, no.3, pp.257-264, 2001.

[LUO96] X. G. Luo, D. Y. Qin and T. A. Lipo, "A novel two phase doubly salient permanent magnet motor," *Proc. IEEE Ind. Appl. Society Ann. Meeting*, pp. 808-815., Oct. 1996.

[MIL93] T. J. E. Miller, Switched reluctance motors and their control. U.K. Oxford University Press, 1993.

[PAN07] Y. Pang, Z. Q. Zhu, D. Howe, S. Iwasaki, R.Deodhar, and A. Pride, "Comparative study of flux-switching and interior permanent magnet machines," in *Proc. Int. Conf. Elect. Mach. Syst*., 2007, pp.757-762.

[PIL99] P. Pillay, and W. Cai, "An investigating into vibration in switched reluctance motors," *IEEE Trans. Ind. Appl*., vol.35, no.3, pp.589-596, May/Jun. 1999.

[POL03] C. Pollock and M. Wallace, "Electronically controlled flux switching motors: a comparison with an induction motor driving an axial fan," in *Proc. IEEE IECON*, 2003, pp. 2465-2470.

[POL06a] H. Polinder, F. F. A. van der Pijl, G. J. de Vilder, and P. J. Tavner, "Comparison of direct-drive and geared generator concepts for wind turbines," *IEEE Trans. Energy Convers*., vol. 21, no. 3, pp. 725-733, Sep. 2006.

[POL06b] C. Pollock, H. Pollock, R. Barron, J. R. Coles, D. Moule, A. Court, and R. Sutton, "Flux-switching motors for automotive applications," *IEEE Trans. Ind. Appl*.,vol. 42, no. 5, pp. 1177–1184, Sep./Oct. 2006.

[POL99] C. Pollock and M. Wallace, "The flux switching motor, a DC motor without magnets or brushes," in *Conf. Rec. IEEE IAS Annu. Meeting*, 1999, vol. 3, pp. 1980–1987.

[PUL88] D.W.J. Pulle, "Performance of split-coil switched reluctance drive," IEE. Elect. Power. Appl., vol. 135, Proc. B, no.6, pp. 318-323, Nov, 1988

[QU13] R. Qu, Y. Liu, and J. Wang, "Review of superconducting generator topologies for direct-drive wind turbines," *IEEE Trans. on Appl. Supercond*., vol. 23, no. 3, pp. 5201108-5201108, Jun. 2013.

[RAU55] S. E. Rauch and L. J. Johnson, "Design principles of flux-switching alternators," *AIEE Trans*., 74III, pp.1261-1268, 1955.

[ROS06] C. Rossi, D. Casadei, A. Pilati, and M. Marano, "Wound rotor salient pole synchronous machine drive for electric traction," in *Conf. Rec. IEEE Industry Appl*., Tampa, Florida, 2006, pp. 1235-1241.

[SCH08] R. Schiferl, A. Flory, W. C. Livoti, and S. D. Umans, "High-temperature superconducting synchronous motors: economic issues for industrial applications," *IEEE Trans. Ind. Appl*., vol. 44, no. 5, pp. 1376-1384, Sep./Oct. 2008.

[SHA93] A. Shakel, Y. Liao, and T. A. Lipo, "A permanent magnet ac machine structure with true field weakening capability," in *Proc. IEEE Int. Symp. Ind. Electron*., 1993, pp. 19-24.

[SHI14a] J. T. Shi, X. Liu, D. Wu and Z. Q. Zhu, "Influence of stator and rotor pole arcs

on electromagnetic torque of variable flux reluctance machines," *IEEE Trans. Magn*., vol.50, no.11, Nov. 2014.

[SHI14b] J. T. Shi, Z. Q. Zhu, D. Wu and X. Liu, "Comparative study of novel synchronous machines having permanent magnets in stator poles," in *Int. Conf. on Electrical Machines (ICEM)*, pp.429-435, Sep.2014.

[SHI14c] J. T. Shi, Z. Q. Zhu, D. Wu and X. Liu, "Influence of flux focusing on electromagnetic torque of novel biased flux PM machines," in *Int. Conf. on Electrical Machines (ICEM)*, pp.523-529, Sep.2014.

[SHI15] J. T. Shi and Z. Q. Zhu, "Analysis of novel multi-tooth variable flux reluctance machines with different stator and rotor pole combinations," *IEEE Trans. Magn*., vol. 51, no. 5, 2015.

[VIJ08] K. Vijayakumar, R. Karthikeyan, S. Paramasivam, R. Arumugam, and K. N. Srinivas, "Switched reluctance motor modeling, design, simulation, and analysis: a comprehensive review," *IEEE Trans. Magn*., vol. 44, no. 12, pp. 4605-4617, Dec. 2008.

[WAN99] C. Wang, S. A. Nasar and I. Boldea, "Three-phase flux reversal machine (FRM)," *IEE Proceedings on Electr. Power. Appl*., vol. 146, no. 2, Mar. 1999.

[WU14] D. Wu, J. T. Shi, Z. Q. Zhu and X. Liu, "Electromagnetic performance of novel synchronous machines with permanent magnets in stator yoke," *IEEE Trans. Magn*., vol. 50, no. 9, Sep. 2014.

[WU15] Z. Z. Wu, Z. Q. Zhu and J. T. Shi, "Novel doubly salient permanent magnet machines with partitioned stator and iron pieces rotor," *IEEE Trans. Magn*., vol. PP, no. 99, 2015.

[ZHA09]] J. Z. Zhang, M. Cheng, Z. Chen and W. Hua, "Comparison of stator-mounted permanent–magnet machines based on a general power equation," *IEEE Trans. Energy Convers*., vol. 24, no. 4, pp. 826-834, Dec. 2009.

[ZHA10] W. X. Zhao, K. T. Chau, M. Cheng, J. H. Ji and X. Y. Zhu, "Remedial brushless AC operation of fault-tolerant doubly salient permanent-magnet motor drives," *IEEE Trans. Ind. Electron*., vol. 57, no.6, pp 2134-2141, Jun. 2010.

[ZHU00] Z. Q. Zhu and D. Howe, "Influence of design parameters on cogging torque in permanent magnet machines," *IEEE Trans. Energy Convers*., vol. 15, no.4, pp. 407-412, Dec. 2000.

[ZHU04] Z. Q. Zhu, K. Ng, N. Schofield, and D. Howe, "Improved analytical modelling of rotor eddy current loss in brushless machines equipped with surface-mounted permanent magnets," in *IEE Proc. Electr. Power Appl*., vol. 151, no. 6, Nov. 2004.

[ZHU05] Z. Q. Zhu, Y. Pang, D. Howe, S. Iwasaki, R. Deodhar, and A. Pride, "Analysis of electromagnetic performance of flux-switching permanent magnet machines by non-linear adaptive lumped parameter magnetic circuit model," *IEEE Trans. Magn*., vol. 41, no. 11, pp. 4277-4287, Nov. 2005.

[ZHU07] Z. Q. Zhu and D. Howe, "Electrical machines and drives for electric, hybrid, and fuel cell vehicles," *Proc. IEEE*, vol. 95, no. 4, pp. 746-765, Apr. 2007.

[ZHU08a] Z. Q. Zhu, J. T. Chen, Y. Pang, D. Howe, S. Iwasaki, and R. Deodhar, "Analysis of a novel multi-tooth flux-switching PM brushless ac machine for high torque direct-drive applications," *IEEE Trans. Magn*., vol.44, no.11, pp.4313-4316, Nov. 2008.

[ZHU08b] Z. Q. Zhu, Y. Pang, J. T. Chen, R. L. Owen, D. Howe, S. Iwasaki, R. Deodhar, and A. Pride, "Analysis and reduction of magnet eddy current loss in flux-switching permanent magnet machines," in Proc. Power Electronices, Machines

and Drives, 2008, pp. 120-124.

[ZHU09] Z. Q. Zhu, "A simple method for measuring cogging torque in permanent magnet machines," in *IEEE Power & Energy Society General Meeting*, Calgary, U.S., Jul. 2009, pp. 1-4.

[ZHU10] Z. Q. Zhu and J. T. Chen, "Advanced flux-switching permanent magnet brushless machines," *IEEE Trans. Magn*.,vol. 46, no. 6, pp. 1447-1453, Jun. 2010.

[ZHU11a] Z. Q. Zhu, "Fractional slot permanent magnet brushless machines and drives for electric and hybrid propulsion systems," *Trans. COMPEL*., vol. 30, no. 1, pp. 9-31, 2011.

[ZHU11b] Z.Q. Zhu, "Switched flux permanent magnet machines – innovation continues", *Proc. Int. Conf. on Electrical Machines and Systems*, 20-23 August 2011, Beijing, paper Keynote Speech-06.

[ZHU15] Z. Q. Zhu and X. Liu, "Novel stator electrically field excited synchronous machines without rare-earth magnet," *IEEE Trans. Magn*., vol. 51, no. 4, 8103609, Apr. 2015.

[ZHO13a] Y. J. Zhou, and Z. Q. Zhu, "Comparison of low-cost wound-field switched-flux machines," In *Proc. Energy Conversion Congress and Exposition (ECCE).*, Sep 15-19, 2013, pp.904-911/

[ZHO13b] Y. J. Zhou, and Z. Q. Zhu, "Torque density and magnet usage efficiency enhancement of sandwiched switched flux permanent magnet machines using V-shape magnets," *IEEE Trans. Magn*. Vol.49, no.7, pp.3834-3837, Jul. 2013

[ZUL10] A. Zulu, B. Mecrow, and M. Armstrong, "A wound-field three-phase flux switching synchronous motor with all excitation sources on the stator," *IEEE Trans. Ind. Appl*. vol.46, no.6 pp.2363-2371, Nov./Dec. 2010.

[ZUL12a A. Zulu, B. Mecrow, and M. Armstrong, "Investigation of the dq-equivalent model for performance prediction of flux-switching synchronous motors with segmented rotors," IEEE Trans. Ind. Electron. Vol. 59, pp. 2393-2402, Jun. 2012.

[ZUL12b] A. Zulu, B. Mecrow, and A. Armstrong, "Permanent-magnet flux-switching synchronous motor employing a segmental rotor," *IEEE Trans. Ind. Appl*., vol. 48, no. 6. pp. 2259–2267, Nov./Dec. 2012.

APPENDIX A
COGGING TORQUE AND STATIC TORQUE TEST METHOD

The test method described in [ZHU09] is employed in this thesis to measure the cogging torque and also to measure the static torque, as shown in Fig. A.1. The stator of measured machine is clamped in the jaws of a lathe, while the rotor shaft is attached with a balanced beam. One side of the balanced beam is resting on the tray of a digital weight gauge, and a screw is used to adjust the level of balanced beam with the aid of gradienter. A pre-load weight is added on the measurement end of balanced beam to ensure that the balanced beam is always in contact with the digital weight gauge during the testing process. The degree calibration on the faceplate of the lathe is used to turn the stator in the precise steps and also indicate the corresponding rotor position.

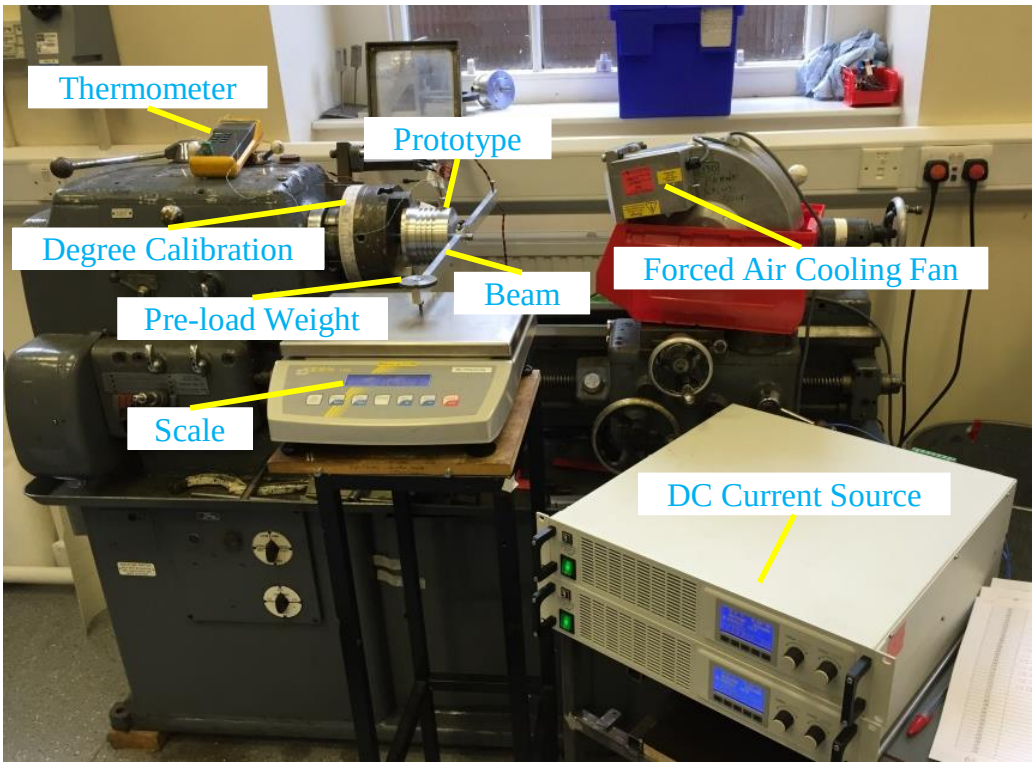

Fig. A.1. Typical test rig set-up for cogging torque and static torque measurements.

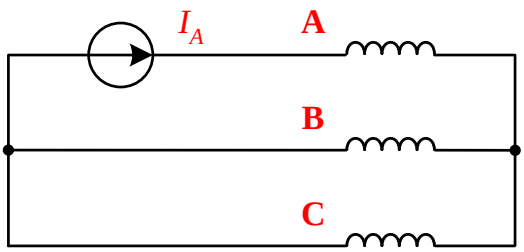

Fig. A.2. DC current supply connection for static torque waveform test.

To measure the cogging torque waveform, the stator is manually rotated within a cogging torque period, and the data displaying on the digital weight gauge (F_w) will be recorded together with corresponding rotor position. Then, according to (A.1), the data can be transferred to cogging torque against with rotor position as cogging torque waveform [ZHU09].

$$T_c = \left(F_w - M_{pre-load}\right)gL \tag{A.1}$$

where F is the reading from the digital weight gauge, $M_{pre\text{-}load}$ is the pre-load weight, g is gravity acceleration and L is arm length of the balanced beam from the center of rotor shaft to the acting point on the digital weight gauge.

Similar to cogging torque waveform, the static torque waveform can be measured in the same method by supplying three-phase armature windings with DC current as $I_{DC}=I_A=-2I_B=-2I_C$, as shown in Fig. A.2. Furthermore, the thermometer and forced air cooling fan are used to ensure the temperature of armature winding within the safety limitation.

APPENDIX B
NOVEL CONSEQUENT POLE SYNCHRONOUS MACHINES WITH CONCENTRATED WINDINGS AND PERMANENT MAGNETS ON STATOR POLE SURFACE

In Chapter 4, the electromagnetic performance of biased flux PM machines (BFPMMs) considering the influence of PM locations have been investigated. Based on the surface mounted BFPMM (SM-BFPMM), when half of PMs (either all S pole PMs or N pole PMs) are removed and replaced by laminations, novel consequent pole SM-BFPMM (CP-SM-BFPMM) is proposed and investigated in this chapter.

B.1 Introduction

Variable flux reluctance machine (VFRM) which adopts doubly salient stator and rotor structure with concentrated windings is proposed and investigated in [LIU12b] [LIU12c] [LIU13] [LIU14] [KAS11] [FUK12]. Similar to doubly fed doubly salient machine (DFDSM), VFRM is also developed from switched reluctance machine (SRM) by introducing stator DC field winding. However, the main difference between these two machines is that the DC field winding is wound around each stator pole in VFRM but full-pitched in DFDSM [LIU13] [LI95]. Hence, the flux paths for each phase in the stator of VFRM are identical. Meanwhile, the choice of rotor pole number in VFRM also significantly exceeds that in SRM and DFDSM, as it can be any integers except the phase number and its multiples. Further, since all the even emf harmonics which cause the emf asymmetry in each coil can be completely cancelled in phase winding when using special stator/rotor pole combinations, such as 6/5, 6/7, 12/10, 12/11, 12/13 and 12/14 etc, more sinusoidal phase flux-linkage and back-EMF waveforms will be obtained in VFRM [LIU12b] [LIU14].

However, similar to other DC excitation machines, the torque density of VFRM is relatively low when compared with permanent magnet (PM) machines. Therefore, the method which replaces DC field windings with PMs to improve the torque performance is adopted in VFRM. Alternate polarity PMs can be equivalently located in the stator back iron at an interval of pole number equal to one or housed in the adjacent stator poles. Correspondingly, these two machines are designated as stator yoke mounted biased flux PM machine (BFPMM) (SYM-BFPMM) and surface mounted BFPMM (SM-BFPMM) in

[WU14] and [SHI14b] respectively. Similar to VFRM, both SYM-BFPMM and SM-BFPMM have flexible stator and rotor pole combination as well as sinusoidal phase flux-linkage and back-EMF. Meanwhile, the copper loss of DC field winding in VFRM is eliminated in both SYM-BFPMM and SM-BFPMM. In addition, the PM positions of SM-BFPMM can be moved from the surface to the bottom of stator pole since the main magnetic circuit is similar (even can be moved to stator yoke as SYM-BFPMM) [SHI14b]. However, the optimal torque performance for BFPMMs with PMs located in the stator pole is obtained when the PMs are mounted on the surface of stator pole due to the lowest flux leakage.

Based on SM-BFPMM, when half of PMs (either all S pole PMs or N poles PMs) are removed and replaced by laminations, novel consequent pole SM-BFPMM (CP-SM-BFPMM) is proposed and investigated in this Appendix. Firstly, the operation principle and stator/rotor pole combinations are illustrated. Then, unequal stator pole arc technique (UT) is used to enhance the torque performance of CP-SM-BFPMMs. The electromagnetic performances of CP-SM-BFPMMs with UT will be compared with the CP-SM-BFPMMs with equal stator pole arc technique (ET) under both 6/5 and 6/7 stator/rotor pole combinations. All of the machines are optimized for maximum average torque at the rated 30W copper loss.

B.2 Operation Principle and Stator/Rotor Pole Combinations

B.2.1 Machine Topologies and Operation Principle

As shown in Fig. B.1(a), doubly salient stator and rotor structure with concentrated armature winding are adopted in SM-BFPMM. Meanwhile, alternate polarity PMs are housed on the surface of adjacent stator poles. Further, when half of PMs (either all S Pole PMs or N pole PMs) are removed and replaced by laminations, novel consequent pole SM-BFPMM (CP-SM-BFPMM) is developed as shown in Fig. B.1(b). Compared with SM-BFPMM, the main difference is that the PM flux produced by PM in one stator pole is flowed into adjacent stator poles without PMs to form complete flux loops with rotor poles together in CP-SM-BFPMM, as shown in Fig. B.1. In other words, the PM flux, which circulated from two adjacent stator poles with PM housed, formed a virtual PM with opposite polarity in the stator pole without PM housed. Hence, similar phase flux-linkage can be obtained in CP-SM-BFPMM.

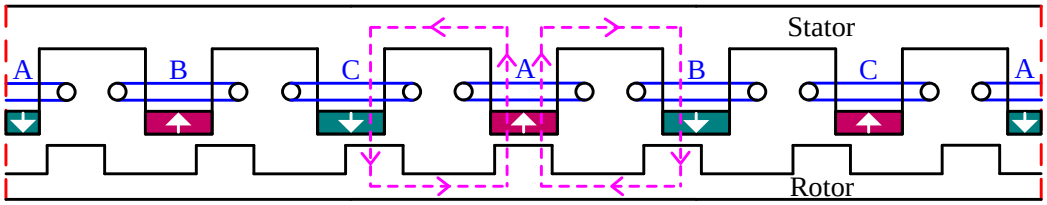

(a) SM-BFPMM.

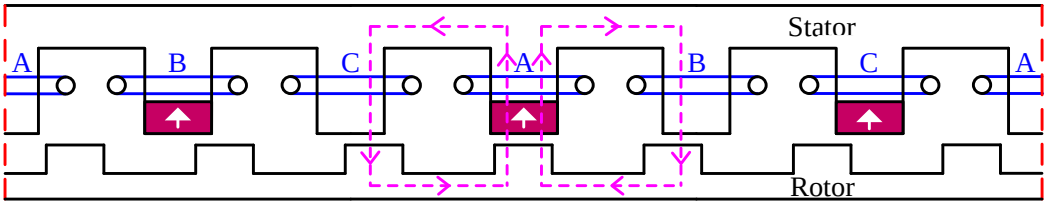

(b) CP-SM-BFPMM.

Fig. B.1. Structure evolution from SM-BFPMM to CP-SM-BFPMM.

In order to produce the positive average torque over one electric period in CP-SM-BFPMM, positive current should be injected into armature coil to enhance the air-gap field around the stator pole by producing the same polarity flux with PM flux when the rotor pole moves from unaligned position to aligned position as well as negative current is injected into armature coil to weaken the air-gap field to help the rotor pole moving smoothly from aligned position to unaligned position, Fig. B.2(a) and (b). (Aligned position is defined as the position of one rotor pole aligned with one stator pole with PM housed.) Further, as a combined result of three phase operation, continuous output torque will be generated.

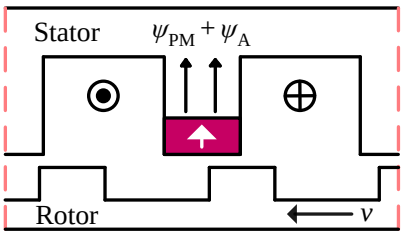

(a) Moving form unaligned to aligned position

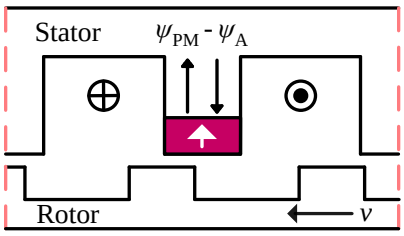

(b) Moving from aligned to unaligned position

Fig. B.2. Operation principle schematics of CP-SM-BFPMM.

Similar to SM-BFPMM, CP-SM-BFPMM is also one kind of stator PM synchronous machines due to similar operation principle. Hence, the expression of electromagnetic torque in PM synchronous machines [ZHU05] can be extended to CP-SM-BFPMM, e.g.

$$T = \frac{3}{2} N_r \psi_{PM} I_q \tag{B.1}$$

where N_r is the number of rotor poles, ψ_{PM} is the PM flux-linkage, I_q is the q-axis current.

B.2.2 Stator and Rotor Pole Combinations

For CP-SM-BFPMM, the choice of stator and rotor pole combinations is flexible. The stator pole number N_s should be the multiples of phase number while the rotor pole number N_r can be any integers except phase number and its multiples. Hence, the selection of N_s and N_r can be summarized as

$$N_s = km \ (k = 1, 2\ldots) \tag{B.2}$$

$$N_r = N_s \pm j \ (N_r \neq k_i m, j = 1, 2\ldots, k_i = 1.\ 2\ldots) \tag{B.3}$$

where m is the phase number, k, j and k_i are integers.

By using the conventional coil-EMF vector method, the coil connection of armature windings for CP-SM-BFPMM can be determined [ZHU10]. According to the equation (B.4), when the mechanical degree α_m and rotor pole number N_r is determined, the electrical degree α_e between two adjacent coil-EMF vectors can be calculated.

$$\alpha_e = N_r \alpha_m \tag{B.4}$$

Fig. B.3 shows the topologies of 6-stator pole CP-SM-BFPMMs with suitable rotor pole numbers. The main geometric parameters of four machines are listed in Table B.1, which are optimized under the constraint of rated 30W copper loss. According to (B.4) and Fig. B.3, the coils belong to same phase are connected in series with same polarity in 4- and 8-rotor pole CP-SM-BFPMMs but with opposite polarity in 5- and 7-rotor pole CP-SM-BFPMMs. Meanwhile, as shown in Fig. B.4, the open-circuit phase flux-linkage is unipolar for 4- and 8-rotor pole CP-SM-BFPMMs but bipolar for 5- and 7-pole CP-SM-BFPMMs. Fig. B.5 shows the open-circuit phase back-EMF waveforms of four machines at rated speed of 400rpm. As shown in Table B.2, it can be seen that 5-rotor pole CP-SM-BFPMM exhibits the highest fundamental back-EMF among the four stator/rotor pole combinations. Fig. B.6 shows the waveform of torque with rotor position over one electrical period. The average torques of 4-, 5-, 7- and 8-rotor pole CP-SM-BFPMMs are 1.28, 1.36, 1.32 and 1.23Nm respectively at the rated copper loss, as shown in Table B.2. Obviously, CP-SM-BFPMMs with 6 stator pole exhibit the highest torque capability when the number of stator and rotor poles differed by one.

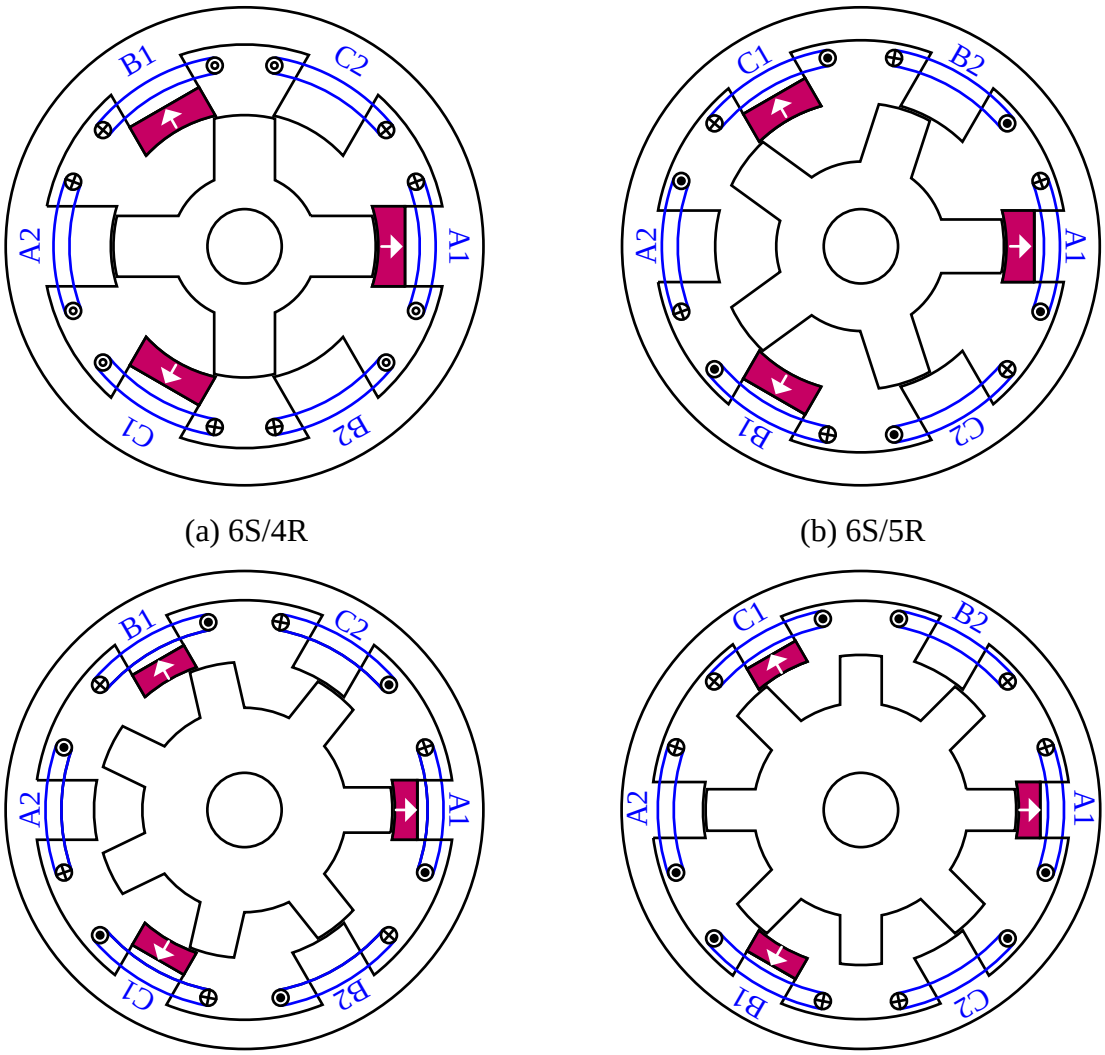

(a) 6S/4R (b) 6S/5R

(c) 6S/7R (d) 6S/8R

Fig. B.3. Topologies of 6-stator pole CP-SM-BFPMMs with different rotor pole number.

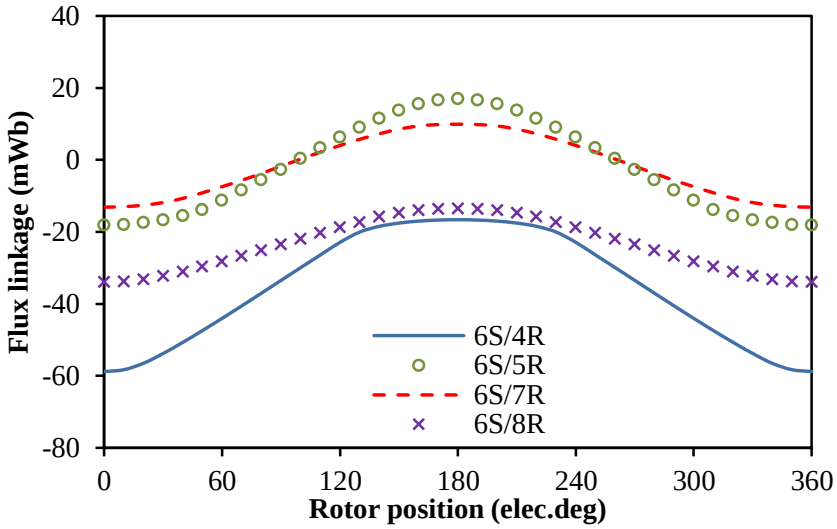

Fig. B.4. Open-circuit phase flux-linkages of CP-SM-BFPMMs.

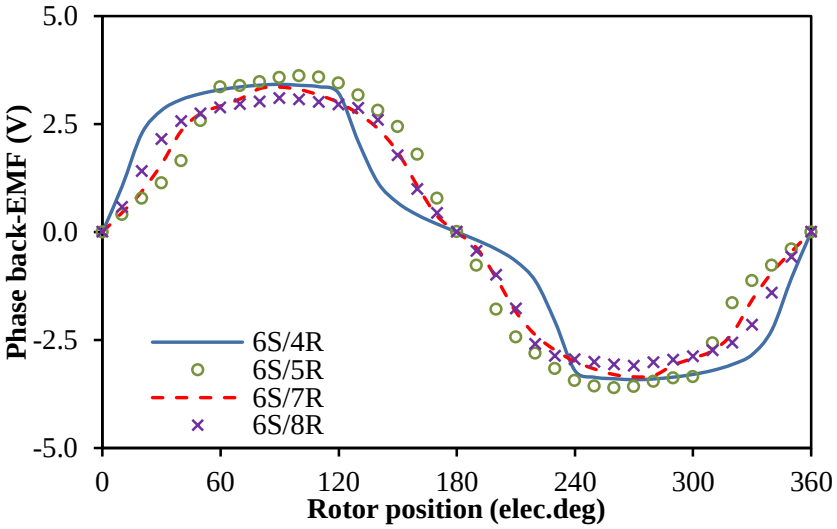

Fig. B.5. Open-circuit phase back-EMFs of CP-SM-BFPMMs, 400rpm.

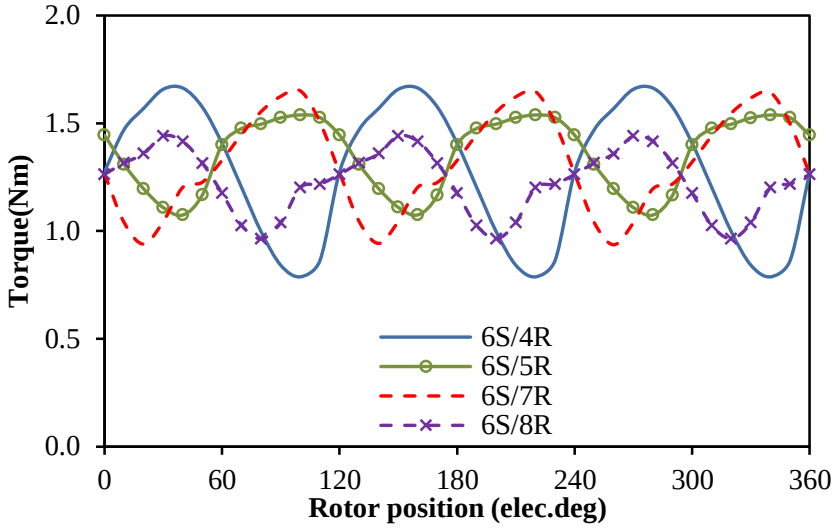

Fig. B.6. Electromagnetic torque of CP-SM-BFPMMs at rated current, p_c=30W.

Table B.1 Parameters of prototype machines for PS-BFPMM and PS-SFPMM

Parameter	**CP-SM-BFPMMs with 6-pole stator**			
Number of phases	3			
Turns per coil	72			
Rated speed (rpm)	400			
Outer radius of stator (mm)	45			
Active axial length (mm)	25			
Airgap length (mm)	0.5			
Packing factor	0.5			
Rated copper loss (W)	30			
Number of stator poles N_s	6			
Number of rotor poles N_r	4	5	7	8
Equal/Unequal stator pole	ET	ET/UT	ET/UT	ET
Split ratio	0.56	0.61/0.62	0.63/0.62	0.66
Stator pole arc (°)	34.8	28.4/39.6 19.6	22.8/32.0 17.6	20.4
Rotor pole arc (°)	26.8	21.6/21.5	17.6/17.0	15.4
Stator back iron (mm)	7.0	6.2/5.7	5.5/5.1	5.6
Slot area (mm^2)	229	240/240	271/282	249
Rated AC current (A_{rms})	7.8	8.0/8.0	8.5/8.7	8.1
Minimum PM thickness (mm)	5.0	5.2/4.5	4.2/5.0	4.0
Magnetic remanence (T)	1.2T			
Relative PM permeability	1.05			

Table B.2 Main parameters of electromagnetic performance

Parameter	**CP-SM-BFPMMs with 6-pole stator**			
Number of rotor poles N_r	4	5	7	8
Equal/Unequal stator pole	ET	ET/UT	ET/UT	ET
1^{st} flux-linkage (mWb)	21.1	17.6/19.6	11.6/13.8	10.1
1^{st} back-EMF (V)	3.52	3.68/4.09	3.41/4.03	3.37
Average torque (Nm)	1.28	1.36/1.54/	1.32/1.54	1.23
Incremental rate (%)		13.2	16.7	

B.3 Unequal Stator Pole Arc Technique

According to the analyses and globe optimizing results in [WU14] and [SHI14a], for the doubly salient stator and rotor pole structure machines which have no PMs in the stator pole, the optimum torque capability are obtained when the rotor pole arc to rotor pole pitch ratio is ~1/3 and the optimal stator pole arc is close to the optimal rotor pole arc. Further, for CP-SM-BFPMMs, since unipolar PMs are housed on the surfaces of alternate stator poles, the widths of half stator poles are restricted by the widths of PMs, as shown in Fig. B.3.

According to (B.1), PM flux-linkage ψ_{PM} and q-axis current I_q are two main parameters should be considered to improve the torque capability. Firstly, according to (B.5), the PM flux φ_{PM} can be enhanced by increasing the width of stator pole with PMs housed since the PM remanence B_r is same but the cross sectional area S_{PM} is increased. Correspondingly, the PM flux-linkage ψ_{PM} is also increased. Secondly, in order to compensate the loss of slot area which is caused by increased width of stator pole with PM housed, the width of stator pole without PM housed can be reduced to around the width of rotor pole to increase the slot area. As shown in Table B.1, for 5- and 7-rotor pole CP-SM-BFPMMs, the slot area of using unequal stator pole arc technique are almost the same as (or even larger than) that of using equal stator pole arc technique. Equation (B.6) shows the number of turns N_a and armature current I_a vary with the slot area S_a under the fixed copper loss. Obviously, when N_a is kept constant, I_a will be increased as the enlarged S_a. Hence, combined with the variation of two main parameters, the unequal stator pole arc technique can be used to improve the torque capability of CP-BFPMM.

$$\varphi_{PM} = B_r S_{PM} \tag{B.5}$$

$$N_a I_a \propto \sqrt{S_a} \tag{B.6}$$

In the following section, the influence of unequal stator pole arc technique on CP-SM-BFPMM will be analysed and compared with the original equal stator pole arc technique under the stator and rotor pole combinations determined by $N_r = N_s \pm 1$ since they exhibit larger average torque than that of $N_r = N_s \pm 2$ at rated copper loss, as shown in Table B.2. In order to simplify the comparison, the original equal stator pole arc technique and unequal stator pole arc technique can be designated as ET and UT respectively. The main geometric parameters of 6/5 and 6/7 stator/rotor pole CP-SM-BFPMMs with ET and UT are listed in Table B.1, which are optimized for maximum average torque under rated 30W copper loss.

B.4 Performance Comparison between Equal and Unequal Stator Pole Arc Techniques

B.4.1 Open-Circuit Field Distribution

The open-circuit flux equipotential and flux density field distribution for four machines at aligned position are shown in Fig. B.7. It can be seen that all machines have short flux path which can result in lower MMF drop in the stator. Meanwhile, the coils belong to the same phase have independently complete flux loops. Moreover, for both 5- and 7- pole CP-SM-BFPMMs, the saturation levels of machines with UT are heavier than those with ET due to the enhanced PM flux which is caused by the increased width of PM.

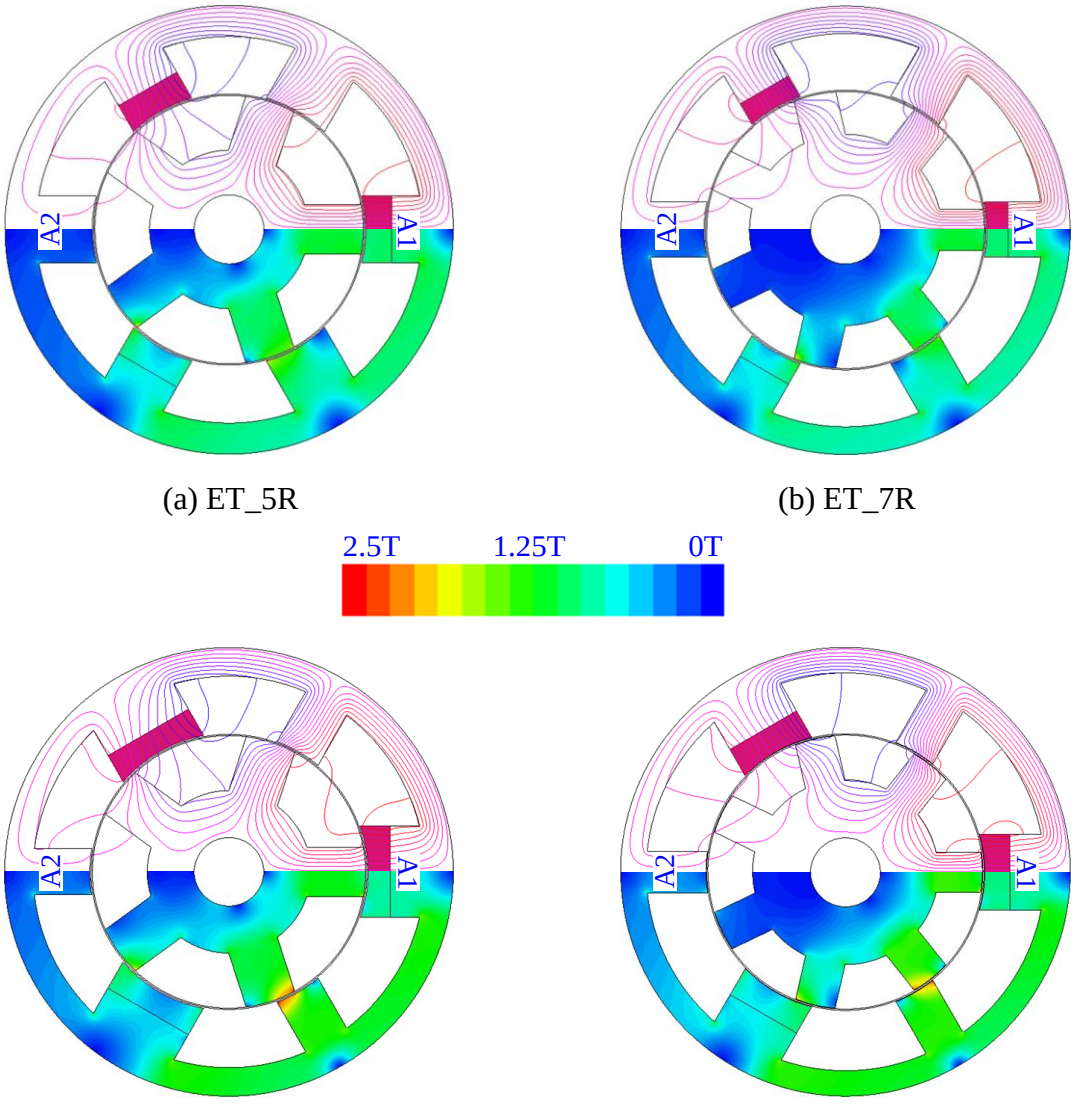

(a) ET_5R (b) ET_7R

(c) UT_5R (d) UT-7R

Fig. B.7. Open-circuit equipotential and flux density field distribution of 6-pole CP-SM-BFPMMs with equal and unequal stator pole arc techniques.

Fig. B.8 shows the open-circuit air-gap flux density distributions at aligned position, which is the same as Fig. B.7. Obviously, for the same rotor pole, machines with UT exhibit higher peak value of flux density, especially in the regions around the adjacent stator poles close to the stator pole which is wound with coil A1. Meanwhile, it also implies that larger back-EMF and torque capability may be obtained in machines with UT.

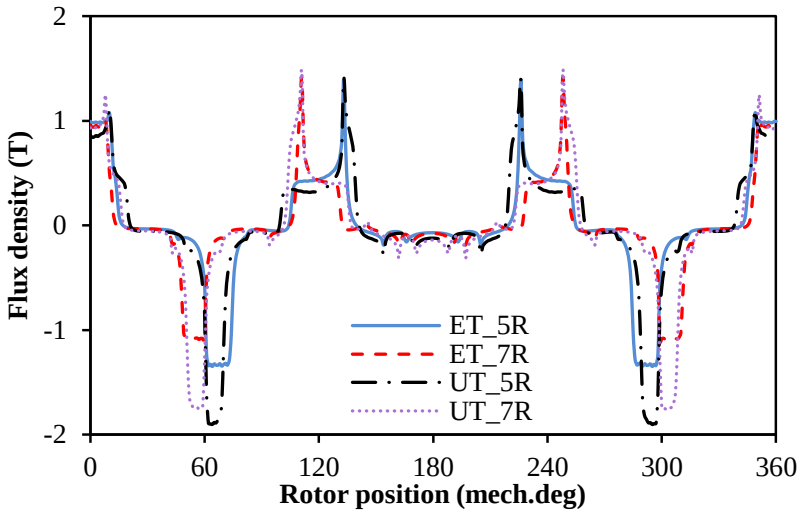

Fig. B.8. Open-circuit air-gap flux density of ET- and UT-CP-SM-BFPMMs at aligned position, *d*-axis.

B.4.2 Open-Circuit Flux-Linkage and Back-EMF Waveforms

Fig. B.9 shows the open-circuit bipolar phase flux-linkages of four machines. Obviously, machines with UT have higher peak to peak value of phase flux-linkage than that with ET when the rotor pole number is same. It means that UT can boost the flux-linkage of CP-SM-BFPMM which agrees with the analysis mentioned above. In addition, since the electric frequency is the same when the rotor pole number is same, the machine with UT should also exhibit larger peak to peak value of back-EMF or fundamental back-EMF than that with ET. It can be evidenced by the waveforms and FFT results of phase back-EMF (rated 400rpm) as shown in Fig. B.10 and Table B.2. Overall, the static performance of CP-SM-BFPMM can be improved by UT. Meanwhile, 5-rotor pole CP-SM-BFPMM with UT has the largest fundamental back-EMF although it also includes the highest even harmonics among four machines.

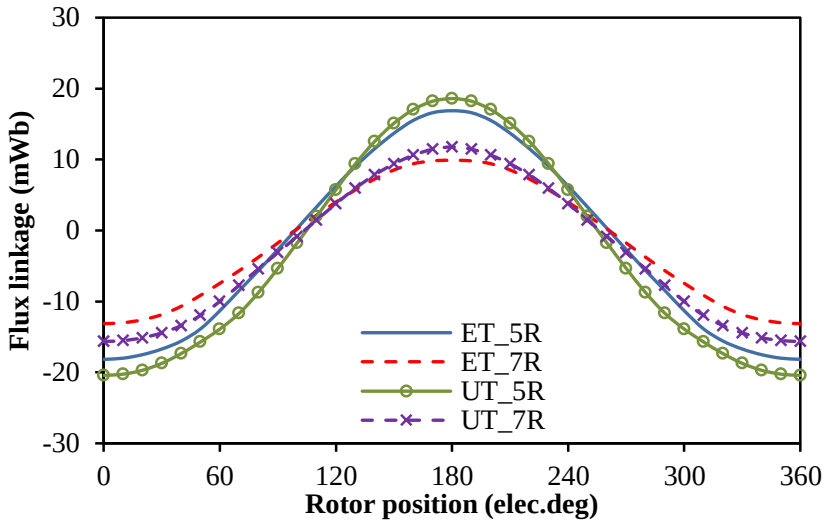

Fig. B.9. Open-circuit phase flux-linkage.

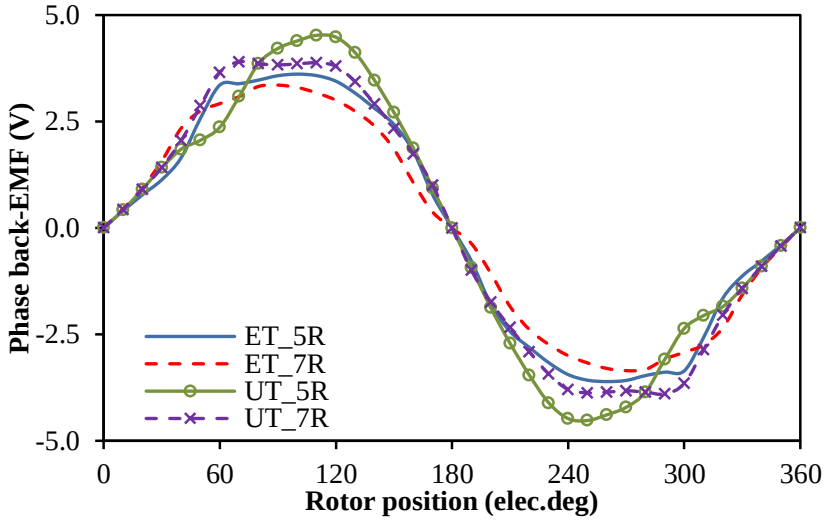

(a) Waveforms

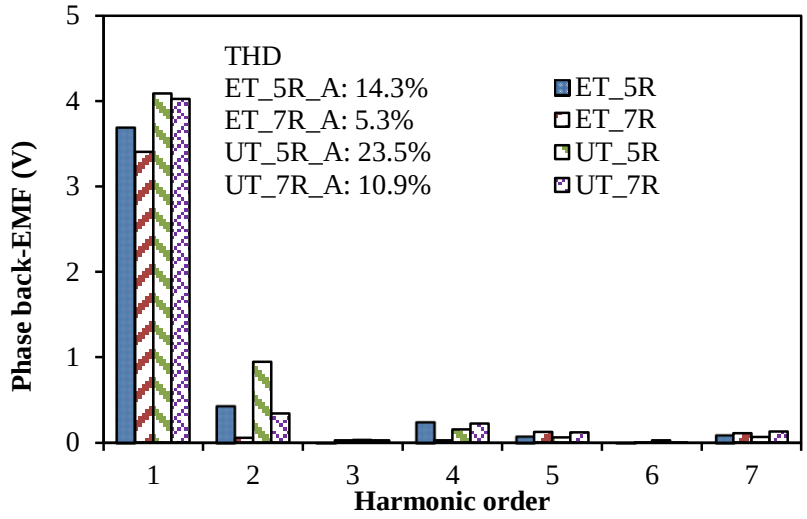

(b) Spectra

Fig. B.10. Open-circuit phase back-EMF, 400rpm.

B.4.3 DQ-Axis Inductances

Fig. B.11 shows the *dq*-axis inductances with different current angles for four machines at rated current (corresponding to rated 30W copper loss). Obviously, the *dq*-axis inductances of machines with UT are both smaller than those of machines with ET during the whole current angle range. Meanwhile, for both types of machines (ET and UT), 7-rotor pole CP-SM-BFPMM has larger *dq*-axis inductances than 5-rotor pole CP-SM-BFPMM. Moreover, since the *d*-axis inductance is close to *q*-axis inductance, the saliency ratio is low and the reluctance torque is negligible in both types of machines. Hence, CP-SM-BFPMMs with ET or UT are both suitable for vector control when I_d=0.

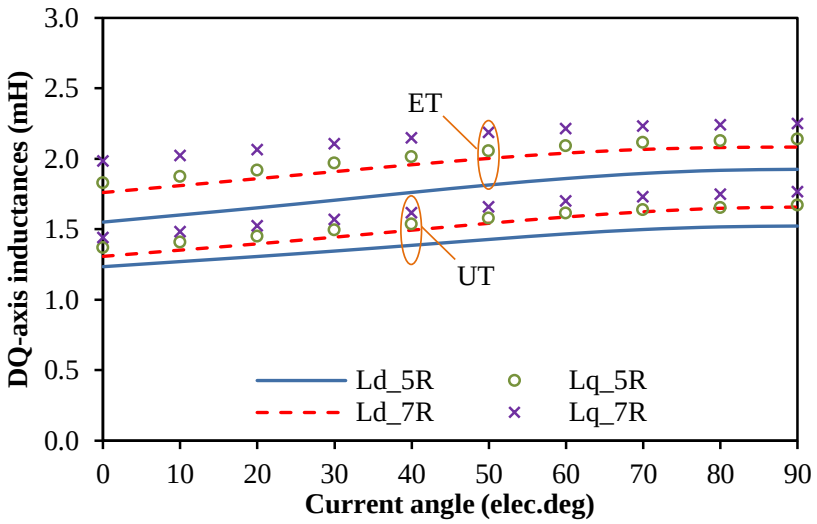

Fig. B.11. Variation of *dq*-axis inductances with current angle under the rated currents as given in Table B.1.

B.4.4 Cogging Torque

Fig. B.12 shows the cogging torque waveforms over one electric period for four machines. Obviously, machines with UT exhibit larger magnitude of cogging torque than those with ET. Meanwhile, for both types of machines, the numbers of cogging torque cycles over one electric period are the same whether the rotor pole number is 5 or 7.

Due to the similar operational principle, the equation (B.7) which is used to calculate the cycles of cogging torque over one electric period in SM-BFPMMs can also be extended to CP-SM-BFPMMs [SHI14b] [ZHU00].

$$N_c = \frac{N_{sscs}}{GCD(N_{sscs}, N_r)} \tag{B.7}$$

where N_c is the number of cogging torque cycles over one electric period, GCD means the greatest common divisor, N_{sscs} is the number of stator structure cyclic symmetry. By way of example, for the CP-SM-BFPMM under investigation, N_r=5, N_{sscs}=3, N_c=3. It can be evidenced by the FFT results shown in Fig. B.12(b) since the main harmonics of cogging torque are multiples of 3 which means that the combined cogging torque will exhibit 3 cycles over one electric period.

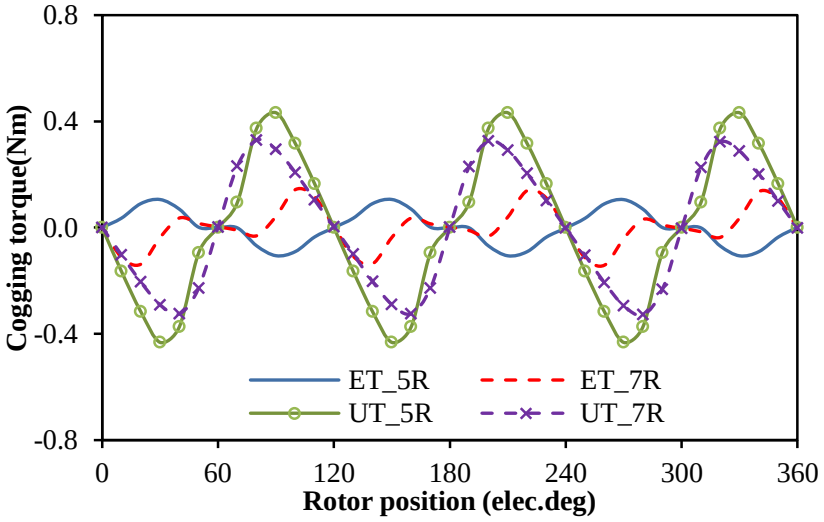

(a) Waveforms

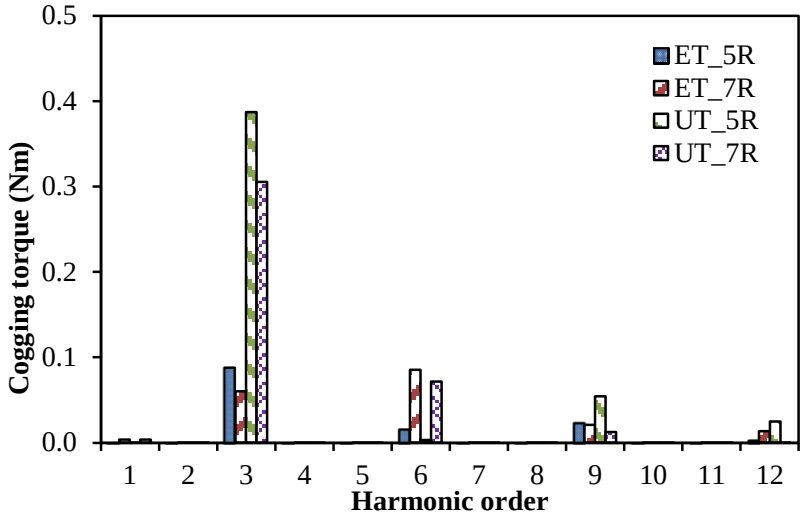

(b) Spectra

Fig. B.12. Open-circuit cogging torque.

B.4.5 Electromagnetic Torque Characteristics

Fig. B.13 shows the waveforms of average torque against current angle at rated current (corresponding to copper loss p_c=30W) for four machines. Obviously, the reluctance torques

can be negligible in four CP-SM-BFPMMs since the optimal current angles are all close to 0°. The results are consistent with the conclusion mentioned in section B.4.3.

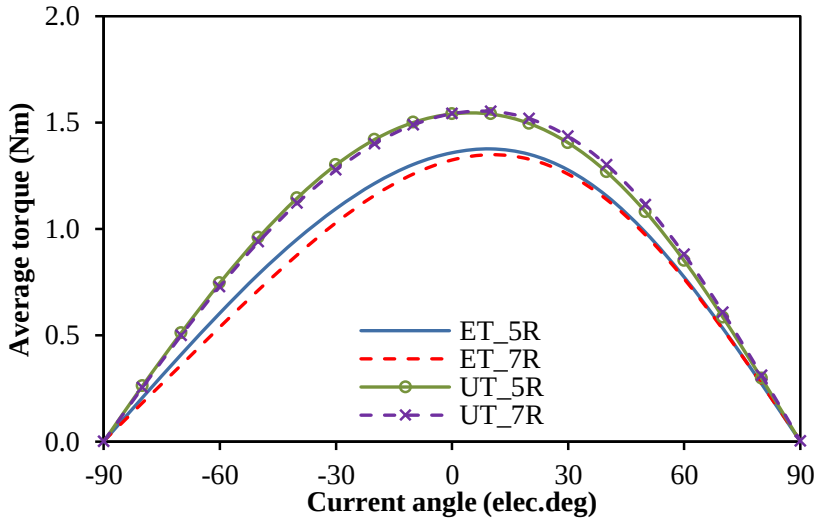

Fig. B.13. Variation of average torque with current angle under the rated currents as given in Table B.1 for all machines, p_c=30W.

The electromagnetic torques of CP-SM-BFPMMs with ET and UT are compared in Fig. B.14 under the rated current as given in Table B.1 (corresponding to p_c=30W) and I_d=0 control. Obviously, the cycle numbers of torque ripple over one electric period for four machines are all equal to three as shown in Fig. B.14(a). It can be explained as the combined influence of the cogging torque and the 2^{th} and 4^{th} harmonics of phase back-EFM. Meanwhile, CP-SM-BFPMMs with UT exhibit larger torque ripple than those with ET when the rotor pole numbers are same.

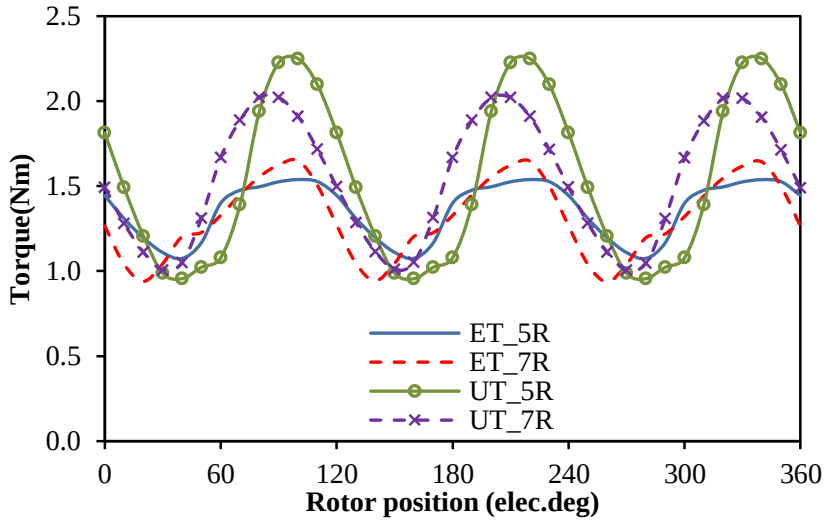

(a) Waveforms

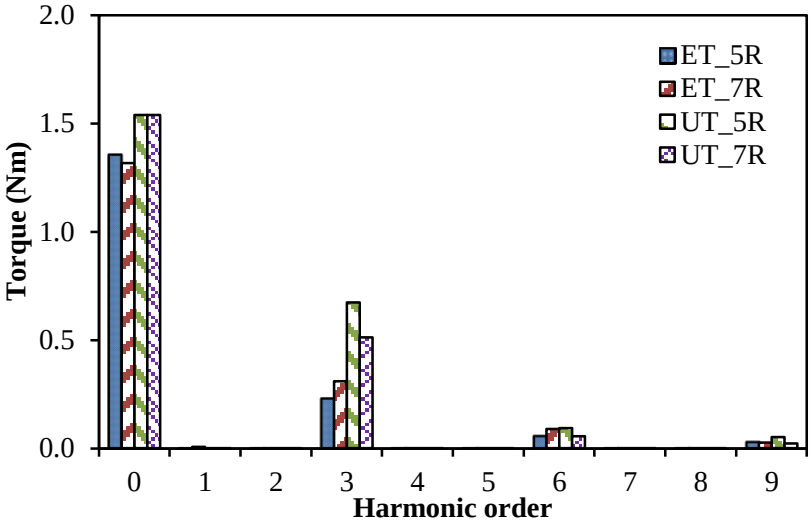

(b) Spectra

Fig. B.14. Variation of electromagnetic torque with rotor position under the rated currents as given in Table B.1 for all machines, p_c=30W.

As shown in Fig. B.14(b), the average torque of CP-SM-BFPMMs is enhanced by employing UT since the PM flux-linkage ψ_{PM} and q-axis current I_q (I_q=I_a under I_d=0 control) which have influence on average torque are both increased as analysed above. Compared with CP-SM-BFPMMs with ET under the rated 30W copper loss, the average torques of CP-SM-BFPMMs with UT are enhanced ~13.2% and 16.7% for 6/5 and 6/7 stator/rotor pole combinations respectively, as shown in Table B.2. Meanwhile, the 6/5 and 6/7 stator/rotor poles CP-SM-BFPMMs with UT have equal average torque as 1.54 Nm at rated 30W copper loss.

Further, the torque capability can also be reflected in the variation of average torque with copper loss as shown in Fig B.15. The vertical dashed and dotted line indicates the rated copper loss which is used to optimize the maximum average torque of four machines. According to (B.1), the average torque will be increased with the increase of copper loss since the corresponding phase current is increased together. However, the increasing rate will gradually decline for all machines due to the magnetic saturation. Overall, for the whole copper loss range as shown in Fig. B.15, CP-SM-BFPMMs with UT exhibit higher average torque than CP-SM-BFPMMs with ET for both 6/5 and 6/7 stator/rotor pole combinations. Meanwhile, for CP-SM-BFPMMs with UT, the average torque of 6/7 stator/rotor pole combination is larger at lower copper loss but lower at higher copper loss when compared with 6/5 stator/rotor pole combination.

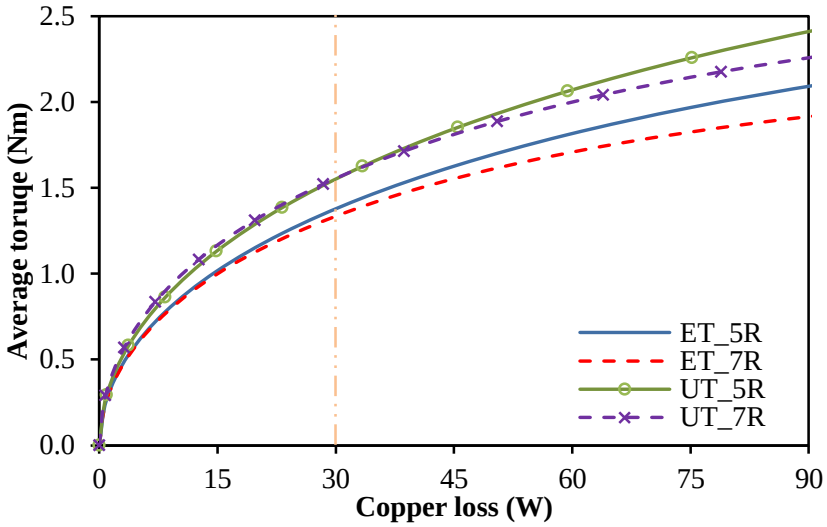

Fig. B.15. Variation of average torque with copper loss (I_d=0 control).

B.5 Summary

In this Appendix, novel CP-SM-BFPMMs which adopt doubly salient stator and rotor structure and concentrated windings are investigated. Unipolar PMs are housed on the surface of stator pole at interval pole number equal to one. The choice of rotor pole number is flexible and can be any integer except the phase number and its multiples.

For 6-stator pole CP-SM-BFPMMs, the phase flux-linkages of $N_r = N_s \pm 1$ are bipolar whilst those of $N_r = N_s \pm 2$ are unipolar. Meanwhile, CP-SM-BFPMMs with $N_r = N_s \pm 1$ exhibit larger torque capability than those of $N_r = N_s \pm 2$. By using unequal stator pole arc technique, the torque capability can be improved since the PM flux-linkage is enhanced and the slot area is enlarged. The results show that the average torque is increased by 13.2% and 16.7% for 6/5 and 6/7 stator/rotor pole combinations respectively at the rated 30W copper loss. Further, 6/5 and 6/7 stator/rotor poles CP-SM-BFPMMs with UT have approximately the same average torque, i.e. 1.54Nm at rated 30W copper loss. Moreover, the reluctance torque of CP-SM-BFPMM is also negligible since the saliency ratio is low.

APPENDIX C
NOVEL PARTITIONED STATOR BIASED FLUX PM MACHINES CONSIDERING CONSEQUENT POLE PM STATOR CONFIGURATION

In chapter 6, partitioned stator biased flux permanent magnet (PM) machines (BFPMMs) (PS-BFPMMs) considering both SPM and Spoke-IPM stator configurations are proposed and investigated. Since the PMs and armature windings are located in two separate inner and outer stators, the positions of two excitation sources are free and can be exchanged. Meanwhile, based on SPM stator, when half of PMs (either all S pole PMs or N pole PMs) are removed and replaced by laminations, novel consequent pole PM stator is proposed. Therefore, in this Appendix, the influence of the PMs and armature windings positions together with consequent pole PM stator configuration on electromagnetic performance of PS-BFPMMs with SPM stator will be analysed and compared.

C.1 Introduction

Biased flux permanent magnet (PM) machines (BFPMMs) were proposed in [WU14] by replacing the DC field windings with PMs in variable flux reluctance machines (VFRMs) [KAS11] [LIU12b] [LIU13] [FUK12]. Correspondingly, the features of VFRMs are inherited in the BFPMMs, and can be concluded as: (1) doubly salient structure, (2) non-overlapping armature windings, (3) flexible choice of rotor pole number (any integers except phase number and its multiples), (4) symmetrical bipolar phase flux-linkage and back-EMF under special stator and rotor pole combinations. Reference [WU14] also shows that the torque density of BFPMM is enhanced by ~ 70% under the same copper loss and the same machine size when compared with VFRMs.

However, similar to other machines with PMs and armature windings are both located in the stator, the possibility of further enhancing the torque performance of BFPMMs are still limited by the conflictions among the PMs, coppers and stator irons due to the limited stator space. Then, partitioned stator configuration proposed in [EVA15] provides one more efficient solution to solve this confliction since the inner space is fully utilized. By introducing this configuration, novel partitioned stator BFPMMs (PS-BFPMMs) which separate the PMs and armature windings into inner and outer stators respectively are

proposed in [WU15]. Reference [WU15] shows that PS-BFPMMs exhibit ~207% higher torque density than the original single stator BFPMMs under the same rated copper loss due to the enlarged slot area (for copper) and volume of PM under the same machine size. Furthermore, since the PMs are located in the separate stator, various PM stator configurations can be employed in PS-BFPMMs, such as Spoke-IPM stator and SPM stator.

Since the PMs and armature windings are located in two separate inner and outer stators, the positions of two excitation sources are free and can be exchanged. Meanwhile, based on SPM stator, when half of PMs (either all S pole PMs or N pole PMs) are removed and replaced by laminations, novel consequent pole PM stator is proposed. Therefore, in this Appendix, the influence of the PMs and armature windings positions together with consequent pole PM stator configuration on electromagnetic performance of PS-BFPMMs with SPM stator will be analysed and compared. Firstly, the machine topologies and operational principle are illustrated. Then, the electromagnetic performance in terms of phase flux-linkages and back-EMFs, cogging torque and torque capability will be analysed and compared under the same machine size and the same rated copper loss.

C.2 Machine Topologies

The basic model of original PS-BFPMM with SPM stator is shown in Fig. C.1(a). It can be seen that the PMs and armature windings of PS-BFPMM are located in separated inner and outer stators respectively. Therefore, the positions of two excitation sources are free and can be exchanged as shown in Fig. C.1(b), which PMs and armature windings are located in outer and inner stator respectively. Further, when half of PMs (either all S Pole PMs or N pole PMs) in the original SPM stator are removed and replaced by laminations, novel consequent pole PM (CPM) stator is proposed, as shown in Fig. C.1(c) and (d). It should be noted that the PM fluxes which circulated from two adjacent PMs with same polarity formed a virtual PM with opposite polarity in the sandwiched iron pole. Therefore, the equivalent pair number of PMs in the consequent pole PM stator can be considered as the same as the original SPM stator. Overall, according to Fig. C.1, the flux paths shown in the PS-BFPMMs with consequent pole PM stator are consistent with those in the original PS-BFPMMs whenever PMs located in the inner stator or outer stator, which imply that the operation principle of PS-BFPMMs with consequent pole PM stator is similar to that of PS-BFPMMs with the original SPM stator.

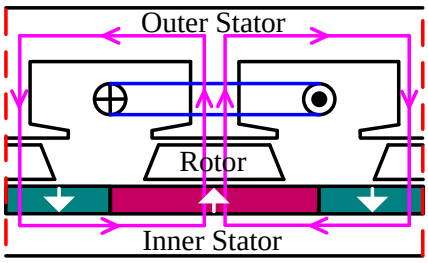

(a) PS-BFPMM-I

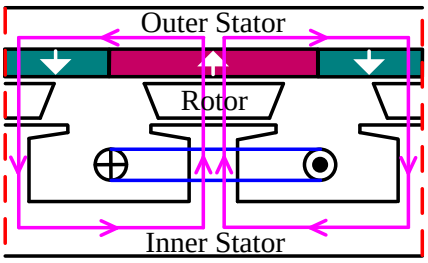

(b) PS-BFPMM-II

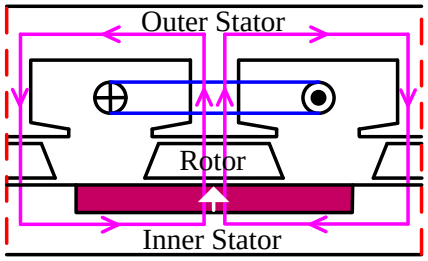

(c) PS-CP-BFPMM-I

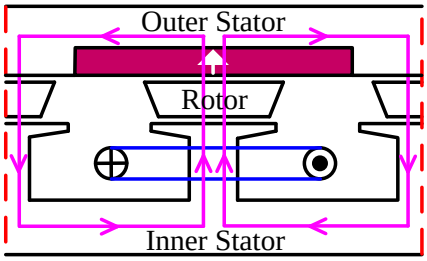

(d) PS-CP-BFPMM-II

Fig. C.1. Schematics of PS-BFPMMs and PS-CP-BFPMMs.

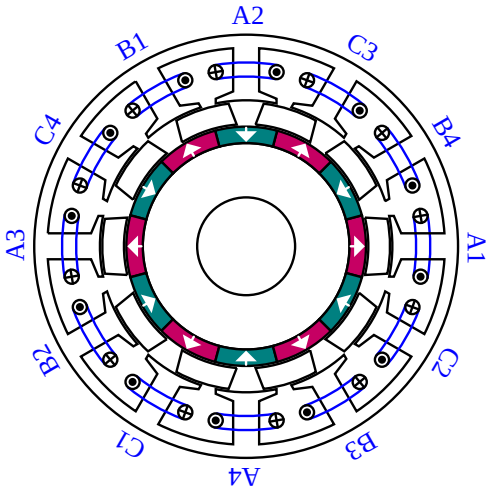

(a) PS-BFPMM-I

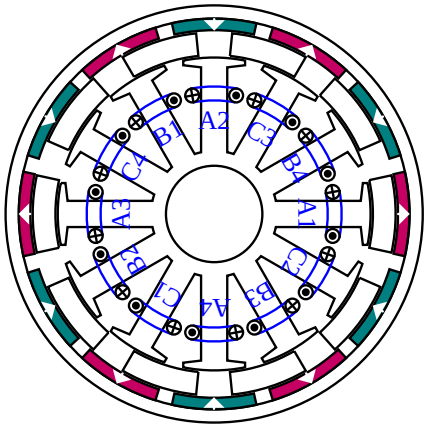

(b) PS-BFPMM-II

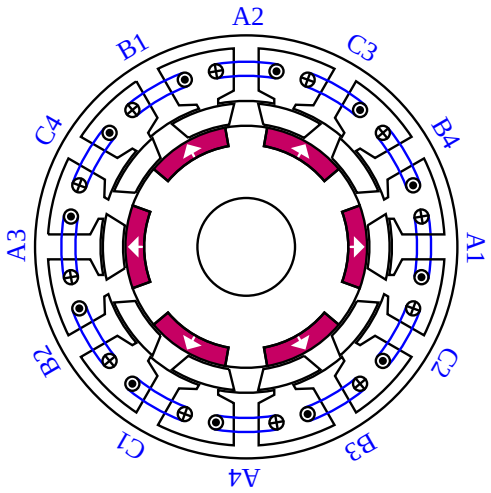

(c) PS-CP-BFPMM-I

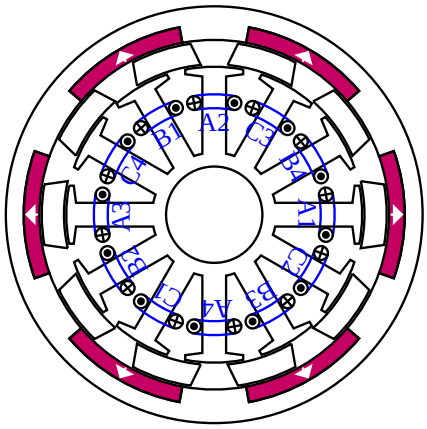

(d) PS-CP-BFPMM-II

Fig. C.2. Machine topologies of PS-BFPMMs with original SPM stator and CPM stator.

Table C.1 Parameters of prototype machines for PS-BFPMMs

Parameters	**PS-BFPMMs**			
Topology	PS-SPM-I	PS-SPM-II	PS-CPM-I	PS-CPM-II
Number of phases	3			
Turns per phase	72			
Rated speed (rpm)	400			
Rated copper loss (W)	30			
Packing factor	0.5			
Air-gap length L_{ag} (mm)	0.5			
Active axial length L_{aa} (mm)	25			
Outer stator outer radius R_{oso} (mm)	45			
Inner stator inner radius R_{isi} (mm)	10.4			
Outer stator (OS) pole number, N_{os}	12	12	12	12
Inner stator (IS) pole number, N_{is}	12	12	6	6
Rotor pole number, N_r	10	10	10	10
OS inner radius R_{osi} (mm)	31.05	39.65	31.05	37.75
IS outer radius R_{iso} (mm)	25.45	33.75	25.75	31.95
OS tooth body pole arc θ_{ostb} (°)	10.2	(IST) 9.6	9.8	(IST) 9.2
OS tooth tip pole arc θ_{ostt} (°)	6.9	(IST) 6.6	6.2	(IST) 6.7
OS tooth tip thickness (Opening) T_{ostto} (mm)	1	(IST) 1	1	(IST) 1
OS tooth tip thickness (Body) T_{osttb} (mm)	2	(IST) 2	2.3	(IST) 2
Rotor outer pole arc θ_{rop} (°)	22.0	24.6	26.4	20.2
Rotor inner pole arc θ_{rip} (°)	27.2	24.6	20.0	25.8
Rotor radial thickness T_{rr} (mm)	4.6	4.9	4.3	4.8
OS yoke thickness T_{osy} (mm)	2.8	(ISY) 3.2	2.7	(ISY)3.0
Rated AC current (A_{rms})	17.10	15.94	17.30	15.25
PM inner pole arc θ_{PM} (°)	30	25	40	39
Minimum PM thickness T_{PM} (mm)	3.5	2.5	4	3.4
Magnetic remanence (T)	1.2			
Relative PM permeability	1.05			

Fig. C.2 shows the topologies of 12-inner/12-outer stator/10 rotor pole (12I/12O/10R) PS-BFPMMs with the original SPM stator and consequent pole PM stator considering two different PM positions. All machines are globally optimized with maximum average torque under the same machine size and the same copper loss. The main geometric parameters are listed in Table C.1. In addition, to simplify the comparison in the following sections, the machines corresponding to the Fig. C.2(a), (b), (c) and (d) can be designated as PS-SPM-I, PS-SPM-II, PS-CPM-I and PS-CPM-II respectively.

C.3 Performance Comparison of PS-BFPMMs with SPM and CPM Stators

C.3.1 Open-Circuit Field Distribution

The open-circuit equipotential and flux density field distributions of PS-BFPMMs with SPM and CPM stators at aligned position are shown in Fig. C.3. Obviously, the flux loop of each coil belong to the same phase is completely independent in PS-BFPMMs with CPM stator (PS-CPM-I and PS-CPM-II), which is consistent with the PS-BFPMMs with SPM stator (PS-SPM-I and PS-SPM-II). Meanwhile, short flux path, which could result in lower MMF drop in the stator and thinner thickness of stator yoke, is also observed in both types of PS-BFPMMs. Moreover, for both PS-BFPMMs with SPM and CPM stators, heavier saturation will be observed when PMs located in the outer stator rather than in the inner stator, especially in the regions of stator yoke which close to the gaps between the adjacent PMs (contact surface between PM and iron pole for CPM stator). It also can be reflected by the waveforms of open-circuit air-gap flux density distributions at aligned position as shown in Fig. C.4. Since the PS-BFPMMs have two layers of air-gap, the corresponding waveforms shown in Fig. C.4 are based on the layers which close to the stator wound with armature windings. It can be seen that PS-BFPMMs with SPM and CPM stators have similar waveform of air-gap flux density. Furthermore, when PMs located in the outer stator, higher peaks of air-gap flux densities are observed in both PS-BFPMMs with SPM and CPM stators.

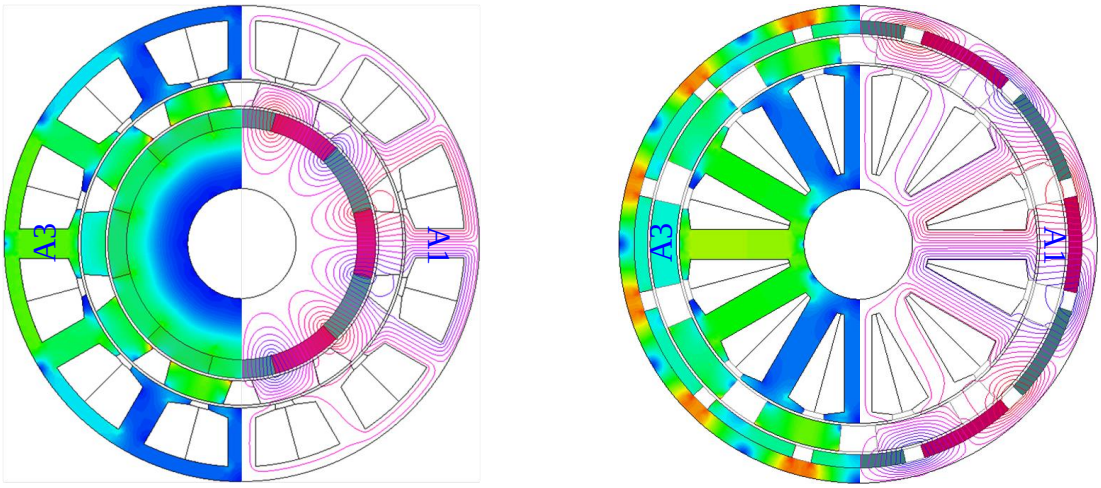

(a) PS-SPM-I (b) PS-SPM-II

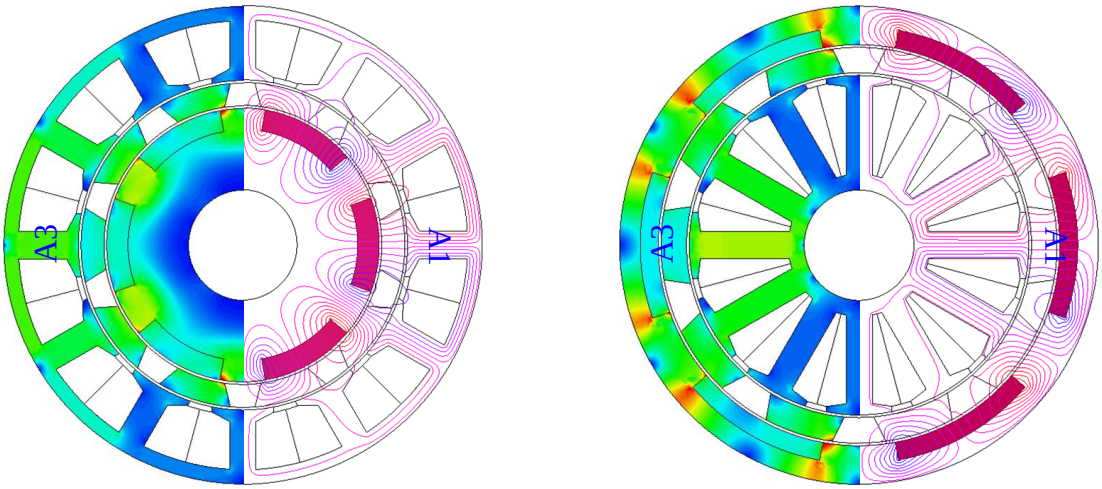

(c) PS-CPM-I (d) PS-CPM-II

Fig. C.3. Open-circuit equipotential and flux density field distributions at aligned position.

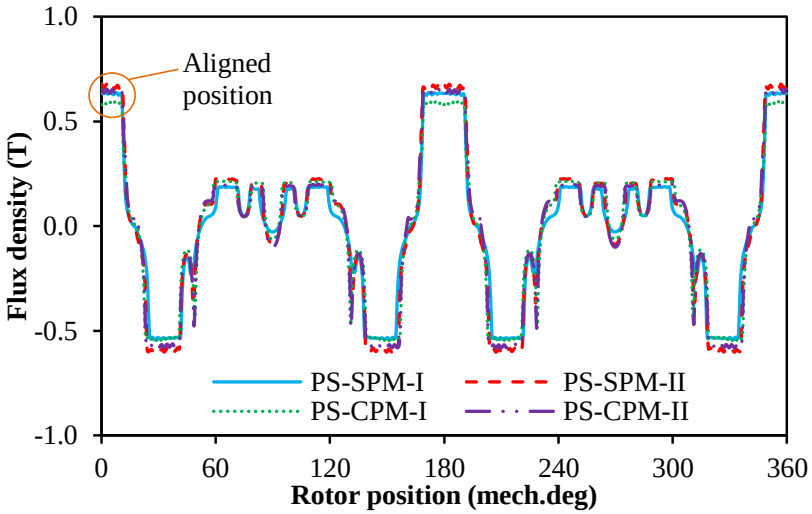

Fig. C.4. Open-circuit air-gap flux density at aligned position.

C.3.2 Flux-Linkage and Back-EMF Waveforms

The open-circuit phase flux-linkages of PS-BFPMMs with SPM and CPM stators are shown in Fig. C.5. Obviously, bipolar phase flux-linkages waveforms are observed in all machines. Further, they are symmetrical in PS-BFPMMs with SPM stator while asymmetric in PS-BFPMMs with CPM stator. It is due to fact that the even harmonics which cause the biased value and asymmetric waveform in each coil are incompletely cancelled in the phase winding of PS-BFPMMs with CPM stator since the magnitude of each order harmonic in coil A1 (A3) and coil A2 (A3) are unequal, which can be evidenced by the FFT results shown in Fig. C.5(b). As shown in Table C.2, the magnitudes of fundamental phase flux-linkage for PS-SPM-I, PS-SPM-II, PS-CPM-I and PS-CPM-II are 8.46, 9.96, 8.60 and 9.36mWb respectively. For both PS-BFPMMs with SPM and CPM stators, higher fundamental phase flux-linkage can be obtained when PMs located in the outer stator rather than PMs located in the inner stator, which are enhanced by 17.7% and 8.8% respectively. Compared with BFPMMs with SPM stator, the fundamental phase flux-linkage of PS-BFPMMs with CPM stators is enhanced by 1.7% when PMs located in the inner stator but declined by 6.0% when PMs located in the outer stator.

Due to the same reason for phase flux-linkage, the phase back-EMF waveform is symmetrical in PS-BFPMMs with SPM stator but asymmetric in PS-BFPMMs with CPM stator, as shown in Fig. C. 6. According to Table C.2, the magnitudes of fundamental phase back-EMF for PS-SPM-I, PS-SPM-II, PS-CPM-I and PS-CPM-II at rated speed (400rpm) are 3.54, 4.17, 3.60 and 3.92V respectively. Since four machines have the same rotor pole number, the rated electrical frequencies are the same and equal to 66.7 Hz. Therefore, the increase rate (or decrease rate) of fundamental phase back-EMFs caused by employing CPM stator and changing the PM position are consistent with those in fundamental phase flux-linkages.

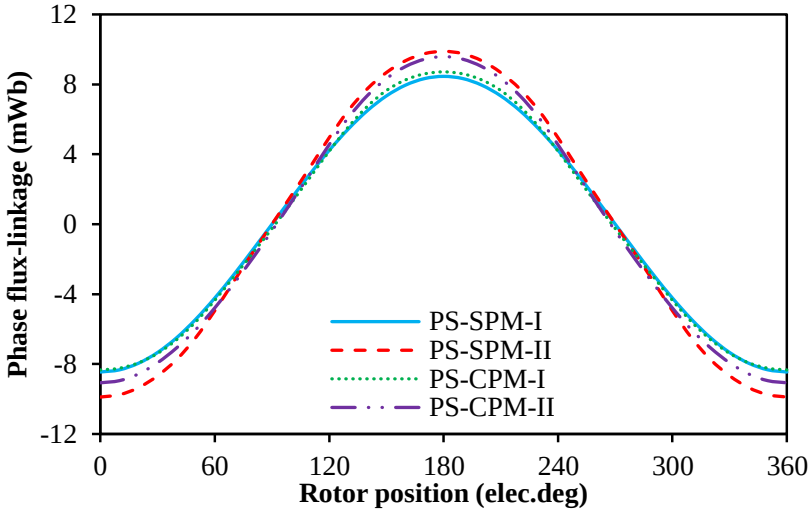

(a) Waveforms

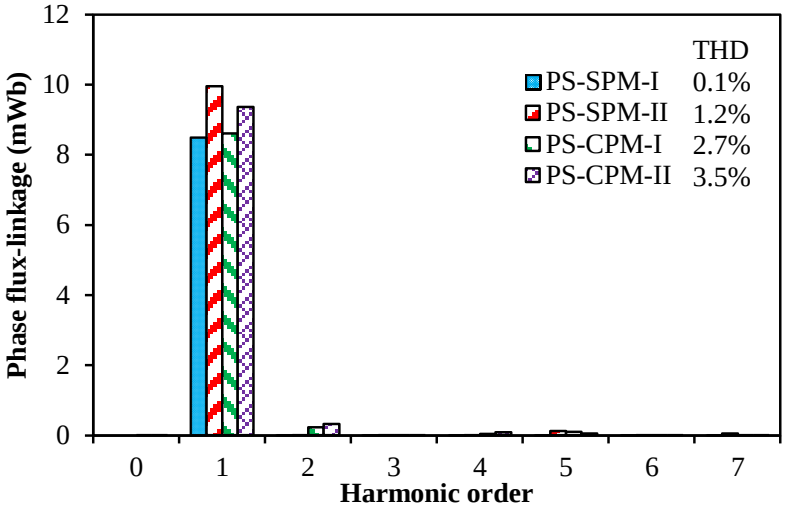

(b) Spectra

Fig. C.5. Open-circuit phase flux-linkages.

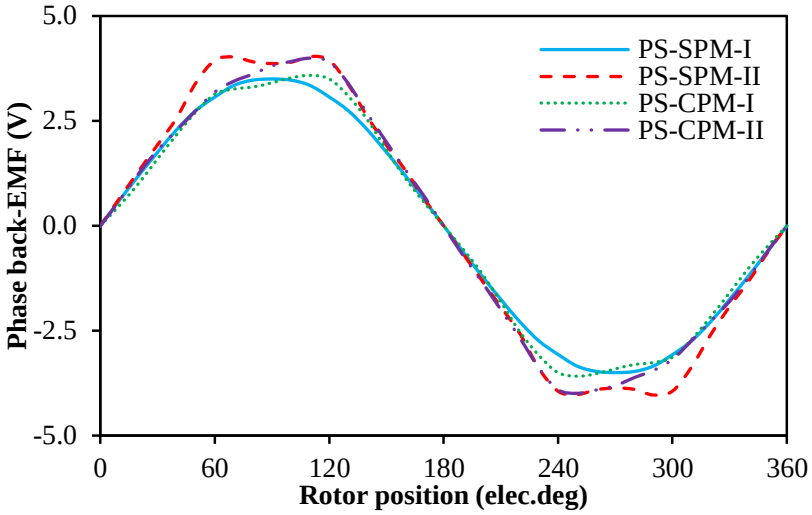

(a) Waveforms

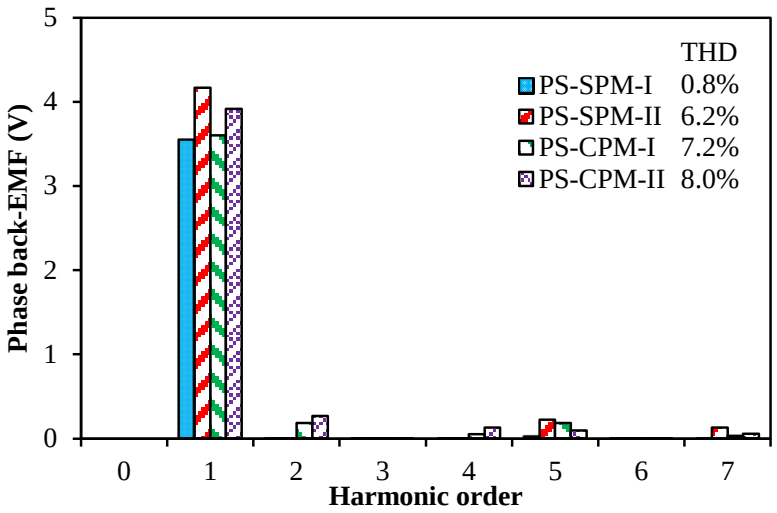

(b) Spectra

Fig. C.6. Open-circuit phase back-EMF, 400rpm.

C.3.3 Cogging Torque

The cogging torque waveforms of PS-BFPMMs with SPM and CPM stators are shown in Fig. C.7. Obviously, whenever PMs located in the inner or outer stators, PS-BFPMMs with CPM stator exhibit larger magnitudes of cogging torque than PS-BFPMMs with SPM stator. Meanwhile, for both BFPMMs with SPM and CPM stators, larger magnitudes of cogging torque is observed in machines with PMs located in outer stator when compared with those with PMs located in the inner stator. Overall, among these four machines, PS-CPM-II has the largest cogging torque.

Since the operational principle of PS-BFPMM with CPM stator is similar to that of PS-BFPMM with SPM stator, equation (6.3) which is used to calculate the cycle number of cogging torque over one electric period in PS-BFPMMs can be extended to PS-SFPMMs with CPM stator. Considering the influence of stator structure cyclic symmetry, equation (6.3) can be changed as (C.1).

$$N_C = \frac{MIN(N_{is},\ N_{os})}{GCD(\ MIN(N_{is},\ N_{os})\ ,\ N_r)} \tag{C.1}$$

where, N_c is the cycle number of cogging torque over one electrical period, N_{is} and N_{os} are the number of inner and outer stator pole, N_r is number of rotor pole.

According to (C.1), the cycle numbers of cogging torque for PS-SPM-I, PS-SPM-II, PS-CPM-I and PS-CPM-II are 6, 6, 3 and 3 respectively. They are evidenced by the waveforms and FFT results shown in Fig. C.7.

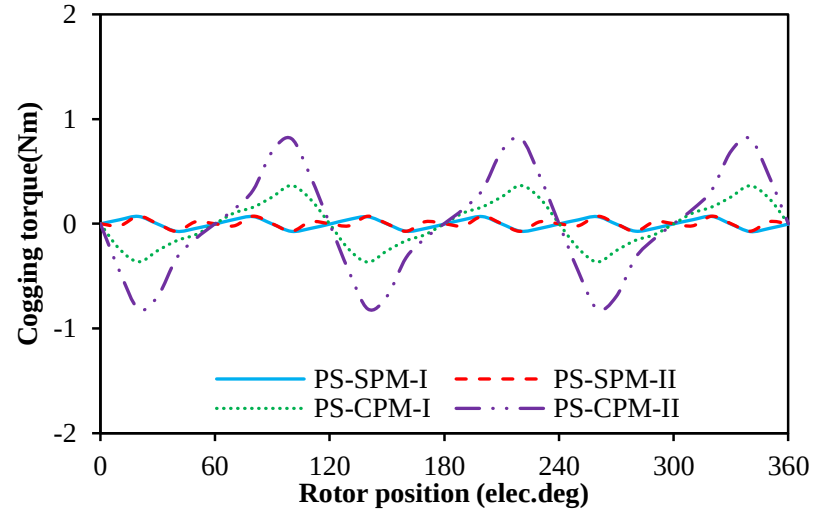

(a) Waveforms

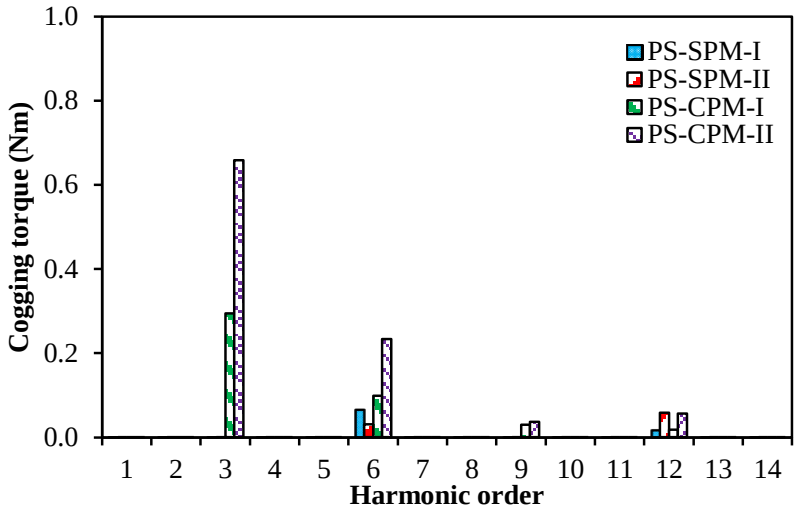

(b) Spectra

Fig. C.7. Open-circuit cogging torque.

C.3.3 Electromagnetic Torque Characteristics

Fig. C.8 shows the waveforms of average torque against current angle at rated currents (corresponding to p_c=30W) for all machines. Obviously, whenever PM located in inner or outer stators, the optimal current angles for both PS-BFPMMs with SPM and CPM stators are close to 0°, which means that the reluctance torque is negligible in all machines.

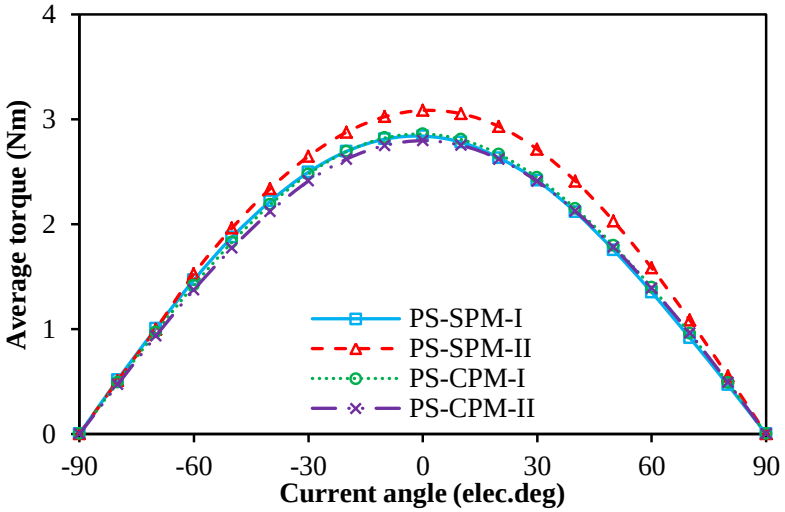

Fig. C.8. Variation of average torque with current angle under the rated currents as given in Table C.1 for all machines, p_c=30W.

Fig. C.9 shows the waveforms of torque against with rotor position at rated currents (p_c=30W) and I_d=0 control. Due to the combined influences of cogging torque and back-EMF harmonics (5^{th} and 7^{th} for SPM stator, 2^{th} and 4^{th} for CPM stator), PS-BFPMMs with SPM stator have 6 torque ripples over one electric period while PS-BFPMMs with CPM have 3 torque ripples. Moreover, the torque ripples of PS-SPM-I, PS-SPM-II, PS-CPM-I and PS-CPM-II are 14.0%, 17.9%, 35.3% and 75.9% respectively. Obviously, whenever PMs located in the inner or outer stator, PS-BFPMM with CPM stator exhibits larger torque ripple than PS-BFPMM with SPM stator. Further, for both SPM and CPM stators, FS-BFPMMs with PMs located in the outer stator have the larger torque ripple than those with PM located in the inner stators. Overall, PS-CPM-II exhibits the largest torque ripple among these four machines.

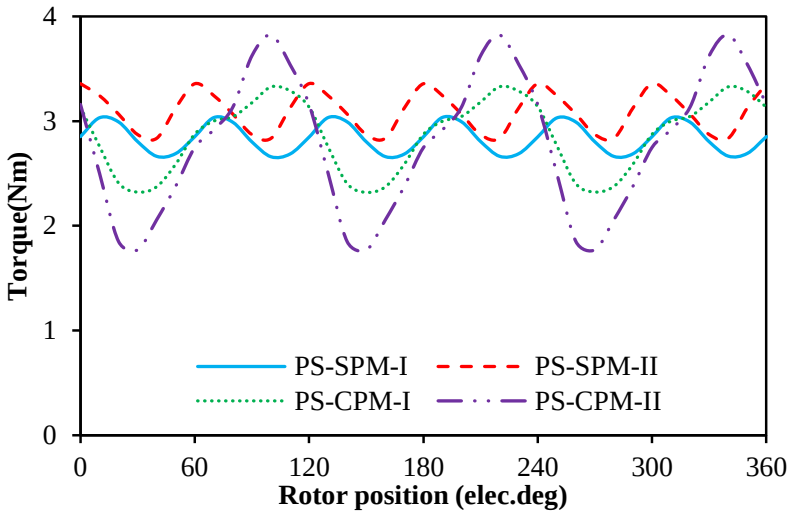

(a) Waveforms

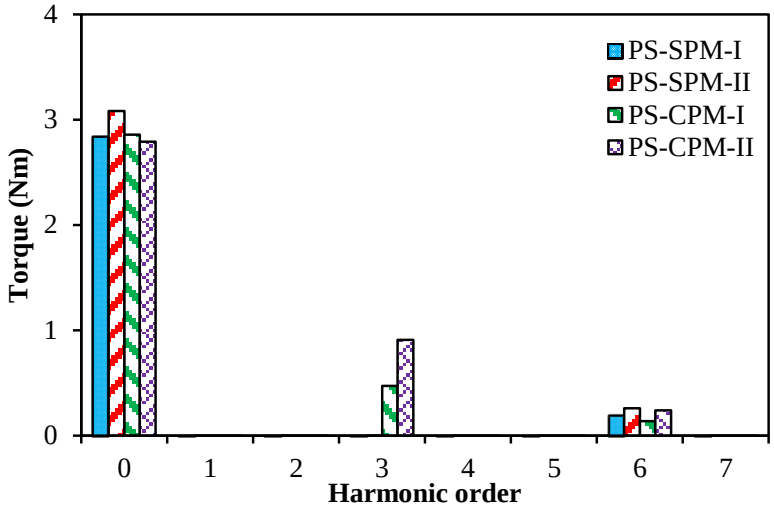

(b) Spectra

Fig. C.9. Variation of electromagnetic torque with rotor position under the rated currents as given in Table C.1 for all machines, p_c=30W.

According to the Table C. 2, the average torque for PS-SPM-I, PS-SPM-II, PS-CPM-I and PS-CPM-II are 2.84, 3.08, 2.86 and 2.79Nm respectively. It can be seen that PS-BFPMM with CPM stator exhibits similar average torque to PS-BFPMM with SPM stator when PMs located in the inner stator while 9.4% lower when PMs located in the outer stator. Further, for PS-BFPMM with SPM stator, the average torque is enhanced by 8.5% when PMs located in the outer stator rather than PMs located in the inner stator. However, the average torque is reduced by 2.5% in PS-BFPMM with CPM stator. Overall, among these four machines, PS-SPM-II has the largest average torque.

The torque density and torque to PM volume of all machine at rated currents (p_c=30W) and I_d=0 control are compared in Fig. C.10. According to Table C.2, the torque densities for PS-SPM-I, PS-SPM-II, PS-CPM-I and PS-CPM-II are 17.85, 19.38, 17.97 and 17.56 kN/m^2 respectively. Since four machines have the same machine size, the increase rate (or decrease rate) of torque density caused by employing CPM stator and changing the PM position are consistent with those in average torque. Moreover, for the ratio of torque to PM volume (PM utilization efficiency), it is increased by ~5.8% when PMs located in the outer stator for PS-BFPMMs with SPM stator but decreased 29.0% for PS-BFPMMs with CPM stator. Overall, among these four machines, PS-CPM-I exhibits the highest PM utilization efficiency.

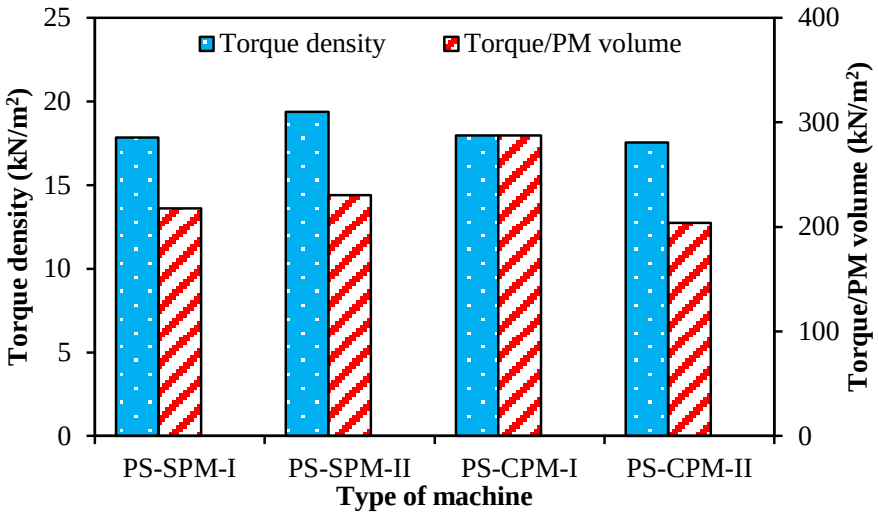

Fig. C.10. Torque density and torque to PM volume ratio, p_c=30W, I_d=0 control.

Fig. C. 11 compares the torque performance of four machines under different copper loss. The vertical dashed and dotted line shows the rated copper loss used for global optimization. Similar to the original PS-SPM-I, the increase rate of average torque for PS-SPM-I, PS-CPM-I and PS-CPM-II will be declined with the rising of copper loss (current) due to the aggravated magnetic saturation. As shown in Fig. C.11, PS-SPM-II exhibits the largest average torque among those four machines under the same copper loss over the whole copper range. Further, the torque capabilities of PS-CPM-I and PS-CPM-II are similar to that of PS-SPM-I over the whole copper loss range.

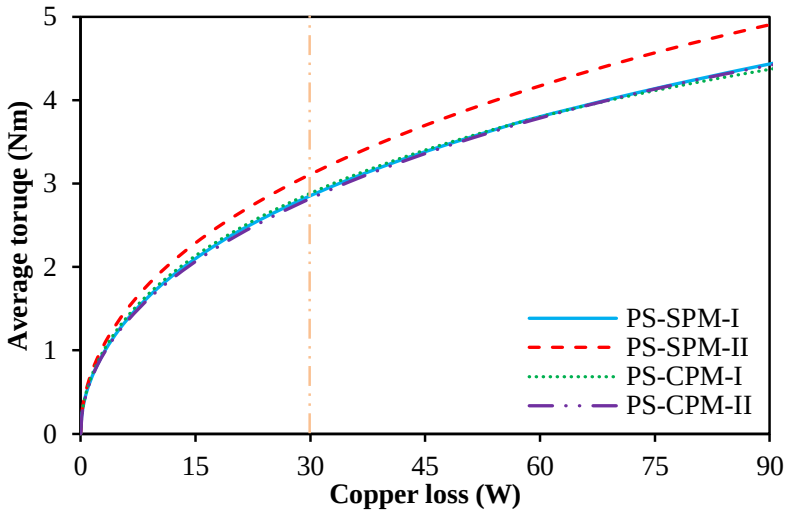

Fig. C.11. Variation of average torque with copper loss, I_d=0 control.

Table C.2 Main electromagnetic performance

Parameter	PS-SPM-I	PS-SPM-II	PS-CPM-I	PS-CPM-II
Fund. flux-linkage (mWb)	8.46	9.96	8.60	9.36
Fund. back-EMF (V)	3.54	4.17	3.60	3.92
Rated electric frequency (Hz)	66.7	66.7	66.7	66.7
Cogging torque (Nm)	0.070	0.072	0.365	0.847
Average torque (Nm)	2.84	3.08	2.86	2.79
Torque ripple (%)	14.0	17.9	35.3	75.9
Torque density (kN/m^2)	17.85	19.38	17.97	17.56
Torque/PM volume (kN/m^2)	217.8	230.4	287.3	203.9

C.4 Summary

In this Appendix, the influence of the PMs and armature windings positions together with consequent pole PM stator configuration on electromagnetic performance of 12-stator/10-rotor pole PS-BFPMMs with SPM stator is investigated.

When PMs located in the inner stator, PS-BFPMM with CPM stator has similar torque density and higher PM utilization efficiency but larger cogging torque and torque ripple when compared with PS-BFPMM with SPM stator. By changing the PM position from inner stator to outer stator, the torque density and PM utilization efficiency can be enhanced by 8.5% and 5.8% respectively in PS-BFPMM with SPM stator but reduced by 2.5% and 29% in PS-BFPMM with CPM stator. Overall, among these four machines, PS-SPM-II has the largest torque density while PS-CPM-I has the highest PM utilization efficiency.

APPENDIX D
DRAWINGS AND PARAMETERS OF LAMINATIONS FOR ALL PROTOTYES

The drawings and parameter of laminations for the prototype machines investigated in this thesis are given as follows. It should be noted that the axial lengths for all of prototype machines are 25mm. Further, the Lamination steel grade is M330-35A and the PM grade is N35SH.

D.1 Optimized Variable Flux Reluctance Machines

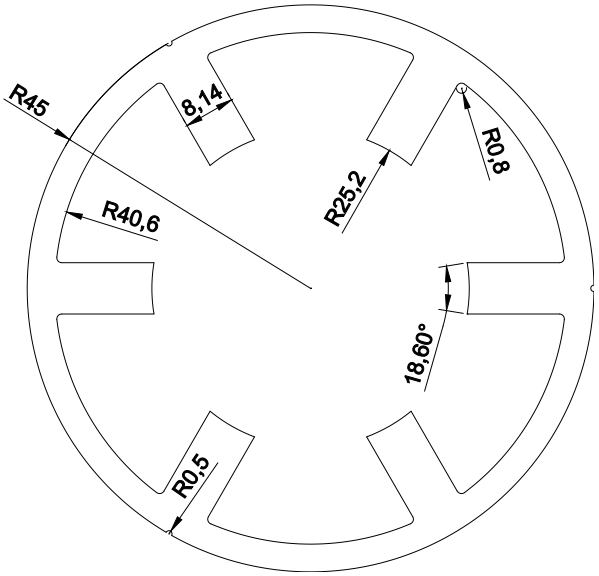

(a) 6-pole stator

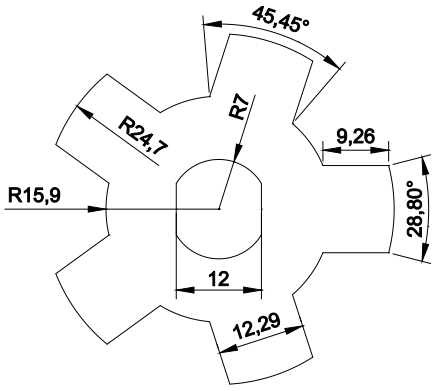

(b) 5-pole rotor

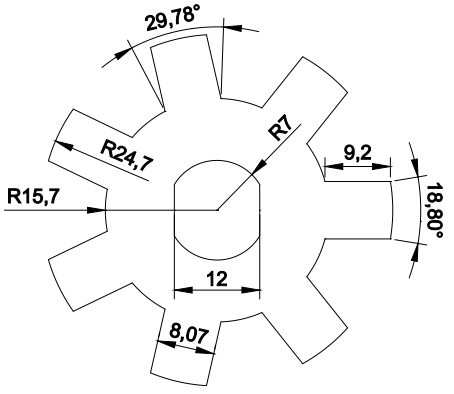

(c) 7-pole rotor

Fig. D.1. Optimized VFRMs with 6-pole stator.

D.2 Multi-Tooth Variable Flux Reluctance Machines

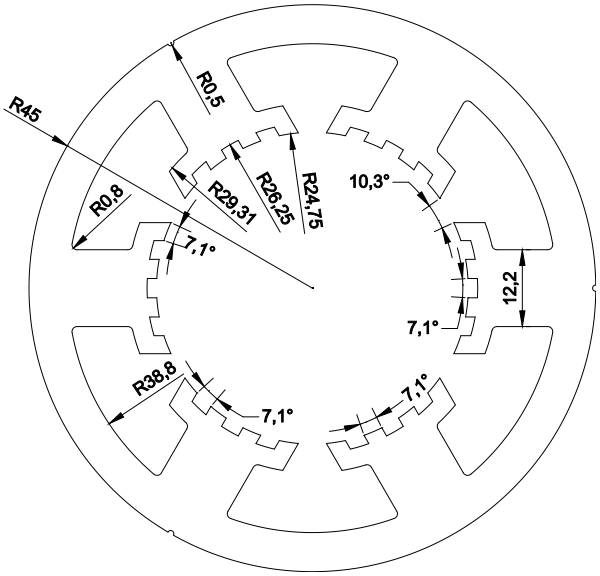

(a) 6-pole stator of 4-tooth VFRM

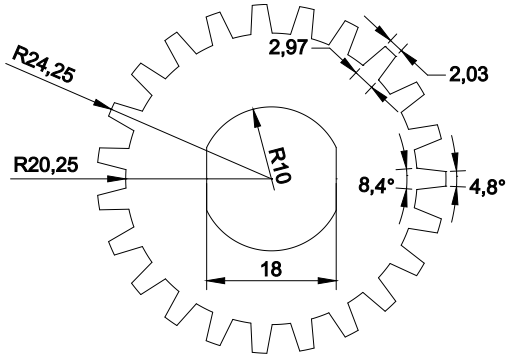

(b) 23-pole rotor

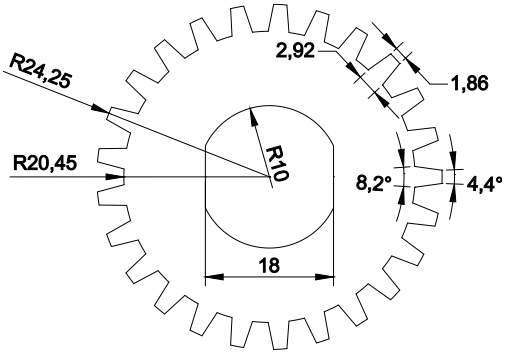

(c) 25-pole rotor

Fig. D.2. 4-tooth VFRMs with 6-pole stator.

D.3 Surface Mounted-Biased Flux PM Machines

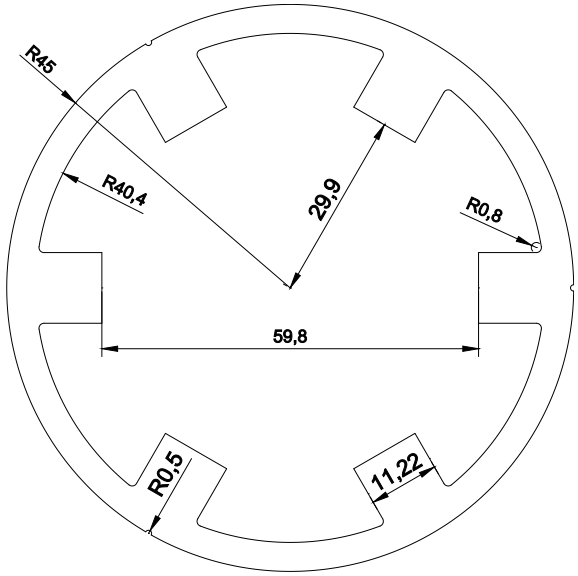

(a) 6-pole stator

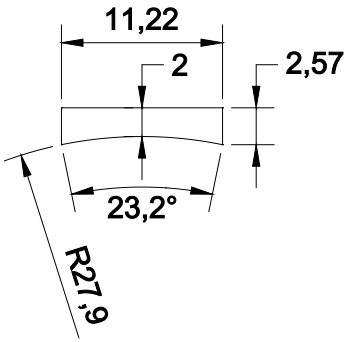

(b) Shape of PM

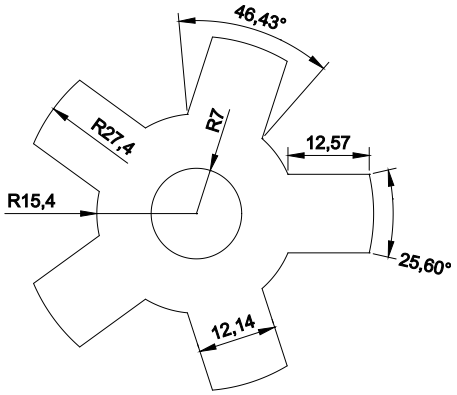

(c) 5-pole rotor

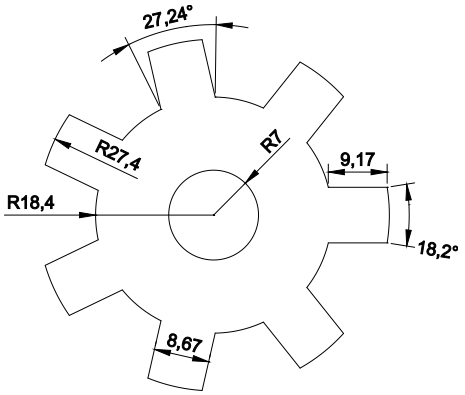

(d) 7-pole rotor

Fig. D.3. SM-BFPMMs with 6-pole stator.

D.4 Stator Yoke Mounted-Biased Flux PM Machines

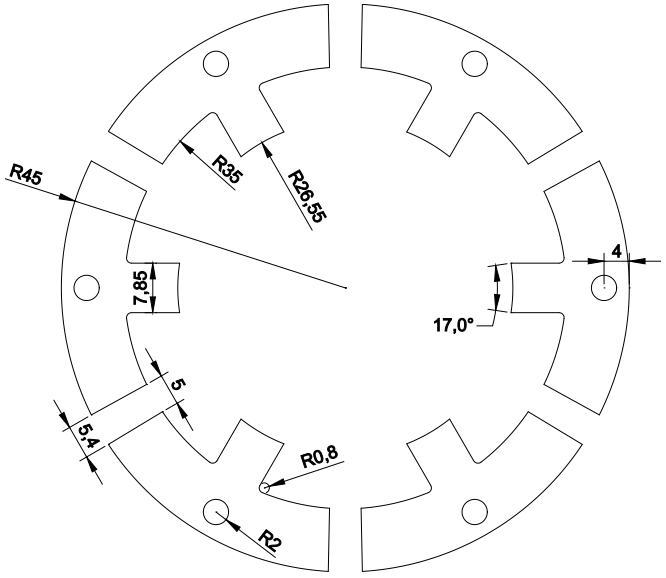

(a) 6-pole stator

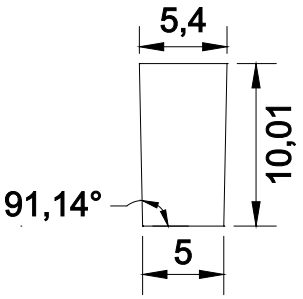

(b) Shape of PM

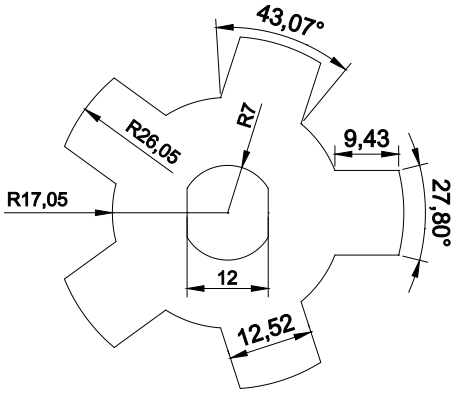

(c) 5-pole rotor

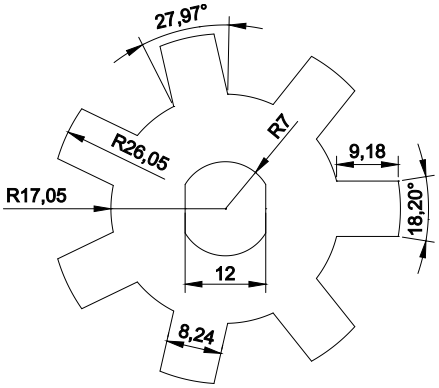

(d) 7-pole rotor

Fig. D.4. SYM-BFPMMs with 6-pole stator.

D.5 Stator Yoke Mounted-Biased Flux PM Machines with Inner Type Flux Focusing Configuration

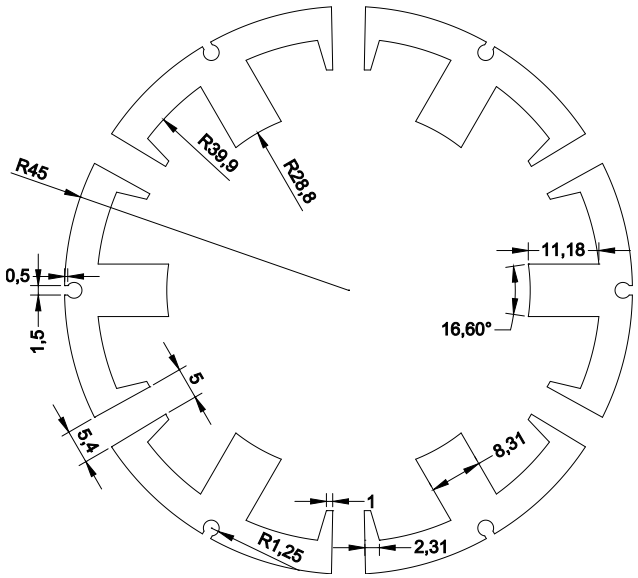

(a) 6-pole stator

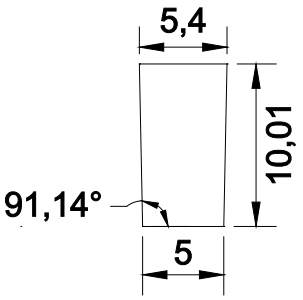

(b) Shape of PM

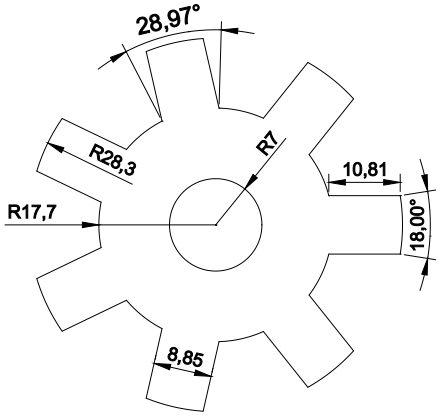

(b) 7-pole Rotor

Fig. D.5. SYM-BFPMMs with 6-pole stator.

D.6 Partitioned Stator PM Synchronous Machines

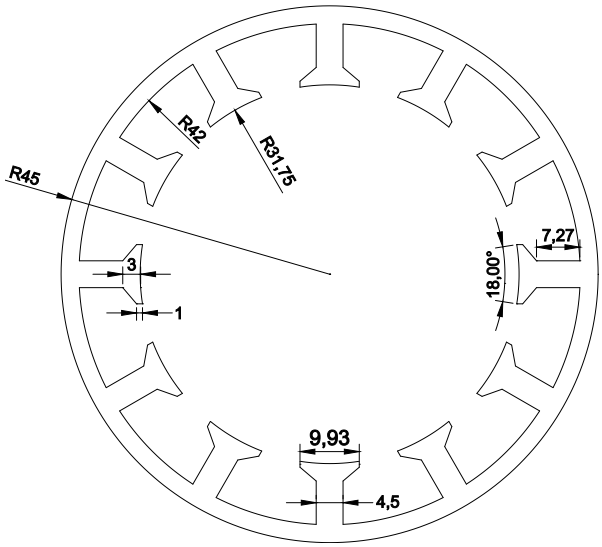

(a) 12-pole outer stator

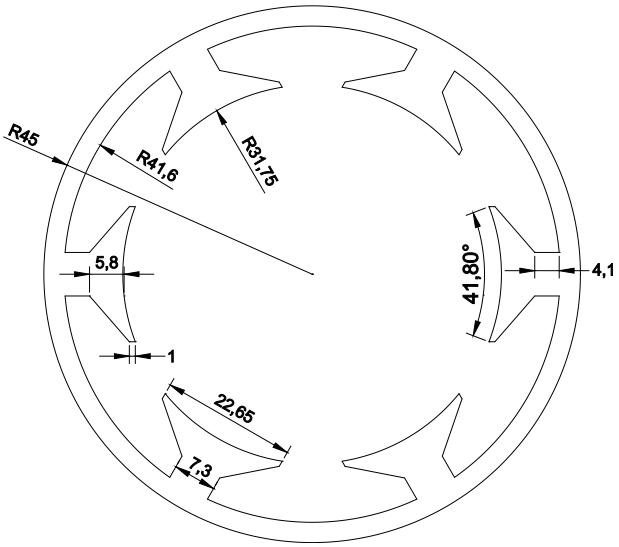

(b) 6-pole outer stator

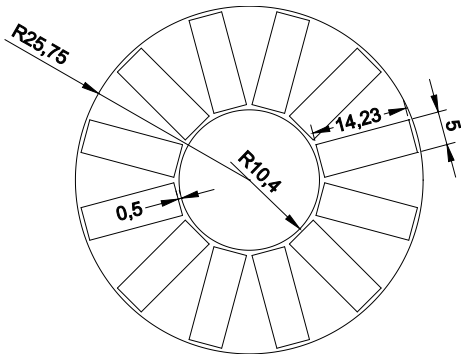

(c) 12-pole outer stator (Spoke-IPM)

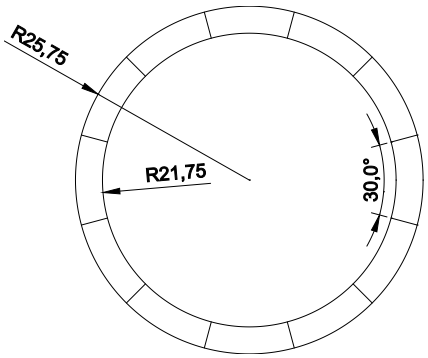

(d) 12-pole outer stator (SPM)

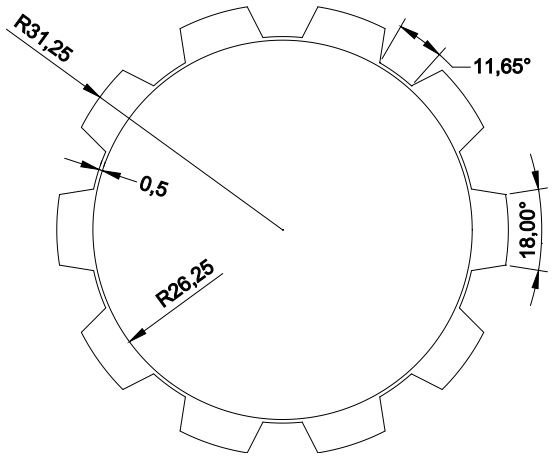

(e) 10-pole rotor

Fig. D.6. Partitioned stator PM synchronous machines, including PS-BFPMMs and PS-SFPMMs.

D.7 Lamination Steel and Permanent Magnet

For laminations, the data and curve of B-H are shown in Table D. 1 and Fig. D.7 respectively, and the parameters for iron loss calculation are given in Table D. 2. Further, the property of permanent magnet is given in Table D. 3.

Table D.1 Data for B-H curve of lamination steel [CHE09]

H(A/m)	B(T)	H(A/m)	B(T)	H(A/m)	B(T)
0	0	508.9904	1.357687	6006.141	1.691965
40	0.432	600	1.385	6963.257	1.716482
60	0.613	723.5518	1.411185	8000	1.74
77.831543	0.728297	883.5636	1.435731	9997.106	1.777656
100	0.83	1037.345	1.454386	12130.73	1.811553
127.2625	0.921704	1290.866	1.47881	14255.09	1.84208
153.7043	0.995235	1569.527	1.50213	17061.12	1.878364
200	1.095	1991.086	1.53152	20000	1.912
244.33569	1.164175	2425.496	1.556268	24660.76	1.955666
300	1.23	2914.226	1.580957	30974.31	2.00358
347.10001	1.273279	3492.226	1.607179	36703.28	2.03723
400	1.31	4000	1.628	40000	2.053
448.56351	1.333929	4882.181	1.658935	133445	2.5

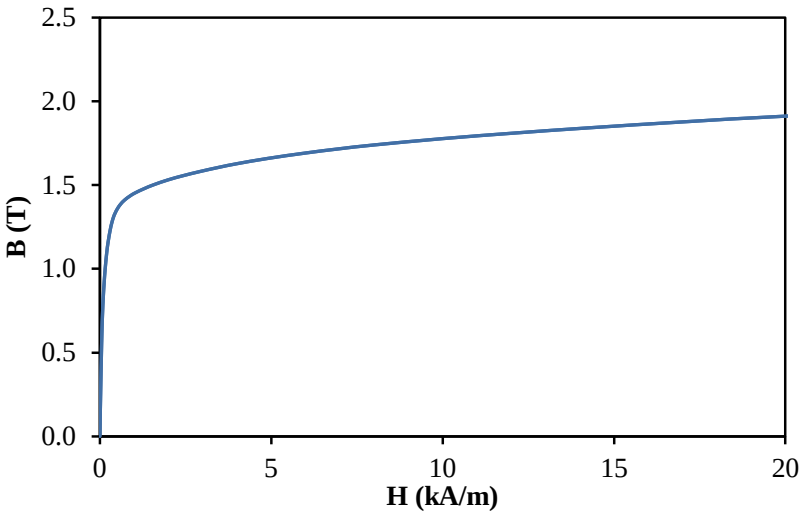

Fig. D.7. B-H curve of lamination steel.

Table D.2 Parameters for iron loss calculation [CHE09]

k_h	0.0179	D_{iron}	0.35 mm
a_h	0.841	m_v	7650 kg/m^3
b_h	1.023	ρ_{iron}	4.5×10^{-7} Ωm
k_c	2.61	k_e	0.002

Table D.3 Property of permanent magnet [CHE09]

Grade	Remanence	Coercive force (kA/m)	Working Temp	Density (G/cm^3)	Electrical conductivity (Ωm^{-1})
N35SH	1.17-1.25	≥860	≤150	≥7.54	6.67×10^5

APPENDIX E

PUBLICATIONS RESULTED FROM PHD STUDY

Journal papers published or in press:

[J1] J. T. Shi, Z. Q. Zhu, D. Wu and X. Liu, "Comparative Study of Synchronous Machines Having Permanent Magnets in Stator," *ELSEVIER Trans. Electric Power Systems Research*, vol. 133, Doi: 10.1016/j.epsr.2015.12.018, pp. 304-312, Apr. 2016.

[J2] J. T. Shi and Z. Q. Zhu, "Analysis of novel multi-tooth variable flux reluctance machines with different stator and rotor pole combinations," *IEEE Trans. Magn.*, vol. 51, no. 5, May. 2015."

[J3] J. T. Shi, X. Liu, D. Wu and Z. Q. Zhu, "Influence of stator and rotor pole arcs on electromagnetic torque of variable flux reluctance machines," *IEEE Trans. Magn.*, vol.50, no.11, Nov. 2014.

[J4] D. Wu, J. T. Shi, Z. Q. Zhu and X. Liu, "Electromagnetic performance of novel synchronous machines with permanent magnets in stator yoke," *IEEE Trans. Magn.*, vol. 50, no. 9, Sep. 2014

[J5] Z. Z. Wu, Z. Q. Zhu and J. T. Shi, "Novel doubly salient permanent magnet machines with partitioned stator and iron pieces rotor," *IEEE Trans. Magn.*, vol. 51, no. 5, May. 2015.

[J6]] Z. Q. Zhu, H. Hua, D. Wu, J. T. Shi and Z. Z. Wu, "Comparative study of partitioned stator machines with different PM excitation stators," *IEEE Trans. Ind. Appl.*, vol. 52, no. 1, pp. 199-208, Jan/Feb. 2016.

[J7] C. C. Awah, Z. Q. Zhu, Z. Z. Wu, H. L. Zhan, J. T. Shi, D. Wu and X. Ge, "Comparison of partitioned stator switched flux permanent magnet machines having single- or double-layer windings," *IEEE Trans. Magn.*, vol. 52, no. 1, Jan. 2016.

Journal papers submitted:

[J8] J. T. Shi and Z. Q. Zhu, "Novel variable flux permanent magnet machines with partitioned stator," submitted to *IEEE Trans on Magnetics*.

[J9] J. T. Shi and Z. Q. Zhu, "Influence of outer stator pole number on electromagnetic performance of partitioned stator biased flux permanent magnet machines," submitted to *IEEE Trans on Magnetics*.

[J10] J. T. Shi and Z. Q. Zhu, "Influence of inner stator and rotor pole number combinations on electromagnetic performance of partitioned stator switched flux permanent magnet machines," submitted to *IEEE Trans on Energy Conversion*.

[J11] J. T. Shi, Z. Q. Zhu, D. Wu and X. Liu, "Comparative study of novel biased flux permanent magnet machines with doubly salient permanent magnet machines considering with influence of flux focusing," *ELSEVIER Trans. Electric Power Systems Research*, Under review.

Conference papers:

[C1] J. T. Shi, Z. Q. Zhu, D. Wu and X. Liu, "Comparative study of novel biased flux permanent magnet machine with doubly salient permanent magnet machine", in *Int. Conf. on Electrical Machines and Systems (ICEMS)*, pp. 415-420, China, Oct. 2014.

[C2] J. T. Shi, Z. Q. Zhu, D. Wu and X. Liu, "Comparative study of novel synchronous machines having permanent magnets in stator poles," in *Int. Conf. on Electrical Machines (ICEM)*, pp.429-435, Germany, Sep.2014.

[C3] J. T. Shi, Z. Q. Zhu, D. Wu and X. Liu, "Influence of flux focusing on electromagnetic torque of novel biased flux PM machines," in *Int. Conf. on Electrical Machines (ICEM)*, pp.523-529, Germany, Sep.2014.

[C4] J. T. Shi, X. Liu, D. Wu and Z. Q. Zhu, "Influence of stator and rotor pole arcs on electromagnetic torque of variable flux reluctance machines," *Int. Conf. on IEEE International Magnetics Conference (Intermag)*, BP-15, Germany, May, 2014.

[C5]] Z. Q. Zhu, H. Hua, D. Wu, J. T. Shi and Z. Z. Wu, "Comparison of partitioned stator machines with different PM excitation stator topologies," in *Int. Conf. on Ecological Vehicles and Renewable Energies (EVER)*, Monaco, Mar/Apr, 2015.

[C6] C. Awah, Z. Q. Zhu, Z. Z. Wu, J. T. Shi, D. Wu and X. Ge, "Comparison of Partitioned Stator Switched Flux Permanent Magnet Machines having Single- or Double-layer Windings," in *Int. Conf. on Ecological Vehicles and Renewable Energies (EVER)*, Monaco, Mar/Apr, 2015.